THE EFFECT OF SELF-GENERATED MAGNETIC FIELDS ON RAYLEIGYH-TAYLOR INSTABILITY IN INERTIALLY CONFINED FUSION TARGETS

Muhammad Mumtaz Raja

Submitted for the degree of Doctor of Philosophy

University of York

Department of Physics

May 1992

Acknowledgements

Over three years the degree course at the University of York has proved to be an excellent and most rewarding intellectual exposure which has culminated in this dissertation. I am indeed grateful to Ministry of Education (Pakistan) and The British Council but for whose generous support, this work could not have materialised.

At the University, I owe the greatest intellectual debt to Professor Geoff J. Pert whose constant guidance and encouragement inspired me to pursue an extensive survey of the research techniques of the classics on the subject. At a time when I was groping in darkness and indecision it was he who encouraged me to keep going. He enlightened me to pick up the threads and tie them into a coherent whole. The final dissertation is a result of a series of critical discussions with Prof. Pert in the process of drafting, re-drafting and tightening of the manuscript. His generous and friendly supervision will remain a pleasant memory for me. Responsibility for omission, if any, is however, mine.

I would like to acknowledge useful discussions with Prof. Malcolm Haines and Dr. Mike Henshaw.

Within our group at York I have had help and support from Dr. Bill Crum, Dr. Phil Holden, Dr. Malcolm Lightbody and Sean Healy. Special thanks for all things computational go to Iain Bruce and to Alan Gebbie for the production of a number of diagrams.

I cannot forget my friend Dr. Muhammad Salahuddin for providing a continous moral support throughout my stay at University of York. I extend my thanks to my parents and many friends for their support during this period

Finally, I owe a special word of thanks to my wife Alam Ara and loving son Muhammad Masood Raja for providing me all possible facilities and tolerating my long study hours.

ABSTRACT

The role of Rayleigh-Taylor instability is a question of crucial importance to the reliability of Inertial Confinement Fusion scheme. Initially as the shell accelerates inwards, defects in target manufacture or non-uniform laser irradiation can generate Rayleigh-Taylor instability on the ablation surface. In previous simulations this effect has been studied either with 2D or 3D simulation codes excluding the effect of self-generated magnetic fields in laser plasma interactions.

The 2D hydrodynamic computer code MAGT2LD is used to simulate laser heated foils in order to study the growth of the instability at the ablation surface. Simulations are performed applying the perturbations through the material density and the laser intensity for different targets and changing the perturbation wavelength both including and excluding the self-generated magnetic field.

A substantial difference is observed in instability growth for field on simulations over no field when the instability is seeded through the laser intensity. The largest fields of the order of 1.8 MG are consistently observed in most of the simulations. The inclusion of the full set of thermo-electric diffusion coefficients of Braginskii has not shown any difference in instability growth over those with more simply determined thermally self-generated magnetic fields. High frequency modes are also observed on the density contour maps in the early stages of the instability growth which generated due to the non-linear field generation. These high frequency modes give rise a phase shift of the high density nodes towards the target axis.

Contents

Chapter 1

INTRODUCTION

1.1 MOTIVATION

The object of this thesis is to investigate, by means of computer simulations, the Rayleigh-Taylor instability arising in a laser produced plasma. In particular our interests and observations are to find the effect of self-generated magnetic fields on the Rayleigh-Taylor instability growth in the corona region of Inertially Confined Fusion pellets.

As conventional energy resources, such as gas, oil and coal are depleted, scientists are endeavouring to produce energy, one of the basic human needs, by different means. Energy can also be produced by other means, such as hydro-electric and solar systems. It is now well-known that substantial energy can be released in nuclear reactions in two physical processes, known as fission and fusion.

In nuclear fission a heavy nucleus, such as Uranium, disintegrates in to smaller fission fragments with the release of some energy. This technique has been in operation for more than three decades to produce commercial energy. However there are important drawbacks in this scheme. Uranium resources are limited and it is costly and dangerous to extract it from mines. A second problem is the reprocessing of fuel which is expensive as well as dangerous due to the amount of radioactive waste generated. Finally the waste nuclear fission products are also radioactive and these must be stored safely for many centuries.

The alternative approach, known as nuclear fusion, in which light nuclei, such as the isotopes of Hydrogen, are fused together to release more energy than was

used to confine them. In a typical DT reaction, Deuterium ($_1D^2$) and Tritium nuclei ($_1T^3$) combine together to produce a Helium nucleus and a neutron. This reaction releases $17 \cdot 6$ Mev of energy, which is carried away as the kinetic energy of the reaction products. The reaction is

$$_1D^2 +_1 T^3 \longrightarrow_2 He^4(3 \cdot 5Mev) + n^1(14 \cdot 1Mev) \tag{1.1}$$

Deuterium is a naturally occurring isotope of Hydrogen. Tritium is not available in nature but can be produced by indirect means such as the D-D and n-Li reactions. Although Tritium is radioactive its half life is far less than the nuclear fission fragments. The fusion process is still is uncontrolled. Great efforts are being made to design fusion reactors, such as JET at Culham Laboratory, all over the world.

Two different techniques, Magnetic Confinement and Inertial Confinement fusion, are being used to achieve this goal. The basic technique used is to heat the nuclei of the fuel to such an extent that they overcome the Coulomb potential barrier. In Magnetic Confinement fusion a hot low density plasma is confined for an appreciable time by applying magnetic field. The approach is limited by the $n\tau - product$ known as the Lawson criterion, and requires a low density plasma confined for an appreciable time (a few seconds) [1].

In the other approach a small DT fuel pellet is irradiated by an intense laser beam. This ionises the outer surface of the target which explodes outwards very rapidly and because of rocket action (Newton's third law) implodes the bulk of fuel inwards compressing the fuel to high densities. The compressed core ignites producing $\alpha - particles$ which propagate outwards through the rest of the fuel, heating it to the required temperature, called 'bootstrap' heating.

Two different approaches, as shown in figure $1 \cdot 1$, are applied to achieve this rapid heating and fuel compression. In the direct approach the laser is directly incident on the target surface which drives the process [25], whereas in the indirect or 'hohlraum' approach the high energy laser system is incident on a shell of high atomic mass emitting X-rays, absorbed by the target forming an ablating plasma expanding outwards [2]. Both of these techniques have advantages and disadvantages over one another.

To attain high compression the target fuel must be compressed nearly isentrop-

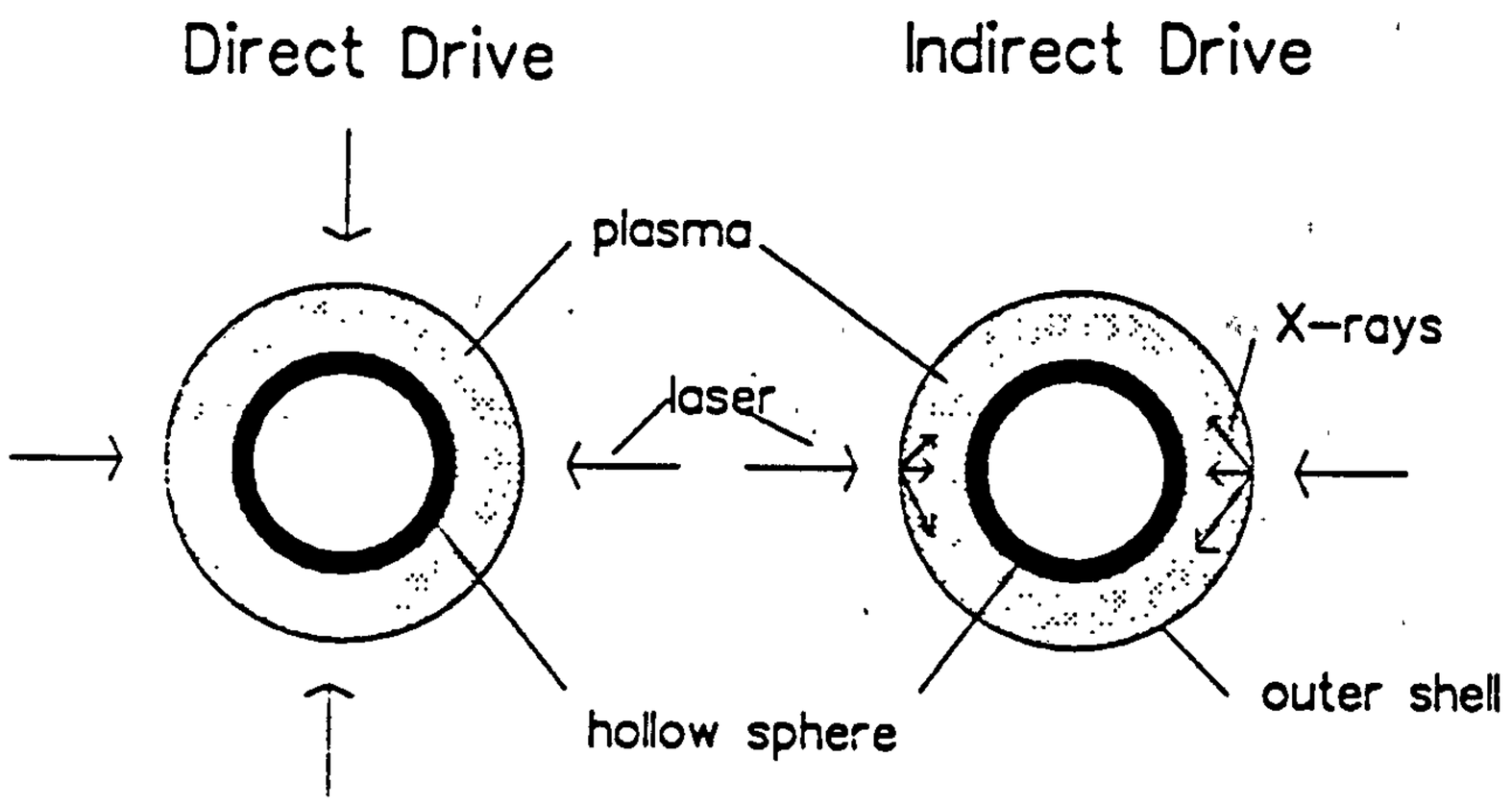

Figure 1.1: A schematic diagram of the two approaches to laser fusion

ically. It is, therefore, necessary to avoid pre-heating of the target. This requires the shock waves to converge at the core of the pellet simultaneously. In addition the core temperature must not be raised beyond desired limit before convergence.

A fluid system in which the density and pressure gradients are opposite i.e. ($\nabla p.\nabla \rho < 0$) in a gravity field, is susceptible to the well-known Rayleigh-Taylor instability. This instability causes the low density fluid, which is pushing a high density fluid, to interchange its position with it. This type of instability may occur at two distinct times in the laser driven targets at different positions, and may eventually preclude the attainment of uniform implosion. In first stage this instability may occur in the ablation zone, where a hot low density plasma is accelerating the more dense fluid. Any non-uniformity in the ablation pressure may initiate the Rayleigh-Taylor instability, leading to an unsymmetric collapse. The second time is at the end of implosion, when the pressure in the collapsed fuel becomes large enough to decelerate the collapsing shell. Here it is the inner surface of the shell which is susceptible to the instability.

Magnetic fields are generated in laser produced plasma by thermally driven, circulating electric currents and for the laser target geometry are directed az-

imuthally about the axis of the incoming laser radiation [80]. The fields have been predicted to reach the level of the order of few megagauss. These self-generated magnetic fields may also affect the growth of Rayleigh-Taylor instability. We have employed the 2D quasi-Lagrangian rezoning code, MAGT2LD, to study the generation of these and their effect on the instability growth. The simulation results are compared with the fields both included and excluded. We have also performed simulations including the thermoelectric diffusion term of Braginskii in the code MAGT2LD and its effect on the instability. It was not possible during our studies to compare our results with other existing experimental and computational work, as we were not able to find any existing work on this specific problem.

1.2 PLAN OF THESIS

The layout of the dissertation is as follows. The instability in general terms as well as Inertial Confinement Fusion is reviewed in Chapter 2. Chapter 3 is based on analytical and computational studies of Rayleigh-Taylor instability in an incompressible system. The physics of the code MAGT2LD is discussed in Chapter 4. In Chapter 5 the code is used to perform numerical tests on different targets by varying the target size and the perturbation wavelength to find the effect of self-generated magnetic field on the instability by applying perturbation through mass. The same effect is studied in Chapter 6 when the perturbation is applied through laser intensity. In Chapter 7 some further simulation results are presented by changing the target geometry, inverting the applied perturbation, lowering the input power and applying the full self-generated field equation. The important points in the study are summarised in Chapter 8.

Chapter 2

REVIEW OF RAYLEIGH-TAYLOR INSTABILITY

In this Chapter, Rayleigh-Taylor instability is reviewed in general terms as well as its appearence in Inertial Confinement Fusion. In section 2 · 1 the instability generation is described with giving review of different stages and the factors which may influence the instability growth. In section 2 · 2 the theoretical basis of the scaling law is developed for the spike and the bubble development. A simple review is given in section 2 · 3 for the instability growth in Inertial Confinement Fusion and in the next two sections the generation of magnetic fields as result of laser plasma interaction and the development of the fluid codes is discussed briefly.

2.1 RAYLEIGH-TAYLOR INSTABILITY

A fluid system in which there exists a density gradient is in a state of unstable equilibrium if it experiences an acceleration in the same direction as the density gradient. A small perturbation to the density or in the velocity field of the fluid in the plane perpendicular to acceleration will tend to grow in time and this known as Rayleigh-Taylor instability [3, 4]. It is commonly studied for incompressible fluids and has been discussed both for superposed and stratified layers. The growth of Rayleigh-Taylor instability for fluid models relating to Inertial Confinement Fusion

has been studied in detail in Chapters 5-7.

This instability occurs in diverse situations such as the overturning of the outer portion of the collapsed core of a massive star [5],and the formation of high luminosity twin exhaust jets in rotating gas clouds in an external gravitational potential [6]. It may also arise in Inertially Confinement Fusion targets [7-9], electromagnetic implosion of a metal liner [10] and in several other physical phenomenon. The phenomena of Rayleigh-Taylor instability is explained by an example [11], where a roof is plastered uniformly with water as shown in figure $2 \cdot 1$. The layer of water will fall down. Why? This is not due to the lack of support from the air, which has enough pressure to hold the water against the ceiling. It is because after preparation of the water surface it is not completely flat, so different portions of the fluid require slightly different pressure to hold it and the air cannot supply the necessary variations in pressure and so the flatness cannot be restored. The irregularities will grow exponentially with time and eventually the water falls to the floor.

2.1.1 Different Stages

The phenomenon of instability growth is very complex and complicated, which lead to the formation of spikes, bubbles, competition among bubbles and their amalgamation (i.e. the breakup of smaller bubbles and making bigger ones), development of Kelvin-Helmholtz instability on spikes and the turbulent mixing of the whole fluid. Different stages of the instability are shown in figure $2 \cdot 2$. To understand these physical processes the growth of this instability can be arranged into a number of different stages [13, 15], as explained below.

The early stages of the growth of the instability can be analysed using the linearized form of the dynamical equations for the fluid. When the amplitude of a perturbation of wavelength ($\lambda = \frac{2\pi}{k}$) grows to a size of the order of $0 \cdot 1\lambda - 0 \cdot 4\lambda$, a significant deviation from the linear theory is observed where the growth rate approaches a limiting value proportional to $\sqrt{g\lambda}$ [15]. This stage is normally referred as the linear phase of the growth.

During the second stage when the amplitude of perturbation grows up to the order λ, the development of the instability is strongly affected by the density

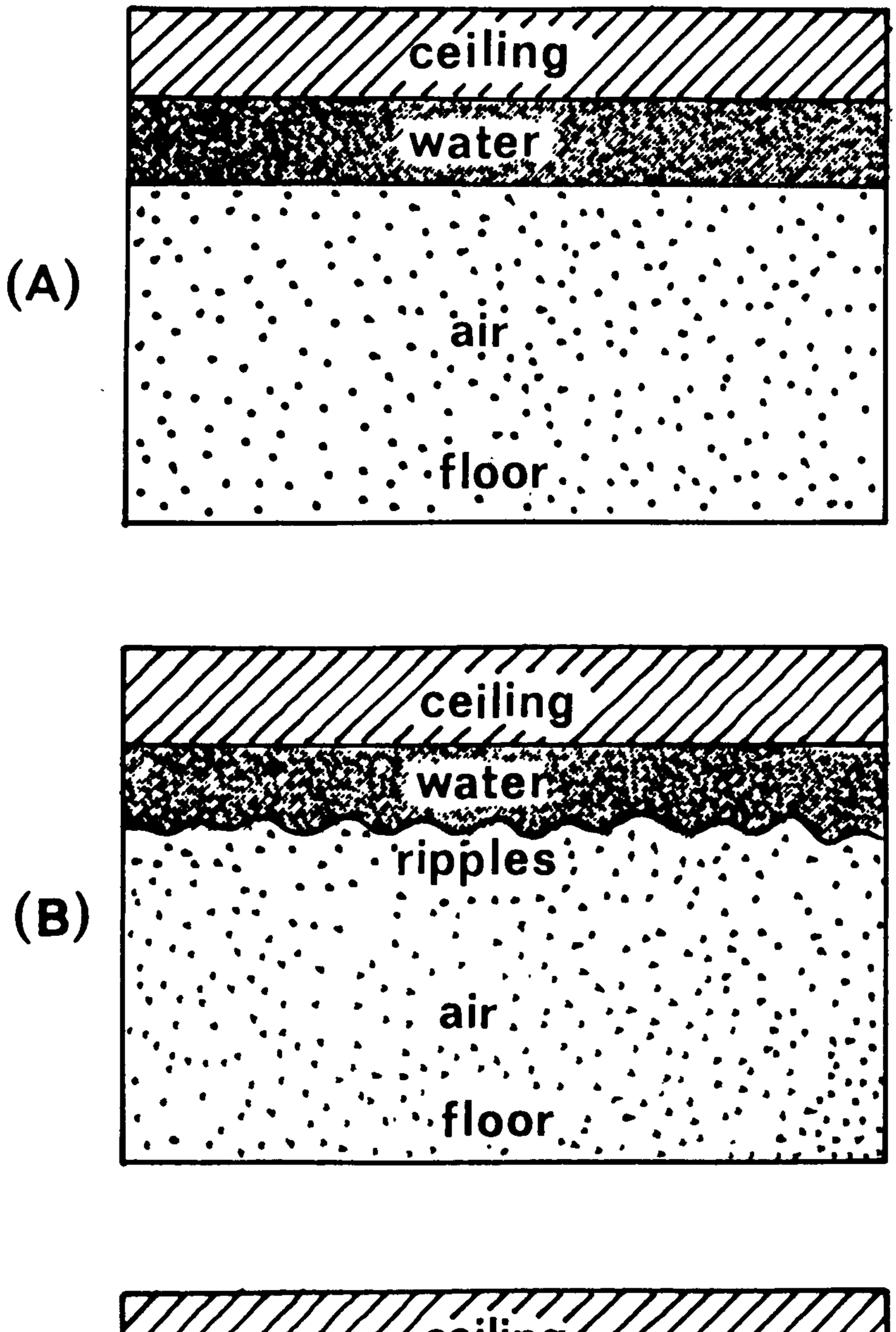

Figure 2.1: Growth of Rayleigh-Taylor instability at different times

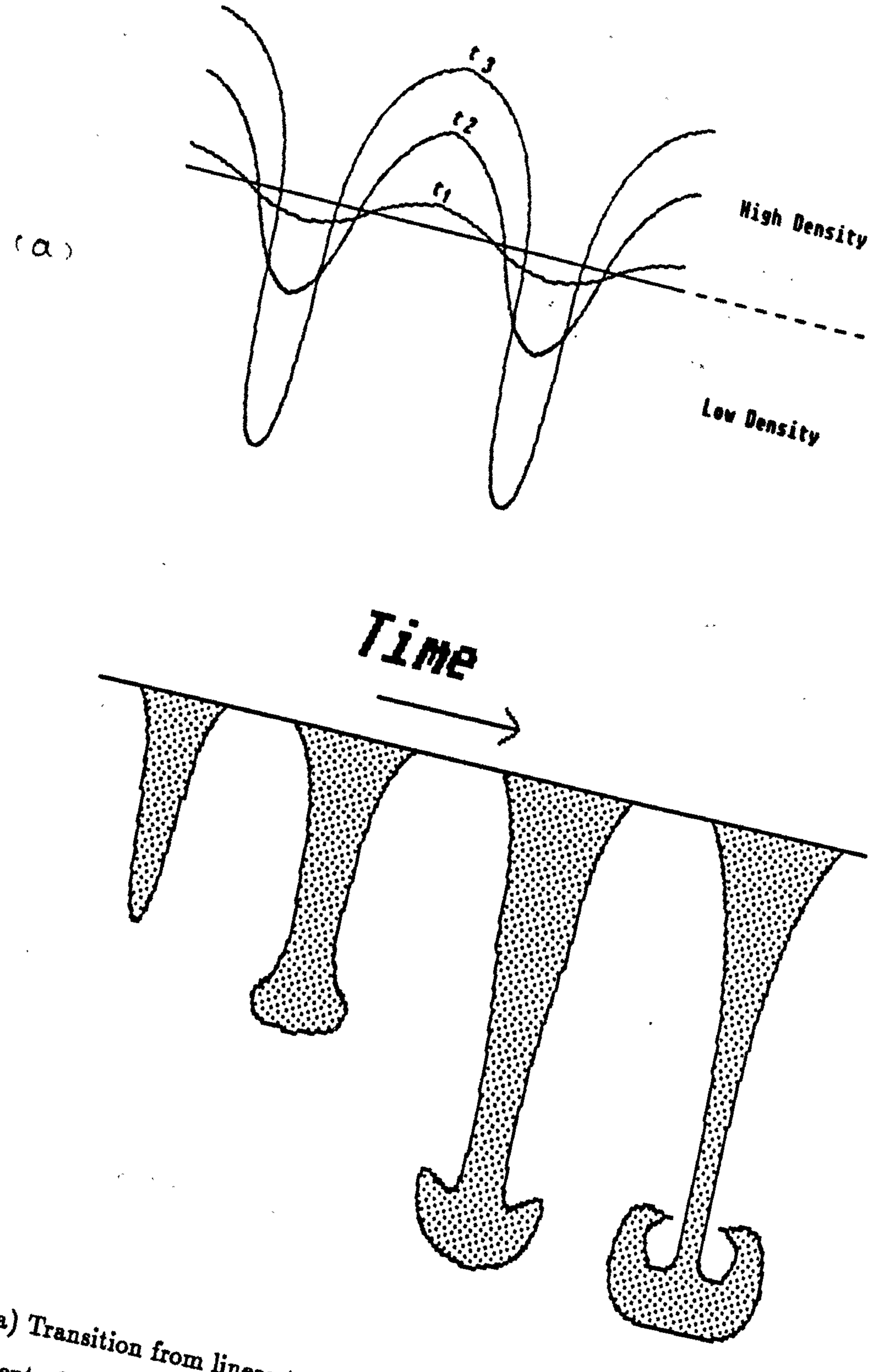

Figure 2.2: (a) Transition from linear to non-linear at different times.
(b) Development of mushroom shape on Rayleigh-Taylor instability spikes due to Kelvin-Helmholtz instability

difference and three dimensional effects. In the case, when the density difference, normally measured in the terms of Atwood's number, is less than one the light fluid will rise up into the heavy fluid in the form of round ended bubbles and the heavy fluid will fall into the light fluid in the form of spikes (figure 2.2 a). In three dimensions the spikes look like curtains of dense fluid, whereas the horizontal section would give a honey comb appearance. The three dimensional effects are not very well understood, although they are expected to be of great importance in the later stages [11]. From the fusion point of view an instability during these late stages would almost certainly constitute failure and so the details of these three dimensional effects may not be of great importance in our studies.

In the next stage structures appear on the spikes due to Kelvin-Helmholtz instability defined as the shearing effect at the interface of the fluid [12, 14]. This occurs at the interface of two fluids of different density when there is a relative motion between the two layers [14, 16, 17]. The shear causes a small perturbation at the interface to grow as it moves downstream so that mixing of the layers occurs to increasing drag. The relative motion of the spike and bubble causes deformation of the spike via Kelvin-Helmholtz instability resulting in the mushroom shape as shown in figure 2 · 2 (b). These vorticity effects are important as they eventually give rise to the break up of spikes. The formation of mushroom shape on spikes is more common for a low density ratio. During this stage the bubbles merge forming larger bubbles which rise with faster velocity.

In the last stage the spikes break up forming droplets by various mechanisms, the penetration of a bubble through a slab of fluid of finite thickness and other complicated behaviour which ends up the turbulent mixing of the two fluids.

2.1.2 Influencing Factors

There are many factors which can influence the development of this instability. These are surface tension, viscosity, shock waves, compressibility, divergence in density and temperature and converging geometry. In natural phenomenon there are other factors which are important in the development of this instability. The most important of these are the material properties and the equation of state of the fluid.

2.2 NON-LINEAR INSTABILITY GROWTH

It has been experimentally suggested that linear theory is only valid until the amplitude of displacement $A(t) \leq 0 \cdot 1\lambda$ for a sinusoidal perturbation [15]. As the disturbance grows, nonlinear effects will cause a change in the shape of disturbance. Although it is sinusoidal in the beginning the phenomenon is converted into nonlinear phase when the high density fluid falls into the low density one in the form of spikes and the low density fluid rises up into the high density one in the form of round ended bubbles.

Jacobs [59] has adopted a synthetic model to describe the Rayleigh-Taylor instability, where in the nonlinear regime, the bubble growth is described by the following equation

$$A(t) = A_0 e^{nt} \quad t \leq t_1 \tag{2.1}$$

$$A(t) = \frac{\dot{A}_t}{n} + \dot{A}_t(t - t_1) \quad t \geq t_1 \tag{2.2}$$

where

$$t_1 = \frac{1}{n} \ln(\frac{\dot{A}_t}{nA_0}) \tag{2.3}$$

and

$$\dot{A}_t = \frac{dA}{dt} = F\sqrt{g\lambda} \tag{2.4}$$

the terminal bubble speed. Here g and λ are the acceleration and the wavelength respectively and F is an empirical constant (Froude number). Different people obtained this constant both experimentally and theoretically and found its value between $0 \cdot 2 - 0 \cdot 3$. Kull [60] adopted a detailed model of non-linear growth and found

$$F \simeq \frac{1}{\sqrt{6\pi}} = 0 \cdot 23 \tag{2.5}$$

These models do not give the real picture because there is only a single bubble considered i.e. no interference and this will exist only for a time until the bubbles (if circular in profile) have penetrated a distance, $\lambda/2$. The bubble and spike growth is discussed in more detail in the next section.

2.2.1 Limitations on Spike and Bubble Growth

The growth of instability is observed by examining the bubble and spike growth with time. An intensive study has been carried out in evaluating the growth rate of bubbles and spikes experimentally, theoretically and via computer simulation. Sharp [11] considers incompressible fluids in a simple calculation without including surface tension and viscosity, gives the growth of perturbation amplitude as

$$A = A_0 \cosh[\sqrt{gkat}] \tag{2.6}$$

where $k = \frac{2\pi}{\lambda}$, the wave number of perturbation, g the constant acceleration and a is the Atwood's number. In laser plasma applications, we know that $\rho_2 >> \rho_1$, then we can put $a \leq 1$.

In the case of incompressible fluids, Fermi [61] in his model worked out that spikes and bubbles to grow as t^2 and $t^{1/2}$ respectively. The spike growth for incompressible fluids follows the gravitational free fall law as $A \simeq \frac{1}{2}gt^2$. Experimental studies show that the bubbles grow with a constant velocity [62-65], for the bounded medium, where as for an unbounded medium the bubble grows as t^2 [28].

In the theoretical calculations, for plane geometry, the bubble steady velocity is $w = 0 \cdot 225\sqrt{g\lambda}$ and the transition from exponential to the steady flow occurs at time τ, given by

$$A_0 \cosh[\sqrt{gk}\tau] \simeq \frac{1}{2}A_0 \exp[\sqrt{gk}\tau] = 0 \cdot 225\sqrt{g\lambda}\tau \tag{2.7}$$

In analytical calculations [66], this coefficient was found to be $0 \cdot 23$ for plane bubbles and $0 \cdot 36$ for axisymmetric cylindrical bubbles. Garabedian [64] points out for initially sinusoidal perturbations, the maximum bubble velocity to be

$$w = 0 \cdot 24\sqrt{g\lambda} \tag{2.8}$$

In a crude dimensional analysis [67], it is noted that in the nonlinear phase $A/\lambda = const.$, where A is the bubble head displacement. Assuming the bubble to be approximately circular, then $A \simeq \frac{1}{2}\lambda$. Therefore, from equation (2.8) it is found

$$\frac{dA}{dt} \simeq 0 \cdot 34\sqrt{gA} \tag{2.9}$$

or

$$A \simeq 0 \cdot 03gt^2 \tag{2.10}$$

It is found that A is a function of g and t only. Youngs [68] in his 2D calculations gives

$$A = 0 \cdot 05gt^2 \tag{2.11}$$

Read [69] in his experimental studies gives

$$A = 0 \cdot 07gt^2 \tag{2.12}$$

These two results differ because of the two dimensional nature of calculations. Layzer's [66] studies for the case of cylindrical, on the basis of above calculations, is in good agreement with equation (2.12).

In an unbounded medium the initial growth of the dominant wave length of non-periodic small displacement from rest is given by equation (2.6). The flow will start to depart from exponential growth at time τ, given by equation (2.7). It is also possible that bubble encroachment will also start to take place. In other words, we can say the motion in an unbounded medium changes progressively from exponential growth to a turbulent mixing phase at time τ, given by

$$\frac{1}{2}A_0 \exp[\Omega\sqrt{gk}\tau] \simeq \eta g\tau^2 \tag{2.13}$$

where Ω is the correction factor.

The solution of this becomes

$$\sqrt{z} = \ln(\beta z) \tag{2.14}$$

where

$$\beta = \frac{2\eta}{A_0 k\Omega^2} \tag{2.15}$$

and

$$z = \Omega^2 gk\tau^2 \tag{2.16}$$

It is easily shown that the solution exists only for

$$\beta < \frac{e^2}{4} = 1 \cdot 847 \tag{2.17}$$

with $z > 4$. The complete solution drawn from equation (2.14) is shown in figure 1 of Henshaw [67]. It is, therefore, concluded that the linear or exponential phase is observed only, if

$$A_0 < \frac{4\eta\lambda}{\pi e^2\Omega^2} = 0 \cdot 1723\frac{\eta\lambda}{\Omega^2} \tag{2.18}$$

The 2D numerical calculations for a spherical target, using the code POLLUX [70], with a laser of wavelength $0{\cdot}53\mu m$ without including the magnetic field effects, it is observed that $\eta = 0 \cdot 05 - 0 \cdot 15$ and $\Omega = 0 \cdot 8 - 1 \cdot 0$. It is, therefore, calculated that in these situations the initial displacement for linear growth is given by

$$A_0 < 0 \cdot 04\lambda \tag{2.19}$$

It is also pointed out that Ω may be dependent on plasma conditions and it is set to be equal to $1 \cdot 0$, which makes it more restrictive.

It has been pointed out that bubbles and spikes can have the same velocity at late time, so the thickness of mix region becomes

$$\tilde{A} = \tilde{\eta} g t^2 \tag{2.20}$$

with $\tilde{\eta}$ to be the function of bubble and spike growth. It is observed that the position of unstable surface is not fixed in the Inertial Confinement Fusion targets. Therefore, the thickness of the mixed region is measured as the growth amplitude in our calculations presented in Chapters 5-7, instead of individual bubble and spike growth.

2.3 RAYLEIGH-TAYLOR INSTABILITY IN ICF

In Inertial Confinement Fusion a target of DT fuel contained with a glass or plastic micro-balloon is uniformly irradiated by drivers such as lasers, or light and heavy ion beams. In an ablative driven target DT fuel pellet is uniformly irradiated by intense laser beams of short wavelength. There are several occasions during pellet compression in which Rayleigh-Taylor instability can become important but two of them one in the coronal region and the other in core region at the time of compression are particularly important as explained below.

The incident energy is absorbed by the abalator, which causes the outer material to blow off, whence as a rocket action this ablated material accelerates the

target inwards. The outer surface is now the interface between the heavy fluid (metal) and the light fluid (vaporized metal). This region is susceptible to hydrodynamic instability and has been observed in the ablating accelerated planar and spherical targets [18, 19, 67]. As is well-known that laser can deposit its energy only up the critical density, where the plasma frequency is equal to the light frequency. Beyond the critical density the energy transportation takes place via electron thermal conduction. The process of energy absorption continues and as a result a shock front implodes inwards, pushing the cold fuel ahead of it to higher and higher densities, causing the central spark to ignite (a thermonuclear ignition), which propagates outwards as a burn wave. The pellet is compressed by this phenomenon to densities up to approximately 1000 times the initial solid density. As the compression of DT fuel nears its peak, the pusher separating the fuel from the abalator will still be slowing down. This will be pushing against the lower density DT fuel, so the pusher fuel interface is unstable as the ignition is getting underway. This causes the mixing of fuel with pusher material, thereby impeding the burn wave and reducing the fractional burn and hence reducing the gain.

To achieve these high densities, it is therefore required that the core must be compressed nearly isentropically, so shock waves and other mechanisms which could heat the core before compression must be avoided [20]. One of these problems is the production of superathermal electrons in the resonance absorption process [21], i.e. a large amount of the absorbed energy goes into a group of hot electrons producing a higher energy tail on the electron distribution function. Because of their long mean free path these penetrate the core before compression and deposit their energy there, as the mean free path reduces in the higher density region. Core pre-heating reduces the peak compression and to avoid this problem it has been suggested that short wavelength lasers are preferable as the electron energy is scaled as $\sqrt{I\lambda^2}$ [20].

There are many effects such as external shape irregularities, target manufacture, geometry and dynamics of the physical process, which can contribute to Rayleigh-Taylor instability growth. The external irregularities could be at wavelengths of the order of or greater than the shell thickness; and gives an indication of

the relative importance of the various sources of perturbation. The non-uniform illumination of laser is also a source of the instability growth, which is present throughout the process of implosion. The factors concerned with the target manufacture can be the non-uniform surface, variation in areal thickness and the material inhomogeneity. The physical phenomenon present in an implosion, such as very large temperature gradients, steep density gradients in the fluid, ablating material, viscosity and compressibility, also affect the growth of this instability. Therefore the situation becomes so complex and complicated that linear as well as non-linear analysis gives only a rough estimate to the solution of the dynamics. Diagnostics of full ablative implosion experiments [35] can assess the degree of symmetry but cannot (so far) sort out the detailed physics of stabilization.

The geometry and the target design of the pellet also plays an important role in the development of the instability. Spherical shells have advantage over spheres requiring lower input optical power, but the shells are more susceptible to Rayleigh-Taylor instability [22]. The power requirement decreases as the aspect ratio (ratio of shell radius to the target thickness) increases. The aspect ratio is likely to be limited by Rayleigh Taylor instability, and a maximum of ≤ 10 has been suggested [23].

High-z materials prevent the pre-heat from the hot electrons, x-rays and may also give velocity multiplication effects (billiard ball effects). Multiple shell targets further reduce the optical power requirement [24], but these targets are rather difficult to manufacture and may create further problems of instability.

There are several different arguments concerning the hydrodynamic stability of the ablation surface. It is reported [25] that the material near ablation zone, from the spikes is ablated more rapidly which stabilizes the surface. In another analysis [26] it is argued that the ablation region is linearly unstable. McCrory [7] indicates that the spike growth is retarded by higher acceleration but it does not imply stability. The ablation process causes a constant flow of material through the unstable region, it has been suggested that by transporting vorticity downstream and away from the unstable region, growth may be reduced. Bodner [27] suggested that vortex shedding might stabilize the implosion, but it is considered in more recent discussions [28-30] to be a relatively insignificant effect in comparison with

the so-called thermal smoothing.

Thermal conduction may also modify the instability development. The energy is transported from the critical surface by the process of thermal conduction. Any variation in the heating can generate uneven pressure distribution which may lead to non-uniform acceleration of the ablation surface. It is possible that pressure variations caused by perturbation sources other than laser may also be controlled by high thermal conductivity. The thermal conductivity in the plasma is very high and it is suggested that lateral thermal conduction may be sufficient to smooth out non-uniformities in the heating before they reach the ablation surface [23]. Therefore, the smoothing of laser non-uniformity is improved by increasing the distance between ablation and critical surface. This can be achieved by preferring long wavelength lasers over the short wavelength lasers, but not so long that corona-core decoupling can occur [31]. The distance between the surfaces plays some role in spherical and planar targets. In planar targets the density fall-off in the underdense plasma is more gradual than in the spherical target expansion. The separation of critical and ablation surface is a function of time in both geometries but in general it is less for spherical expansion. A wavelength of $0 \cdot 53 \mu m$ with a power of $\geq 10^{14} W/cm^2$ has been suggested [23] as a suitable laser. Gardner and Bodner [32] also suggested intensities of a few times $10^{14} W/cm^2$ and the wavelength in the range $0 \cdot 5 - 2.7 \mu m$.

As the absorption takes place, the laser beam is refracted in the plasma, which may also generate the non-uniformity. A variation of about 30% in the laser intensity is expected to take place at the critical surface [23]. This beam non-uniformity is now controlled by the technique called Induced Spatial Incoherence (ISI) [33, 34]. This technique involves fluctuating spatial variations in intensity with time on a short time scale ($\simeq 10ps$) so that at the time of laser fusion ($\simeq 1ns$) these variations are averaged out. Time jitter, the effect of all the laser beams reaching the peak power at slightly different times may also destroy the symmetry of implosion [24].

Finally, we can conclude that a great many efforts have been made in designing the computer codes [35] and many experiments are performed using implosion calculations. The code modelling and experimental success give us a confidence

that implosion stability can be designed. But there are certain questions which remain to be investigated amongst which are performance limits of high aspect ratio targets, self generated magnetic effects and fuel mixing [35]. The latter question is particularly important because it affects the limits of target gain. Because the process occurs at the end of such a long chain of complex process, we cannot yet have a confidence in theoretical (code) predictions [35]. Experiments will also be able to establish a sufficient confidence.

2.4 SELF-GENERATED MAGNETIC FIELDS

In laser produced plasmas, a short powerful pulse of laser radiation is focused on a small target. This laser produced plasma contains spontaneous magnetic fields. We may refer to these as self-generated magnetic fields because they do not require any initial field but only require plasma inhomogeneity to form. There are several sources which can generate these high fields. The most important factors of these are the energy absorption [36] and transport [37, 38], superathermal electron generation [39], thermally generated magnetic instabilities including thermal magnetic waves and 'hot spots' in the electron plasma [40-44], field generation at composition boundaries and the field generation and amplification during the compression and burn phases [46, 47].

Large scale thermal magnetic source fields can be produced in electron pressure in the expanding ablated plasma. If there is an angle between the density and temperature gradients in the electrons as shown in figure $2 \cdot 3$, the electric field arising from the charge separation will have a curl including a magnetic field by Faraday's law. In our studies we will mainly include the simple thermal magnetic source although occasionally the full thermoelectric terms (Braginskii) [81] have been included. The full equation is given below

$$\nabla \times \mathbf{S} = -\frac{ck}{en_e}\nabla n_e \times \nabla T_e + \frac{c}{e}\nabla \times (\beta_0 . \nabla k T_e) \tag{2.21}$$

which will be discussed and its application in the code MAGT2LD, using the finite difference method in Chapter 4.

Fields of several megagauss have been observed at the junction of materials of differing atomic numbers due to the large gradients in the electron density which

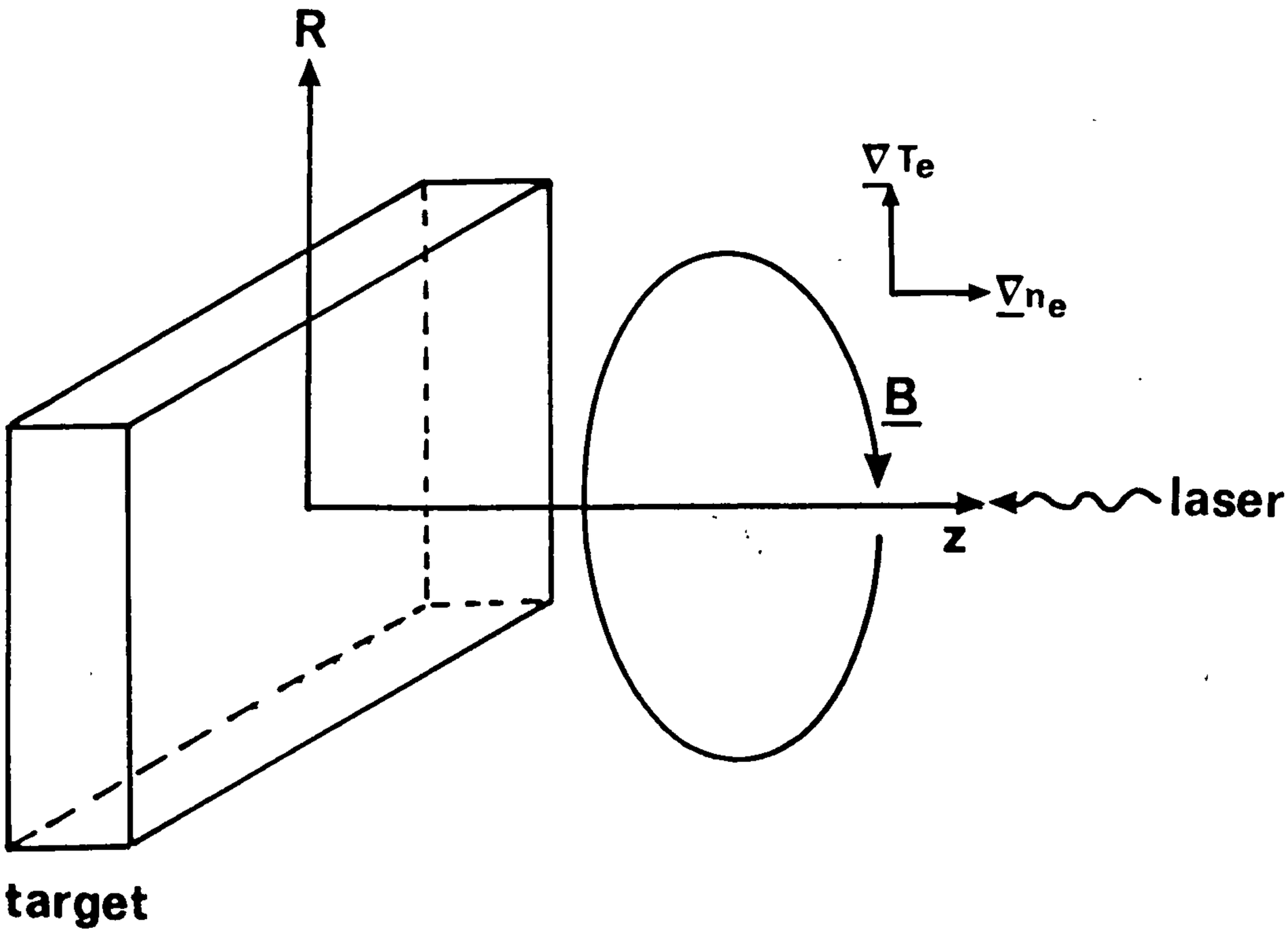

Figure 2.3: The mechanism of generation of magnetic field

would in principle arise there [48]. Similarly, magnetic fields between $10^5 G$ and $2 \times 10^6 G$ have been observed in computer simulations if large z, spherical impurity grains embedded in dense plasma [45]. Pert [41] has shown analytically that thermal magnetic waves may be generated in the absorption region and propagate along lines of constant density in the plasma. It is anticipated that their growth would be limited by propagation of energy out of the absorption region whence dissipative mechanisms such as thermal conduction, ohmic heating and phase effects would operate.

The fields produced by these mechanisms tend to be toroidal in shape surrounding the focal spot [49]. But the field strengths produced by these relatively well ordered fields are not sufficient to explain transport inhibition in the overdense region, where it matters most. At higher intensities ($\geq 10^{15} W/cm^2$), where the direct effect of laser radiation are important, field generation also depends on the laser polarization (resonance absorption) and local direction of the Poynting flux (field momentum deposition).

The magnetic fields can affect the pellet performance in several ways. The greatest initial concern is the pellet performance which can be degraded due to re-

duced thermal transport and its effect on implosion symmetry. This is because the magnetic fields are generated in the low density absorption region by non-uniform laser irradiation. Later studies of the magnetic fields generated in the ablation region and associated with the Rayleigh-Taylor instability raised concerns of inhibited heat thermal flux from the absorption to ablation region and consequence decrease in ablation pressure.

2.5 FLUID CODES

The fluid codes can be of three different types, Lagrangian, Eulerian and the hybrid of these two, called quasi-Lagrangian. In Eulerian codes, the finite difference mesh is fixed in space and the fluid is transported (or advected) from cell to cell. In Lagrangian codes mesh is fixed in space and there is no transportation of fluid between the cells or in other words the mesh is stationary in the fluid frame of reference. Both of these schemes have advantages and disadvantages according to the nature of flow.

Eulerian schemes give good results for steady and incompressible flow. The disadvantage of such a scheme is that the mesh cannot adopt the changing requirements for supersonic flows. Near the shock fronts, the quantities change rapidly so fixed Eulerian grids give poor finite difference representation. Lagrangian mesh is more suitable for compressive and expansive flow, because the cells can change their shape and size according to the flow, giving better accuracy. Also, as there is no fluid flow between the cells, the problem of numerical instability associated from advection is removed [50]. The two-dimensional Lagrangian scheme is not suitable as each cell cannot maintain orthogonality because of shearing in the flow and the mesh structure may become distorted [72]. The mesh entanglement problem can be solved by introducing artificial viscosity [51] or the successful use of rezoning schemes but may lead to error during compression.

The Eulerian and Lagrangian schemes are used in laser driven ablatively accelerated targets. In Lagrangian formulation there is an advantage that the solid target material is used as initial state [52] but the mesh tangling problem complicates this scheme. In Eulerian formulation a low density plasma tail must be

included (through which the ablated plasma flows) as initial state variable [82]. It is pointed out by Pert [55] that in the initial state when the density profile is still evolving, Lagrangian grid is most suitable whereas when the flow becomes steady the Eulerian grid gives should be used.

In laser-plasma ablation it is difficult to use simple Eulerian and Lagrangian formulations. The other examples could be shock propagation and the simulation of magnetic flux surfaces [57]. Therefore the rezoning schemes within Eulerian Flux Corrected Transport (FCT) schemes are used simultaneously and the cells are moved according to physical simulations required.

The code MAGT2LD used in our calculations is Eulerian in radial direction (where large scale motion is not expected) and quasi-Lagrangian in the axial direction. So the rezoning is essentially in one dimension which closely resembles to a one-dimensional Lagrangian formulations [53]. Mass, velocity and momentum is transported between the cells by FCT method [54].

The quasi-Lagrangian formulation consists of two stages:

1. First the calculation is advanced through one time step in a purely Lagrangian way and

2. In the second stage the mesh is rezoned so as to conform to the desired configuration.

The shift of fluid variables on the new rezoned mesh corresponds to transport if the relative velocity between the mesh and fluid should be used. The basic rezoning algorithms are given by Pert [55]. Two methods, velocity [56, 57] and mass [58] rezoning have been suggested. The physics of the code MAGT2LD is discussed briefly in Chapter 4 whereas it is applied in the next Chapters.

Chapter 3

RAYLEIGH-TAYLOR INSTABILITY IN INCOMPRESSIBLE FLUIDS

This chapter deals with the general problem of Rayleigh-Taylor instability in incompressible fluids. The fluid equations have been solved for a simple physical problem without including the effects of viscosity, surface tension and other physical phenomena. In section 3.1 the standard fluid equations have been given in a three dimensional coordinate system. Whereas in section 3.2 the equations have been solved to find a second order differential equation which is used to study instability problem. Section 3.3 deals with transforming the variables in non-dimensional form in order to avoid the dimensional problem of units. In sections 3.4 & 3.5, two different cases of density profiles are studied to investigate how the instability is affected by varying their wavelength for different Atwood's number.

3.1 GOVERNING EQUATIONS

The equations used to study the Rayleigh-Taylor instability are the equation of motion in a gravitational field, the equation of continuity and the equation of incompressibility. The fluid is allowed to have a non-uniform density but is assumed to be incompressible. All the variables which affect the Rayleigh-Taylor growth e.g. surface tension, viscosity and magnetic field effects etc. are not considered in

the model used in these calculations. Therefore the basic governing equations are written as [14, 59]:

$$\rho(\frac{\partial}{\partial t} + \mathbf{v}.\nabla)\mathbf{v} = -\nabla p + \rho \mathbf{g} \tag{3.1}$$

the equation of continuity can be written as

$$(\frac{\partial}{\partial t} + \mathbf{v}.\nabla)\rho = -\rho \nabla \cdot \mathbf{v} \tag{3.2}$$

As the fluid has non-uniform density although it is incompressible, therefore, equation (3.2) can be simplified by putting both sides of the equation equal to zero.

$$(\frac{\partial}{\partial t} + \mathbf{v}.\nabla)\rho = 0 \tag{3.3}$$

$$\nabla.\mathbf{v} = 0 \tag{3.4}$$

Where ρ, $\mathbf{v}$ and p are the fluid density, velocity and pressure respectively. Equation (3.3) states that the density of the fluid is unchanged moving with the fluid whereas equation (3.4) indicates that the divergence of the fluid velocity or net dilation is zero. These equations are to be solved using the normal mode method for the five independent variables $\mathbf{v}(v_x, v_y, v_z)$, p and ρ.

Applying a small perturbation to the fluid, the above equations are linearised by splitting the variables into the steady state value (equilibrium) and the increment due to the disturbance [14]. Therefore in the perturbed system the variables are written as the sums

$$\rho = \rho_0 + \rho' \tag{3.5}$$

$$p = p_0 + p' \tag{3.6}$$

$$v = v_0 + v' \tag{3.7}$$

where the subscripts zero refer to the equilibrium variables and the superscript prime denote the perturbed variables.

3.1.1 Equilibrium and Perturbed Equilibrium

Considering the fluid model in which density varies in the direction of g but is taken to be constant in the other directions as illustrated in figure 3 · 1.

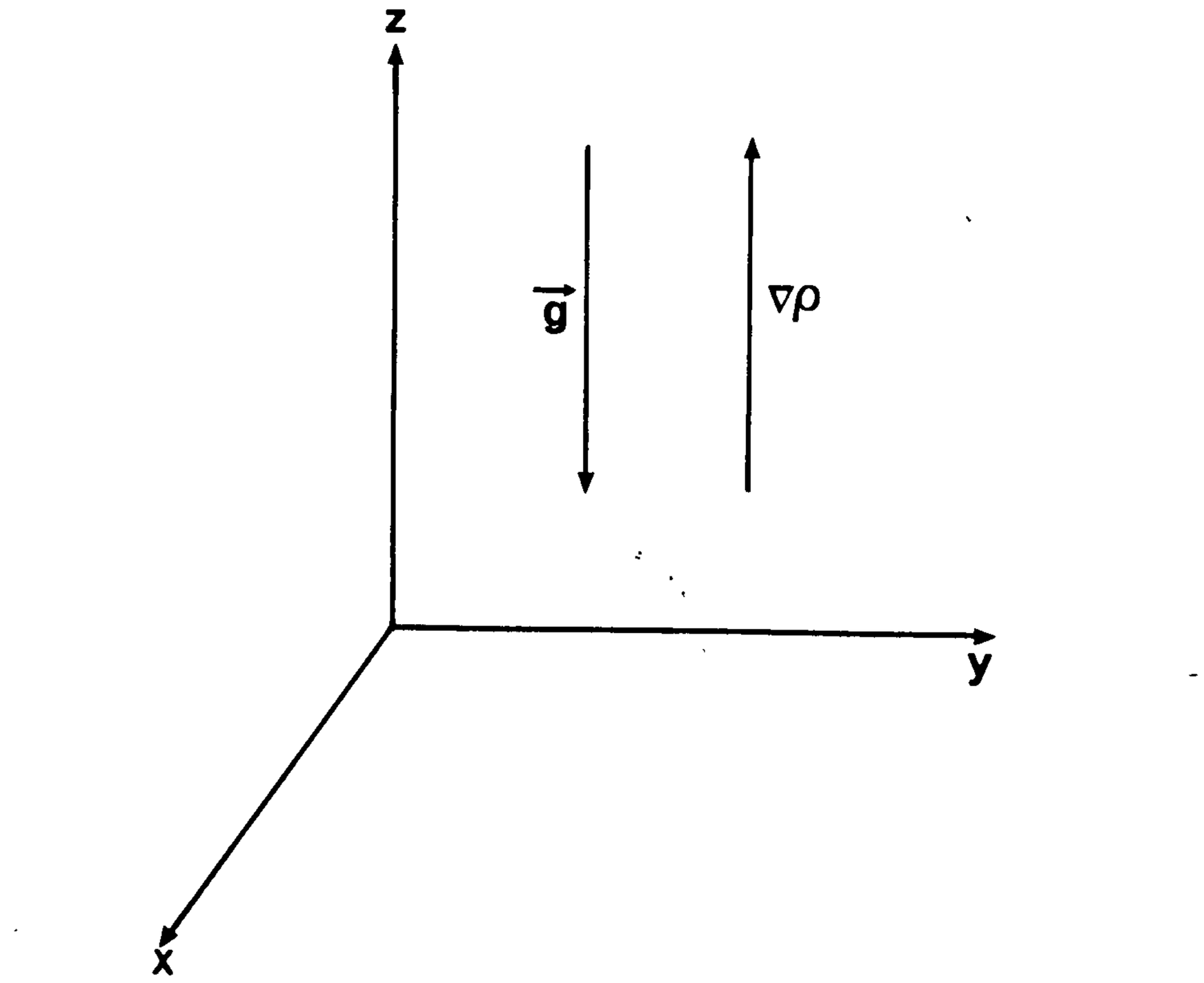

Figure 3.1: Geometry of equilibrium for Rayleigh-Taylor instability

In equilibrium the fluid velocity and its derivative are zero so equations (3.1,3.3 & 3.4) can be written as

$$\nabla p_0 = \rho_0 \mathbf{g} \tag{3.8}$$

$$\frac{\partial \rho_0}{\partial t} = 0 \tag{3.9}$$

$$\mathbf{v}_0 = 0 \tag{3.10}$$

The perturbed equations (3.1,3.3, 3.4) can now be written with the help of equations (3.5-3.7) in the following form

$$(\rho_0 + \rho')(\frac{\partial}{\partial t} + \mathbf{v}'.\nabla)\mathbf{v}' = -\nabla(p_0 + p') + (\rho_0 + \rho')\mathbf{g} \tag{3.11}$$

$$(\frac{\partial}{\partial t} + \mathbf{v}'.\nabla)(\rho_0 + \rho') = 0 \tag{3.12}$$

$$\nabla.\mathbf{v}' = 0 \tag{3.13}$$

3.1.2 Linearization

It is just as difficult to solve equations (3.11-3.13) as the original equations but fortunately the question of stability is answered by determining whether small

perturbations grow in time. The perturbations applied are considered to be arbitrarily small so that their non-linear terms can be ignored. Therefore retaining only the first order perturbations and dropping the second and higher order terms, equations (3.11-3.13) can be written as

$$\rho_0 \frac{\partial \mathbf{v}'}{\partial t} = -\nabla p' + \rho' \mathbf{g} \tag{3.14}$$

$$\frac{\partial \rho'}{\partial t} + \mathbf{v}'.\nabla \rho_0 = 0 \tag{3.15}$$

$$\nabla.\mathbf{v}' = 0 \tag{3.16}$$

3.2 FOURIER TRANSFORMATIONS

Since the fluid is initially uniform in x and y directions, variables can be expanded as a Fourier series. There is no loss of generality in taking perturbations which vary only in x, each Fourier component having the form $e^{\iota(kx-nt)}$ and taking $\mathbf{g} = (o, o, -g)$ as in figure $3 \cdot 1$; we obtain from equations (3.14-3.16)

$$-\iota\rho_0 n v_z = -\frac{dp'}{dz} - \rho' g \tag{3.17}$$

$$-\iota\rho_0 n v_x = -\iota k p' \tag{3.18}$$

$$-\iota n \rho' = v_z \frac{d\rho_0}{dz} \tag{3.19}$$

$$\frac{dv_z}{dz} + \iota k v_x = 0 \tag{3.20}$$

The linear variables in these equations are actually the Fourier components. These equations combine to give the following differential equation

$$\rho_0 \frac{d^2 v_z}{dz^2} + \frac{d\rho_0}{dz} \cdot \frac{dv_z}{dz} + k^2 \left(\frac{g}{n^2} \cdot \frac{d\rho_0}{dz} - \rho_0\right) v_z = 0 \tag{3.21}$$

This is a second order differential equation and the problem is therefore completely specified by giving the boundary conditions in z to give an eigenvalue equation for n^2. It is important to note from equation (3.21), it depends on n^2, so both signs ($\pm$) of n can be used. Also, because, the above equation is linear, so the linear combination of e^{nt} and e^{-nt} is a solution.

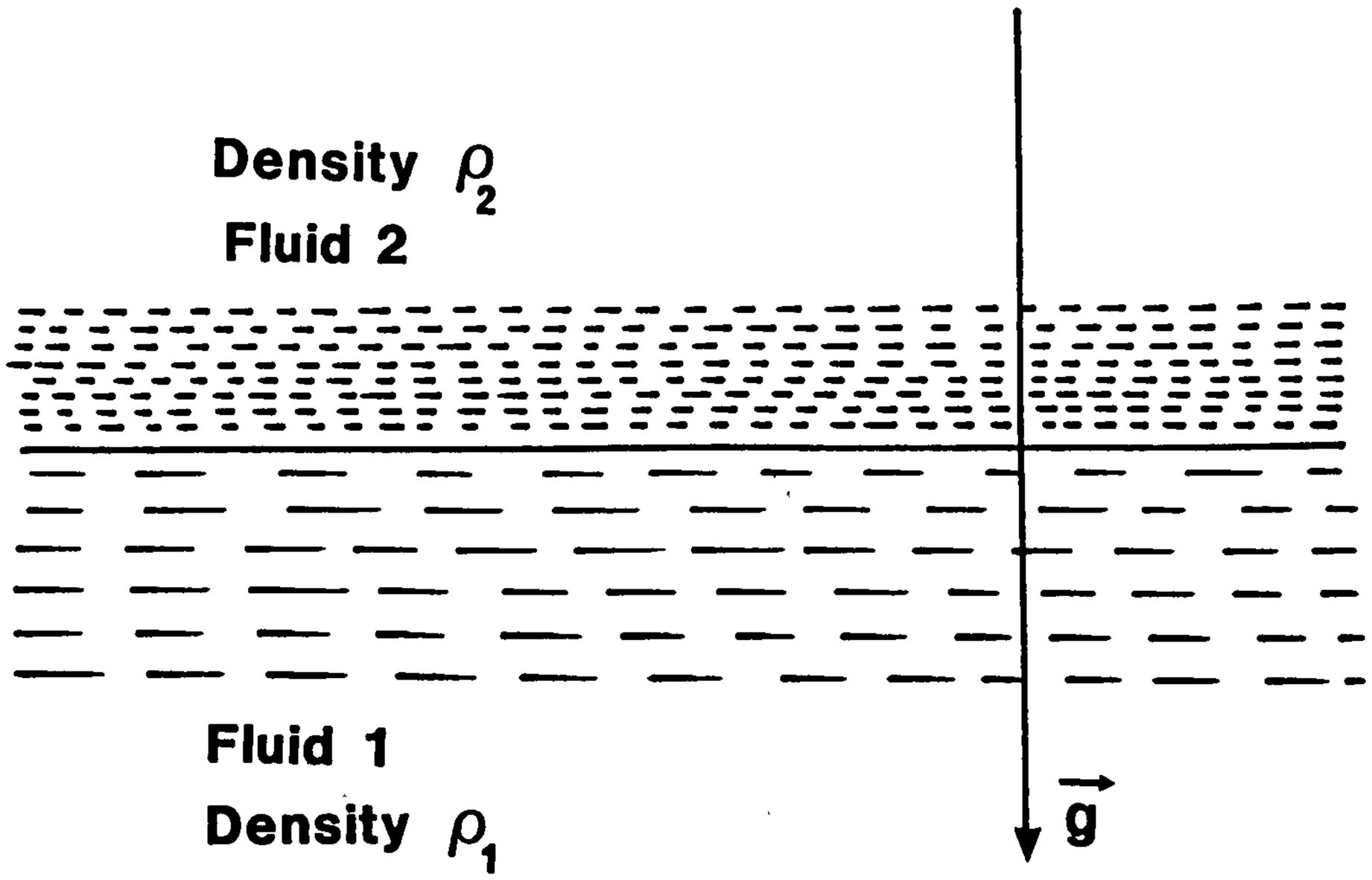

Figure 3.2: Two uniform fluids of different densitites superposed on one another

3.2.1 Two Uniform Fluids of Constant Density Separated by a Horizontal Boundary

Consider the case of two uniform fluids separated by a horizontal boundary [14] at $z = 0$ as shown in figure $3 \cdot 2$. In regions 1 and 2 there is no change in density i.e. $d\rho_0/dz$ is zero in these two regions. Therefore equation (3.21) reduces to

$$\frac{d^2 v_z}{dz^2} - k^2 v_z = 0 \tag{3.22}$$

and

$$\left.\frac{dv_z}{dz}\right|_{z_-=2} = -kv_z \tag{3.23}$$

$$\left.\frac{dv_z}{dz}\right|_{z_+=1} = kv_z \tag{3.24}$$

The remaining condition for the inviscid case is obtained by integrating equation (3.21) across the boundary.

$$\left[\rho_0 \frac{dv_z}{dz}\right]_1^2 + k^2 \int_1^2 (\frac{g}{n^2} . \frac{d\rho_0}{dz} - \rho_0) v_z dz = 0 \tag{3.25}$$

or since v_z must be continuous, therefore

$$\rho_2 \left.\frac{dv_z}{dz}\right|_2 - \rho_1 \left.\frac{dv_z}{dz}\right|_1 + \frac{gk^2}{n^2} v_z(\rho_2 - \rho_1) = 0 \tag{3.26}$$

Hence using the values obtained earlier, we can find the growth rate

$$n^2 = \frac{gk(\rho_2 - \rho_1)}{(\rho_2 + \rho_1)} \tag{3.27}$$

Including the surface tension effect the growth rate can be of the form as given below [14]:

$$n^2 = gk\left\{\frac{\rho_2 - \rho_1}{\rho_2 + \rho_1} - \frac{k^2 T}{g(\rho_2 + \rho_1)}\right\} \tag{3.28}$$

According to equations (3.27), if $\rho_2 < \rho_1$ the arrangement is stable: while if $\rho_2 > \rho_1$ the arrangement is unstable for the all the wave numbers. It is important to note when surface tension is present, there is a mode of maximum instability for which the amplitude of the disturbance grows more rapidly [14].

3.3 TRANSITION TO NON-DIMENSIONAL VARIABLES

The coordinates in equation (3.21) are simplified by transforming into the non-dimensional variables [59], therefore, defining

$$\zeta = kz \tag{3.29}$$

$$Y = \frac{n^2}{gk} \tag{3.30}$$

and using these new set of non-dimensional variables in equation (3.21) we obtain the following differential equation to be used in the different study cases.

$$\rho_0 \frac{d^2 v_z}{d\zeta^2} + \frac{d\rho_0}{d\zeta} \cdot \frac{dv_z}{d\zeta} - (\rho_0 - \frac{1}{Y} \cdot \frac{d\rho_0}{d\zeta}) v_z = 0 \tag{3.31}$$

This equation will now be used to find the eigenvalues for different cases studied both analytically and numerically in the forthcoming sections.

3.4 LINEAR DENSITY RAMP

The problem is studied by taking the density profile of finite width L with ρ_1 and ρ_2; the initial and final densities respectively as shown in figure $3 \cdot 3$. Therefore, mathematically the density profile can be written in the following way

$$\rho_0 = \rho_1 + (\rho_2 - \rho_1)(Z + \tfrac{1}{2}); \quad -\tfrac{1}{2} \leq Z \leq \tfrac{1}{2} \tag{3.32}$$

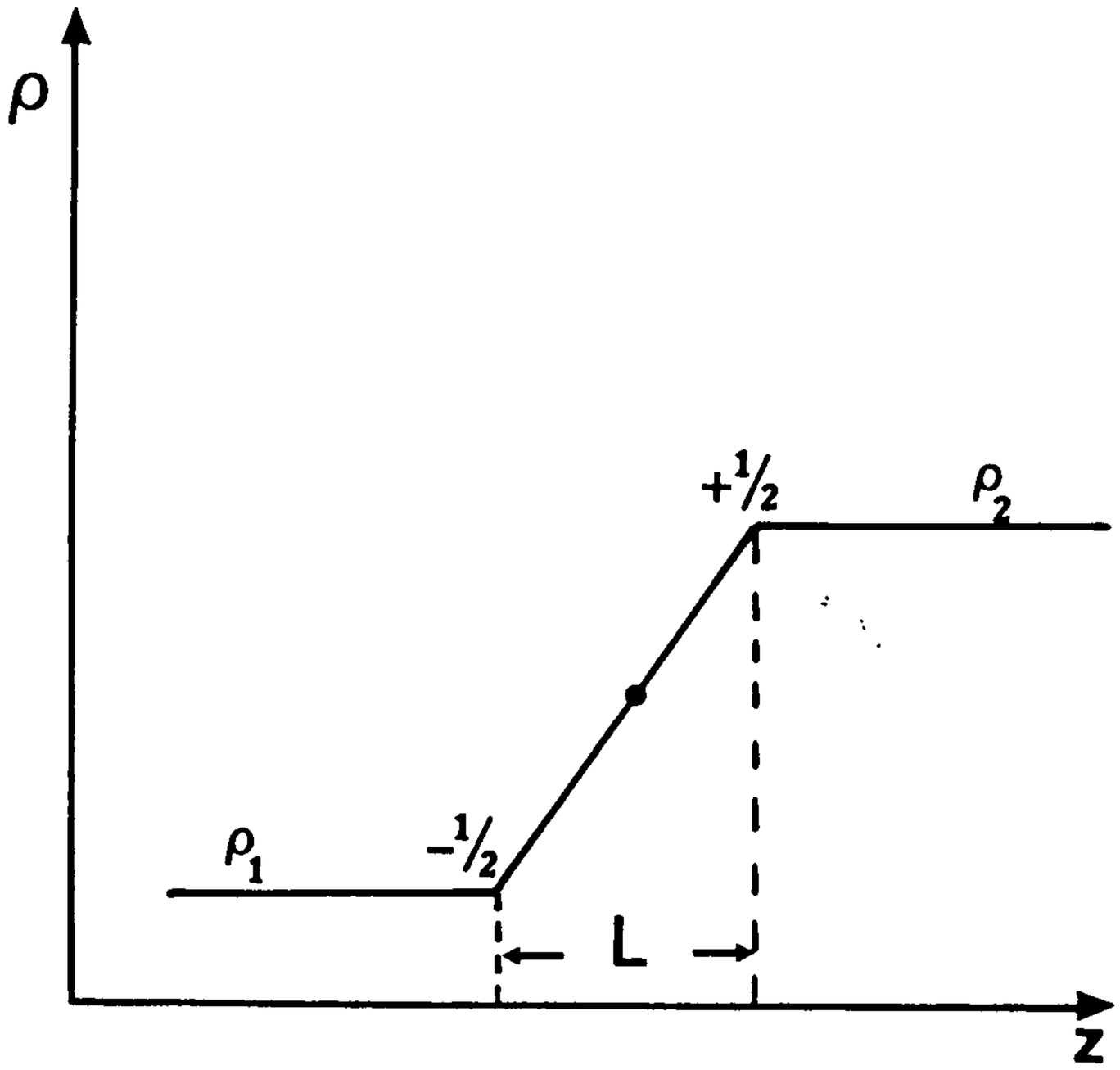

Figure 3.3: Geometry of gradual varying density profile.

where

$$Z = \frac{\zeta}{kL} \tag{3.33}$$

The boundary conditions for density transition region is given by

$$\left.\frac{dv_z/dZ}{v_z}\right|_{\frac{1}{2}} = kL \tag{3.34}$$

$$\left.\frac{dv_z/dZ}{v_z}\right|_{-\frac{1}{2}} = -kL \tag{3.35}$$

The Atwood's number, or density ratio is defined as

$$a = \frac{\rho_2 - \rho_1}{\rho_2 + \rho_1} \tag{3.36}$$

Therefore equation (3.31) becomes

$$\frac{d^2v_z}{dZ^2} + \frac{1}{(1/2a + Z)} \cdot \frac{dv_z}{dZ} - \left[(kL)^2 - \frac{kL}{Y(1/2a + Z)}\right] v_z = 0 \tag{3.37}$$

This is a complicated differential equation and it is not possible to find the exact solution analytically, however an approximate solution is presented in the subsection 3.4.1. It was solved numerically using the routine INTS (Integrate a System of Ordinary Differential Equation) using the computer VAX at York University,

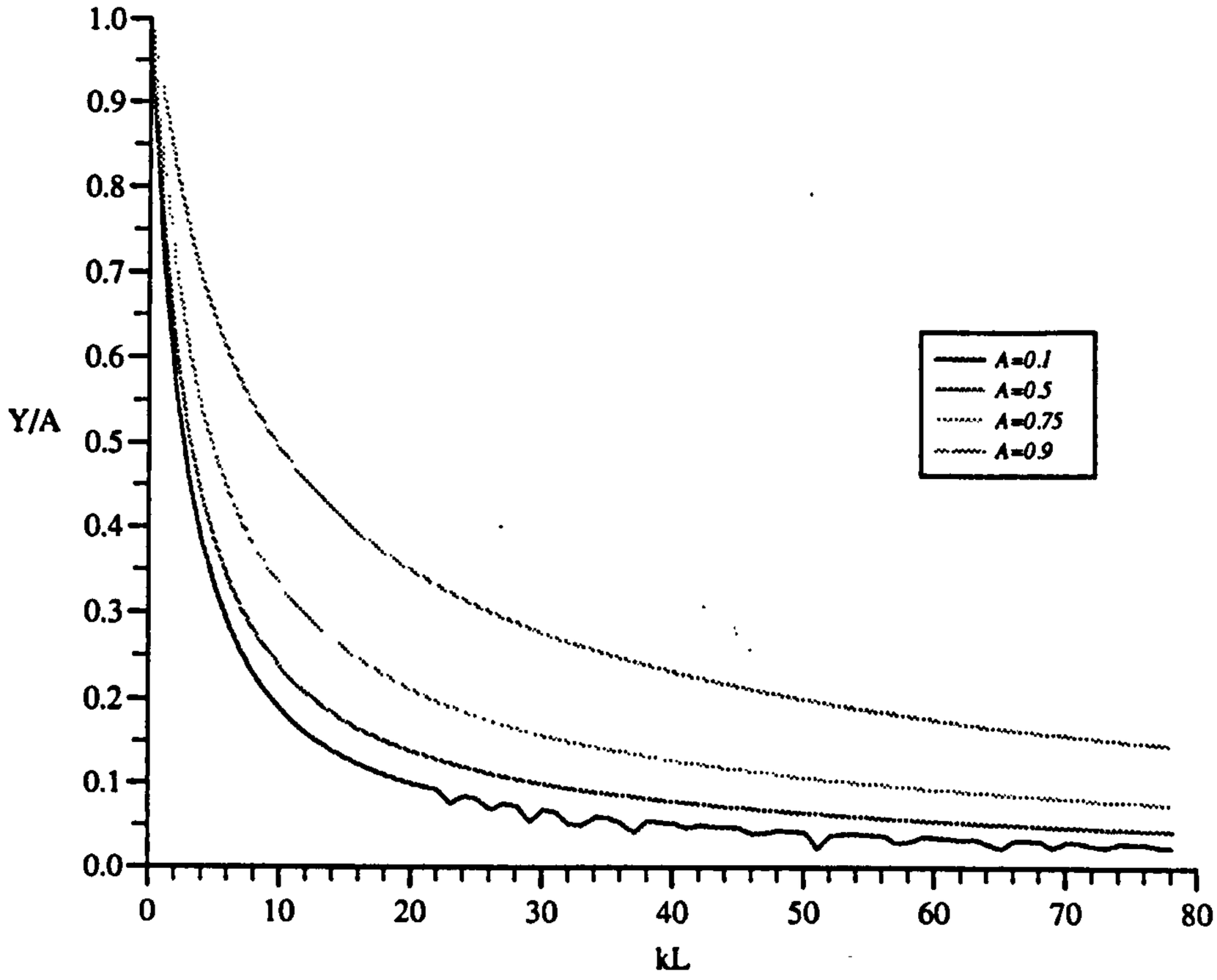

Figure 3.4: Growth rate of instability for a gradual varying density profile for different Atwood's numbers.

changing the wave vector for different Atwood's numbers. It took about 1 CPU hour for each case by giving an increment of 1 in the kL value to cover the range. The growth rate, $Y = n^2/gk$, plotted against the wave vector, kL, is shown in figure $3 \cdot 4$.

As we notice from the graph, the instability grows exponentially. For small Atwood's numbers i.e. $a = 0 \cdot 1$, the instability growth is much slower than for higher values of a, as is shown from figure $3 \cdot 4$. We were not able to run the programme for very high wave vectors, because it crashed for $kL > 100$ in most cases. It is also important to note that the instability grows much faster for small kL (longer wavelengths), than the higher wave vectors.

3.4.1 Approximate Solution

We will try to find the approximate solution of the general differential equation for the problem considered in the previous section in the following way. Integrating the equation (3.21) directly, keeping in mind that v_z is continuous, the equation

becomes

$$\rho_0 \frac{dv_z}{d\zeta}\bigg|_1^2 + \alpha^2 \int_1^2 \left[\frac{1}{\alpha Y}\frac{d\rho_0}{d\zeta} - \rho_0\right] v_z d\zeta = 0 \tag{3.38}$$

where $\alpha = kL$ and $\zeta = z/L$ are the non-dimensional parameters.

Infinitely Thin Profile $kL << 1$

Considering the case when the profile is infinitely thin in the boundary region ζ_1 to ζ_2, we obtain

$$\int_1^2 v_z \frac{d\rho_0}{d\zeta} d\zeta \simeq v_z \rho_0|_1^2 \tag{3.39}$$

and

$$\int_1^2 v_z \rho_0 d\zeta \simeq 0 \tag{3.40}$$

Using these equations in equation (3.38) we find that

$$Y = \frac{\rho_2 - \rho_1}{\rho_2 + \rho_1} \tag{3.41}$$

Very Wide Profile $kL >> 1$

In the case when the density profile is very wide, we approximate v_z by sinusoidal function

$$v_z \simeq v_0 \cos(\pi\zeta) \tag{3.42}$$

with the condition that $\zeta_1 = -1/2$ and $\zeta_2 = 1/2$. Using this form, we find

$$\int_{\zeta_1}^{\zeta_2} v_z \frac{d\rho_0}{d\zeta} d\zeta = \frac{2}{\pi}(\rho_2 - \rho_1) \tag{3.43}$$

From equation (3.31) and with the boundary conditions, we have

$$\rho_0 \frac{dv_z}{d\zeta}\bigg|_{-1/2}^{\zeta} + \frac{\alpha}{Y}(\rho_2 - \rho_1)\int_{-1/2}^{\zeta} v_z d\zeta - \alpha^2 \int_{-1/2}^{\zeta} [\rho_1 + (\rho_2 - \rho_1)\zeta] v_z d\zeta = 0 \tag{3.44}$$

As for the first approximation $v_z = v_0 \cos(\pi\zeta)$, we have

$$\int_{-1/2}^{\zeta} v_z d\zeta = \frac{1}{\pi} v_0 \{1 + \sin(\pi\zeta)\} \tag{3.45}$$

$$\int_{-1/2}^{\zeta} \zeta v_z d\zeta = -\frac{1}{\pi} v_0 \zeta \sin(\pi\zeta) + \frac{1}{\pi^2} v_0 \cos(\pi\zeta) \tag{3.46}$$

Using these equations in equation (3.44), we can have

$$\rho_0 \frac{dv_z}{d\zeta}\bigg|_{-1/2}^{\zeta} + \frac{\alpha}{Y}(\rho_2 - \rho_1)\int_{-1/2}^{\zeta} v_z d\zeta - \alpha^2 \int_{-1/2}^{\zeta} [\rho_1 + (\rho_2 - \rho_1)\zeta] v_z d\zeta = 0 \tag{3.47}$$

Now using equation (3.42), we find

$$\int_{-1/2}^{\zeta} v_z d\zeta = \frac{1}{\pi} v_0[1 + \sin(\pi\zeta)] \tag{3.48}$$

$$\int_{-1/2}^{\zeta} \zeta v_0 d\zeta = -\frac{1}{\pi} v_0 \zeta \sin(\pi\zeta) + \frac{1}{\pi^2} v_0 \cos(\pi\zeta) \tag{3.49}$$

Also noting that the first term in equation (3.47) gives

$$\rho_0 \frac{dv_z}{d\zeta}\Big|_{-1/2}^{\zeta} = -\pi(\rho_2 + \rho_1)v_0 \tag{3.50}$$

Therefore using the above calculated values in equation (3.47), we can find the growth rate as

$$Y = \frac{2\alpha}{(\pi^2 + \alpha^2)} \cdot \frac{(\rho_2 - \rho_1)}{\rho_2 + \rho_1)} \tag{3.51}$$

This equation can be used to find the approximate solution in conjuction with the full solution of equaiton (3.37).

3.4.2 Residual in the Differential Equation

The residual occurring in the differential equation is given by

$$\begin{aligned} -\pi^2[\rho_1 + (\rho_2 - \rho_1)\zeta]\cos(\pi\zeta) - \pi[\rho_2 - \rho_1]\sin(\pi\zeta) - \alpha^2[\rho_1 + (\rho_2 - \rho_1)\zeta]cos(\pi\zeta) \\ +\alpha/Y[\rho_2 - \rho_1]\cos(\pi\zeta) \end{aligned} \tag{3.52}$$

At $\zeta = 0$

$$-\frac{1}{2}(\alpha^2 + \pi^2)(\rho_2 + \rho_1) + \alpha(\rho_2 - \rho_1)/Y = 0$$

and at $\zeta = \pm 1/2$

$$\pm\pi[\rho_2 - \rho_1]$$

More generally we can have

$$-(\alpha^2 + \pi^2)(\rho_2 - \rho_1)(\zeta - \frac{1}{2})\cos(\pi\zeta) - \pi(\rho_2 - \rho_1)\sin(\pi\zeta)$$

This will have a small value if $\rho_2 - \rho_1$ is small and agree with the numerical values for $kL >> 1$.

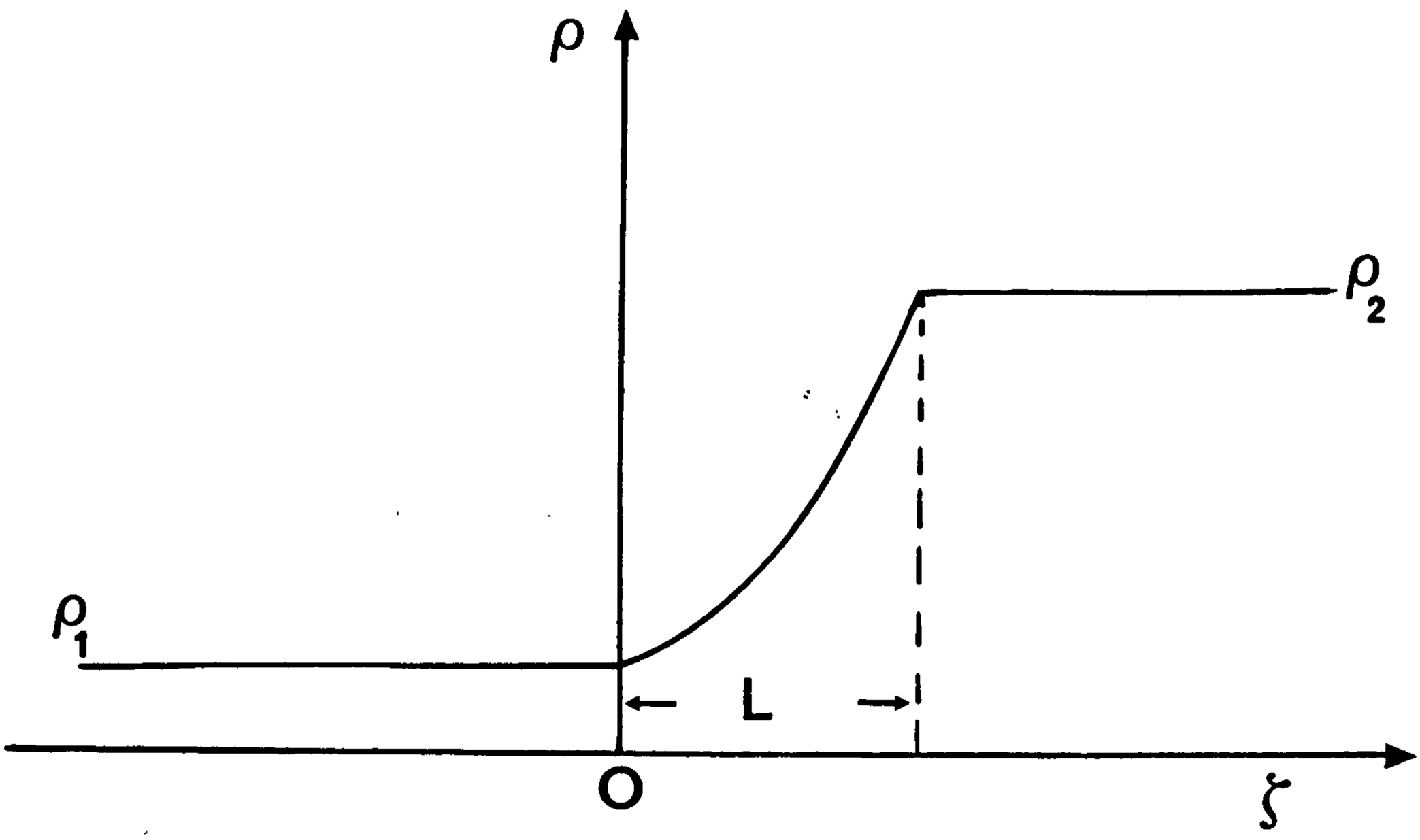

Figure 3.5: An exponentially varying density profile.

3.5 EXPONENTIAL DENSITY TRANSITION PROFILE

In the case of incompressible fluids, there exist simple solutions for the differential equation (3.21) for exponential density variations as is considered by [14, 59, 60]. These will be used to solve the boundary value problem for a density transition profile as shown in figure 3 · 5. Mathematically the exponential density transition profile given below will be studied under the conditions given below:

$$\rho_0(\zeta) = \begin{cases} \rho_1 & \zeta \leq 0 \\ \rho_1 \exp \beta\zeta & 0 \leq \zeta \leq L \\ \rho_2 = \rho_1 \exp \beta L & \zeta \geq L \end{cases} \tag{3.53}$$

where β is a constant, defined as

$$\beta = \frac{L}{l} \tag{3.54}$$

Also, defining

$$l = \frac{L}{ln(\rho_2/\rho_1)} \tag{3.55}$$

where

$$\frac{\rho_2}{\rho_1} = \frac{1-a}{1+a} \tag{3.56}$$

The differential equation (3.31) then becomes

$$\frac{d^2v_z}{d\zeta^2} + \beta\frac{dv_z}{d\zeta} - \alpha^2\left\{1 - \frac{\beta}{\alpha Y}\right\}v_z = 0 \tag{3.57}$$

This equation is solved to find the numerical solution to compare with the analytical solutions.

3.5.1 Analytical Solution

The above equation satisfies the solution of the type,

if $\sigma^2 > 0$, then

$$v_z = Ae^{-\frac{\beta}{2}\zeta}\cos(\sigma\zeta + \Gamma) \tag{3.58}$$

Differentiating this equation twice and using the the resulting values into equation (3.57), we can find out

$$\sigma^2 = -\left[\frac{\beta^2}{4} + \alpha^2 - \frac{\alpha\beta}{Y}\right] \tag{3.59}$$

Now for the boundary condition, we can find out at $\zeta = 0$ and in the region of constant density we can have

$$\frac{dv_z/d\zeta}{v_z} = \alpha \tag{3.60}$$

$$\frac{dv_z/d\zeta}{v_z} = -\frac{\beta}{2} - \sigma\tan(\Gamma) \tag{3.61}$$

These equations combine to give

$$\tan\Gamma = -\frac{(\alpha + \beta/2)}{\sigma} \tag{3.62}$$

For the other boundary condition, in the region of constant density we can have at $\zeta = 1$

$$\frac{dv_z/d\zeta}{v_z} = -\alpha \tag{3.63}$$

$$\frac{dv_z/d\zeta}{v_z} = -\frac{\beta}{2} - \sigma\tan(\sigma + \Gamma) \tag{3.64}$$

Therefore, these could give us the equation of the form

$$\tan(\sigma + \Gamma) = \frac{(\alpha - \frac{\beta}{2})}{\sigma} \tag{3.65}$$

Combining equations (3.62 & 3.65), we find

$$2\sigma \cot \sigma = \frac{\sigma^2 + (\beta/2)^2 - \alpha^2}{\alpha} \tag{3.66}$$

Alternatively, we can have the solution of the type,

if $\sigma^2 < 0$, then

$$v_z = Ae^{-\frac{\beta}{2}\zeta} \cosh(\sigma\zeta + \Gamma) \tag{3.67}$$

Differentiating this equation twice and using the result in the equation (3.57) we can find

$$\sigma^2 = (\beta^2/4 + \alpha^2 - \alpha\beta/Y) \tag{3.68}$$

Therefore for the boundary condition at $\zeta = 0$

$$\frac{dv_Z/d\zeta}{v_z} = \alpha \tag{3.69}$$

$$\frac{dv_z/d\zeta}{v_z} = -\frac{\beta}{2} + \sigma \tanh \Gamma \tag{3.70}$$

these equations combine to give

$$\tanh \Gamma = \frac{(\beta/2 + \alpha)}{\alpha} \tag{3.71}$$

and at $\zeta = 1$

$$\frac{dv_z/d\zeta}{v_z} = -\alpha \tag{3.72}$$

$$\frac{dv_z/d\zeta}{v_z} = -\beta/2 - \sigma \tanh(\sigma + \gamma) \tag{3.73}$$

therefore, we can have

$$\tanh(\sigma + \Gamma) \doteq \frac{(\beta/2 - \alpha)}{\sigma} \tag{3.74}$$

Using equation (3.71) in equation (3.74) and with the help of trigonometric algebra we can write

$$2\sigma \coth \sigma = \frac{(\beta/2)^2 - \sigma^2 - \alpha^2}{\alpha} \tag{3.75}$$

If $\alpha \to 0$ i.e. $(kL \to 0)$ then we can have from equation (3.75)

$$\begin{aligned} \sigma^2 &= (\beta/2)^2 - 2\alpha\sigma \coth \sigma - \alpha^2 \\ &\simeq (\beta/2)^2 - \alpha\beta \coth(\beta/2) \end{aligned} \tag{3.76}$$

but

$$a = (\rho_2 - \rho_1)/(\rho_2 + \rho_1) = (e^{-\beta} - 1)/(e^{-\beta} + 1) = \tanh(\beta/2) \tag{3.77}$$

Therefore we can write

$$Y = \frac{\alpha\beta}{(\beta/2)^2+\alpha^2-\sigma^2} \simeq \frac{\alpha\beta}{\alpha\beta\coth(\beta/2)} = a \tag{3.78}$$

and if $\alpha \to \infty$ i.e. (limit $kL \to \infty$), so in this situation we can write $2\sigma\cot\sigma \to \infty$, therefore, $\sigma \to \pi$ or $(n\pi)$

$$Y = \frac{\alpha\beta}{\alpha^2+(\beta/2)^2-\sigma^2} = \frac{\beta/\alpha}{1+(\beta/2\alpha)^2} \tag{3.79}$$

but $\beta/\alpha = 1/kl$, therefore we can have

$$Y \simeq \frac{kl}{1/4 + (kl)^2} \tag{3.80}$$

with

$$l = \frac{L}{\ln(1-a)/(1+a)} \tag{3.81}$$

3.5.2 General Solution

The general solution is found from the two solutions in the appropriate range. Considering the case with β to be fixed and vary α. For small values of α the solution is a hyperbolic function. Taking $\alpha \simeq 0$, we find

$$\sigma \simeq \pm\{(\beta/2) - \frac{\alpha}{\beta}\coth(\beta/2).....\}$$

Thus as α is increased σ increases up the line $\sigma\coth\sigma$ until $\sigma = 0$ when $\sigma\coth\sigma = 1$ as shown in figure $3 \cdot 6$ and

$$\alpha = \sqrt{([1 \pm (\beta/2)^2] - 1)}$$

At this point the solution changes to the circular functions. Further increase in α, σ moves along the branch $0 - \pi$ of $\sigma\cot\sigma$ with $\sigma = \pi/2$ at

$$\alpha = \sqrt{[(\pi/2)^2 + (\beta/2)^2]}$$

Further increase in α leads to

$$\sigma^2 + (\beta/2)^2 - \alpha^2 < 0$$

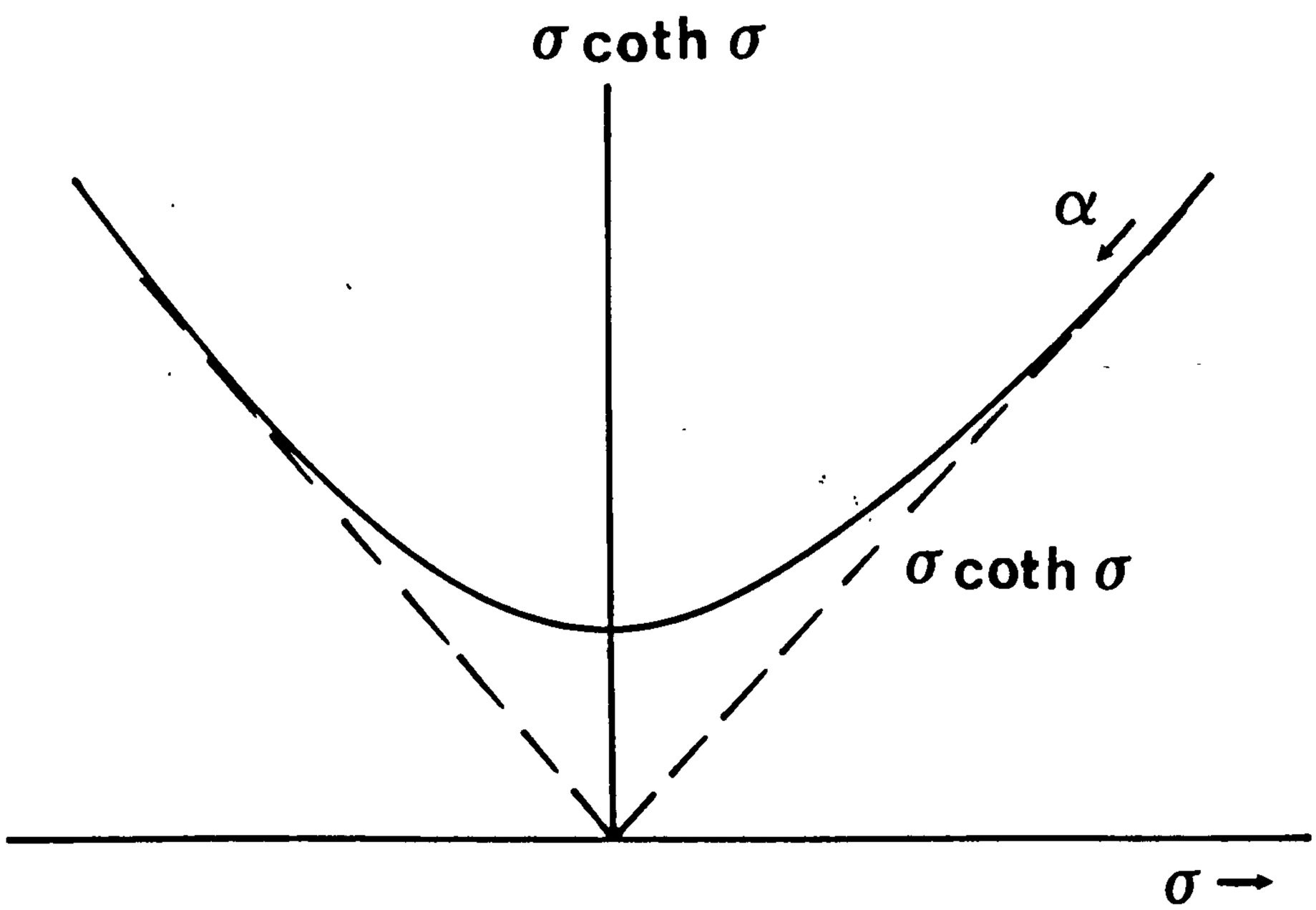

Figure 3.6: Graph of σ vs $\sigma \coth \sigma$

with $\sigma \to \pi$ as $\alpha \to \infty$. This behaviour is shown in figure $3 \cdot 7$

This solution is the fundamental mode with no zeros in the range $0 < z < L$.

Additional modes with the zeros occur on the branch as $\sigma = n\pi$ to $(n+1)\pi$.

For $\alpha = 0$, $(n+1)\pi \geq \sigma \geq n\pi$ such that

$$\sigma = cot^{-1}\{[(n\pi)^2 + (\beta/2)^2]/(2n\pi\alpha)\}$$

and the growth rate will become

$$Y = \frac{\alpha\beta}{(n\pi)^2+\beta^2/4} << \tanh(\beta/2) \quad for \quad n = 0$$

Therefore for small Atwood number $a \simeq 0$, the exponential profile has

$$\beta = \ln(1+a)/(1-a) \simeq 2a$$

with growth rate

$$Y = \frac{\alpha\beta}{\alpha^2 + (\beta^2/4) + \pi^2} \simeq \frac{2\alpha}{\alpha^2+\pi^2}a \tag{3.82}$$

which is similar to the gradual density transition profile for $kL << 1$.

We have plotted equation (3.57) for different Atwood's numbers and have compared these results with the numerical results shown in figure $3 \cdot 8$. Looking at the

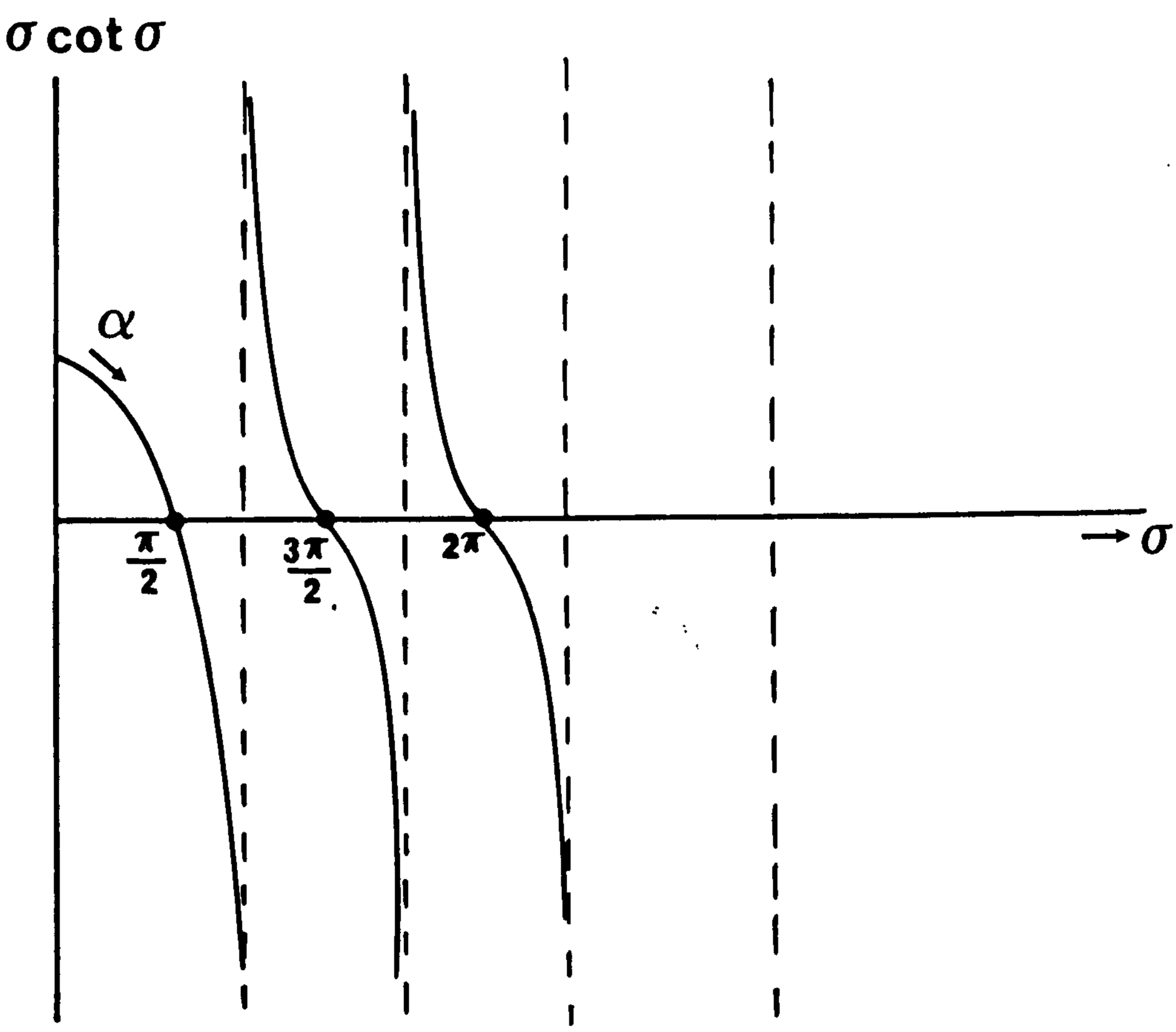

Figure 3.7: Graphical representation of σ vs $\sigma \cot \sigma$

results we notice that the values of the growth of the instability are similar for the kL values up 20 for the numerical and approximate analytical treatment as can be seen from figure 3 · 8. But for higher wavelengths the growth of instability shows differences for analytical and computational cases. The lower growth rates in the case of computational results are due to mode switching in the configuration of the eigenfunction where a higher order mode than the fundamental is evaluated due to numerical error.

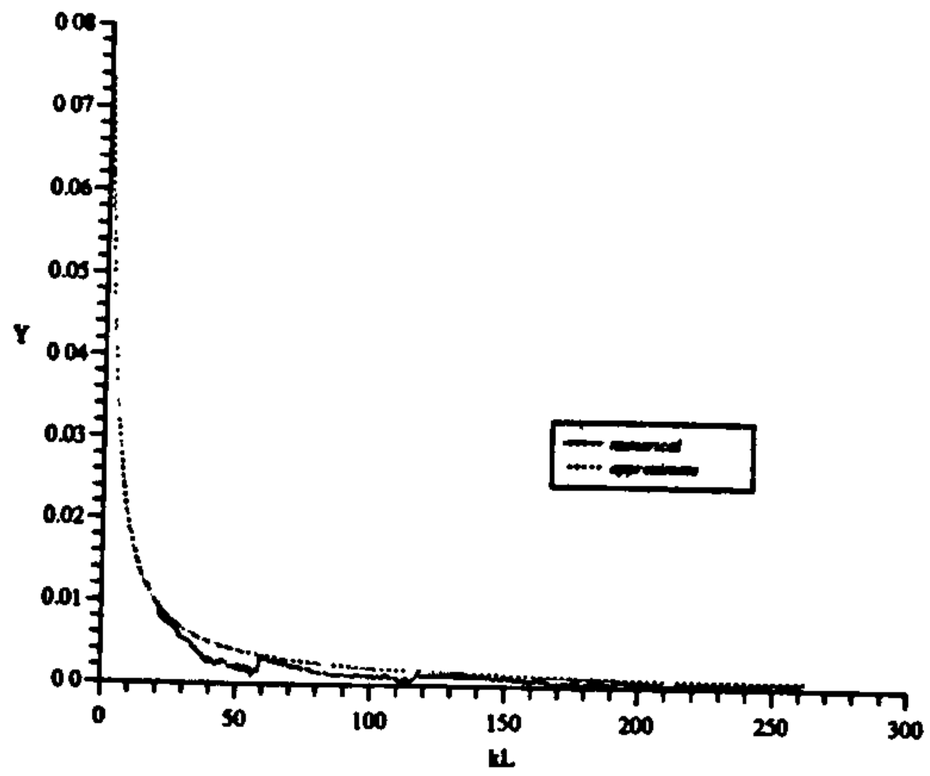

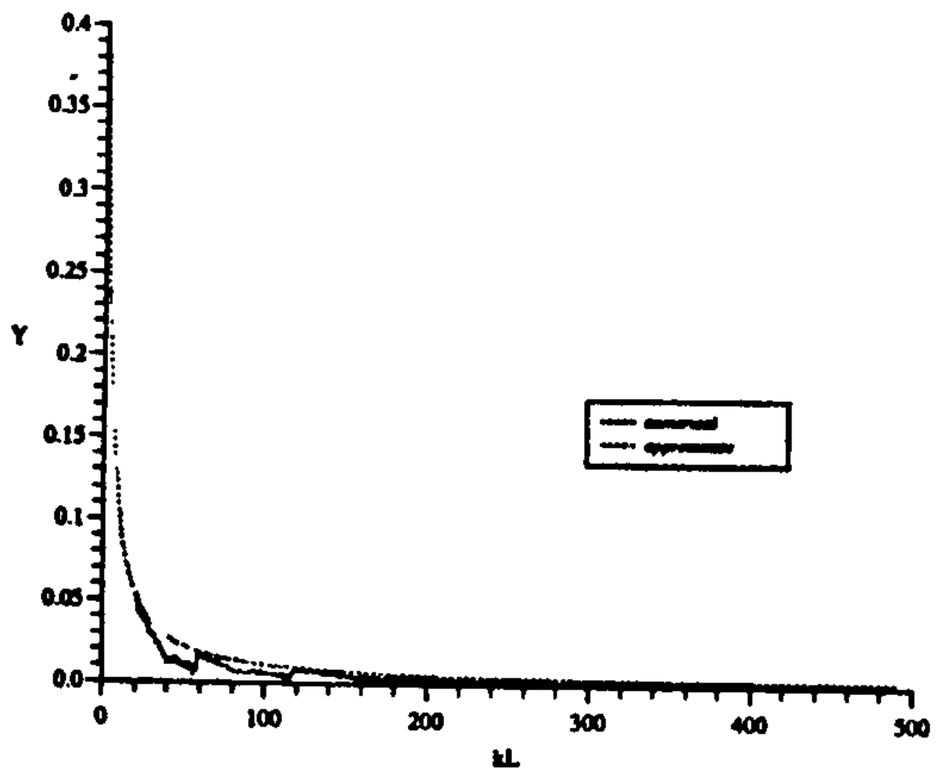

Figure 3.8: Growth rate for exponential profile for different Atwood's numbers

Comparison of Growth Rate for
Exponential Profile for A=0.75

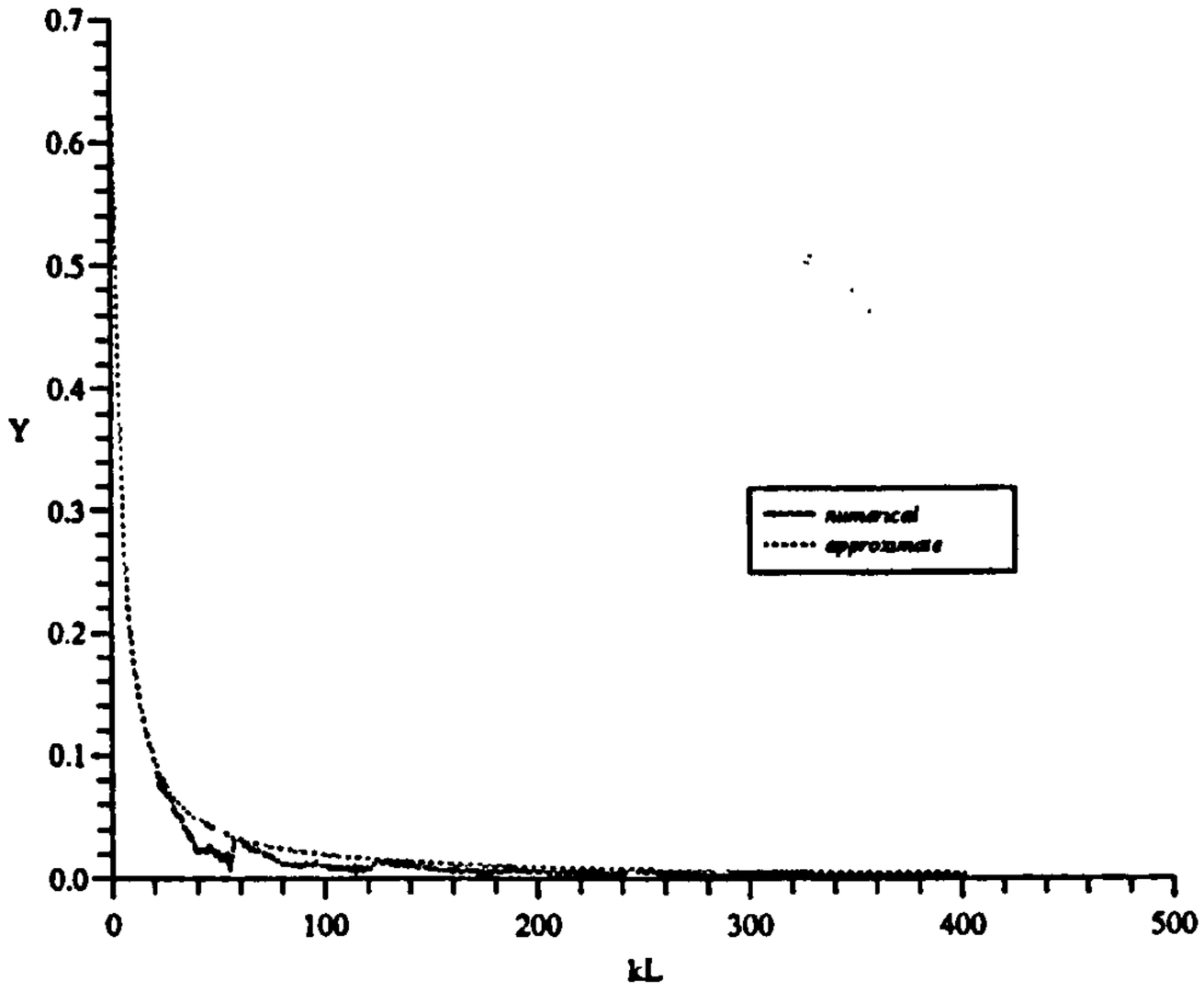

Comparison of Growth Rate for
Exponential Profile for A=0.9

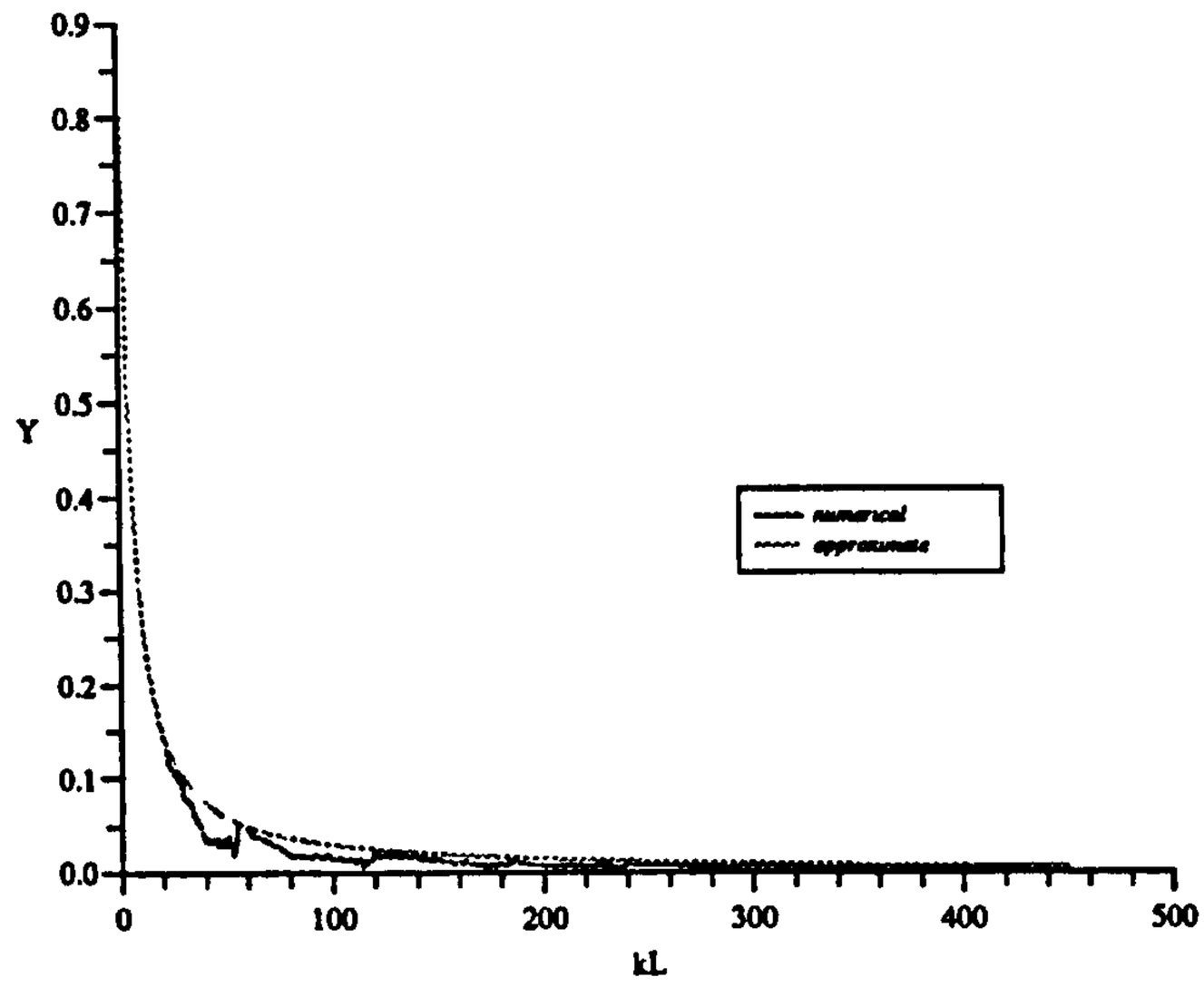

Chapter 4

THE PHYSICAL PROCESSES AND THE CODE MAGT2LD

4.1 INTRODUCTION

The computer code MAGT2LD is used to study the Rayleigh-Taylor instability. The code has been described in detail elsewhere by Pert [70, 72]. It is a two temperature (T_e, T_i) finite difference hydrodynamic code in which the fluid equations are solved on a 2D quasi-Lagrangian rezoning mesh. A cylindrical coordinate system (r,z) is used because of its symmetry about the axis of the incoming laser beam. The mesh is divided into a number of cells as shown in figure 4 · 1. The boundaries in axial direction are free to move in lagrangian fashion whereas the coordinates are fixed in radial direction. The code includes laser absorption by inverse bremsstrahlung and a dump of 20% of energy penetrating to the critical density, the remaining is reflected back which undergoes further absorption. This has been discussed in section 4 · 2. Electron-ion equilibration is studied in section 4 · 4. A flux limited electron ion thermal conduction is included in the code, discussed in section 4 · 5. Megagauss magnetic field are generated when the density and temperature gradients are antiparallel to each other. The field generation and its related phenomenon is reviewed in section 4 · 6.

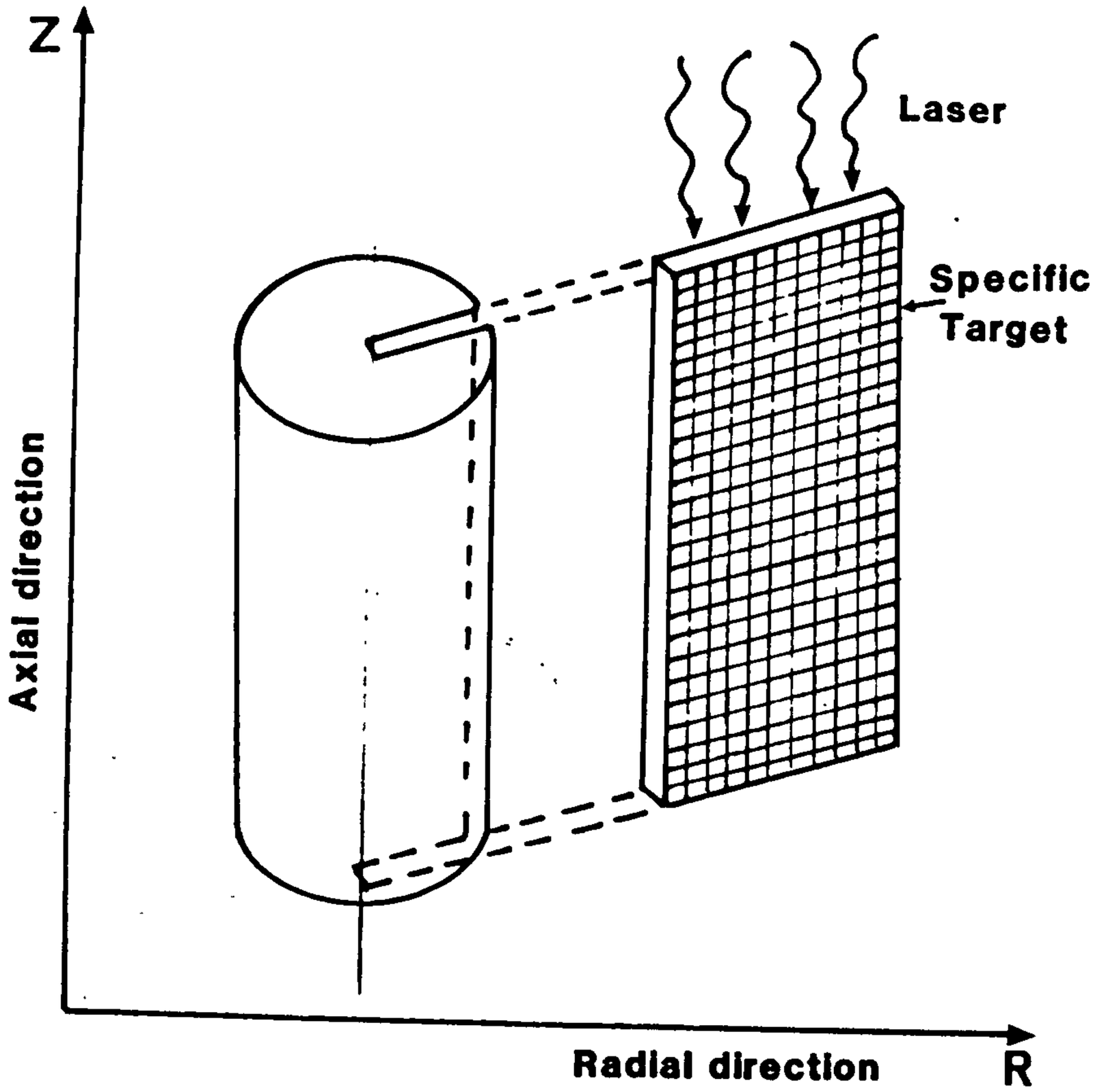

Figure 4.1: The schematic drawing of the computational mesh.

4.2 ENERGY ABSORPTION PROCESS

In Inertial Confinement Fusion, the input laser energy is deposited in the outer region of a tiny pellet to implode the fuel to very high densities for its ignition and efficient thermonuclear burn. The laser light can interact with the plasma in a number of ways. In this section different mechanisms will be discussed by which the incident energy is transported from the deposition region to the ablation surface of the target.

As is well-known the driver beam cannot penetrate beyond the critical density, where the plasma frequency is equal to the light frequency ($\omega_p = \omega_l$). This critical density is usually quite low and most of the input energy is deposited in the corona region, far from the ablation surface. Beyond the critical surface the energy transportation takes place by the process of electron thermal conduction (and possibly other less important mechanisms). Different physical processes and their regions are shown in figure $4 \cdot 2$. In this section two of these processes Inverse bremsstrahlung and Resonance absorption, which are of great importance will be discussed in detail and how they are implemented in the working code MAGT2LD.

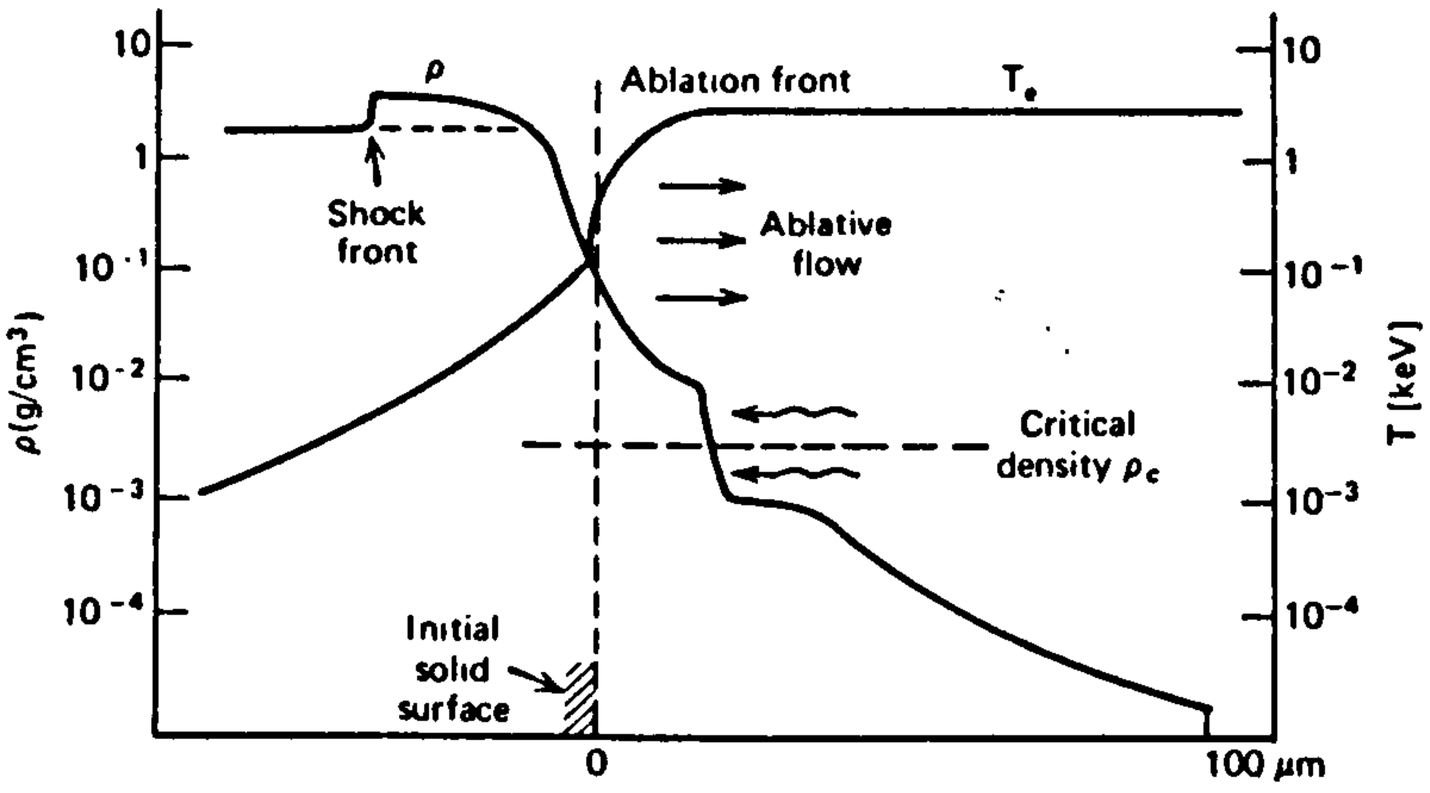

Figure 4.2: Density and temperature profiles in laser produced plasma.

4.2.1 Inverse Bremsstrahlung Process

Energy is absorbed by the process of inverse bremsstrahlung when the incident photon is absorbed by an electron in the ion Coulomb field. This can be explained in the following way. Consider an electron which moves in the oscillating field of an incident electromagnetic wave. These oscillating electrons collide with ions and their 'quiver' kinetic energy is converted into thermal energy. In other words, the incident laser electric field drives electron currents that lead to resistive heating (Joule heating) of the plasma due to charged particle collision. In this way, the incident light energy is deposited in the form of increased electron thermal energy (temperature), which leads to the collisional or Inverse bremsstrahlung process.

In the code MAGT2LD the incoming beam travels parallel to the axial direction in the cylindrical geometry. The intensity (I) is constant over the face upon which laser is incident. In cells whose density is lower than the critical density, the energy is absorbed by this process. Therefore the energy deposition rate per unit volume is given as:

$$\frac{dI}{dZ} = -\alpha I \tag{4.1}$$

where Z is the axis parallel to the laser beam and the absorption coefficient α is given by [71]

$$\alpha = \frac{32\pi^2 Z^2 n_i n_e e^6 \ln \Lambda}{3c\omega_l^2 (2\pi m_e k T_e)^{3/2}} (1 - \frac{\omega_p^2}{\omega_l^2})^{-1/2} \tag{4.2}$$

where ω_l and ω_p are the frequency of incident light and the plasma frequency and n_e, n_i, m_e & $\ln \Lambda$ are the electron and ion number densities, the electron mass and coulomb logarithm respectively.

Integrating equation (4.1) in cylindrical geometry, we obtain

$$I(r, Z, t) = I_0(r, t) \exp\{-\int_Z^\infty \alpha(Z')dZ'\} \tag{4.3}$$

Pert [72] integrated this equation up to the critical density where a fraction (20% in our case) of incident energy is absorbed by resonance absorption. In the code MAGT2LD dumped energy is deposited in the two cells bordering the critical density using finite differencing technique. The remaining energy is reflected back which undergoes further absorption by inverse bremsstrahluing process.

4.2.2 Resonance Absorption

An other method of absorption is the coupling of the incident light into waves in plasma. More specifically the oscillation of the electrons in the electric field of the incident light may directly drive a density fluctuations. The energy is absorbed by this process if it satisfies the conditions that the light must be obliquely incident upon the local density gradient near the critical density and it must have a non-zero p-polarization component of electric field vector parallel to the plasma density gradient which drives the plasma waves. Near the critical density the electric field becomes very large and will resonantly excite these waves. Hence the energy transfer mechanism from light into waves and eventually through the damping of the waves into electron temperature is called the process of resonance absorption.

The phenomenon of resonance absorption can become clear from the figure $4 \cdot 3$, where the electric field of the incident laser light is perpendicular to the plane of the wave vector, k, and density gradient, ∇n, at the turning point there is no electric field component along density gradient. Therefore, near the critical density, the electric field becomes large enough to resonantly excite these waves.

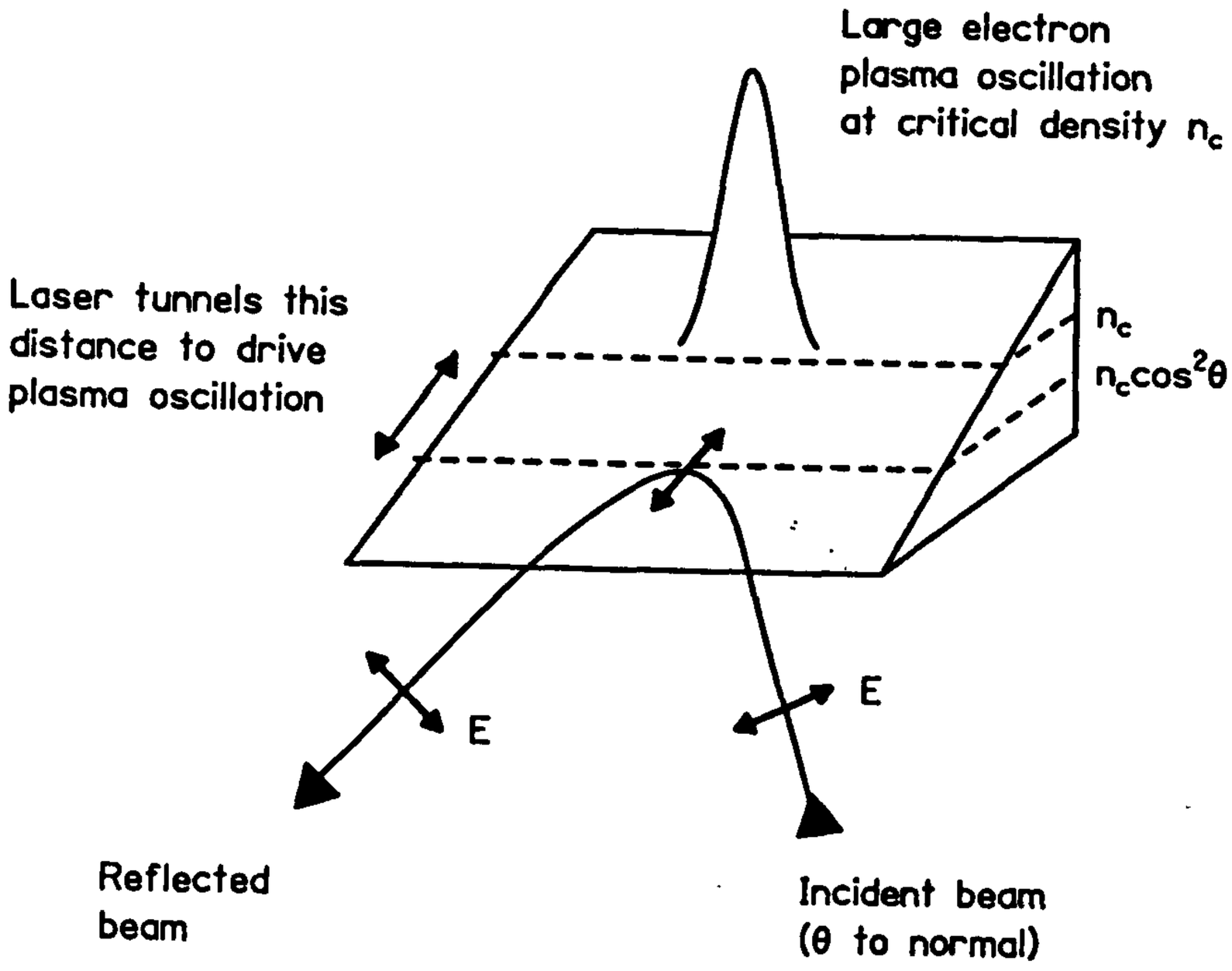

Figure 4.3: Resonance absorption occurs when the light is obliquely incident upon a density gradient.

This becomes absorption as the energy is transferred from the light into the waves and eventually through the damping of the waves into electron temperature.

Considering a p-polarized light in yz-plane, the component of electronic field along the density gradient is given by [73]

$$E_d = E \simeq \frac{E_0}{(\omega_0 L/c)^{1/16}} \sin\theta \left[-\frac{2}{3}\left(\frac{\omega_0 L}{c}\right)\sin^3\theta\right] \tag{4.4}$$

where L (assuming a linear density gradient) is the density gradient scale height given by

$$L = \left[\frac{d(\ln n_e)}{dx}\right]^{-1} \tag{4.5}$$

The fractional absorption is then given by

$$f = \frac{1}{2}\phi^2(\tau) \tag{4.6}$$

where

$$\tau = (k_0 L)^{1/3}\sin\theta \tag{4.7}$$

and

$$\phi(\tau) = 2.31\tau\exp(-\frac{2}{3}\tau^3) \tag{4.8}$$

The electric field becomes [73]

$$E_d = \frac{E_0\phi(\tau)}{\sqrt{2\pi k_0 L}} \quad k_0 >> \frac{1}{L} \tag{4.9}$$

For the resonance absorption to occur, the electric field of the incident light must tunnel from the turning point at $n_c \cos^2\theta$ to the critical density n_c. This fractional absorption of light has been studied by many authors and found to peak at $\tau \simeq 0{\cdot}5$. For typical initial density scale height and laser frequency, the corresponding angle of incidence lies between 20° and 25° [73, 74]. In any event the fraction of incident light that can be absorbed by resonance absorption at the maximum is approximately 50%.

In the code MAGT2LD , 20% of the incident energy is dumped by the process of resonance absorption [72] and the remaining energy is reflected back which is again absorbed by inverse bremsstrahlung process. The dumped energy is deposited in the finite differencing cells bordering the critical surface in the ratio $\rho(high) - \rho(critical) : \rho(critical) - \rho(low)$, to avoid the creation of artificial shocks.

4.3 EQUATION OF STATE

The ideal gas equation of state is used in the code MAGT2LD for the electrons and the ions. The pressure equation for both species are given by

$$P_e = \rho_e(\gamma_e - 1)\epsilon_e \tag{4.10}$$

$$P_i = \rho_i(\gamma_i - 1)\epsilon_i \tag{4.11}$$

and the temperature equations are then given by

$$T_e = \frac{\epsilon_e}{RG_e} \quad T_i = \frac{\epsilon_i}{RG_i} \tag{4.12}$$

where

$$RG_e = \frac{1{\cdot}248 \times 10^8 Z}{m_i}$$

and

$$RG_i = \frac{8{\cdot}32 \times 10^7}{m_i(\gamma - 1)}$$

where γ is the adiabatic constant ($\gamma = 5/3$) and ρ and ϵ are the density and specific internal energy of both electrons and ions.

Atomic processes are not treated the code. It is however understood that their inclusion might modify the magnitude and distribution of the magnetic field [82].

4.4 ELECTRON ION EQUILIBRATION

The plasma in the code MAGT2LD is treated as fully ionized with ions and electrons having different temperatures T_i and T_e respectively. The laser energy is absorbed by the electrons whence there arises a large difference between the two species temperature (i.e. $T_e >> T_i$). The electrons collide with the ions and the rate of thermal energy transfer is given by [75]

$$\frac{d\epsilon_i}{dt} = -\frac{d\epsilon_e}{dt} = -\frac{c_{v_i}(T_i - T_e)}{\tau_{eq}} = -\frac{\epsilon_i - \frac{c_{v_i}}{c_{v_e}}\epsilon_e}{\tau_{eq}} \tag{4.13}$$

where c_{v_i} and c_{v_e} are the electron and the ion specific heats per unit volume and τ_{eq}, is the equilibration time, given by [75]

$$\tau_{eq} = \frac{3m_e m_i k^{3/2}}{8(2\pi)^{1/2} n_i Z^2 e^4 \ln\Lambda}\left(\frac{T_i}{m_i} + \frac{T_e}{m_e}\right)^{3/2} \tag{4.14}$$

where n_i is the ion number density and $\ln\Lambda$ is the Coulomb logarithm. The problem is solved by treating the two species temperatures different. If the equilibration time is kept constant, equation (4.13) is integrated to give the solution [72]

$$\epsilon_e + \epsilon_i = const. \quad \Delta = \Delta_0 \exp(-\tfrac{t}{\tau'_{eq}}) \tag{4.15}$$

where

$$\Delta = \left(\epsilon_i - \frac{c_{v_i}}{c_{v_e}}\epsilon_e\right) \tag{4.16}$$

and

$$\tau'_{eq} = \frac{\tau_{eq}}{(1 + \frac{c_{v_i}}{c_{v_e}})} \tag{4.17}$$

and Δ_0 is the value of Δ at $t = 0$. The finite difference solution of equation (4.15) is given by [72]

$$\Delta^{n+1}_{i+1/2,j+1/2} = \Delta^{n}_{i+1/2,j+1/2} exp\left(-\frac{Dt}{\tau'_{i+1/2,j+1/2}}\right) \tag{4.18}$$

which is stable and positivity maintaining. This is relatively slow during the computation because of its exponential form and could be avoided using its approximate solution provided $Dt \leq L^{-1}$. The total energy is given by

$$\epsilon_i^{n+1} + \epsilon_e^{n+1} = \epsilon_i^n + \epsilon_e^n = \epsilon_{tot} \tag{4.19}$$

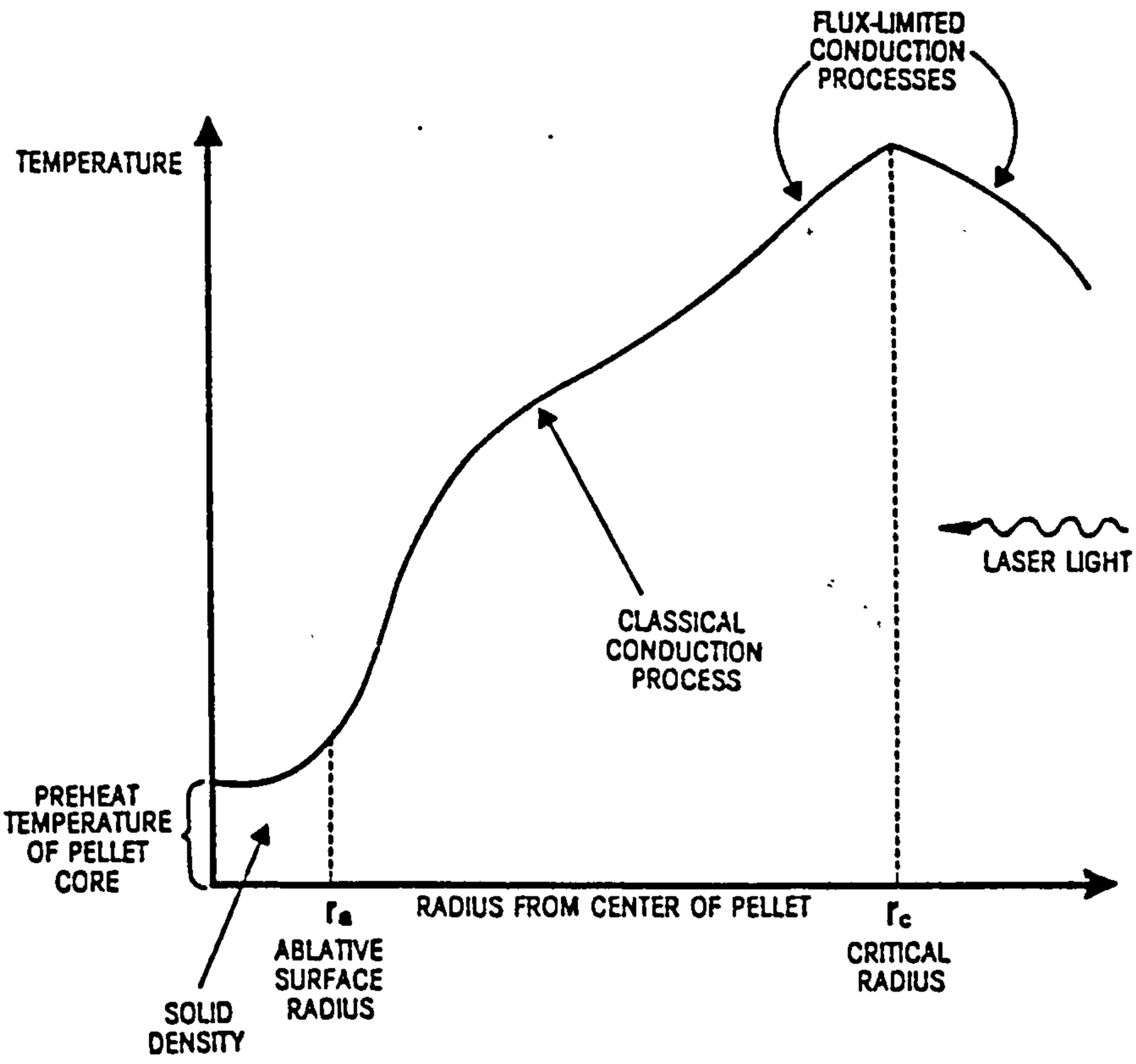

Figure 4.4: Schematic drawing of the temperature profile during ablative process.

and the updated values are then found to be of the form

$$\epsilon_e^{n+1} = \frac{1}{1 + \frac{c_{v_i}}{c_{v_e}}} \left(\epsilon_{tot} - \Delta^{n+1} \right) \epsilon_i^{n+1} \tag{4.20}$$

4.5 FLUX LIMITED THERMAL CONDUCTION

As is well known laser energy deposited near the critical density creates a very high temperature there. The heat is conducted inwards by thermal conduction through the colder plasma until it reaches the solid surface of the pellet, from which the material is being ablated. This heated and ablated material from the pellet flows rapidly outwards as a rarefaction generating very high inwards pressure by conservation of momentum. Different processes are shown in figure 4 · 4. Two features of the profile are very important to note:

1. The finite distance across which the absorbed energy must be conducted between the ablation and critical surface.

2. The temperature profile breaks sharply at the critical surface i.e. the temperature gradients very close to the critical surface become very sharp so that the length of temperature gradients becomes short compared to the electron-ion mean free path.

The classical heat flux is given by [83]

$$q_c = -\kappa \nabla T_e \tag{4.21}$$

where κ is the thermal conductivity defined by [75]

$$\kappa = 20(\frac{2}{\pi})^{3/2} \left\{ \frac{\kappa(\kappa T_e)^{5/2}}{m_e^{1/2} e^4 Z \ln \Lambda} \right\} \tag{4.22}$$

The classical heat flux is valid for small values of temperature gradients, where the electron mean free path is very much smaller than the temperature scale lengths ($\lambda_e << \frac{T_e}{\nabla T_e}$). But in the situation when the temperature changes significantly (e.g. laser produced plasmas) over the distances of the order of λ_e,the heat flux q_c might exceed its physical upper limit giving unrealistically large fluxes. An upper limit, called free streaming limit, allows the heat flux to move no faster than the electron thermal velocity, given as the product of the thermal velocity and energy density [76]. i.e.

$$q_{fs} = f(\frac{3}{2} n k T_e) \left(\frac{3kT_e}{m_e} \right) \tag{4.23}$$

where f is an empirical factor.

Several authors have attempted to drive an appropriate value of f from basic physical considerations. In computer models, the heat flux, a harmonic mean of both classical heat flux and inhibited flux, is used, given by

$$\frac{1}{q} = \frac{1}{q_c} + \frac{1}{q_{fs}} \tag{4.24}$$

Different experiments have been performed, using thin foils, thick layered disk targets and spherical layered targets. Thin layered experimental targets of Malone and others [76] represented empirically $f = 0{\cdot}03$, as the best fit with the numerical models. Solving the Fokker-Plank equation numerically [77], in the study of large temperature gradients on thermal conductivity, the value of f was found to be $0{\cdot}1$. Evans [78] has pointed out how the smoothing is affected in varying the value of f. It has been observed that reducing the flux limit changes the expansion profile

which reduces the distance between the critical and the ablation surface, hence the effective smoothing distance becomes smaller, but at the same time the rate of smoothing is increased because the plasma is hotter. He concludes the increase in smoothing rate does not compensate the reduction in smoothing distance.

When the currents are not co-linear but circulate then we can expect the generation of magnetic fields in the regions of critical density [79, 80] which has been observed of the order of few megagauss. If these fields are large enough so that $\omega\tau \geq 1$ (ω is the electron-ion collision frequency and τ is the cyclotron period), then the thermal flux may be severely limited predicted from the transport coefficients of Braginskii [81].

Bennett [82] in his simulations, using the similar code investigated that the magnetic field effects, for a neodymium glass laser ($\lambda = 1 \cdot 06\mu m$), could be accounted by using more restrictive flux limit of the order of $0 \cdot 01 \leq f \leq 0 \cdot 035$. More recently, thermal heat transport in the presence of magnetic fields has been modified to include effects associated with steep temperature gradients. For the magnetic fields of the value ($\omega_0 \tau_{ei} > 0 \cdot 2$) a strong reduction occurs in heat flux. The flux limiting factor for these magnetic field values was found to be of the order of $0 \cdot 05$ or even less.

4.6 MAGNETIC SOURCE TERM

The equations which give the evolution of magnetic field generation are derived by Pert [41].

$$\frac{\partial \mathbf{B}}{\partial t} - \nabla \times (\mathbf{v} \times \mathbf{B}) + \nabla \times [\eta.(\nabla \times \mathbf{B})] = \nabla \times \mathbf{S} \qquad (4.25)$$

The second and third terms on the left hand side of this equation are called the advection and magnetic diffusion respectively whereas the term on the right hand side is the magnetic source term. Here $\mathbf{v}$ is the plasma bulk velocity and η is called magnetic diffusivity tensor. The source and the diffusivity tensor are written in the convenient form [41]

$$\mathbf{S} = \frac{c}{e}\left[\frac{1}{n_e}\nabla(p_e) + \beta^{\circ}.\nabla(kT_e)\right] \qquad (4.26)$$

and

$$\eta = \left(\frac{c^2}{4\pi}\right)\xi' \tag{4.27}$$

with

$$\xi'_{\|} = \xi_{\|} \quad \xi'_{\perp} = \xi_{\perp} \quad \xi'_{\wedge} = \xi_{\wedge} + \frac{B}{en_e c} \tag{4.28}$$

where the subscript $\|$, $\perp$ and $\wedge$ are called parallel, perpendicular and cross present components to the magnetic field and the component perpendicular to both of these, respectively. The thermo-electric diffusivity tensor β is explained in detail by Braginskii [81].

If the effect of β° is very small, then for the ideal gas we may write equation (4.25) as

$$\begin{aligned} \nabla \times \mathbf{S} &= \nabla \times (\tfrac{c}{en_e}\nabla p_e) \\ &= \tfrac{c}{e}\nabla(kT_e) \times \nabla(\ln n_e) \\ &= \tfrac{ck}{en_e}\nabla T_e \times \nabla n_e \end{aligned} \tag{4.29}$$

For a cylindrical symmetric system, T_e and n_e are function of r and z only, so the azimuthal component of equation (4.29) is given by

$$\nabla \times \mathbf{S} = \frac{ck}{en_e}\left[\frac{\partial T_e}{\partial z}\cdot\frac{\partial n_e}{\partial r} - \frac{\partial T_e}{\partial r}\cdot\frac{\partial n_e}{\partial z}\right] \tag{4.30}$$

In the code, MAGT2LD, the incoming laser beam is in the axial direction, so the main effective terms are $\frac{\partial T_e}{\partial r}$ and $\frac{\partial n_e}{\partial z}$ as shown in figure $2 \cdot 3$. This means that magnetic flux is generated negatively closed loops perpendicular to (r, z) plane about the z-axis as shown in figure $2 \cdot 3$. It is also clear from the second term in equation (4.26) that when $\mathbf{B} = 0$ then

$$\beta^\circ_{\|} = \beta^\circ_{\perp} = const \quad \beta^\circ_{\wedge} = 0 \tag{4.31}$$

Therefore

$$\nabla \times \mathbf{S} = \nabla \times \{\tfrac{c}{e}\beta^\circ_{\|}.\nabla(kT_e)\} = 0 \tag{4.32}$$

This shows that thermoelectric term is not a source generating magnetic field but modifyies the existing fields in the plasma. It can now be written in modified form [41].

$$\mathbf{S} = \tfrac{c}{e}\beta.\nabla(kT_e) \tag{4.33}$$

where

$$\beta_{\|} = \beta^\circ_{\|} - \ln(n_e), \quad \beta_{\perp} = \beta^\circ_{\perp} - \ln(n_e) and \quad \beta_{\wedge} = \beta^\circ_{\wedge} \tag{4.34}$$

Equation (4.25) satisfies a conservation law for the magnetic flux [41, 70]

$$\phi = \int \mathbf{B}.d\mathbf{S} \tag{4.35}$$

4.6.1 Energy Equations

With the above form of source term, the electron energy equation is written as [41, 70]

$$\frac{\partial \epsilon_e}{\partial t} + \nabla.(\epsilon_e \mathbf{v}) + \mathbf{p_e}\nabla.\mathbf{v} + \nabla.\mathbf{q_t} = W_e - G - J + j.\nabla\left[\frac{3}{2}\frac{kT_e}{e}\right] + \xi j^2 + \frac{kT_e}{e}\nabla.(j.\beta) \tag{4.36}$$

where the current density is given by

$$j = \frac{c}{4\pi}\nabla \times \mathbf{B} \tag{4.37}$$

and ϵ_e, p_e & T_e are the electron energy density, pressure and temperature respectively. G is the electron ion equilibration transfer rate [75] which has already been explained in section $4 \cdot 4$. W_e is the laser energy deposition rate per unit volume and $J = n_e e(\xi.j)\mathbf{v}$ an additional ion electron exchange rate not included in the code.

The thermal heat flux is the usual thermal conduction term plus contribution from the thermoelectric effect because the quantities j and β° do not commute. Therefore, we may write

$$\mathbf{q}_t = -\kappa_e.\nabla(kT_e) - [2\beta_\wedge(\mathbf{h} \times \mathbf{j})kT_e/e] \tag{4.38}$$

where $\mathbf{h} = \frac{\mathbf{B}}{|B|}$, a unit vector in the direction of **B**.

In a similar fashion, the ion energy equation is written as

$$\frac{\partial \epsilon_i}{\partial t} + \nabla.(\epsilon_i \mathbf{v}) + p_i\nabla.\mathbf{v} + \nabla.\mathbf{q}_i = W_i + G + J \tag{4.39}$$

W_i is the external heating rate per unit volume taken to be zero in the code and $\mathbf{q}_i = -\kappa_i.\nabla T$ the ion thermal conduction flux and ϵ_i and p_i are the pressure and energy of heavy particle respectively.

Equations (4.36) and (4.39) can be written together in conservation forms and Pert [41] notes the existence of fluxes due to magnetic source and ohmic heating.

The bulk Lorentz force has also an effect on the flow velocity because of magnetic field effects. Therefore the Euler's equation becomes:

$$\rho(\frac{\partial \mathbf{v}}{\partial t} + (\mathbf{v}.\nabla)\mathbf{v}) = \frac{1}{4\pi}(\mathbf{B}.\nabla)\mathbf{B} - \frac{1}{8\pi}\nabla(B^2) - \nabla(p_e + p_i) \tag{4.40}$$

The plasma must obey the equation of continuity:

$$\frac{\partial \rho}{\partial t} + \nabla.(\rho \mathbf{v}) = 0 \tag{4.41}$$

4.6.2 Source Terms

In the cylindrical coordinate system, the equations (4.25) and (4.36) can be written in the following form

$$\begin{aligned} \frac{\partial B}{\partial t} = \; & \frac{\alpha c}{e}\left[\frac{\partial}{\partial r}\left(E\frac{\partial \beta_\perp}{\partial z}\right) - \frac{\partial}{\partial z}\left(E\frac{\partial \beta_\perp}{\partial r}\right)\right. \\ & \left. + \frac{\partial}{\partial z}\left(\beta_\wedge \frac{\partial E}{\partial z}\right) + \frac{\partial}{\partial r}\left(\beta_\wedge \frac{\partial E}{\partial r}\right)\right] \end{aligned} \tag{4.42}$$

$$\begin{aligned} \frac{\partial}{\partial t}(\ln E) = \; & \frac{\alpha c}{4\pi c \rho}\left[\frac{\partial \beta_\perp}{\partial z}.\frac{1}{r}\frac{\partial}{\partial r}(Br) - \frac{\partial \beta_\perp}{\partial r}\frac{\partial B}{\partial z}\right. \\ & \left. - \frac{\partial}{\partial z}\left(\beta_\wedge \frac{\partial B}{\partial z}\right) - \frac{1}{r}\frac{\partial}{\partial r}\left\{\beta_\wedge \frac{\partial}{\partial r}(Br)\right\}\right] \end{aligned} \tag{4.43}$$

It is important to note that the term $E/\rho\frac{\partial \rho}{\partial t}$ which is expected from $\frac{\partial \epsilon}{\partial t}$, is not used in equation (4.43), because it is more appropriately used in the energy convection equation. In finite difference form the equation becomes

$$\begin{aligned} B^{n+1}_{i+1/2,j+1/2} = \; & B^n_{i+1/2,j+1/2} \\ & \frac{\alpha c Dt}{e}\left[\frac{1}{\Delta z \delta R}\left\{\delta(E\Delta\beta_\perp)_{i+1/2,j+1/2} - \Delta(E\delta\beta_\perp)_{i+1/2,j+1/2}\right\}\right. \\ & \left. + \{\Delta(\beta_\wedge \Delta E)/\Delta z^2\}_{i+1/2,j+1/2} + \{\delta(\beta_\wedge \delta E)/\delta R^2\}_{i+1/2,j+1/2}\right] \end{aligned} \tag{4.44}$$

and

$$\begin{aligned} E^{n+1}_{i+1/2,j+1/2} = \; & E^n_{i+1/2,j+1/2} \exp\left[\frac{\alpha c Dt}{4\pi e \rho_{i+1/2,j+1/2}}\right. \\ & \left\{\frac{1}{\Delta z \delta R}\left[\{\Delta\beta_\perp \delta(Br)/r\}_{i+1/2,j+1/2} - \{\delta\beta_\perp \Delta B\}_{i+1/2,j+1/2}\right]\right. \\ & \left.\left. - \Delta\{\beta_\wedge \Delta B/\Delta z^2\}_{i+1/2,j+1/2} - [\delta\{\beta_\wedge \delta(Br)\}/r\delta R^2]_{i+1/2,j+1/2}\right\}\right] \end{aligned} \tag{4.45}$$

The solution of the difference equations for B and E are obtained by ADI technique [70].

4.6.3 Magnetic Diffusion and Ohmic Heating

Pert [70] grouped these effects together since the magnetic energy dissipated by diffusion is seen as ohmic heating in the electron energy balance equation. In cylindrical geometry the magnetic diffusion from equation (4.25) can be written in the following form

$$\begin{aligned}\frac{\partial B}{\partial t} = \; & \frac{\partial}{\partial z}\left\{\eta_{\perp}\frac{\partial B}{\partial z}\right\} + \frac{\partial}{\partial r}\left\{\frac{\eta_{\perp}}{r}\frac{\partial}{\partial r}(Br)\right\} \\ & + \frac{\partial}{\partial r}\left(\frac{\eta_{\wedge}}{r}\right)\frac{\partial}{\partial z}(Br) - \frac{\partial}{\partial z}\left(\frac{\eta_{\wedge}}{r}\right)\frac{\partial}{\partial r}(Br)\end{aligned} \tag{4.46}$$

and the equation for the ohmic heating is given by

$$\frac{\partial w}{\partial t} = \frac{1}{4\pi}\eta_{\perp}\left\{\left(\frac{\partial B}{\partial z}\right)^2 + \left(\frac{1}{r}\frac{\partial}{\partial r}(Br)\right)^2\right\} \tag{4.47}$$

This involves only $\eta_{\perp}$, since B is purely azimuthal.

The equation for magnetic diffusion can now be written in its finite difference form in the following

$$\begin{aligned}B^{n+1}_{i+1/2,j+1/2} = \; & B^{n}_{i+1/2,j+1/2} + Dt\left[\Delta\left\{\eta_{\perp}\Delta B\right\}_{i+1/2,j+1/2}/\Delta z^2\right. \\ & + \delta\left\{\eta_{\perp}/r\delta(Br)\right\}_{i+1/2,j+1/2}/\delta R^2 \\ & \left. + \left\{\delta[\eta_{\wedge}\Delta B]_{i+1/2,j+1/2} - \Delta[\eta_{\wedge}/r\delta(Br)]_{i+1/2,j+1/2}\right\}/\Delta z\delta R\right]\end{aligned} \tag{4.48}$$

In a similar way the finite difference equation for the ohmic heating term is written as

$$\begin{aligned}w_{i+1/2,j+1/2} = \; & \frac{Dt}{8\pi}\left[\left(\eta_{\perp_{i+1,j+1/2}}[\Delta B]^2_{i+1,j+1/2} + \eta_{\perp_{i,j+1/2}}[\Delta B]^2_{i,j+1/2}\right)/\Delta z^2\right. \\ & \left. + \left(\eta_{\perp_{i+1/2,j+1}}[\delta(Br)/r]^2_{i+1/2,j+1} + \eta_{\perp_{i+1/2,j}}[\delta(Br)/r]^2_{i+1/2,j}\right)/\delta R^2\right]\end{aligned} \tag{4.49}$$

The implicit equations are solved by asymmetric ICCG [70] method in the code MAGT2LD.

4.6.4 Thermal Energy Diffusion

In these terms we consider the individually energy conservative terms involving electron thermal conduction, current convection and the residual thermo-electric flux. In cylindrical geometry the governing differential equation can be written as

$$\begin{aligned}\frac{\partial E}{\partial t} = \; & \frac{\partial}{\partial z}\left(\chi_{\perp}\frac{\partial E}{\partial z}\right) + \frac{1}{r}\frac{\partial}{\partial r}\left(r\chi_{\perp}\frac{\partial E}{\partial r}\right) \\ & + \frac{1}{r}\left[\frac{\partial}{\partial r}(r\chi'_{\wedge})\frac{\partial E}{\partial z} - \frac{\partial(r\chi'_{\wedge})}{\partial z}\frac{\partial E}{\partial r}\right] \\ & + \frac{\alpha c}{4\pi e\rho}\left\{\frac{1}{r}\frac{\partial}{\partial r}\left[2\beta_{\wedge}E\frac{\partial}{\partial r}(Br)\right] + \frac{\partial}{\partial z}\left[2\beta_{\wedge}E\frac{\partial B}{\partial}\right]\right\}\end{aligned} \tag{4.50}$$

The current convection term is included with the cross product heat conduction (Righi-Leduc) term by defining the coefficients

$$\chi_\perp = \alpha k_\perp / k \quad \chi'_\wedge = \alpha(k_\wedge / k + cB/4\pi) \tag{4.51}$$

where $k_\perp$ and $k_\wedge$ are the coefficients of electron thermal conduction. In the finite difference form this equation is written by Pert [70]

$$\begin{aligned} E^{n+1}_{i+1/2,j+1/2} = \; & E^n_{i+1/2,j+1/2} + Dt\left[\Delta\left[\chi_\perp \Delta E\right]_{i+1/2,j+1/2}/\Delta z^2\right. \\ & + \left[\tfrac{1}{r}\delta\left\{r\chi_\perp \delta E\right\}\right]_{i+1/2,j+1/2}/\delta R^2 \\ & + \tfrac{1}{2}\tfrac{1}{r_{j+1/2}}\left\{\left[\Delta E \delta(r\chi'_\wedge)\right]_{i+1,j+1/2} + \left[\Delta E \delta(r\chi'_\wedge)\right]_{i,j+1/2}\right. \\ & \left. - \left[\delta E \Delta(r\chi'_\wedge)\right]_{i+1/2,j+1} - \left[\delta E \Delta(r\chi'_\wedge)\right]_{i+1/2,j}\right\}/\Delta z \delta R \\ & \tfrac{2\alpha c}{4\pi c \rho_{i+1/2,j+1/2}}\left\{\tfrac{1}{r_{j+1/2}}\delta\left[\beta_\wedge E \delta(Br)\right]_{i+1/2,j+1/2}/\delta R^2\right. \\ & \left.\left. + \Delta\left[\beta_\wedge E \Delta B\right]_{i+1/2,j+1/2}/\Delta z^2\right\}\right] \end{aligned} \tag{4.52}$$

Pert [70] again used ICCG method in the code MAGT2LD.

4.6.5 Magnetic Stress/Advection

In this case the complementary terms are the Lorentz force terms in Euler's equation. Therefore, In cylindrical geometry, we have

$$\rho\frac{\partial u}{\partial t} = -\frac{1}{8\pi}\frac{\partial}{\partial z}(B^2) \tag{4.53}$$

$$\rho\frac{\partial v}{\partial t} = -\frac{1}{4\pi}\frac{B^2}{r} - \frac{1}{8\pi}\frac{\partial}{\partial r}(B^2) \tag{4.54}$$

and the advection equation

$$\frac{\partial B}{\partial t} = -\frac{\partial}{\partial z}(uB) - \frac{\partial}{\partial z}(vB) \tag{4.55}$$

The face-centered differencing is

$$\left.\frac{\partial}{\partial r}(B^2)\right|_{i+1/2,j+1/2} \Rightarrow \frac{1}{2}\left\{\frac{r_{j+1}[\delta(B^2)]_{i+1/2,j+1} + r_j[\delta(B^2)]_{i+1/2,j}}{r_{j+1/2}}\right\}/\delta R \tag{4.56}$$

we use a face-centered form of B^2

$$\left.\frac{B^2}{r}\right|_{i+1/2,j+1/2} \Rightarrow \frac{1}{2}\frac{[(B)_{i+1/2,j+1}]^2 + [(B)_{i+1/2,j}]^2}{r_{j+1/2}} \tag{4.57}$$

or in direct difference form

$$\left.\frac{\partial}{\partial r}(B^2)\right|_{i+1/2,j+1/2} \Rightarrow \frac{1}{2}\left\{(B^2)_{i+1/2,j+3/2} - (B^2)_{i+1/2,j+1/2}\right\}/\delta R \tag{4.58}$$

and

$$\left.\frac{B^2}{r}\right|_{i+1/2,j+1/2} \Rightarrow \frac{1}{2}\frac{[B_{i+1/2,j+3/2}B_{i+1/2,j+1} + B_{i+1/2,j}B_{i+1/2,j+1/2}]}{r_{j+1/2}} \tag{4.59}$$

It is easily shown that the contribution of these two terms is identical from both prescriptions.

4.7 RUNNING THE CODE

The input data in the code are the parameters describing the laser pulse and the target composition. The mesh coordinates are fixed in radial direction and the quasi-Lagrangian rezoning scheme is applied in the axial direction as the incoming laser beam is along this direction. The code is written in Fortran and is run on IBM-3070 at Rutherford Appleton Laboratory. The mesh is divided into 80×50 cells in Z and R respectively. As it is not possible to run the code up to the required time, therefore, the Dump/Restart facilities are written within the code to perform very long runs, especially when the magnetic field terms are included.

Chapter 5

INSTABILITY DEVELOPMENT FROM A DENSITY PERTURBATION

5.1 INTRODUCTION

In our computational study of the Rayleigh-Taylor instability a polythene target, $(CH_2)_n$, with mass and charge numbers 4.67 and 2.67 respectively is uniformly irradiated by a $0 \cdot 53\mu m$ laser pulse. The target thickness and radius are not fixed parameters during our studies, and may vary in different simulations. The perturbation wavelength is also varied in these simulations and we have applied one of two wavelength perturbations in most of the cases discussed in our studies. During the study of the Rayleigh-Taylor instability presented in this chapter, a sinusoidal perturbation is applied to the mass (through the density) with different wavelengths and for different simulations we have used amplitude as a fixed parameter, $0 \cdot 1\mu m$.

In all the simulations the mesh is radially Eulerian because there is no hydrodynamical expansion in that direction and the quasi-Lagrangian rezoning scheme is applied in the axial direction as the incoming laser is irradiated parallel in this direction. The computational mesh is divided into (80×50) cells in the axial and the radial directions respectively. We have run the code twice having all the parameters the same for a specified run except the magnetic field is included in

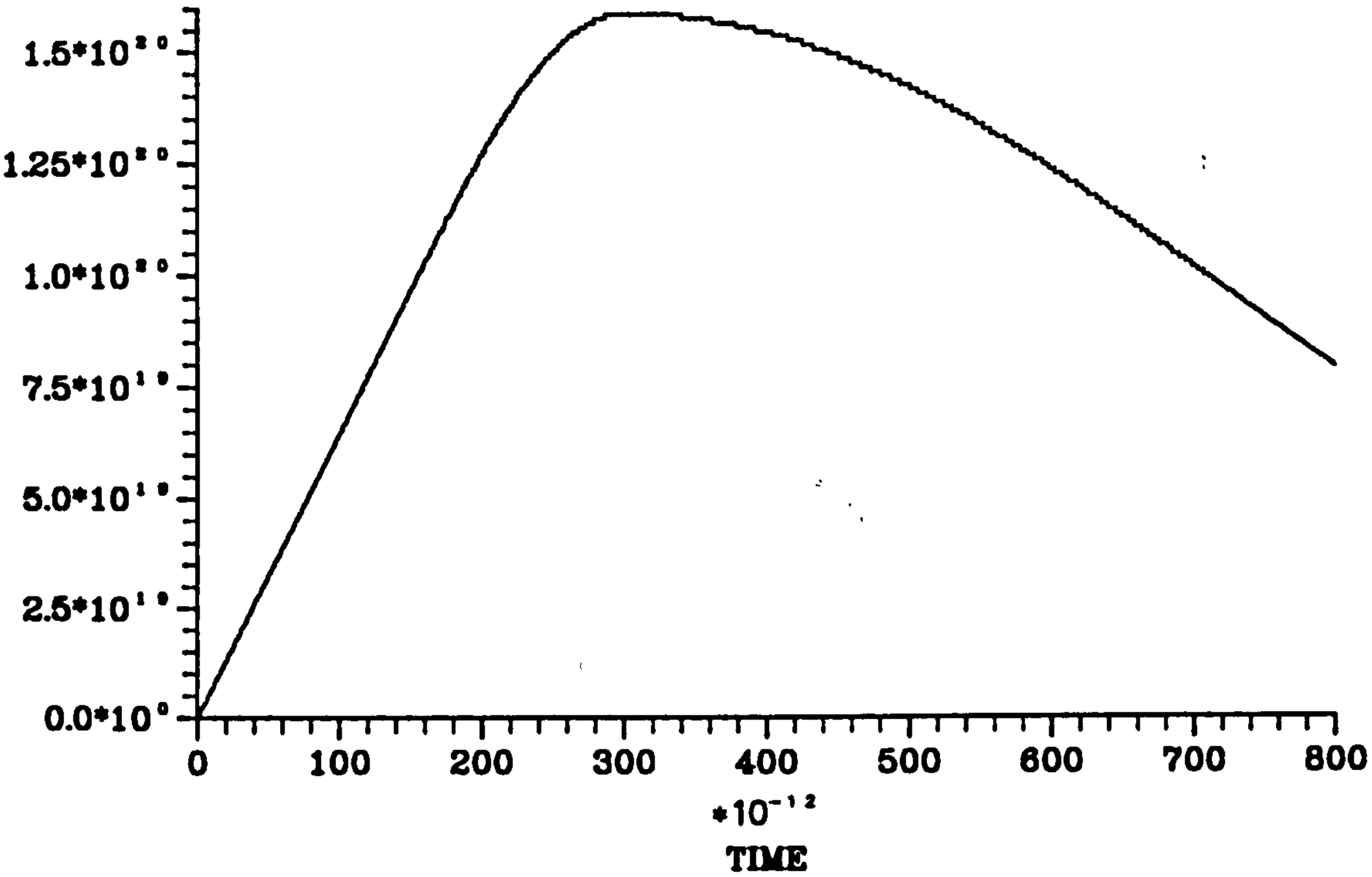

Figure 5.1: Laser pulse shape used during the computer simulation

one run, and not in the other.

The laser intensity is uniform in space and the laser pulse is shown in figure $5 \cdot 1$. The pulse has a very fast rise time which reaches to its peak in 300ps and a gradual fall off to its minimum in 2ns. The simulations are stopped at 800ps because at this time mixing starts to take place and most of the target material has burnt through.

The reflection coefficient, REF, a fixed parameter in our studies, is set to $0 \cdot 8$ so that only 20% of the incident energy reaching the critical density is dumped into the plasma there and the remaining is reflected back. The flux limiter is also a fixed fraction, $f = 0 \cdot 1$, of the classical free streaming limit in all the simulations.

5.2 STANDARD TEST RUN NO. 1

In the simulations presented in this section a polythene target of thickness $5 \cdot 0 \mu m$ and a radius of $2 \cdot 5 \mu m$ is irradiated uniformly by a $0 \cdot 53 \mu m$ laser. A sinusoidal perturbation of wavelength $1 \cdot 25 \mu m$ with a $0 \cdot 1 \mu m$ perturbation amplitude is applied in the axial direction. All the necessary laser, target and the transport

parameters are given in table 5 · 1.

The code MAGT2LD is run on IBM-3090 computer at Rutherford Appleton Laboratory with magnetic field included and excluded for up to 800ps of the laser pulse duration. It took about 4 CPU hours when the magnetic field routines are not switched on and about 25 CPU hours when the magnetic field routines are included. The enormous difference of CPU time is because considerable time is required to solve the magnetic energy routines.

5.2.1 Discussion

The time history of plasma density for both cases when the magnetic field is on and off over this period is shown by contour maps in figure 5 · 2 with a time difference of 10ps for up to 100ps and 50ps for the rest of the run. For the sake of comparison of the time history development of Rayleigh-Taylor instability we have presented these maps for both cases on the same page. It is clear from these figures that until the time reaches 30ps the behaviour of the growth of the instability is almost similar in both cases. When the time approaches 40ps some high frequency modes start to be generated at the front edge when the magnetic field is included whereas in absence of magnetic field we see no such effect and the behaviour on the back edge is same in both cases. As the time progresses, more high frequency modes are generated up to 60ps and these modes start growing with time whereas in the case when there is no magnetic field the instability growth is of the same pattern as the input perturbation.

The original instability becomes more apparent in the non-magnetic field case at 70ps. On the other hand faster growth rate of the higher frequency modes in the magnetic field case is clearly seen at the time of 80ps when the high frequency modes saturate and start to interfere and disappear. When the time passes on to 200ps these high frequency modes have completely disappeared and the behaviour again becomes almost the same at the start where the initial applied perturbation dominates these short wavelengths.

The pattern of the instability in the density remains the same in both the cases when the time reaches up to 350ps but we observe a phase shift towards the axis when the magnetic field is included. Another interesting feature is the generation

TARGET PARAMETERS	
Target thickness	$5 \cdot 0 \mu m$
Target Radius	$2 \cdot 5 \mu m$
Geometry	Cylindrical
Material	Polythene $(CH_2)_n$
Solid Density	$1 \cdot 2 g/cm^3$
Perturbation Wavelength	$1 \cdot 25 \mu m$
Perturbation Amplitude	$0 \cdot 1 \mu m$
Mass No. (F)	$4 \cdot 67$
Charge No.(Z)	$2 \cdot 67$
Ratio of Specific heat	$1 \cdot 667$
Initial Temperature	$10^1 K°$
LASER PARAMETERS	
Peak Power on Axis	$1 \cdot 0 \times 10^{14} W/cm^2$
Focal Radius	$1 \cdot 0 \times 10^4 cm$
Laser wavelength	$0 \cdot 53 \mu m$
Laser Rise Time	300ps
Total Duration of Laser Pulse	2ns
Total Run Time	800ps
Reflection Coefficient	$0 \cdot 8$
TRANSPORT PARAMETERS	
Flux limit Factor (f)	$0 \cdot 1$
Diffusion	Classical

Table 5.1: Input parameters for the target $(5 \cdot 0 \mu m \times 2 \cdot 5 \mu m)$ in both directions.

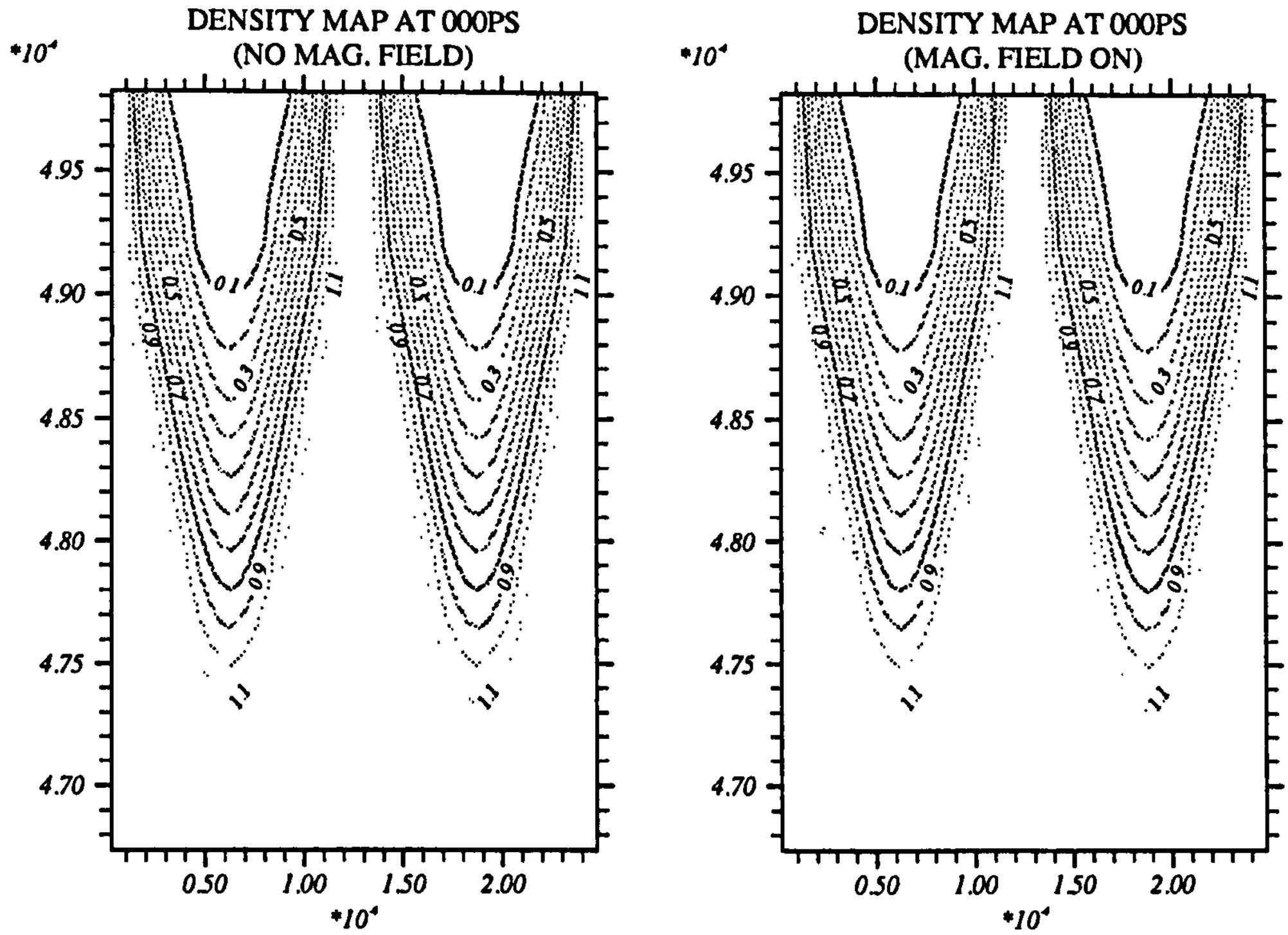

Figure 5.2: Density contour map for target of $(5 \cdot 0\mu m \times 2 \cdot 5\mu m)$ with the perturbation applied through density.

DENSITY MAP AT 20PS
(NO MAG. FIELD)

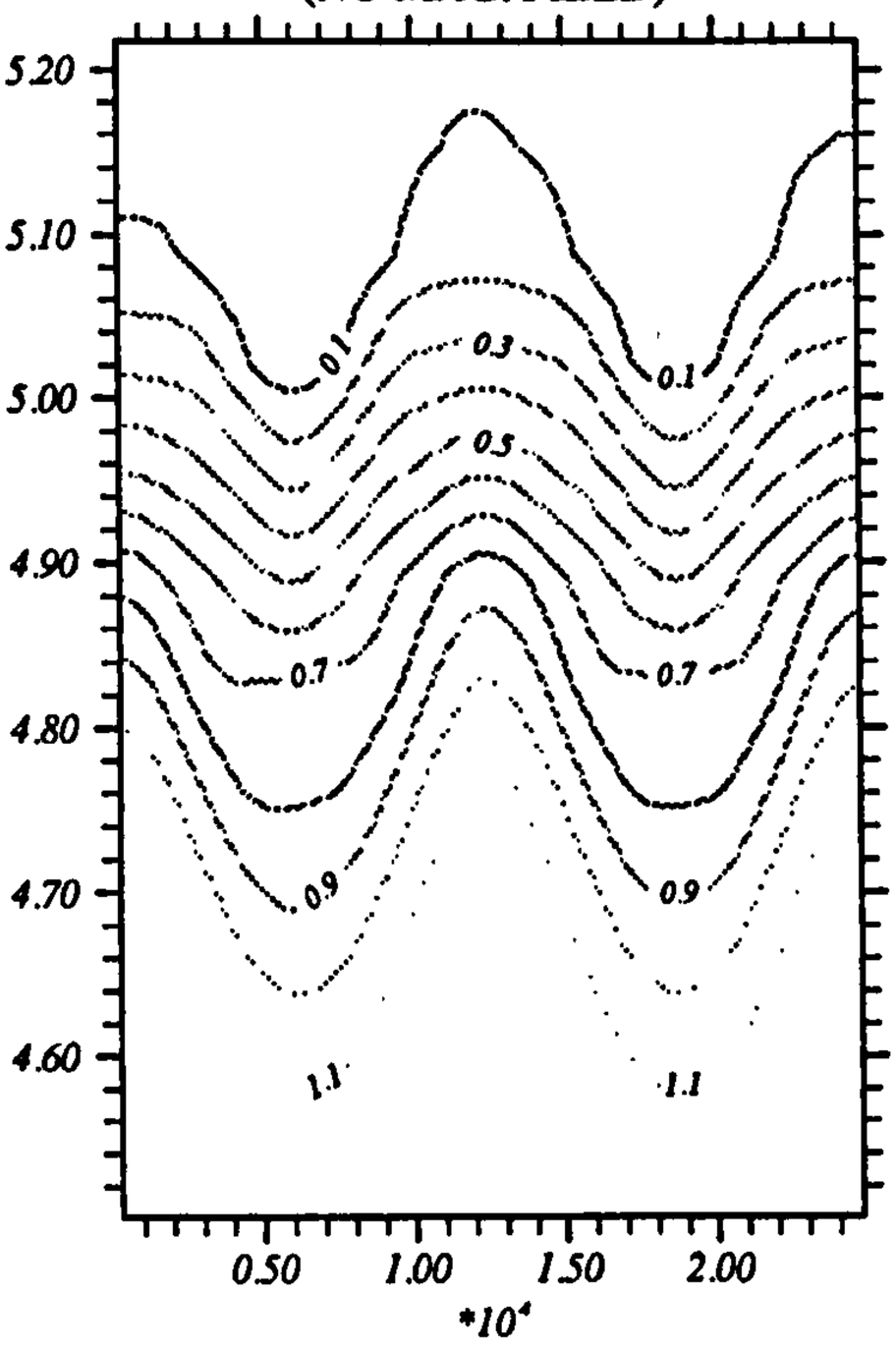

DENSITY MAP AT 20PS
(MAG. FIELD ON)

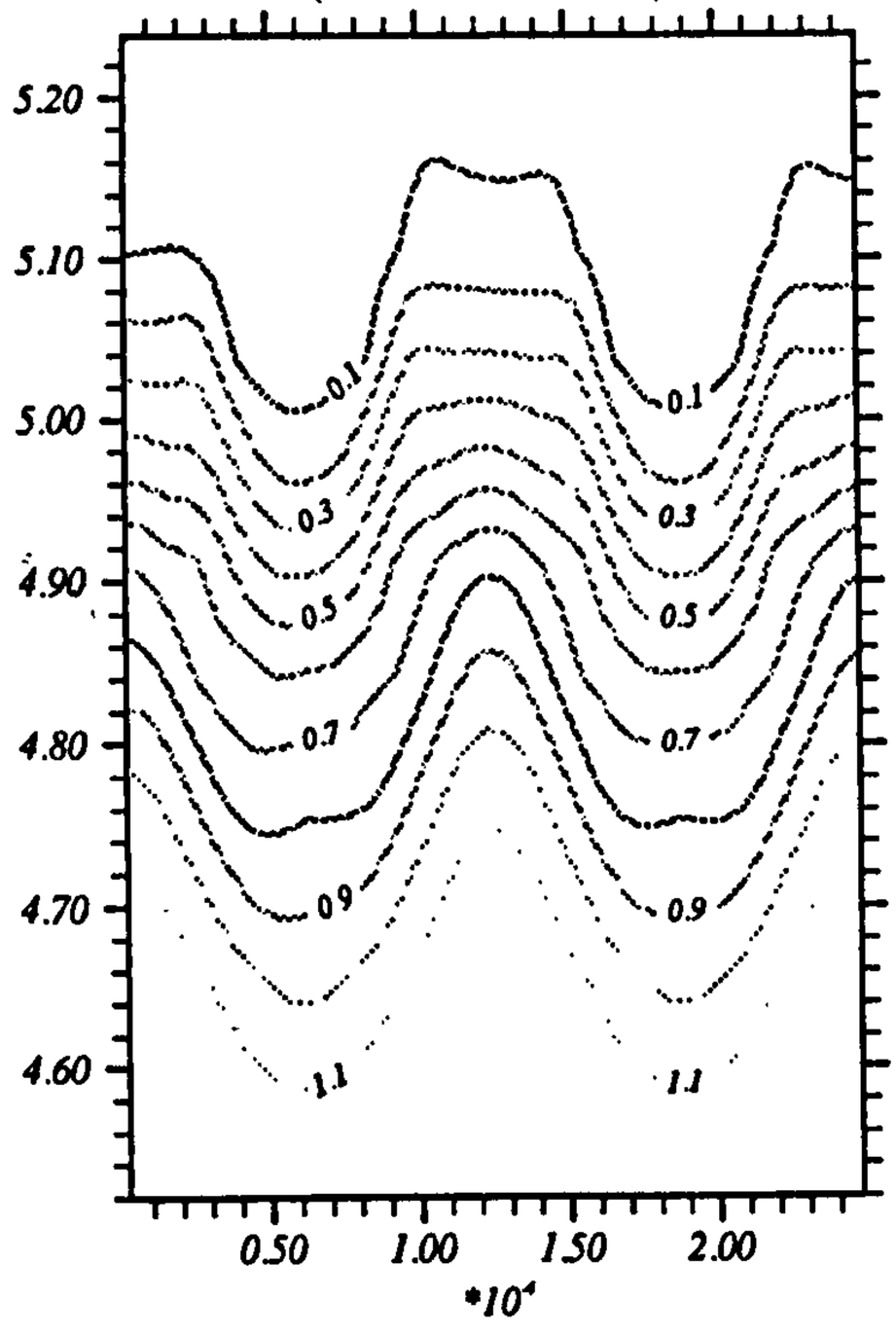

DENSITY MAP AT 30PS
(NO MAG. FIELD)

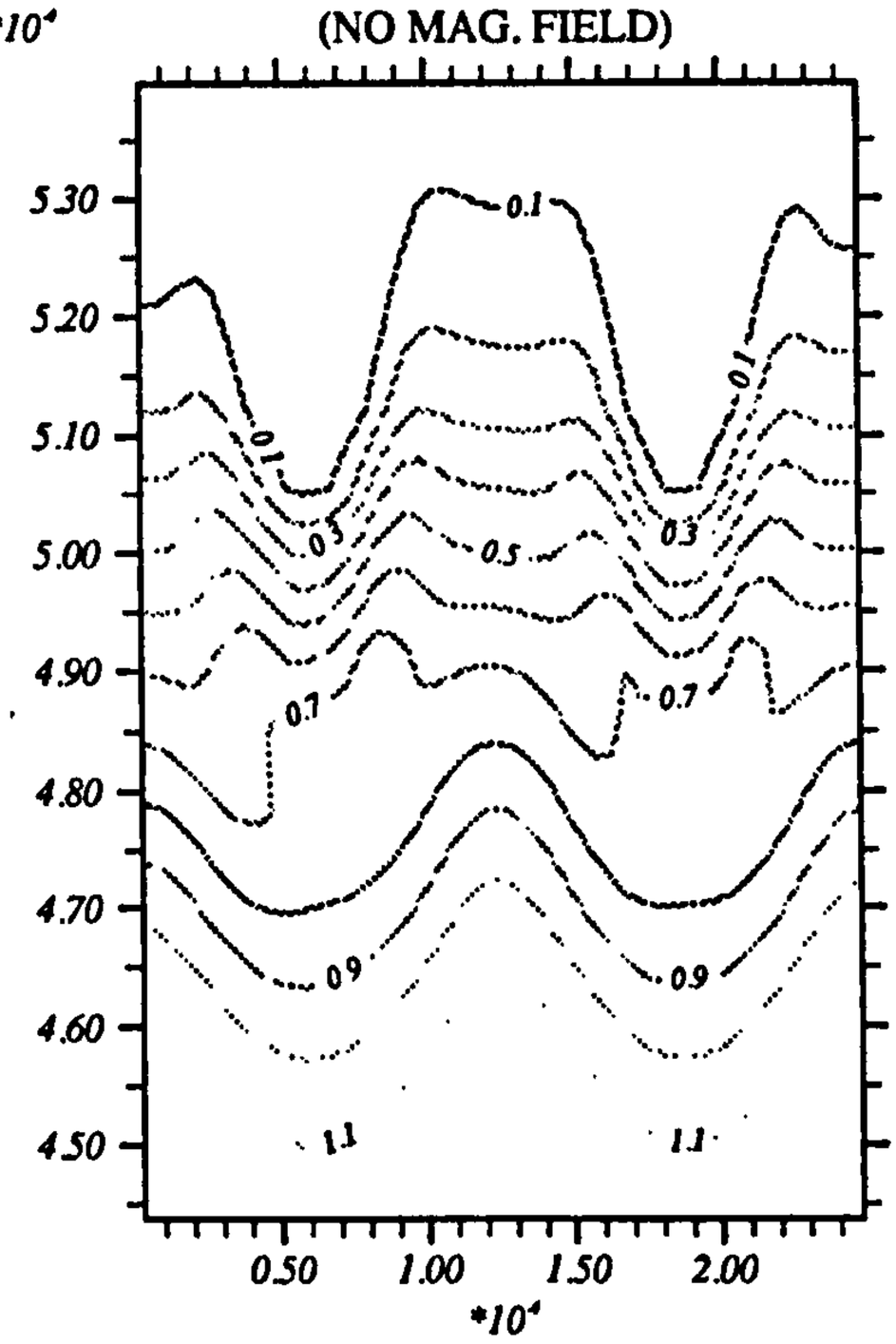

DENSITY MAP AT 30PS
(MAG. FIELD ON)

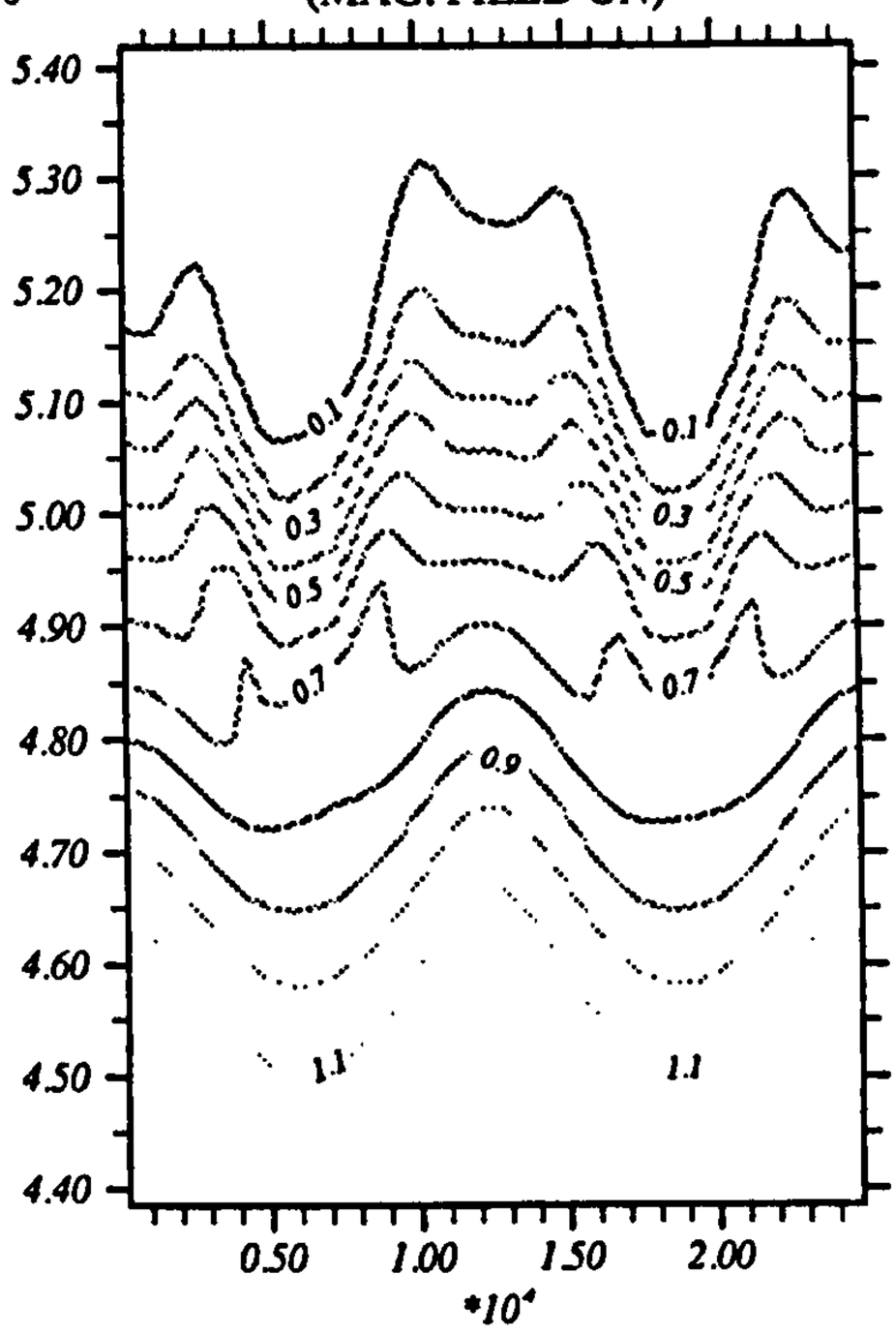

DENSITY MAP AT 60PS
(NO MAG. FIELD)

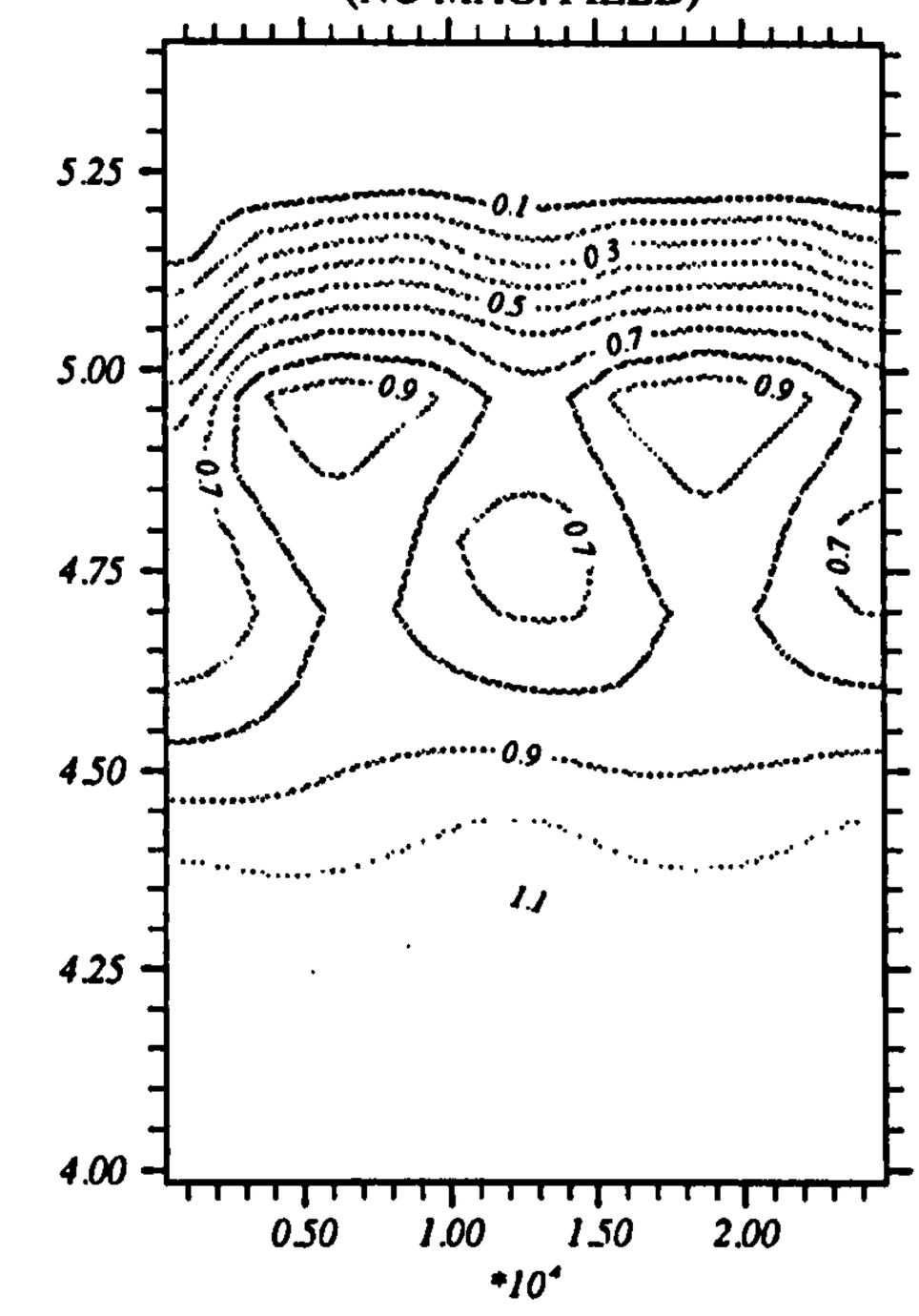

DENSITY MAP AT 60PS
(MAG. FIELD ON)

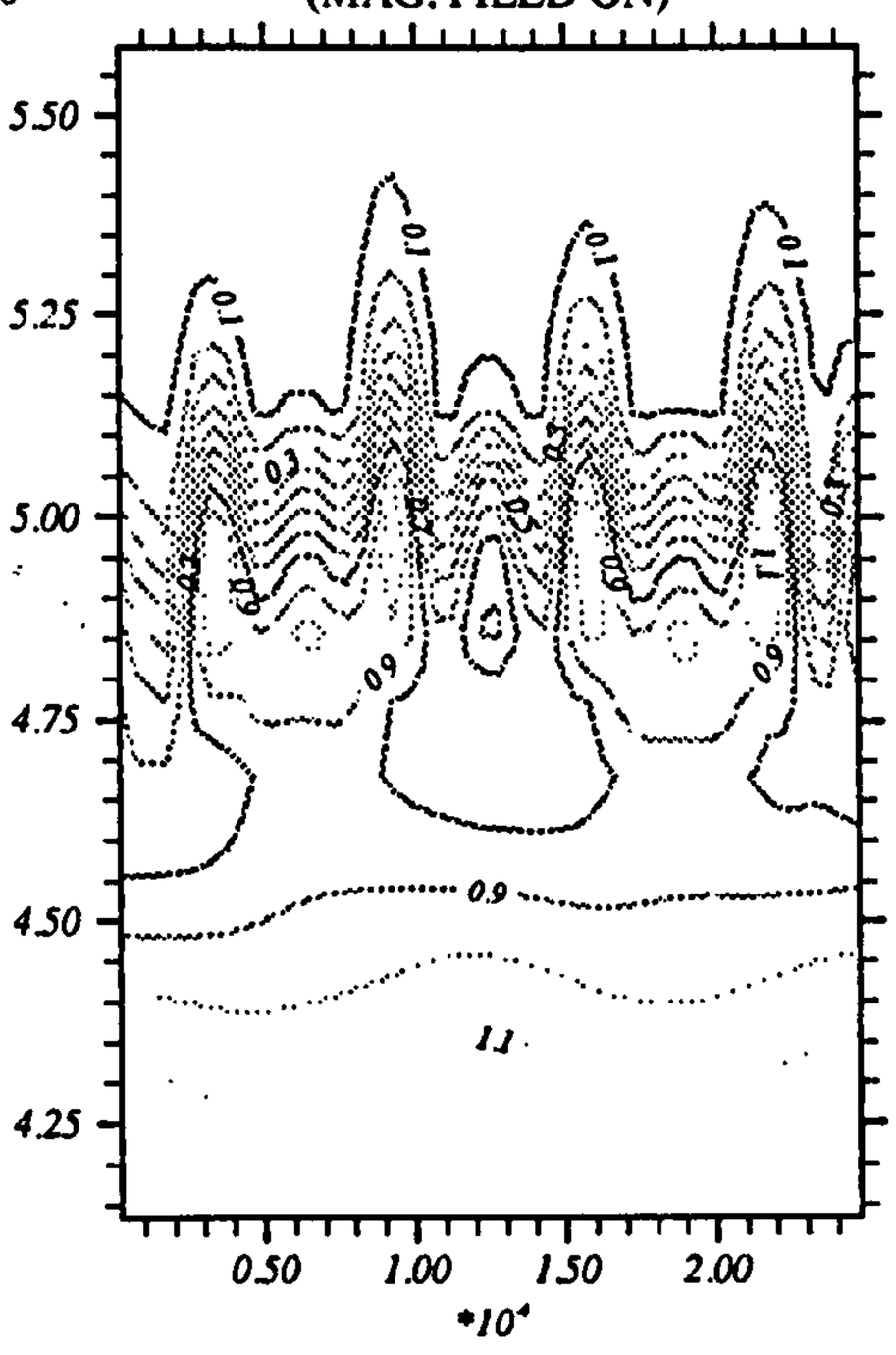

DENSITY MAP AT 70PS
(NO MAG. FIELD)

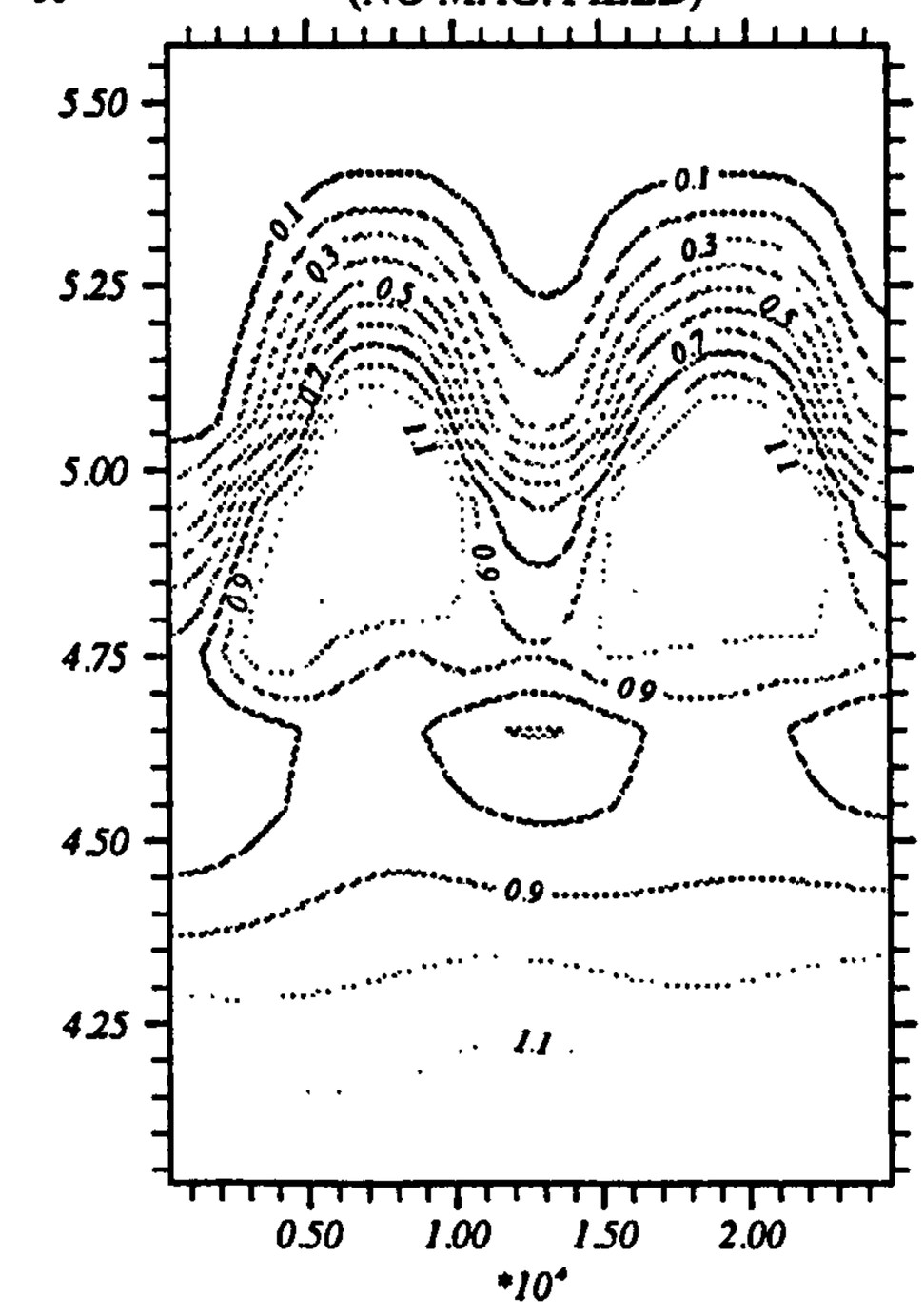

DENSITY MAP AT 70PS
(MAG. FIELD ON)

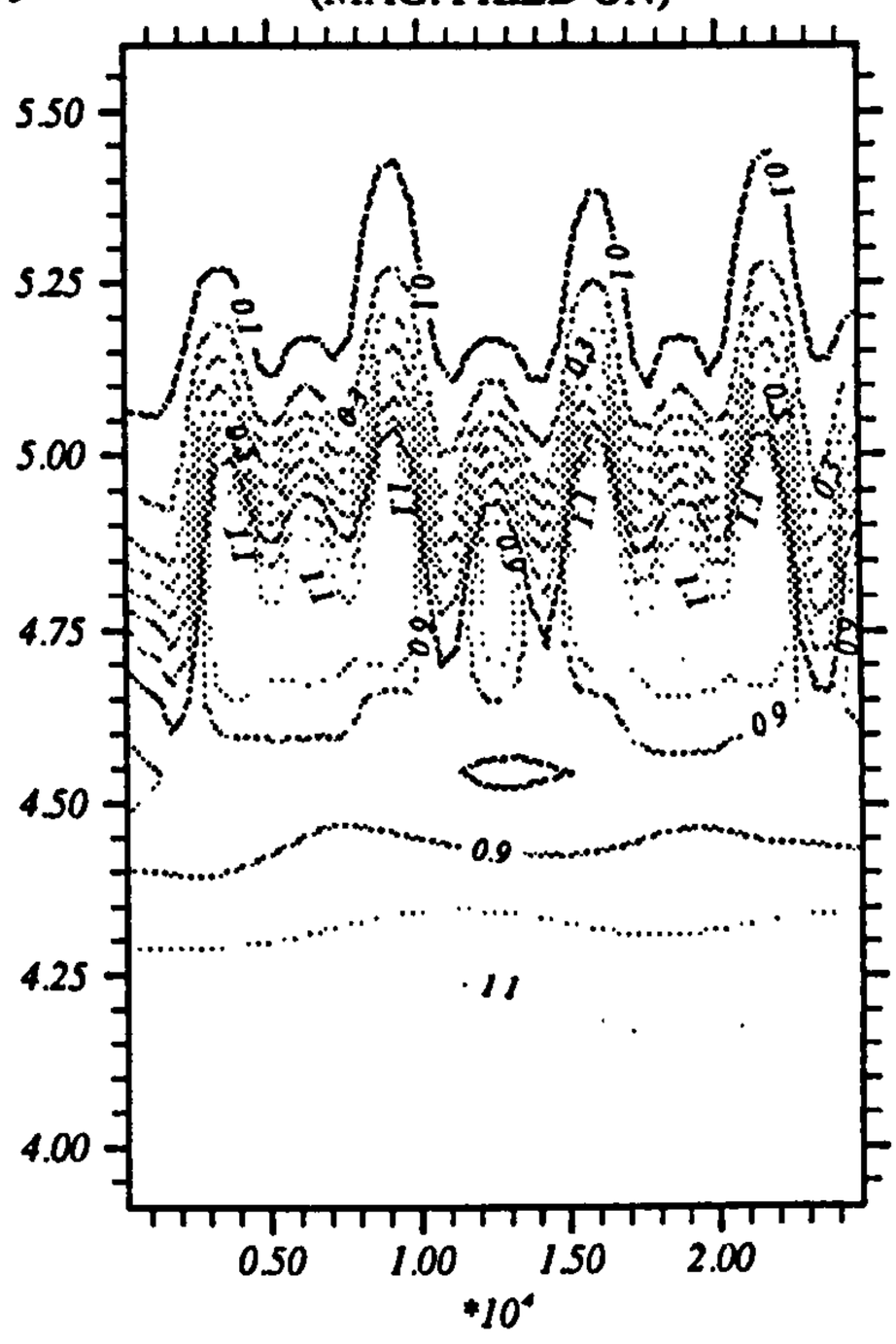

DENSITY MAP AT 80PS
(NO MAG. FIELD)

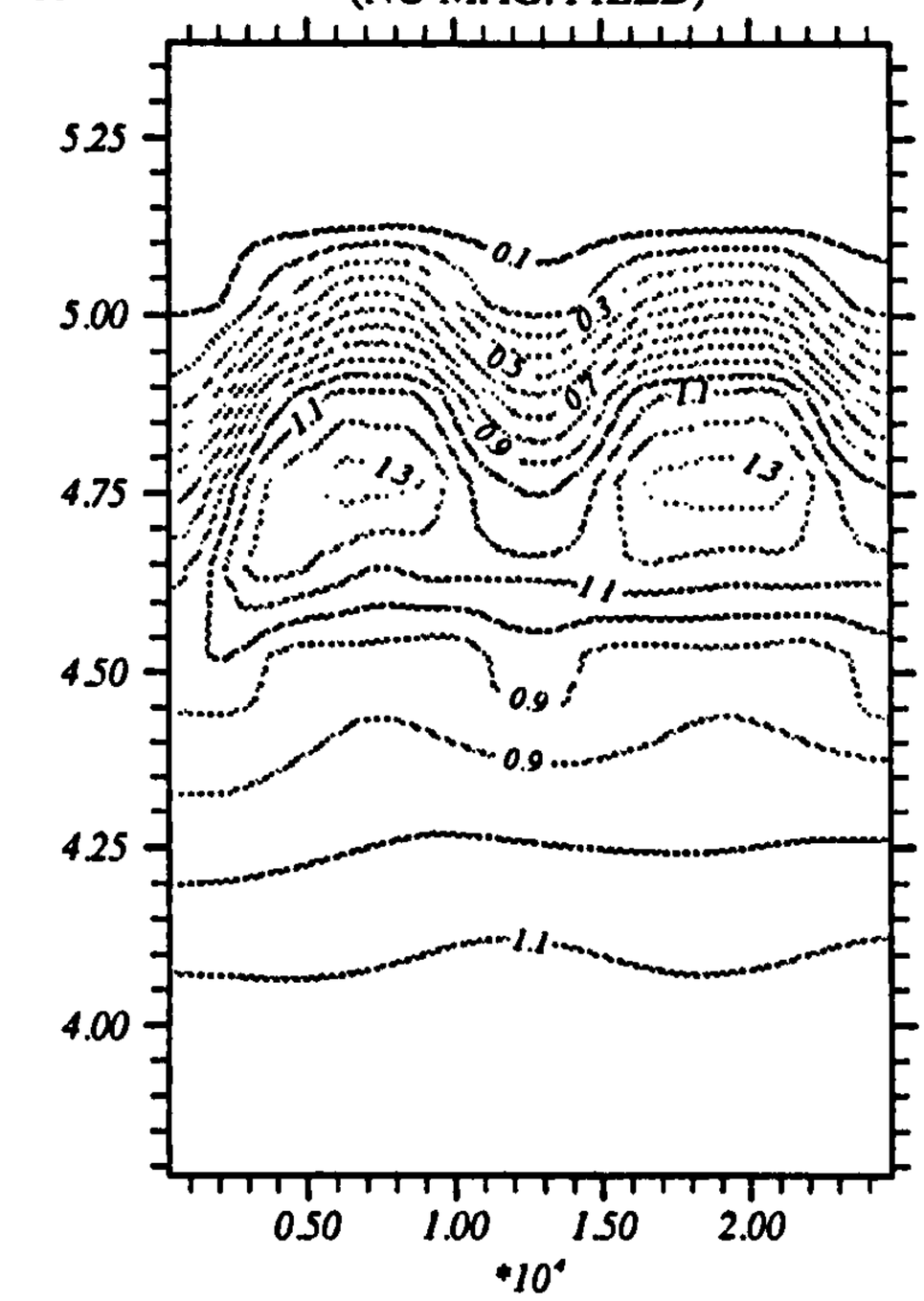

DENSITY MAP AT 80PS
(MAG. FIELD ON)

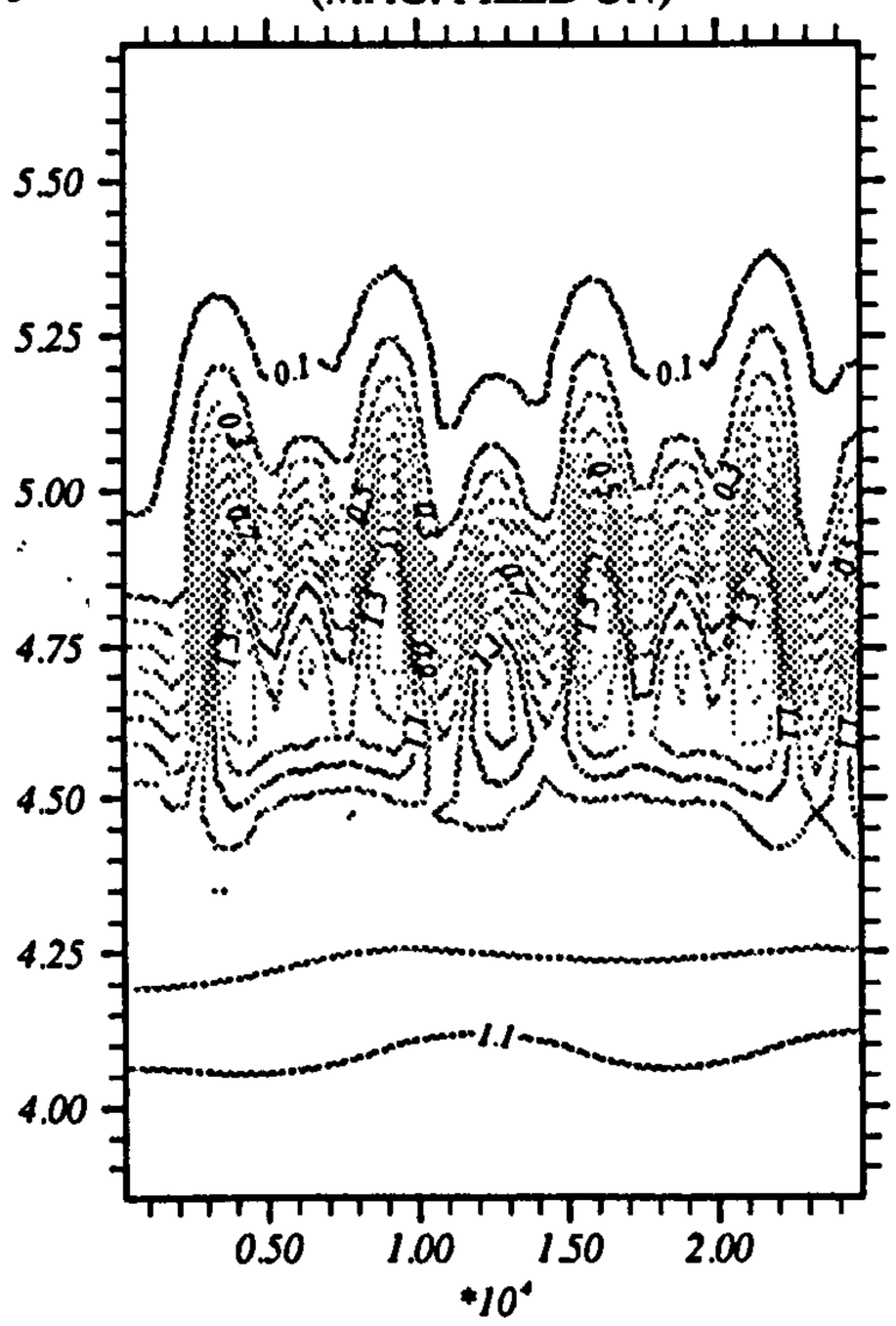

DENSITY MAP AT 90PS
(NO MAG. FIELD)

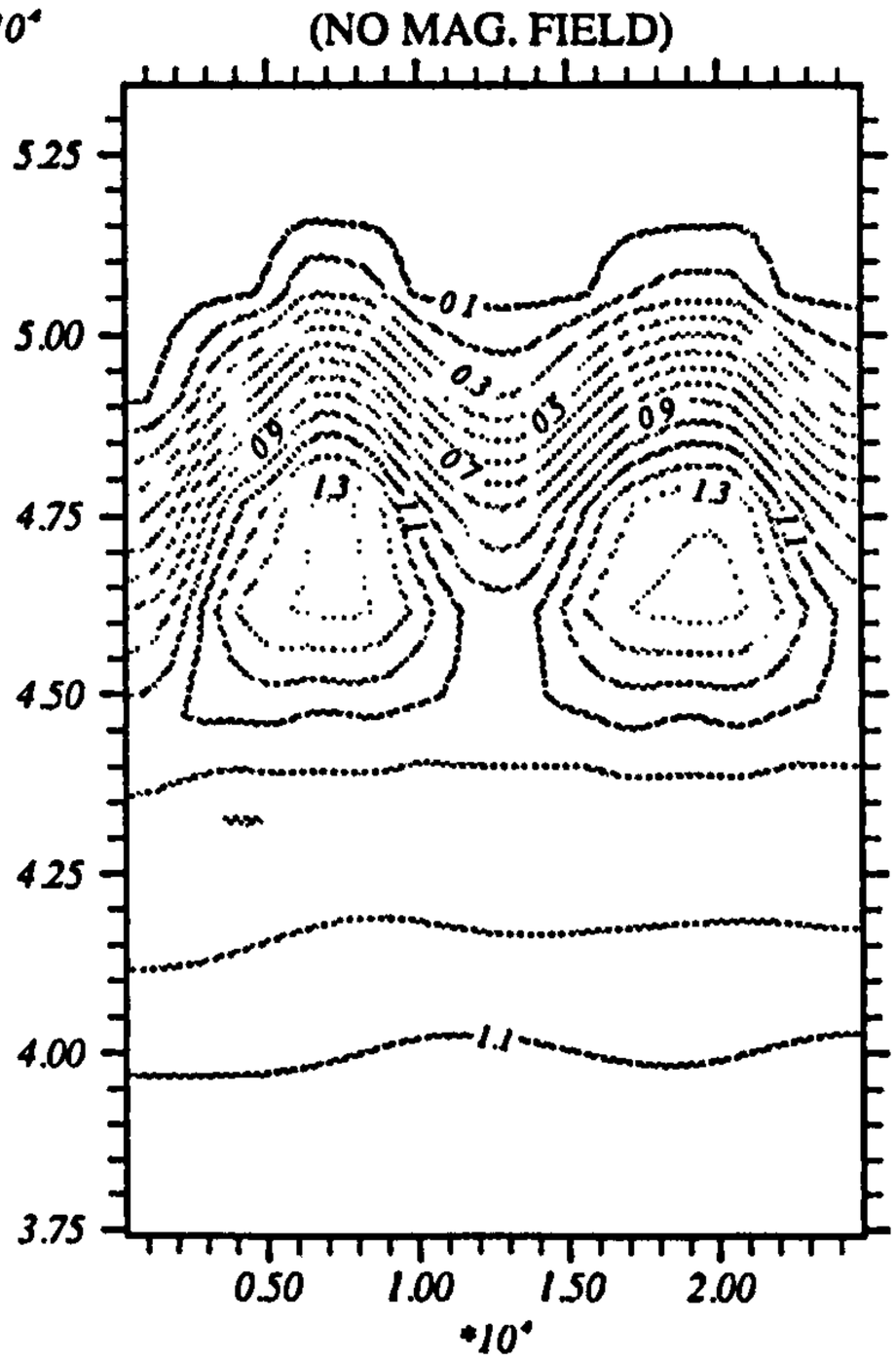

DENSITY MAP AT 90PS
(MAG. FIELD ON)

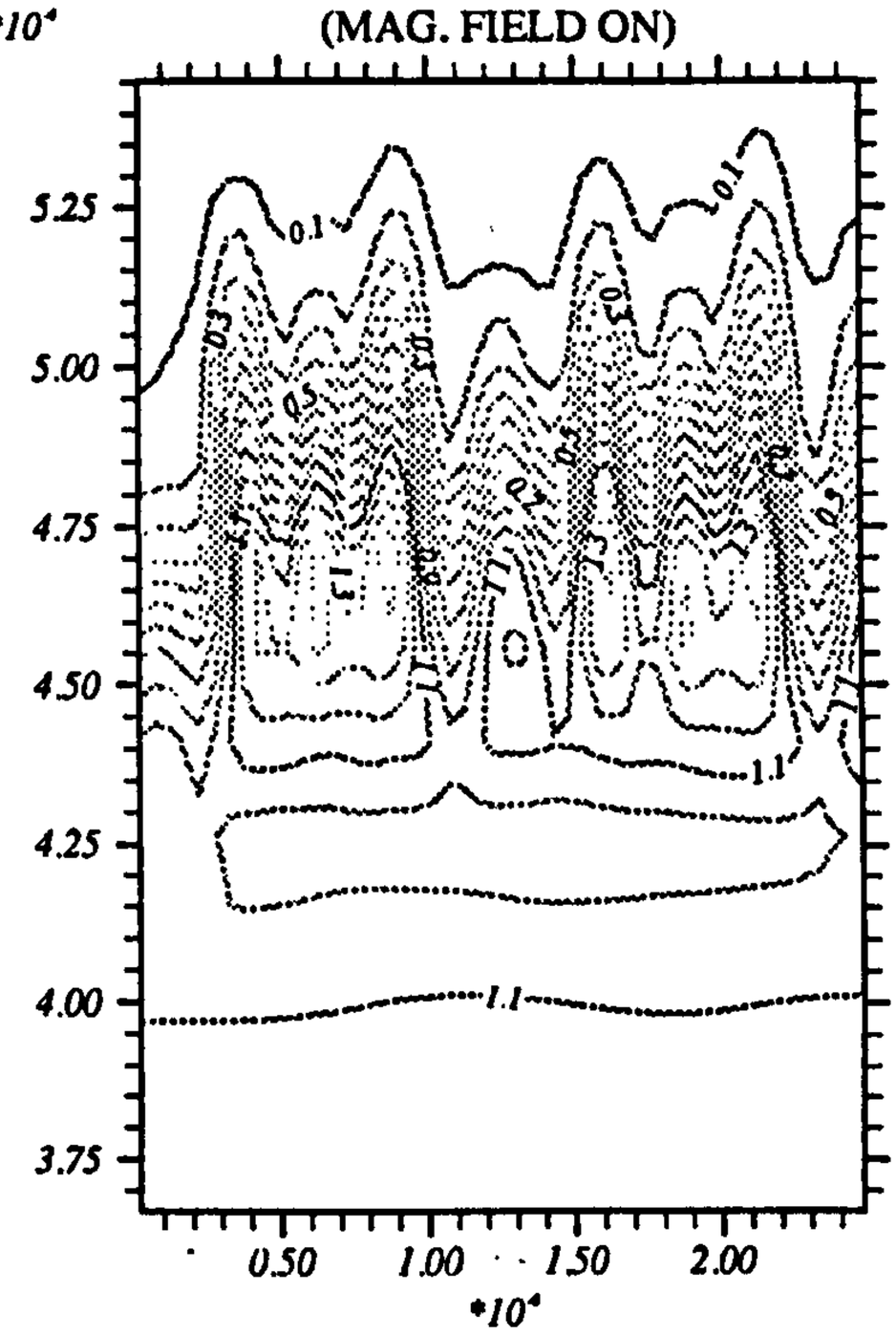

DENSITY MAP AT 100PS
(NO MAG. FIELD)

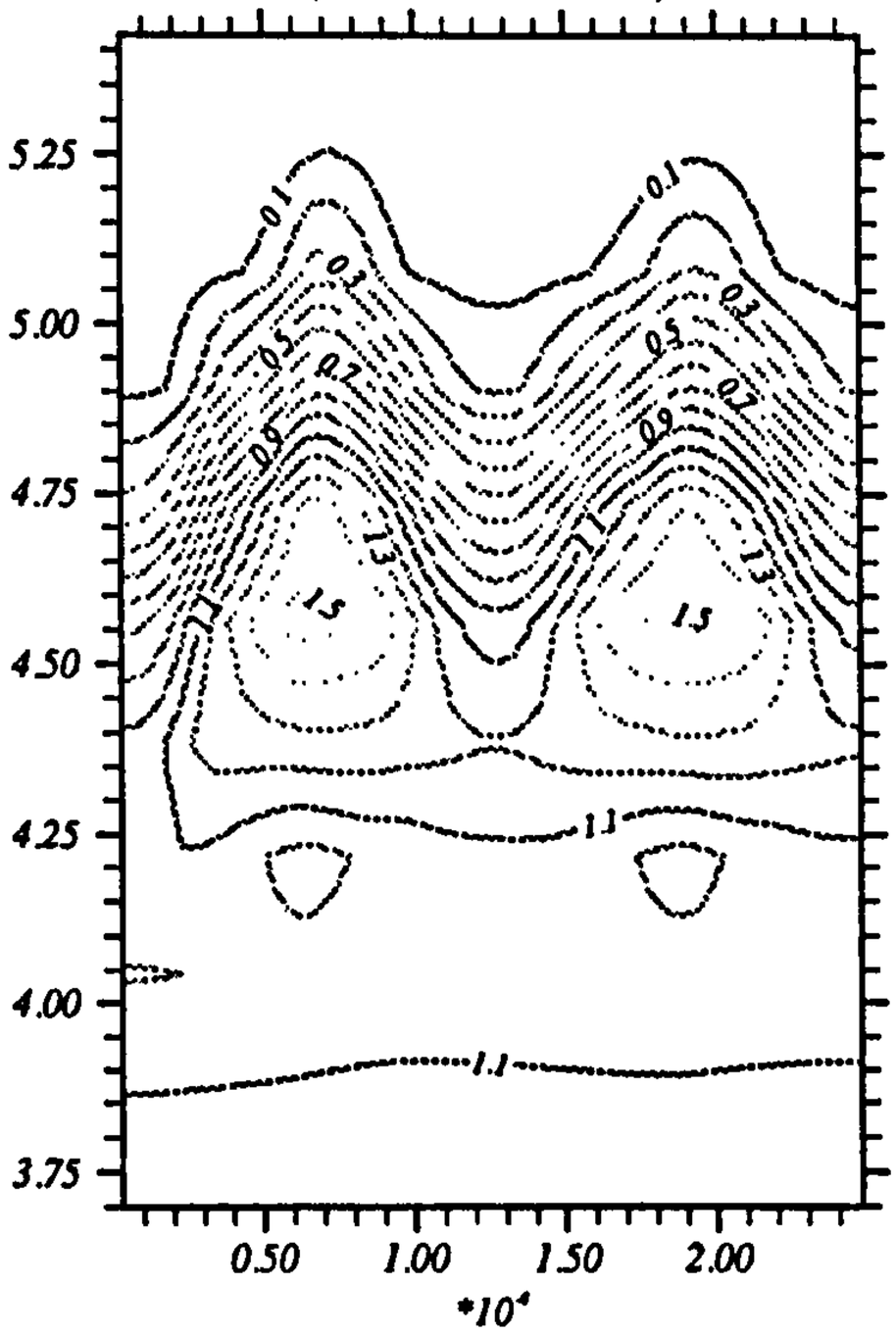

DENSITY MAP AT 100PS
(MAG. FIELD ON)

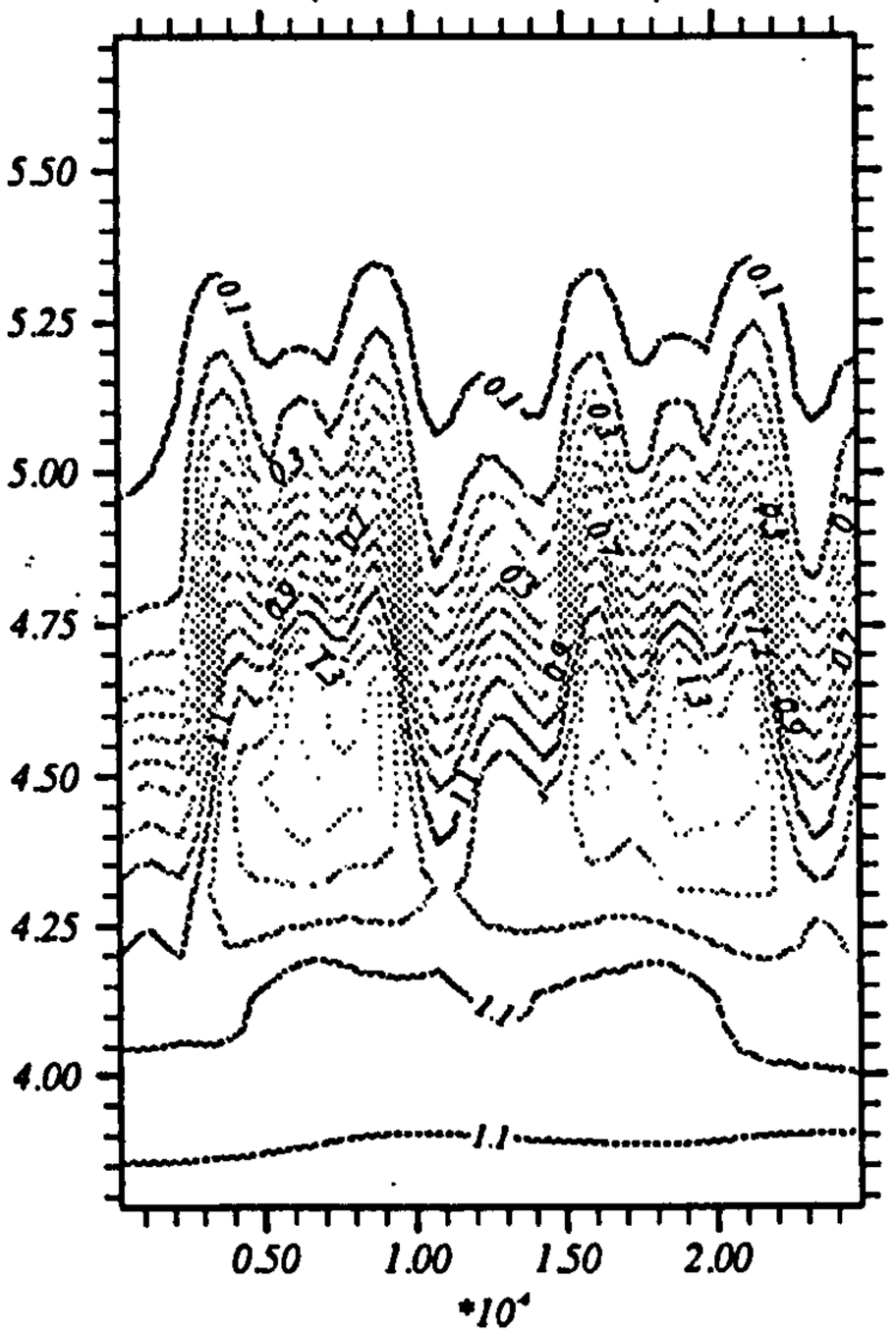

DENSITY MAP AT 150PS
(NO MAG. FIELD)

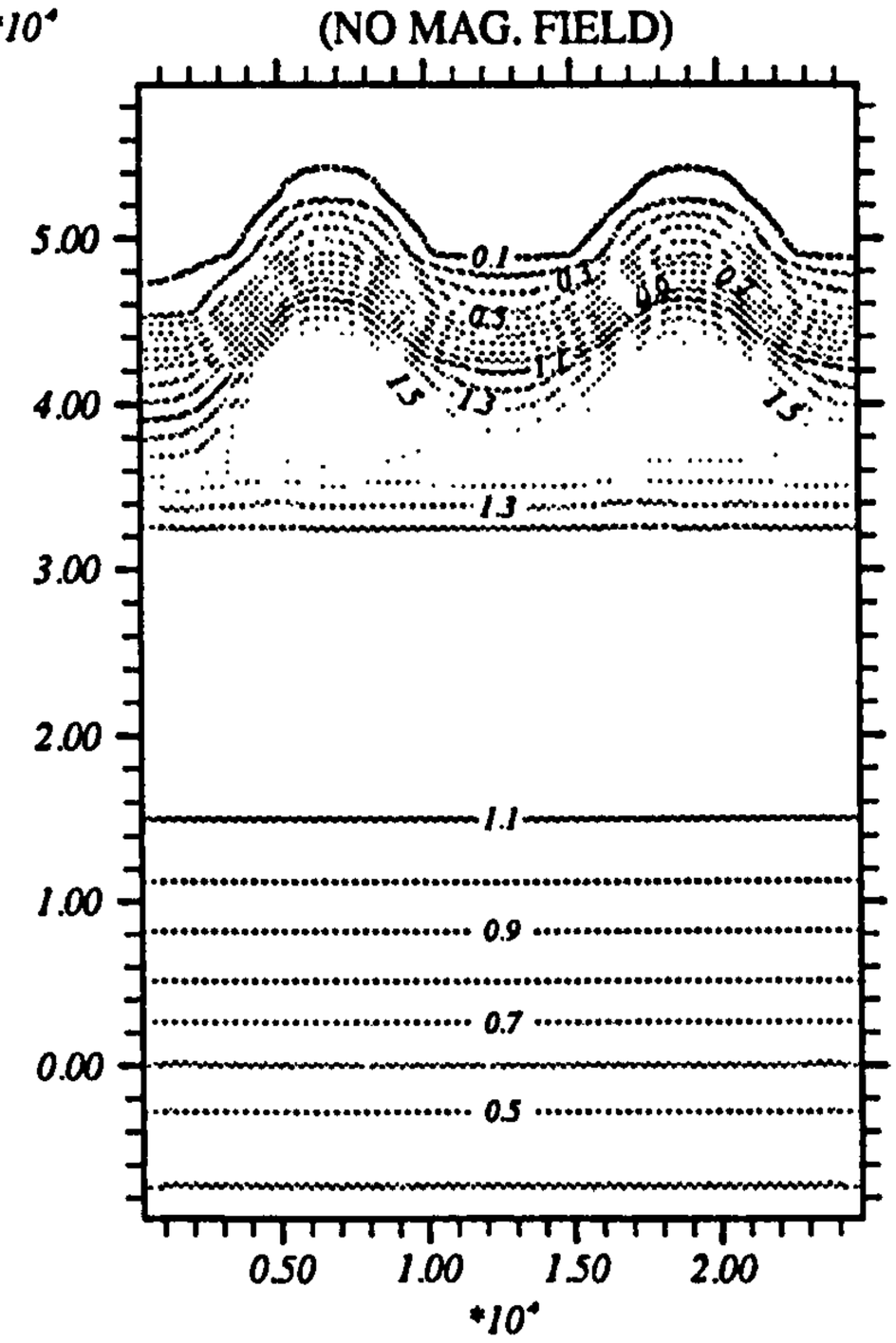

DENSITY MAP AT 150PS
(MAG. FIELD ON)

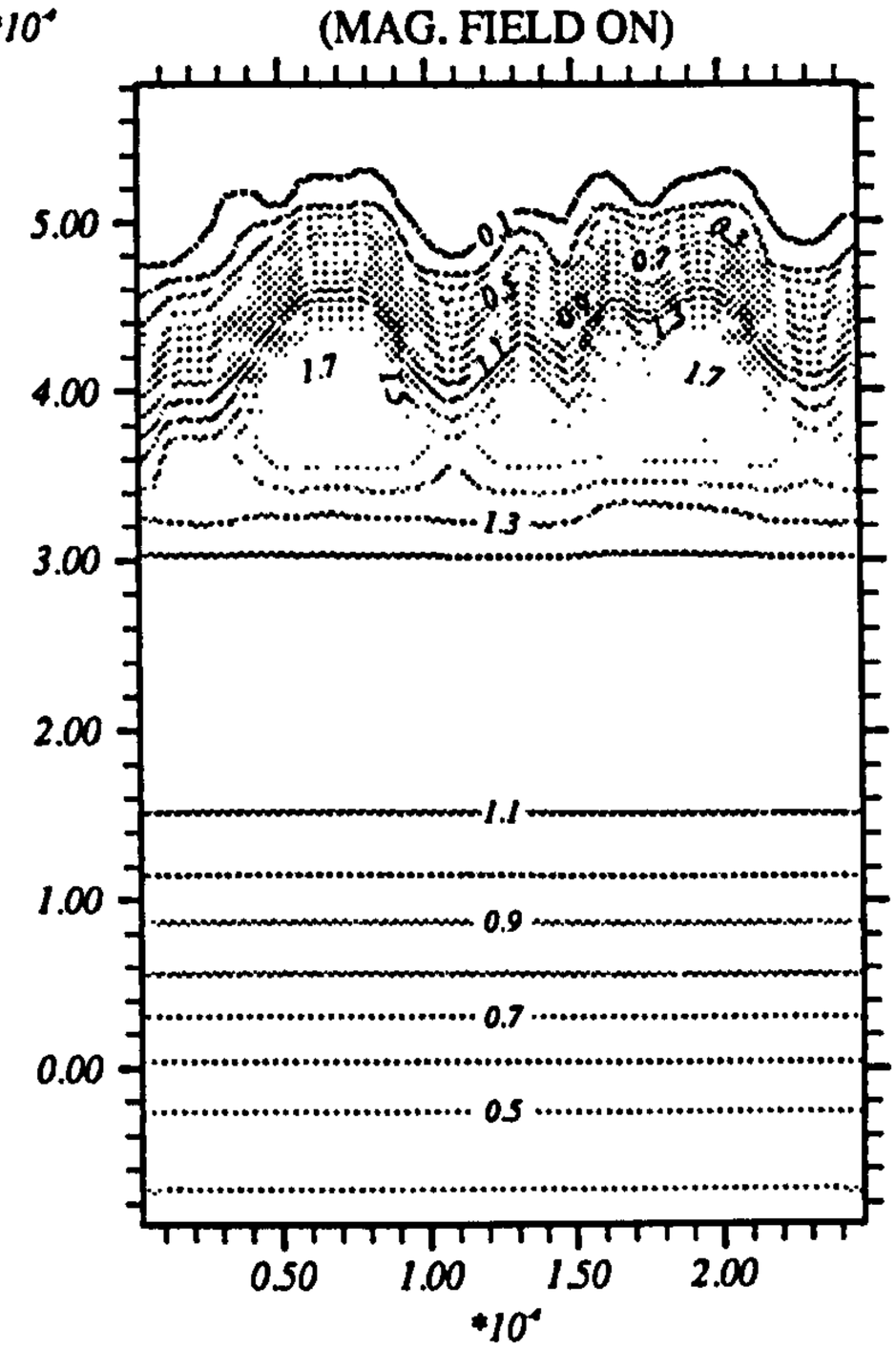

DENSITY MAP AT 200PS
(NO MAG. FIELD)

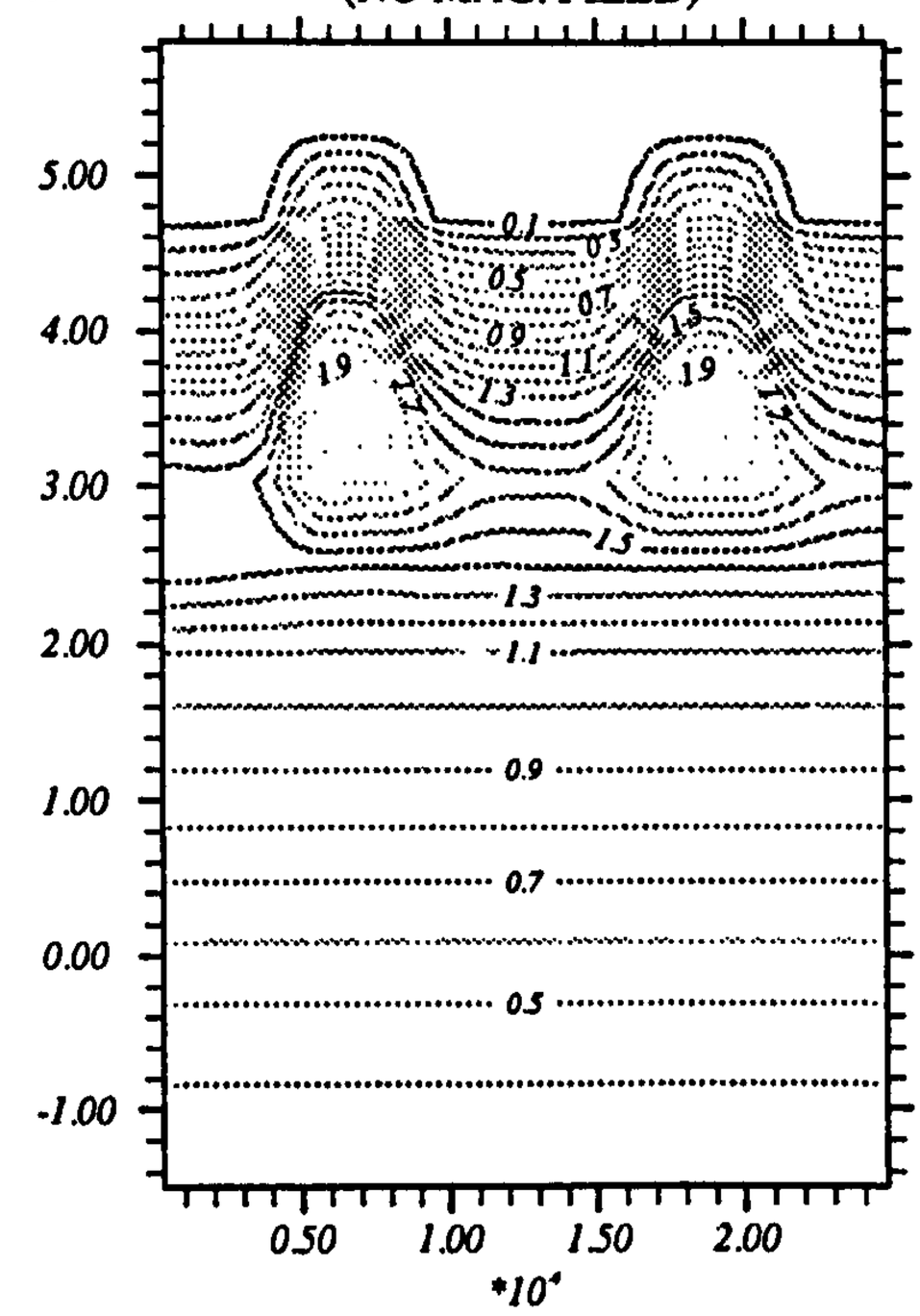

DENSITY MAP AT 200PS
(MAG. FIELD ON)

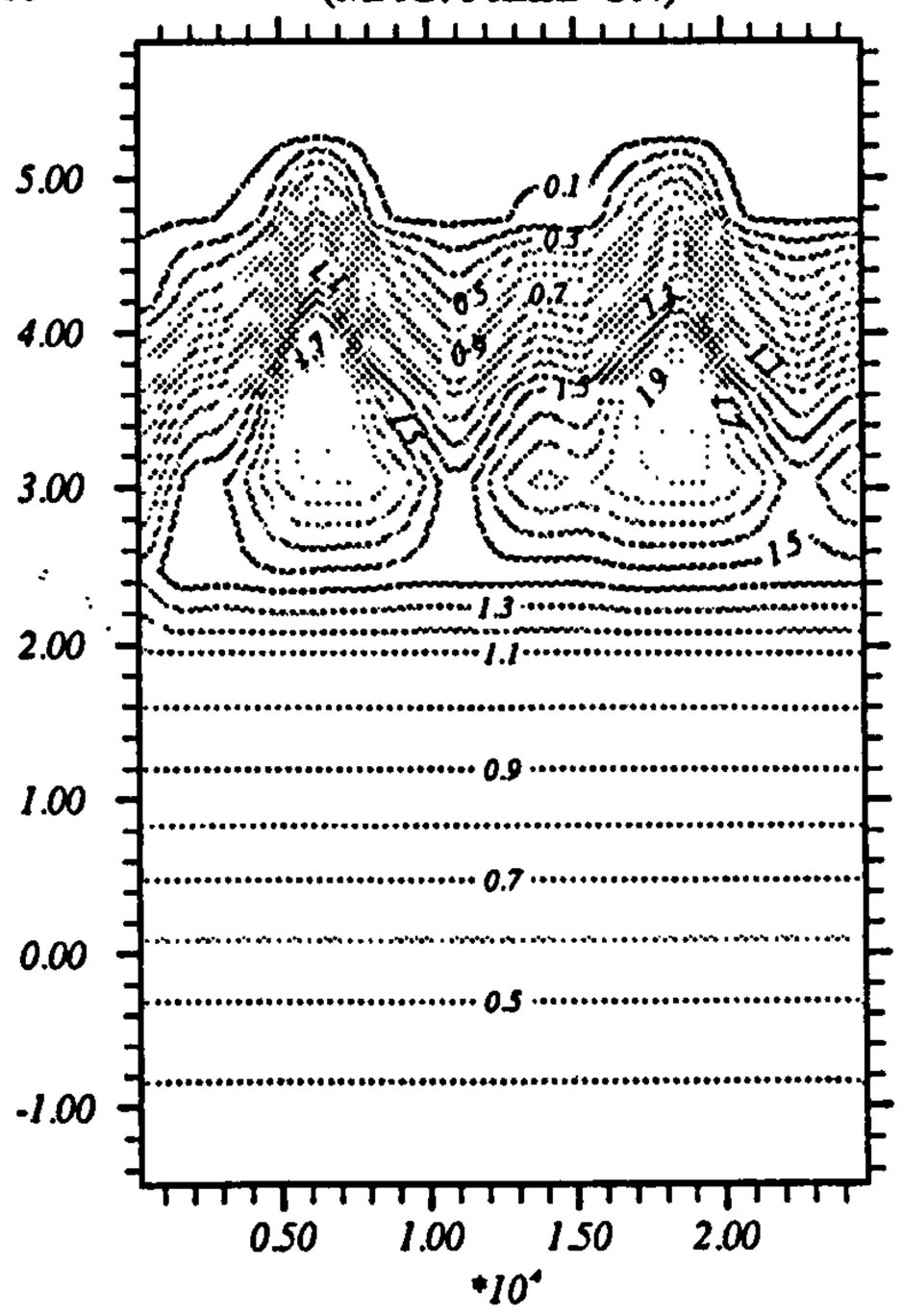

DENSITY MAP AT 250PS
(NO MAG. FIELD)

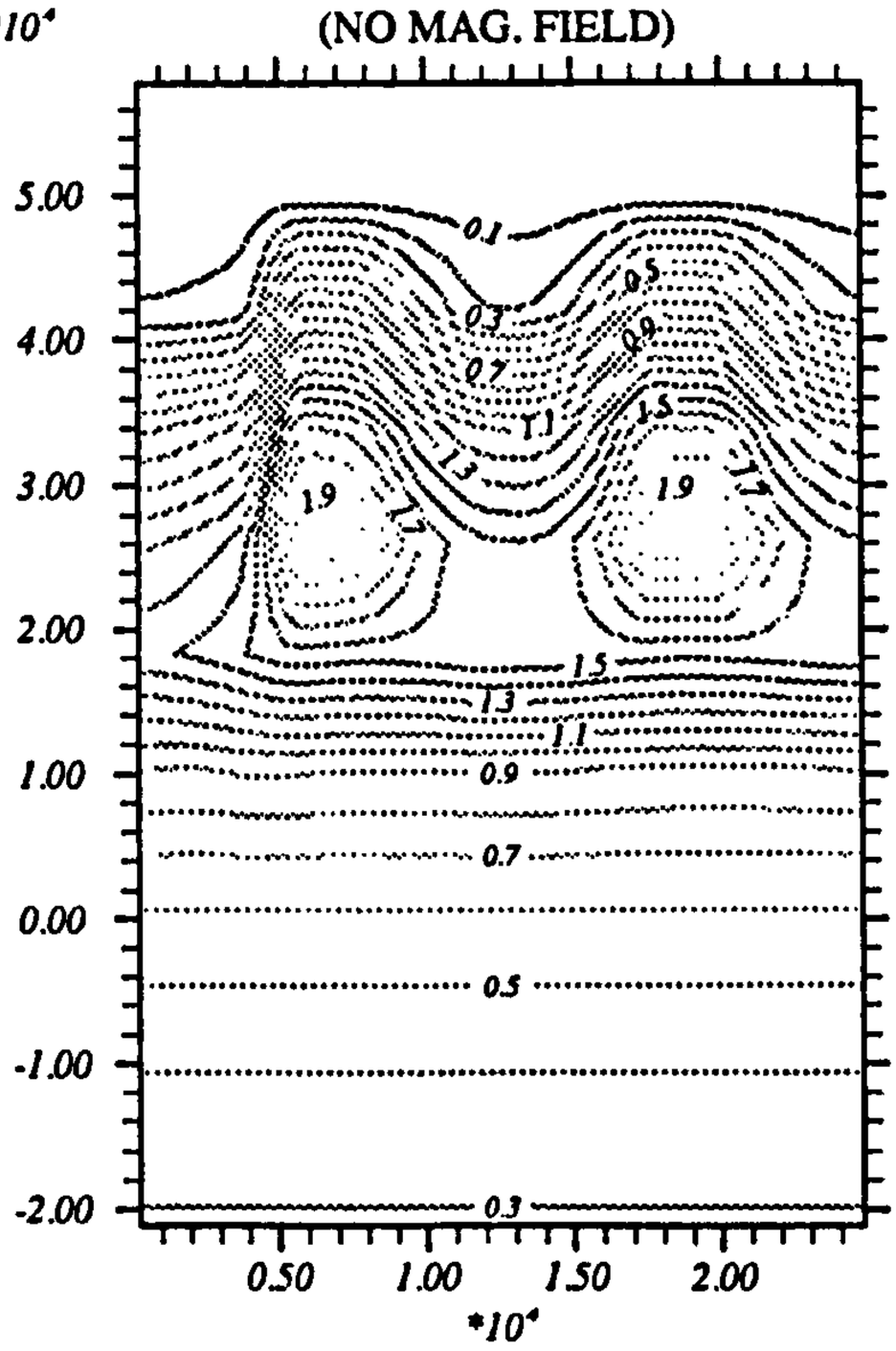

DENSITY MAP AT 250PS
(MAG. FIELD ON)

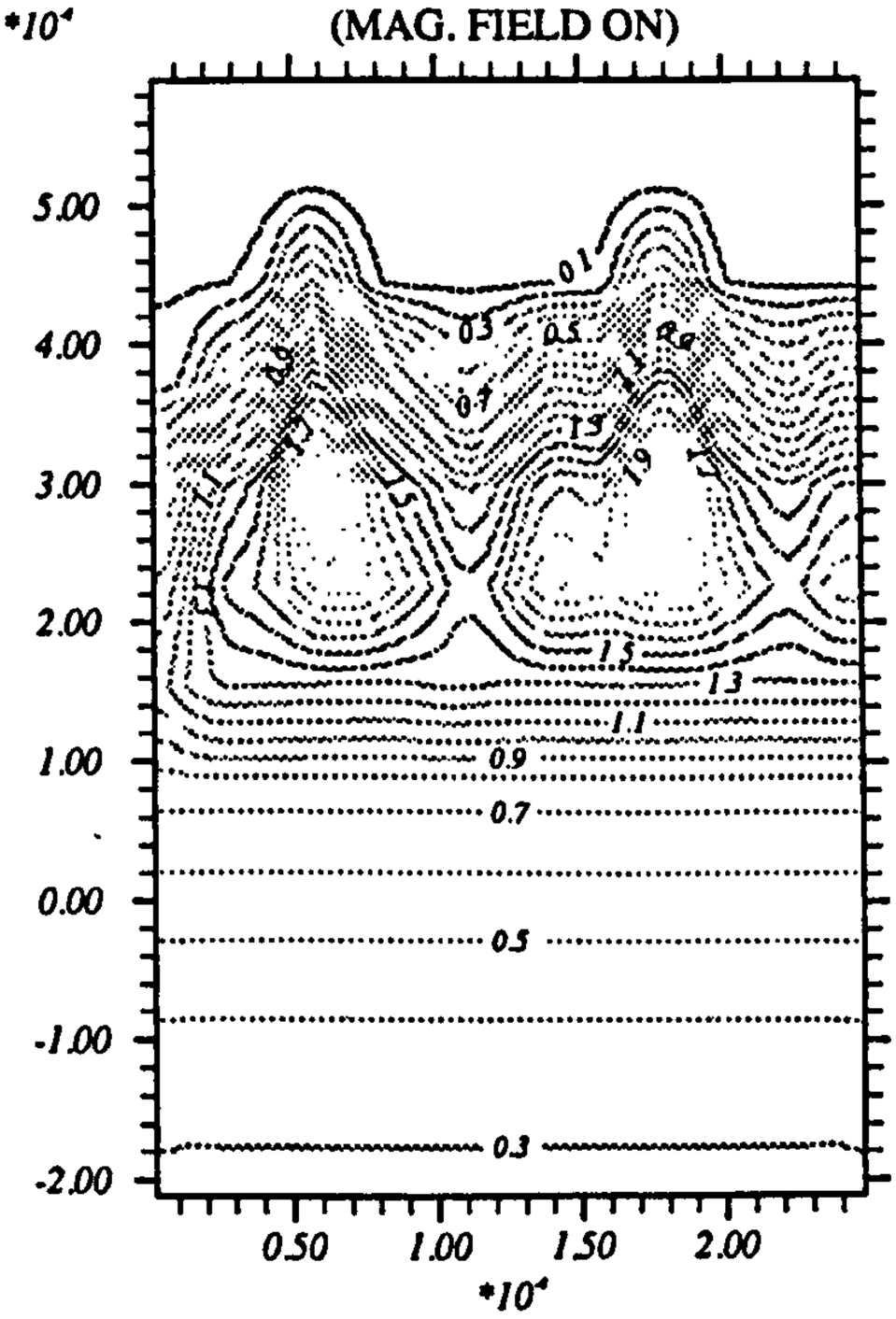

DENSITY MAP AT 300PS
(NO MAG. FIELD)

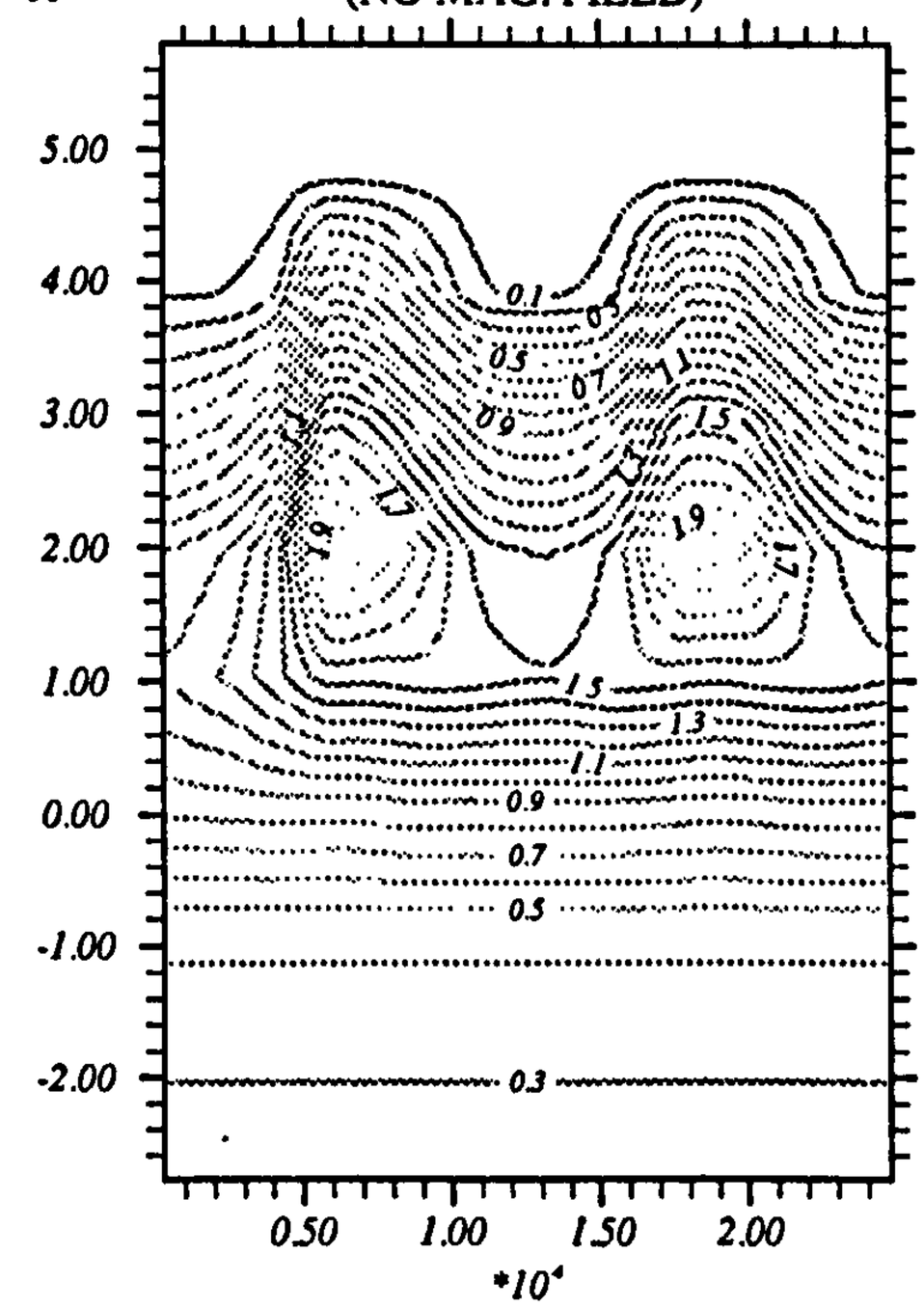

DENSITY MAP AT 300PS
(MAG. FIELD ON)

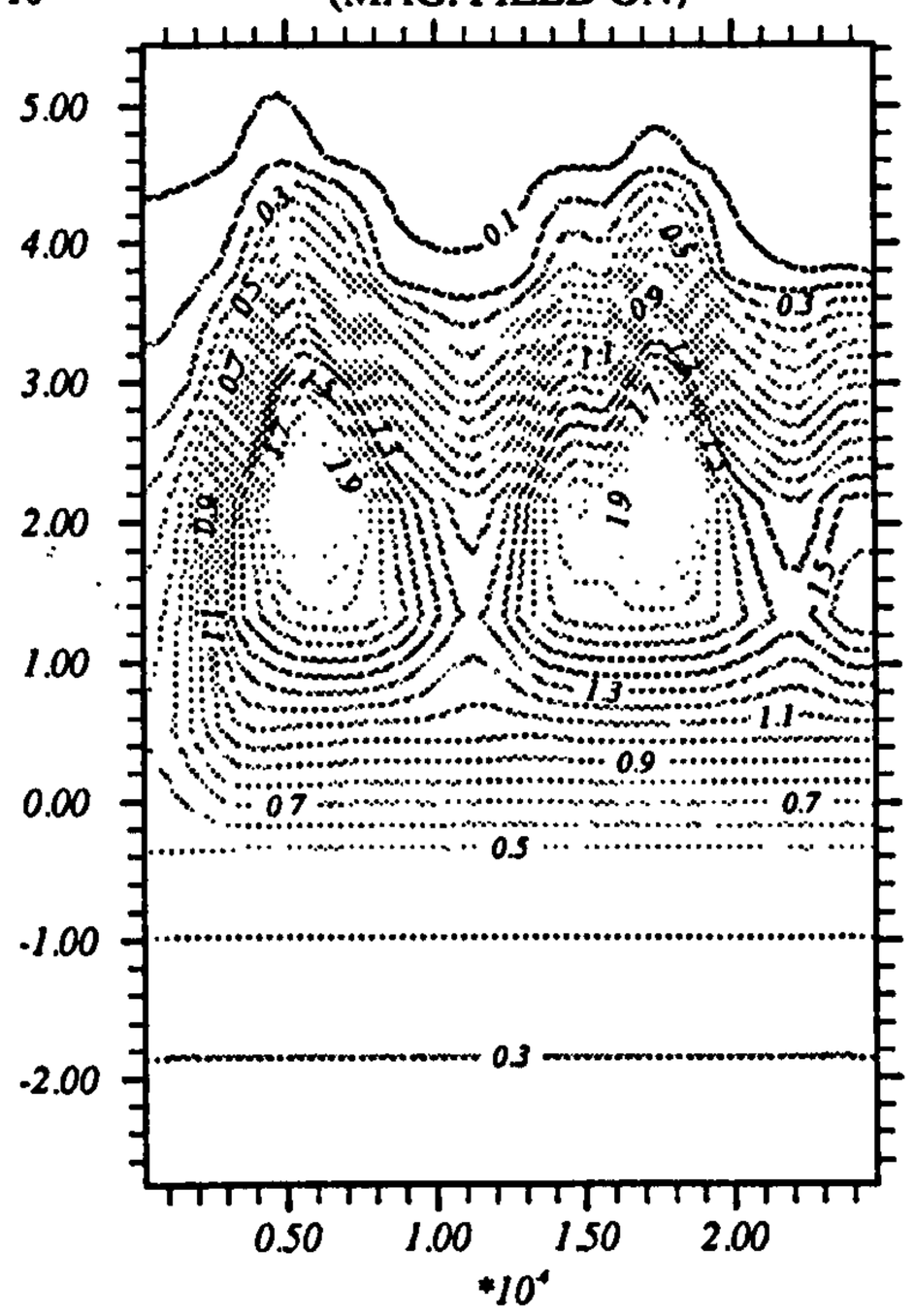

DENSITY MAP AT 350PS
(NO MAG. FIELD)

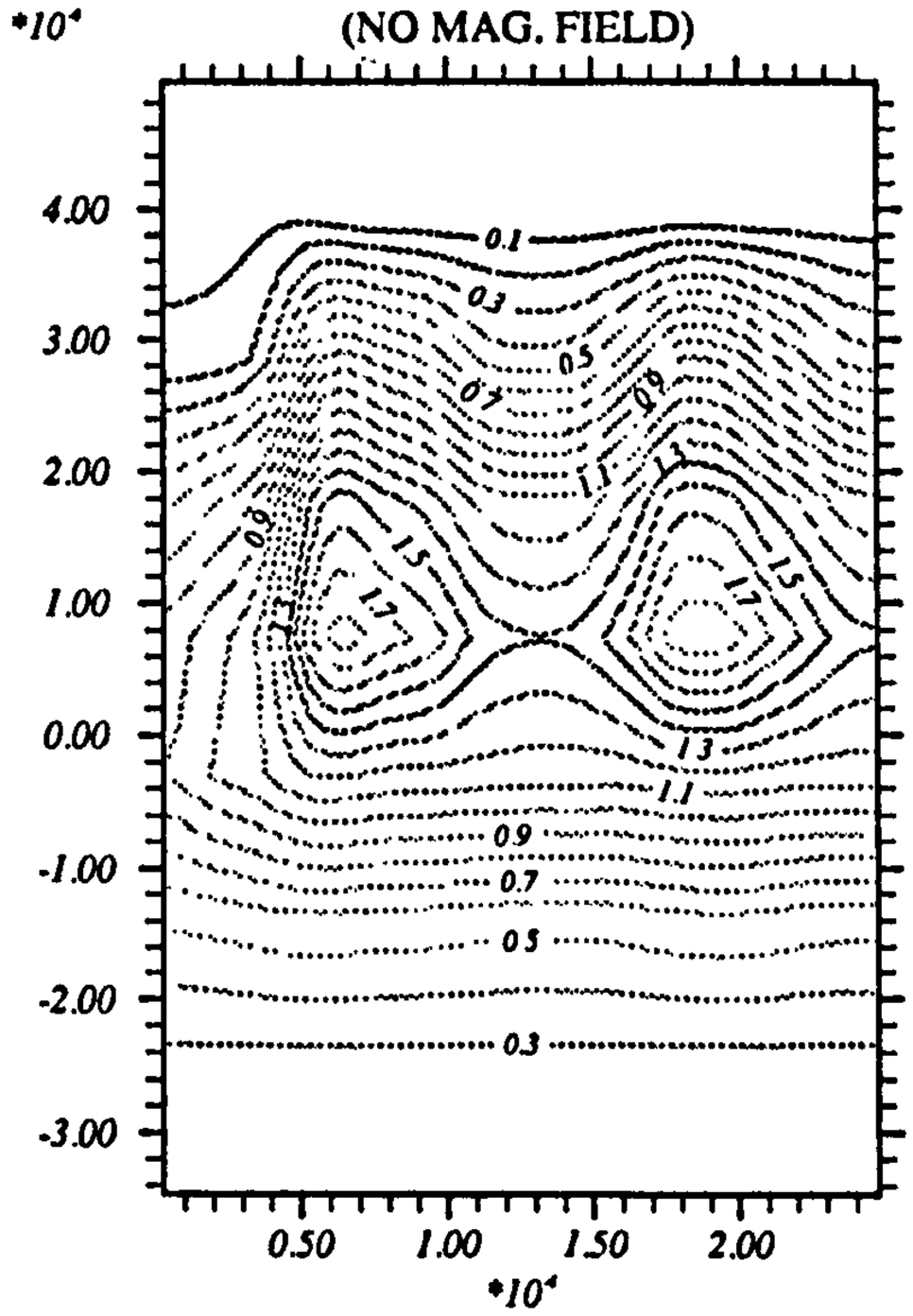

DENSITY MAP AT 350PS
(MAG. FIELD ON)

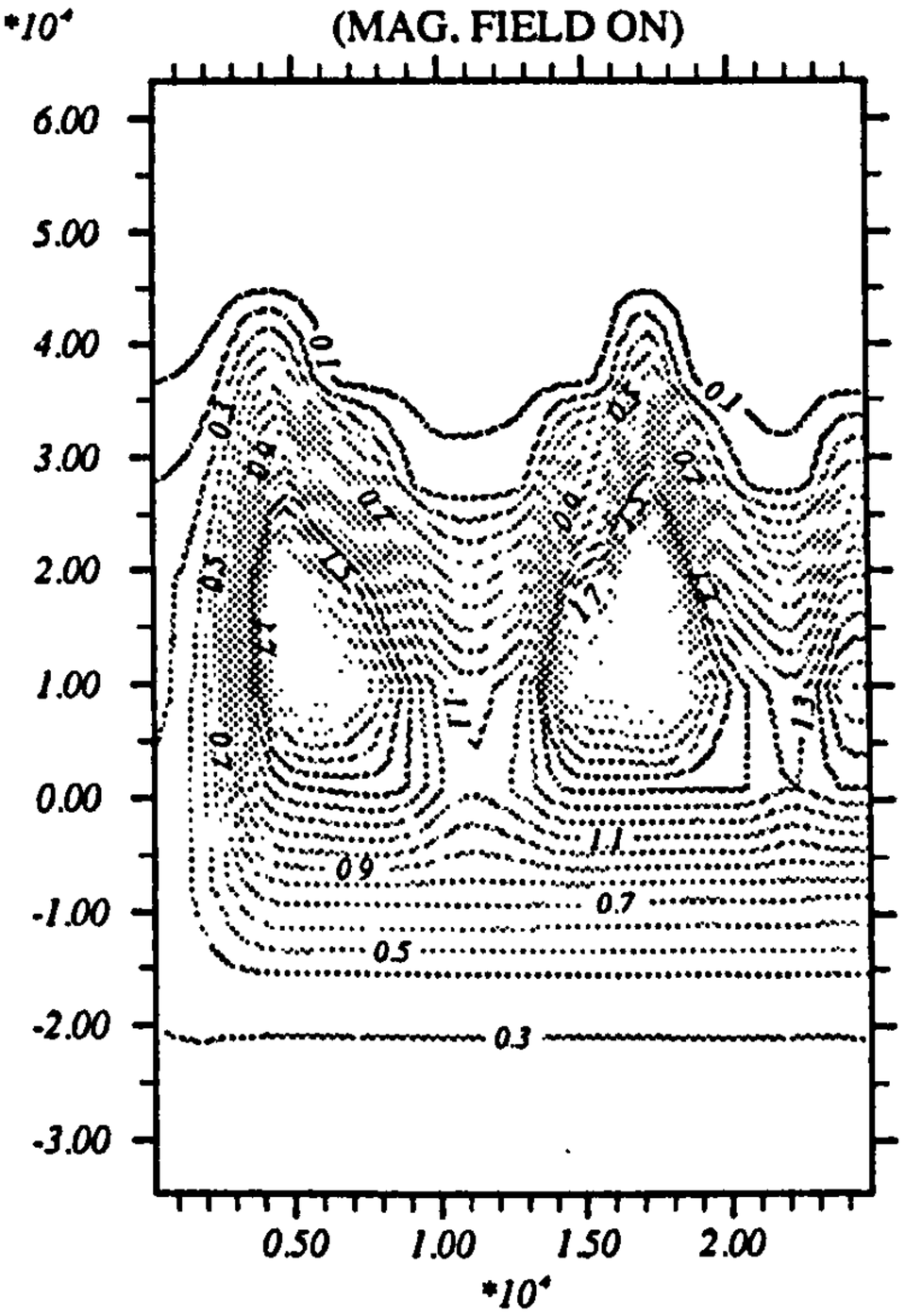

DENSITY MAP AT 400PS
(NO MAG. FIELD)

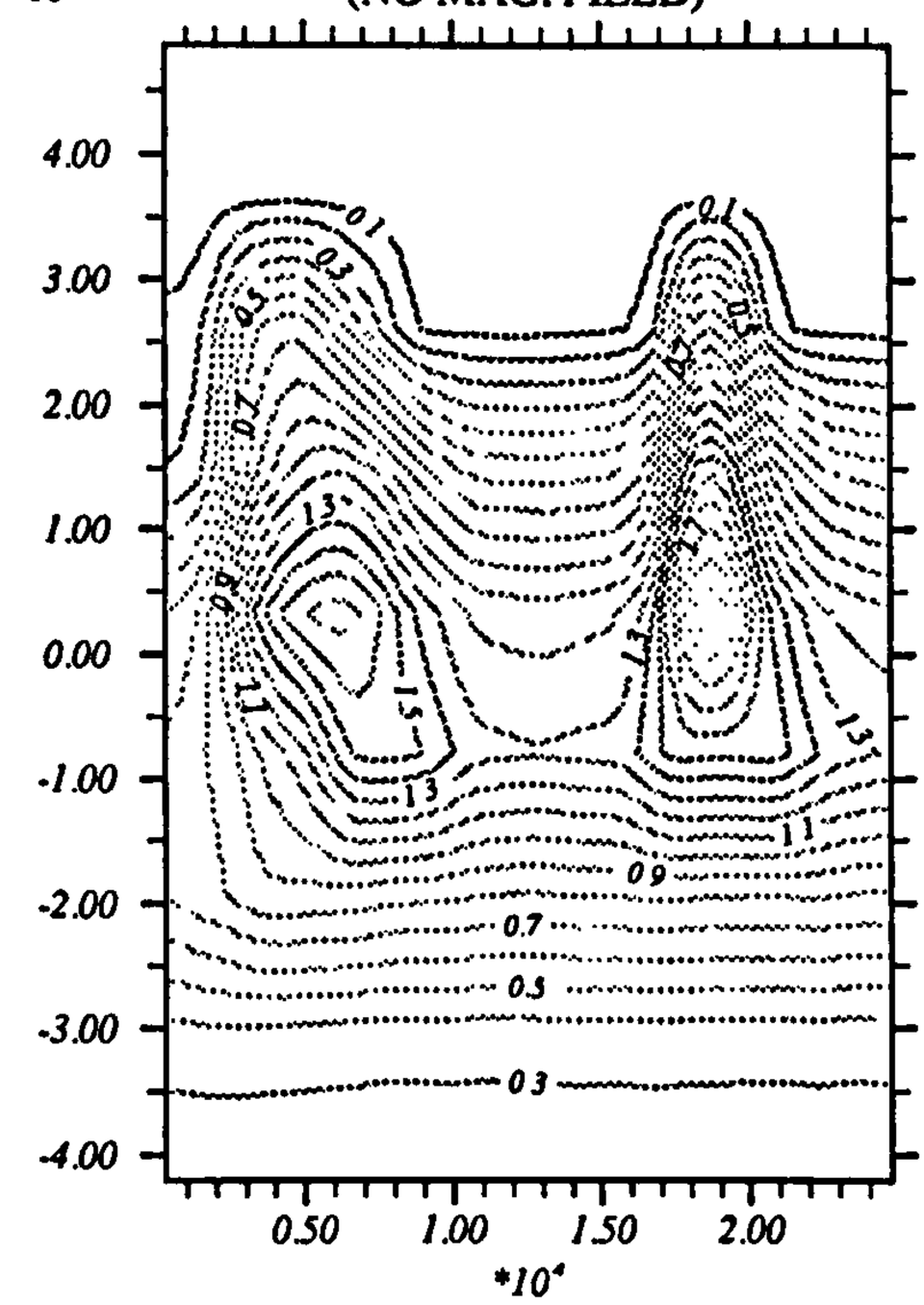

DENSITY MAP AT 400PS
(MAG. FIELD ON)

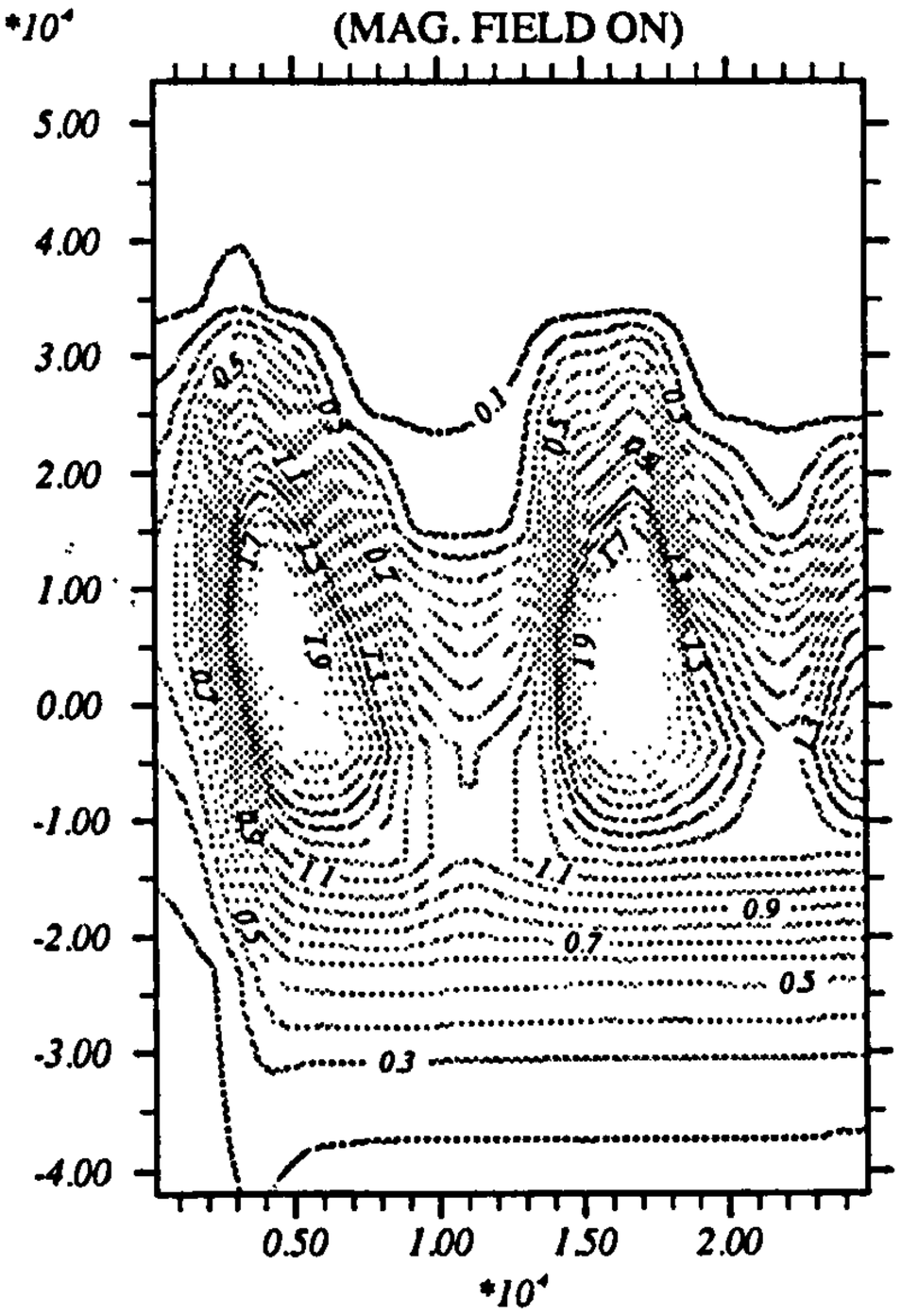

DENSITY MAP AT 450PS
(NO MAG. FIELD)

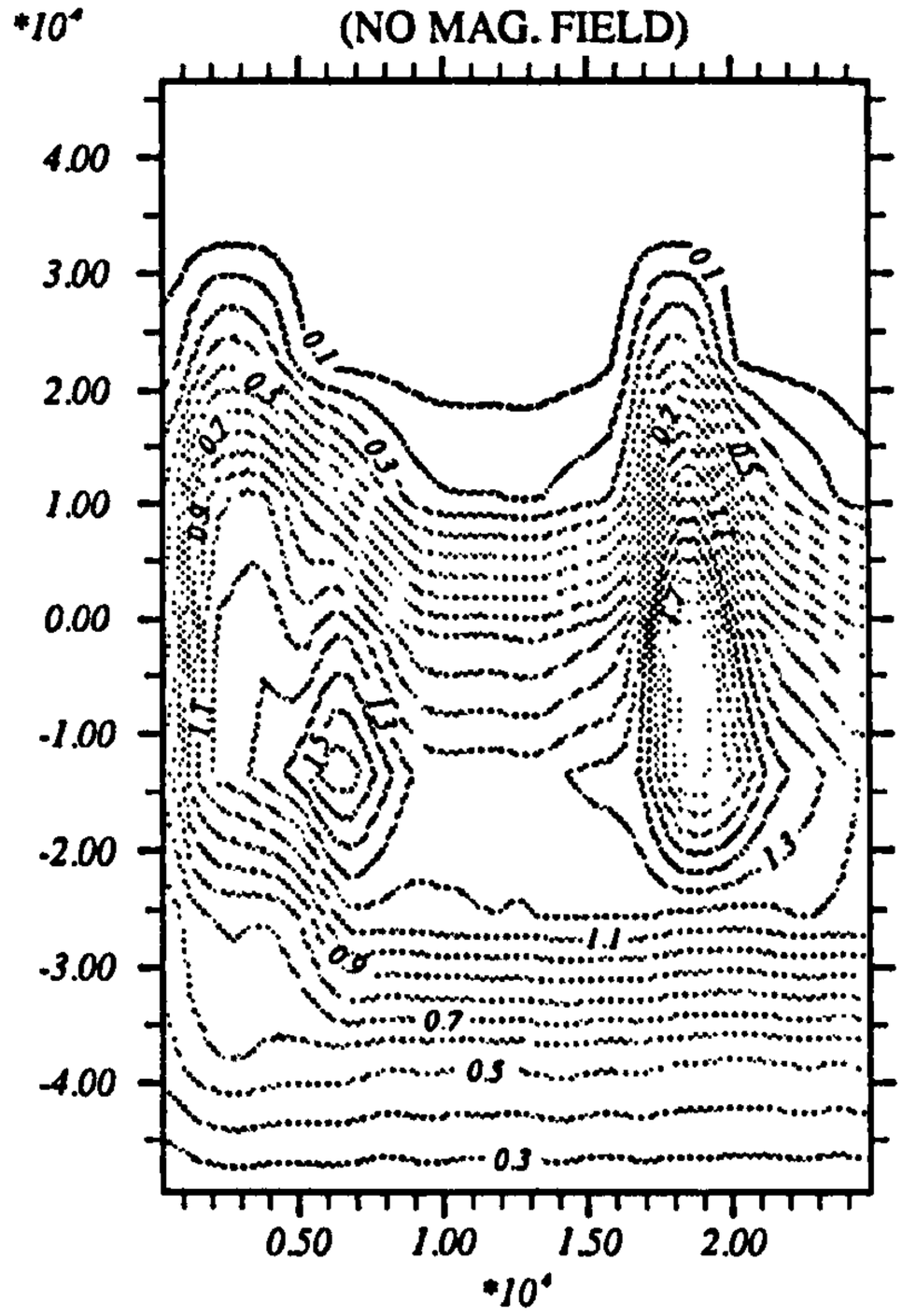

DENSITY MAP AT 450PS
(MAG. FIELD ON)

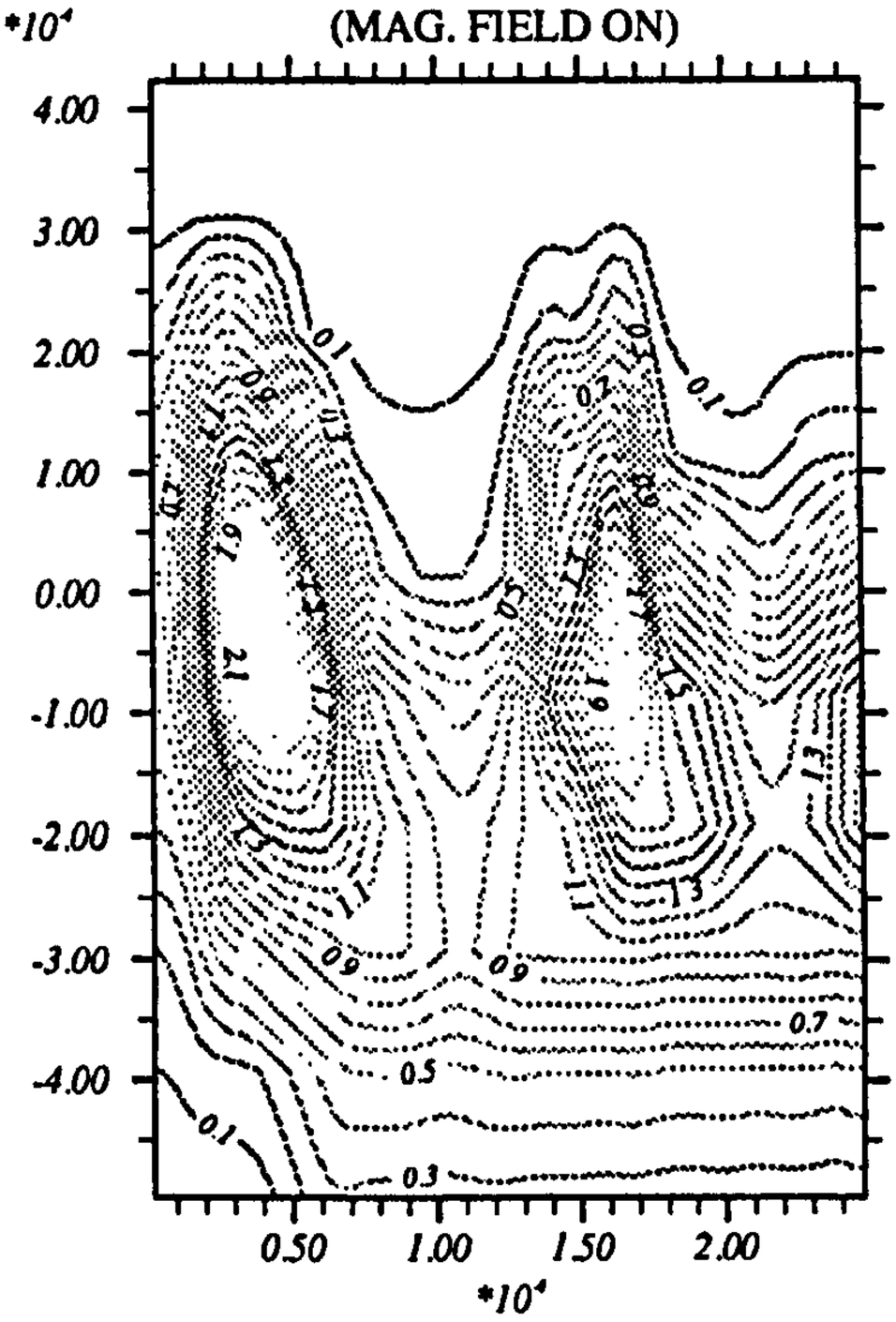

DENSITY MAP AT 500PS
(NO MAG. FIELD)

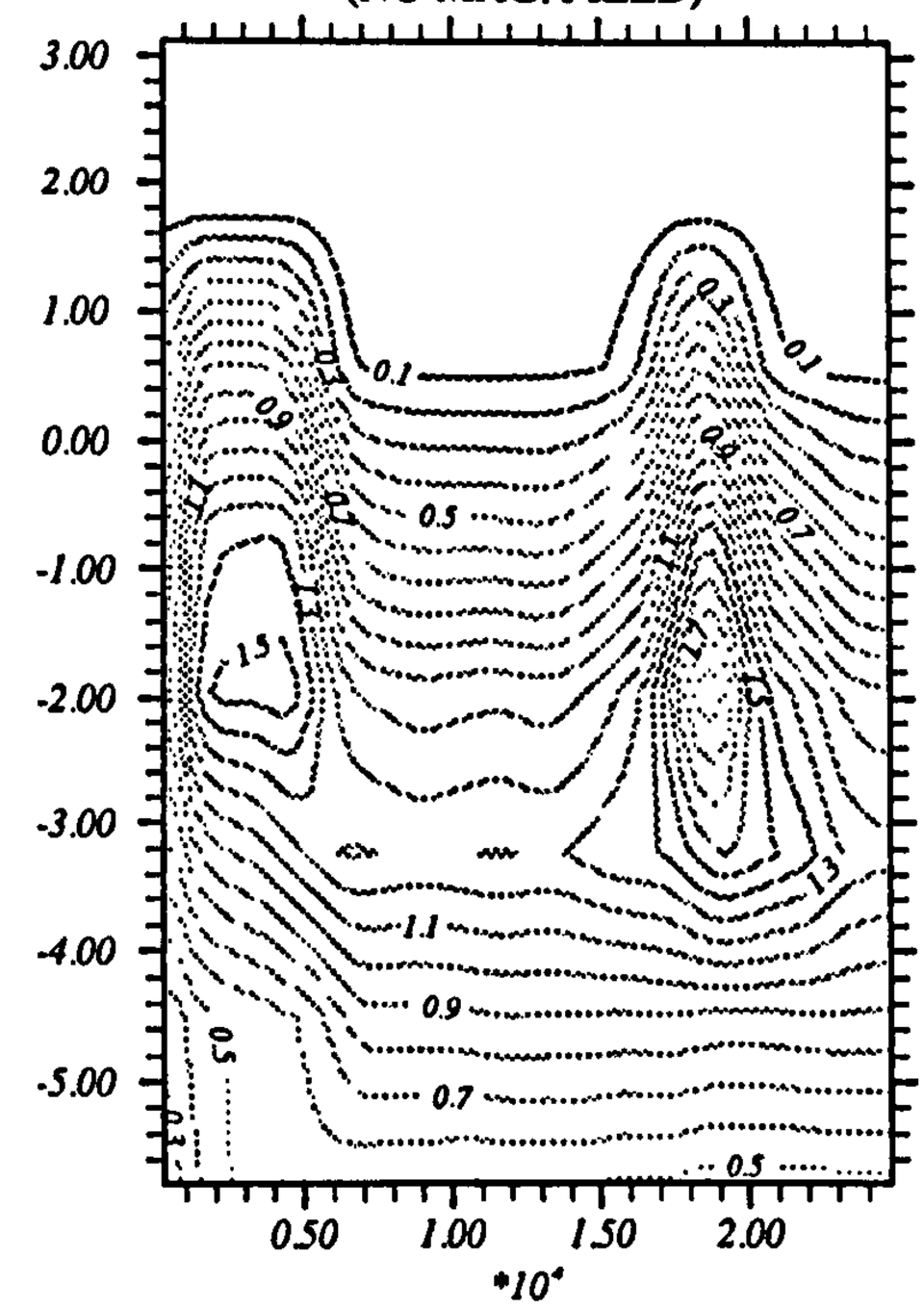

DENSITY MAP AT 500PS
(MAG. FIELD ON)

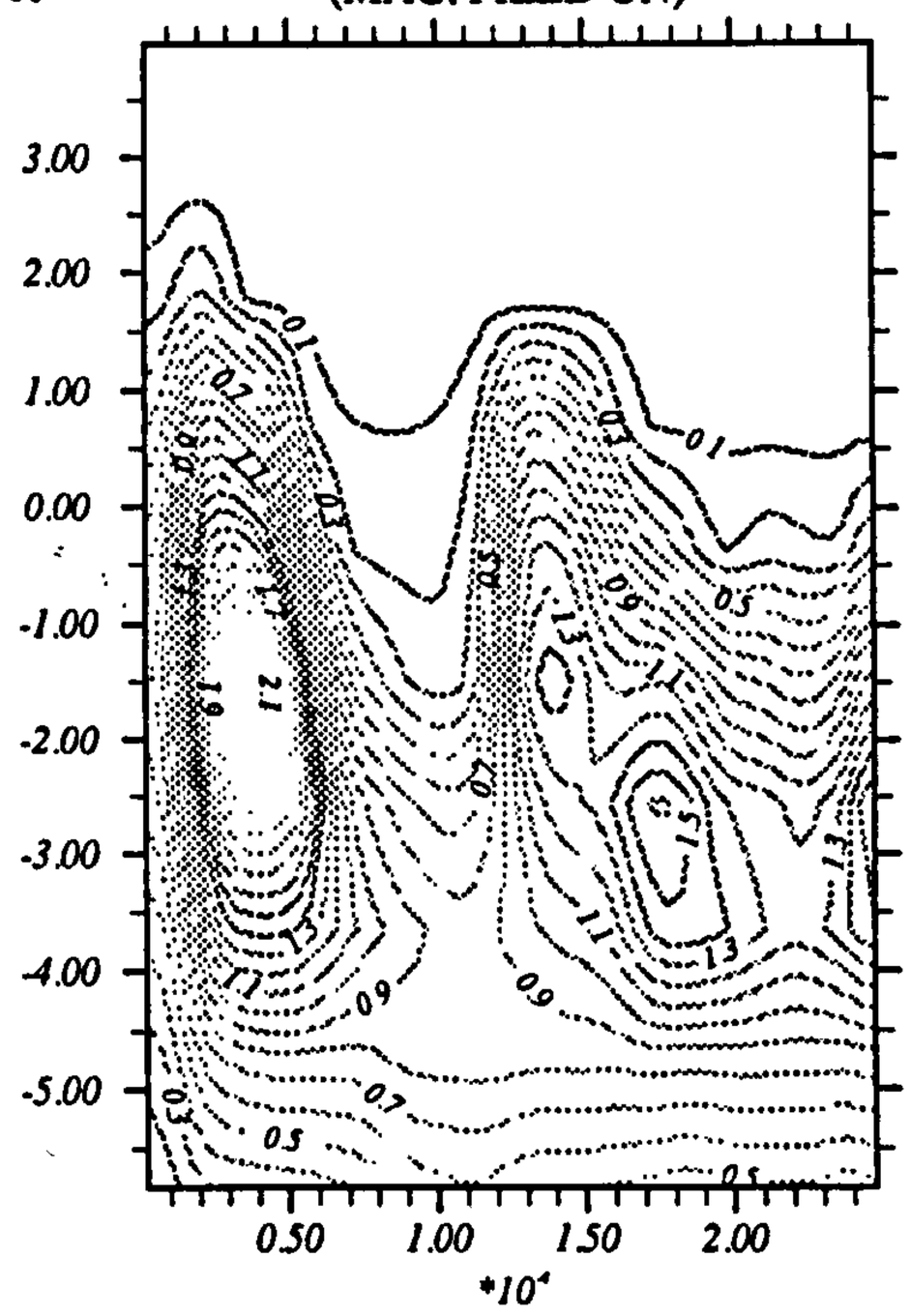

DENSITY MAP AT 550PS
(NO MAG. FIELD)

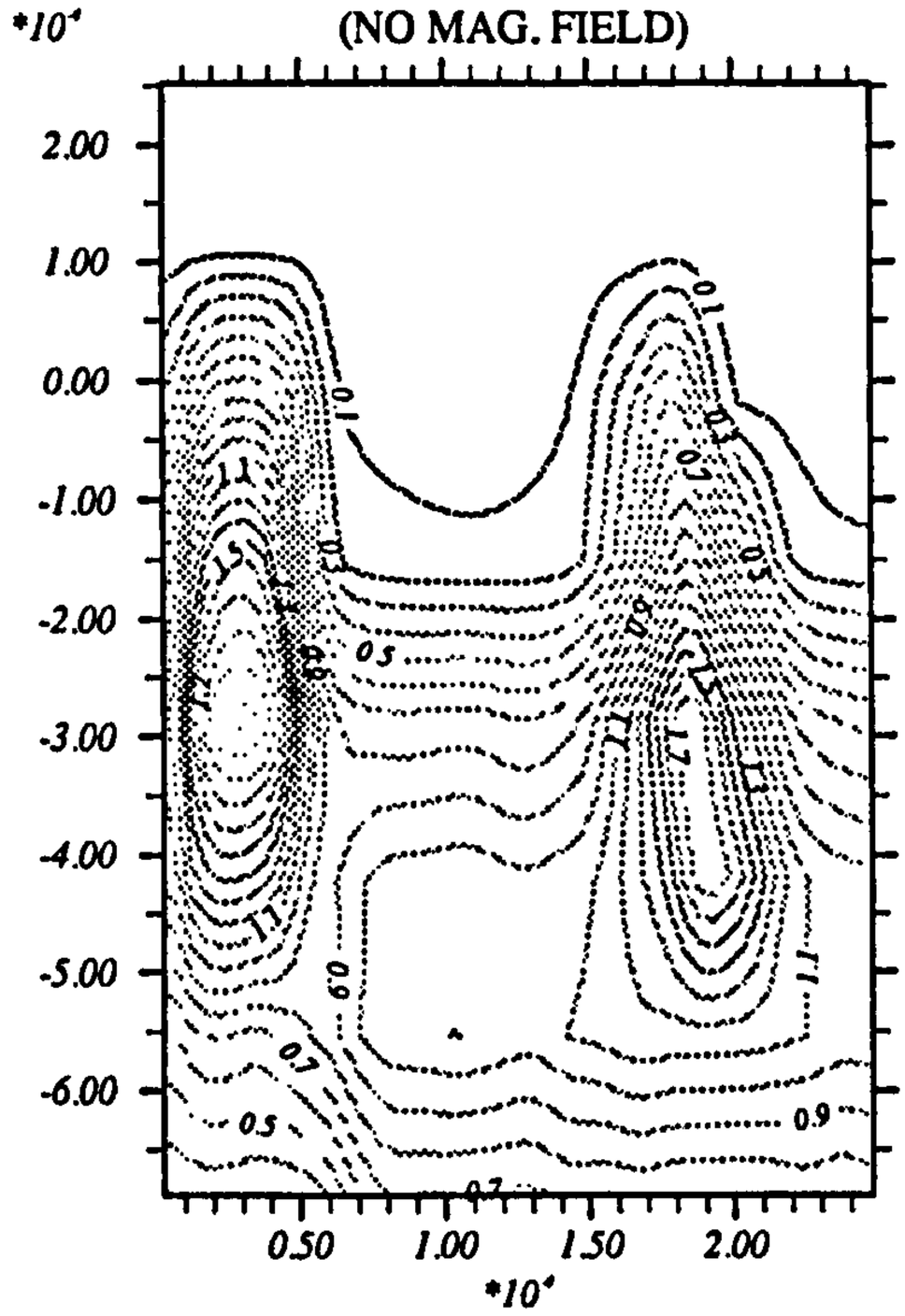

DENSITY MAP AT 550PS
(MAG. FIELD ON)

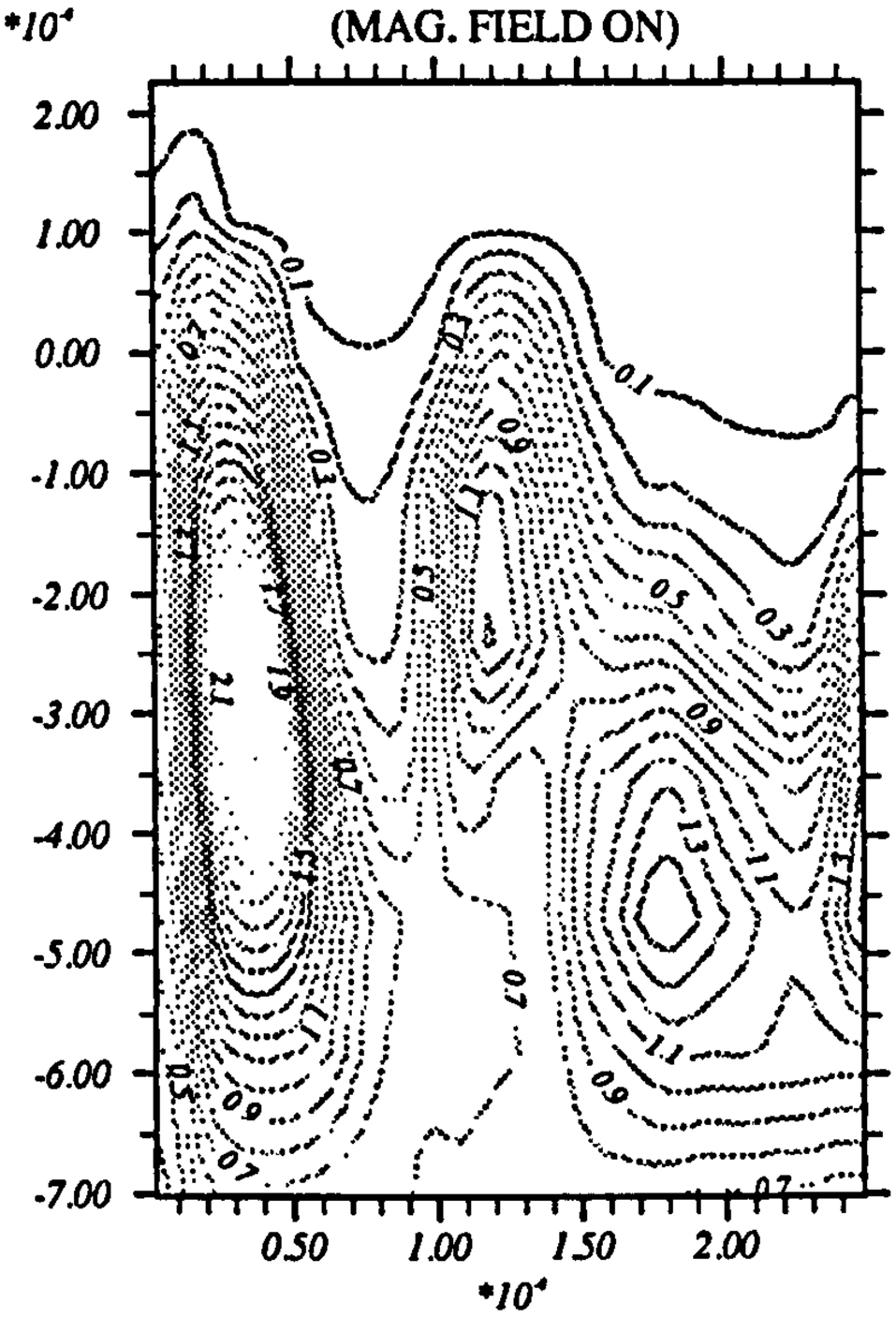

DENSITY MAP AT 600PS
(NO MAG. FIELD)

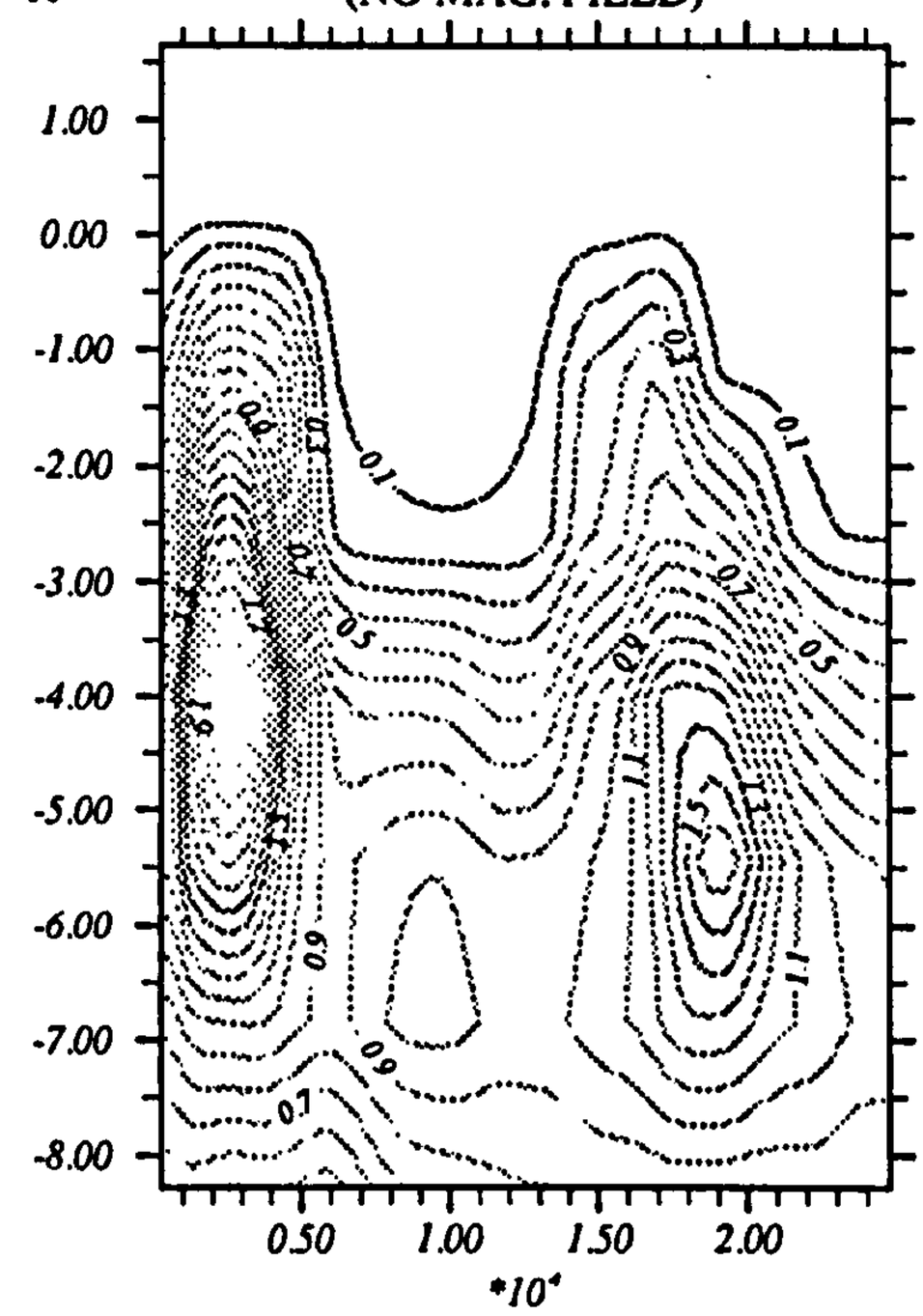

DENSITY MAP AT 600PS
(MAG. FIELD ON)

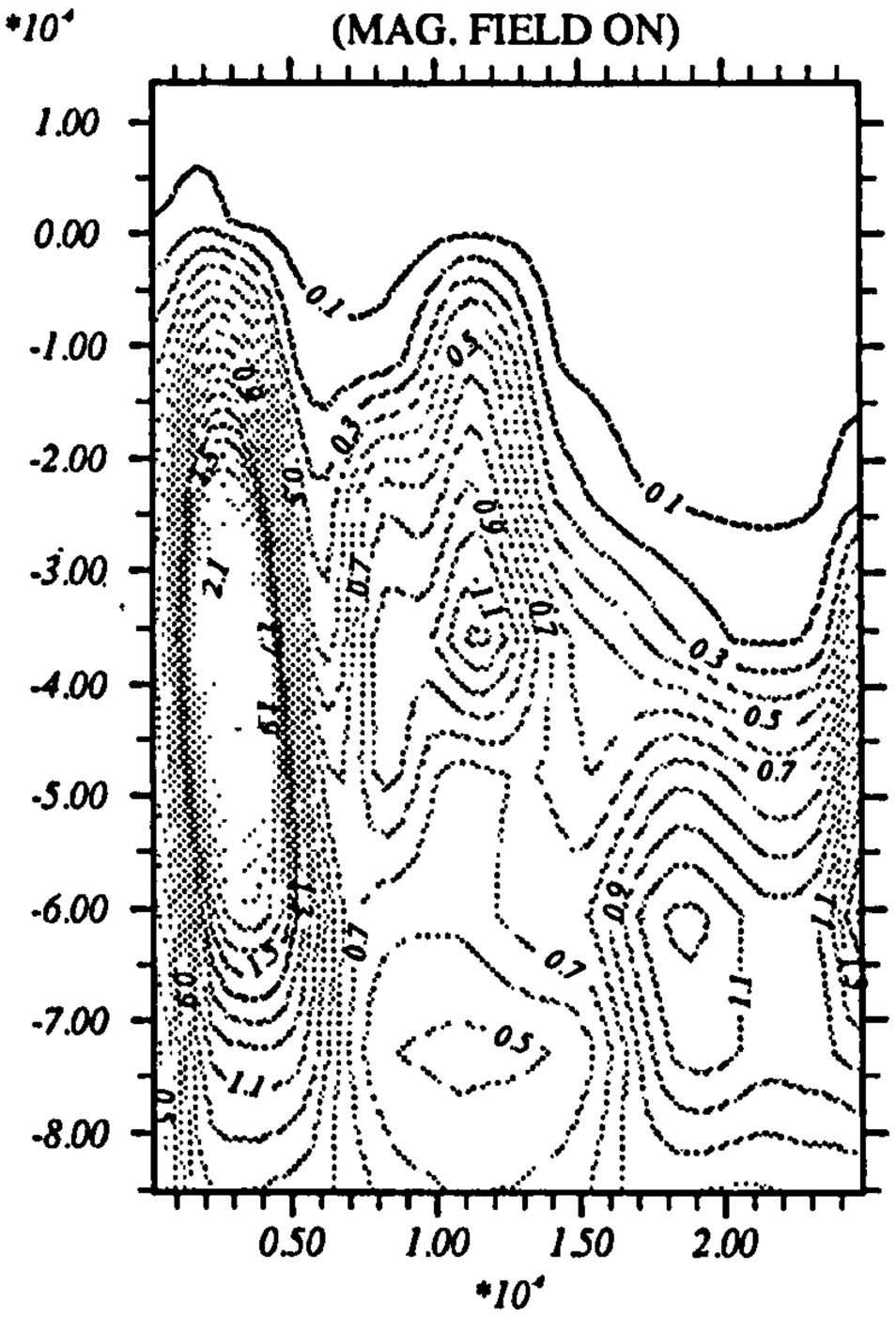

DENSITY MAP AT 650PS
(NO MAG. FIELD)

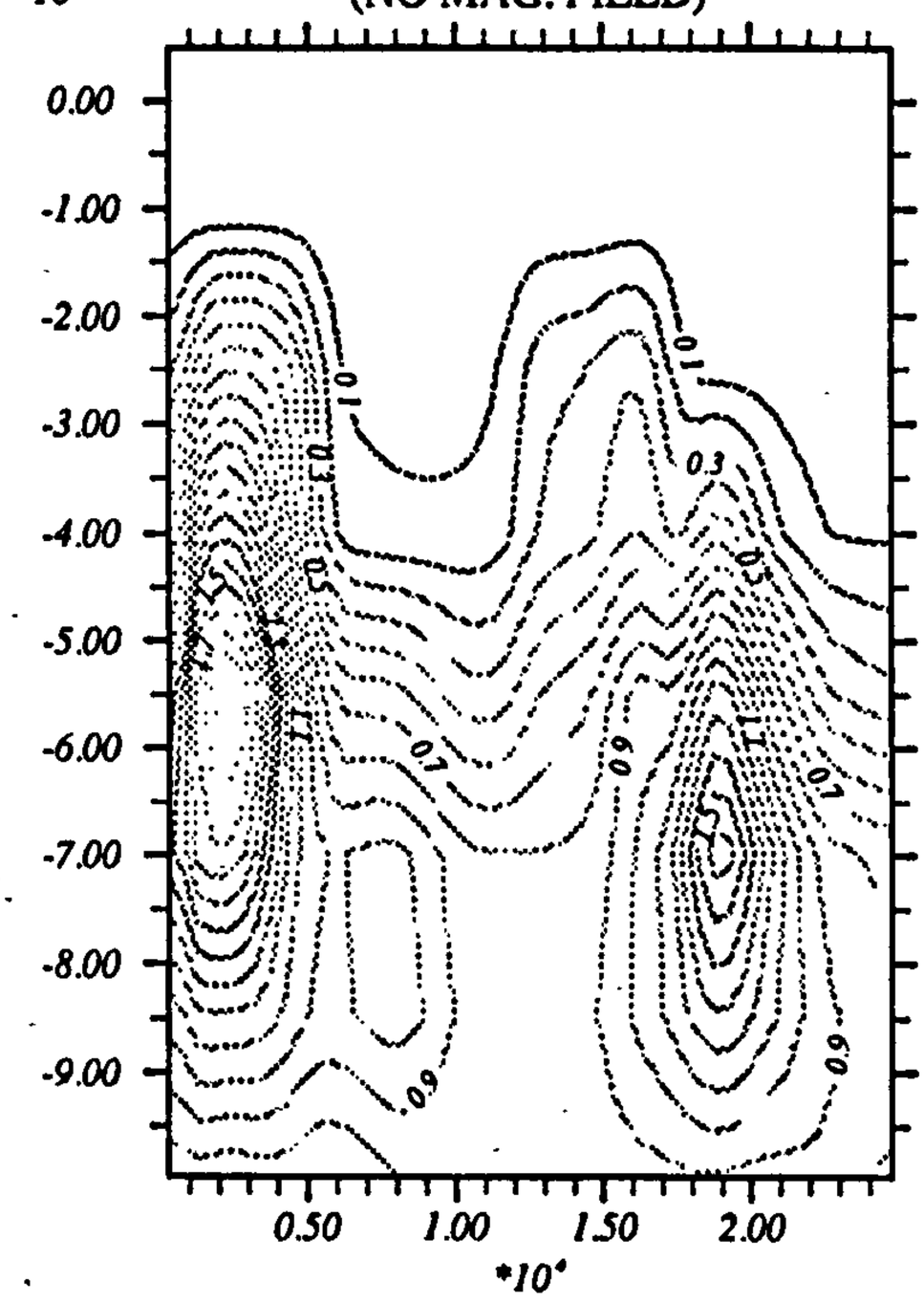

DENSITY MAP AT 650PS
(MAG. FIELD ON)

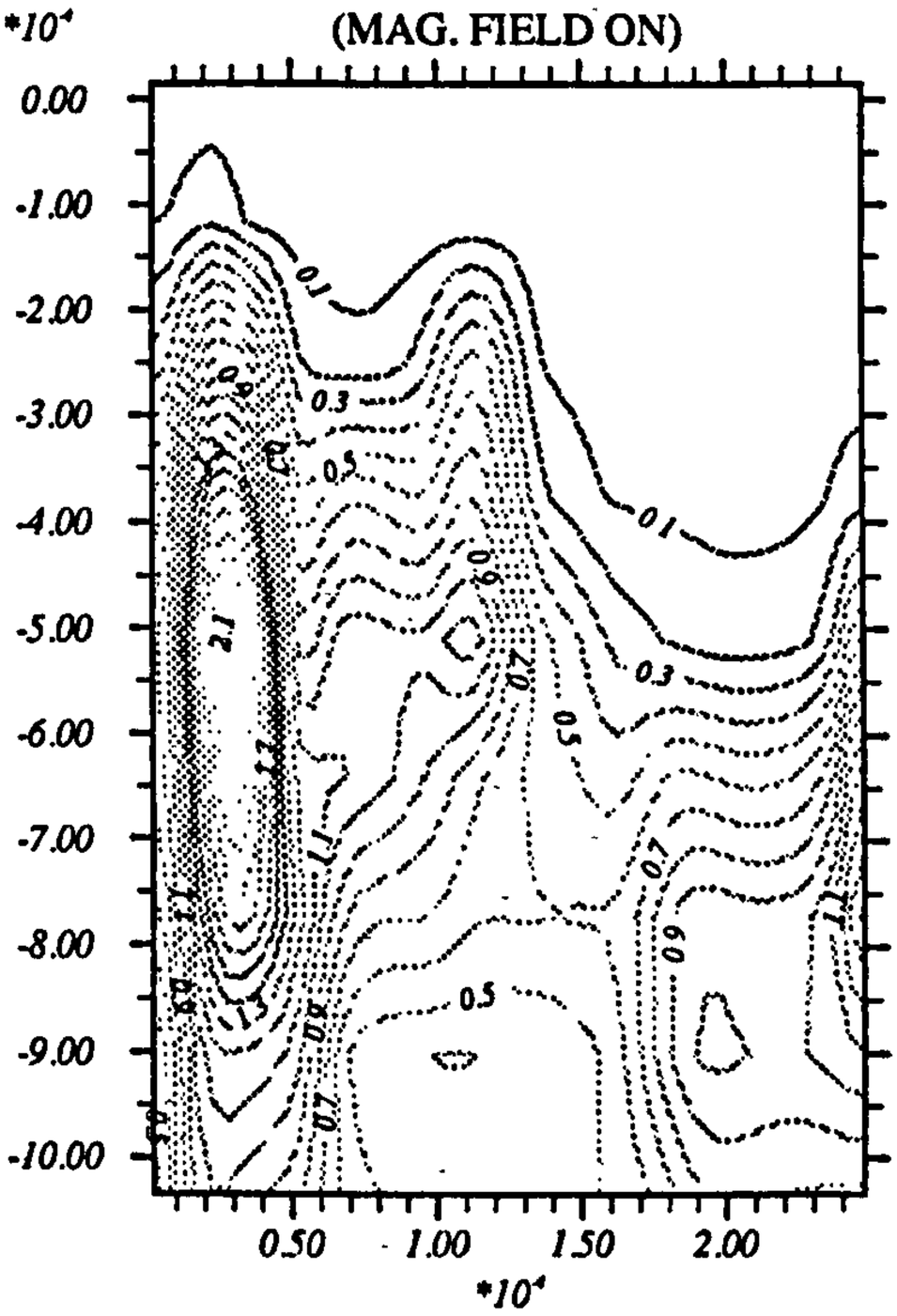

DENSITY MAP AT 700PS
(NO MAG. FIELD)

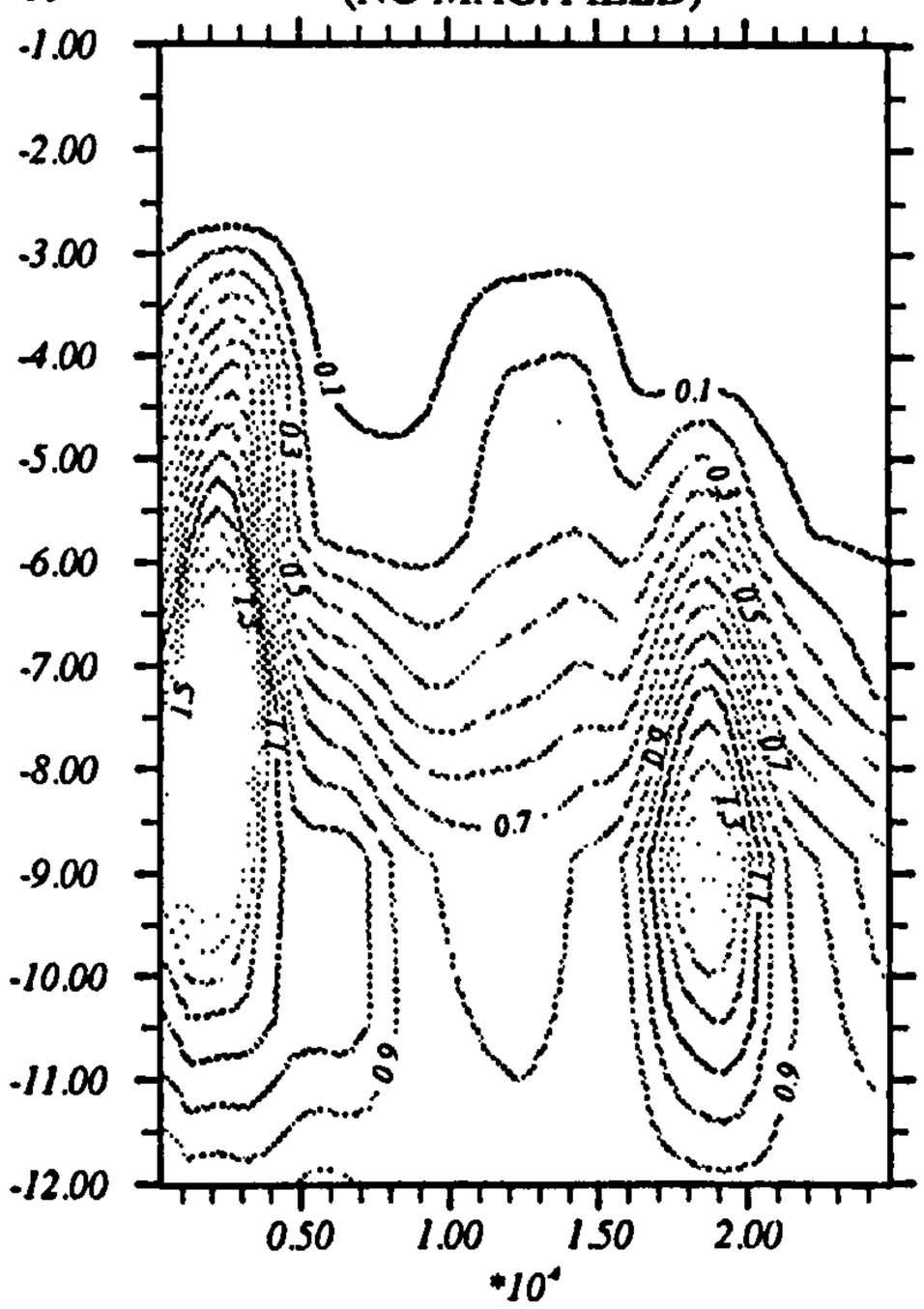

DENSITY MAP AT 700PS
(MAG. FIELD ON)

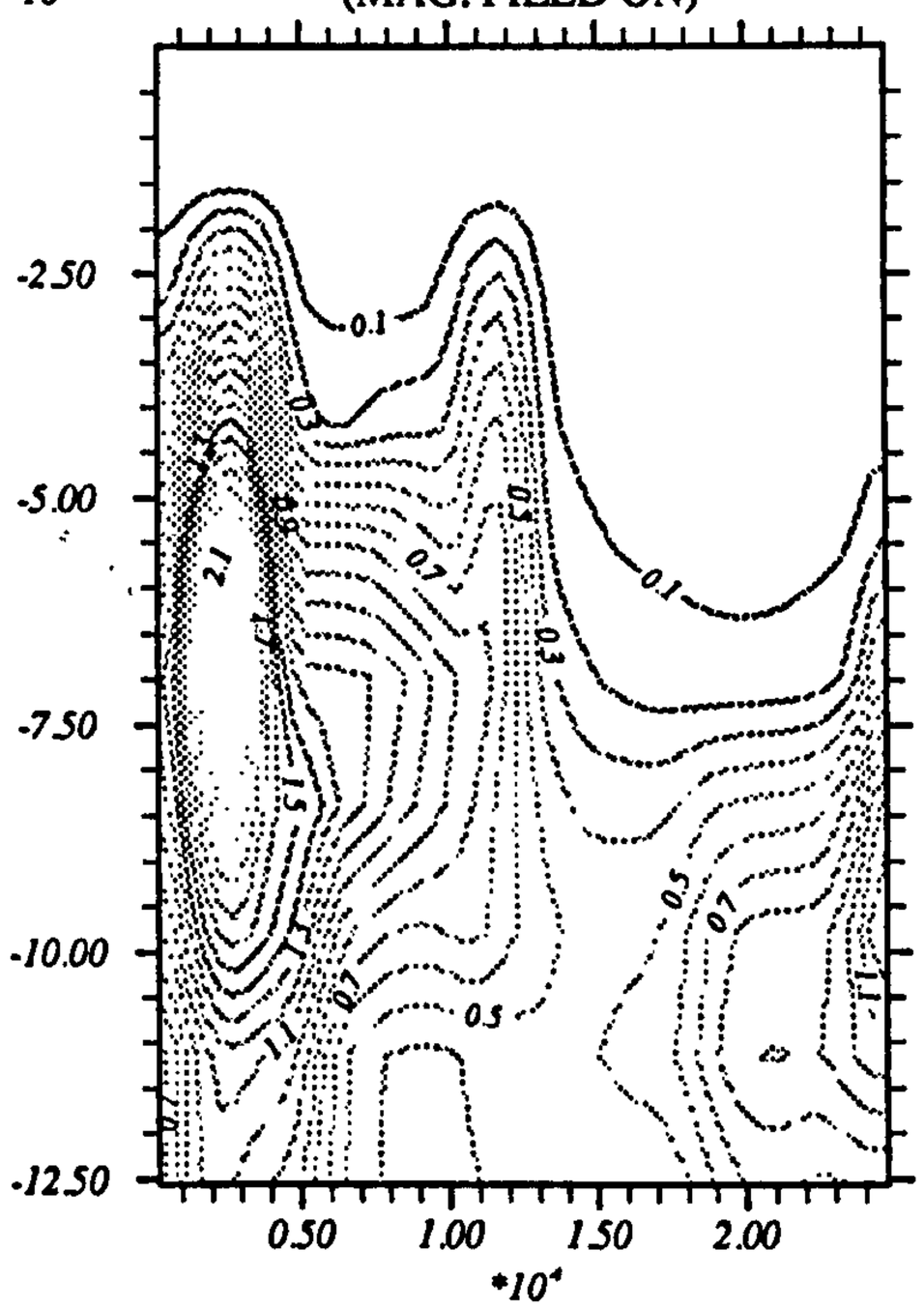

DENSITY MAP AT 750PS
(NO MAG. FIELD)

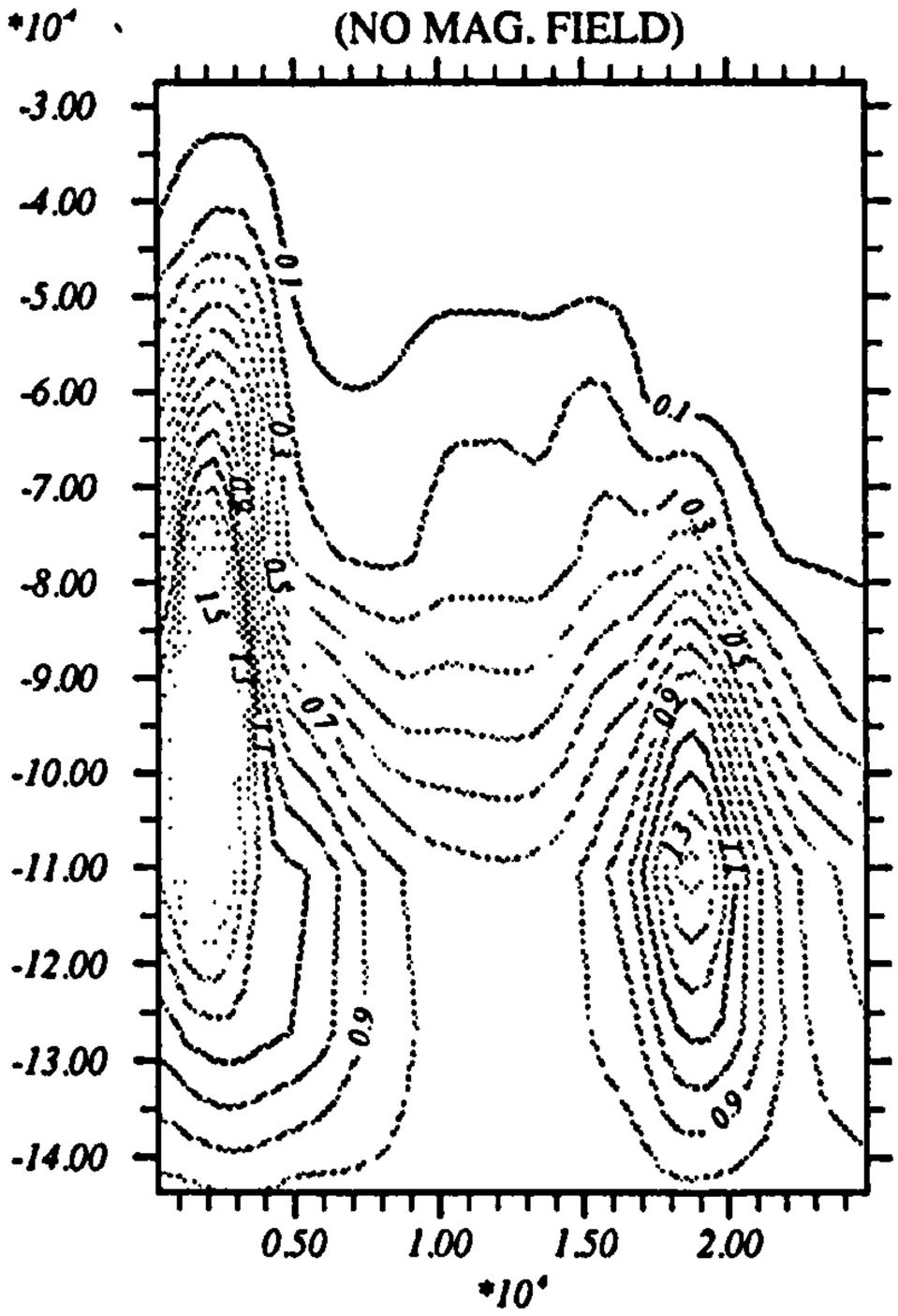

DENSITY MAP AT 750PS
(MAG. FIELD ON)

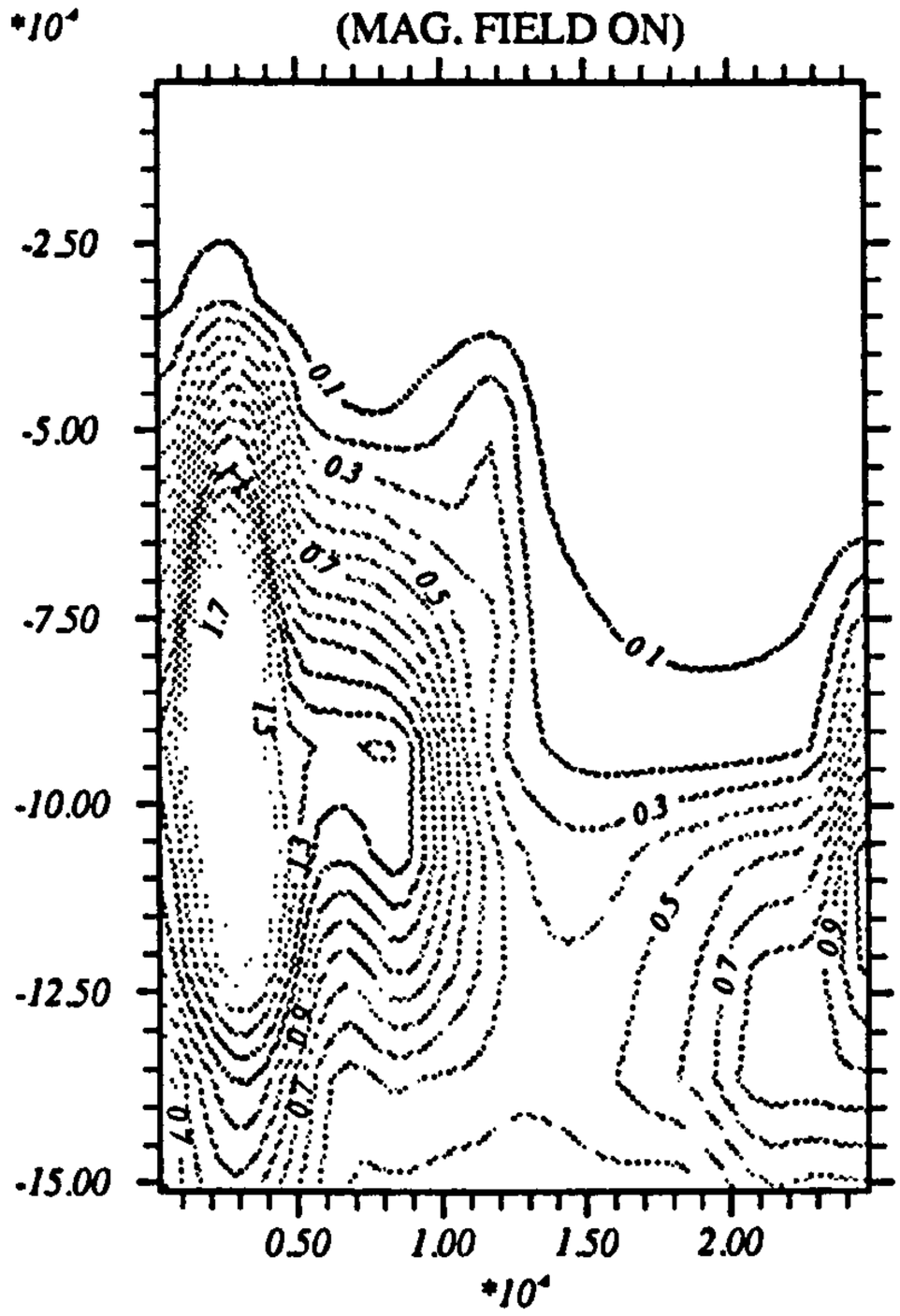

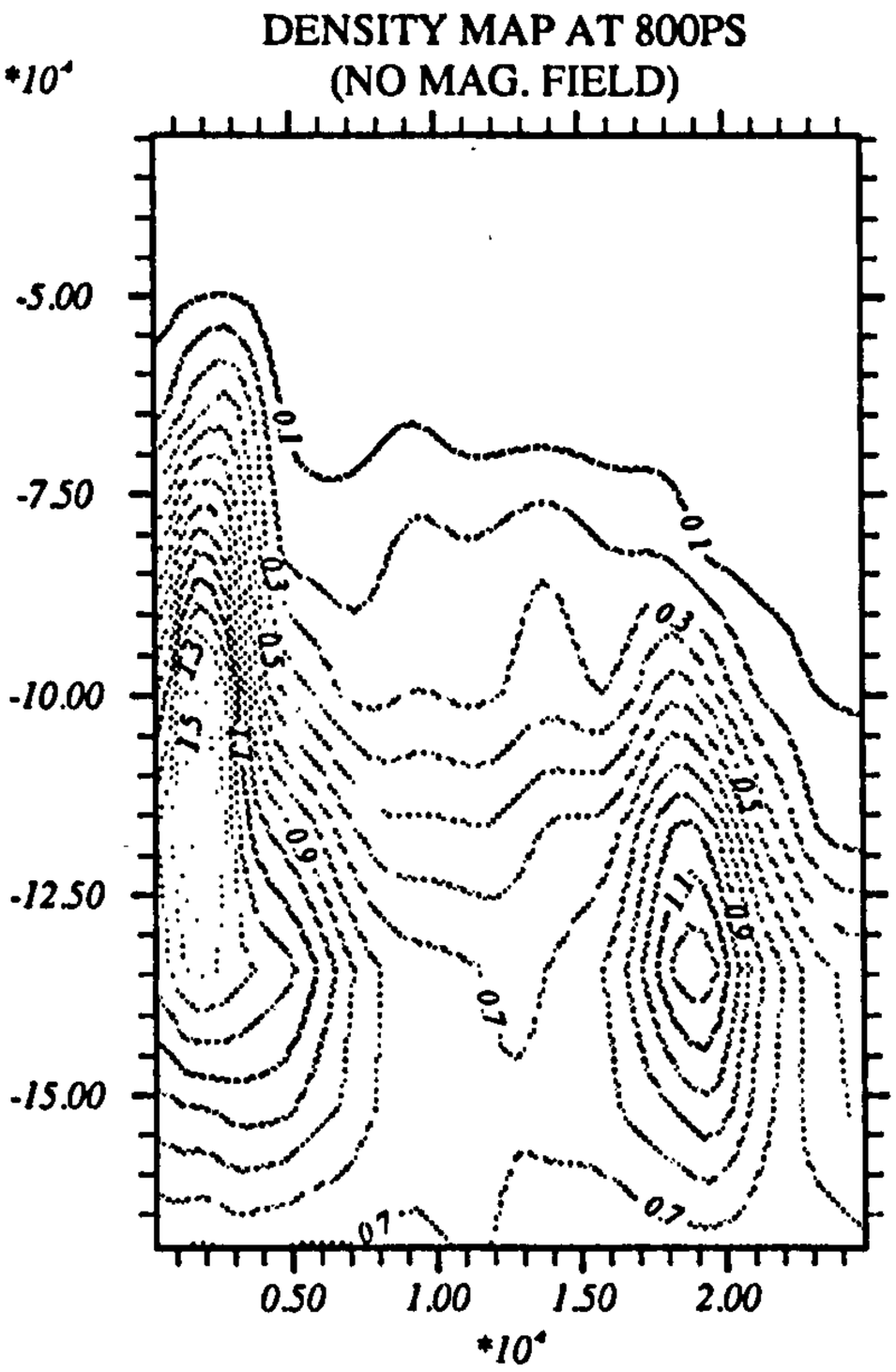
DENSITY MAP AT 800PS
(NO MAG. FIELD)
*10⁴
-5.00
-7.50
-10.00
-12.50
-15.00
0.50
1.00
1.50
2.00
*10⁴

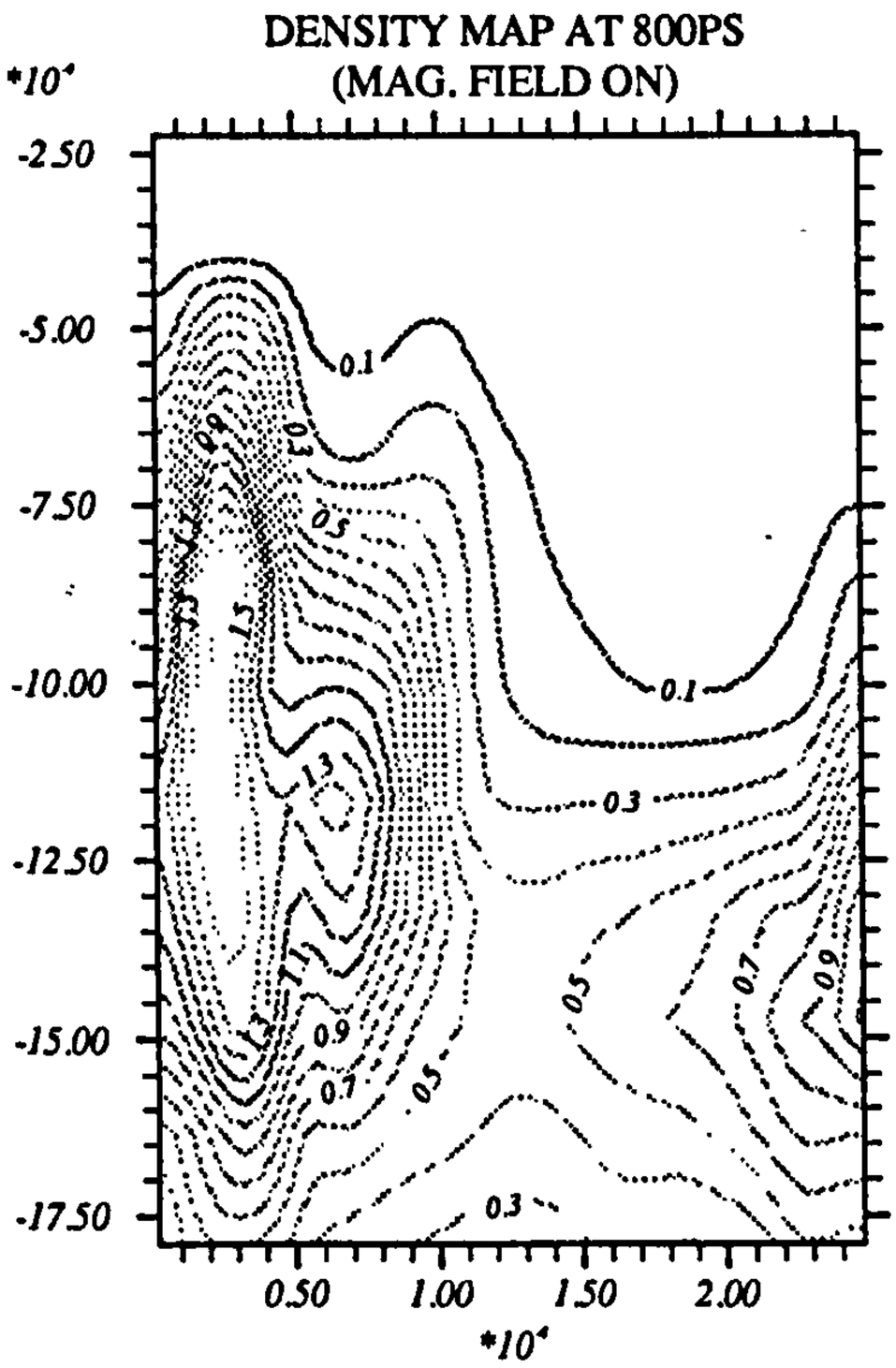
DENSITY MAP AT 800PS
(MAG. FIELD ON)
*10⁴
-2.50
-5.00
-7.50
-10.00
-12.50
-15.00
-17.50
0.50
1.00
1.50
2.00
*10⁴

of a high density node on the outer boundary. It appears that the high frequency modes which were observed in the early time have caused this shift towards the axis. When the time reaches up to 550ps one of the spikes grows substantially and the other disappears along with a very big bubble. The bubbles have affected the neighbourhood by pushing the material towards the edges. At the same time the mixing starts taking place when the magnetic fields are included. At 650ps the wave has completely burnt through the target and in the case when the magnetic field is on the target has almost completely disintegrated.

The situation becomes similar at 800ps when one of the spikes has completely disappeared and because of the hydro effects the other spike is pushed towards the axis of the target. We also observe another interesting feature, in the case of magnetic field being switched on the target is pushed back possibly as a result of the magnetic pressure.

It was difficult to measure the exact amplitude of bubbles and spikes. Therefore, the width of the mix region is specified as the amplitude of the instability which is the mean distance between the spike head and the bubble tip. In figure 5 · 3 we have plotted the amplitude of Rayleigh-Taylor instability (the width of the mix region) versus time. The growth of the Rayleigh-Taylor instability is slightly higher when the magnetic field is switched on. Some evidence of the phase shift in the behaviour between the two cases can be seen from this amplitude vs time graph. We observe that at the time of 350ps the instability growth is somewhat bigger for the magnetic field switched on over no field studies. We see at 600ps the growth of Rayleigh-Taylor instability is higher for non-magnetic field case which may be because of the mixing in the simulations with the magnetic field on. Soon after that time the instability again shoots up which is about twice over non-magnetic field case at later stage at 750ps.

The magnetic field, plasma beta and omega times tau contours are plotted in figures 5 · 4-5 · 6. It is clear that the positive values of the field come out of the paper whereas the negative values go into the page. These fields form loops around the cylindrical axis. A large number of these magnetic field loops are generated soon after the magnetic field is switched on and these are the source to generate the noise in density contours on the same time, their structure being closely related

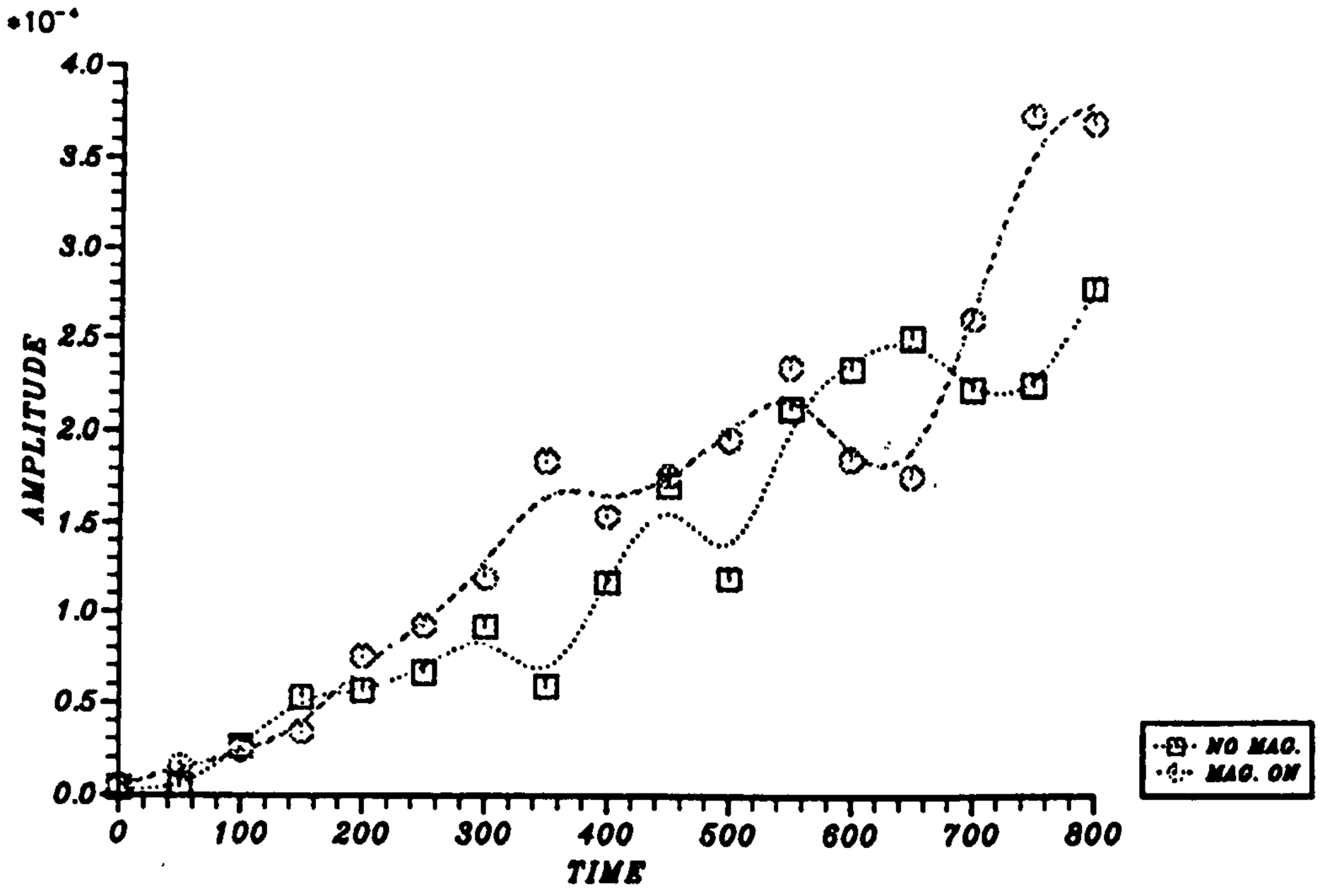

Figure 5.3: Amplitude vs time graph for a target of thickness $5 \cdot 0\mu m$ and radius $2 \cdot 5\mu m$

to the density perturbations.

5.3 Target size $(5 \cdot 0\mu m \times 5 \cdot 0\mu m)$

In these simulations the target size and the perturbation wavelength is changed. The computational mesh considered is $5 \cdot 0\mu m$ thick with the same radius. We again have applied two perturbation waves across the foil with the initial perturbation wavelength of $2 \cdot 5\mu m$. The code was run on the same computer for both cases magnetic field on/off which again took the same order of CPU time in each calculations as in the previous section. The complete target parameters are given in table $5 \cdot 2$.

The time history of instability growth for both magnetic field included and excluded is shown in figure $5 \cdot 7$ In these simulations high frequency modes again appear in the density contour maps when the magnetic field is on, in the early time up to 150ps and the spikes grow longer in the linear phase of the growth of the instability. The growth rate of instability is much slower in the case when

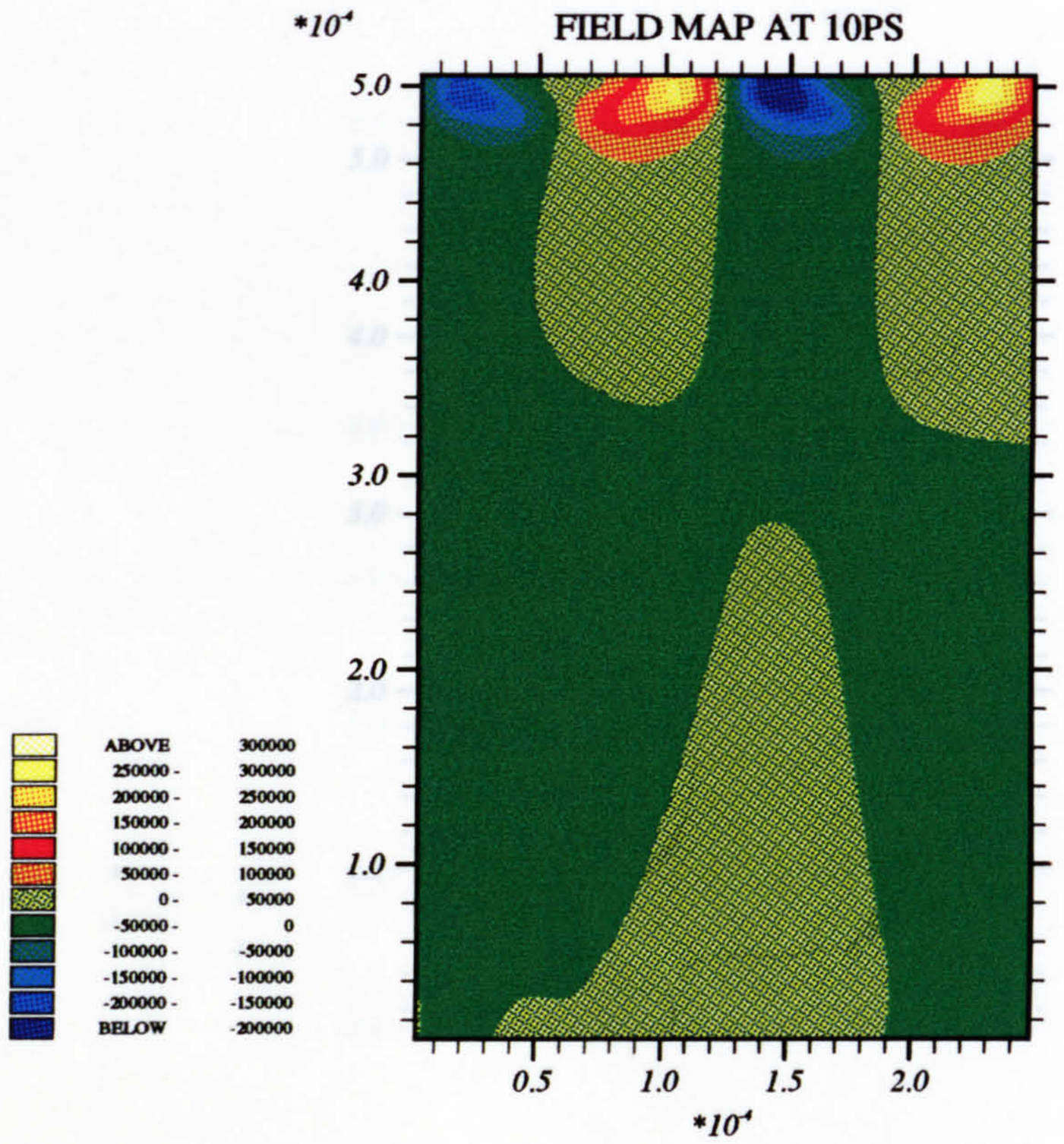

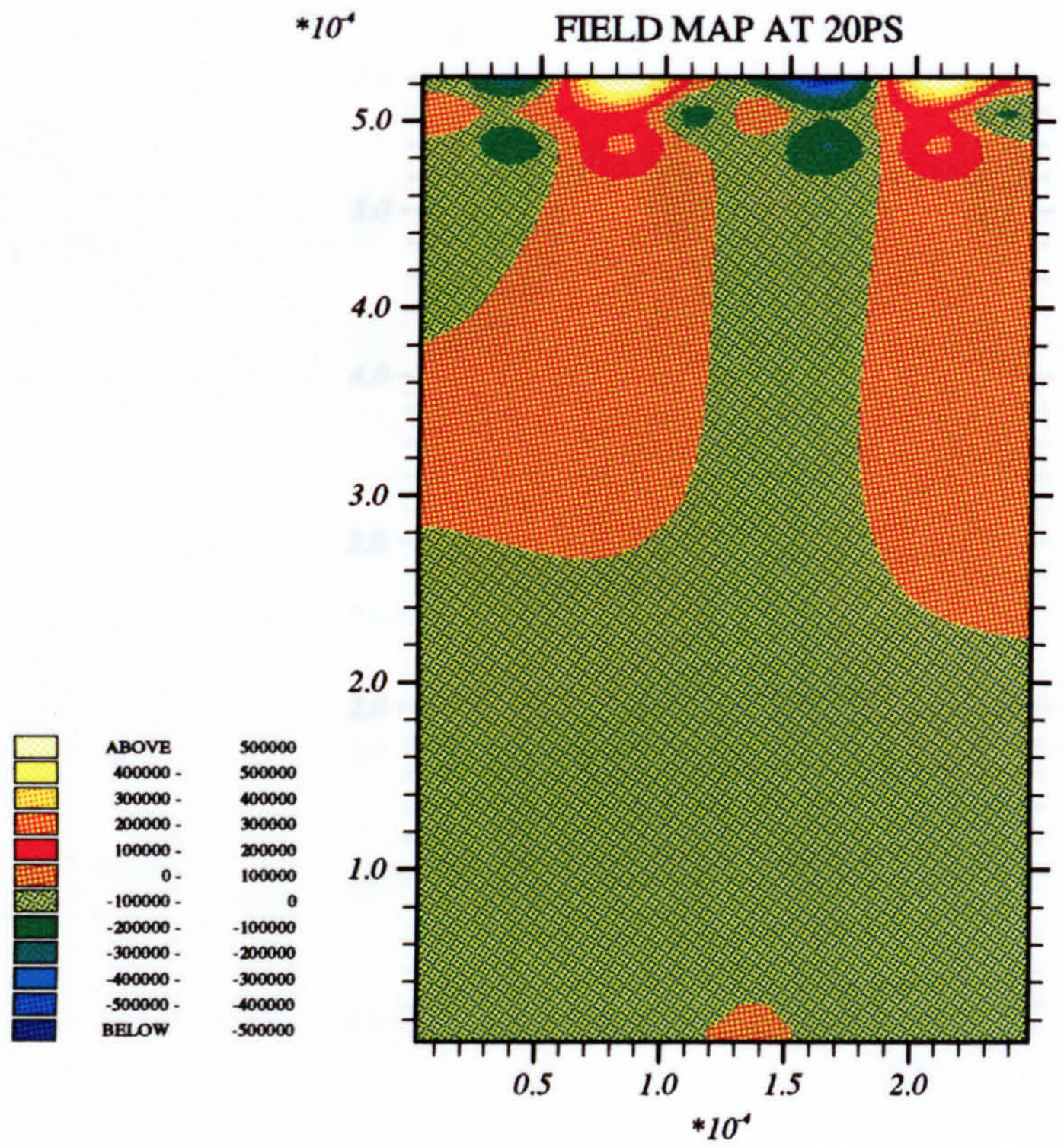

Figure 5.4: Magnetic field map for the target (5·0μm x 2·5μm) with the applied perturbation through density.

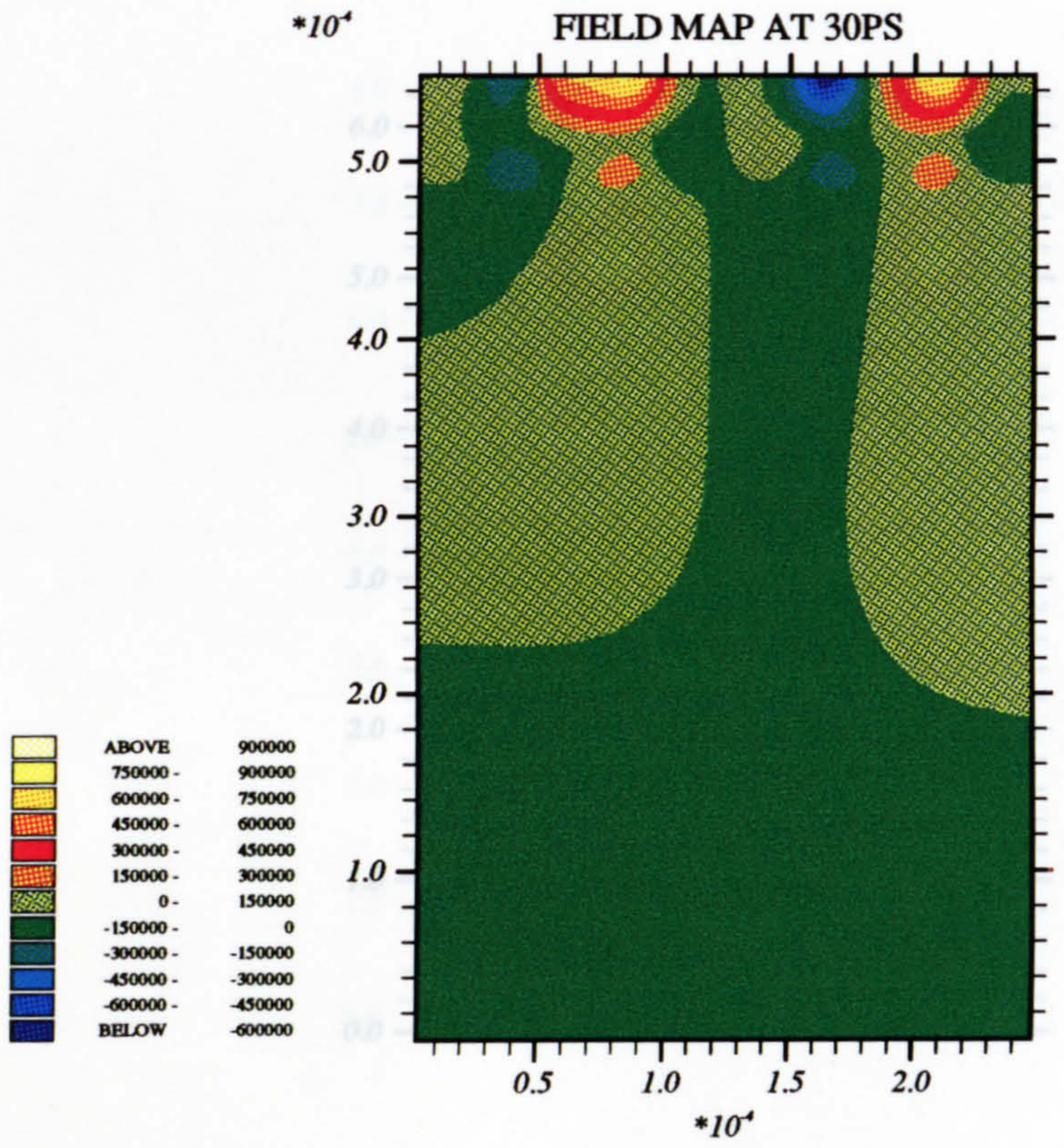
FIELD MAP AT 30PS
*10⁻⁴
5.0
4.0
3.0
2.0
1.0
0.5
1.0
1.5
2.0
*10⁻⁴
ABOVE 900000
750000 - 900000
600000 - 750000
450000 - 600000
300000 - 450000
150000 - 300000
0 - 150000
-150000 - 0
-300000 - -150000
-450000 - -300000
-600000 - -450000
BELOW -600000

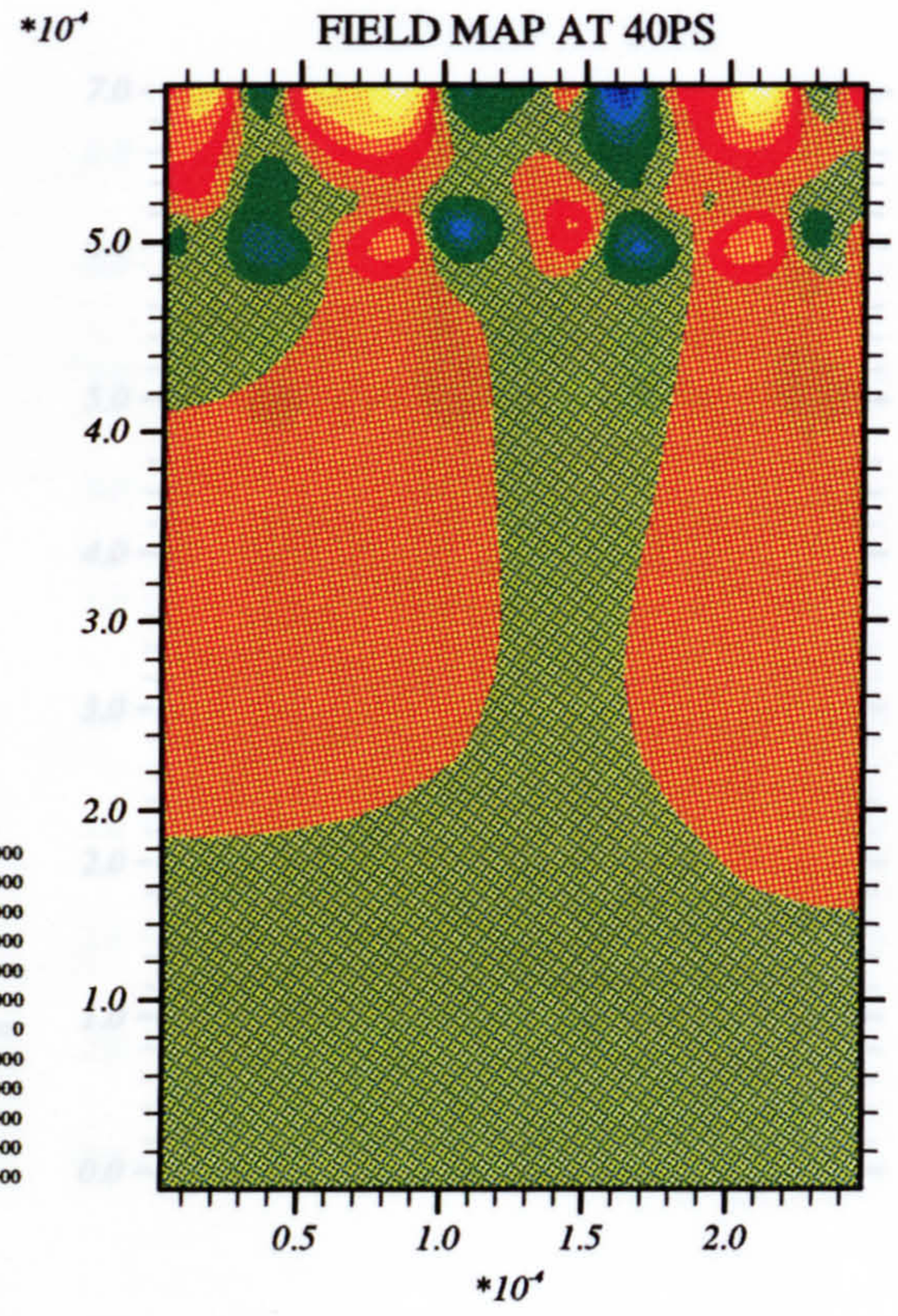
FIELD MAP AT 40PS
*10⁻⁴
5.0
4.0
3.0
2.0
1.0
0.5
1.0
1.5
2.0
*10⁻⁴
ABOVE 475000
380000 - 475000
285000 - 380000
190000 - 285000
95000 - 190000
0 - 95000
-95000 - 0
-190000 - -95000
-285000 - -190000
-380000 - -285000
-475000 - -380000
BELOW -475000

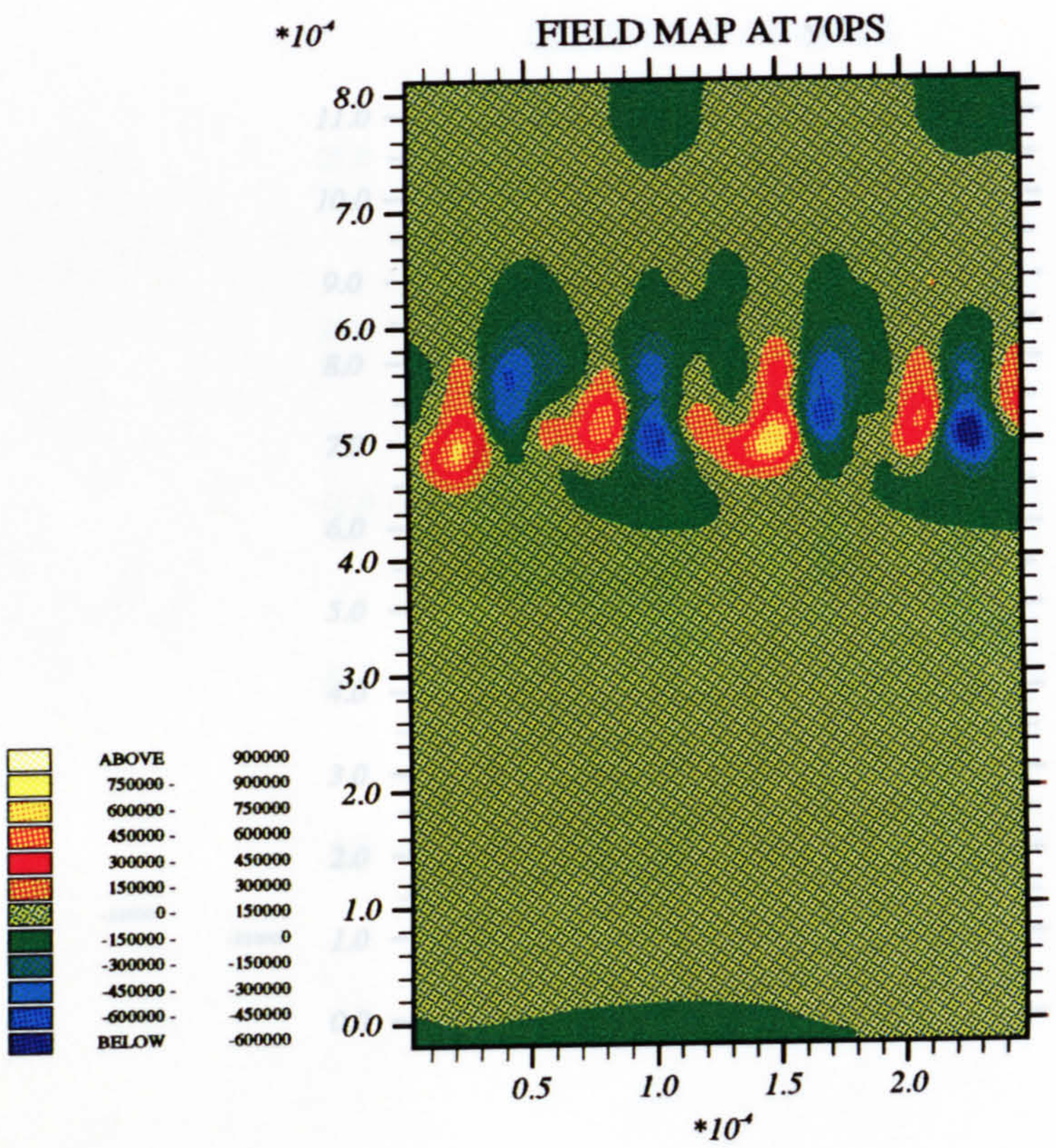
FIELD MAP AT 70PS
*10⁻⁴
8.0
7.0
6.0
5.0
4.0
3.0
2.0
1.0
0.0
0.5
1.0
1.5
2.0
*10⁻⁴
ABOVE 900000
750000 - 900000
600000 - 750000
450000 - 600000
300000 - 450000
150000 - 300000
0 - 150000
-150000 - 0
-300000 - -150000
-450000 - -300000
-600000 - -450000
BELOW -600000

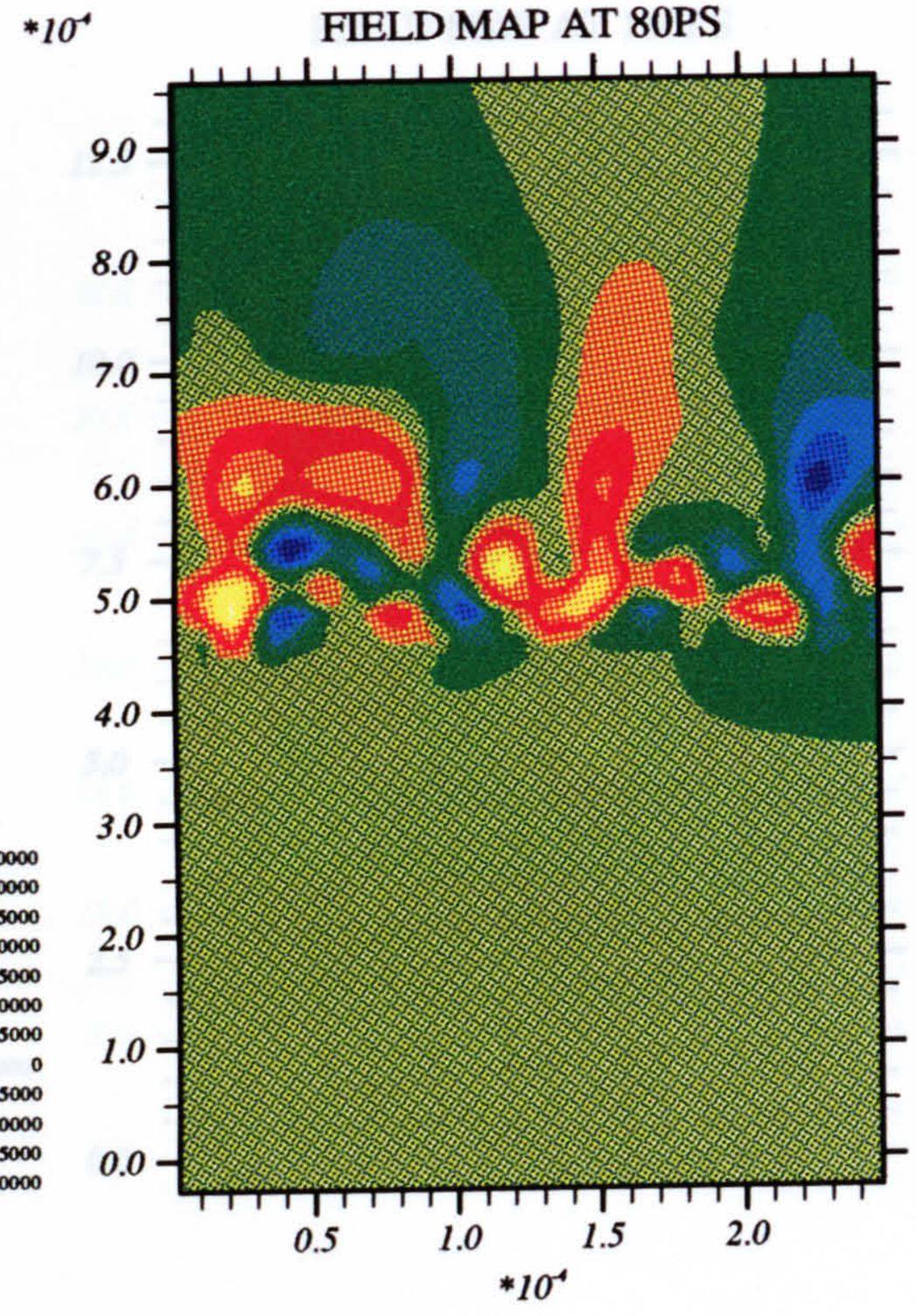
FIELD MAP AT 80PS
*10⁻⁴
9.0
8.0
7.0
6.0
5.0
4.0
3.0
2.0
1.0
0.0
0.5
1.0
1.5
2.0
*10⁻⁴
ABOVE 270000
225000 - 270000
180000 - 225000
135000 - 180000
90000 - 135000
45000 - 90000
0 - 45000
-45000 - 0
-90000 - -45000
-135000 - -90000
-180000 - -135000
BELOW -180000

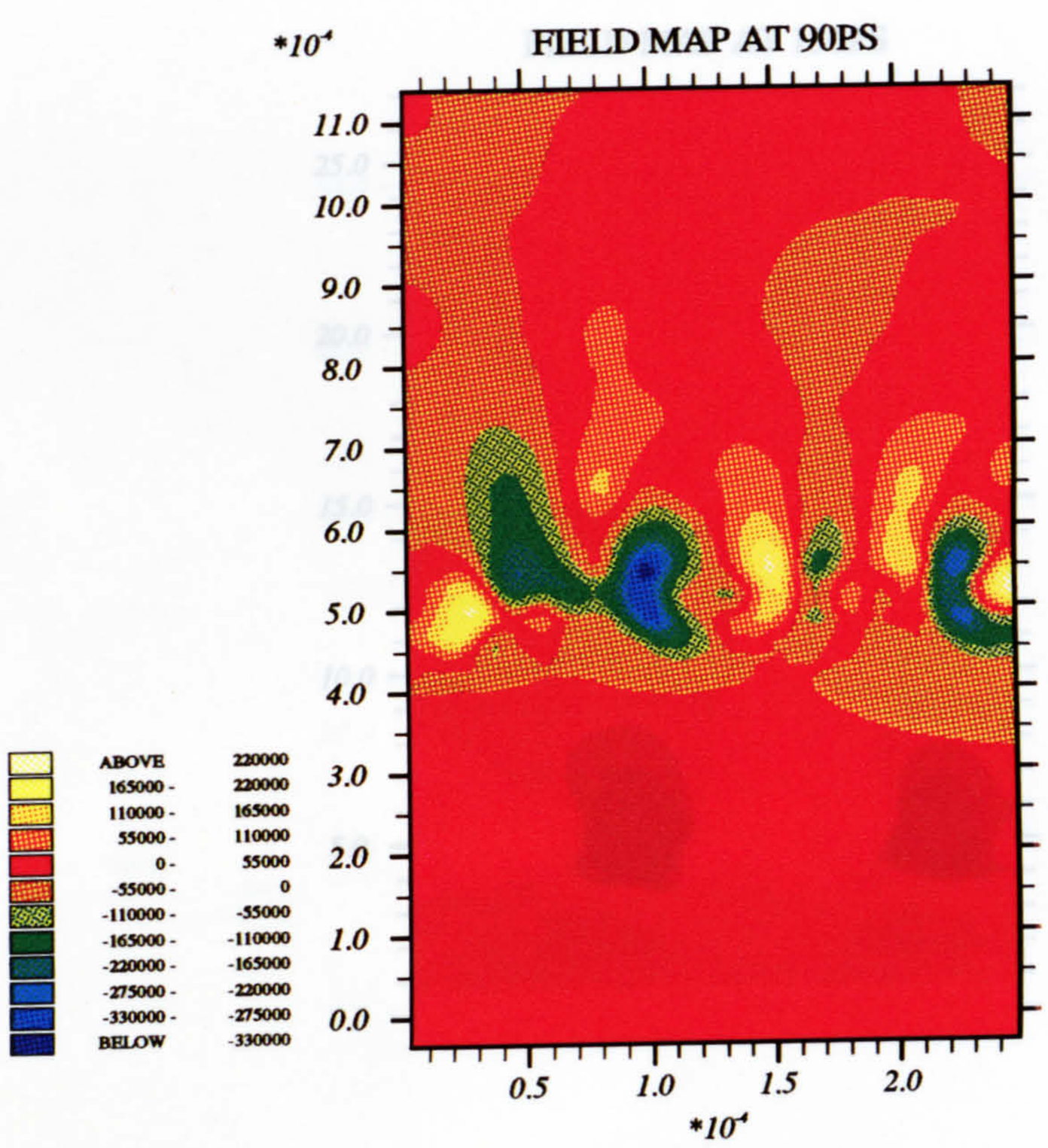
FIELD MAP AT 90PS
*10⁴
11.0
10.0
9.0
8.0
7.0
6.0
5.0
4.0
3.0
2.0
1.0
0.0
0.5
1.0
1.5
2.0
*10⁴
ABOVE 220000
165000 - 220000
110000 - 165000
55000 - 110000
0 - 55000
-55000 - 0
-110000 - -55000
-165000 - -110000
-220000 - -165000
-275000 - -220000
-330000 - -275000
BELOW -330000

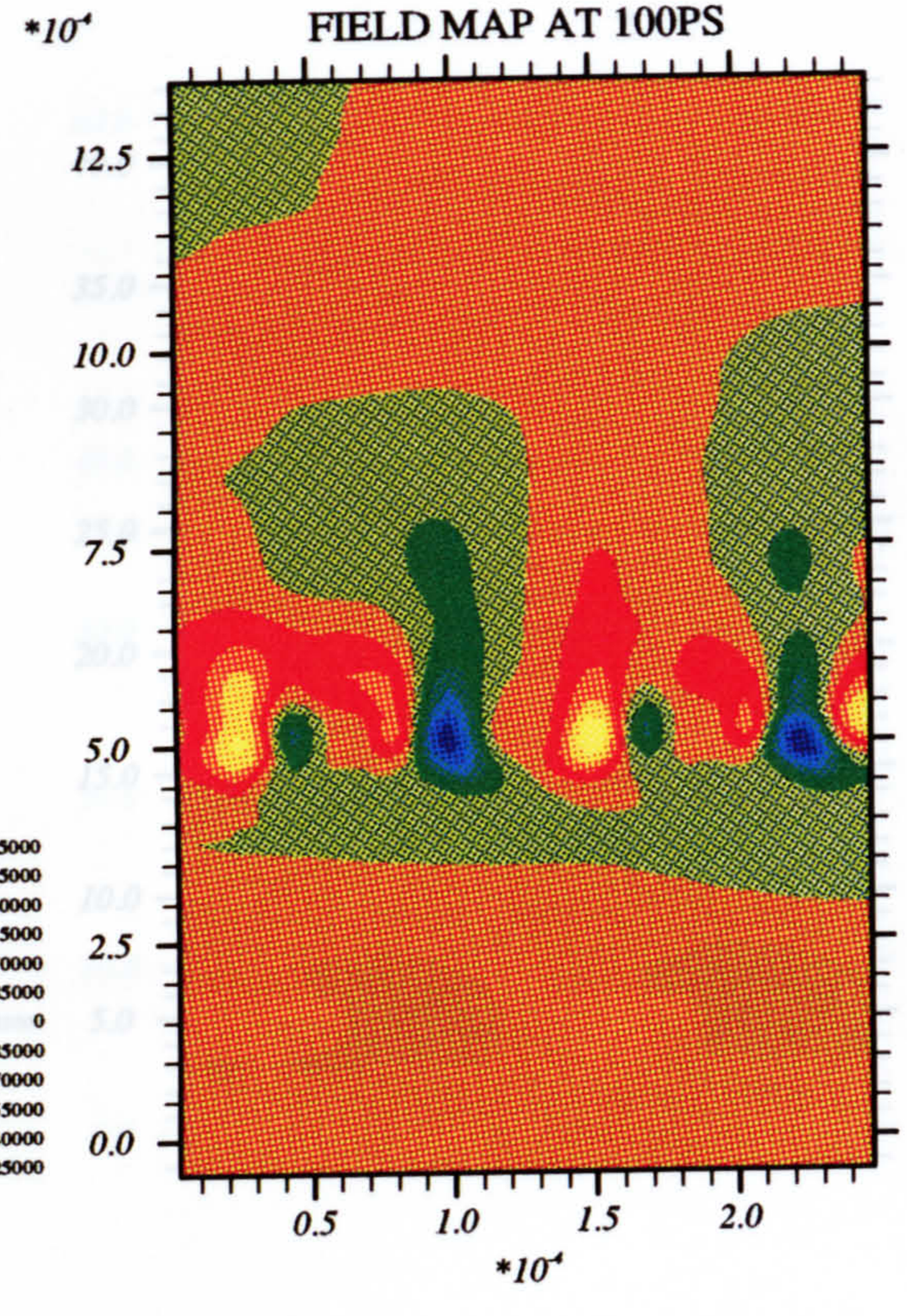
FIELD MAP AT 100PS
*10⁴
12.5
10.0
7.5
5.0
2.5
0.0
0.5
1.0
1.5
2.0
*10⁴
ABOVE 425000
340000 - 425000
255000 - 340000
170000 - 255000
85000 - 170000
0 - 85000
-85000 - 0
-170000 - -85000
-255000 - -170000
-340000 - -255000
-425000 - -340000
BELOW -425000

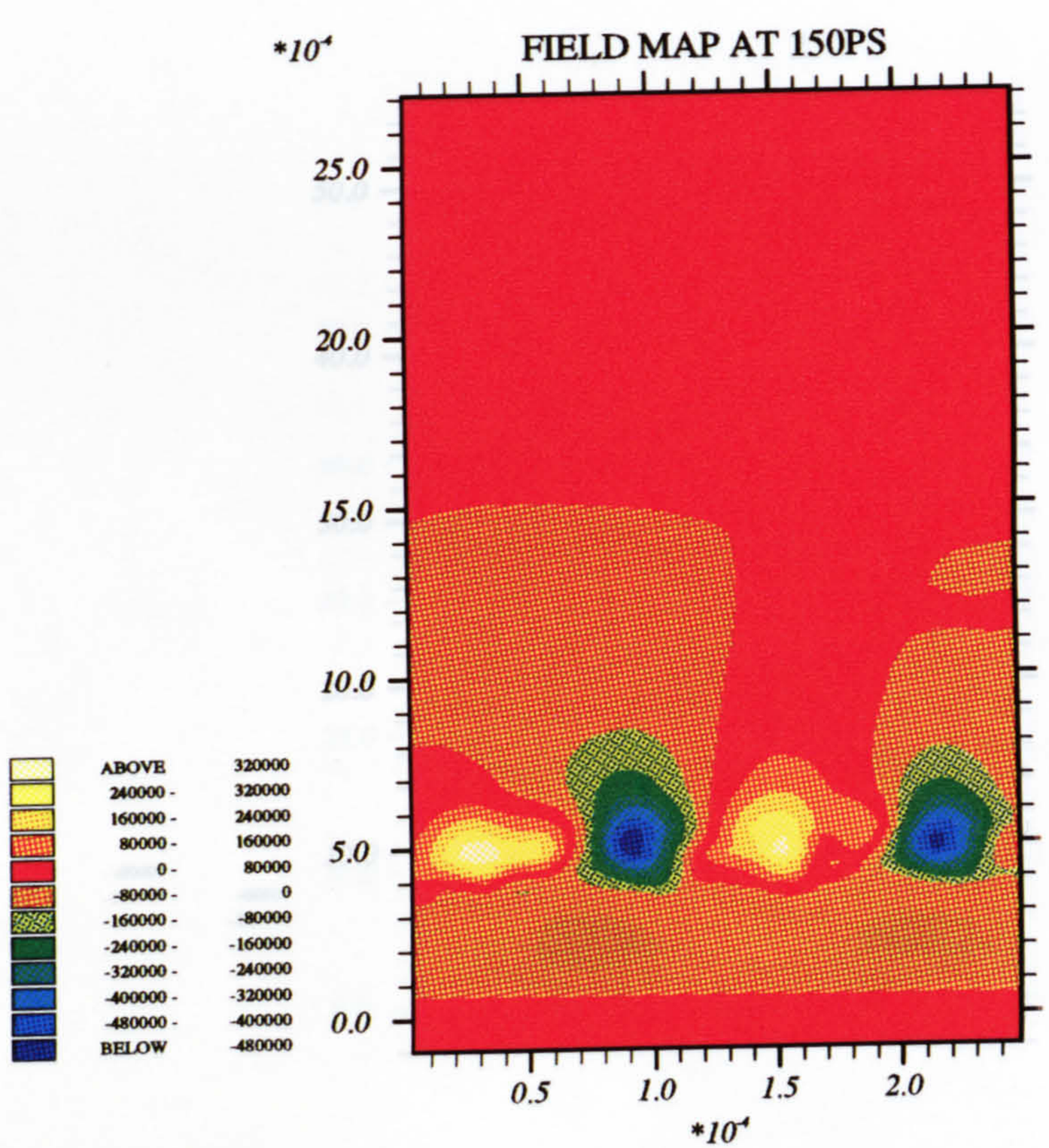
FIELD MAP AT 150PS
*10⁻⁴
25.0
20.0
15.0
10.0
5.0
0.0
0.5
1.0
1.5
2.0
*10⁻⁴
ABOVE 320000
240000 - 320000
160000 - 240000
80000 - 160000
0 - 80000
-80000 - 0
-160000 - -80000
-240000 - -160000
-320000 - -240000
-400000 - -320000
-480000 - -400000
BELOW -480000

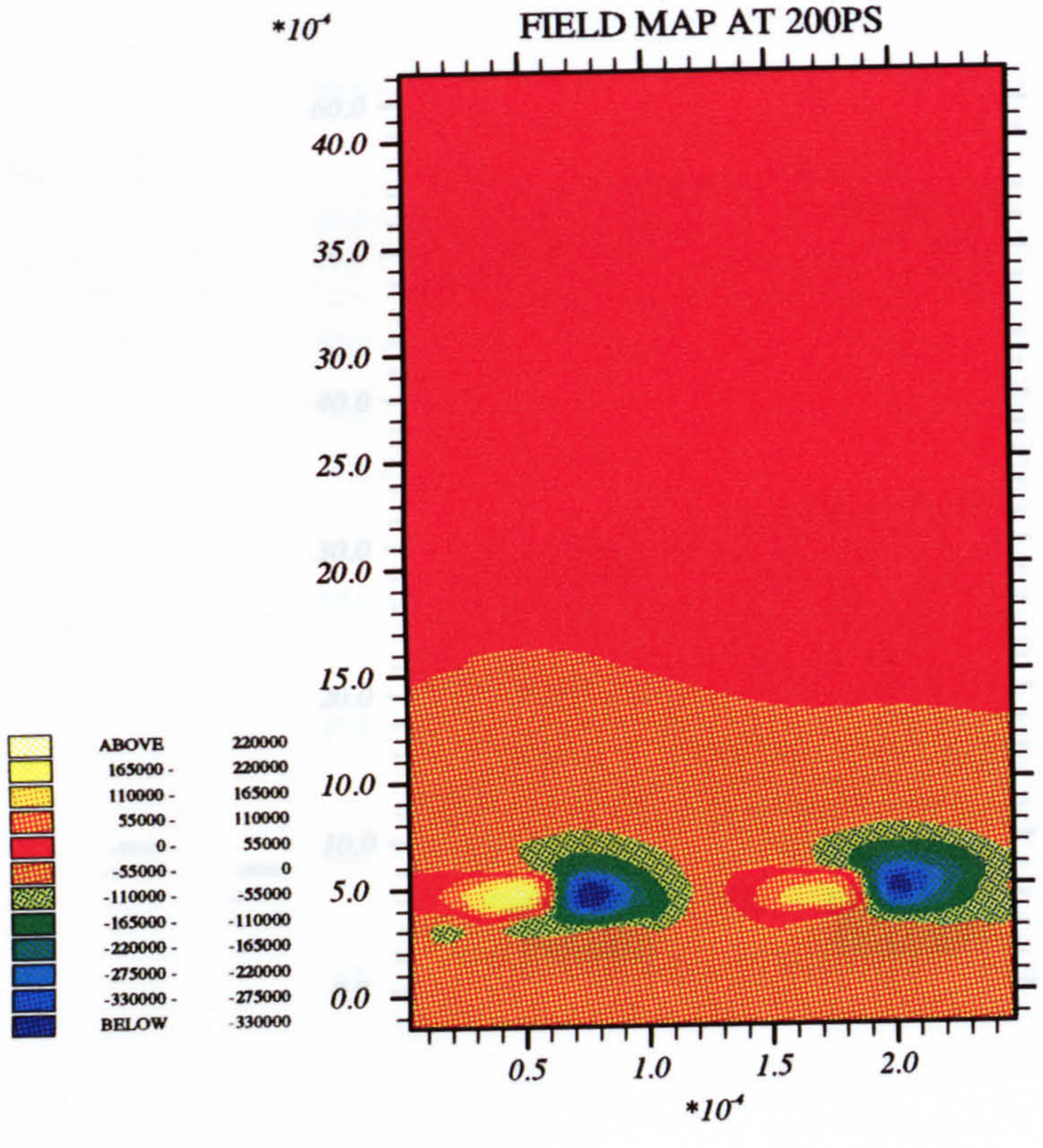
FIELD MAP AT 200PS
*10⁻⁴
40.0
35.0
30.0
25.0
20.0
15.0
10.0
5.0
0.0
0.5
1.0
1.5
2.0
*10⁻⁴
ABOVE 220000
165000 - 220000
110000 - 165000
55000 - 110000
0 - 55000
-55000 - 0
-110000 - -55000
-165000 - -110000
-220000 - -165000
-275000 - -220000
-330000 - -275000
BELOW -330000

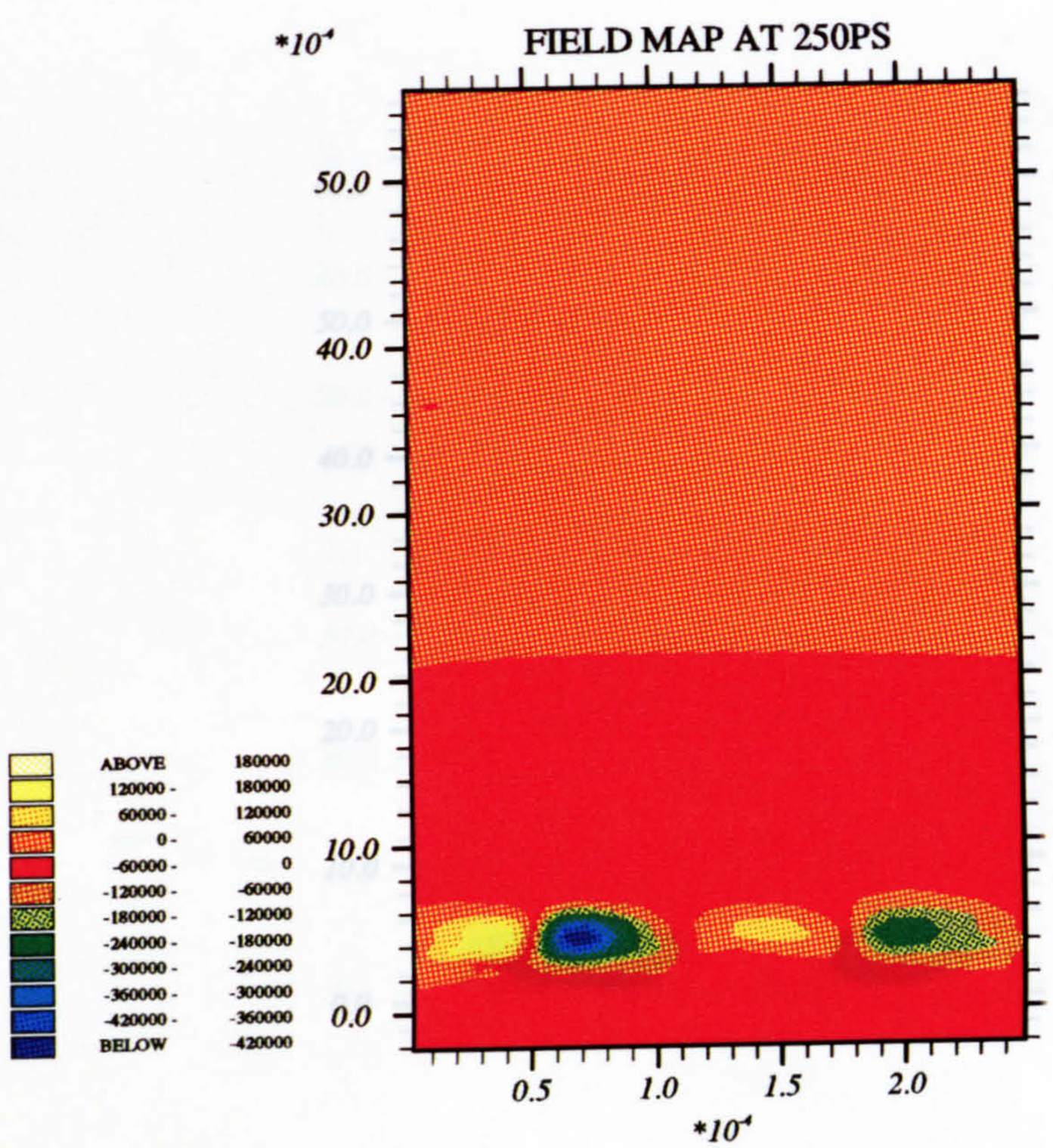
FIELD MAP AT 250PS
*10⁻⁴
50.0
40.0
30.0
20.0
10.0
0.0
0.5
1.0
1.5
2.0
*10⁻⁴
ABOVE 180000
120000 - 180000
60000 - 120000
0 - 60000
-60000 - 0
-120000 - -60000
-180000 - -120000
-240000 - -180000
-300000 - -240000
-360000 - -300000
-420000 - -360000
BELOW -420000

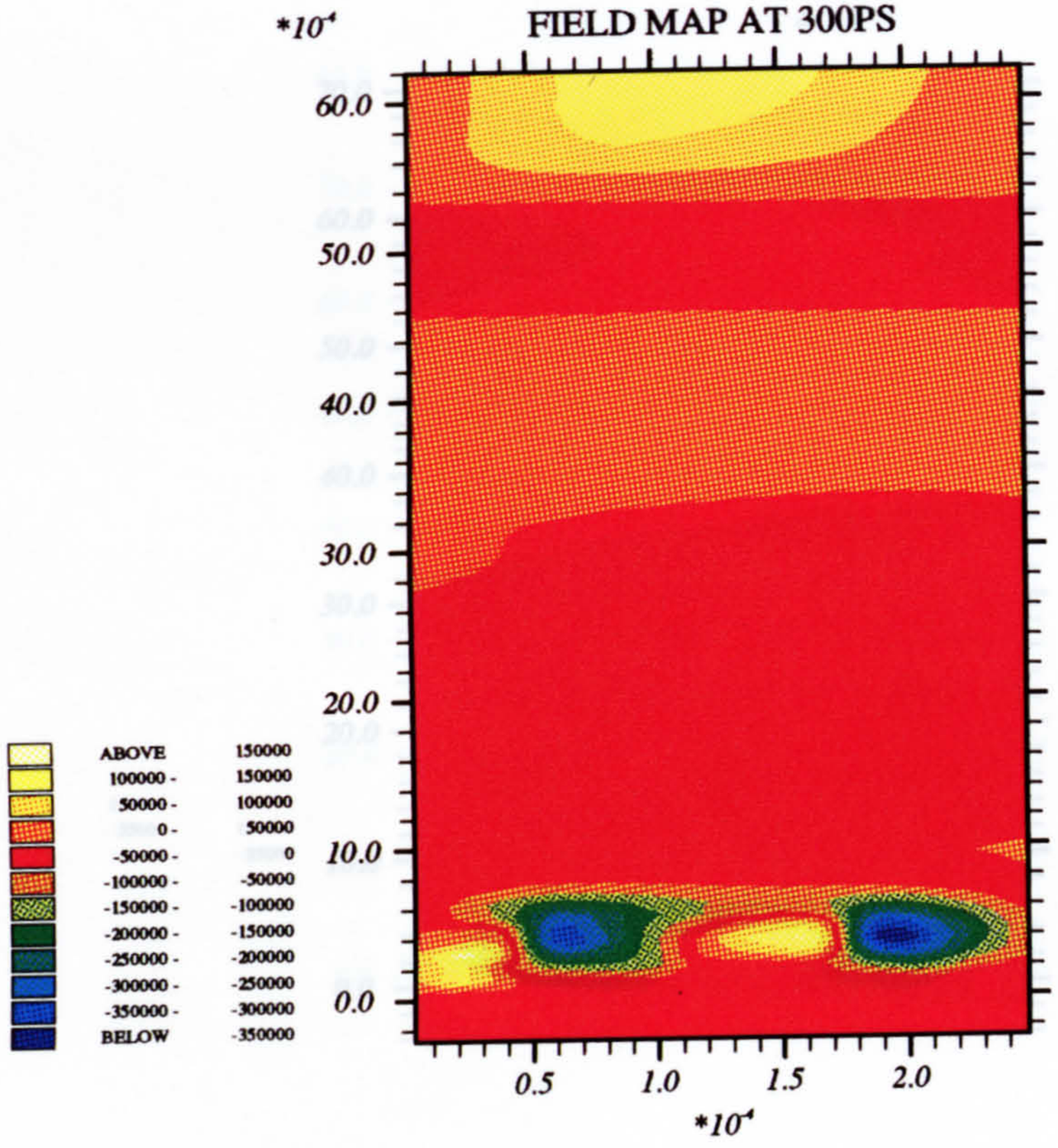
FIELD MAP AT 300PS
*10⁻⁴
60.0
50.0
40.0
30.0
20.0
10.0
0.0
0.5
1.0
1.5
2.0
*10⁻⁴
ABOVE 150000
100000 - 150000
50000 - 100000
0 - 50000
-50000 - 0
-100000 - -50000
-150000 - -100000
-200000 - -150000
-250000 - -200000
-300000 - -250000
-350000 - -300000
BELOW -350000

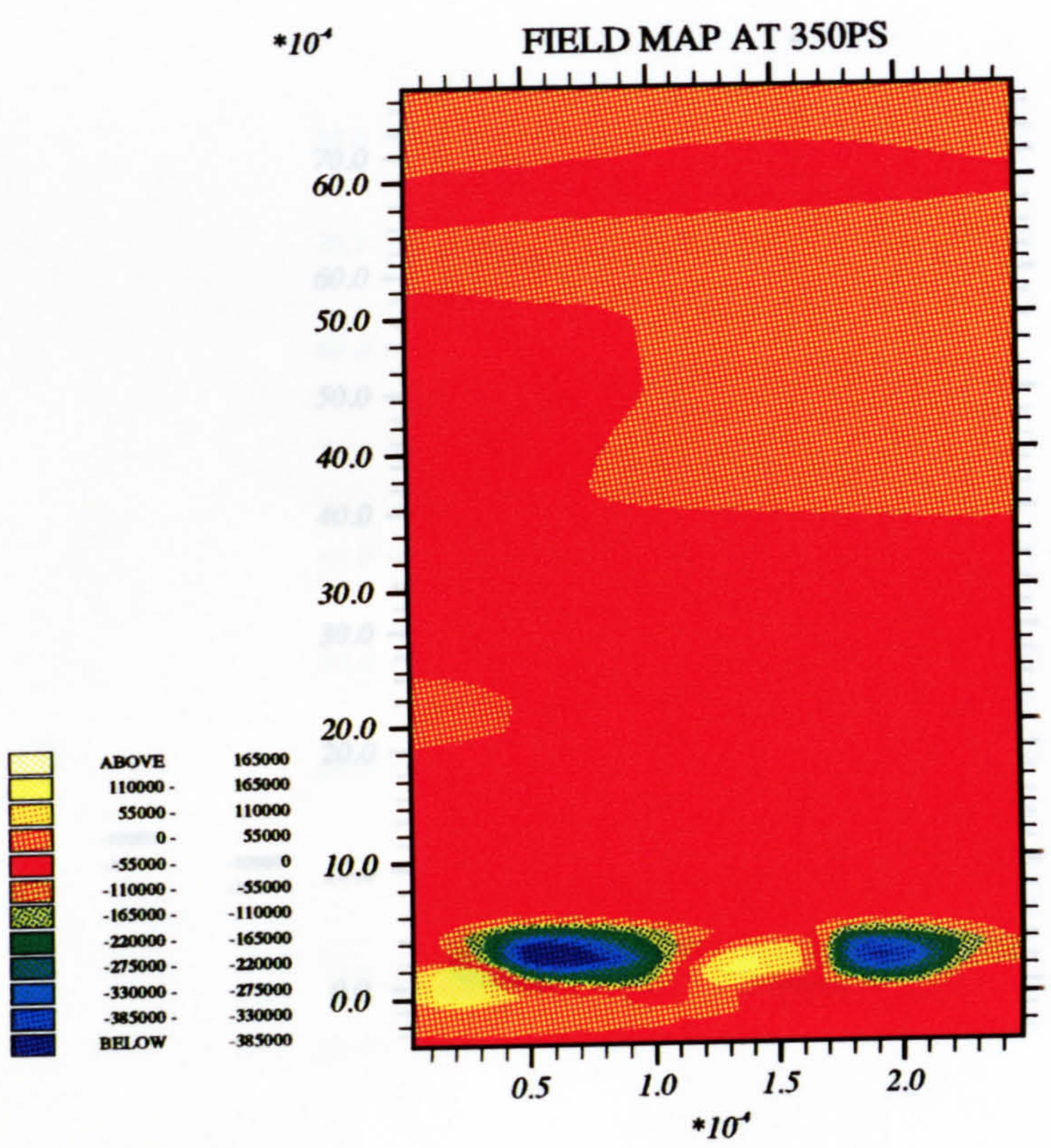
FIELD MAP AT 350PS
*10⁻⁴
60.0
50.0
40.0
30.0
20.0
10.0
0.0
0.5
1.0
1.5
2.0
*10⁻⁴
ABOVE 165000
110000 - 165000
55000 - 110000
0 - 55000
-55000 - 0
-110000 - -55000
-165000 - -110000
-220000 - -165000
-275000 - -220000
-330000 - -275000
-385000 - -330000
BELOW -385000

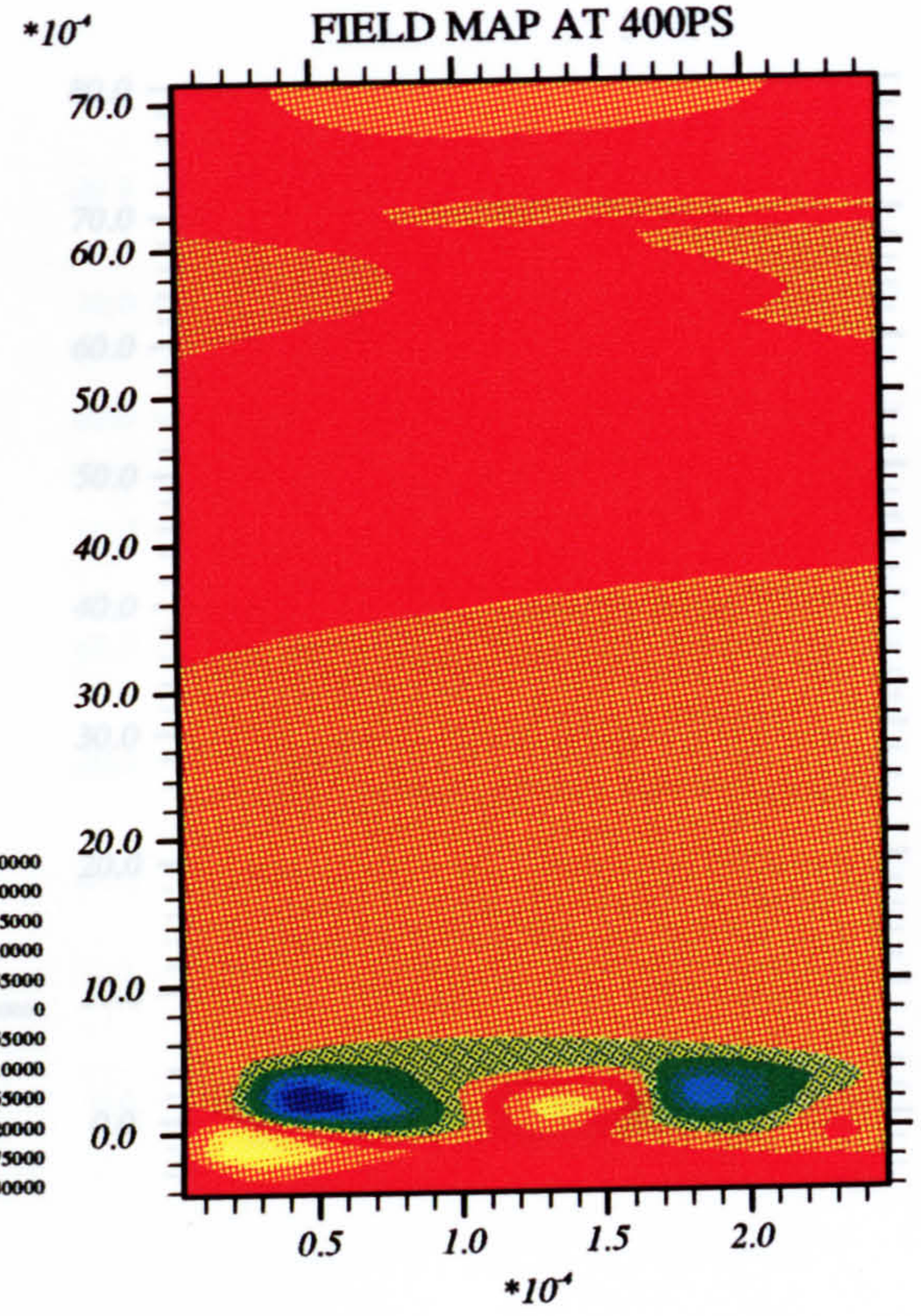
FIELD MAP AT 400PS
*10⁻⁴
70.0
60.0
50.0
40.0
30.0
20.0
10.0
0.0
0.5
1.0
1.5
2.0
*10⁻⁴
ABOVE 220000
165000 - 220000
110000 - 165000
55000 - 110000
0 - 55000
-55000 - 0
-110000 - -55000
-165000 - -110000
-220000 - -165000
-275000 - -220000
-330000 - -275000
BELOW -330000

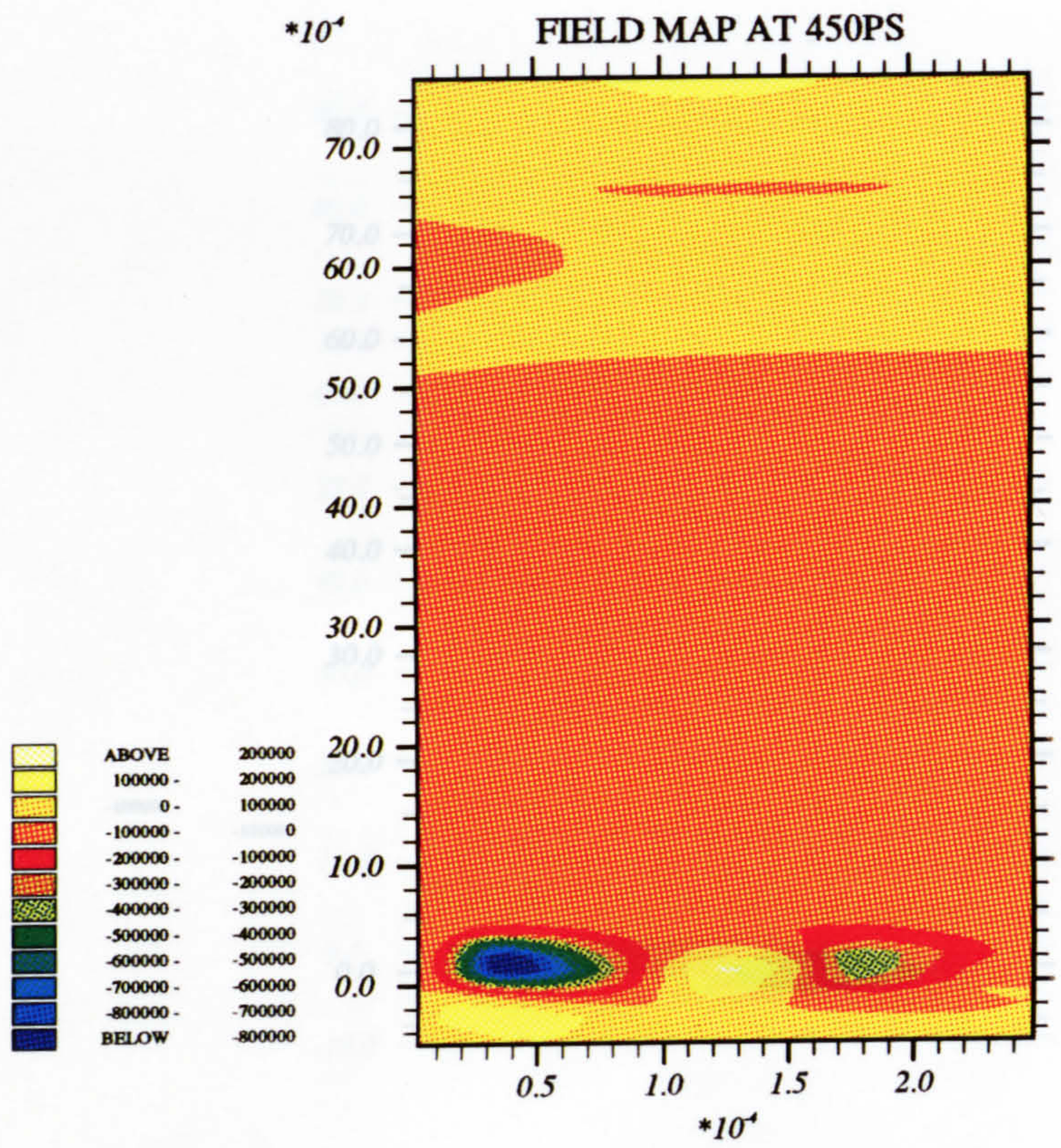
FIELD MAP AT 450PS
*10⁻⁴
70.0
60.0
50.0
40.0
30.0
20.0
10.0
0.0
0.5
1.0
1.5
2.0
*10⁻⁴
ABOVE 200000
100000 - 200000
0 - 100000
-100000 - 0
-200000 - -100000
-300000 - -200000
-400000 - -300000
-500000 - -400000
-600000 - -500000
-700000 - -600000
-800000 - -700000
BELOW -800000

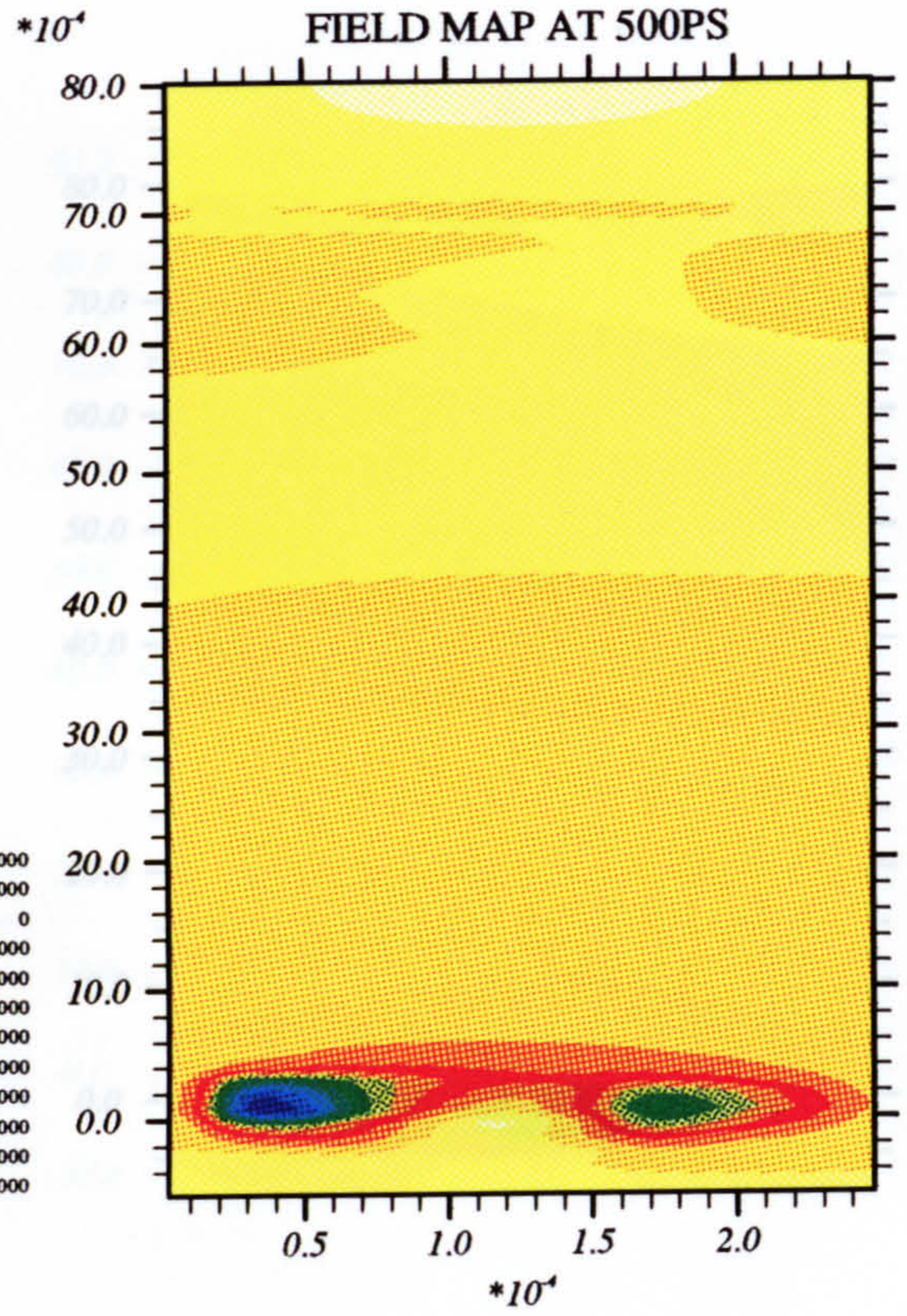
FIELD MAP AT 500PS
*10⁻⁴
80.0
70.0
60.0
50.0
40.0
30.0
20.0
10.0
0.0
0.5
1.0
1.5
2.0
*10⁻⁴
ABOVE 65000
0 - 65000
-65000 - 0
-130000 - -65000
-195000 - -130000
-260000 - -195000
-325000 - -260000
-390000 - -325000
-455000 - -390000
-520000 - -455000
-585000 - -520000
BELOW -585000

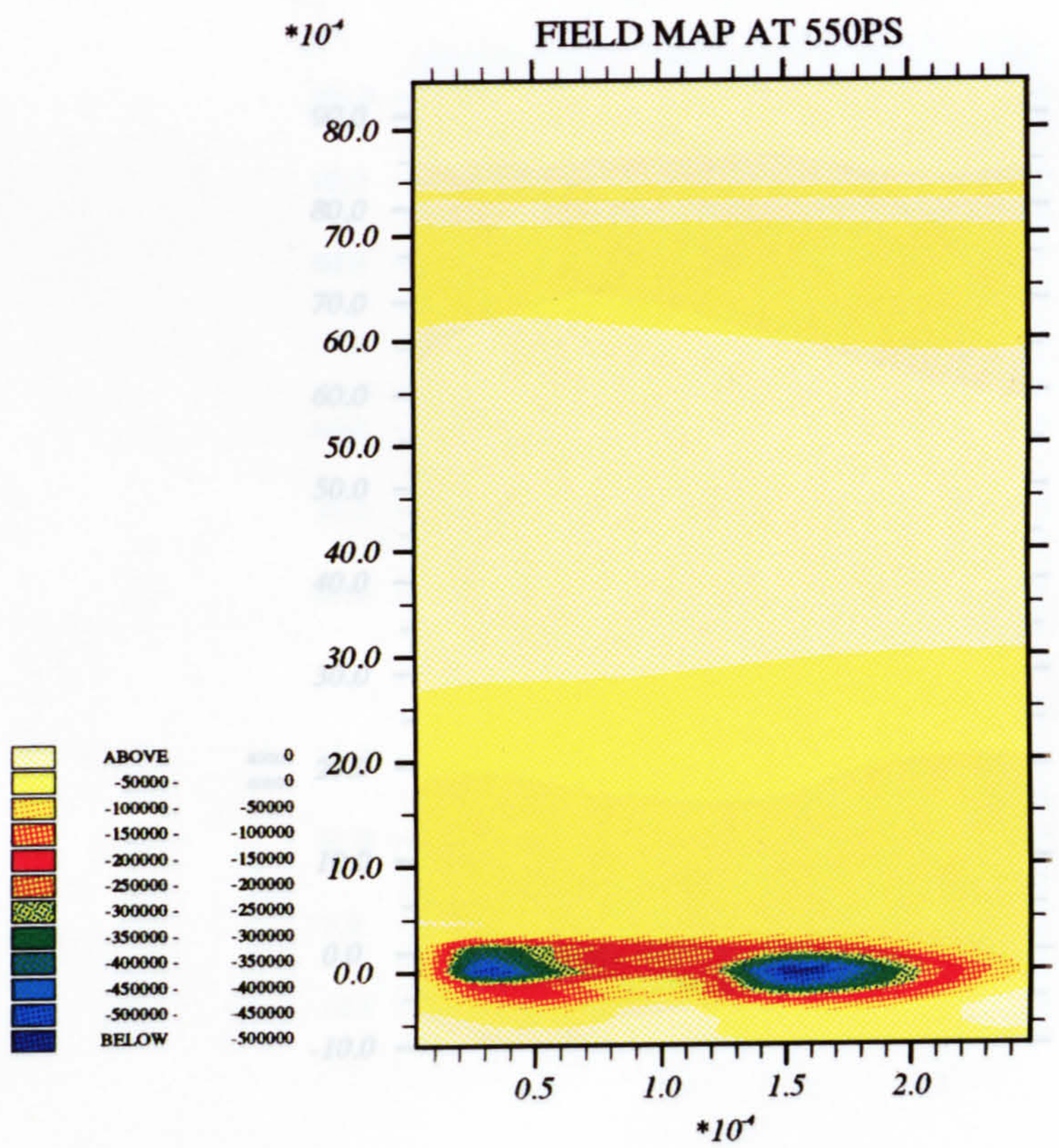
FIELD MAP AT 550PS
*10⁻⁴
80.0
70.0
60.0
50.0
40.0
30.0
20.0
10.0
0.0
0.5
1.0
1.5
2.0
*10⁻⁴
ABOVE 0
-50000 - 0
-100000 - -50000
-150000 - -100000
-200000 - -150000
-250000 - -200000
-300000 - -250000
-350000 - -300000
-400000 - -350000
-450000 - -400000
-500000 - -450000
BELOW -500000

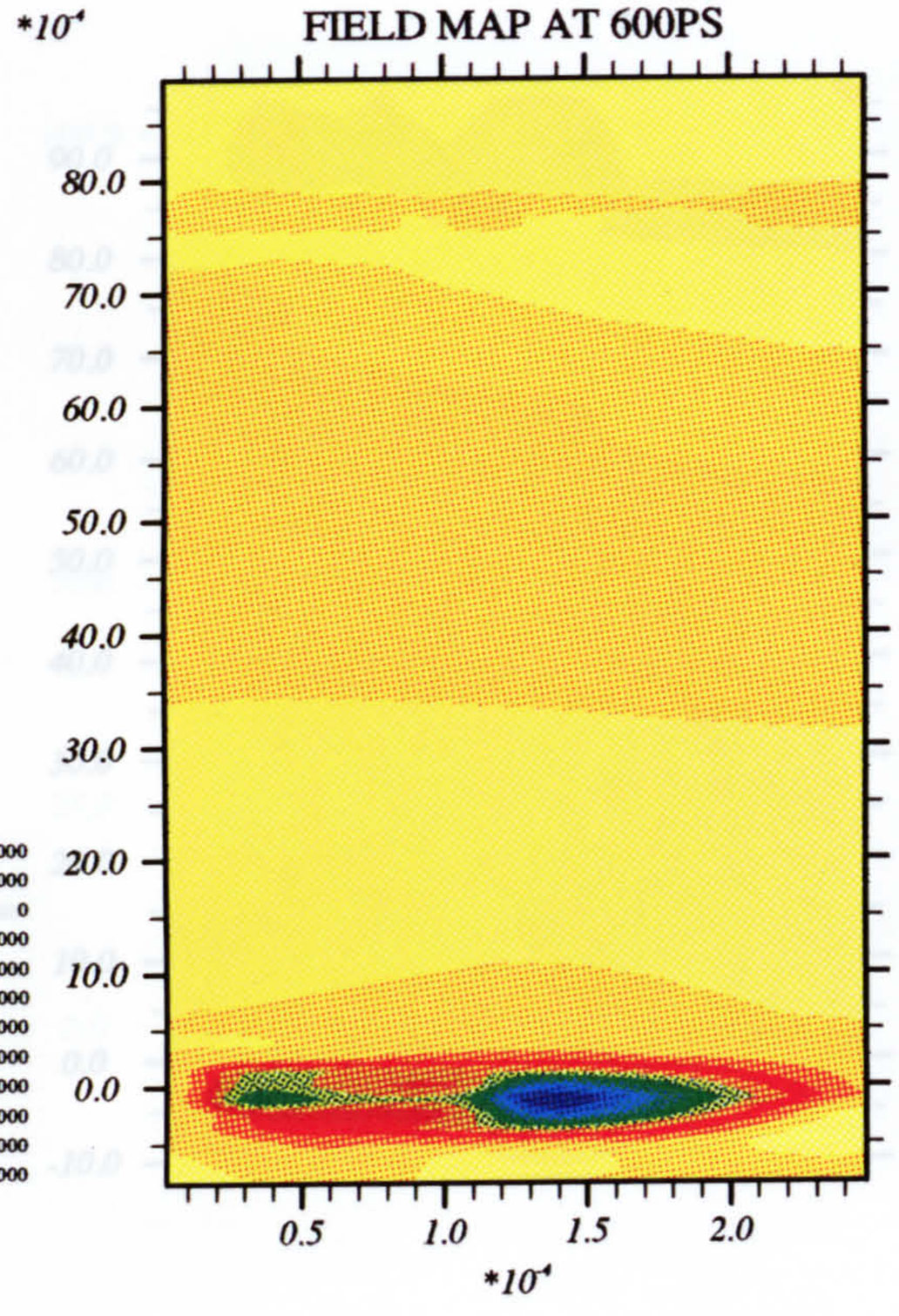
FIELD MAP AT 600PS
*10⁻⁴
80.0
70.0
60.0
50.0
40.0
30.0
20.0
10.0
0.0
0.5
1.0
1.5
2.0
*10⁻⁴
ABOVE 25000
0 - 25000
-25000 - 0
-50000 - -25000
-75000 - -50000
-100000 - -75000
-125000 - -100000
-150000 - -125000
-175000 - -150000
-200000 - -175000
-225000 - -200000
BELOW -225000

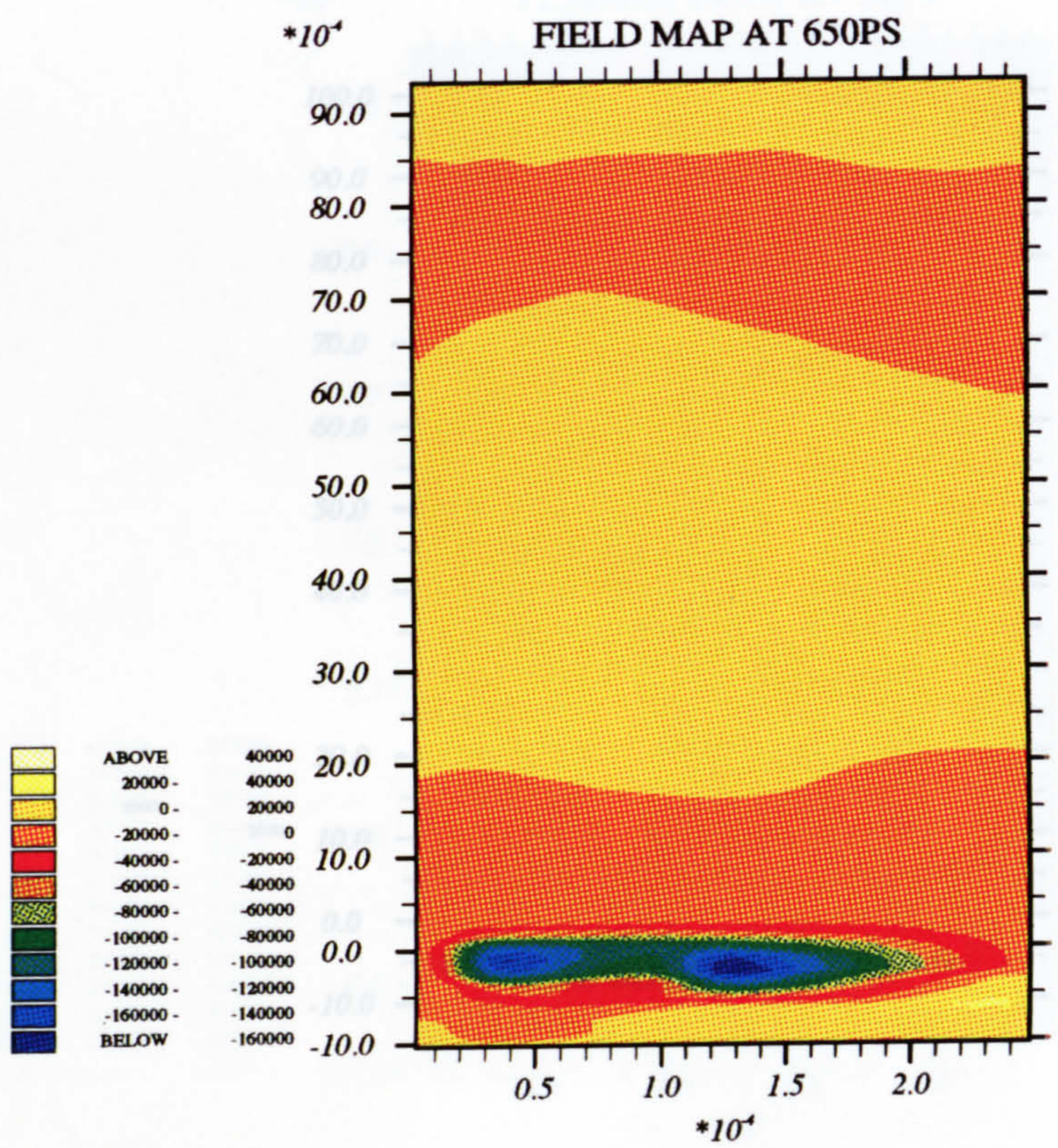
FIELD MAP AT 650PS
*10⁻⁴
90.0
80.0
70.0
60.0
50.0
40.0
30.0
20.0
10.0
0.0
-10.0
0.5
1.0
1.5
2.0
*10⁻⁴
ABOVE
20000 -
0 -
-20000 -
-40000 -
-60000 -
-80000 -
-100000 -
-120000 -
-140000 -
-160000 -
BELOW
40000
40000
20000
0
-20000
-40000
-60000
-80000
-100000
-120000
-140000
-160000

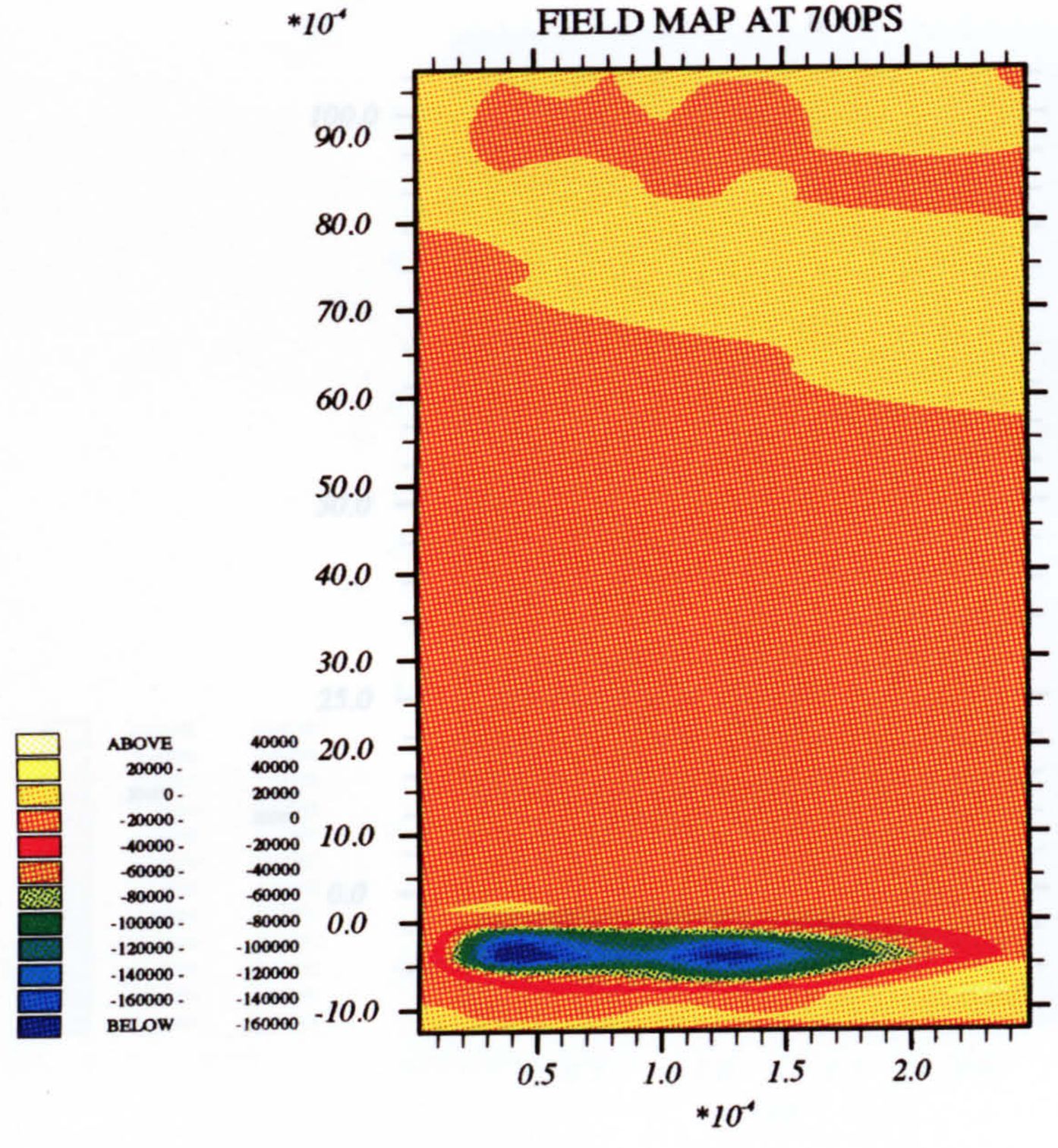
FIELD MAP AT 700PS
*10⁻⁴
90.0
80.0
70.0
60.0
50.0
40.0
30.0
20.0
10.0
0.0
-10.0
0.5
1.0
1.5
2.0
*10⁻⁴
ABOVE
20000 -
0 -
-20000 -
-40000 -
-60000 -
-80000 -
-100000 -
-120000 -
-140000 -
-160000 -
BELOW
40000
40000
20000
0
-20000
-40000
-60000
-80000
-100000
-120000
-140000
-160000

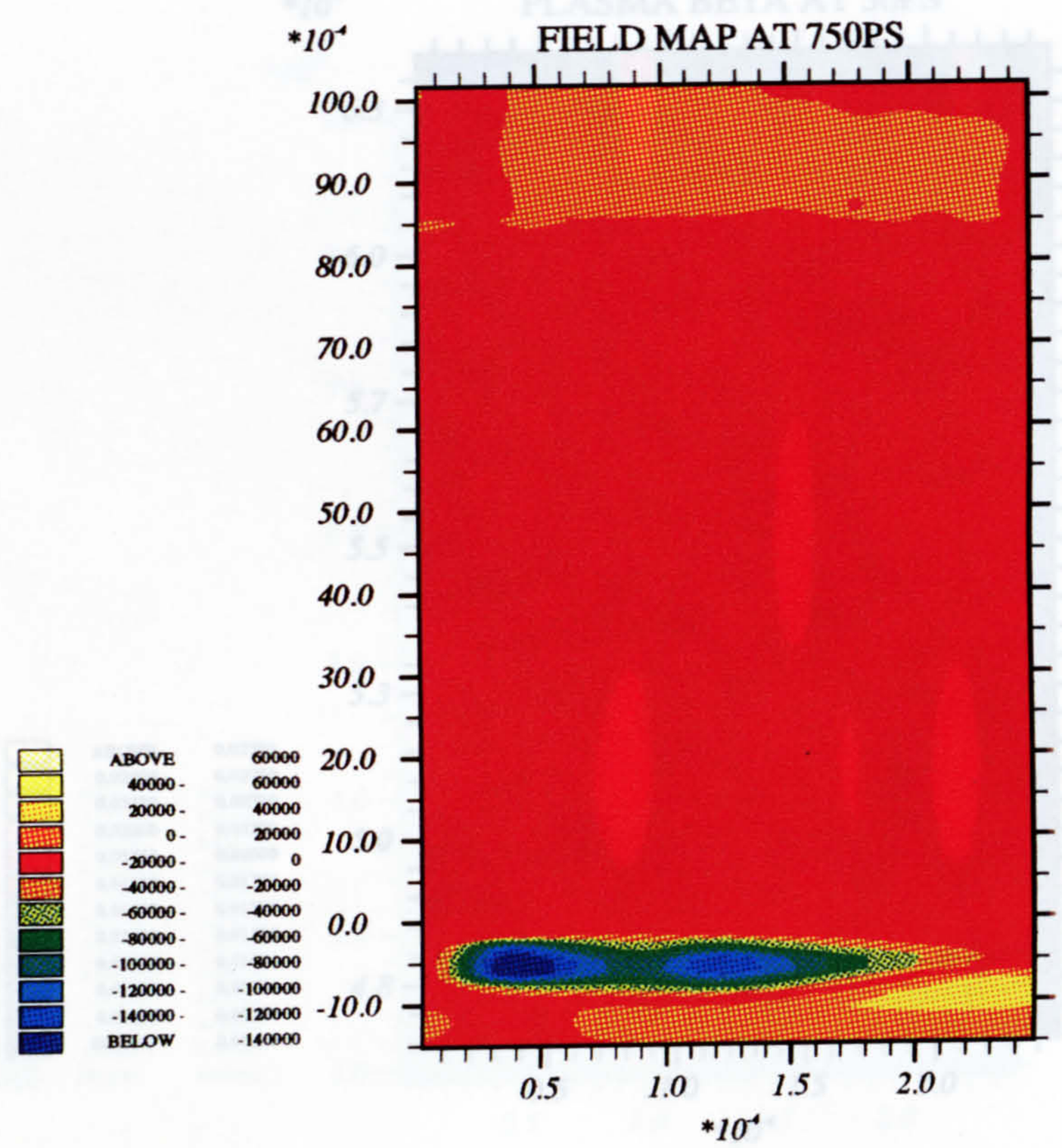
FIELD MAP AT 750PS
*10⁻⁴
100.0
90.0
80.0
70.0
60.0
50.0
40.0
30.0
20.0
10.0
0.0
-10.0
0.5
1.0
1.5
2.0
*10⁻⁴
ABOVE
40000 -
20000 -
0 -
-20000 -
-40000 -
-60000 -
-80000 -
-100000 -
-120000 -
-140000 -
BELOW
60000
60000
40000
20000
0
-20000
-40000
-60000
-80000
-100000
-120000
-140000

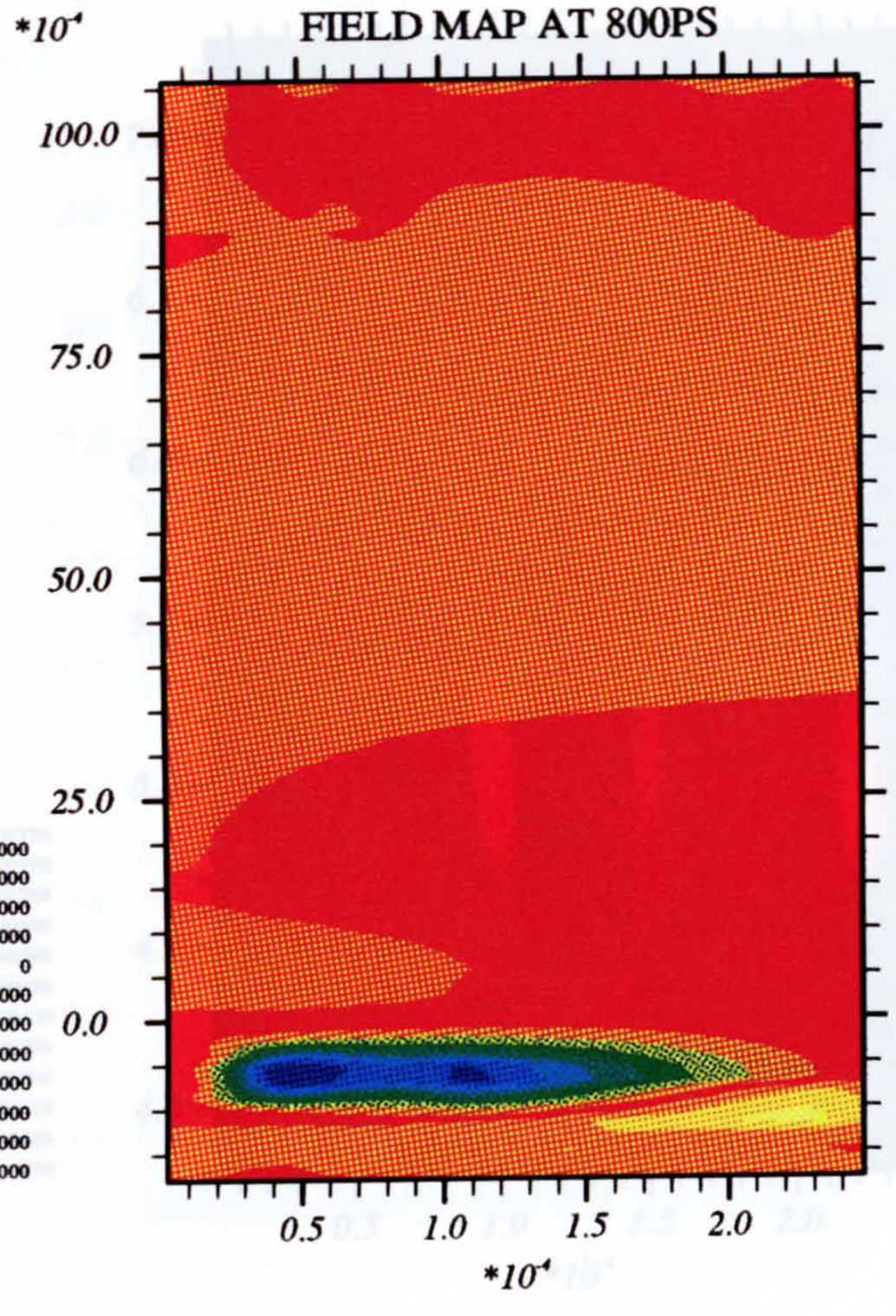
FIELD MAP AT 800PS
*10⁻⁴
100.0
75.0
50.0
25.0
0.0
0.5
1.0
1.5
2.0
*10⁻⁴
ABOVE
40000 -
20000 -
0 -
-20000 -
-40000 -
-60000 -
-80000 -
-100000 -
-120000 -
-140000 -
BELOW
60000
60000
40000
20000
0
-20000
-40000
-60000
-80000
-100000
-120000
-140000

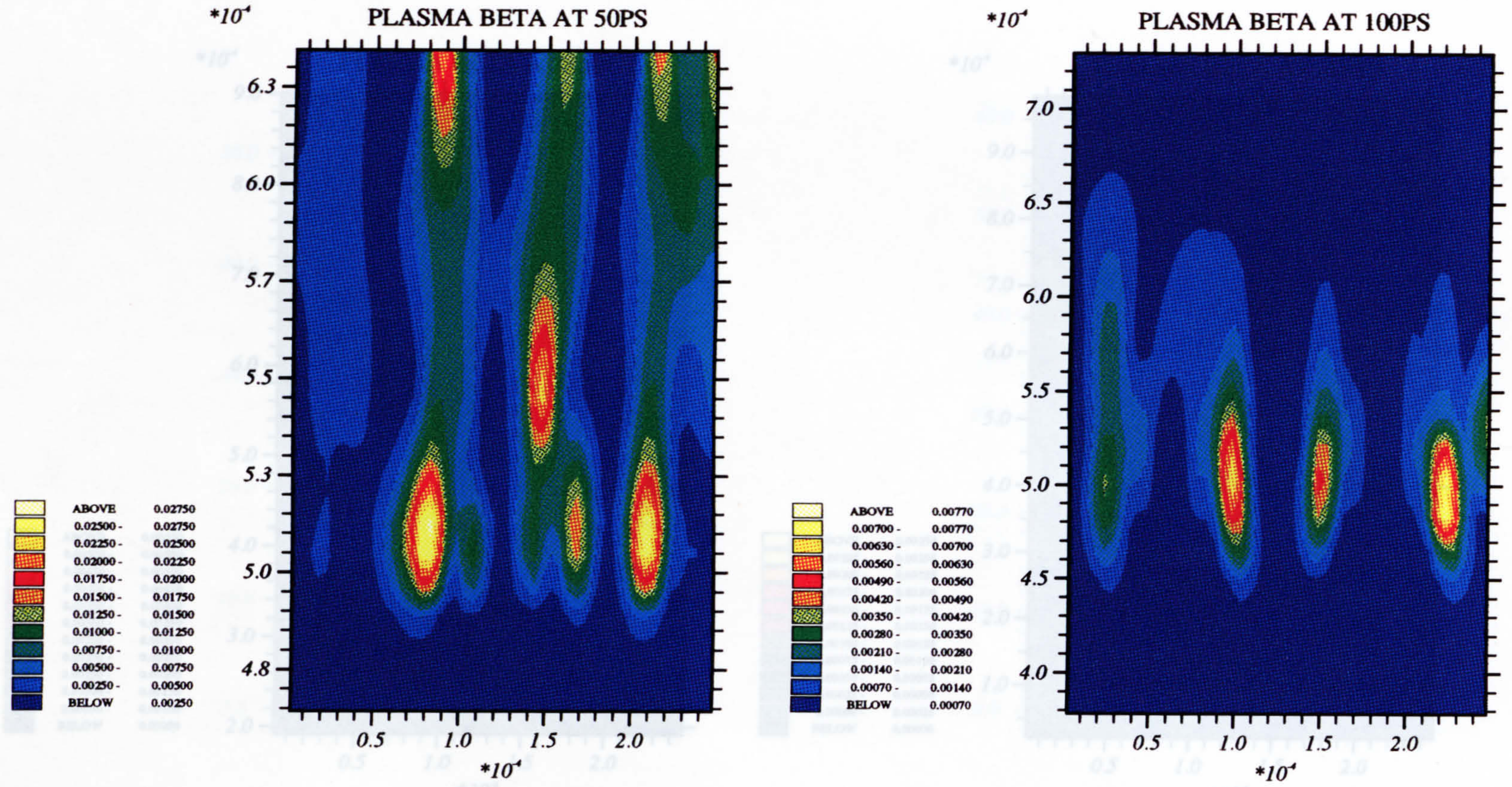

Figure 5.5: Plasma beta map for the target (5.0μm x 2.5μm).

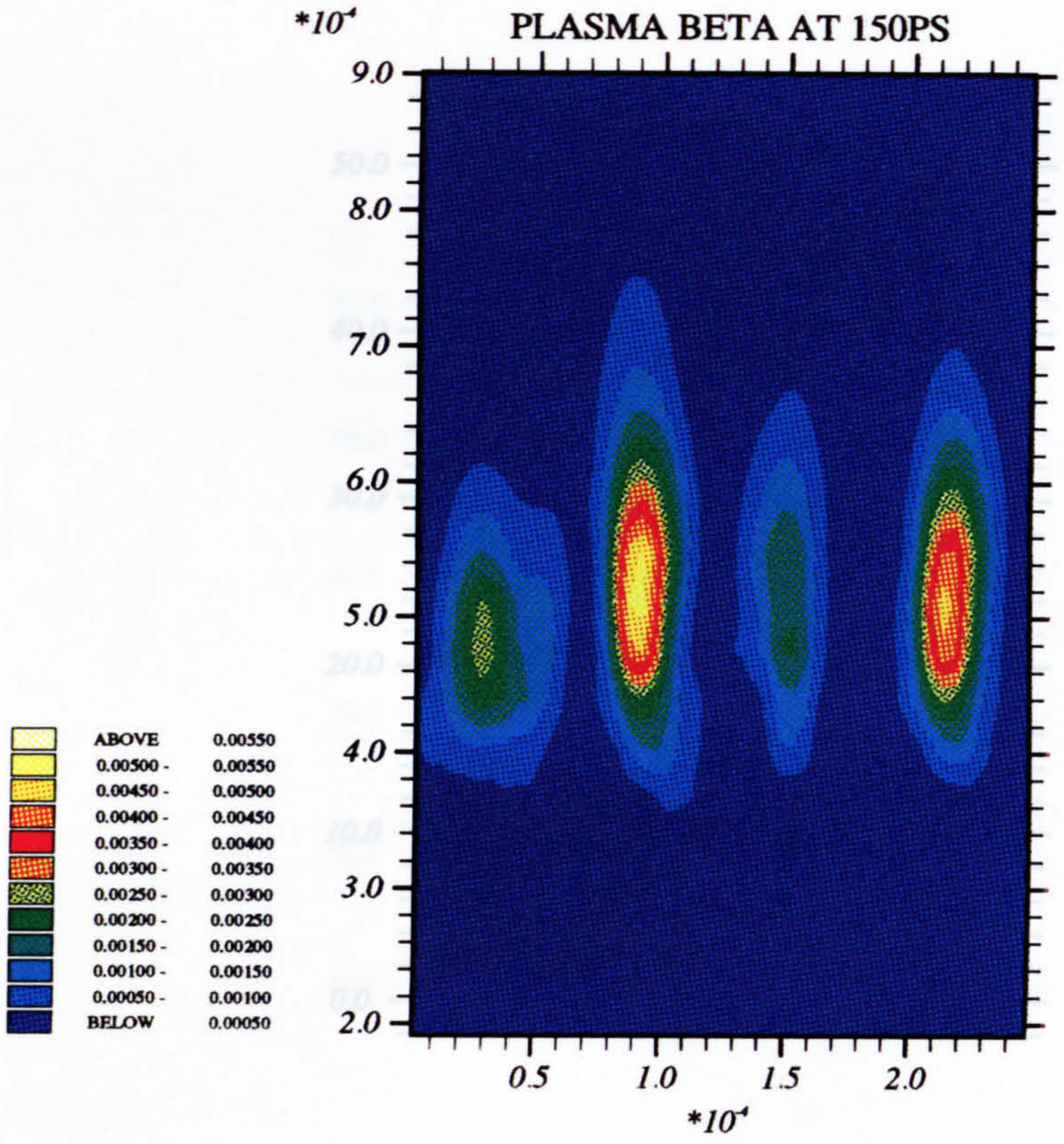
PLASMA BETA AT 150PS
*10⁻⁴
9.0
8.0
7.0
6.0
5.0
4.0
3.0
2.0
0.5
1.0
1.5
2.0
*10⁻⁴
ABOVE 0.00550
0.00500 - 0.00550
0.00450 - 0.00500
0.00400 - 0.00450
0.00350 - 0.00400
0.00300 - 0.00350
0.00250 - 0.00300
0.00200 - 0.00250
0.00150 - 0.00200
0.00100 - 0.00150
0.00050 - 0.00100
BELOW 0.00050

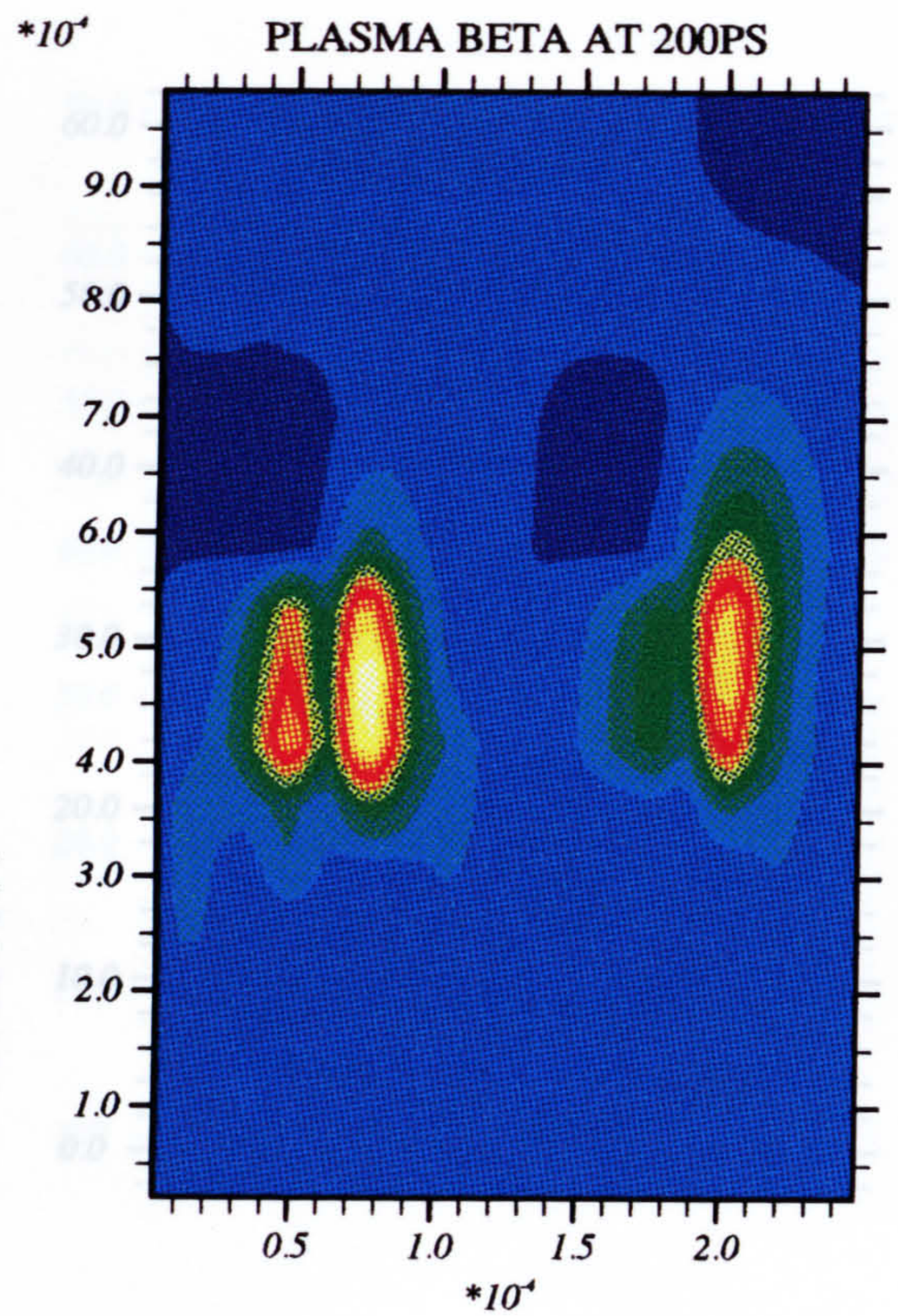
PLASMA BETA AT 200PS
*10⁻⁴
9.0
8.0
7.0
6.0
5.0
4.0
3.0
2.0
1.0
0.5
1.0
1.5
2.0
*10⁻⁴
ABOVE 0.00250
0.00225 - 0.00250
0.00200 - 0.00225
0.00175 - 0.00200
0.00150 - 0.00175
0.00125 - 0.00150
0.00100 - 0.00125
0.00075 - 0.00100
0.00050 - 0.00075
0.00025 - 0.00050
0.00000 - 0.00025
BELOW 0.00000

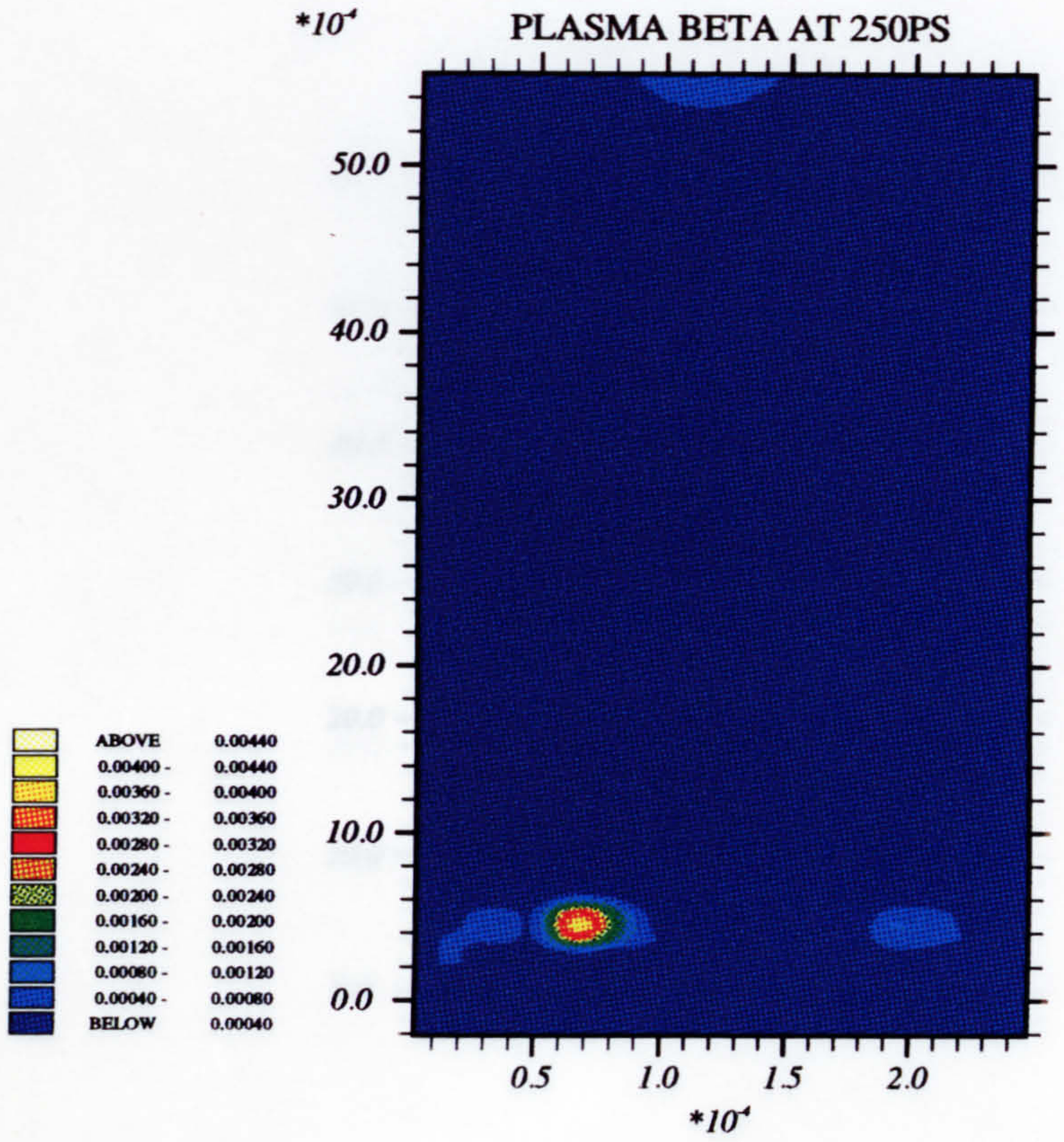
PLASMA BETA AT 250PS
*10⁻⁴
50.0
40.0
30.0
20.0
10.0
0.0
0.5
1.0
1.5
2.0
*10⁻⁴
ABOVE 0.00440
0.00400 - 0.00440
0.00360 - 0.00400
0.00320 - 0.00360
0.00280 - 0.00320
0.00240 - 0.00280
0.00200 - 0.00240
0.00160 - 0.00200
0.00120 - 0.00160
0.00080 - 0.00120
0.00040 - 0.00080
BELOW 0.00040

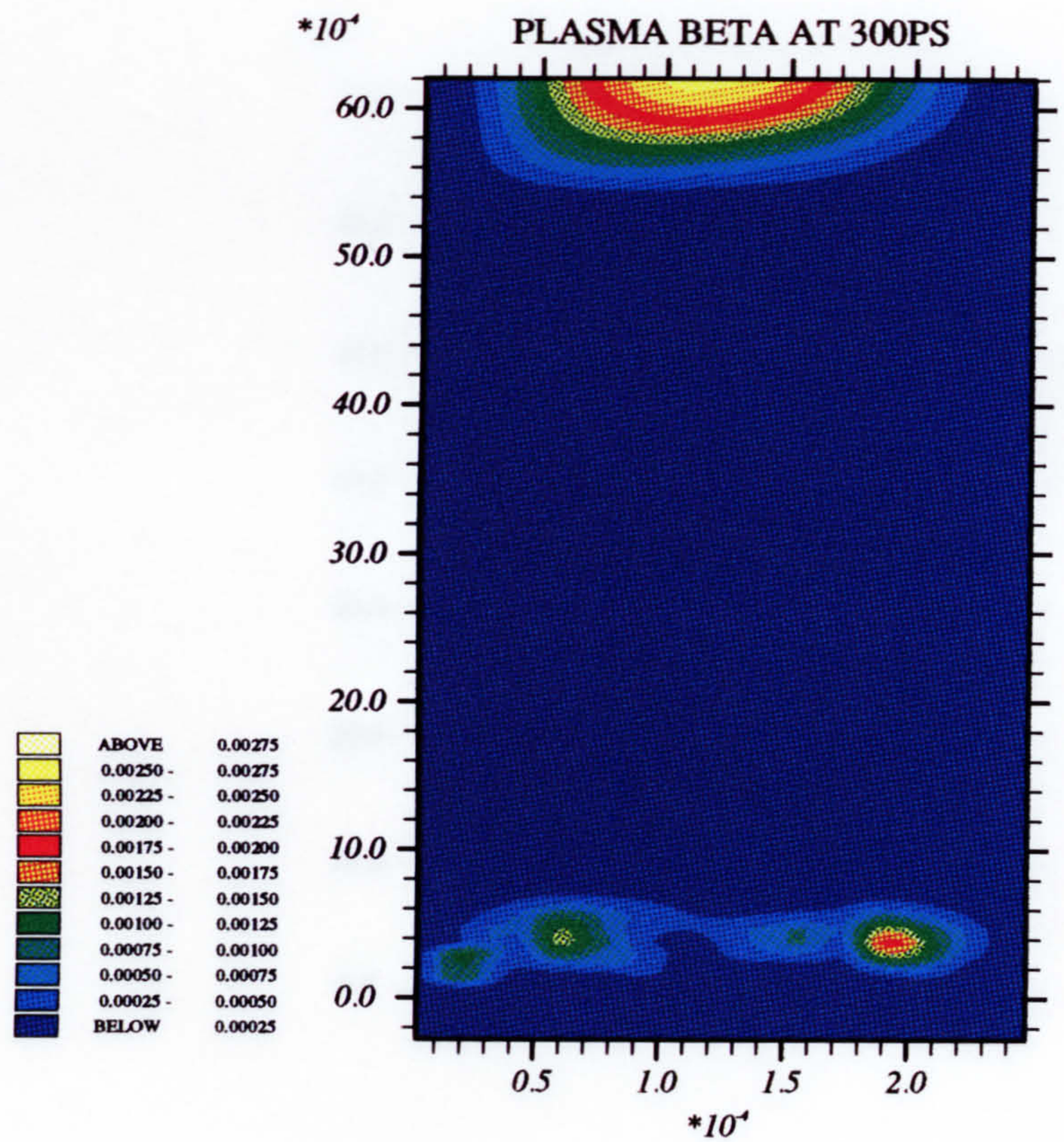
PLASMA BETA AT 300PS
*10⁻⁴
60.0
50.0
40.0
30.0
20.0
10.0
0.0
0.5
1.0
1.5
2.0
*10⁻⁴
ABOVE 0.00275
0.00250 - 0.00275
0.00225 - 0.00250
0.00200 - 0.00225
0.00175 - 0.00200
0.00150 - 0.00175
0.00125 - 0.00150
0.00100 - 0.00125
0.00075 - 0.00100
0.00050 - 0.00075
0.00025 - 0.00050
BELOW 0.00025

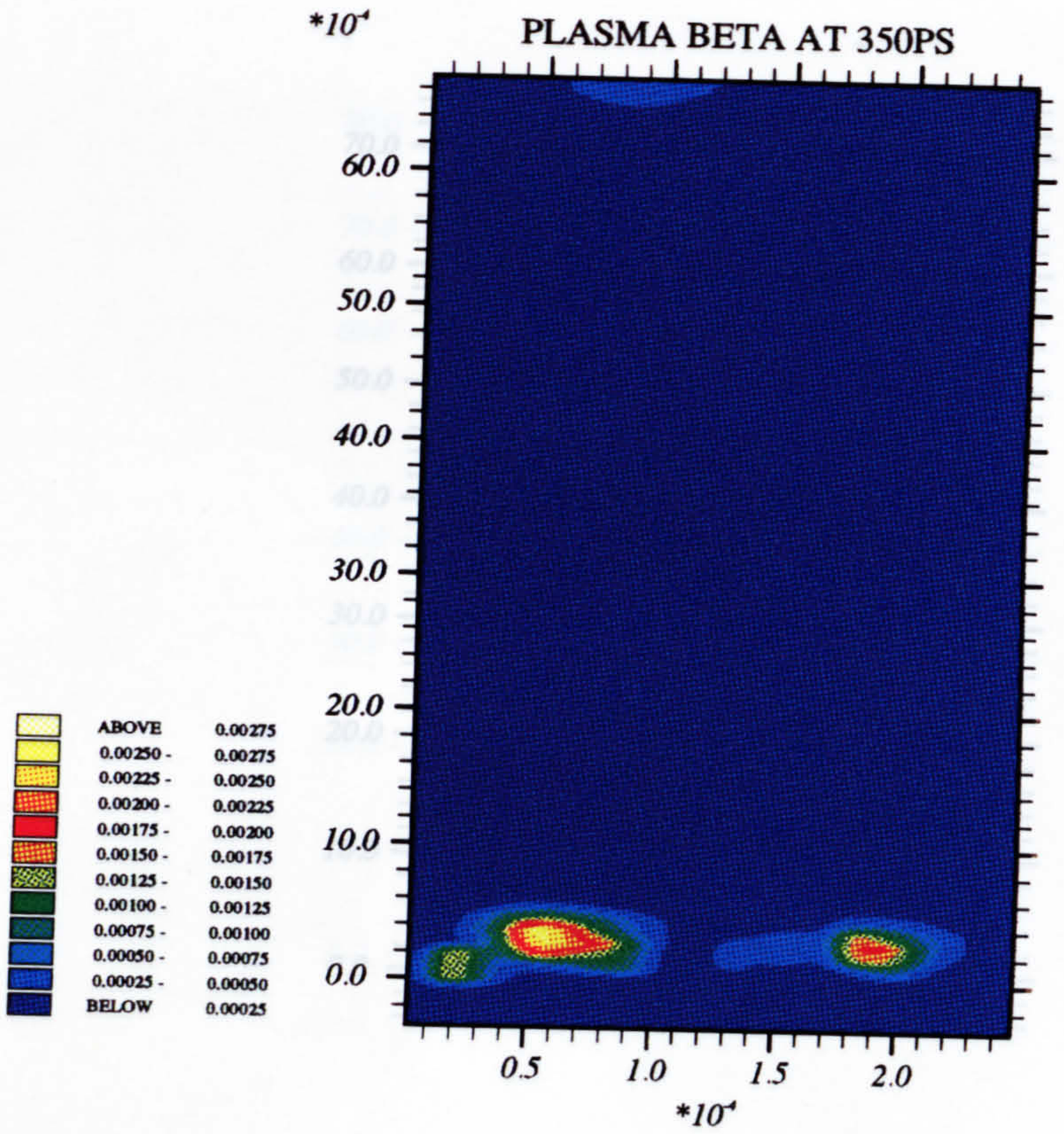
*10⁻⁴
PLASMA BETA AT 350PS
60.0
50.0
40.0
30.0
20.0
10.0
0.0
0.5
1.0
1.5
2.0
*10⁻⁴
ABOVE 0.00275
0.00250 - 0.00275
0.00225 - 0.00250
0.00200 - 0.00225
0.00175 - 0.00200
0.00150 - 0.00175
0.00125 - 0.00150
0.00100 - 0.00125
0.00075 - 0.00100
0.00050 - 0.00075
0.00025 - 0.00050
BELOW 0.00025

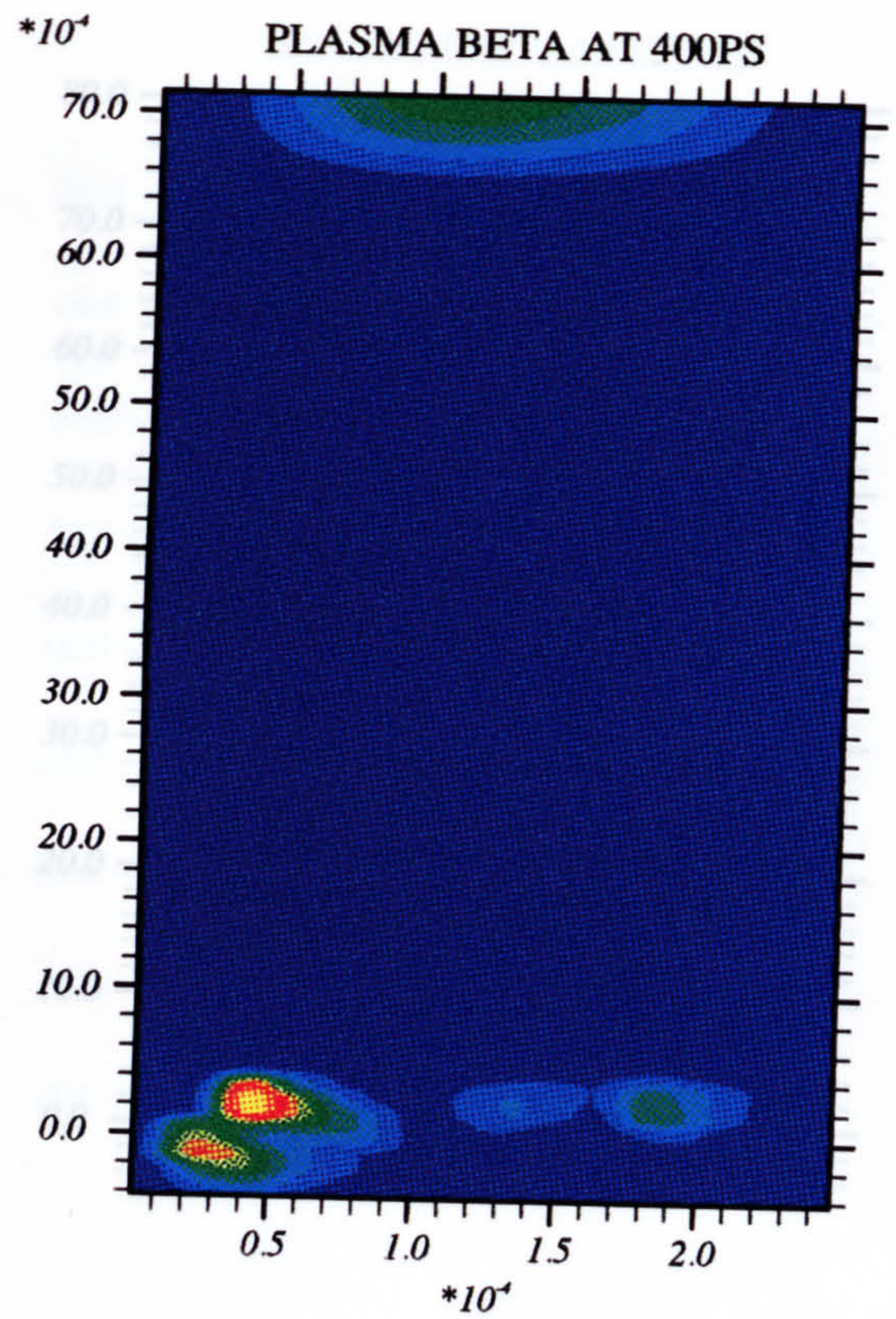
*10⁻⁴
PLASMA BETA AT 400PS
70.0
60.0
50.0
40.0
30.0
20.0
10.0
0.0
0.5
1.0
1.5
2.0
*10⁻⁴
ABOVE 0.00275
0.00250 - 0.00275
0.00225 - 0.00250
0.00200 - 0.00225
0.00175 - 0.00200
0.00150 - 0.00175
0.00125 - 0.00150
0.00100 - 0.00125
0.00075 - 0.00100
0.00050 - 0.00075
0.00025 - 0.00050
BELOW 0.00025

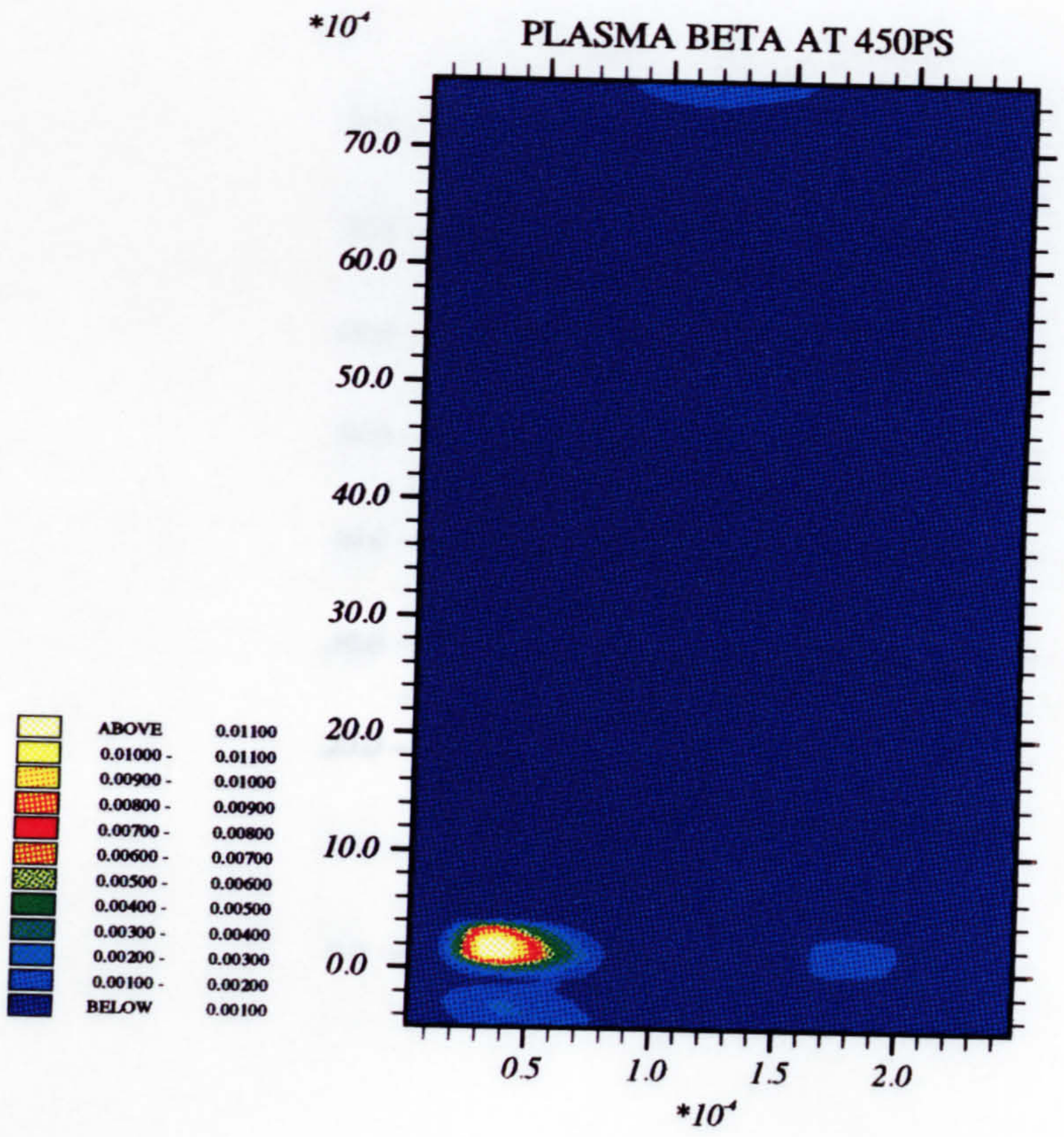
PLASMA BETA AT 450PS
*10⁻⁴
70.0
60.0
50.0
40.0
30.0
20.0
10.0
0.0
0.5
1.0
1.5
2.0
*10⁻⁴
ABOVE 0.01100
0.01000 - 0.01100
0.00900 - 0.01000
0.00800 - 0.00900
0.00700 - 0.00800
0.00600 - 0.00700
0.00500 - 0.00600
0.00400 - 0.00500
0.00300 - 0.00400
0.00200 - 0.00300
0.00100 - 0.00200
BELOW 0.00100

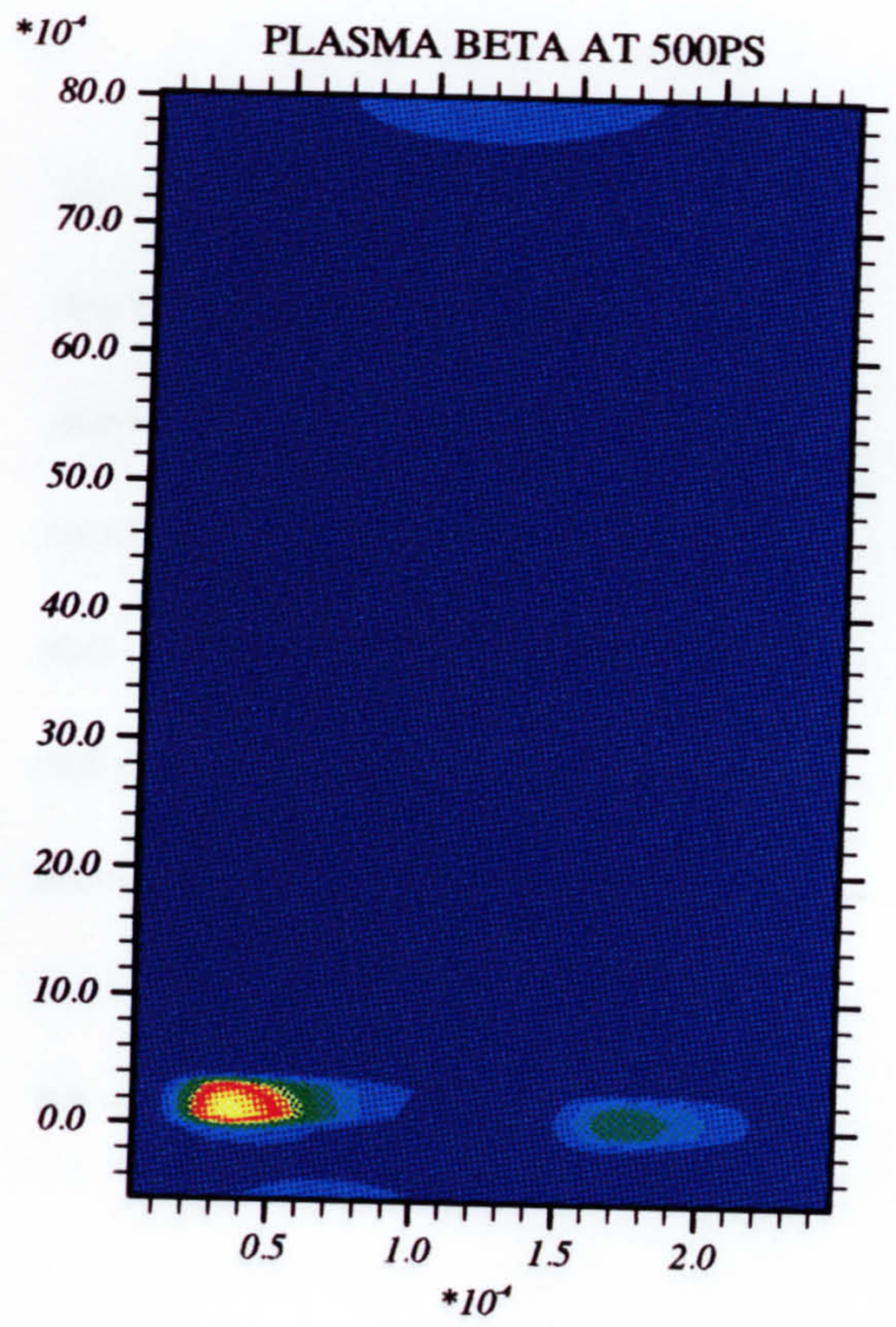
PLASMA BETA AT 500PS
*10⁻⁴
80.0
70.0
60.0
50.0
40.0
30.0
20.0
10.0
0.0
0.5
1.0
1.5
2.0
*10⁻⁴
ABOVE 0.00605
0.00550 - 0.00605
0.00495 - 0.00550
0.00440 - 0.00495
0.00385 - 0.00440
0.00330 - 0.00385
0.00275 - 0.00330
0.00220 - 0.00275
0.00165 - 0.00220
0.00110 - 0.00165
0.00055 - 0.00110
BELOW 0.00055

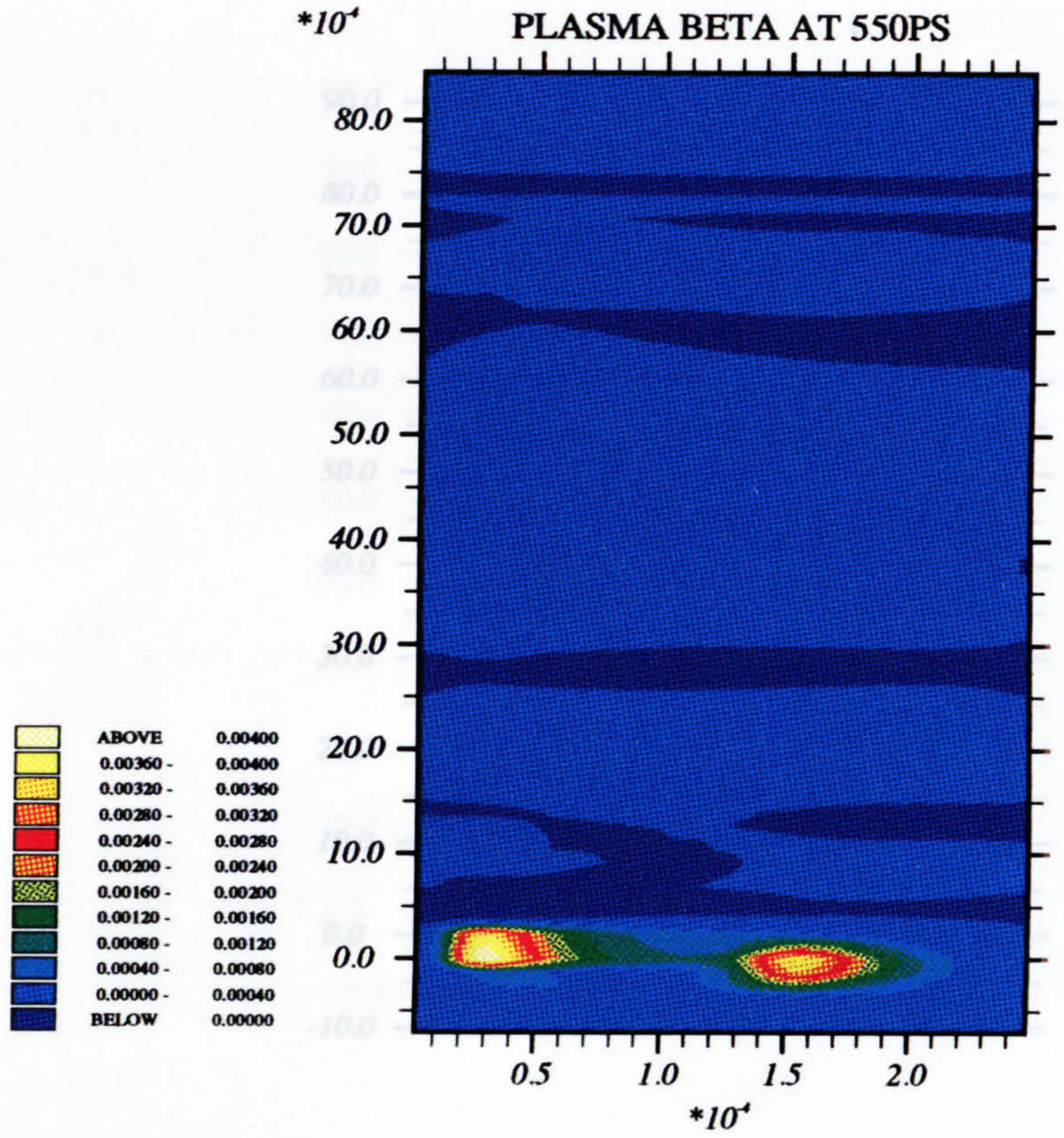
*10⁻⁴
PLASMA BETA AT 550PS
80.0
70.0
60.0
50.0
40.0
30.0
20.0
10.0
0.0
0.5
1.0
1.5
2.0
*10⁻⁴
ABOVE 0.00400
0.00360 - 0.00400
0.00320 - 0.00360
0.00280 - 0.00320
0.00240 - 0.00280
0.00200 - 0.00240
0.00160 - 0.00200
0.00120 - 0.00160
0.00080 - 0.00120
0.00040 - 0.00080
0.00000 - 0.00040
BELOW 0.00000

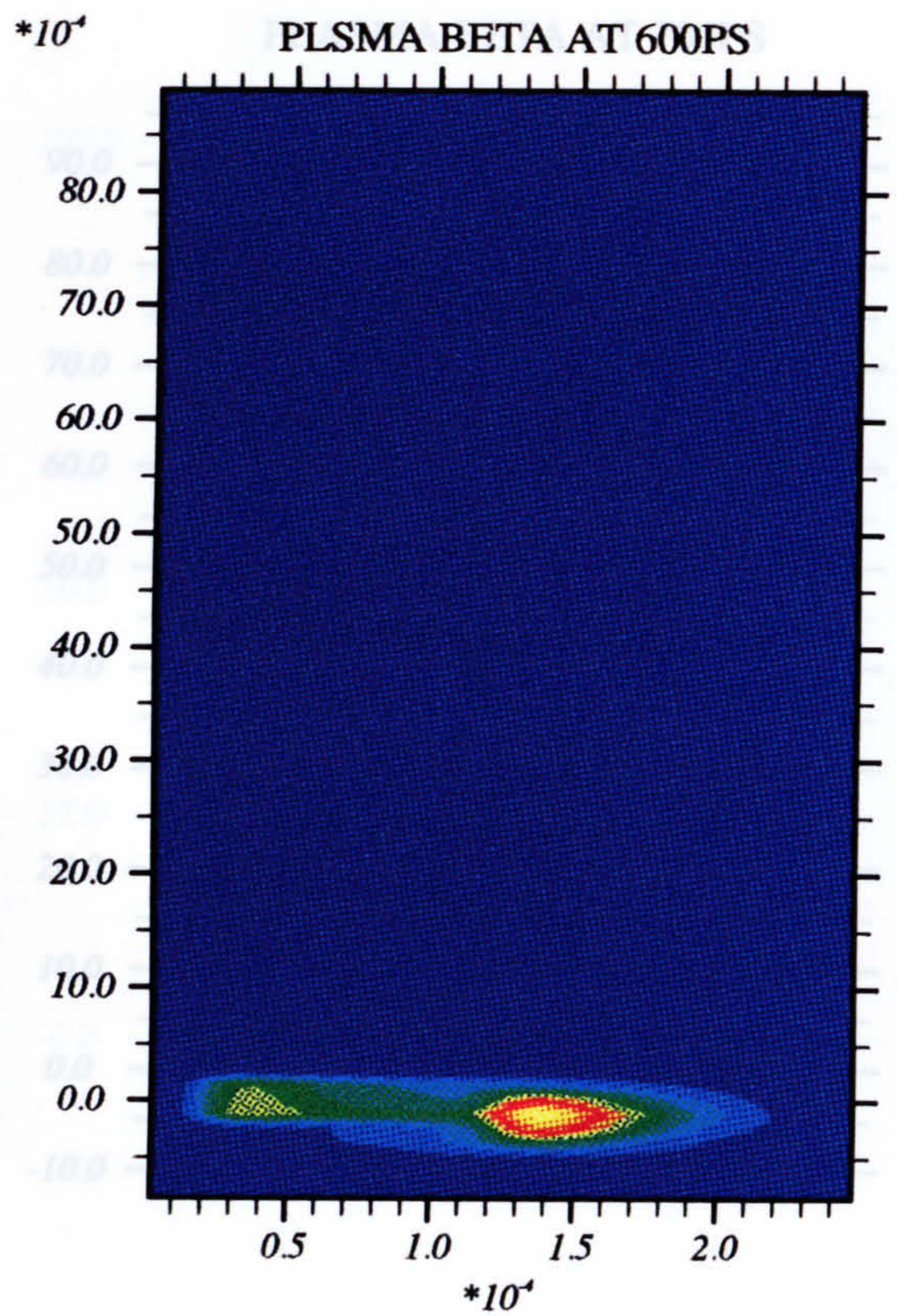
*10⁻⁴
PLSMA BETA AT 600PS
80.0
70.0
60.0
50.0
40.0
30.0
20.0
10.0
0.0
0.5
1.0
1.5
2.0
*10⁻⁴
ABOVE 0.00088
0.00080 - 0.00088
0.00072 - 0.00080
0.00064 - 0.00072
0.00056 - 0.00064
0.00048 - 0.00056
0.00040 - 0.00048
0.00032 - 0.00040
0.00024 - 0.00032
0.00016 - 0.00024
0.00008 - 0.00016
BELOW 0.00008

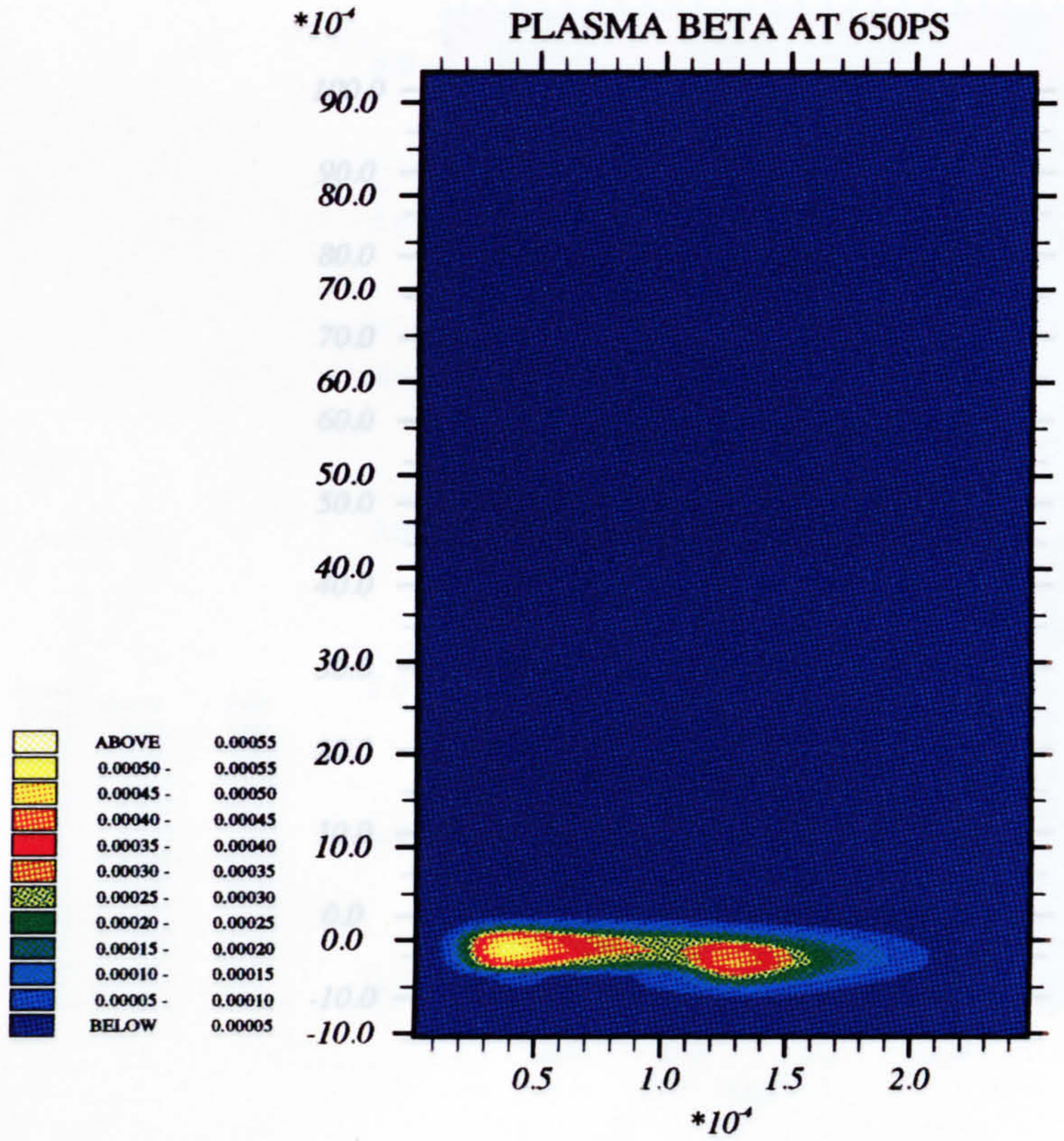
*10⁻⁴
PLASMA BETA AT 650PS
90.0
80.0
70.0
60.0
50.0
40.0
30.0
20.0
10.0
0.0
-10.0
0.5
1.0
1.5
2.0
*10⁻⁴
ABOVE 0.00055
0.00050 - 0.00055
0.00045 - 0.00050
0.00040 - 0.00045
0.00035 - 0.00040
0.00030 - 0.00035
0.00025 - 0.00030
0.00020 - 0.00025
0.00015 - 0.00020
0.00010 - 0.00015
0.00005 - 0.00010
BELOW 0.00005

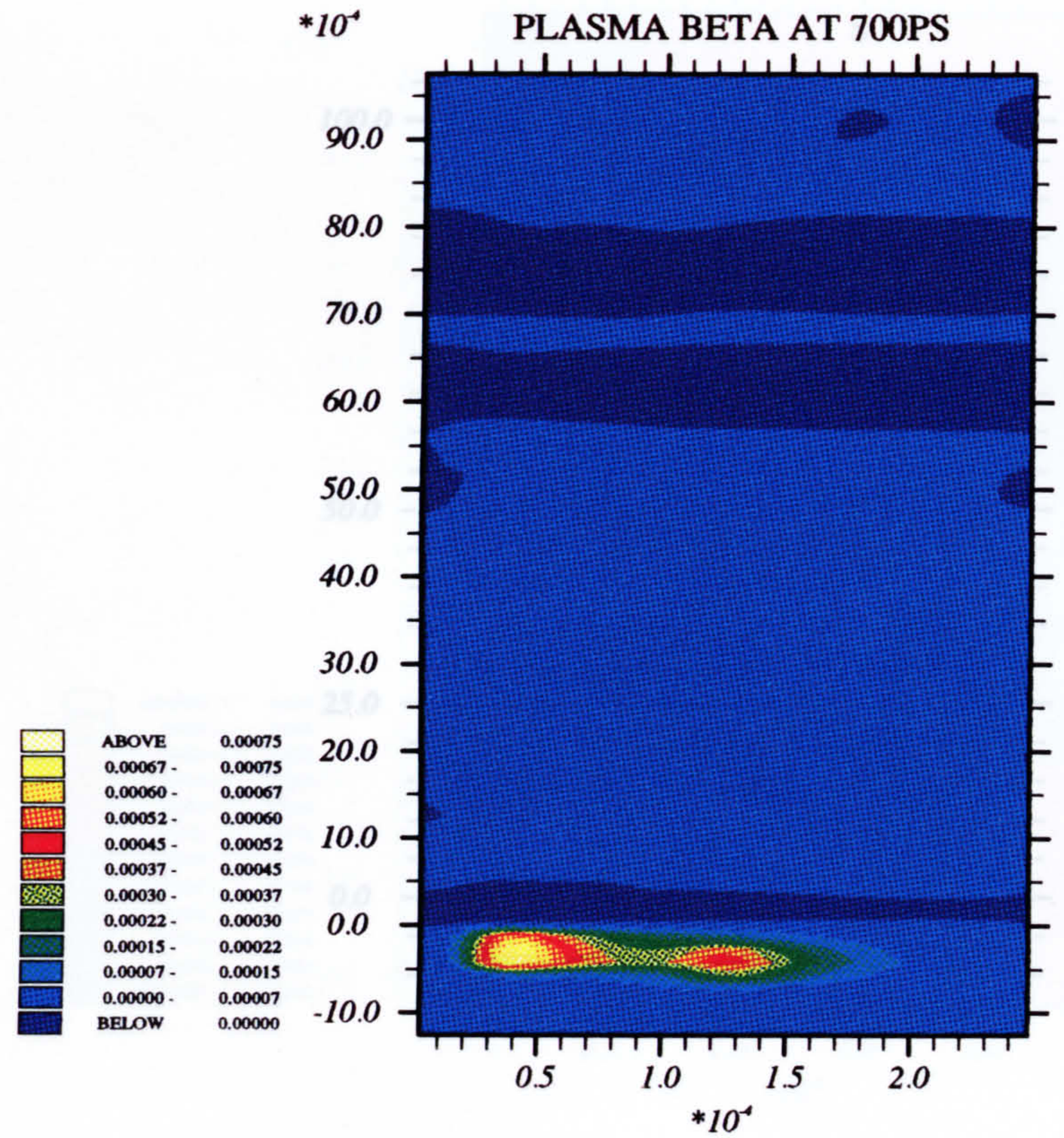
*10⁻⁴
PLASMA BETA AT 700PS
90.0
80.0
70.0
60.0
50.0
40.0
30.0
20.0
10.0
0.0
-10.0
0.5
1.0
1.5
2.0
*10⁻⁴
ABOVE 0.00075
0.00067 - 0.00075
0.00060 - 0.00067
0.00052 - 0.00060
0.00045 - 0.00052
0.00037 - 0.00045
0.00030 - 0.00037
0.00022 - 0.00030
0.00015 - 0.00022
0.00007 - 0.00015
0.00000 - 0.00007
BELOW 0.00000

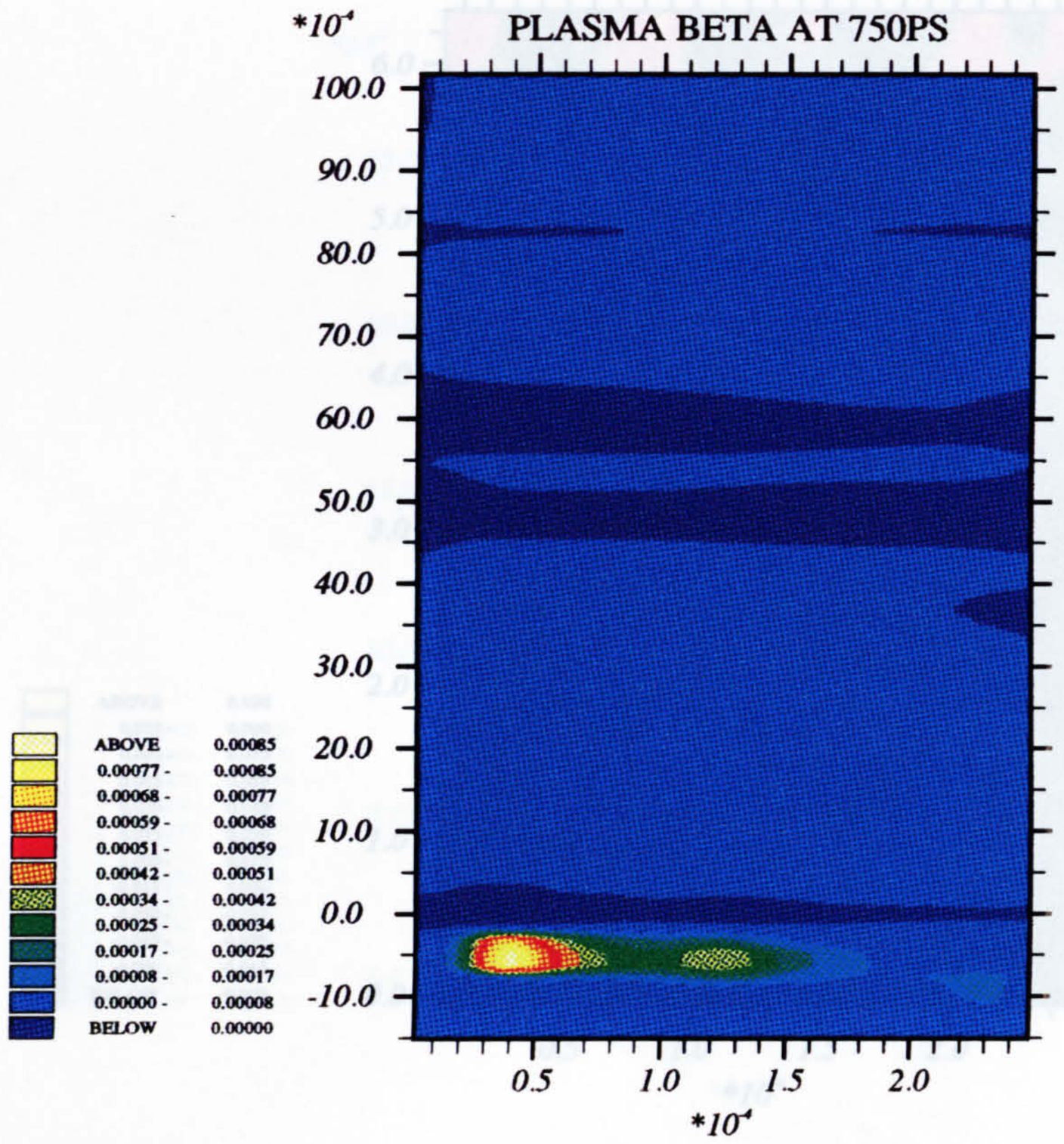
*10⁻⁴
PLASMA BETA AT 750PS
100.0
90.0
80.0
70.0
60.0
50.0
40.0
30.0
20.0
10.0
0.0
-10.0
0.5
1.0
1.5
2.0
*10⁻⁴
ABOVE 0.00085
0.00077 - 0.00085
0.00068 - 0.00077
0.00059 - 0.00068
0.00051 - 0.00059
0.00042 - 0.00051
0.00034 - 0.00042
0.00025 - 0.00034
0.00017 - 0.00025
0.00008 - 0.00017
0.00000 - 0.00008
BELOW 0.00000

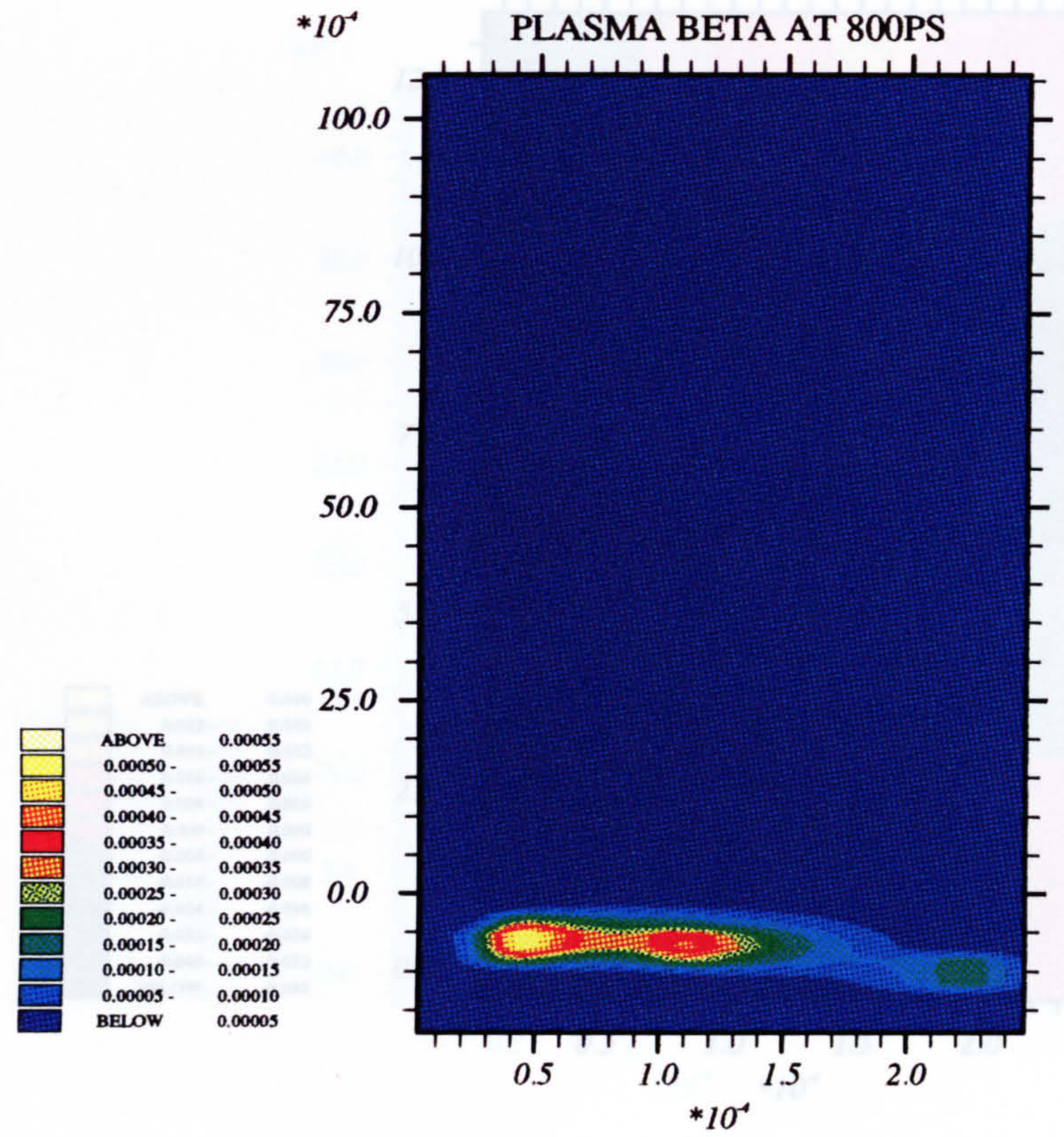
*10⁻⁴
PLASMA BETA AT 800PS
100.0
75.0
50.0
25.0
0.0
0.5
1.0
1.5
2.0
*10⁻⁴
ABOVE 0.00055
0.00050 - 0.00055
0.00045 - 0.00050
0.00040 - 0.00045
0.00035 - 0.00040
0.00030 - 0.00035
0.00025 - 0.00030
0.00020 - 0.00025
0.00015 - 0.00020
0.00010 - 0.00015
0.00005 - 0.00010
BELOW 0.00005

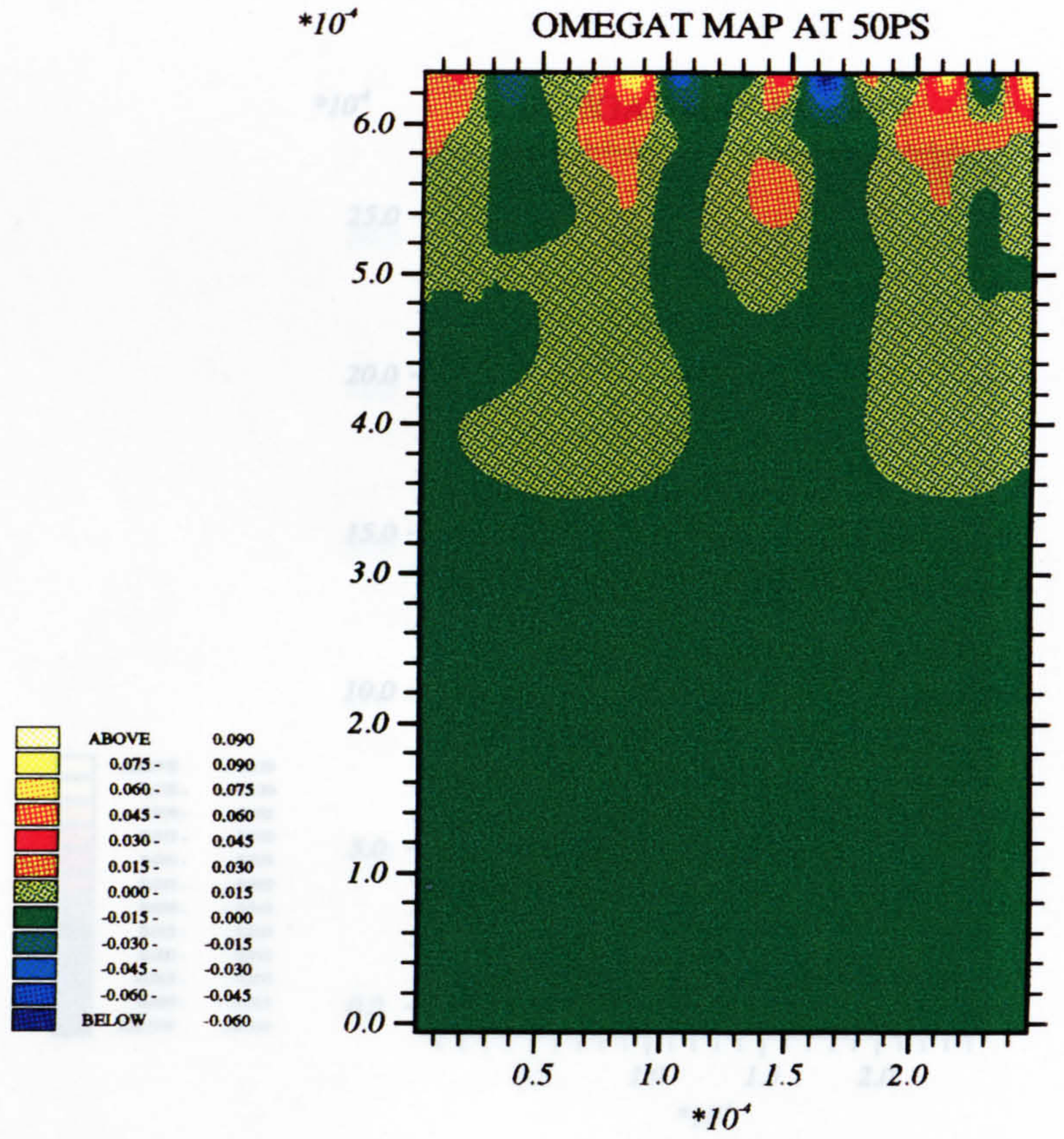

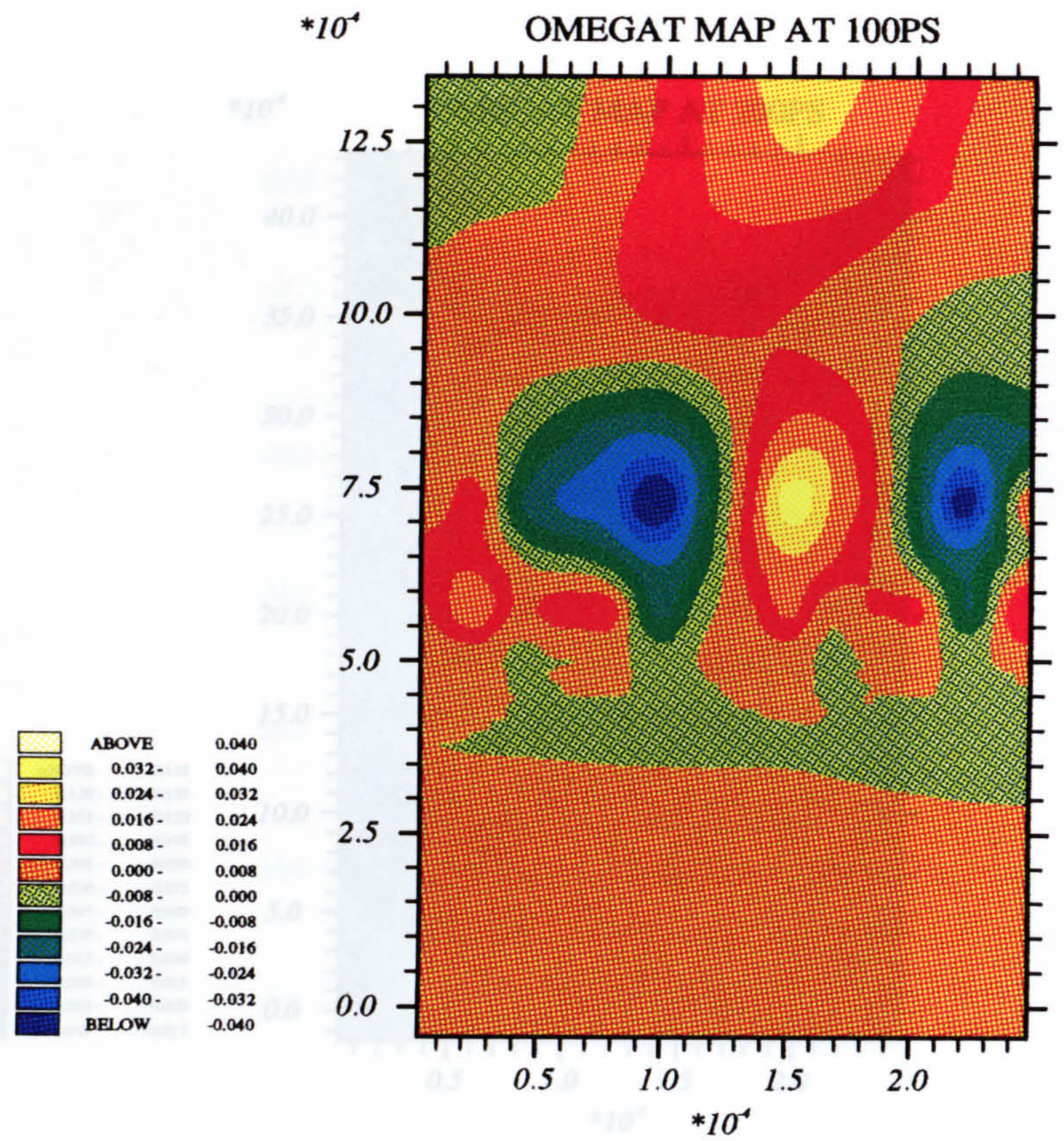

Figure 5.6: $\omega\tau$ map for the target (5.0μm x 2.5μm).

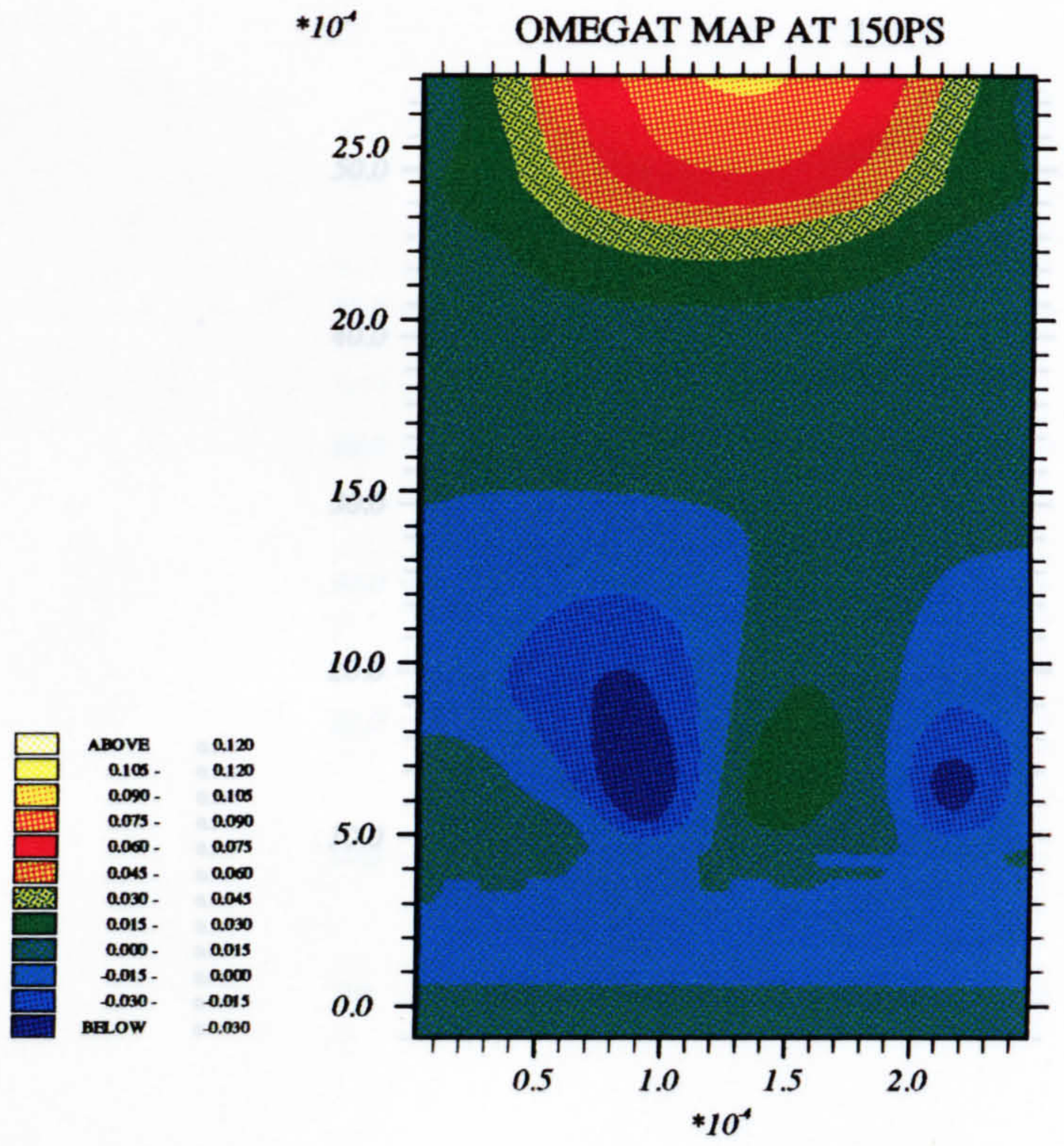
*10⁻⁴
OMEGAT MAP AT 150PS
25.0
20.0
15.0
10.0
5.0
0.0
0.5
1.0
1.5
2.0
*10⁻⁴
ABOVE 0.120
0.105 - 0.120
0.090 - 0.105
0.075 - 0.090
0.060 - 0.075
0.045 - 0.060
0.030 - 0.045
0.015 - 0.030
0.000 - 0.015
-0.015 - 0.000
-0.030 - -0.015
BELOW -0.030

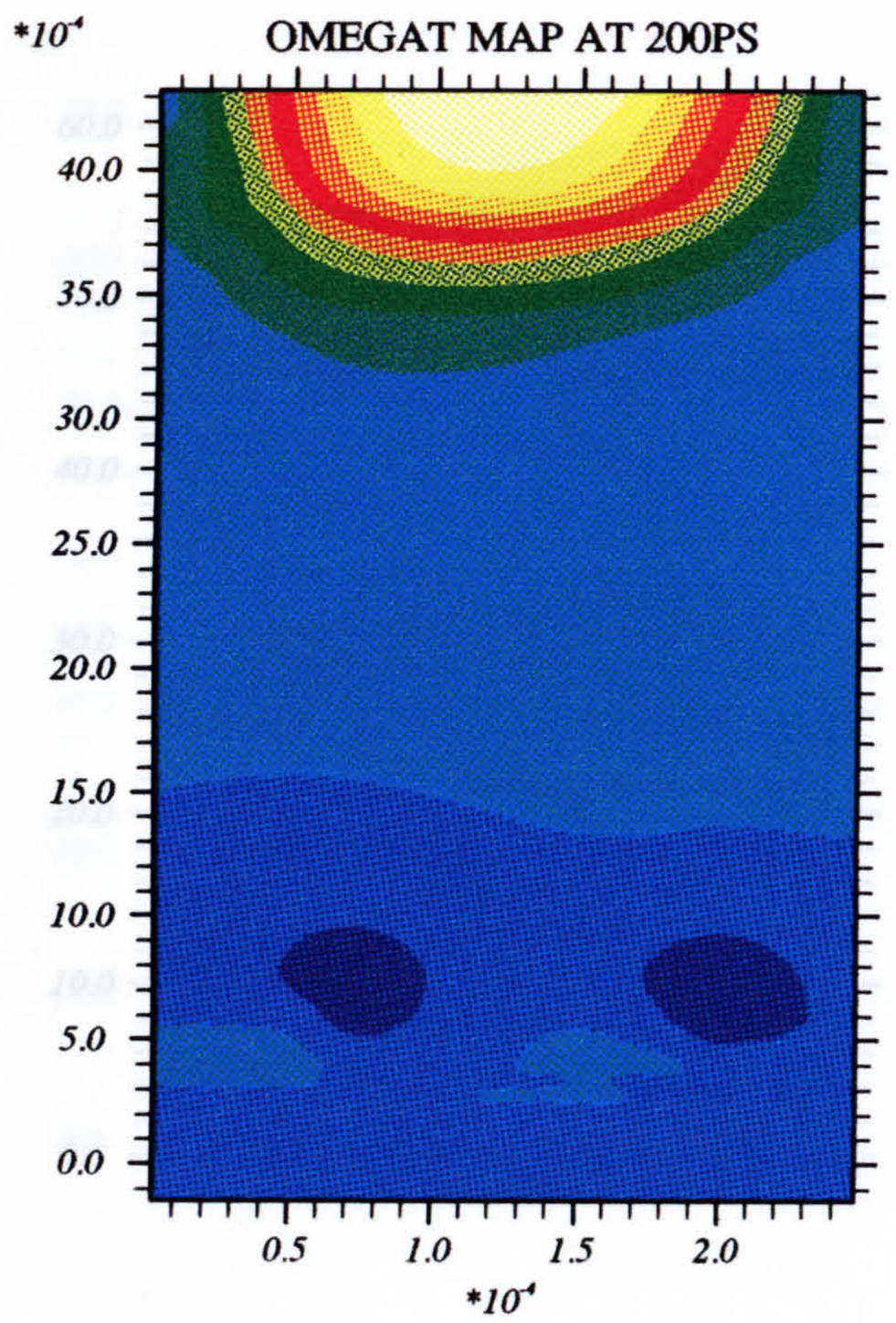
*10⁻⁴
OMEGAT MAP AT 200PS
40.0
35.0
30.0
25.0
20.0
15.0
10.0
5.0
0.0
0.5
1.0
1.5
2.0
*10⁻⁴
ABOVE 0.135
0.120 - 0.135
0.105 - 0.120
0.090 - 0.105
0.075 - 0.090
0.060 - 0.075
0.045 - 0.060
0.030 - 0.045
0.015 - 0.030
0.000 - 0.015
-0.015 - 0.000
BELOW -0.015

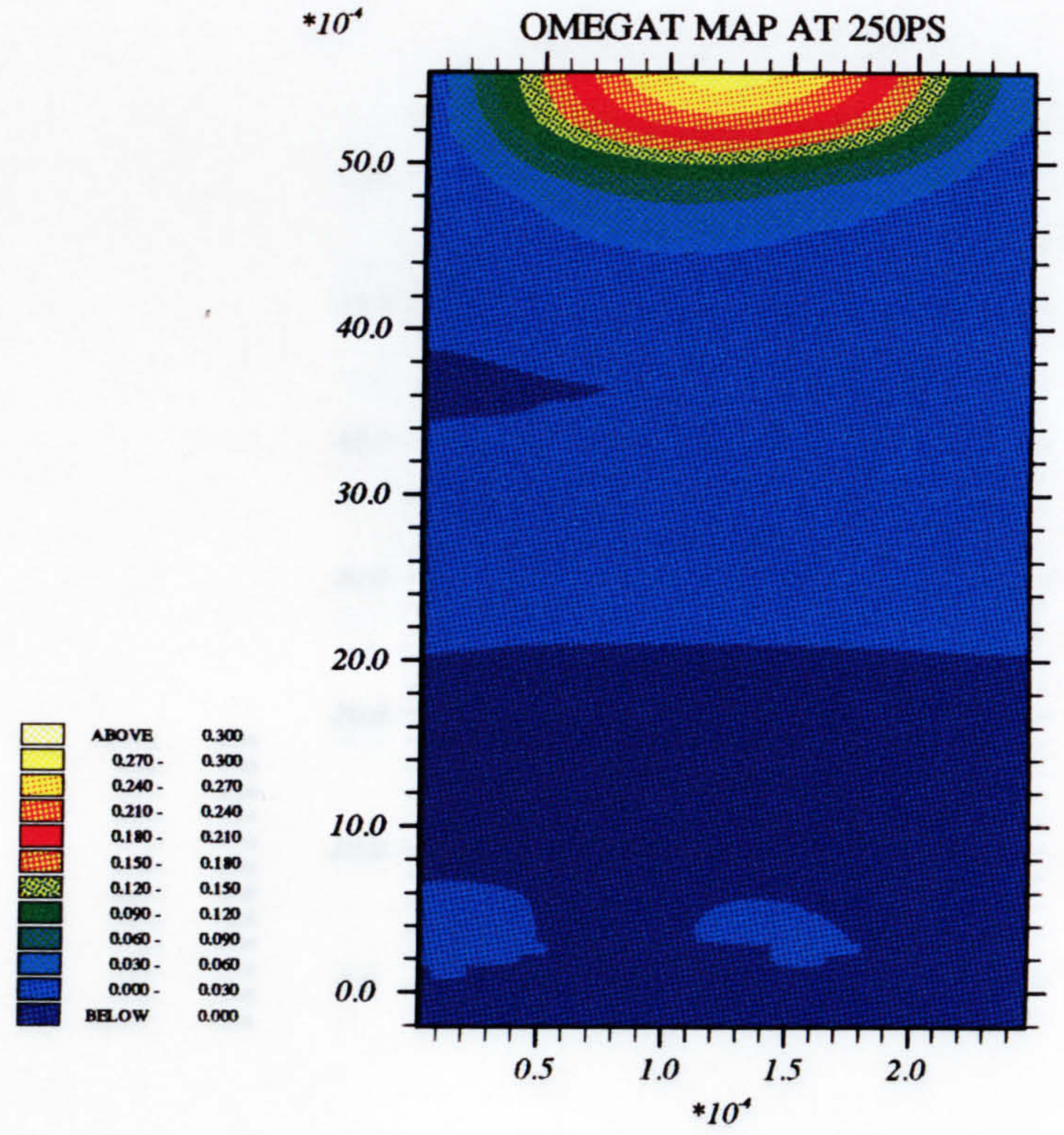
*10⁻⁴
OMEGAT MAP AT 250PS
50.0
40.0
30.0
20.0
10.0
0.0
0.5
1.0
1.5
2.0
*10⁻⁴
ABOVE 0.300
0.270 - 0.300
0.240 - 0.270
0.210 - 0.240
0.180 - 0.210
0.150 - 0.180
0.120 - 0.150
0.090 - 0.120
0.060 - 0.090
0.030 - 0.060
0.000 - 0.030
BELOW 0.000

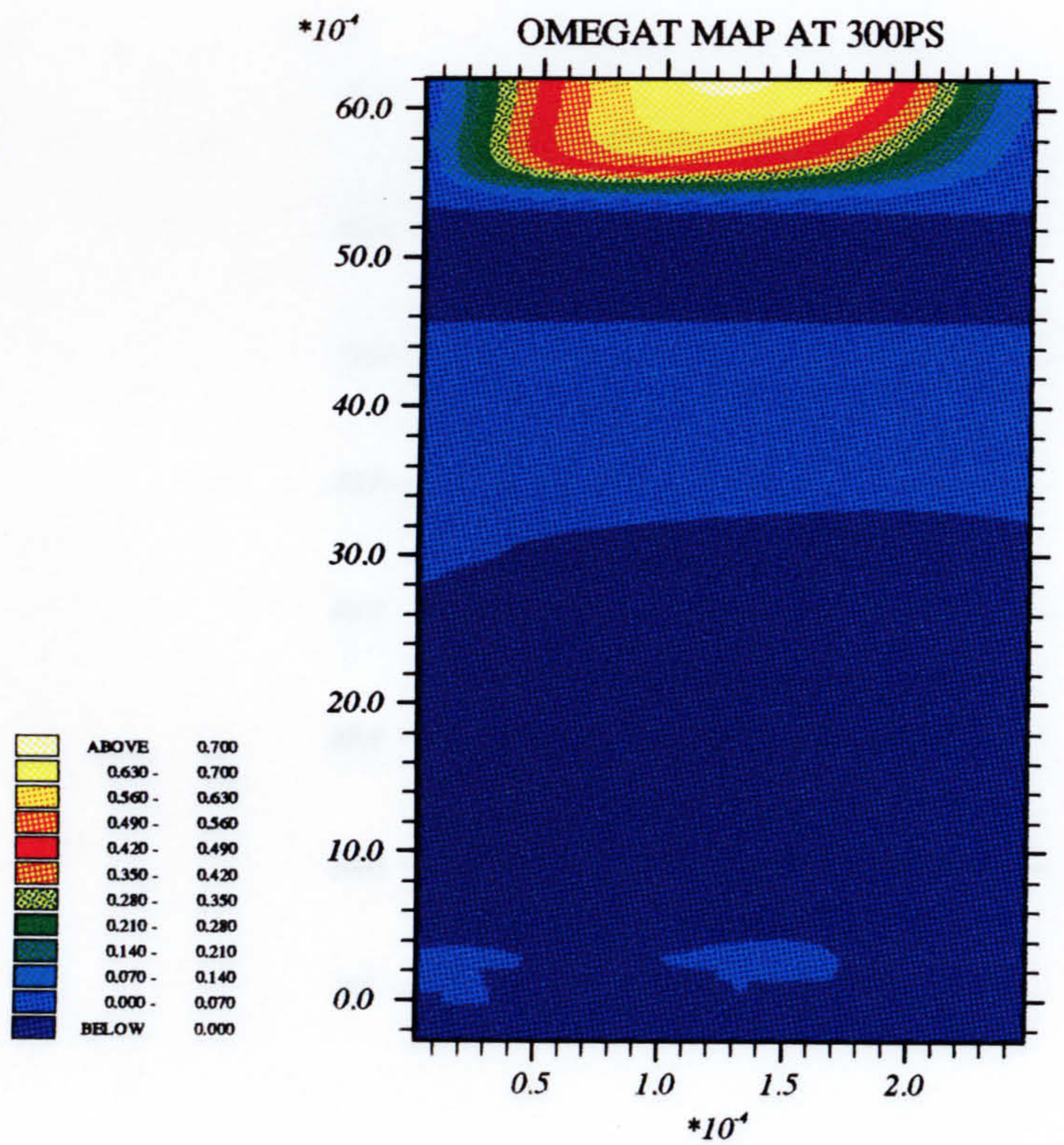
*10⁻⁴
OMEGAT MAP AT 300PS
60.0
50.0
40.0
30.0
20.0
10.0
0.0
0.5
1.0
1.5
2.0
*10⁻⁴
ABOVE 0.700
0.630 - 0.700
0.560 - 0.630
0.490 - 0.560
0.420 - 0.490
0.350 - 0.420
0.280 - 0.350
0.210 - 0.280
0.140 - 0.210
0.070 - 0.140
0.000 - 0.070
BELOW 0.000

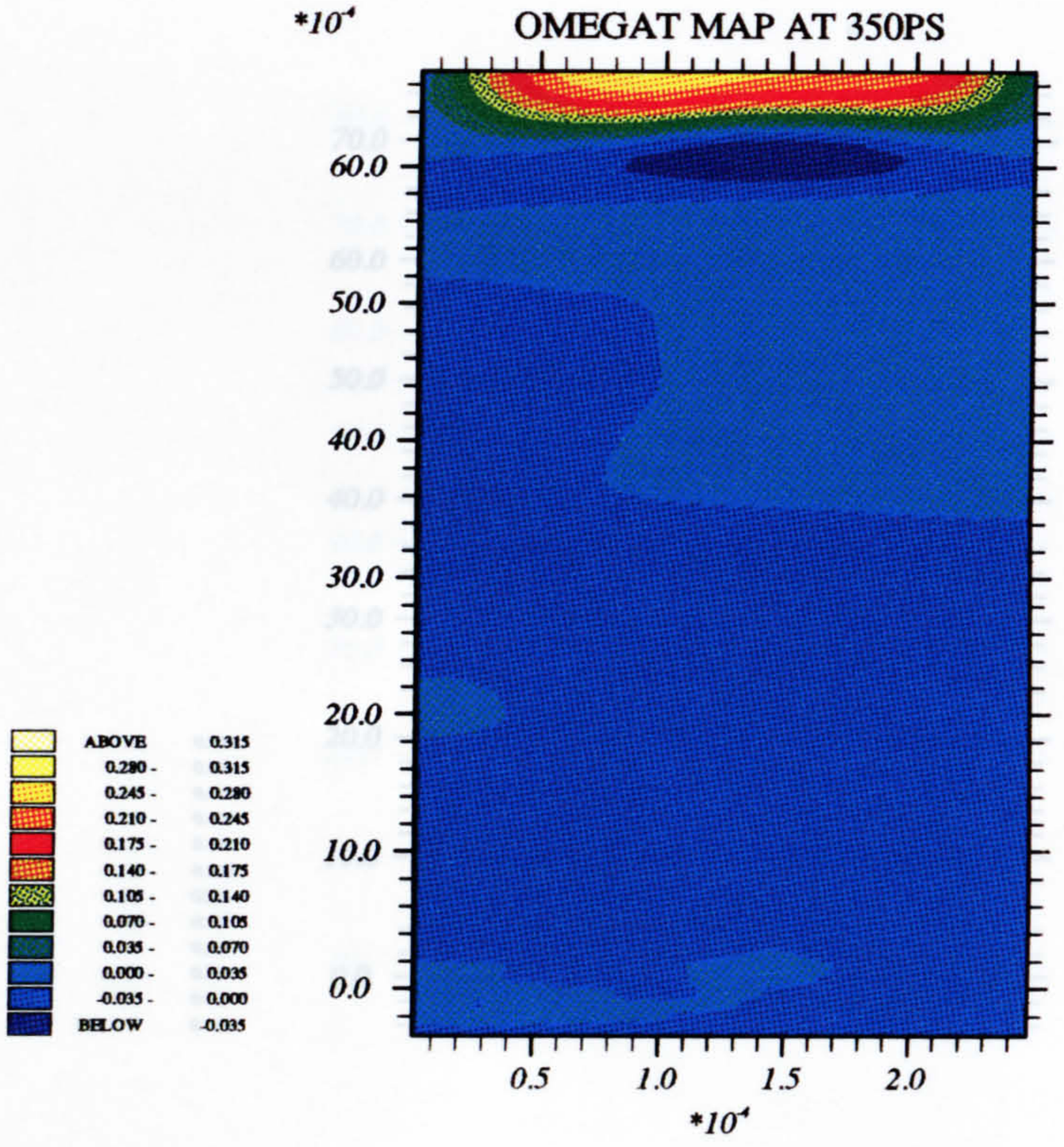
*10⁻⁴
OMEGAT MAP AT 350PS
60.0
50.0
40.0
30.0
20.0
10.0
0.0
0.5
1.0
1.5
2.0
*10⁻⁴
ABOVE 0.315
0.280 - 0.315
0.245 - 0.280
0.210 - 0.245
0.175 - 0.210
0.140 - 0.175
0.105 - 0.140
0.070 - 0.105
0.035 - 0.070
0.000 - 0.035
-0.035 - 0.000
BELOW -0.035

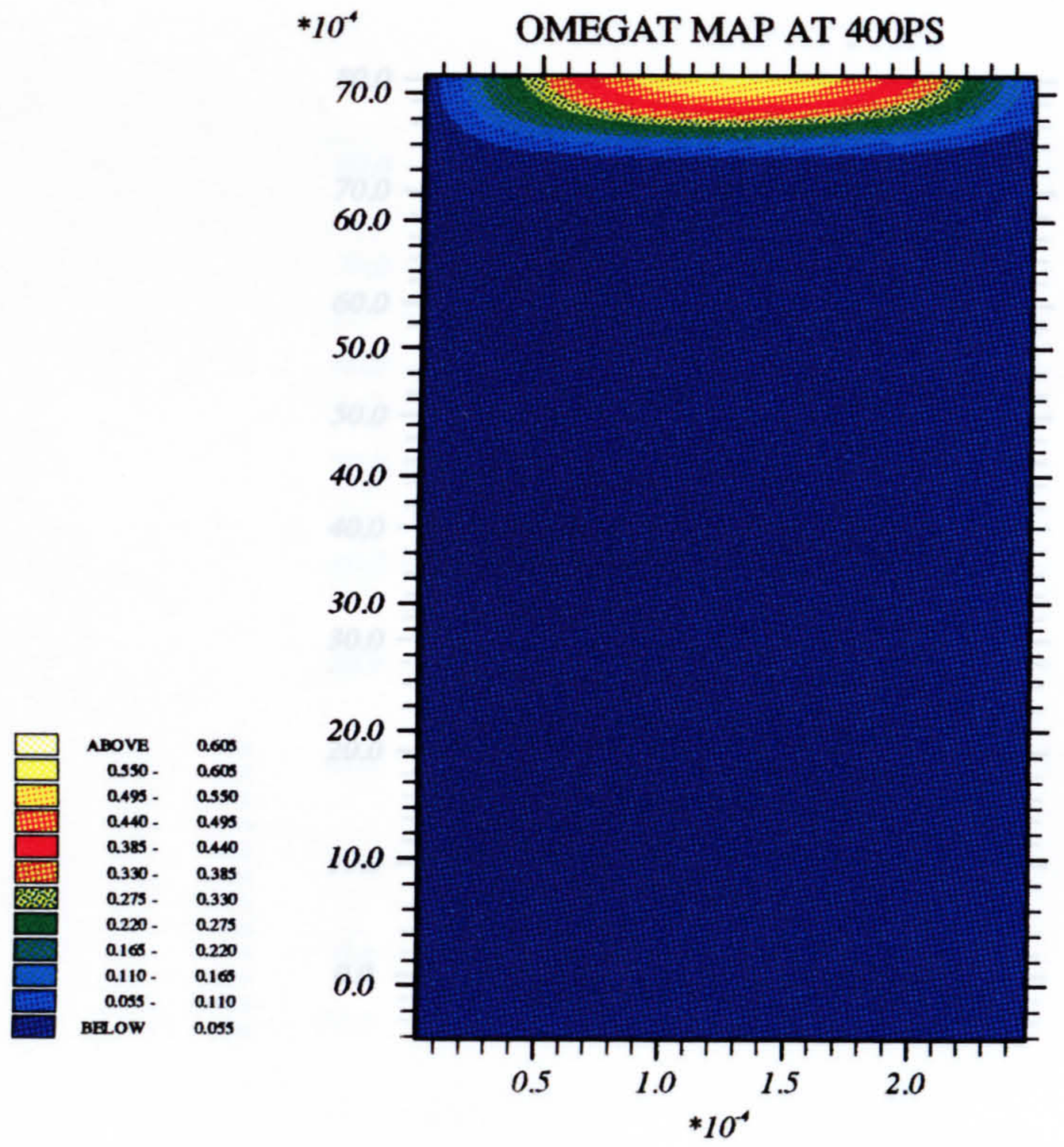
*10⁻⁴
OMEGAT MAP AT 400PS
70.0
60.0
50.0
40.0
30.0
20.0
10.0
0.0
0.5
1.0
1.5
2.0
*10⁻⁴
ABOVE 0.605
0.550 - 0.605
0.495 - 0.550
0.440 - 0.495
0.385 - 0.440
0.330 - 0.385
0.275 - 0.330
0.220 - 0.275
0.165 - 0.220
0.110 - 0.165
0.055 - 0.110
BELOW 0.055

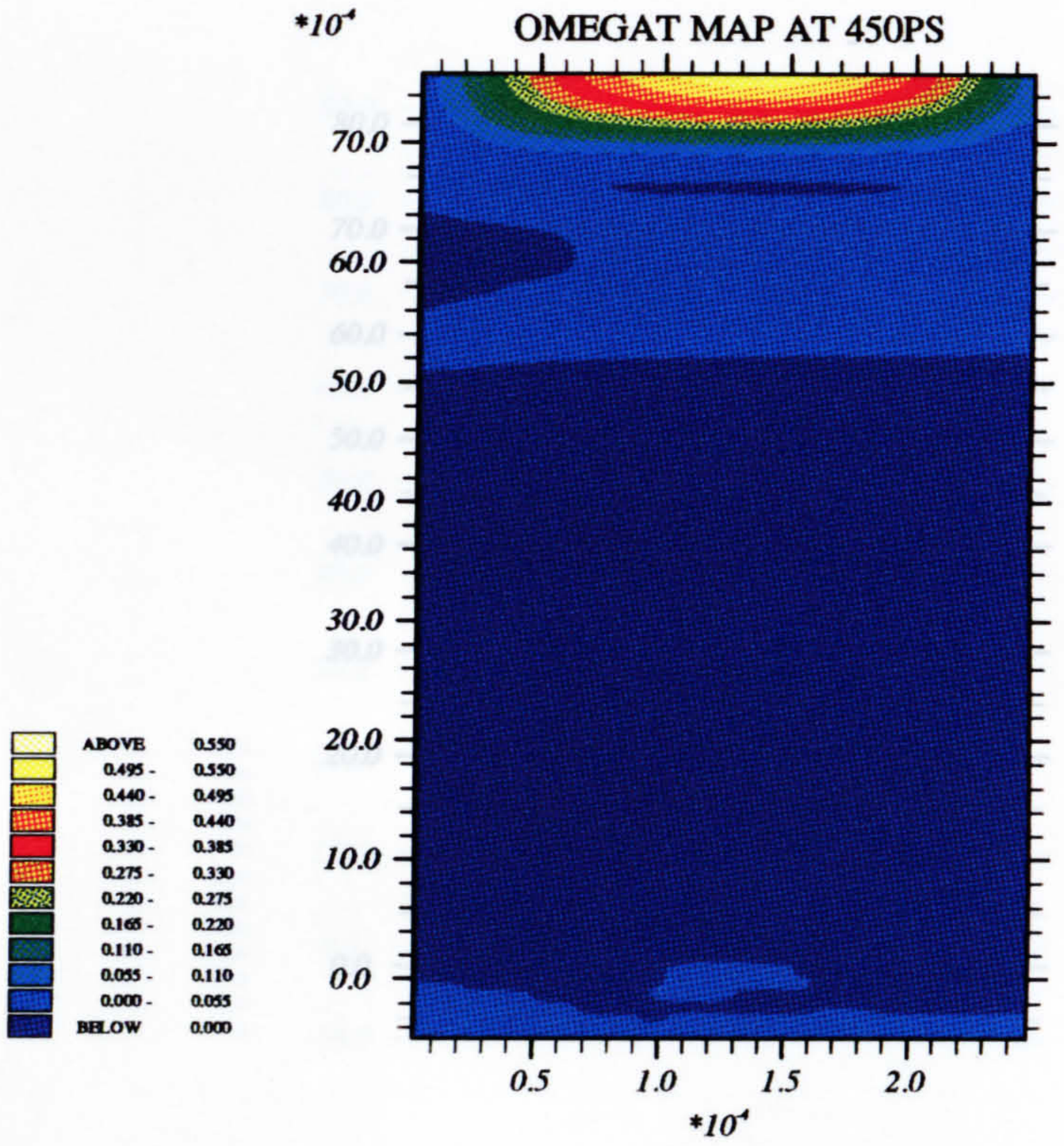
*10⁻⁴
OMEGAT MAP AT 450PS
70.0
60.0
50.0
40.0
30.0
20.0
10.0
0.0
0.5
1.0
1.5
2.0
*10⁻⁴
ABOVE 0.550
0.495 - 0.550
0.440 - 0.495
0.385 - 0.440
0.330 - 0.385
0.275 - 0.330
0.220 - 0.275
0.165 - 0.220
0.110 - 0.165
0.055 - 0.110
0.000 - 0.055
BELOW 0.000

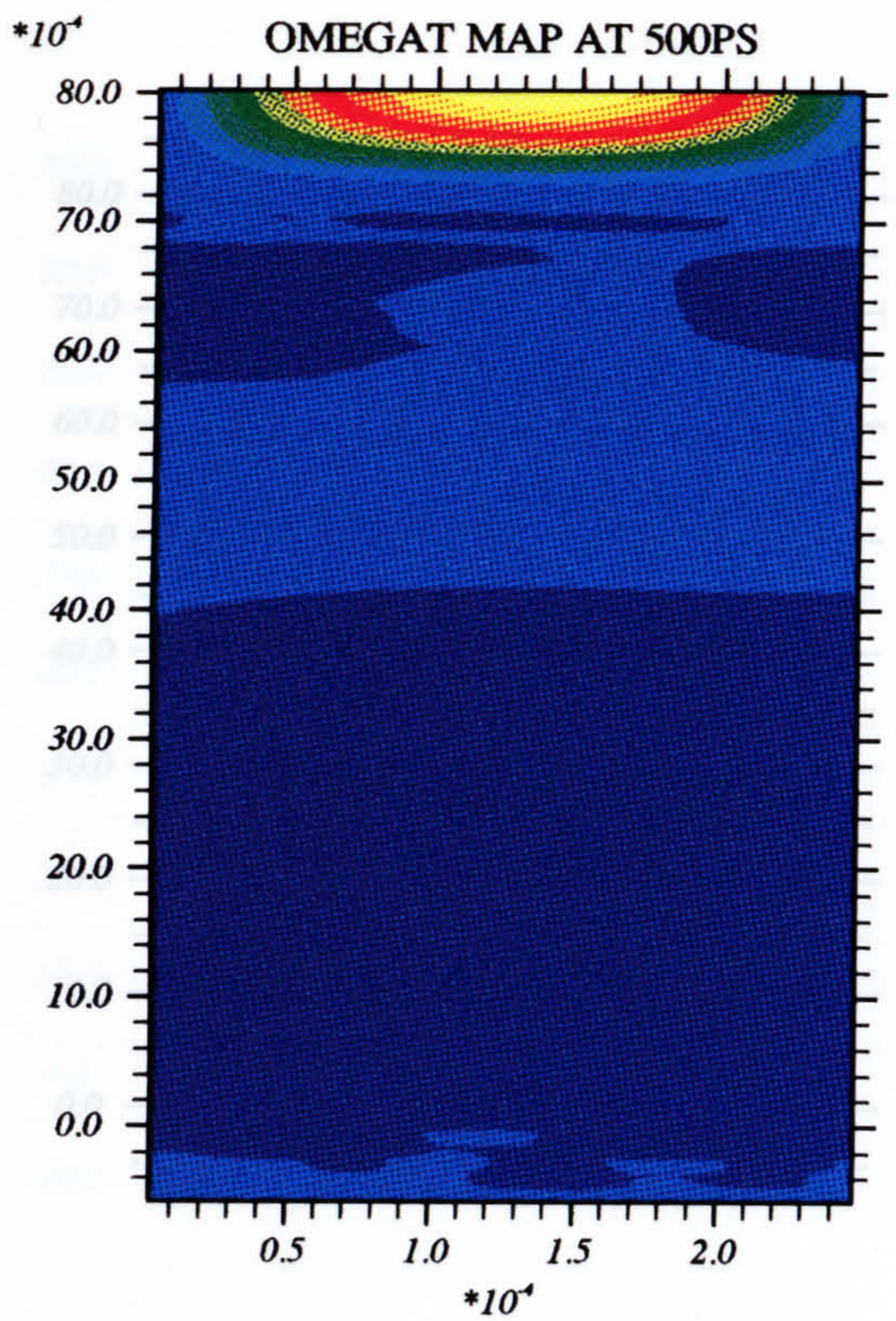
*10⁻⁴
OMEGAT MAP AT 500PS
80.0
70.0
60.0
50.0
40.0
30.0
20.0
10.0
0.0
0.5
1.0
1.5
2.0
*10⁻⁴
ABOVE 0.450
0.405 - 0.450
0.360 - 0.405
0.315 - 0.360
0.270 - 0.315
0.225 - 0.270
0.180 - 0.225
0.135 - 0.180
0.090 - 0.135
0.045 - 0.090
0.000 - 0.045
BELOW 0.000

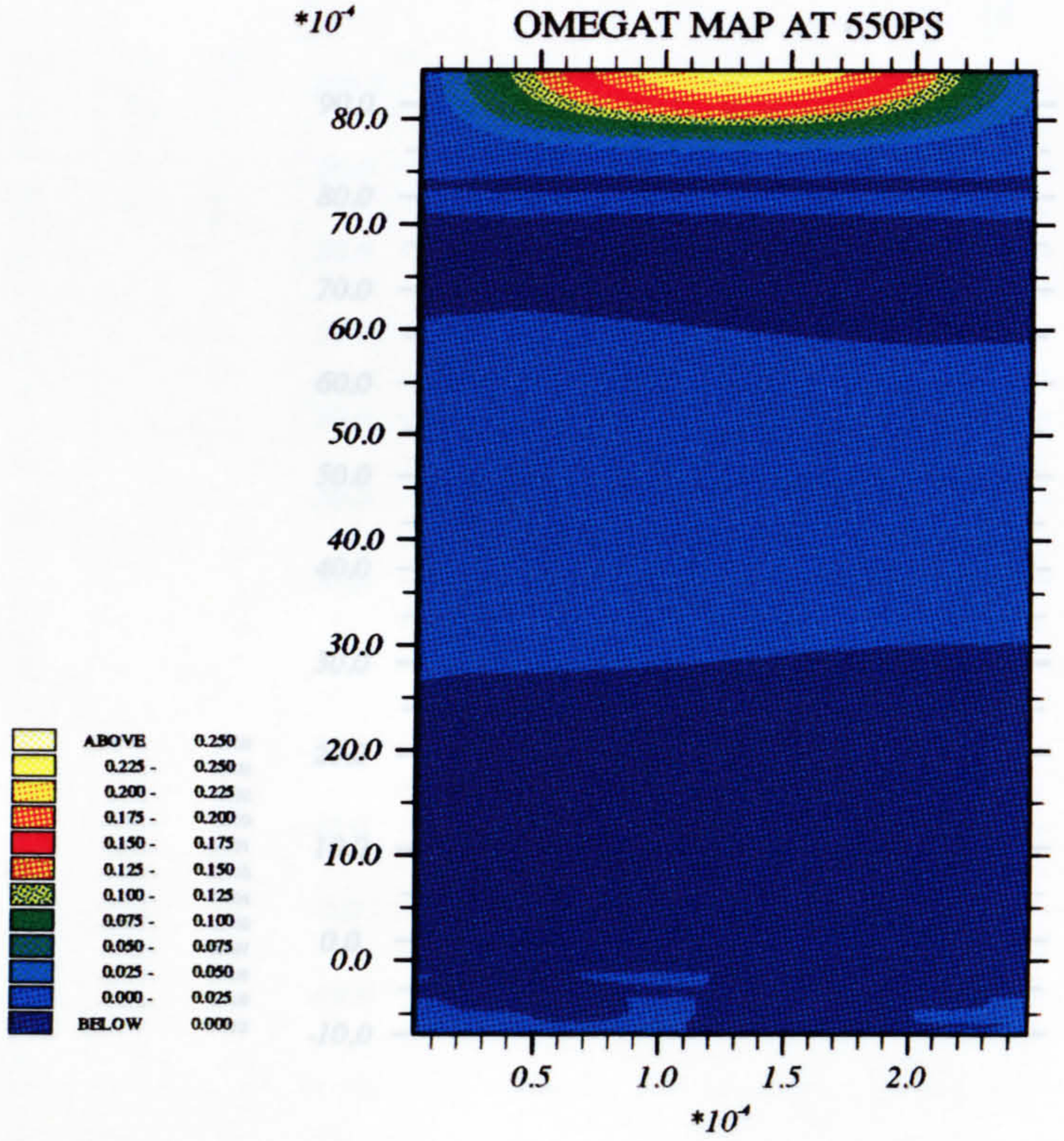
OMEGAT MAP AT 550PS
*10⁻⁴
80.0
70.0
60.0
50.0
40.0
30.0
20.0
10.0
0.0
0.5
1.0
1.5
2.0
*10⁻⁴
ABOVE 0.250
0.225 - 0.250
0.200 - 0.225
0.175 - 0.200
0.150 - 0.175
0.125 - 0.150
0.100 - 0.125
0.075 - 0.100
0.050 - 0.075
0.025 - 0.050
0.000 - 0.025
BELOW 0.000

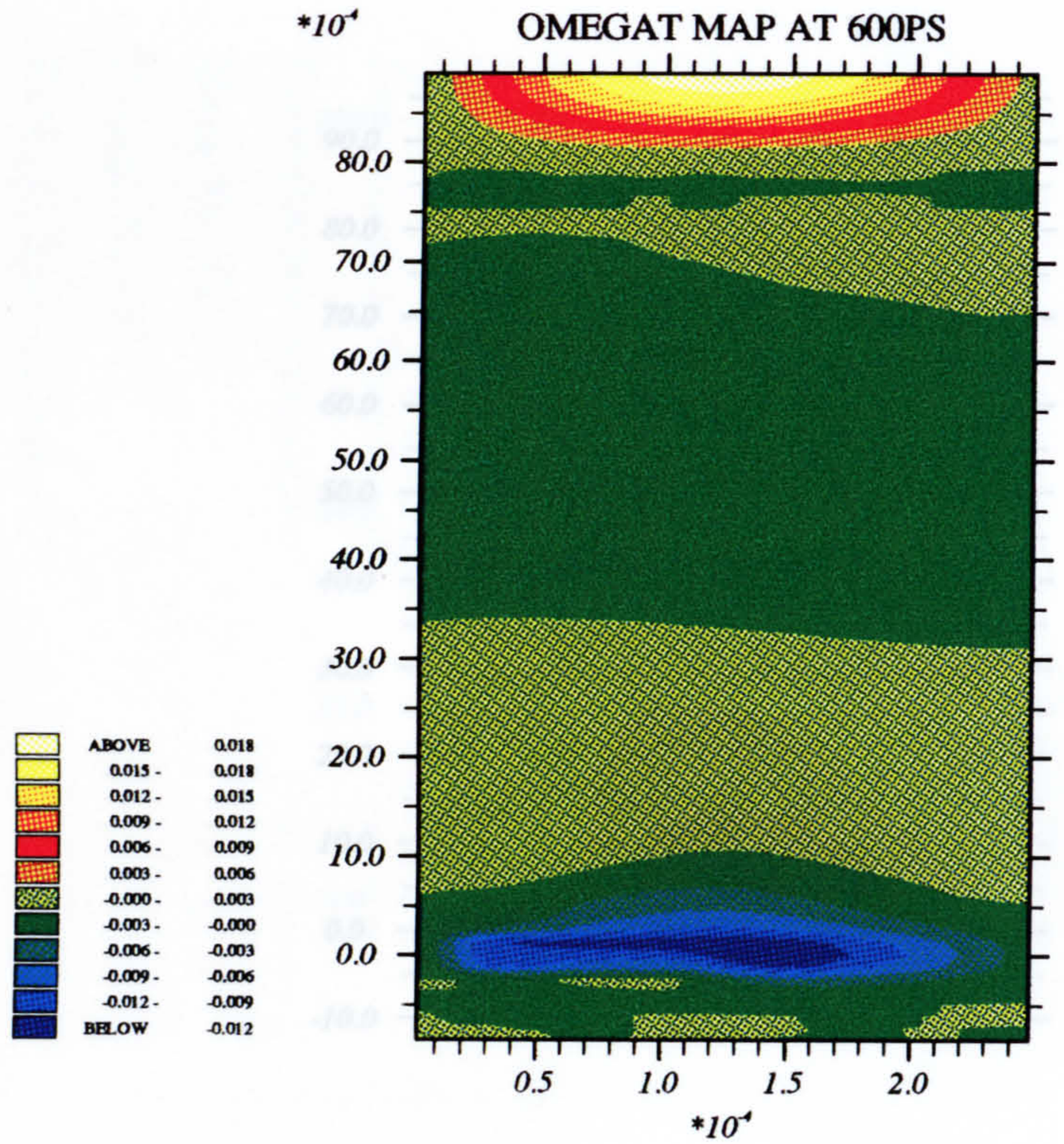
OMEGAT MAP AT 600PS
*10⁻⁴
80.0
70.0
60.0
50.0
40.0
30.0
20.0
10.0
0.0
0.5
1.0
1.5
2.0
*10⁻⁴
ABOVE 0.018
0.015 - 0.018
0.012 - 0.015
0.009 - 0.012
0.006 - 0.009
0.003 - 0.006
-0.000 - 0.003
-0.003 - -0.000
-0.006 - -0.003
-0.009 - -0.006
-0.012 - -0.009
BELOW -0.012

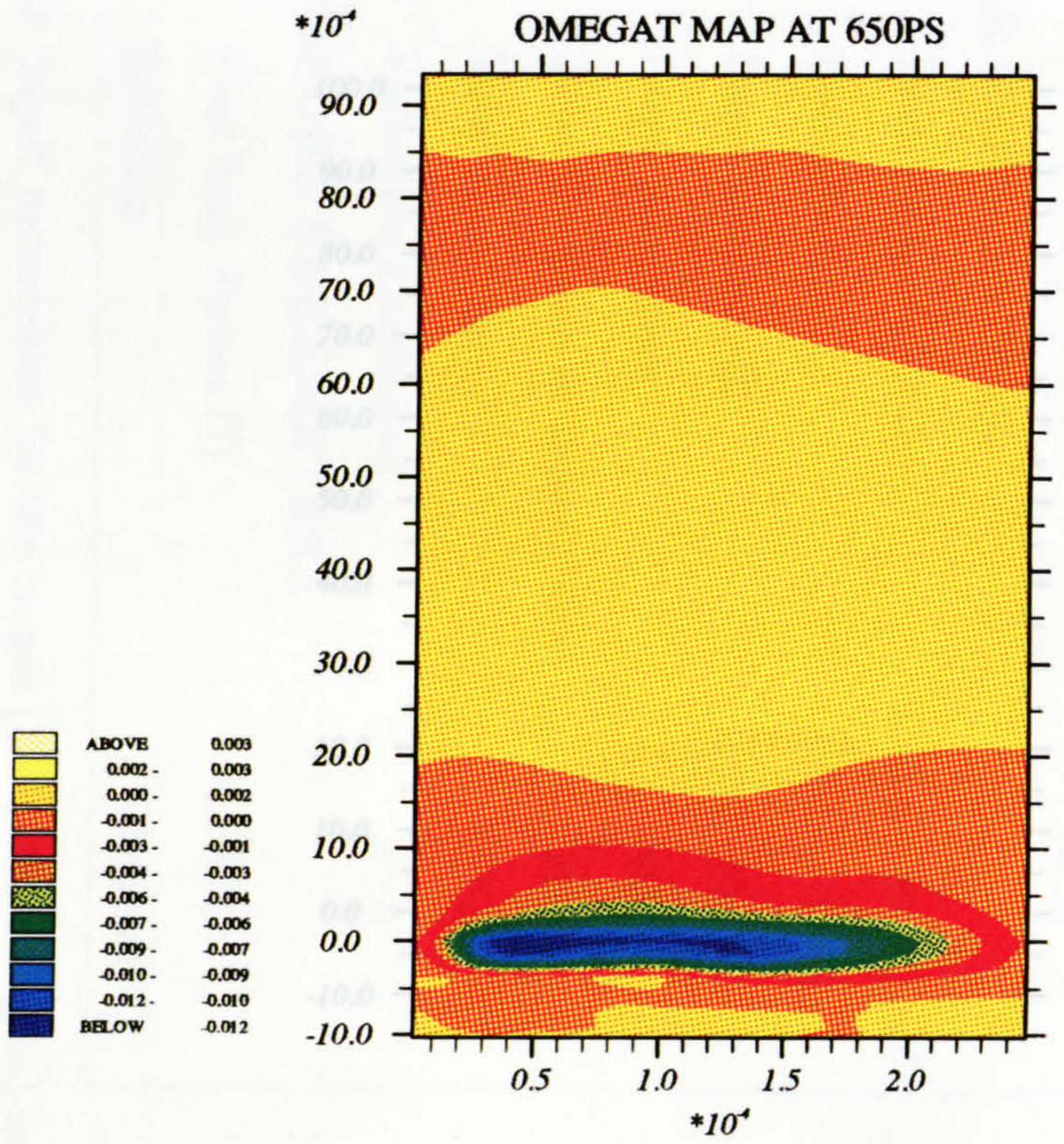
OMEGAT MAP AT 650PS
*10⁻⁴
90.0
80.0
70.0
60.0
50.0
40.0
30.0
20.0
10.0
0.0
-10.0
0.5
1.0
1.5
2.0
*10⁻⁴
ABOVE 0.003
0.002 - 0.003
0.000 - 0.002
-0.001 - 0.000
-0.003 - -0.001
-0.004 - -0.003
-0.006 - -0.004
-0.007 - -0.006
-0.009 - -0.007
-0.010 - -0.009
-0.012 - -0.010
BELOW -0.012

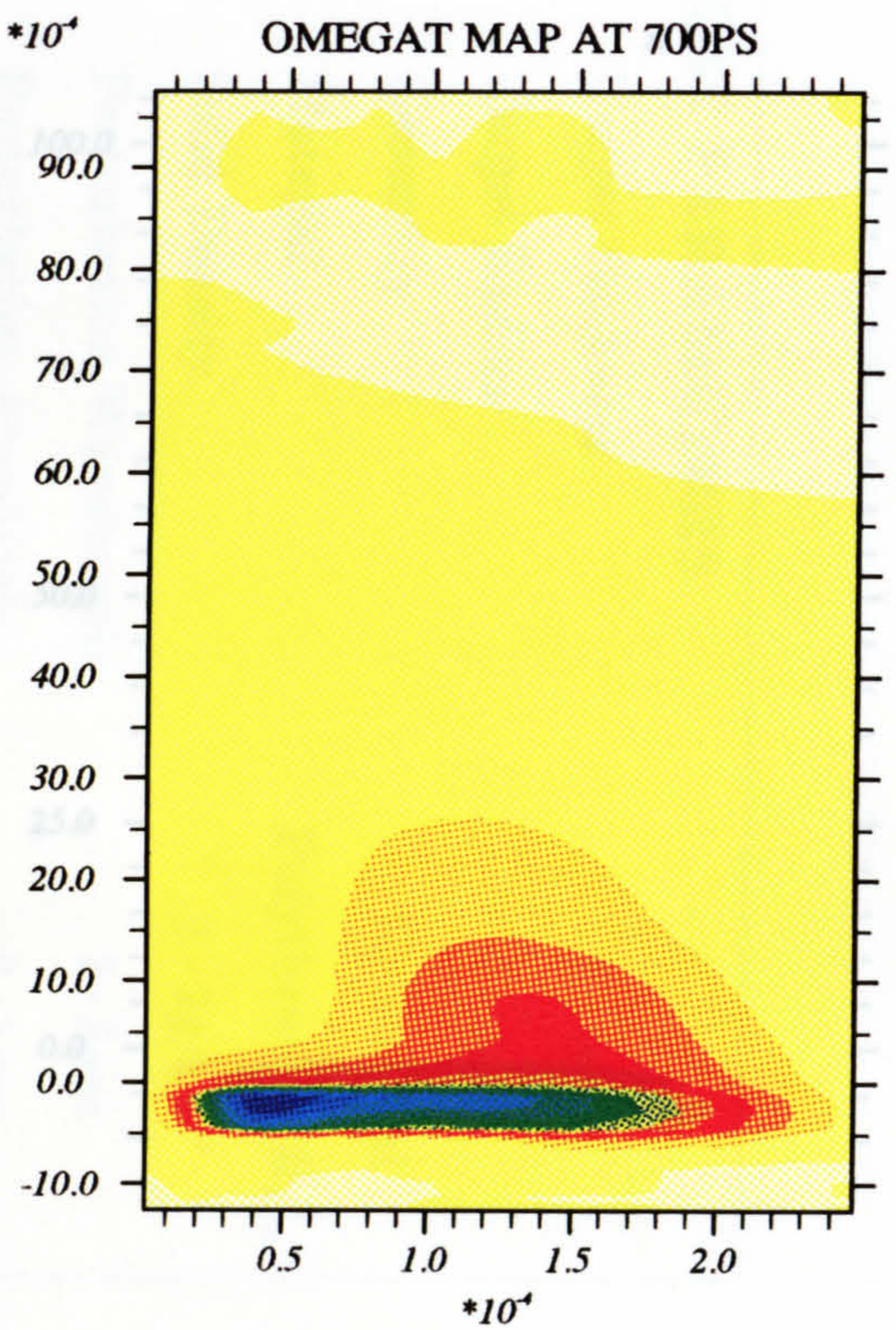
OMEGAT MAP AT 700PS
*10⁻⁴
90.0
80.0
70.0
60.0
50.0
40.0
30.0
20.0
10.0
0.0
-10.0
0.5
1.0
1.5
2.0
*10⁻⁴
ABOVE -0.000
-0.001 - -0.000
-0.002 - -0.001
-0.003 - -0.002
-0.004 - -0.003
-0.005 - -0.004
-0.006 - -0.005
-0.007 - -0.006
-0.008 - -0.007
-0.009 - -0.008
-0.009 - -0.009
BELOW -0.009

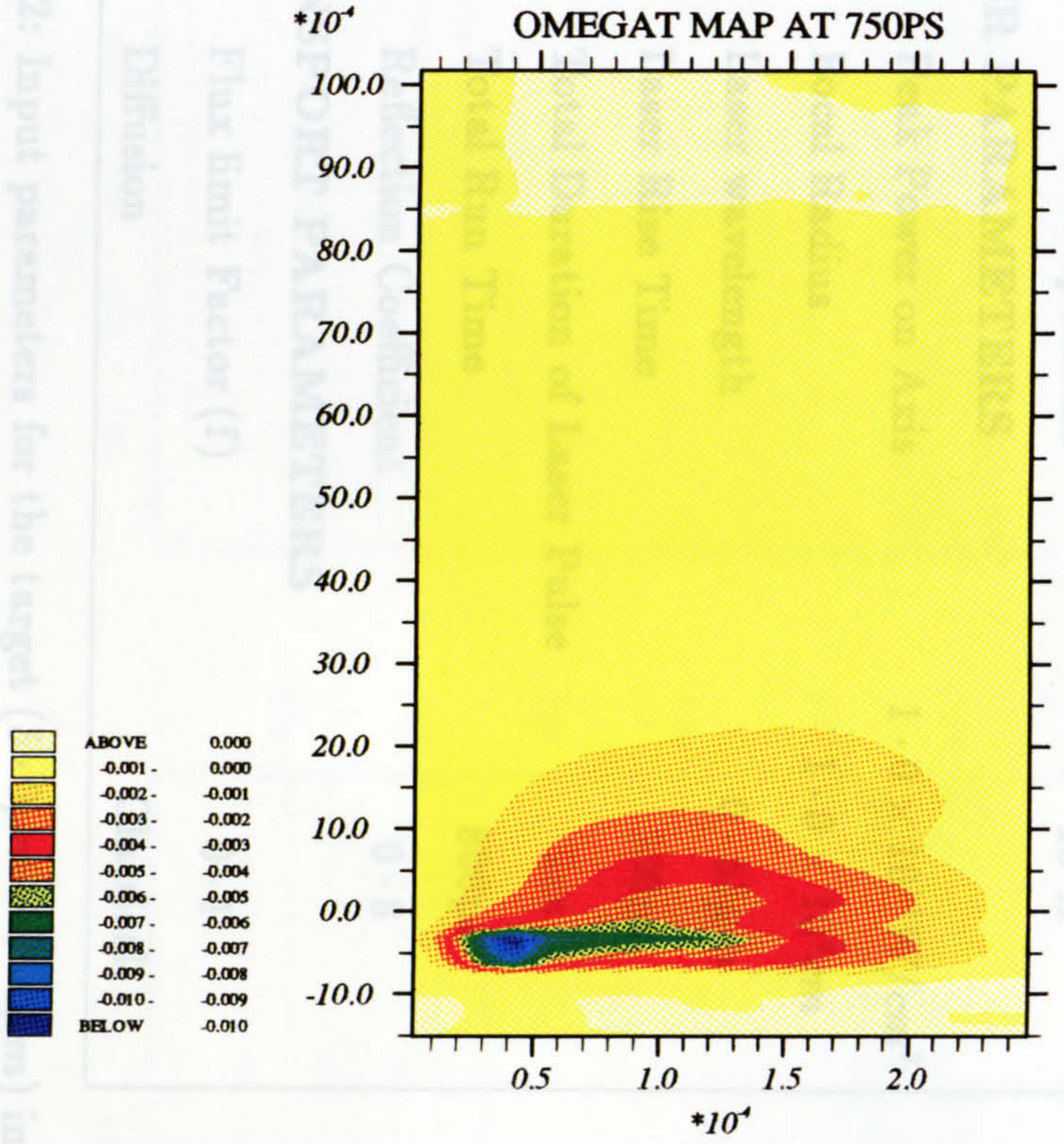
OMEGAT MAP AT 750PS
*10⁻⁴
100.0
90.0
80.0
70.0
60.0
50.0
40.0
30.0
20.0
10.0
0.0
-10.0
0.5
1.0
1.5
2.0
*10⁻⁴
ABOVE 0.000
-0.001 - 0.000
-0.002 - -0.001
-0.003 - -0.002
-0.004 - -0.003
-0.005 - -0.004
-0.006 - -0.005
-0.007 - -0.006
-0.008 - -0.007
-0.009 - -0.008
-0.010 - -0.009
BELOW -0.010

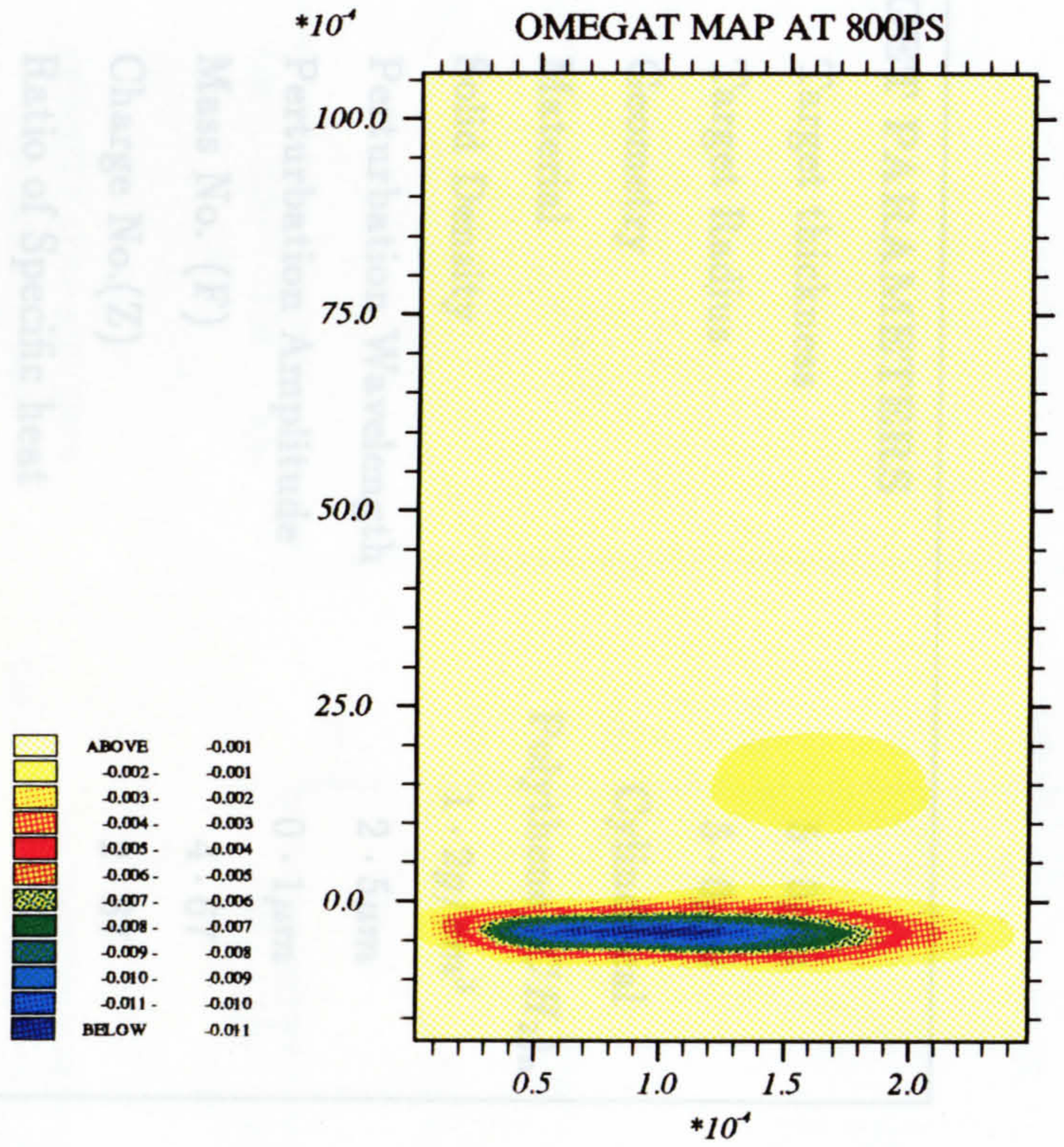
OMEGAT MAP AT 800PS
*10⁻⁴
100.0
75.0
50.0
25.0
0.0
0.5
1.0
1.5
2.0
*10⁻⁴
ABOVE -0.001
-0.002 - -0.001
-0.003 - -0.002
-0.004 - -0.003
-0.005 - -0.004
-0.006 - -0.005
-0.007 - -0.006
-0.008 - -0.007
-0.009 - -0.008
-0.010 - -0.009
-0.011 - -0.010
BELOW -0.011

TARGET PARAMETERS	
Target thickness	$5 \cdot 0 \mu m$
Target Radius	$5 \cdot 0 \mu m$
Geometry	Cylindrical
Material	Polythene $(CH_2)_n$
Solid Density	$1 \cdot 2 g/cm^3$
Perturbation Wavelength	$2 \cdot 5 \mu m$
Perturbation Amplitude	$0 \cdot 1 \mu m$
Mass No. (F)	$4 \cdot 67$
Charge No.(Z)	$2 \cdot 67$
Ratio of Specific heat	$1 \cdot 667$
Initial Temperature	$10^4 K°$
LASER PARAMETERS	
Peak Power on Axis	$1 \cdot 0 \times 10^{14} W/cm^2$
Focal Radius	$1 \cdot 0 \times 10^4 cm$
Laser wavelength	$0 \cdot 53 \mu m$
Laser Rise Time	300ps
Total Duration of Laser Pulse	2ns
Total Run Time	800ps
Reflection Coefficient	$0 \cdot 8$
TRANSPORT PARAMETERS	
Flux limit Factor (f)	$0 \cdot 1$
Diffusion	Classical

Table 5.2: Input parameters for the target $(5 \cdot 0 \mu m \times 5 \cdot 0 \mu m)$ in both directions.

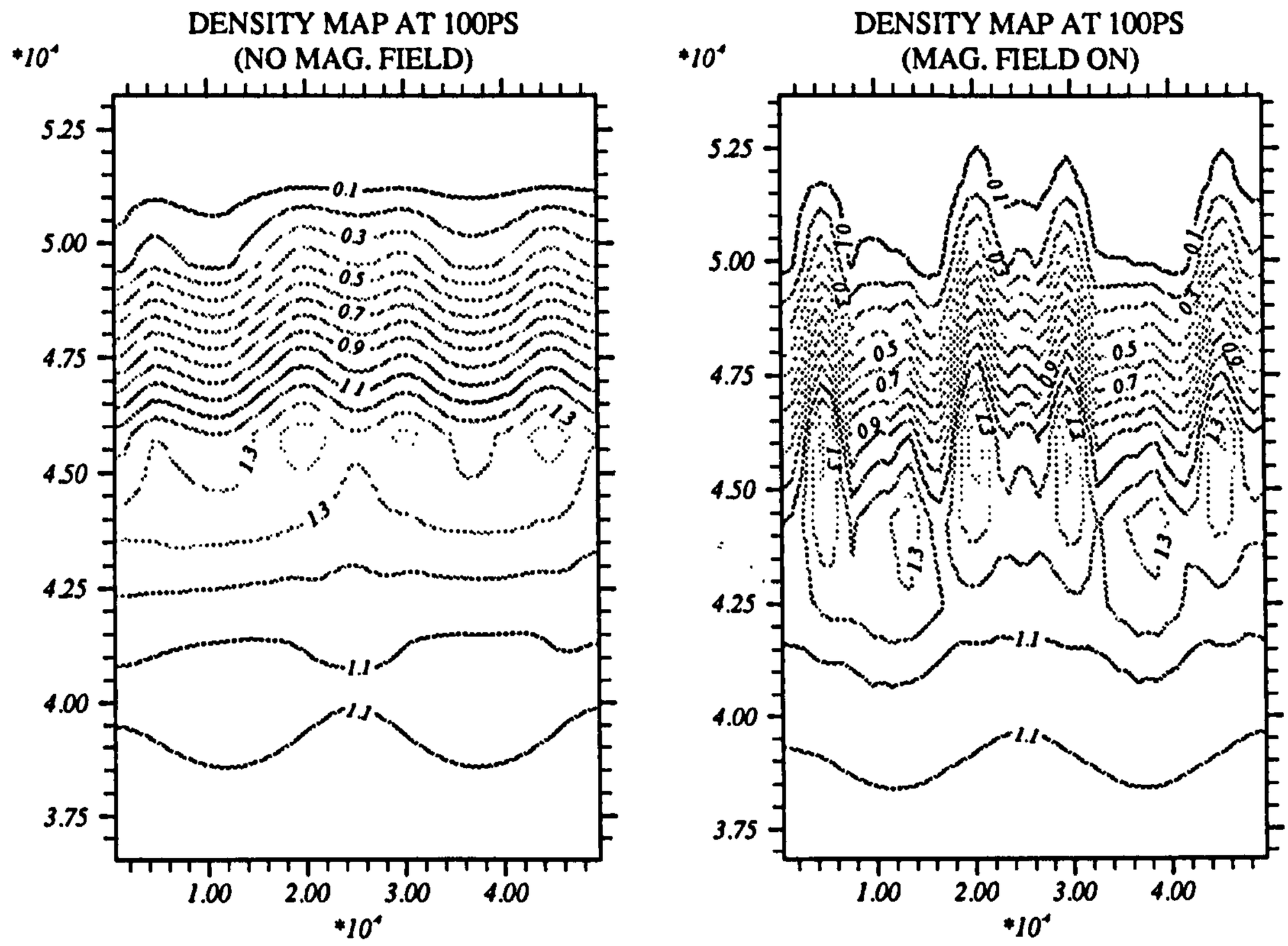

Figure 5.7: Density contour map for the target ($5 \cdot 0\mu m \times 5 \cdot 0\mu m$) axial and radial directions.

DENSITY MAP AT 200PS
(NO MAG. FIELD)

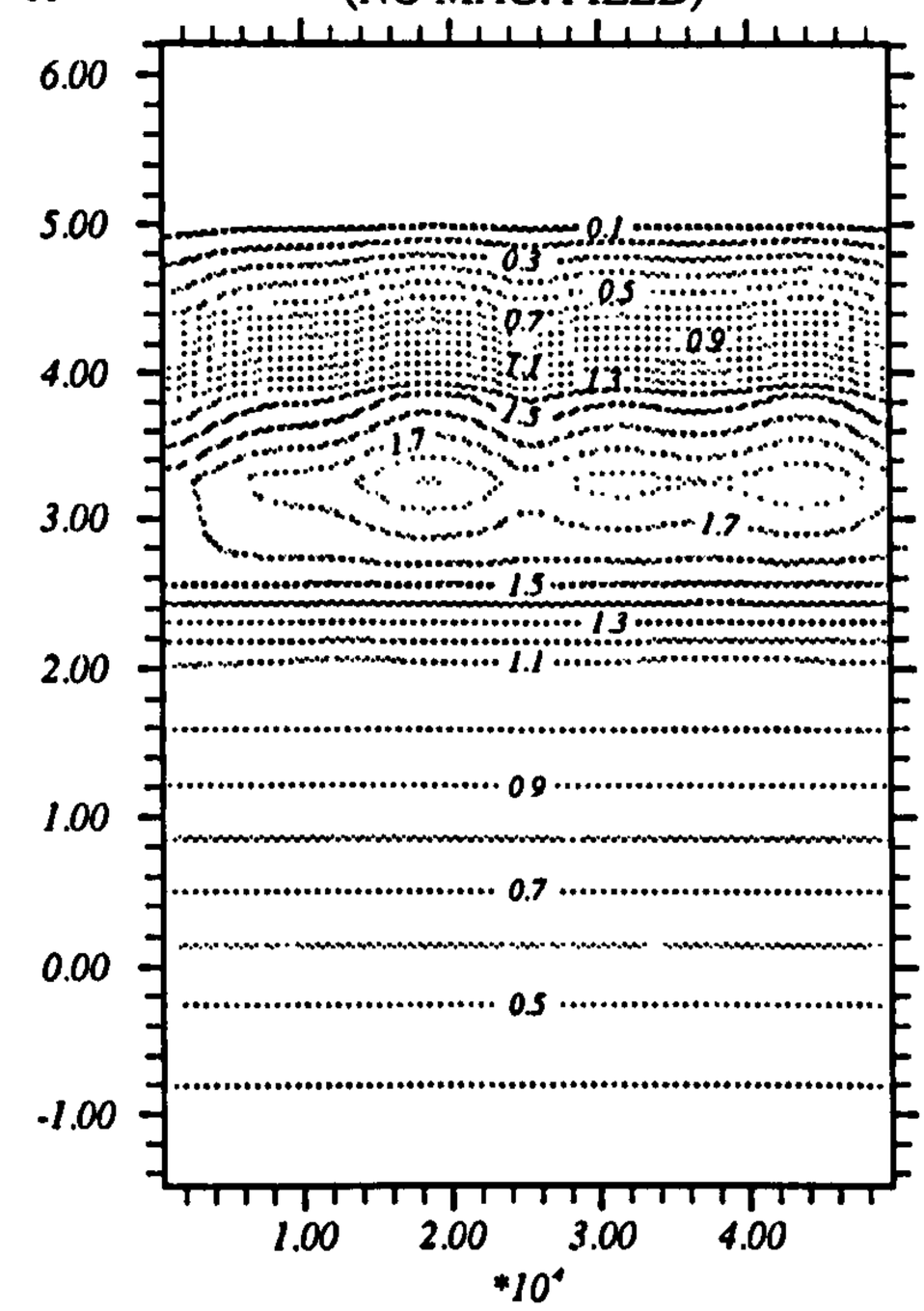

DENSITY MAP AT 200PS
(MAG. FIELD ON)

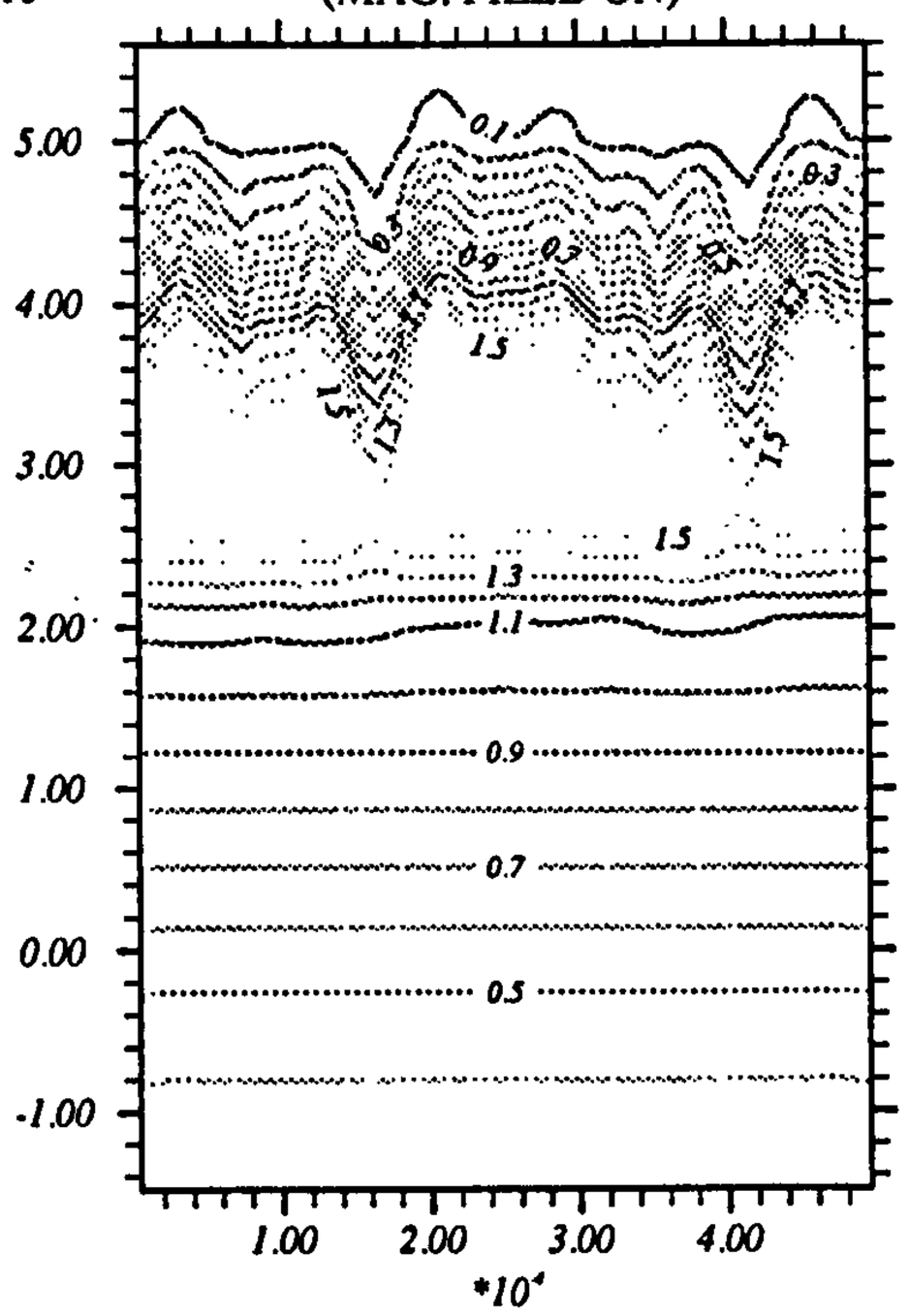

DENSITY MAP AT 250PS
(NO MAG. FIELD)

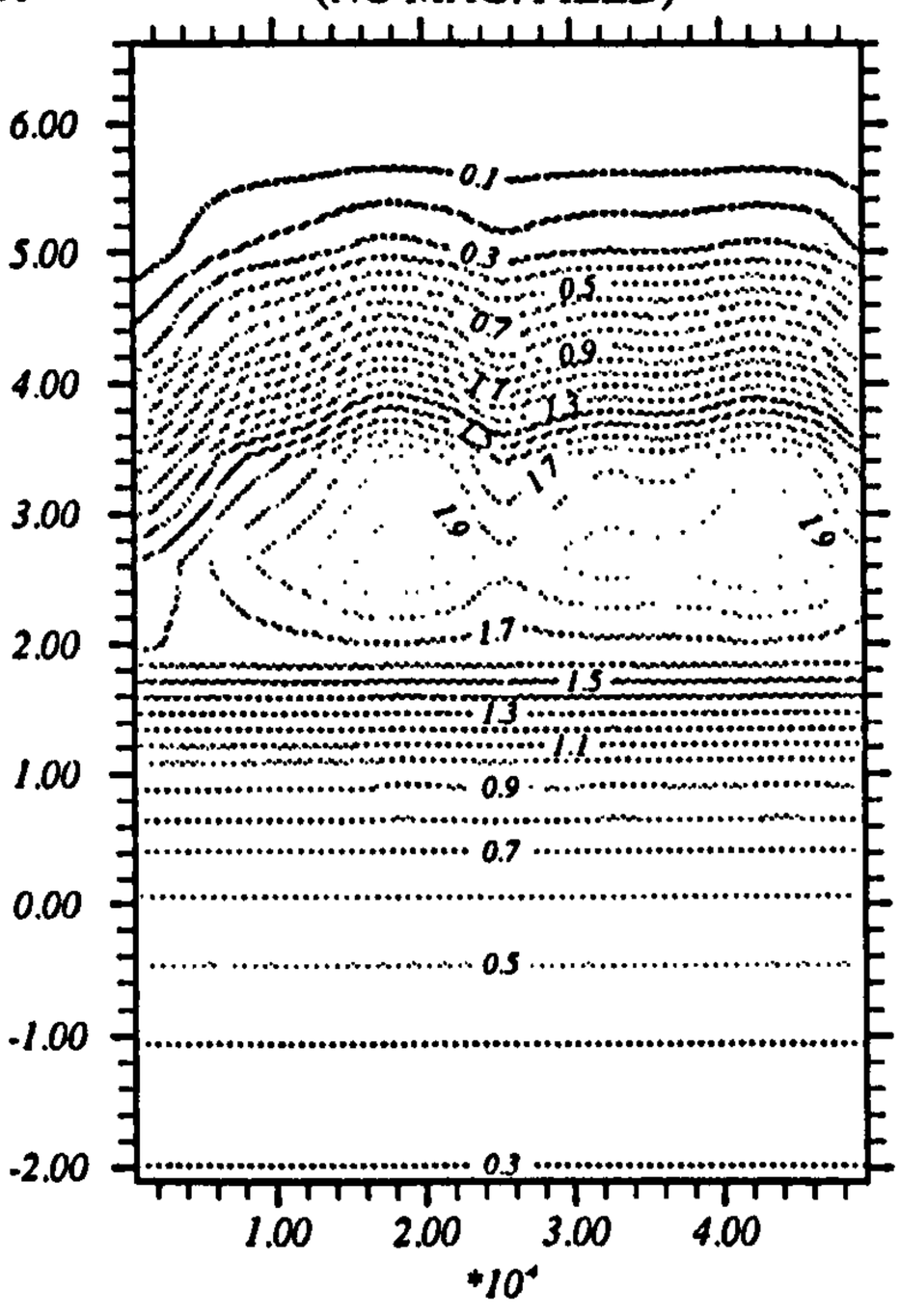

DENSITY MAP AT 250PS
(MAG. FIELD ON)

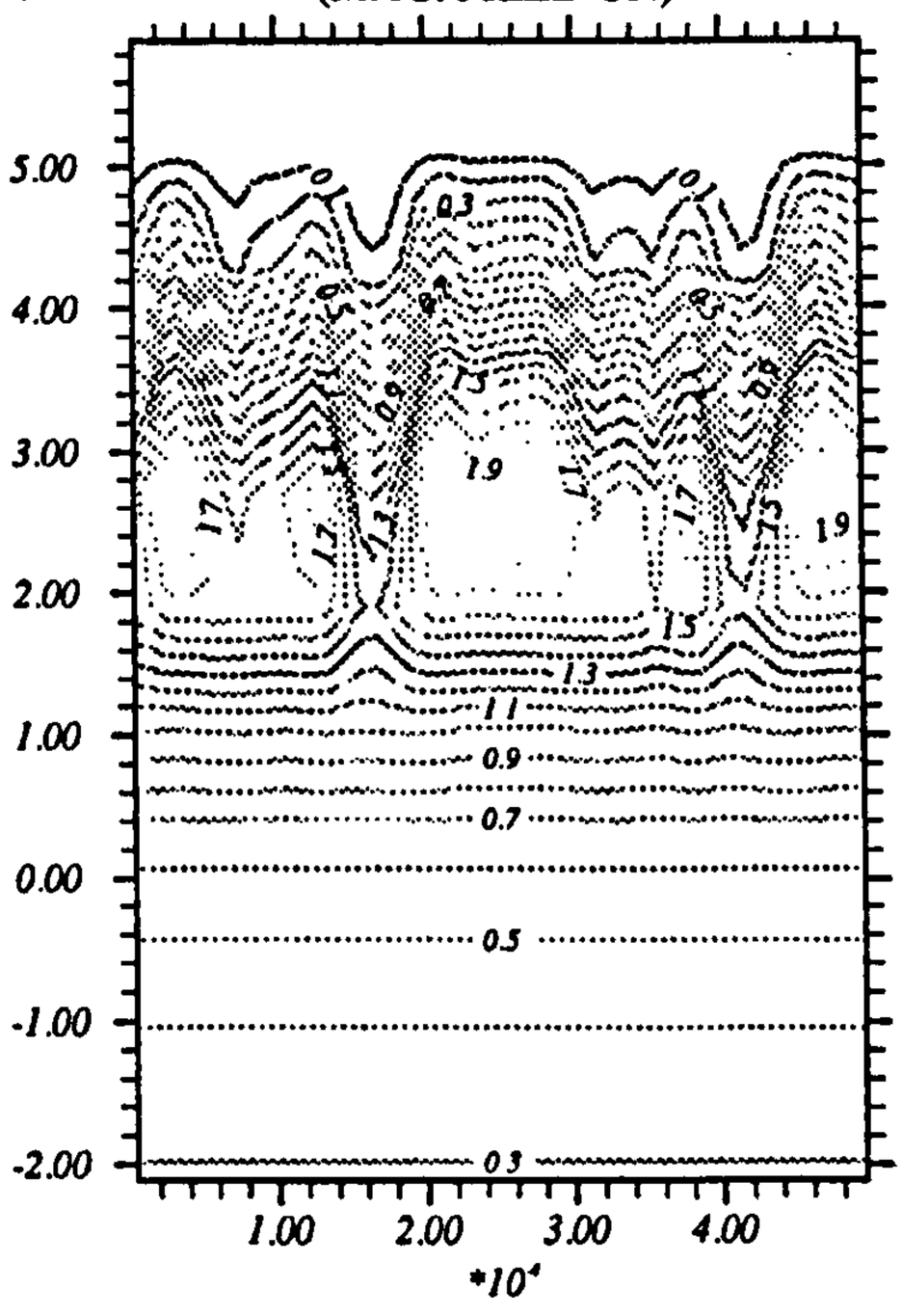

DENSITY MAP AT 300PS
(NO MAG. FIELD)

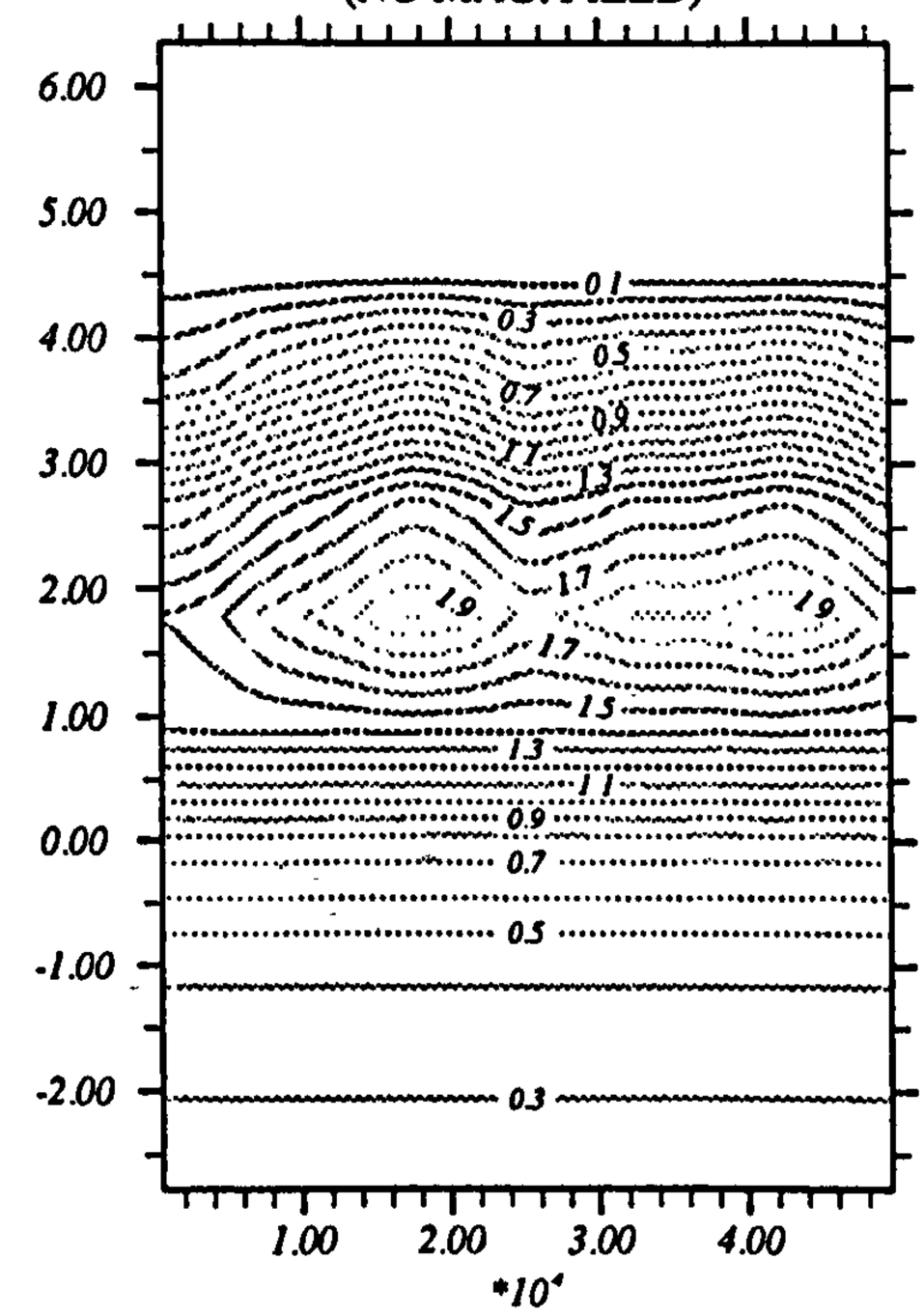

DENSITY MAP AT 300PS
(MAG. FIELD ON)

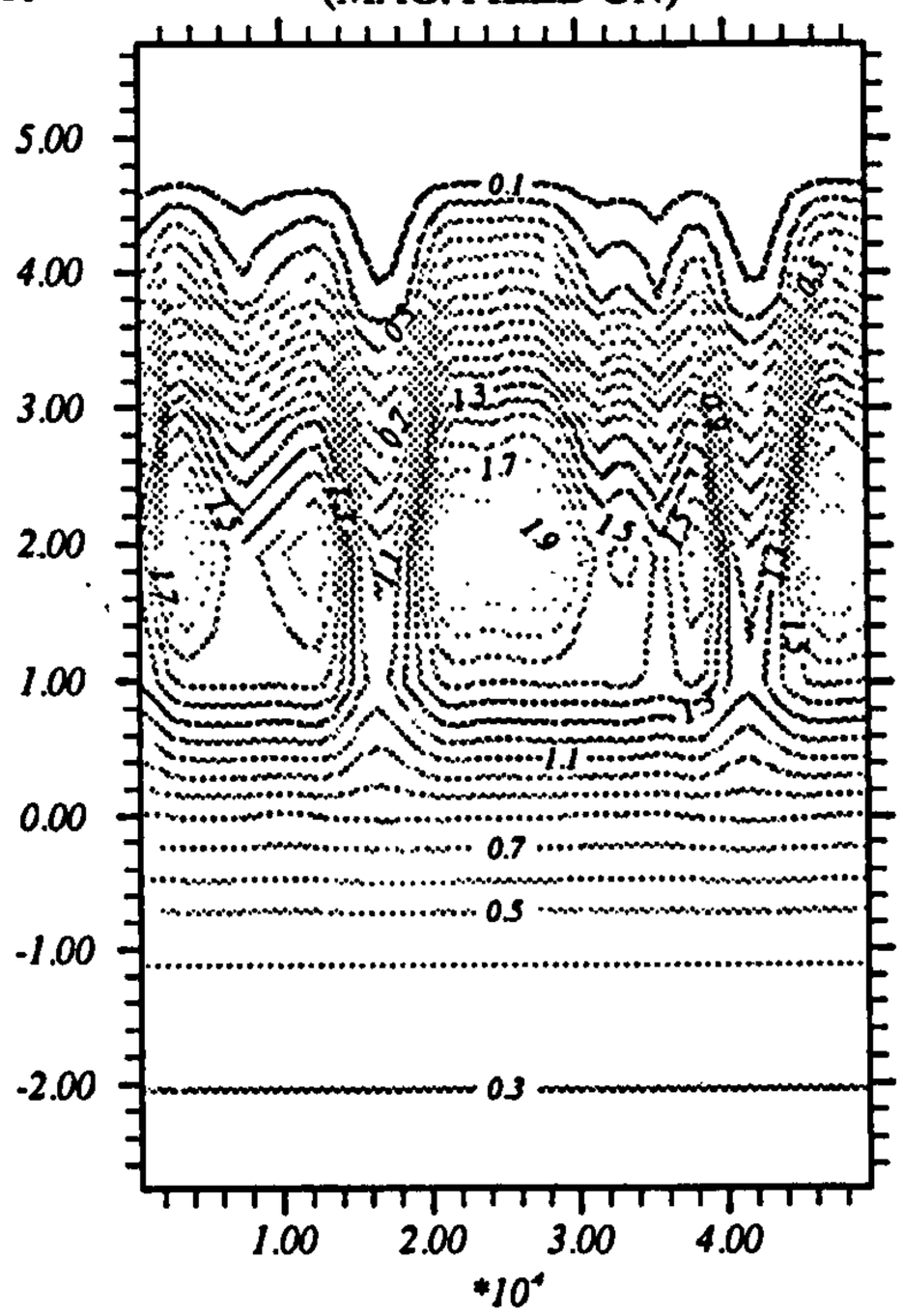

DENSITY MAP AT 350PS
(NO MAG. FIELD)

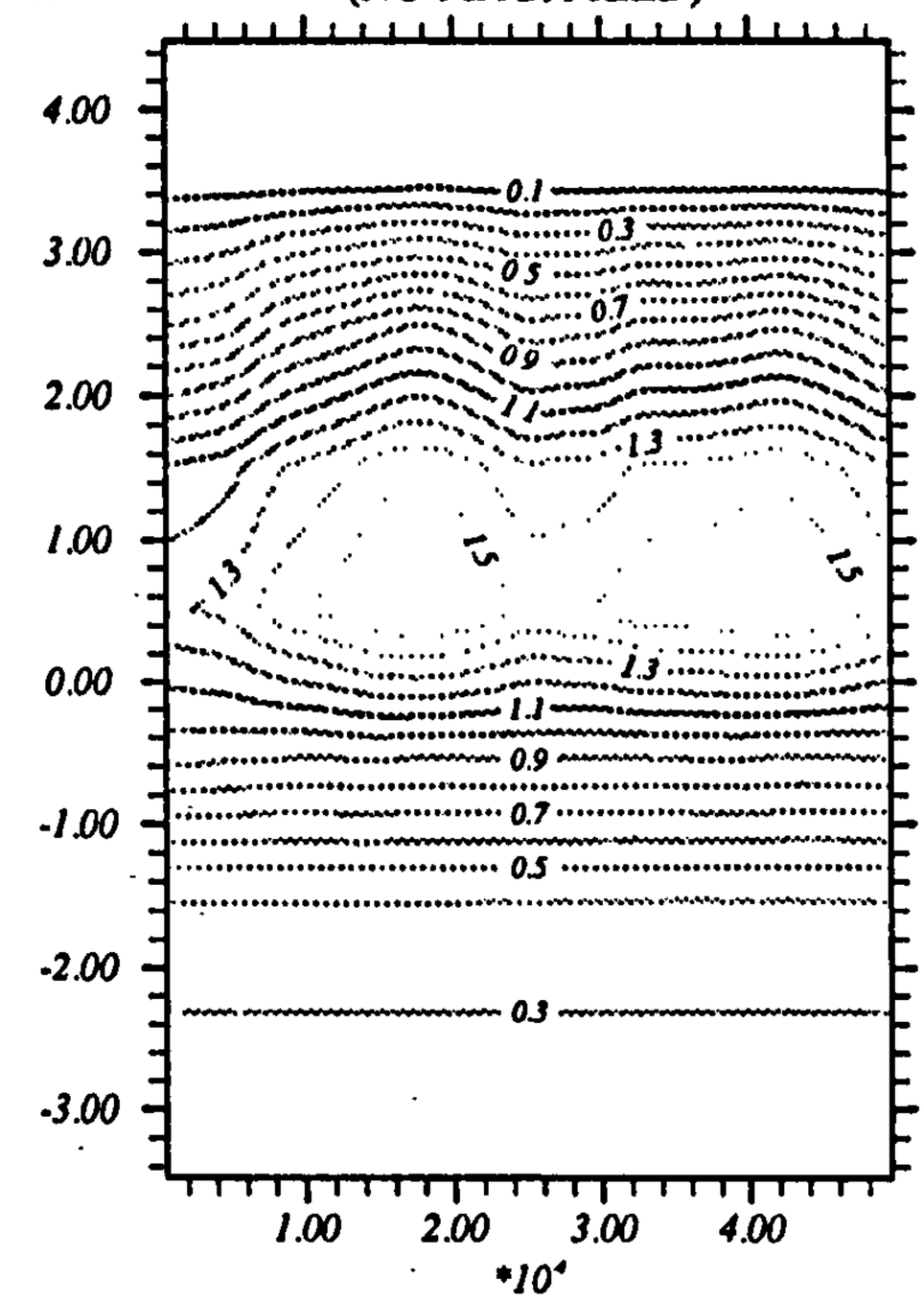

DENSITY MAP AT 350PS
(MAG. FIELD ON)

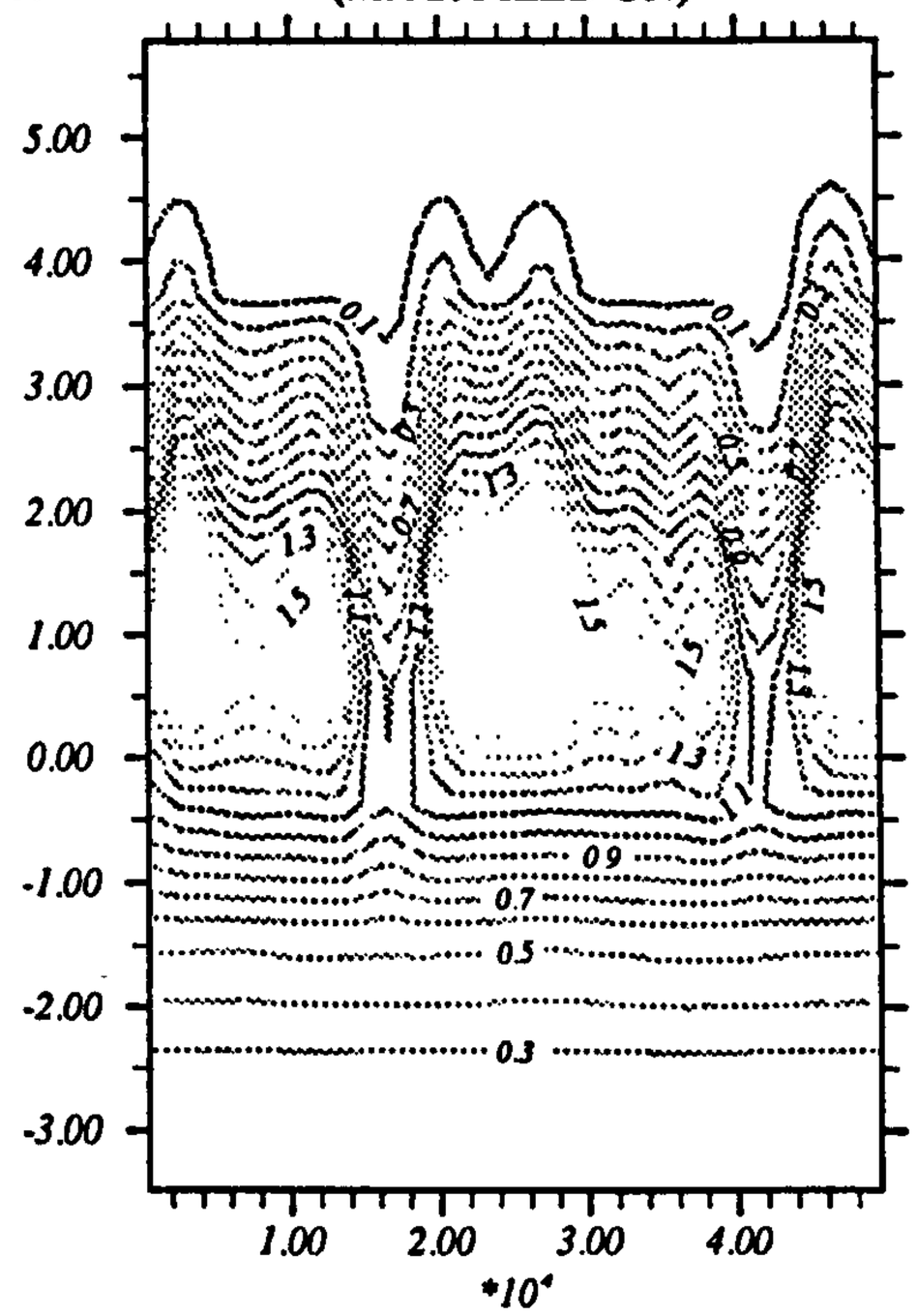

DENSITY MAP AT 400PS
(NO MAG. FIELD)

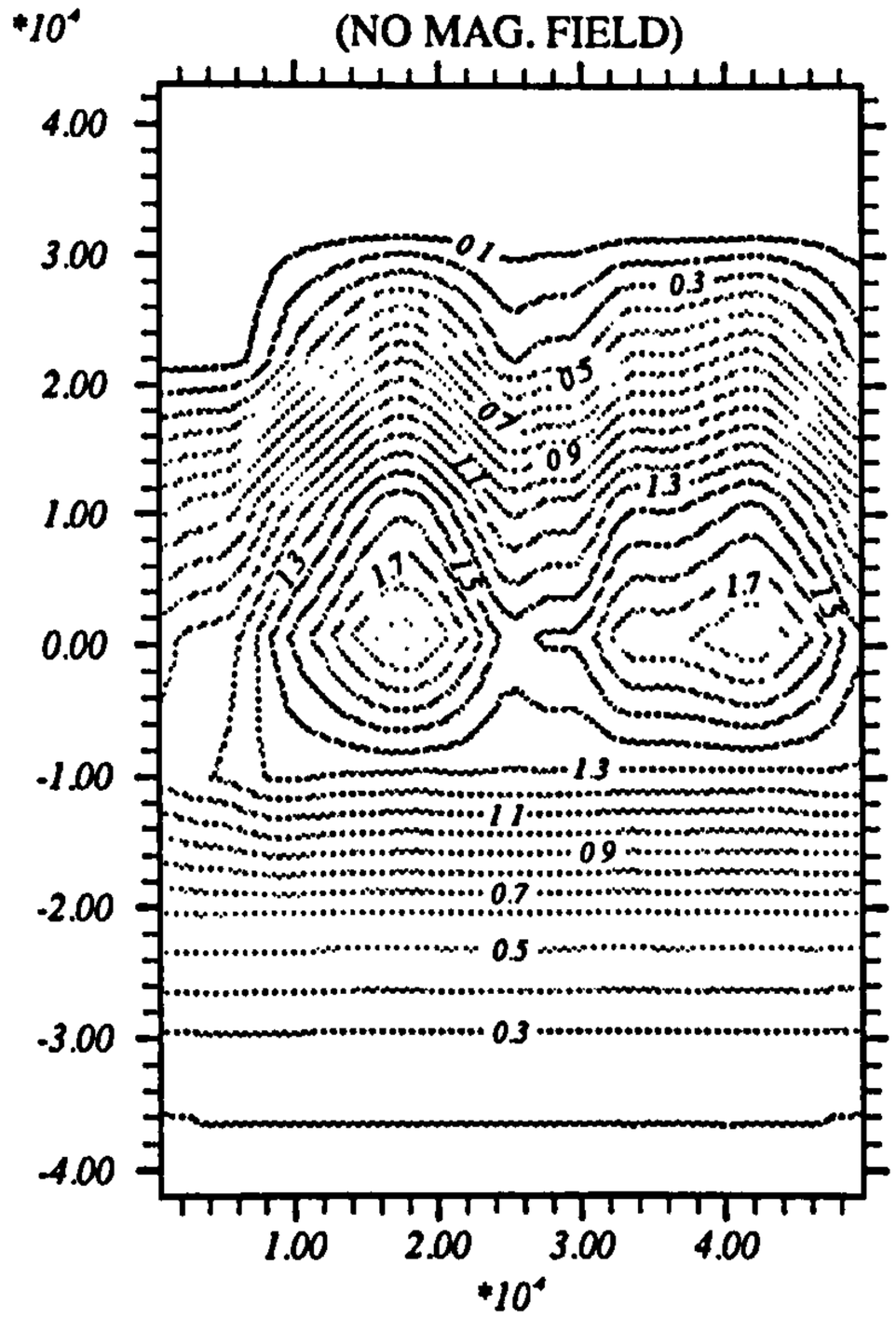

DENSITY MAP AT 400PS
(MAG. FIELD ON)

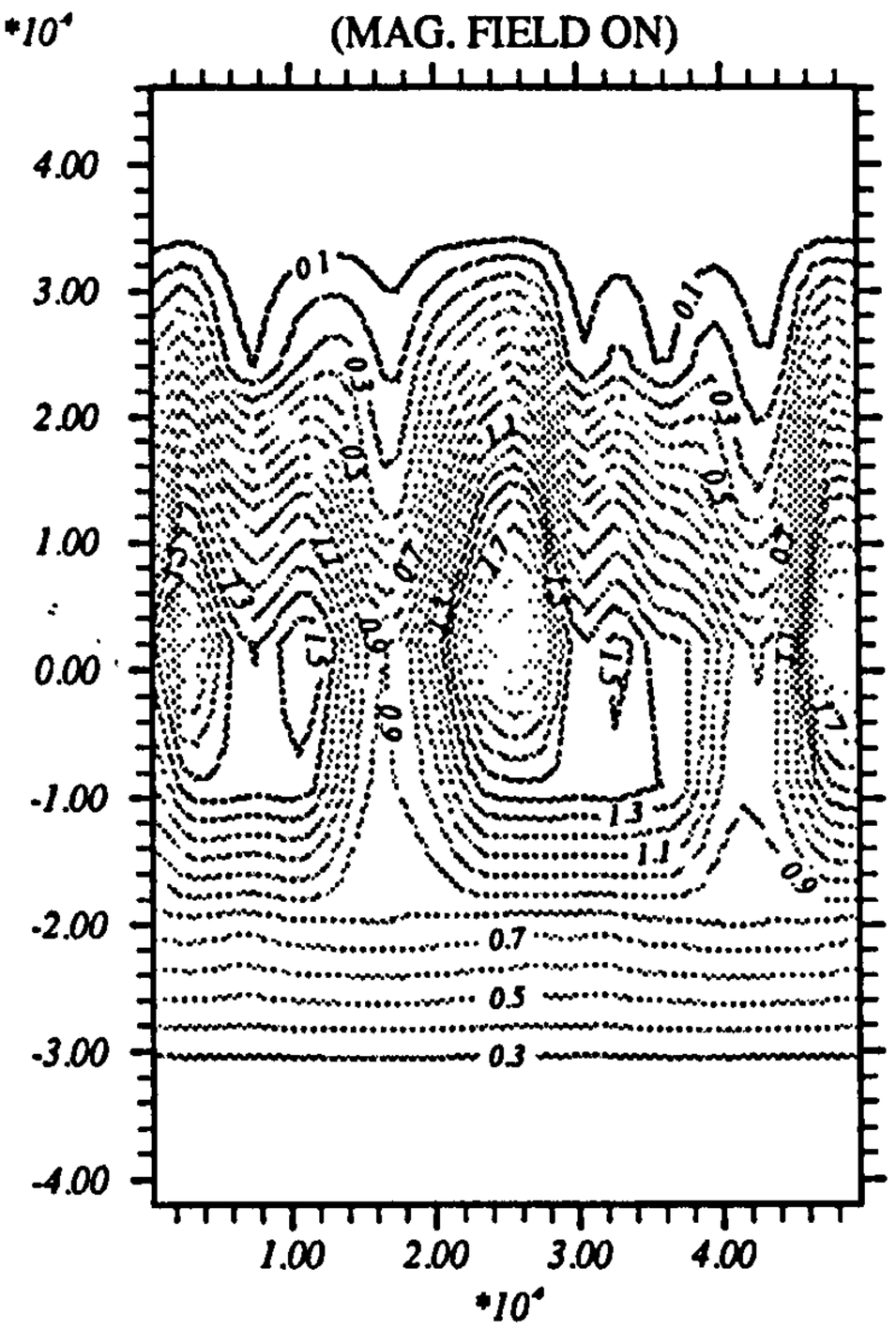

DENSITY MAP AT 450PS
(NO MAG. FIELD)

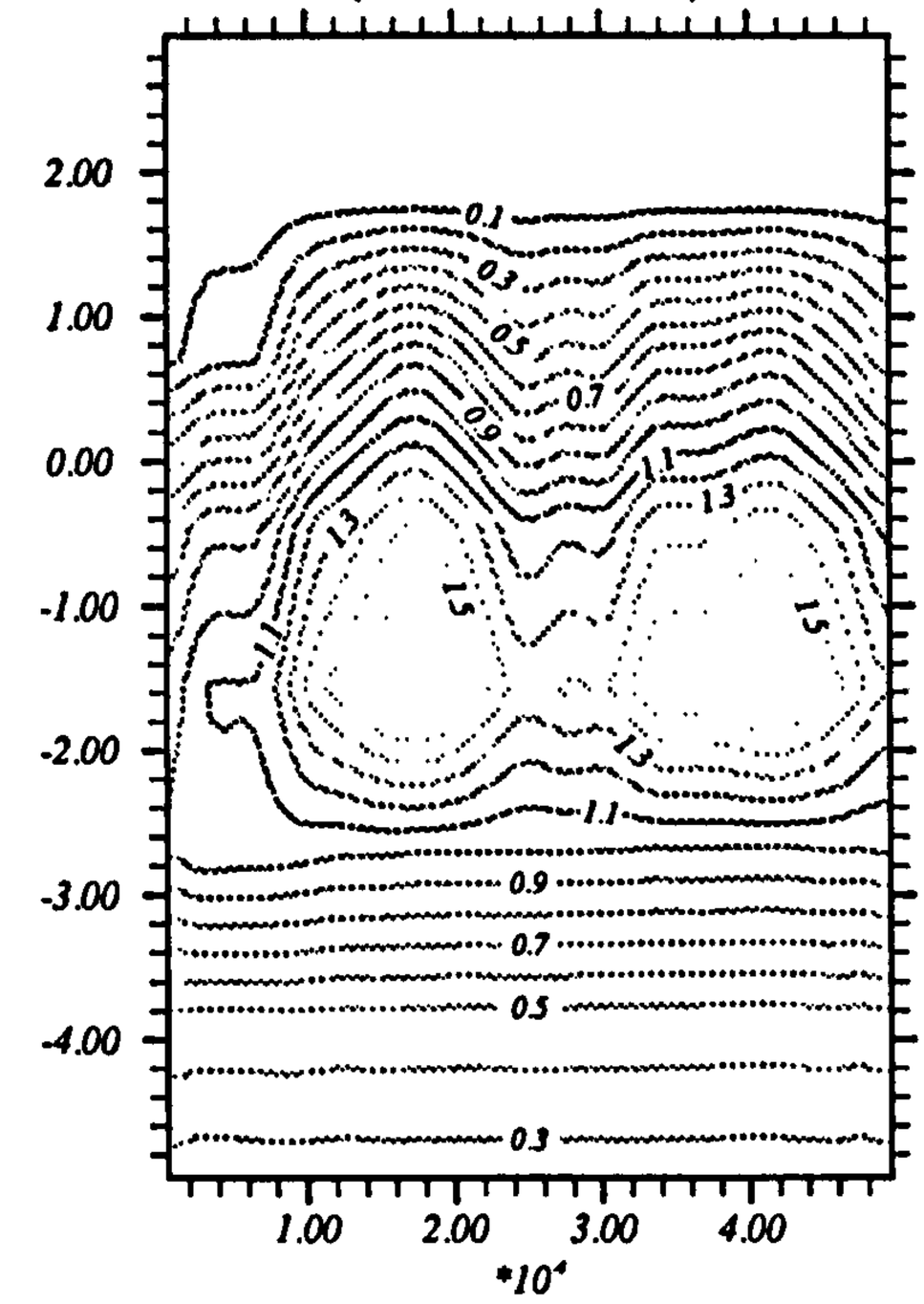

DENSITY MAP AT 450PS
(MAG. FIELD ON)

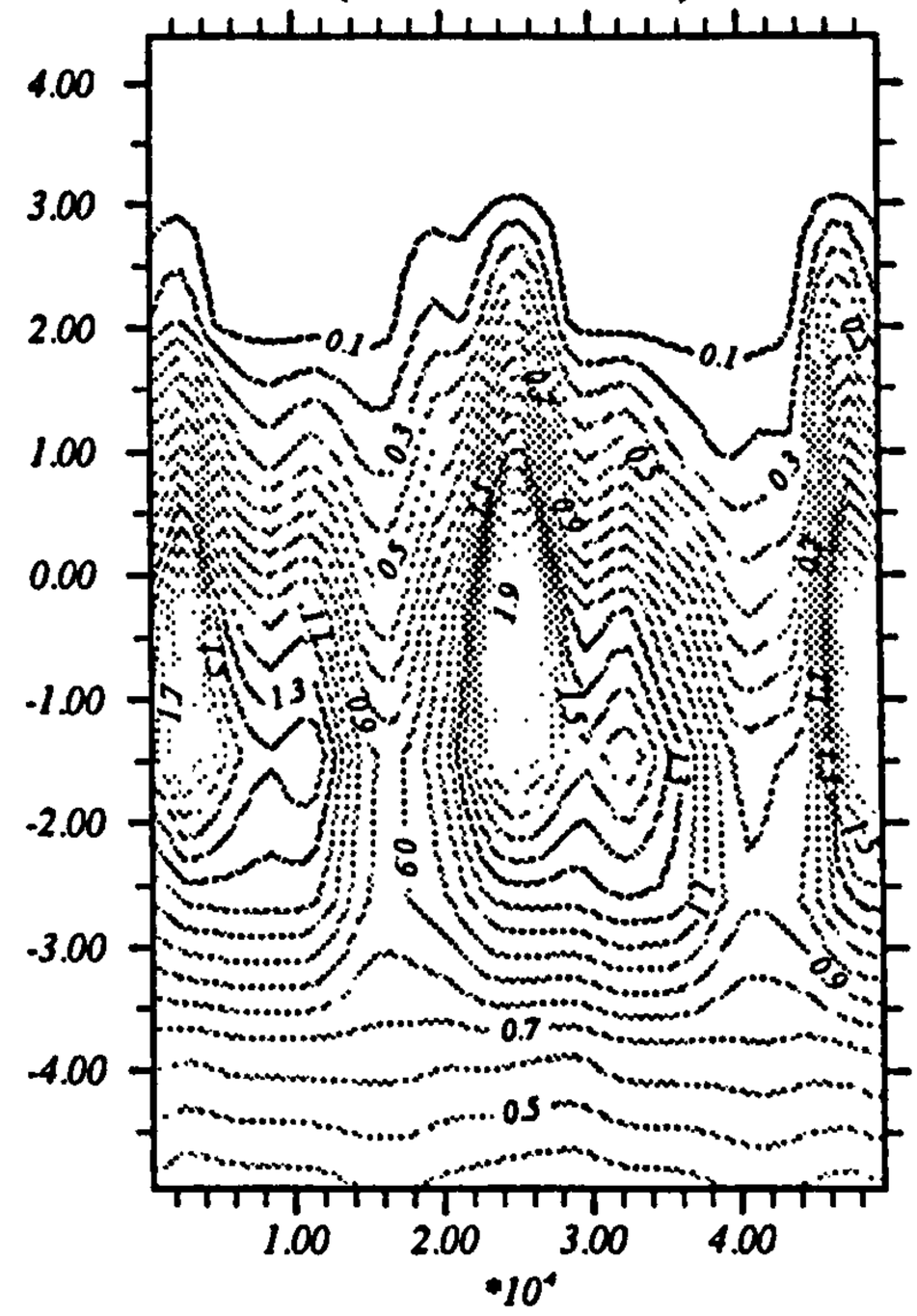

DENSITY MAP AT 500PS
(NO MAG. FIELD)

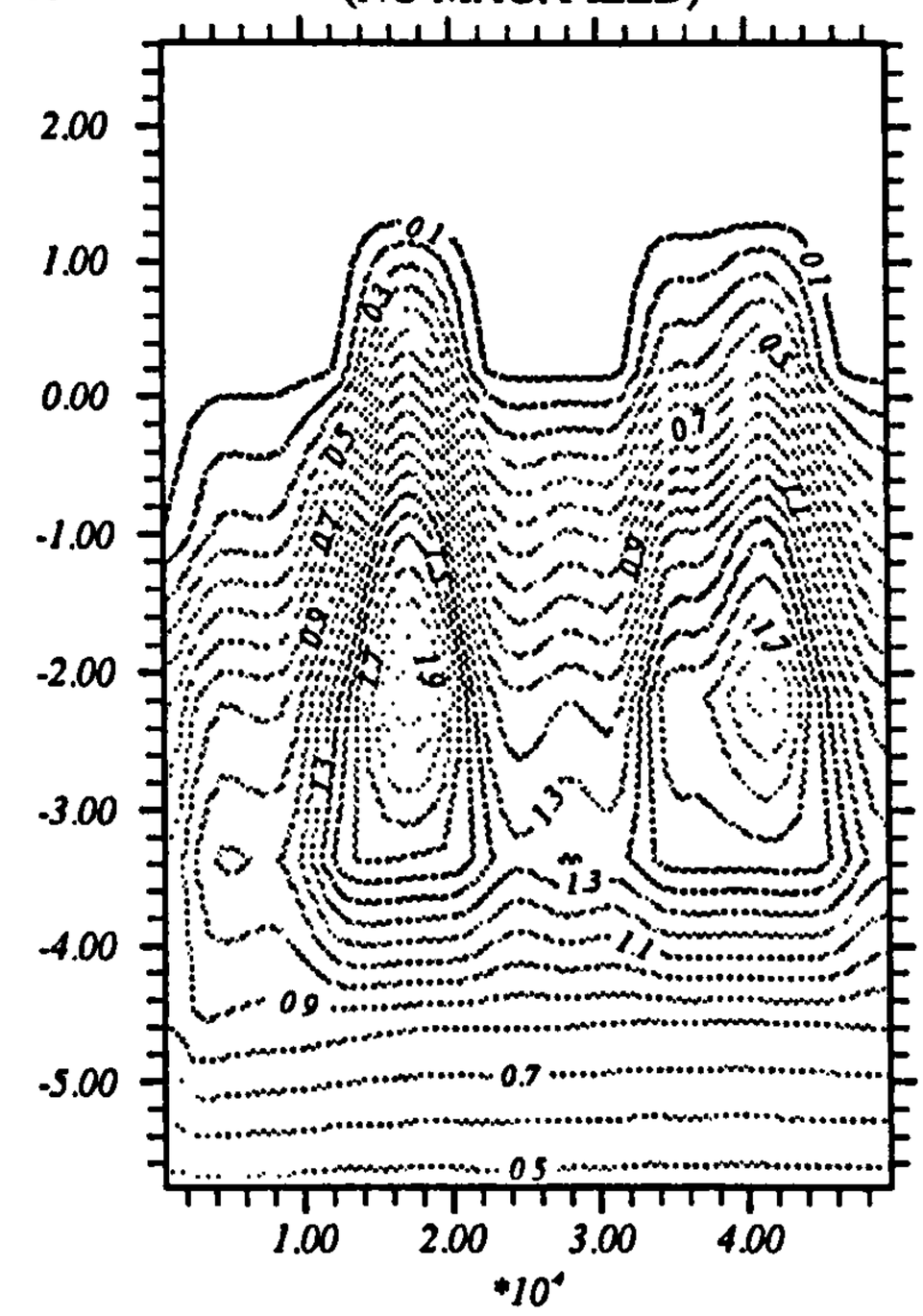

DENSITY MAP AT 500PS
(MAG. FIELD ON)

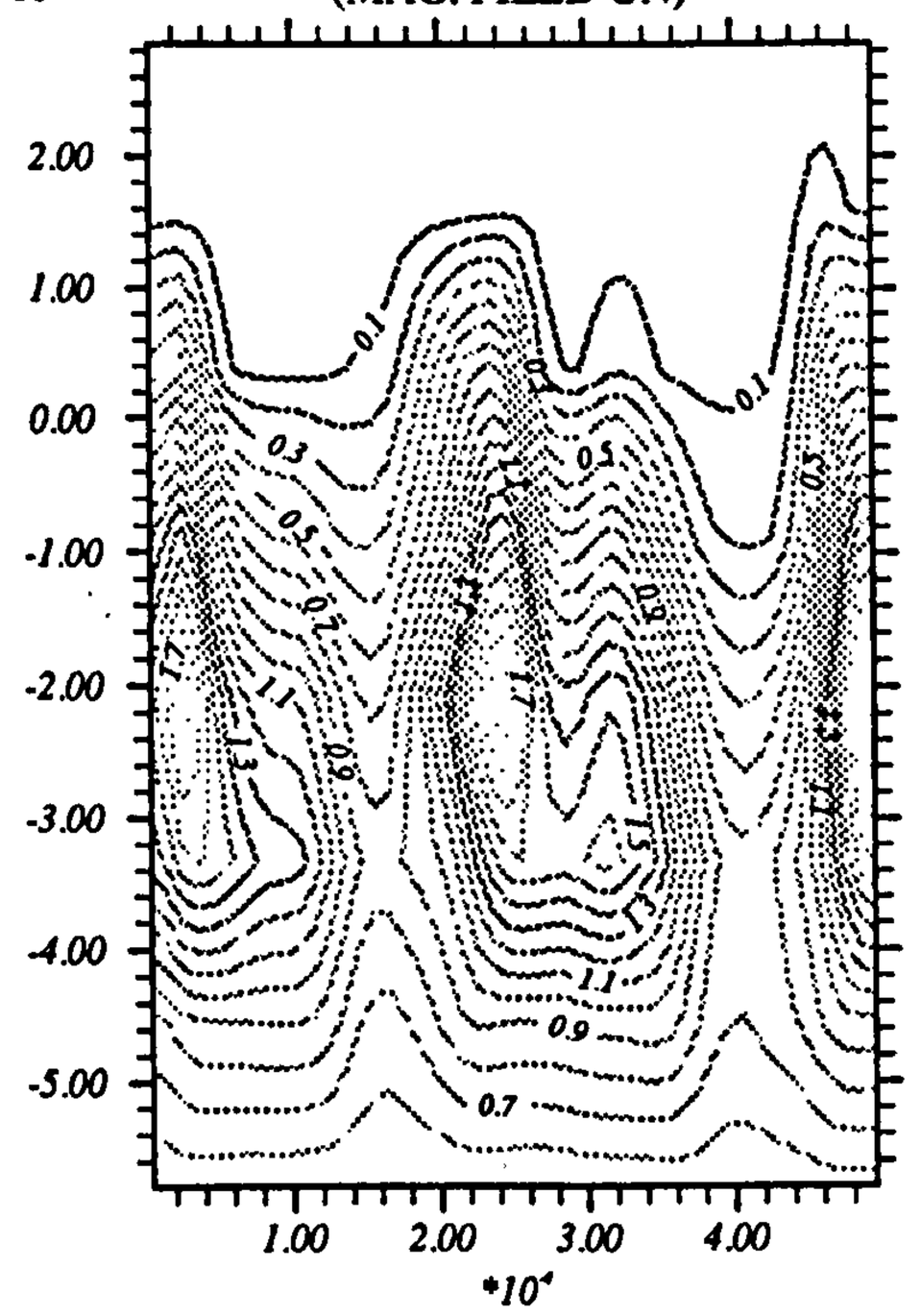

DENSITY MAP AT 550PS
(NO MAG. FIELD)

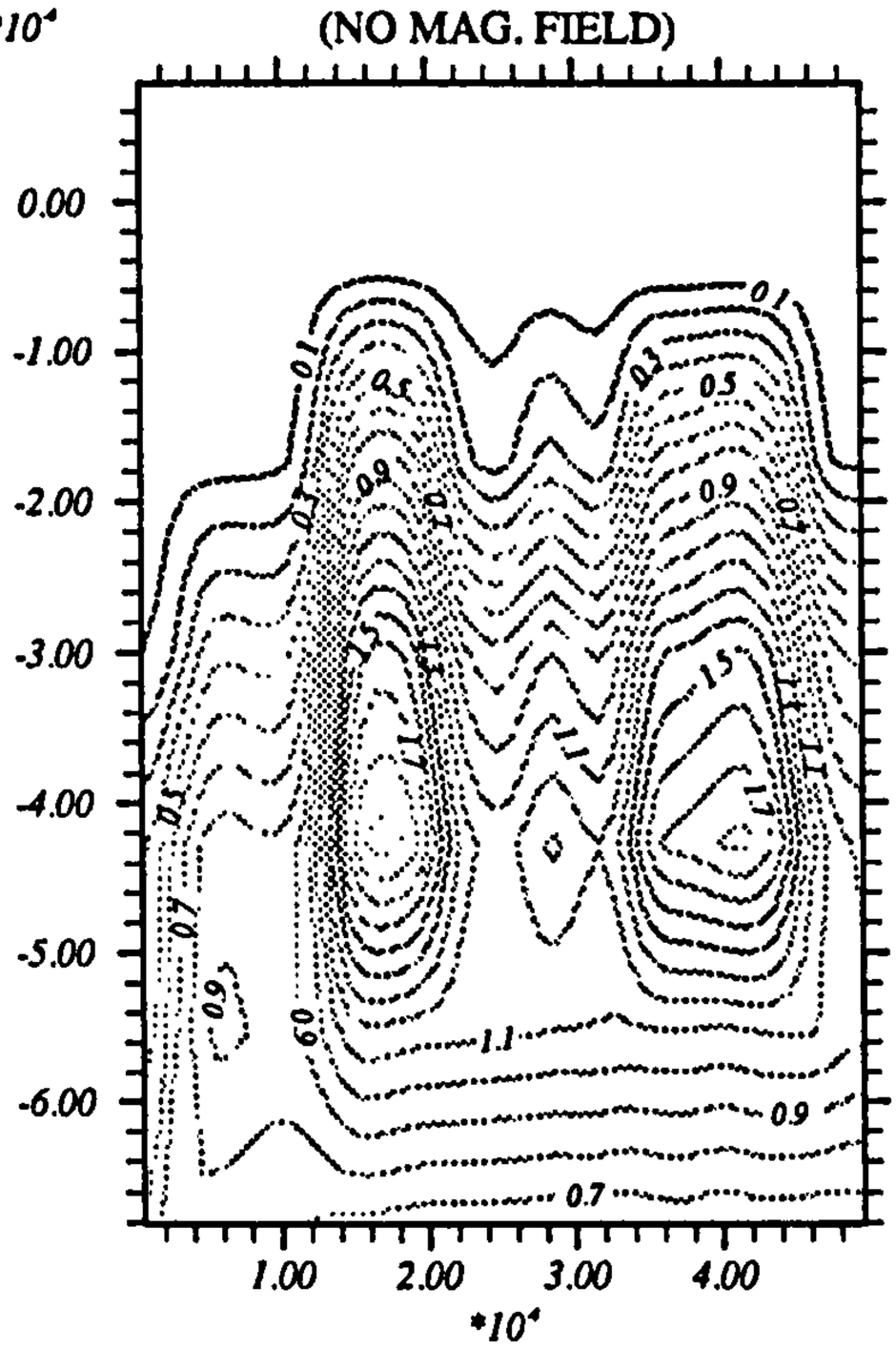

DENSITY MAP AT 550PS
(MAG. FIELD ON)

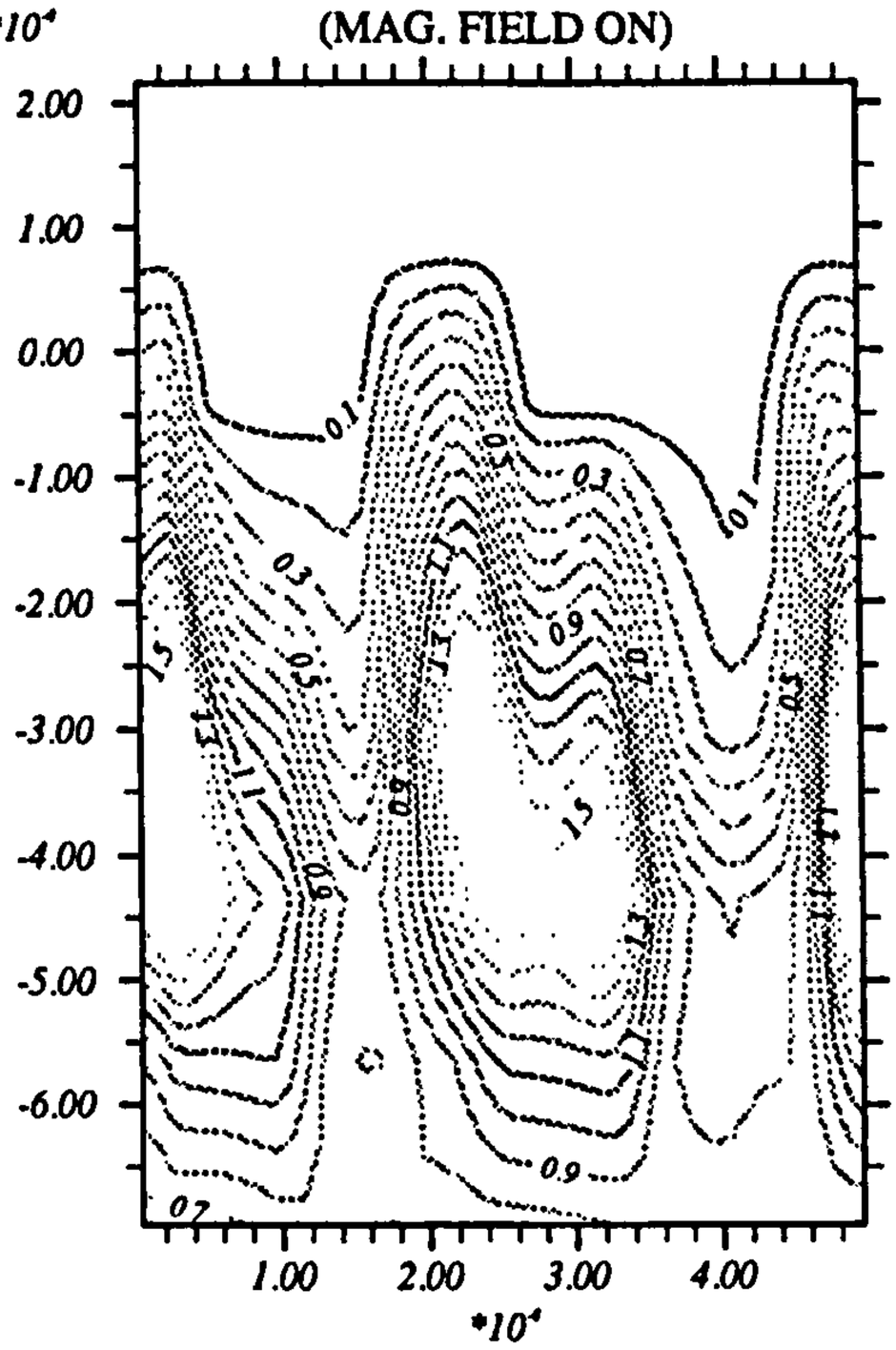

DENSITY MAP AT 600PS
(NO MAG. FIELD)

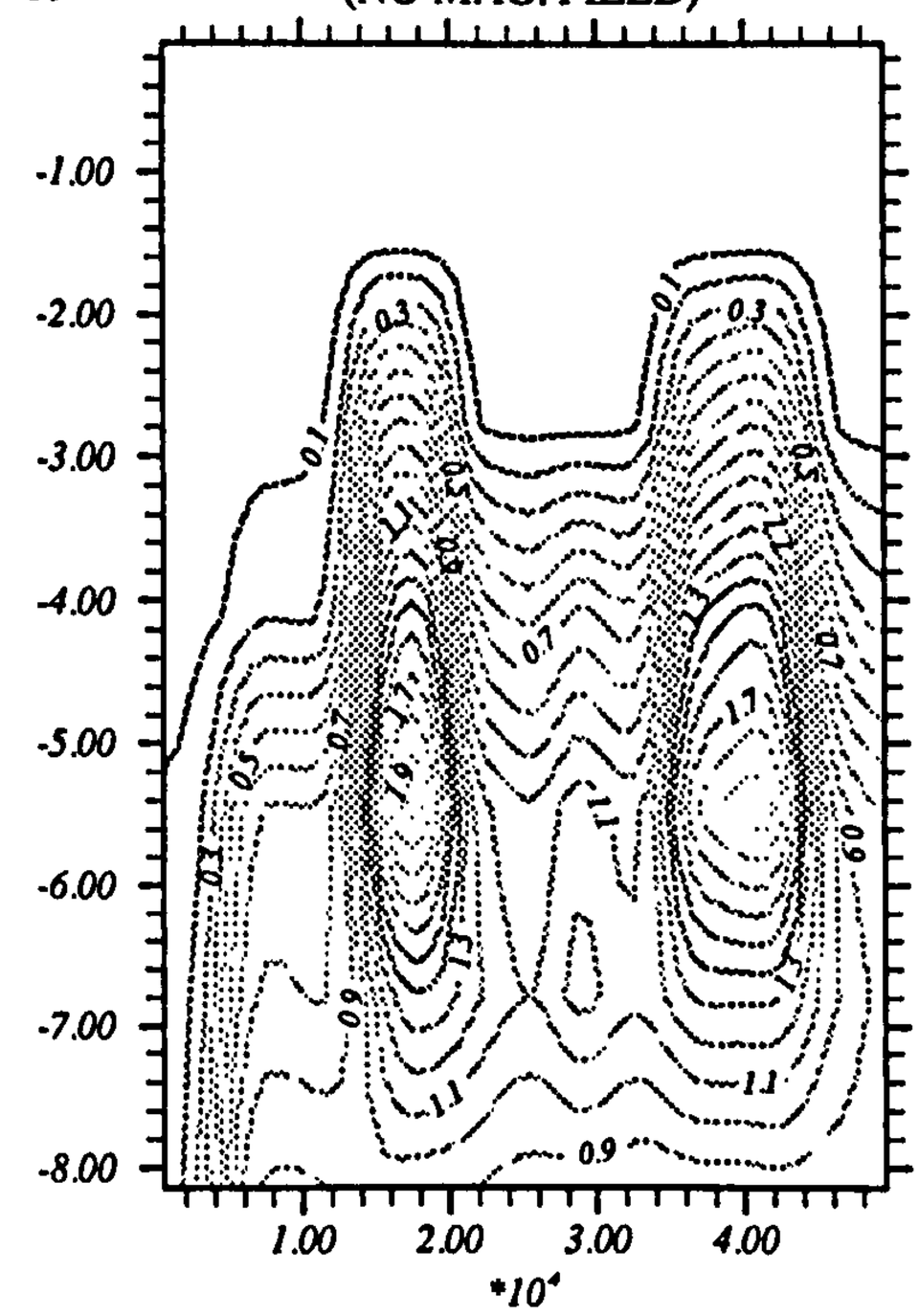

DENSITY MAP AT 600PS
(MAG. FIELD ON)

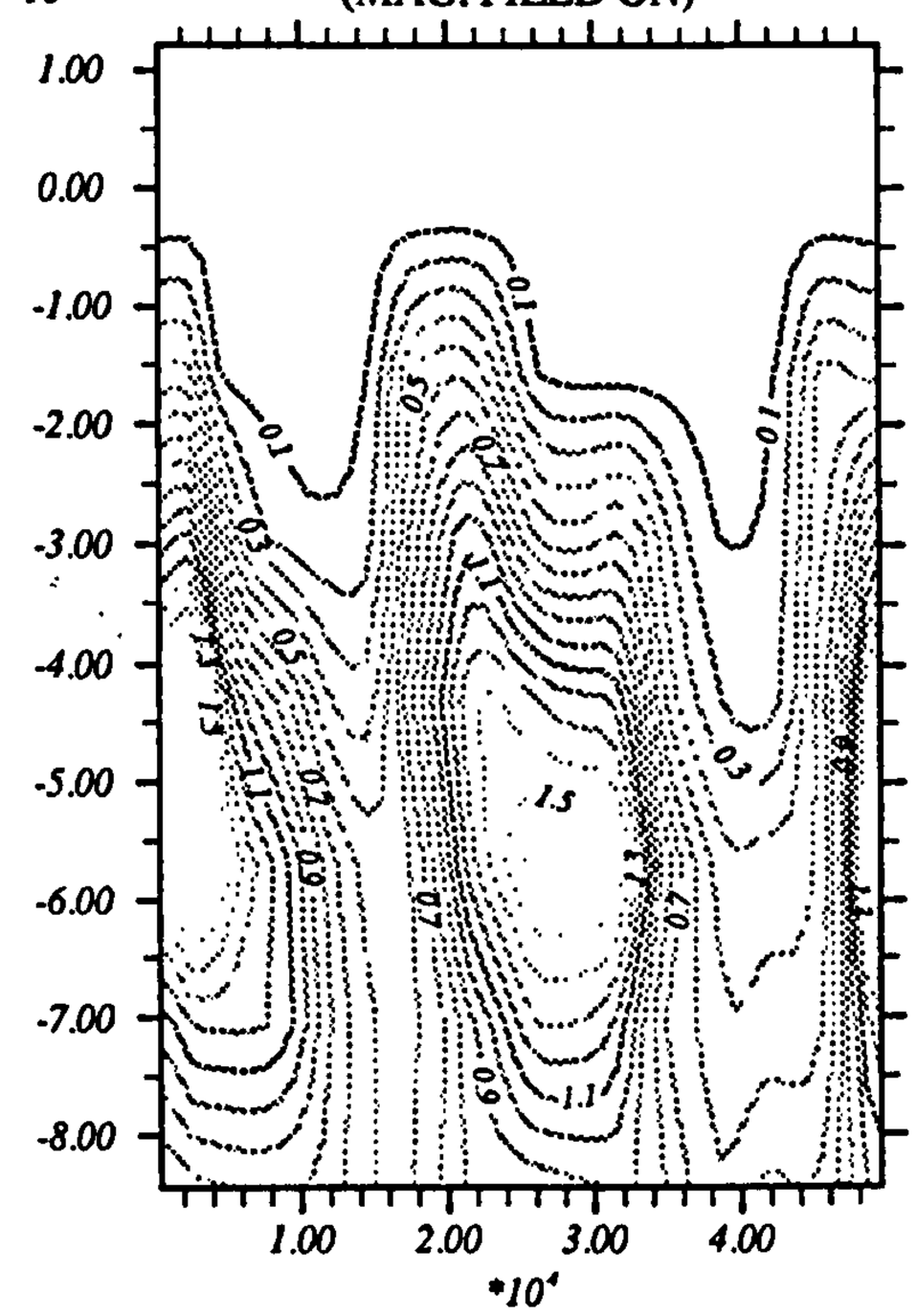

DENSITY MAP AT 650PS
(NO MAG. FIELD)

DENSITY MAP AT 650PS
(MAG. FIELD ON)

DENSITY MAP AT 700PS
(NO MAG. FIELD)

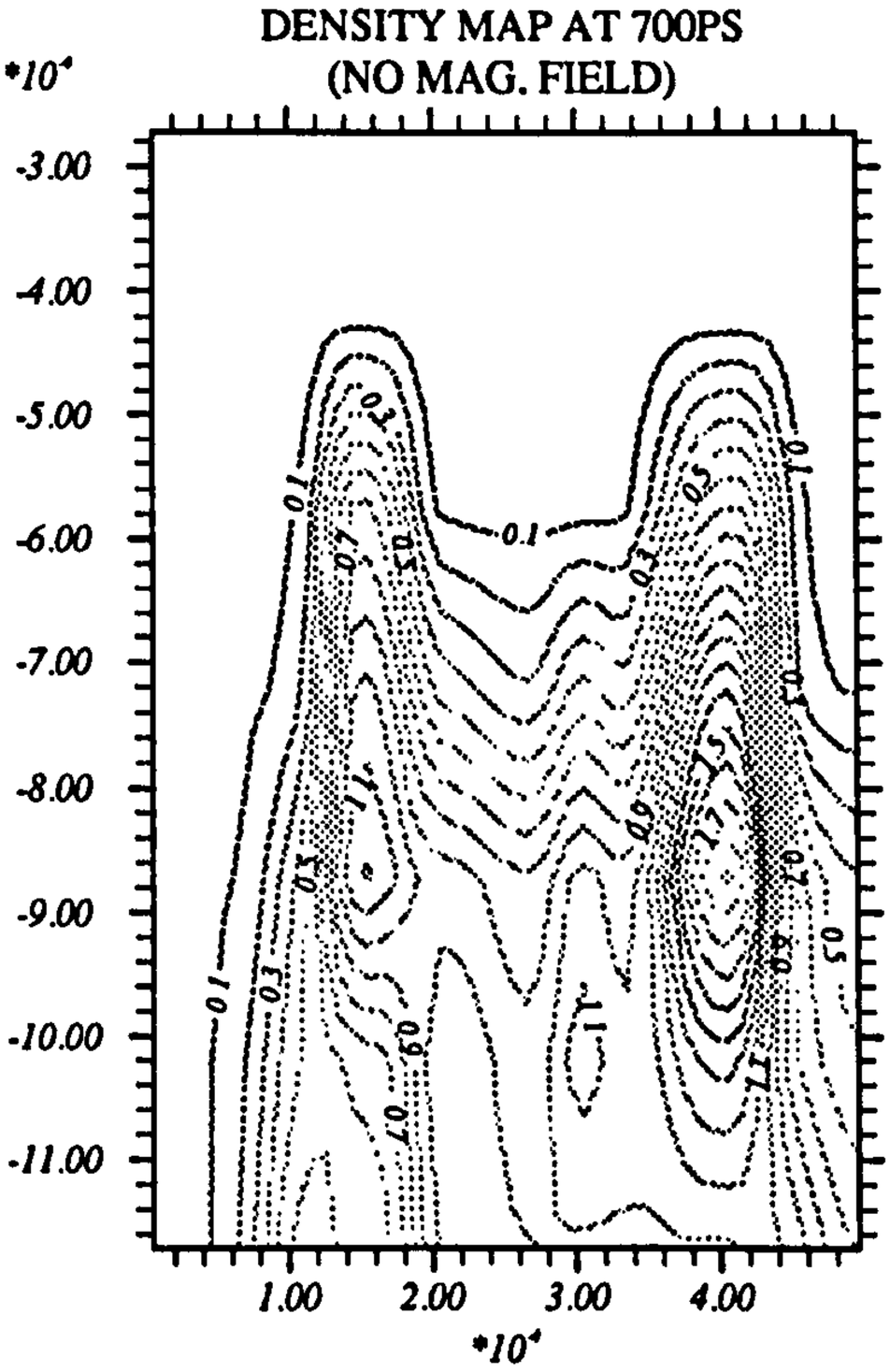

DENSITY MAP AT 700PS
(MAG. FIELD ON)

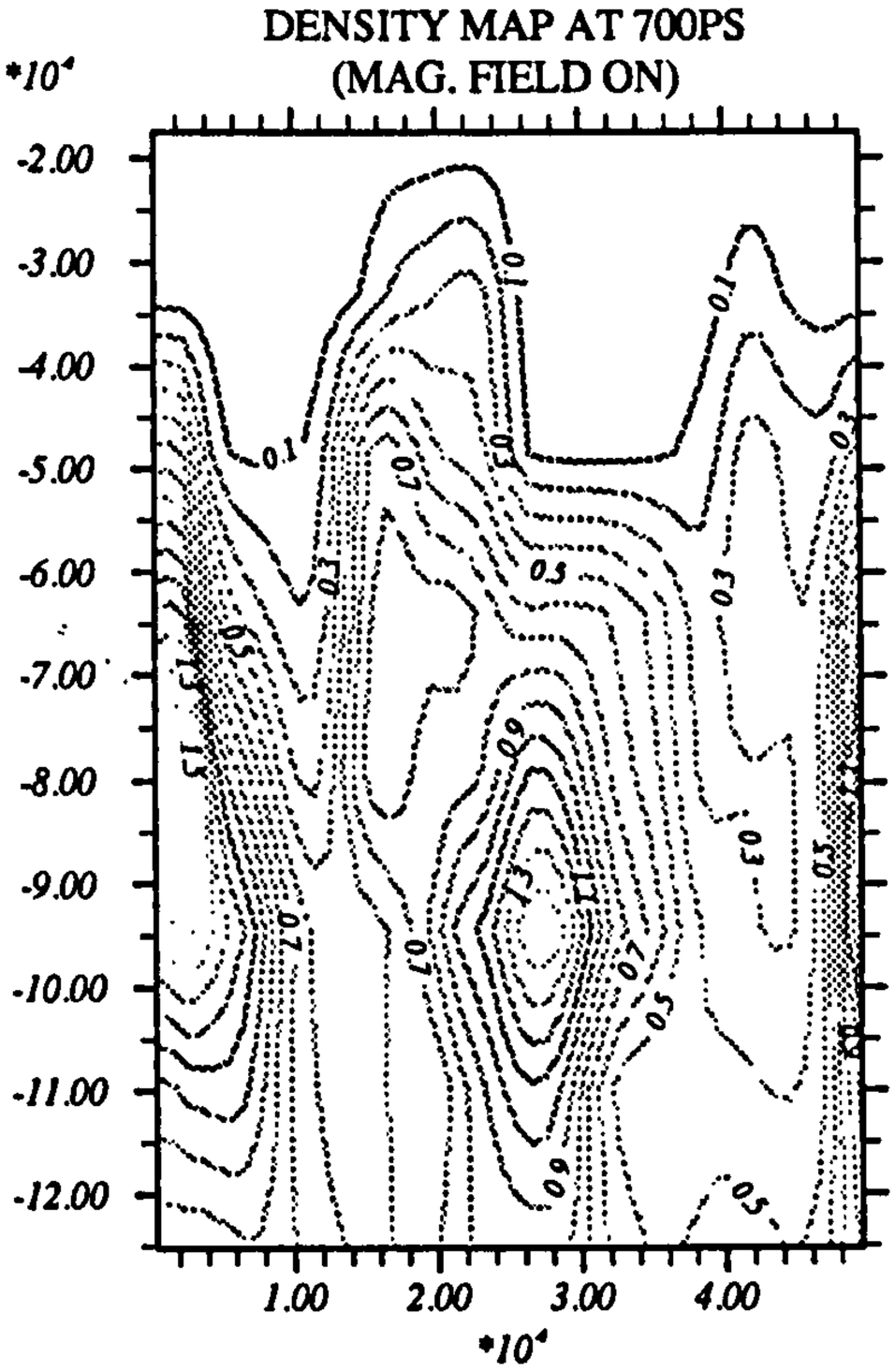

DENSITY MAP AT 750PS
(NO MAG. FIELD)

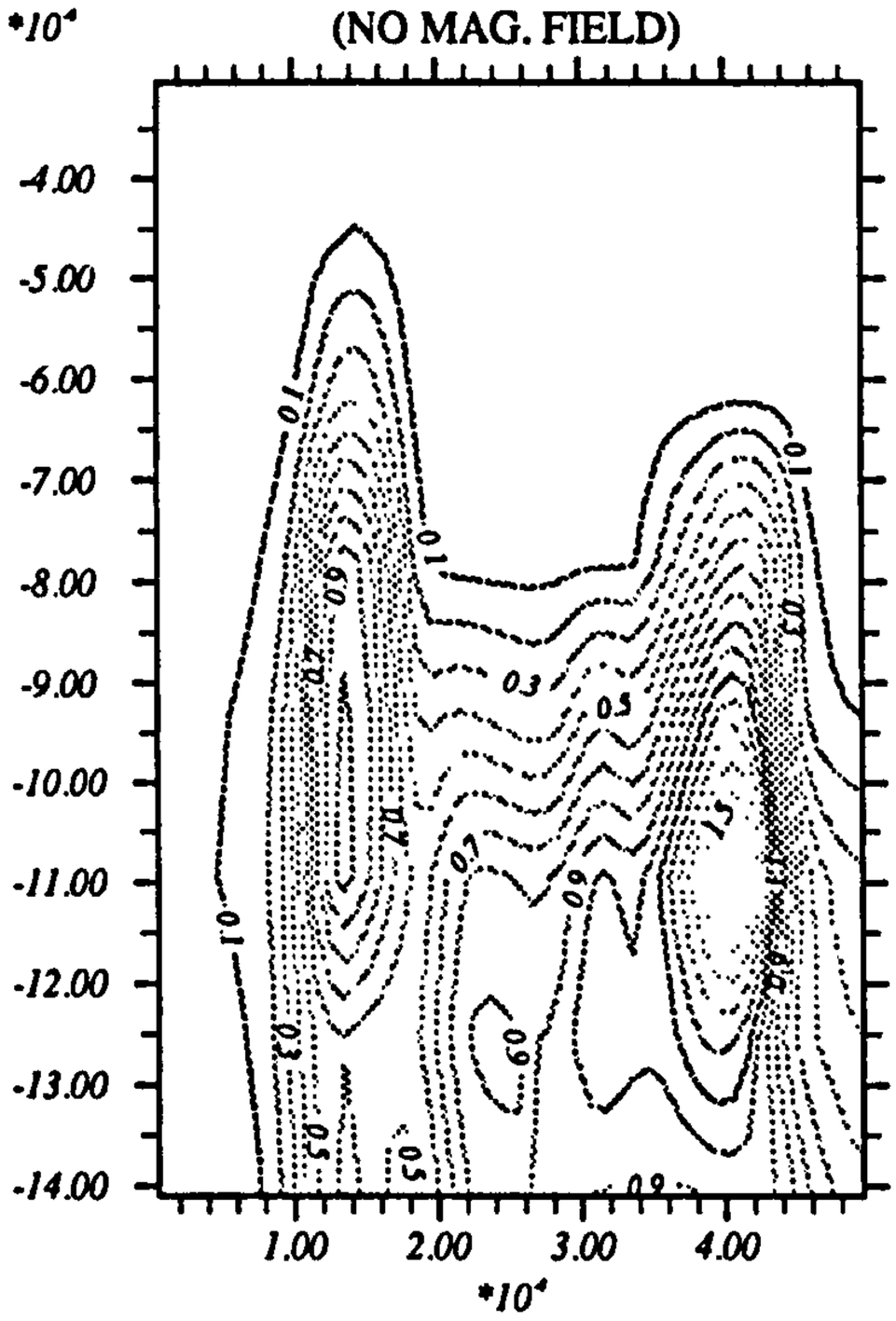

DENSITY MAP AT 750PS
(MAG. FIELD ON)

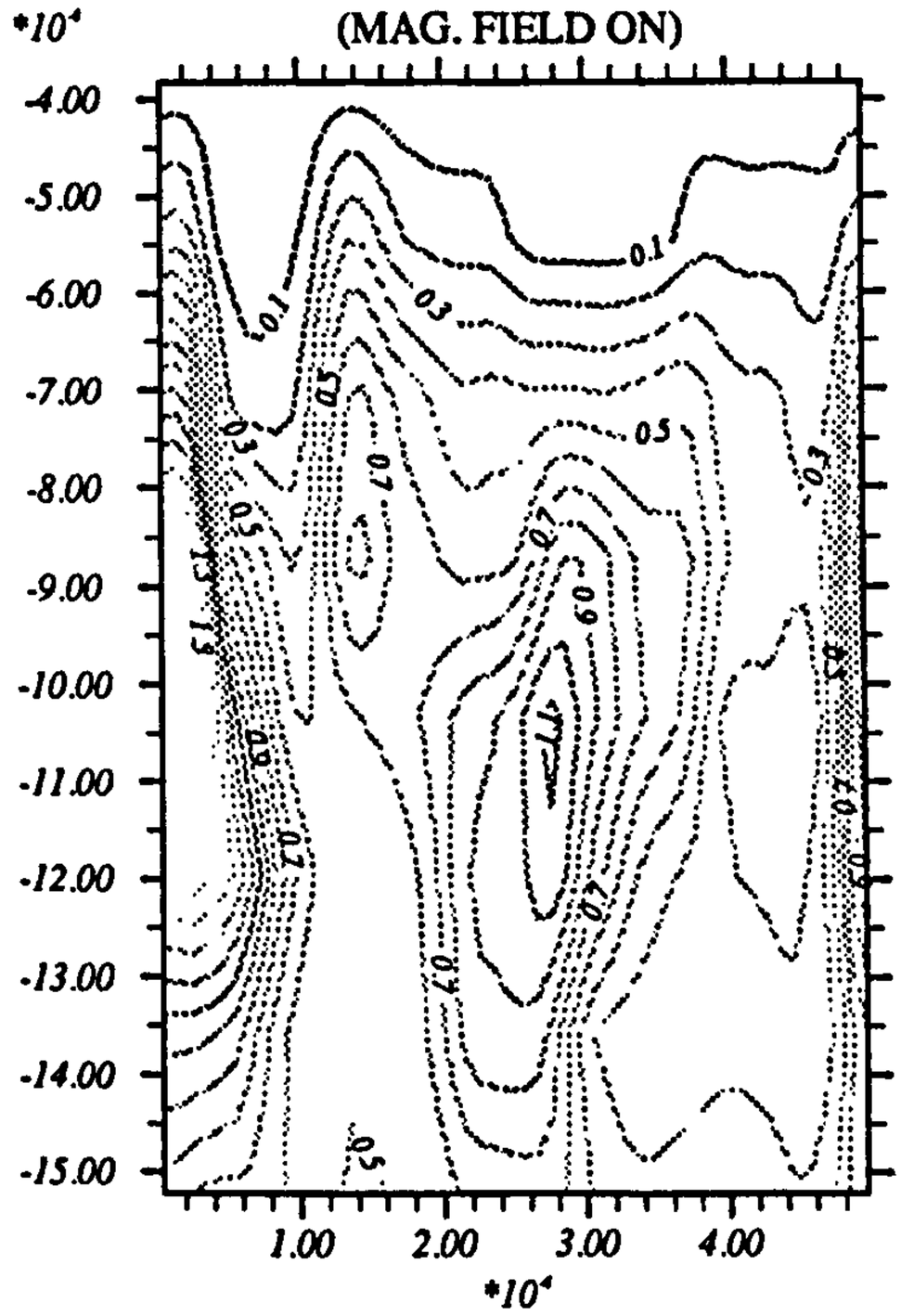

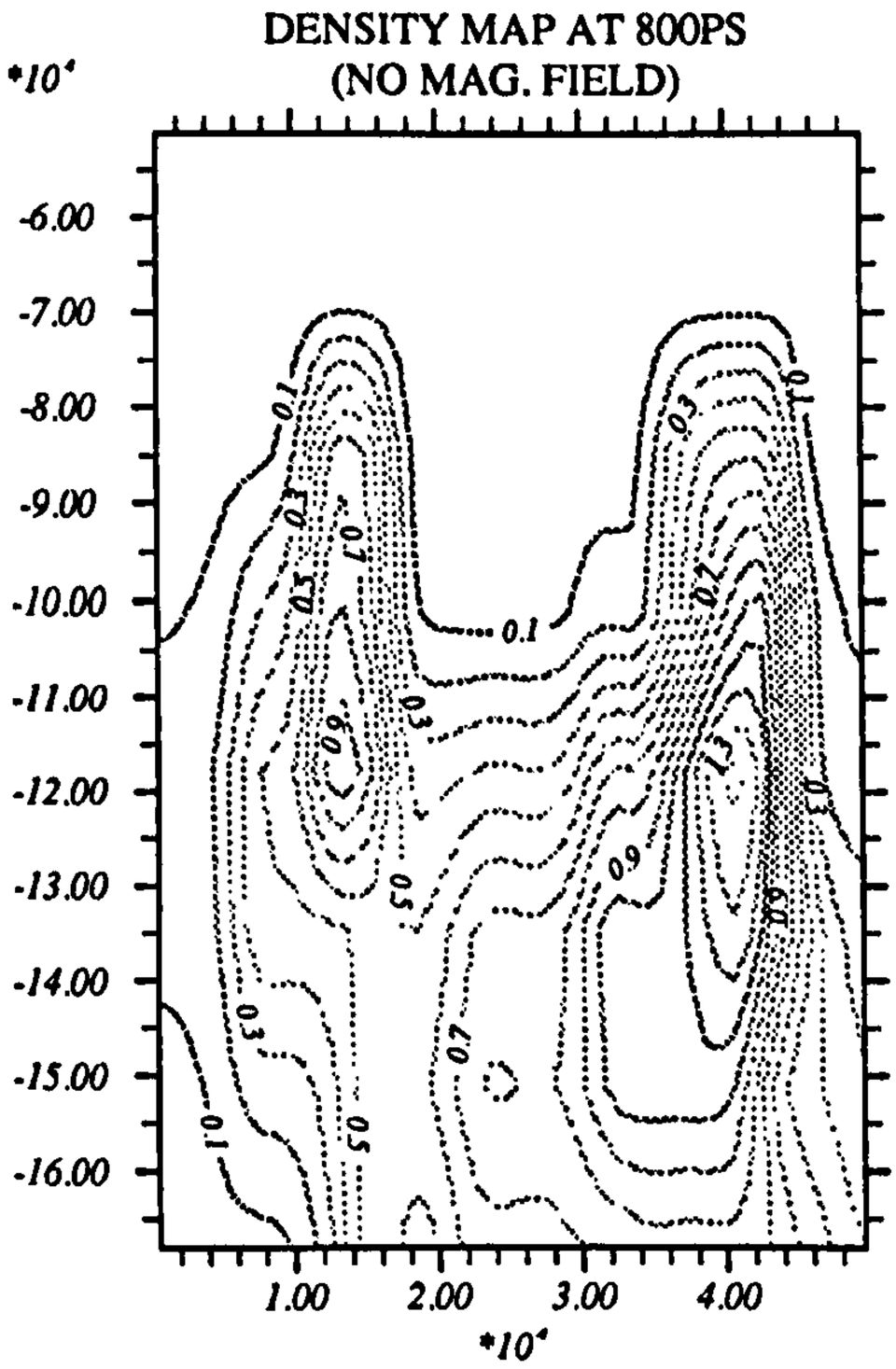
DENSITY MAP AT 800PS
(NO MAG. FIELD)
*10⁴
-6.00
-7.00
-8.00
-9.00
-10.00
-11.00
-12.00
-13.00
-14.00
-15.00
-16.00
1.00
2.00
3.00
4.00
*10⁴

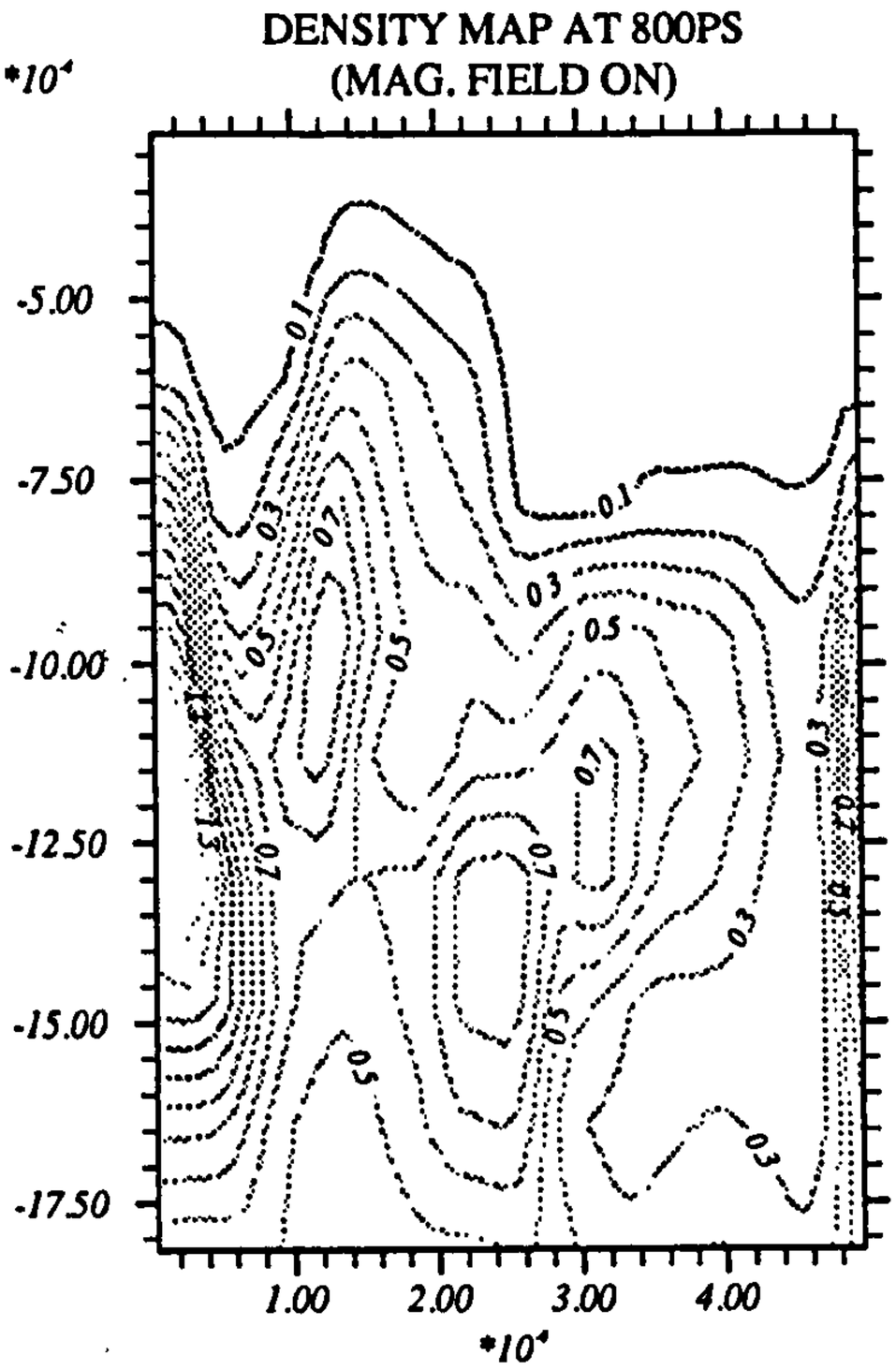
DENSITY MAP AT 800PS
(MAG. FIELD ON)
*10⁴
-5.00
-7.50
-10.00
-12.50
-15.00
-17.50
1.00
2.00
3.00
4.00
*10⁴

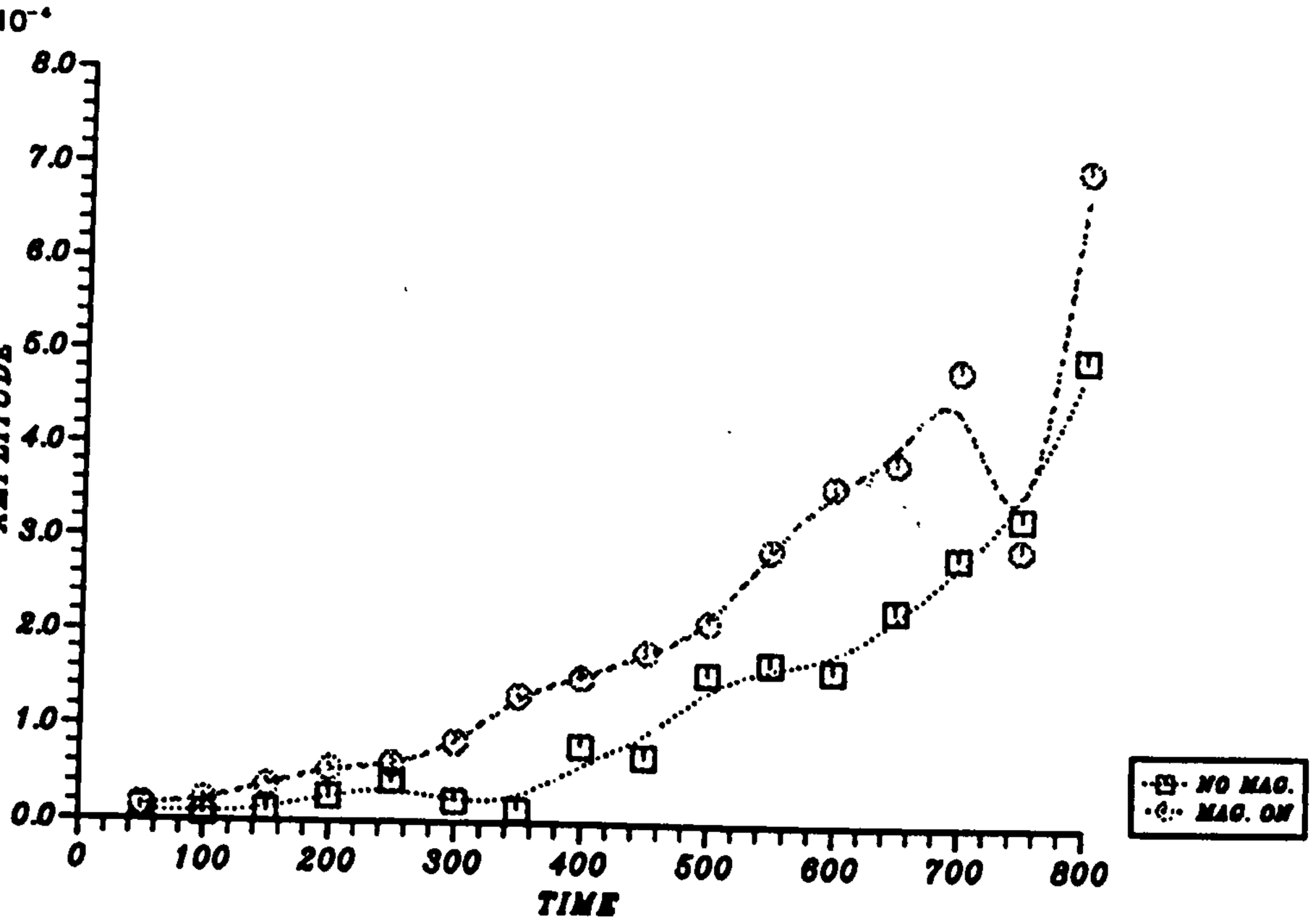

Figure 5.8: Amplitude vs time graph for a target of thickness $5 \cdot 0\mu m$ and radius $5 \cdot 0\mu m$

the magnetic field is not switched on compared to the case when the magnetic is included up to 350ps. In this case we again see the phase shift towards the axis and a high density node develops both on axis and at the outer edge when the field is on, which again is the effect of the high frequency modes generated in the early stages of the instability growth. In contrast in the absence of the field we observe that when the time reaches to about 550ps the beam penetrates deep into the axis and starts creating a hole there. At the time of 650ps a distinct hole is created on the axis in this case when the magnetic field term is ignored.

In both cases spikes develop at the time of 600ps whereas the bubbles rise up in the heavy fluid in almost round ended shape. When the time reaches up to 700ps the target mixing starts to develop and at 800ps a strong mixing of the target is observed in the case when the magnetic is switched on. The target is pushed back in these studies and a long width of the mixed region is generated.

In figure $5 \cdot 8$ the density perturbation displacement amplitude-time plot is drawn to make the comparison of instability growth in both cases. It is observed that the instability growth in the early stages for magnetic field is significantly

larger over non-magnetic field studies. For the target and the perturbation wavelength of this size, the growth amplitude is always higher when magnetic field switched on over magnetic field off.

The time history of the magnetic field contours is shown in figure $5 \cdot 9$ which in fact is the source of creating high frequency modes in the density contours.

5.4 TARGET SIZE $(5 \cdot 0\mu m \times 2 \cdot 5\mu m)$

In this simulation the target thickness is kept the same as in the previous set but its radius is halved to, $2 \cdot 5\mu m$, which is the same as in the first set of simulations. This time instead of applying two wavelength perturbations we used only a single wavelength perturbation of $2 \cdot 5\mu m$. All the necessary input parameters are given in table $5 \cdot 3$ The density contour map for magnetic field included/excluded is shown in figure $5 \cdot 10$. At 50ps the main structure of the instability growth is quite similar in both cases although some short wavelength modes appear in the case when the magnetic field is included. As the time progresses on up to 300ps the growth of instability is slower with no magnetic field whereas the high frequency modes continue their effect on the instability generation.

At 350ps, a broad spike has developed without magnetic field but a bubble with the field. At this time with the magnetic field switched on high density nodes enhance the growth, and by 450ps the mixing starts taking place.

Once again we observe in these simulations that at 600ps a hole starts to develop on the axis of the target with no field where as a strong mixing is observed at the same time in the simulations when the magnetic field switched on. The complete hole is developed on the axis at 750ps in the non magnetic field studies. When the time reaches to 800ps three high density nodes still remain in the case of magnetic field.

The amplitude as a function of time graph is shown in figure $5 \cdot 11$. In the early time the growth of instability is higher with the magnetic field on but after 500ps we see that the growth for no magnetic field is higher over magnetic field studies. This is clearly the effect of mixing and the laser burning through the target.

The magnetic field contours are shown in figure $5 \cdot 12$. In the early stages

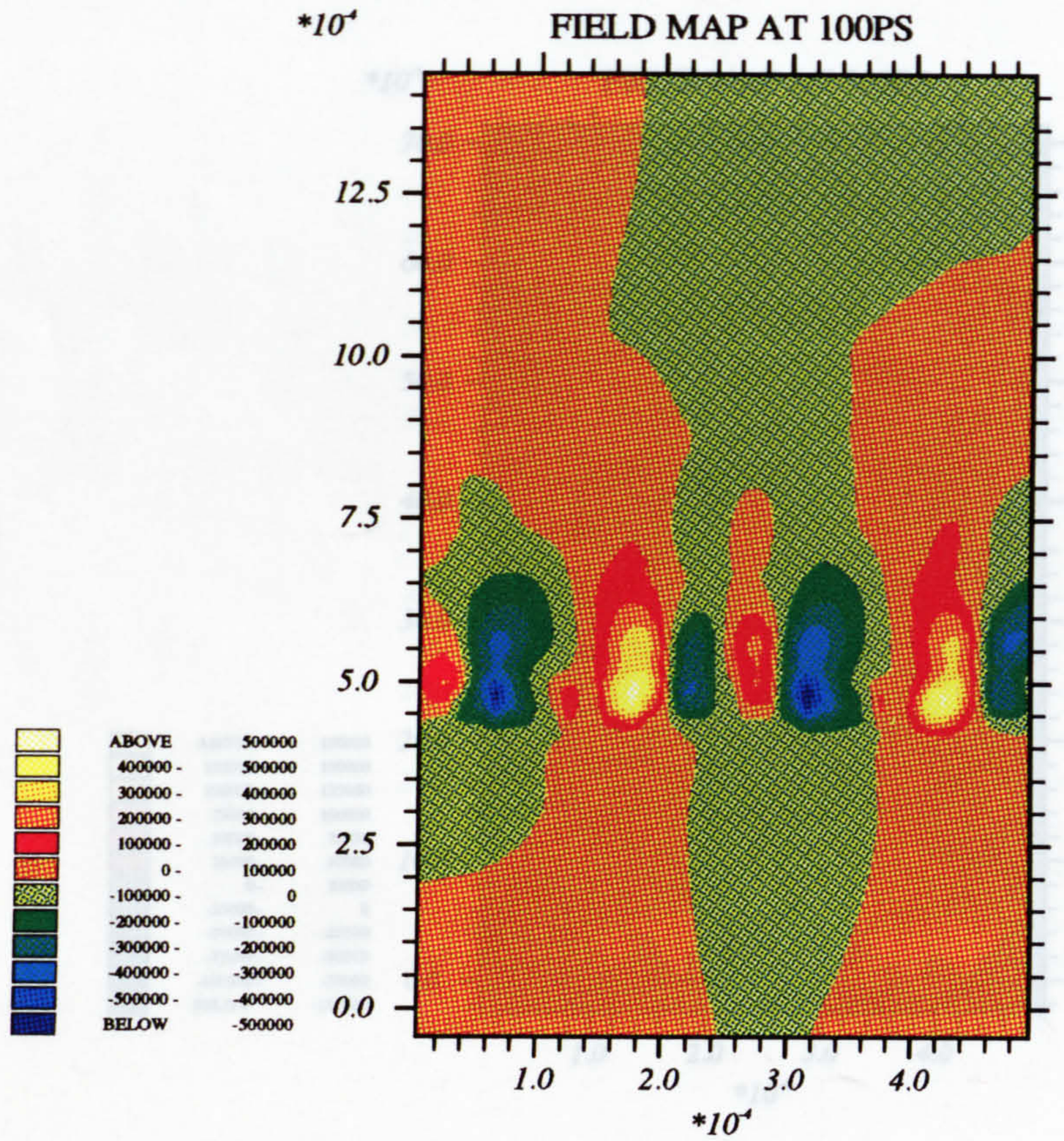

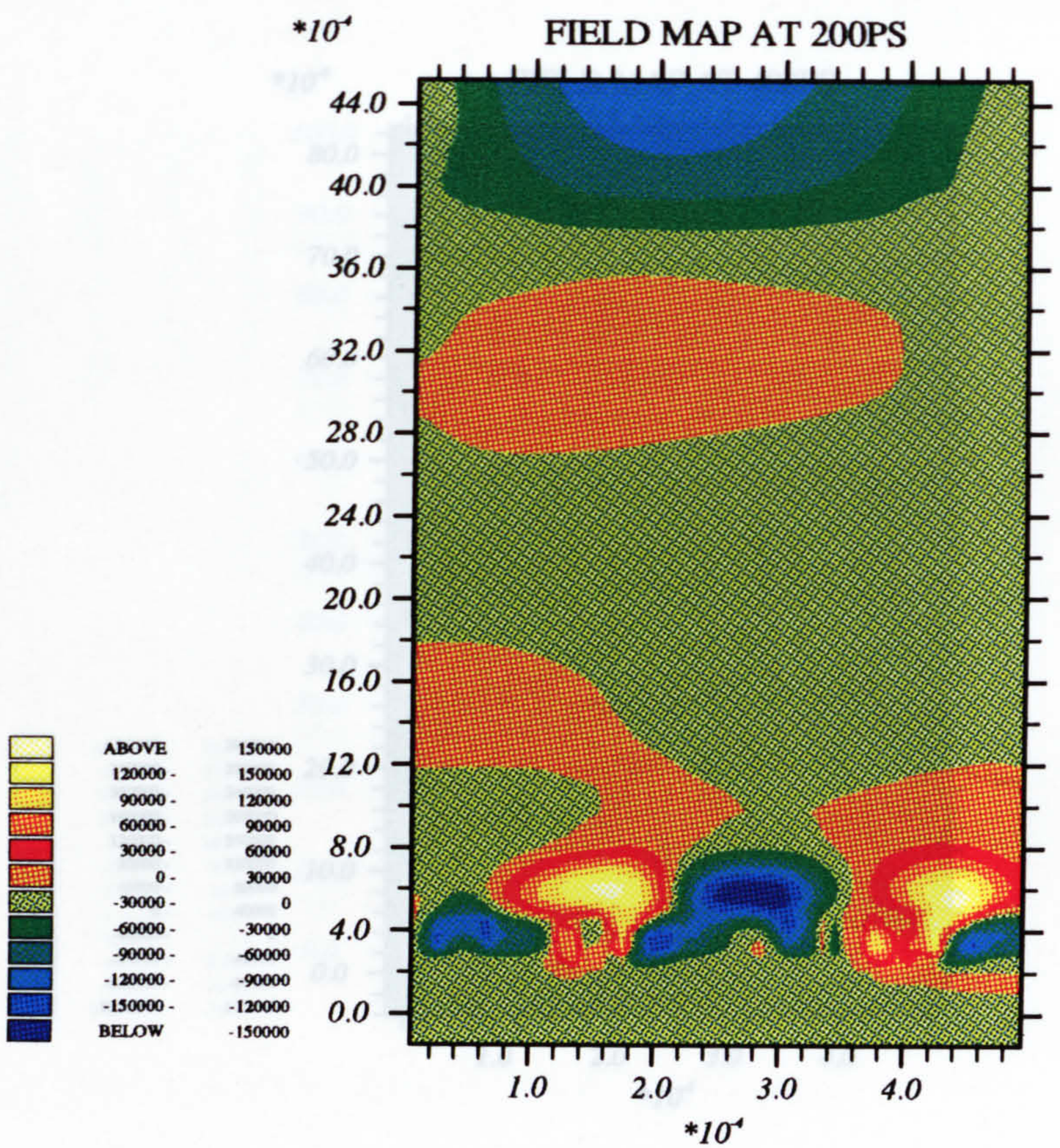

Figure 5.9: Magentic field map for the target (5.0μm x 5.0μm) in both directions.

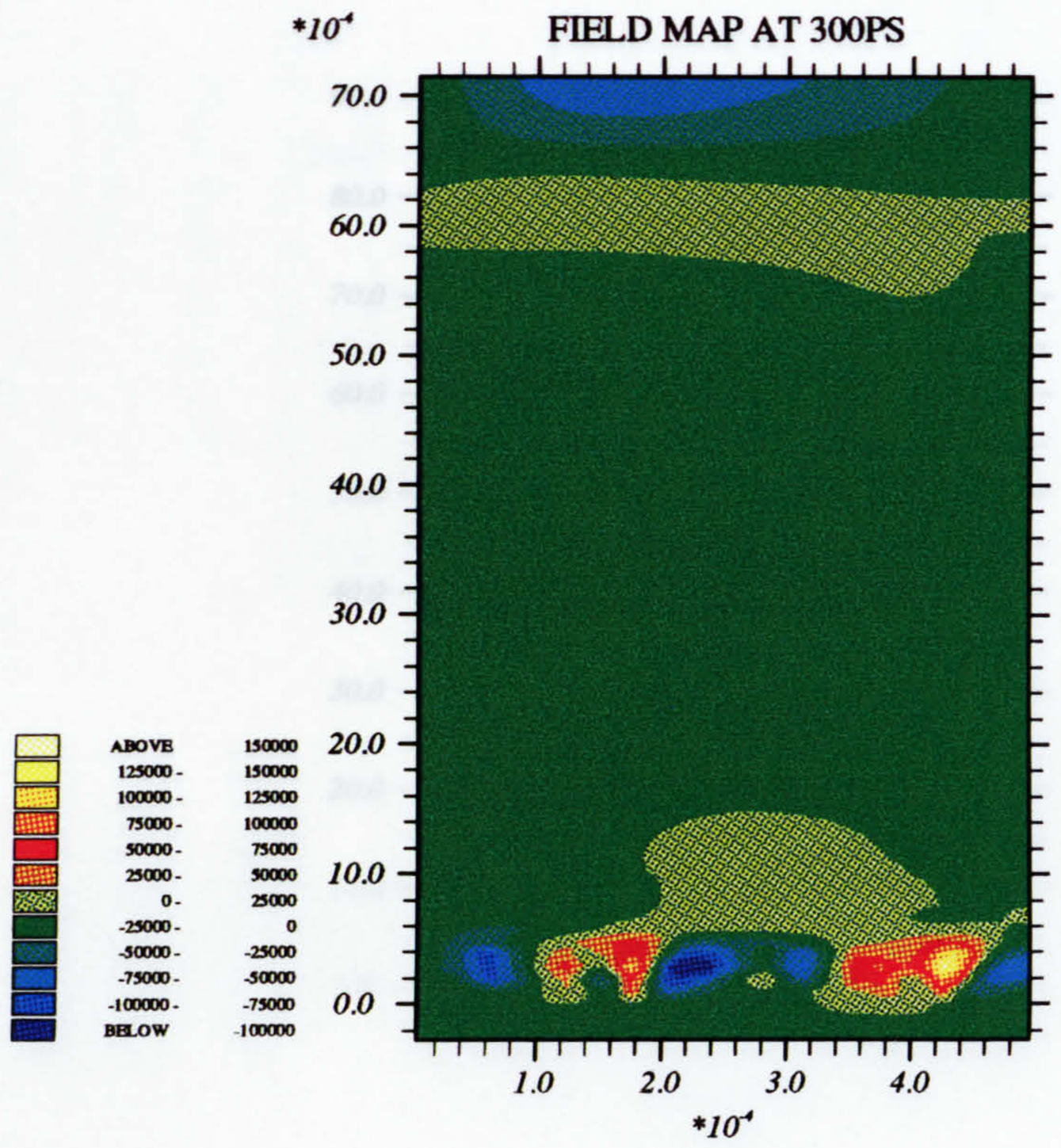
*10⁻⁴
FIELD MAP AT 300PS
70.0
60.0
50.0
40.0
30.0
20.0
10.0
0.0
1.0
2.0
3.0
4.0
*10⁻⁴
ABOVE 150000
125000 - 150000
100000 - 125000
75000 - 100000
50000 - 75000
25000 - 50000
0 - 25000
-25000 - 0
-50000 - -25000
-75000 - -50000
-100000 - -75000
BELOW -100000

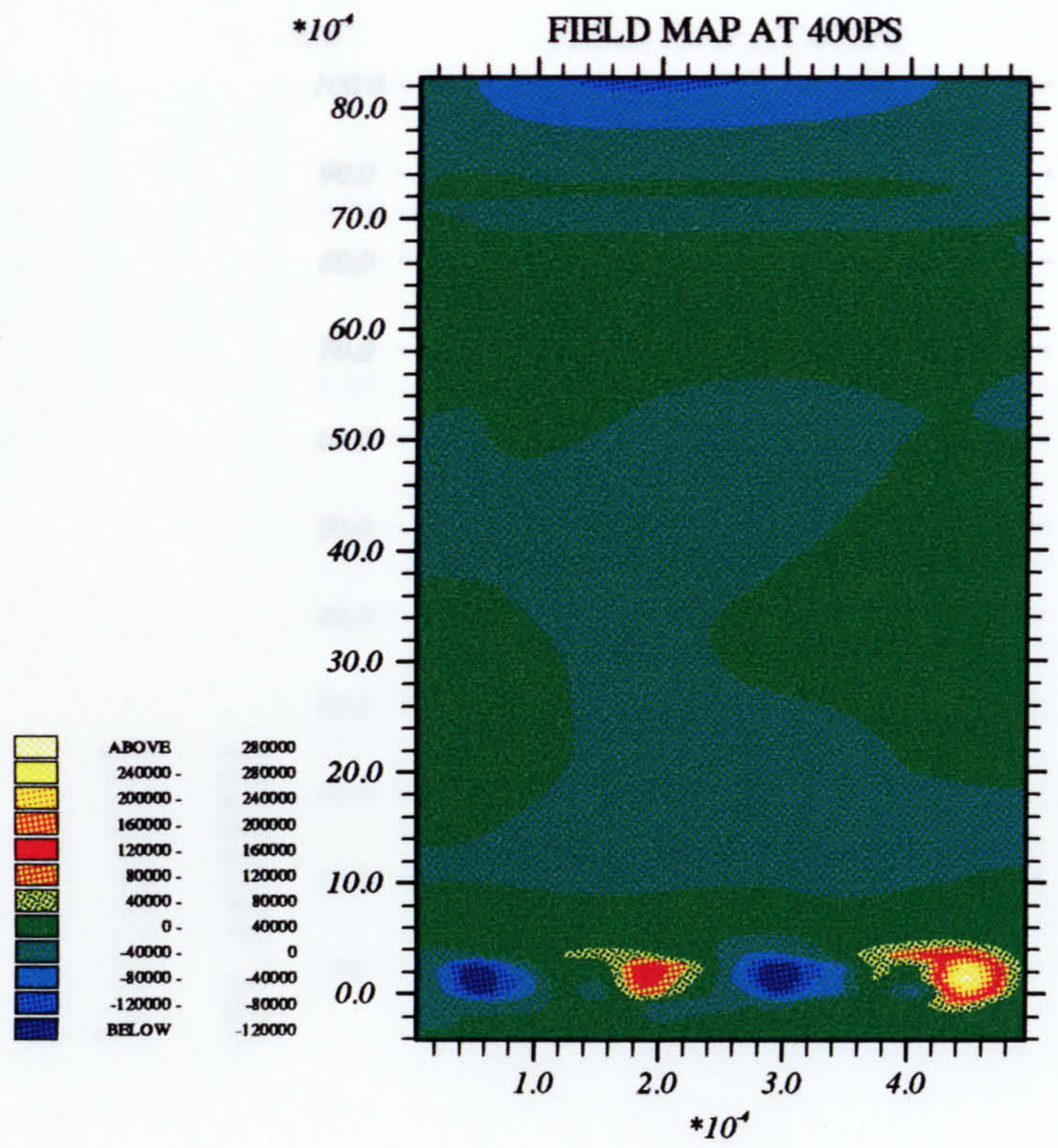
*10⁻⁴
FIELD MAP AT 400PS
80.0
70.0
60.0
50.0
40.0
30.0
20.0
10.0
0.0
1.0
2.0
3.0
4.0
*10⁻⁴
ABOVE 280000
240000 - 280000
200000 - 240000
160000 - 200000
120000 - 160000
80000 - 120000
40000 - 80000
0 - 40000
-40000 - 0
-80000 - -40000
-120000 - -80000
BELOW -120000

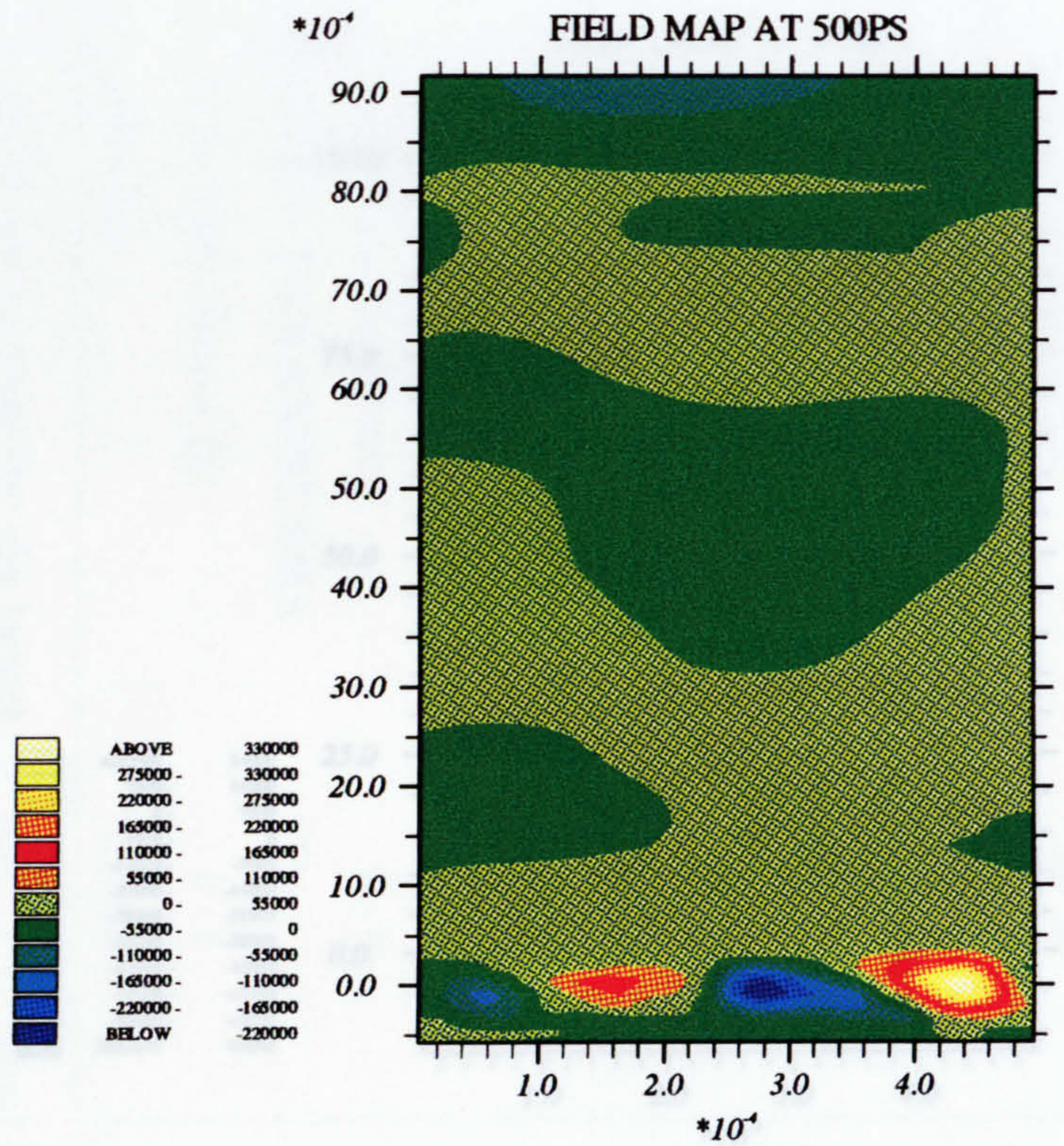
FIELD MAP AT 500PS
*10⁻⁴
90.0
80.0
70.0
60.0
50.0
40.0
30.0
20.0
10.0
0.0
1.0
2.0
3.0
4.0
*10⁻⁴
ABOVE 330000
275000 - 330000
220000 - 275000
165000 - 220000
110000 - 165000
55000 - 110000
0 - 55000
-55000 - 0
-110000 - -55000
-165000 - -110000
-220000 - -165000
BELOW -220000

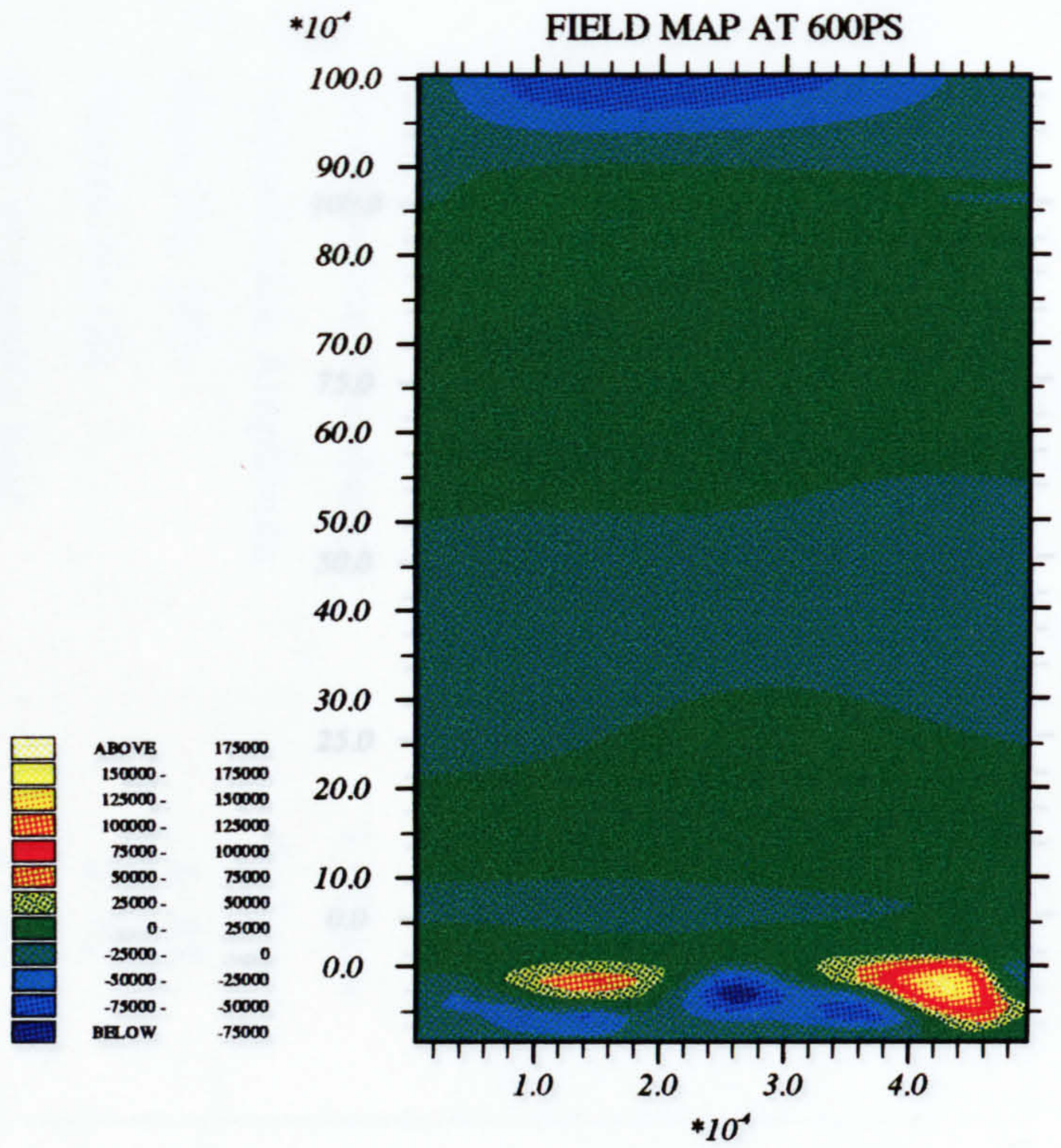
FIELD MAP AT 600PS
*10⁻⁴
100.0
90.0
80.0
70.0
60.0
50.0
40.0
30.0
20.0
10.0
0.0
1.0
2.0
3.0
4.0
*10⁻⁴
ABOVE 175000
150000 - 175000
125000 - 150000
100000 - 125000
75000 - 100000
50000 - 75000
25000 - 50000
0 - 25000
-25000 - 0
-50000 - -25000
-75000 - -50000
BELOW -75000

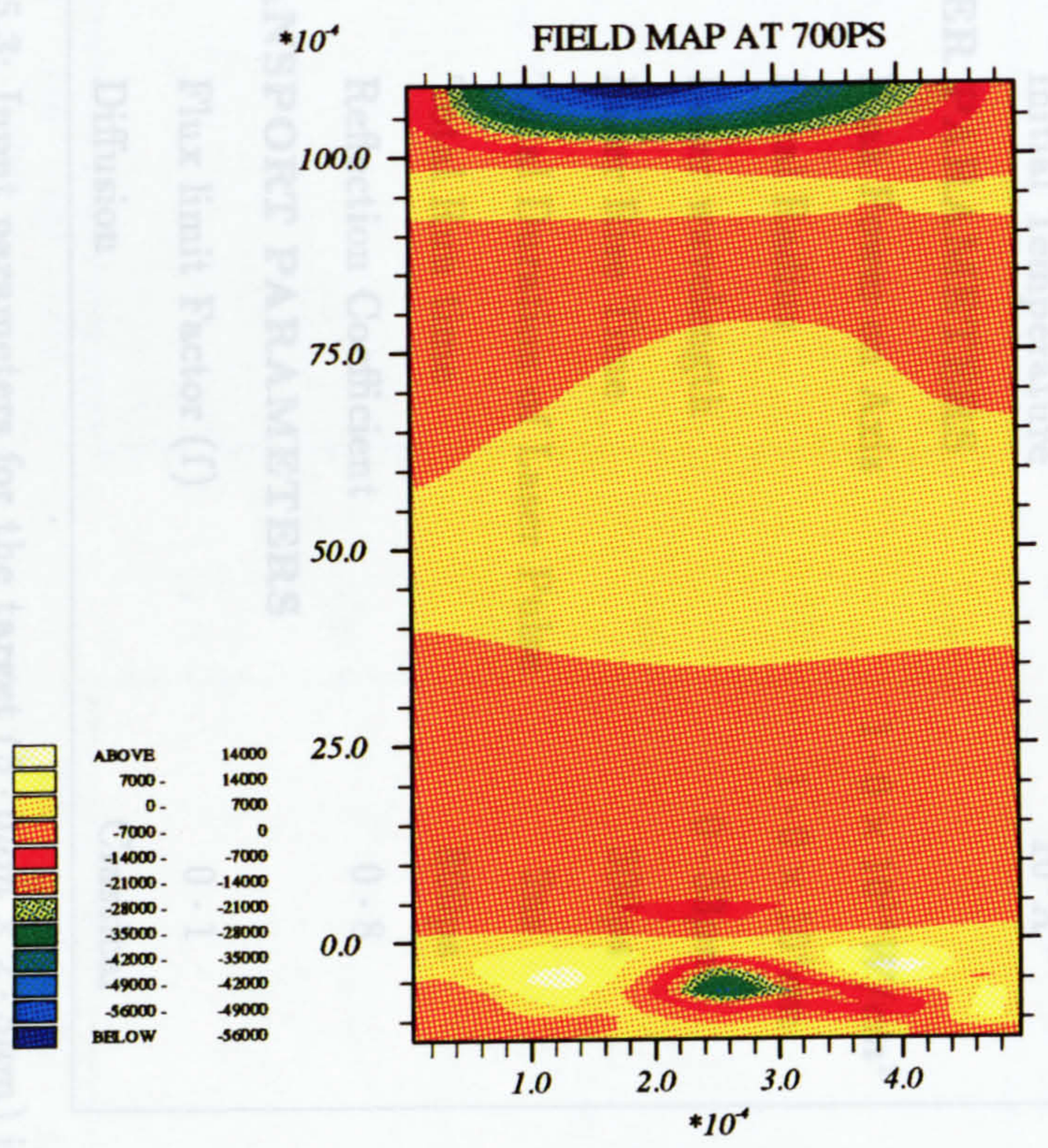
*10⁻⁴
FIELD MAP AT 700PS
100.0
75.0
50.0
25.0
0.0
1.0
2.0
3.0
4.0
*10⁻⁴
ABOVE 14000
7000 - 14000
0 - 7000
-7000 - 0
-14000 - -7000
-21000 - -14000
-28000 - -21000
-35000 - -28000
-42000 - -35000
-49000 - -42000
-56000 - -49000
BELOW -56000

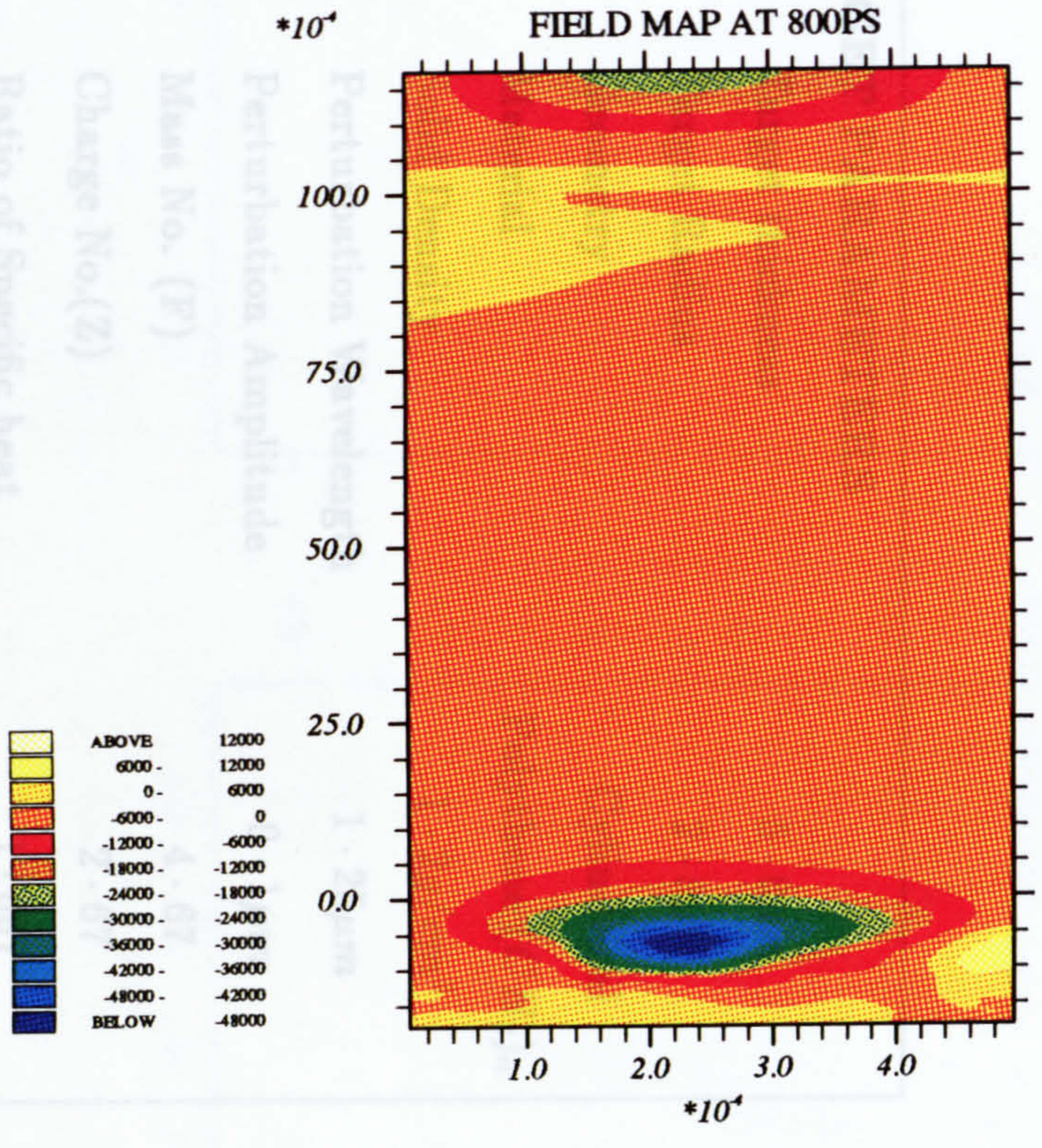
*10⁻⁴
FIELD MAP AT 800PS
100.0
75.0
50.0
25.0
0.0
1.0
2.0
3.0
4.0
*10⁻⁴
ABOVE 12000
6000 - 12000
0 - 6000
-6000 - 0
-12000 - -6000
-18000 - -12000
-24000 - -18000
-30000 - -24000
-36000 - -30000
-42000 - -36000
-48000 - -42000
BELOW -48000

TARGET PARAMETERS	
Target thickness	$5 \cdot 0 \mu m$
Target Radius	$2 \cdot 5 \mu m$
Geometry	Cylindrical
Material	Polythene $(CH_2)_n$
Solid Density	$1 \cdot 2 g/cm^3$
Perturbation Wavelength	$1 \cdot 25 \mu m$
Perturbation Amplitude	$0 \cdot 1 \mu m$
Mass No. (F)	$4 \cdot 67$
Charge No.(Z)	$2 \cdot 67$
Ratio of Specific heat	$1 \cdot 667$
Initial Temperature	$10^1 K°$
LASER PARAMETERS	
Peak Power on Axis	$1 \cdot 0 \times 10^{14} W/cm^2$
Focal Radius	$1 \cdot 0 \times 10^4 cm$
Laser wavelength	$0 \cdot 53 \mu m$
Laser Rise Time	300ps
Total Duration of Laser Pulse	2ns
Total Run time	800ps
Reflection Coefficient	$0 \cdot 8$
TRANSPORT PARAMETERS	
Flux limit Factor (f)	$0 \cdot 1$
Diffusion	Classical

Table 5.3: Input parameters for the target ($5 \cdot 0 \mu m \times 2 \cdot 5 \mu m$) in axial and radial directions.

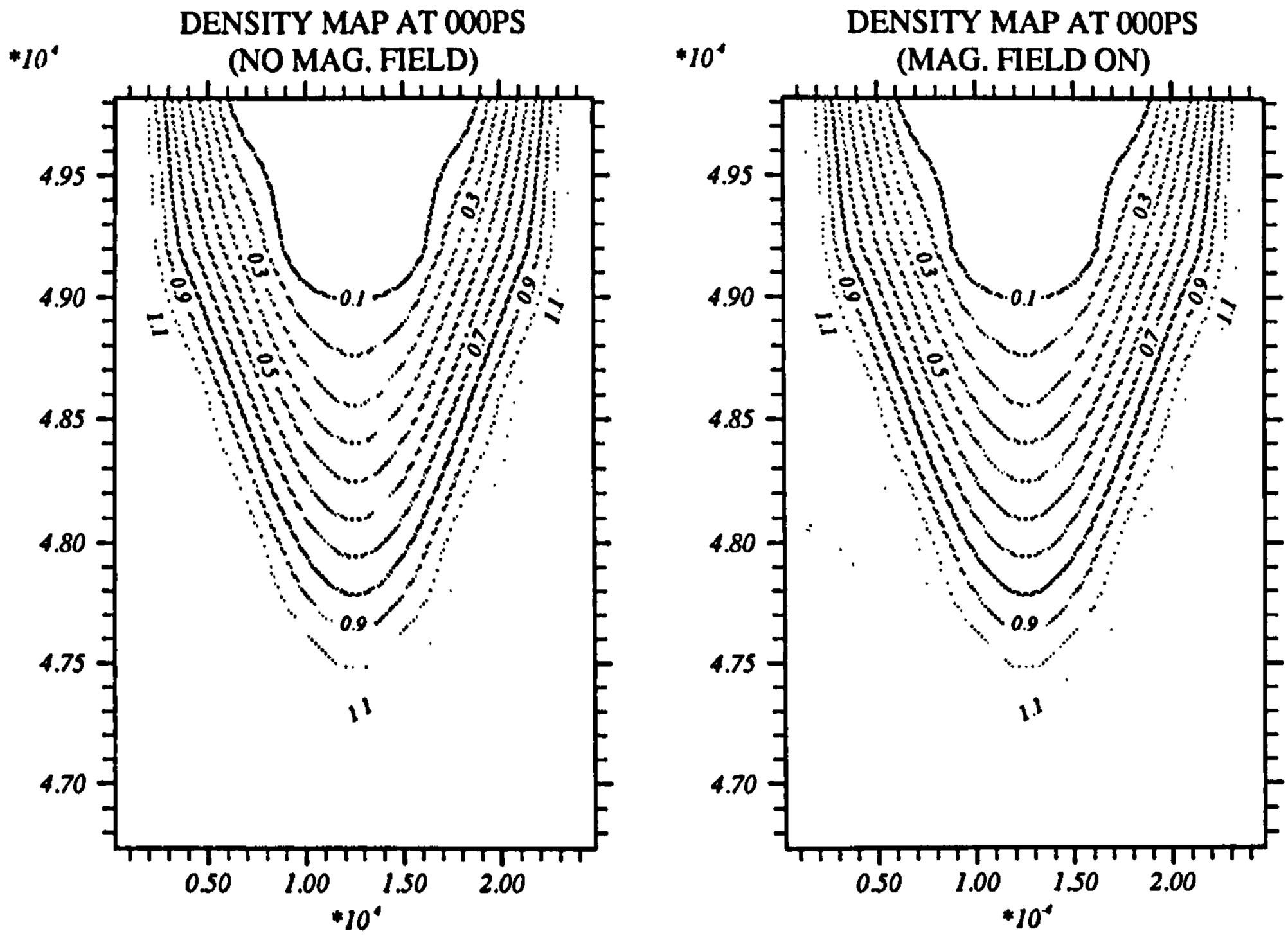

Figure 5.10: Density contour map for the target ($5 \cdot 0\mu m \times 2 \cdot 5\mu m$) in axial and radial direction.

DENSITY MAP AT 100PS
(NO MAG. FIELD)

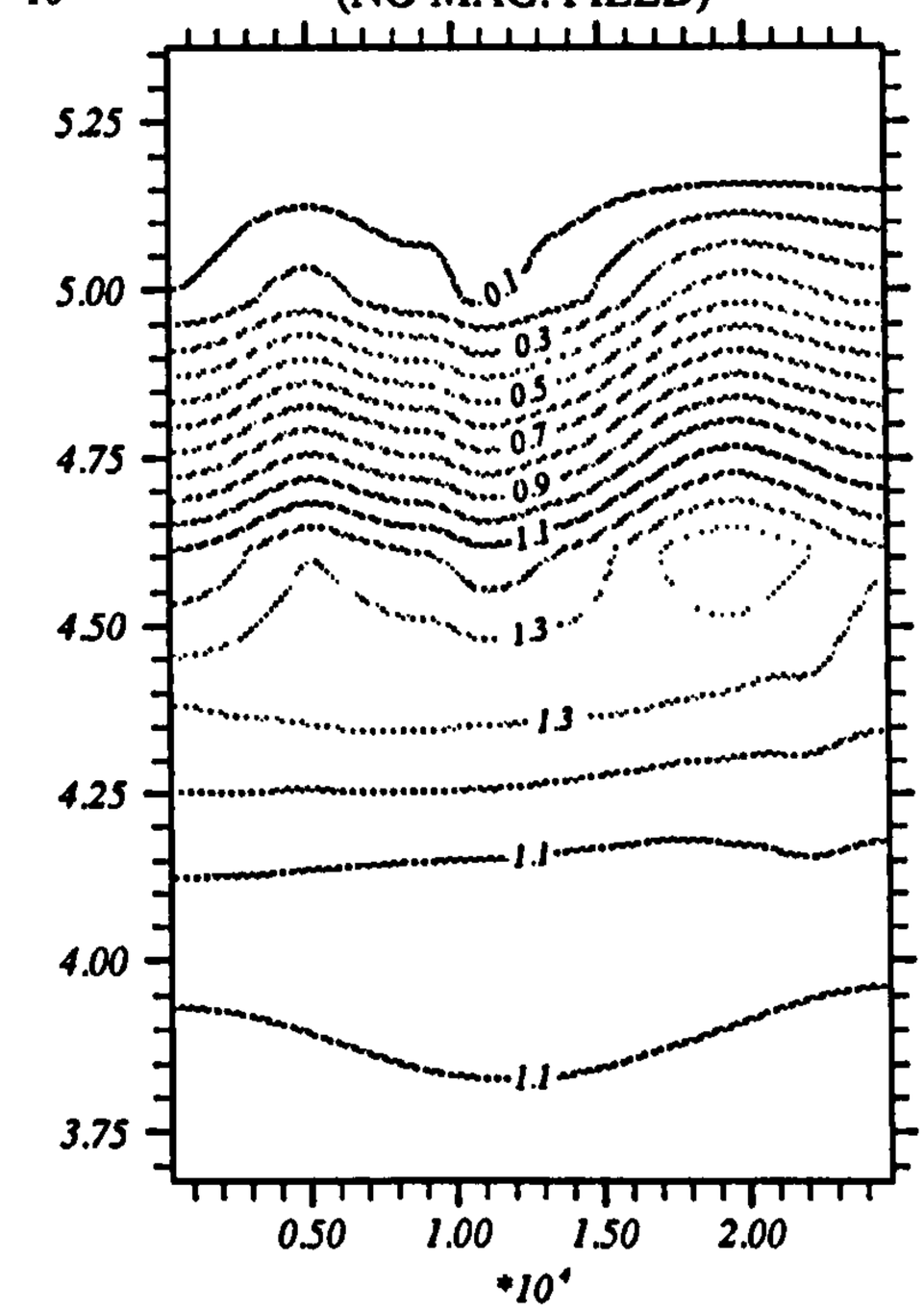

DENSITY MAP AT 100PS
(MAG. FIELD ON)

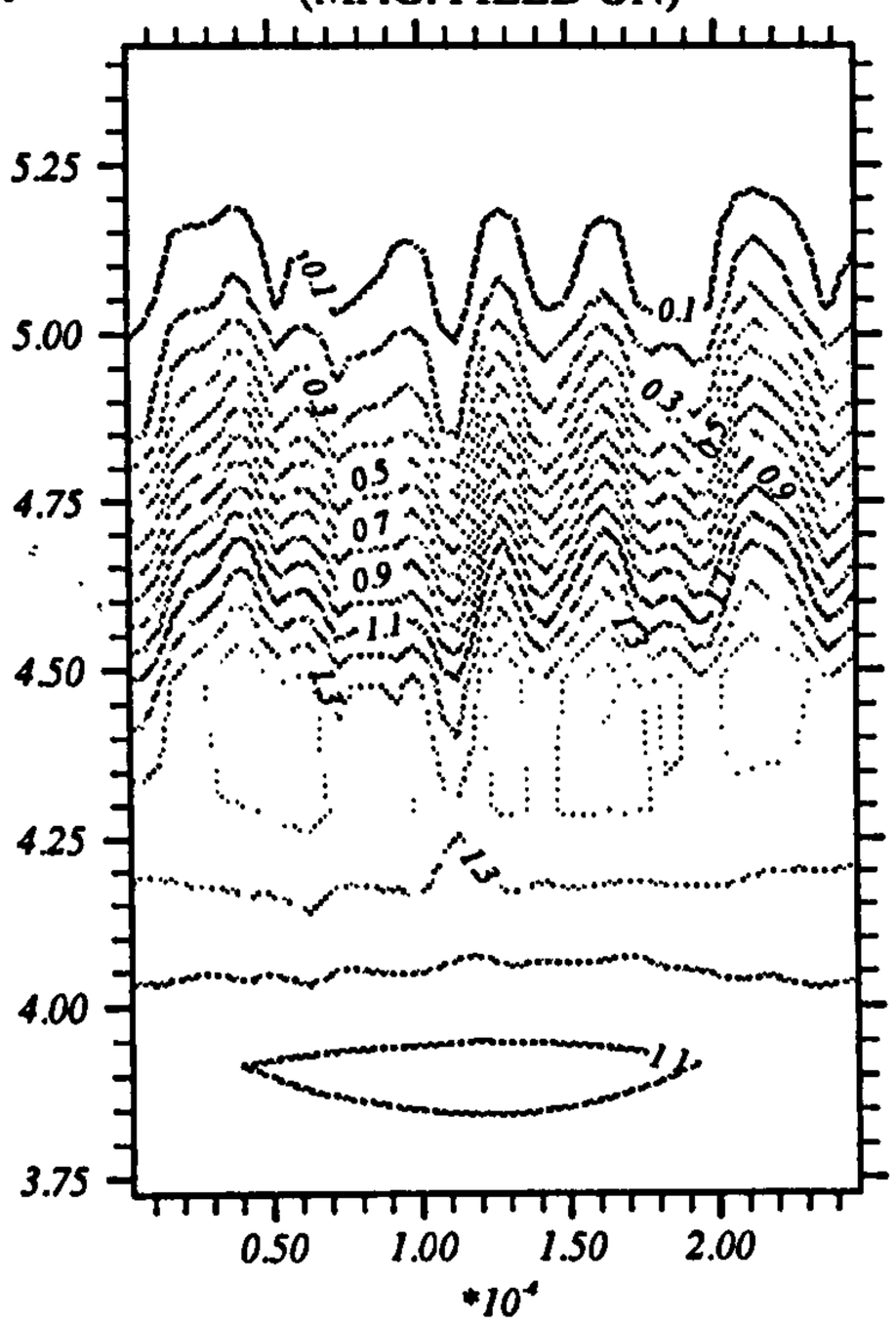

DENSITY MAP AT 150PS
(NO MAG. FIELD)

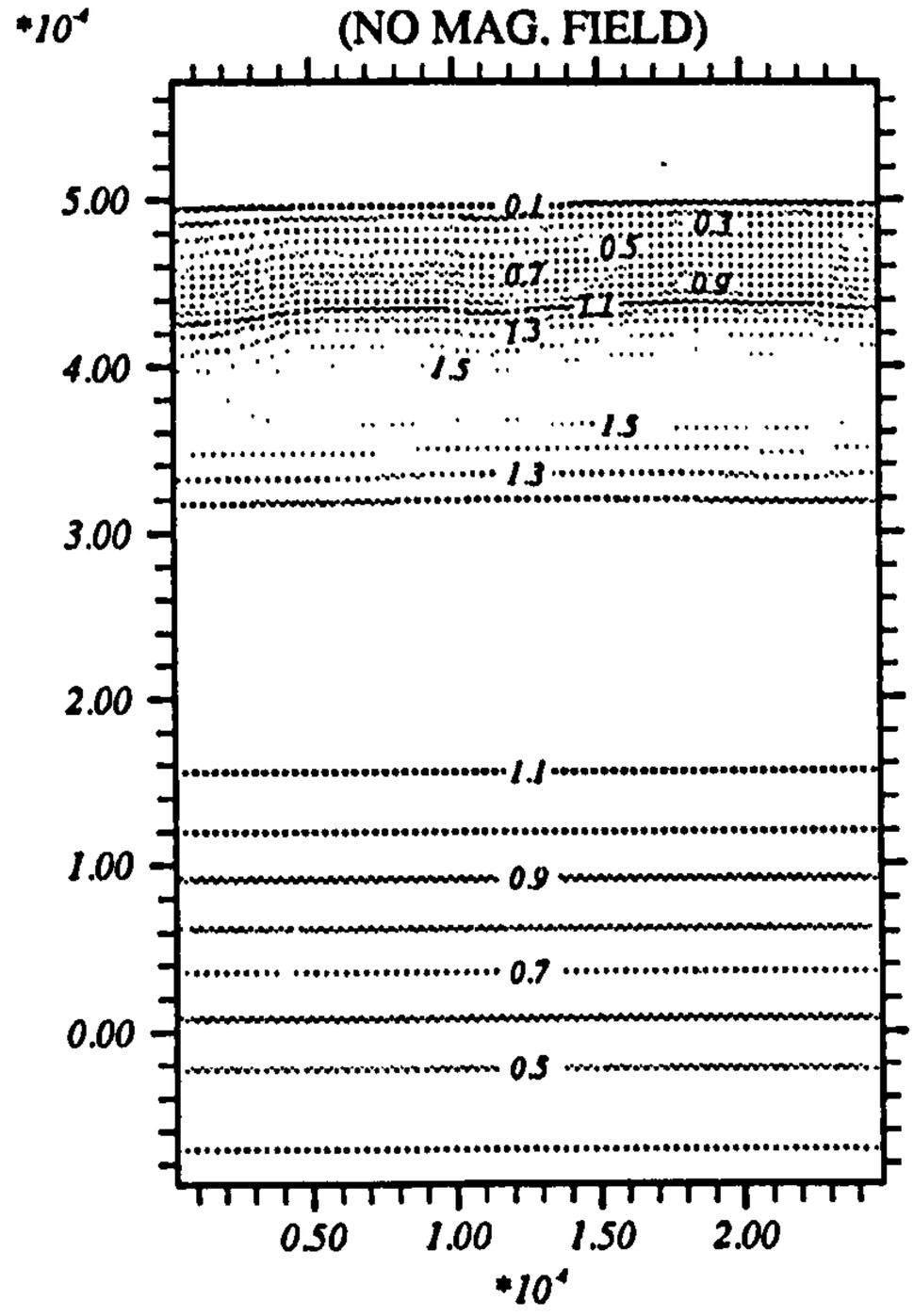

DENSITY MAP AT 150PS
(MAG. FIELD ON)

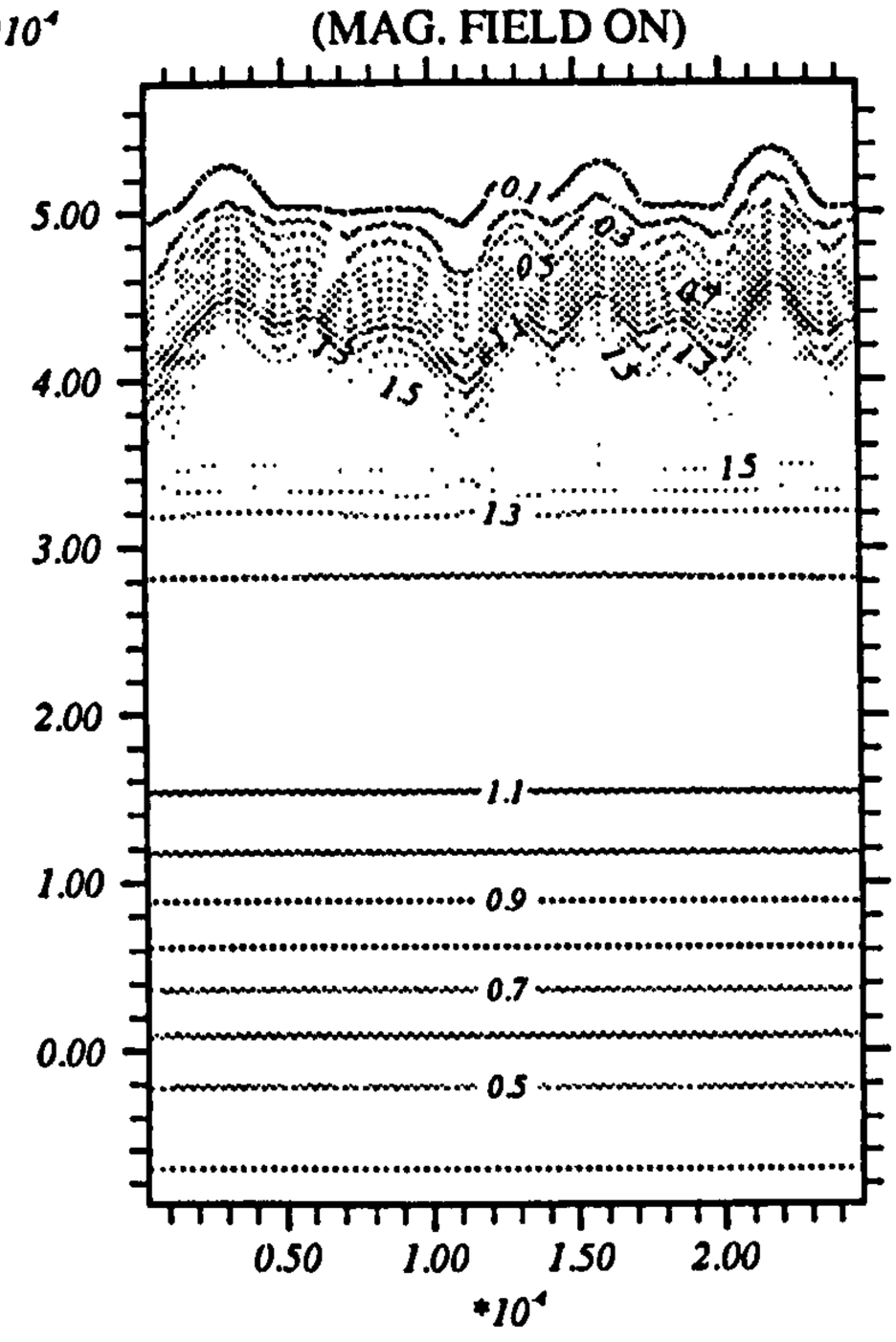

DENSITY MAP AT 200PS
(NO MAG. FIELD)

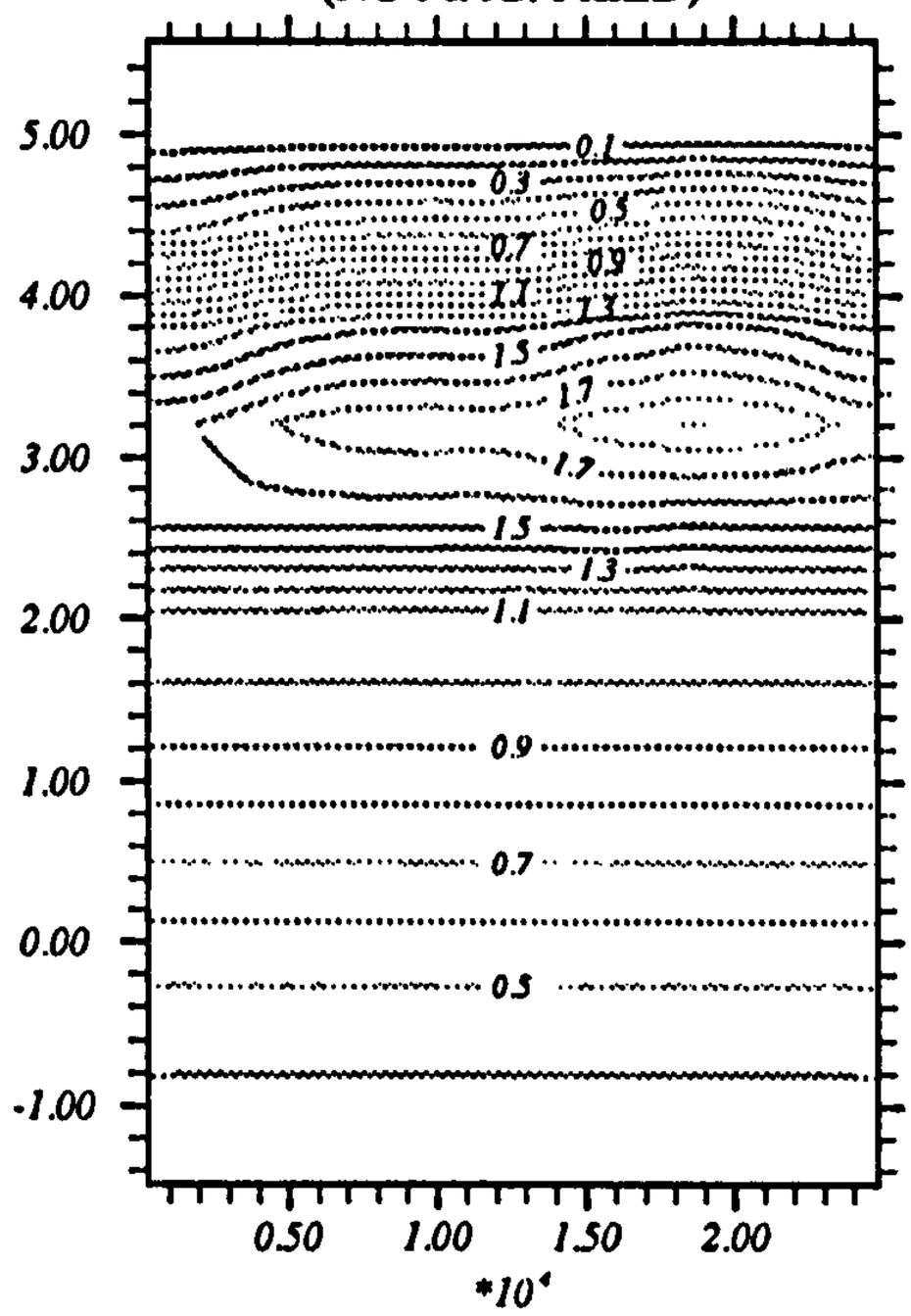

DENSITY MAP AT 200PS
(MAG. FIELD ON)

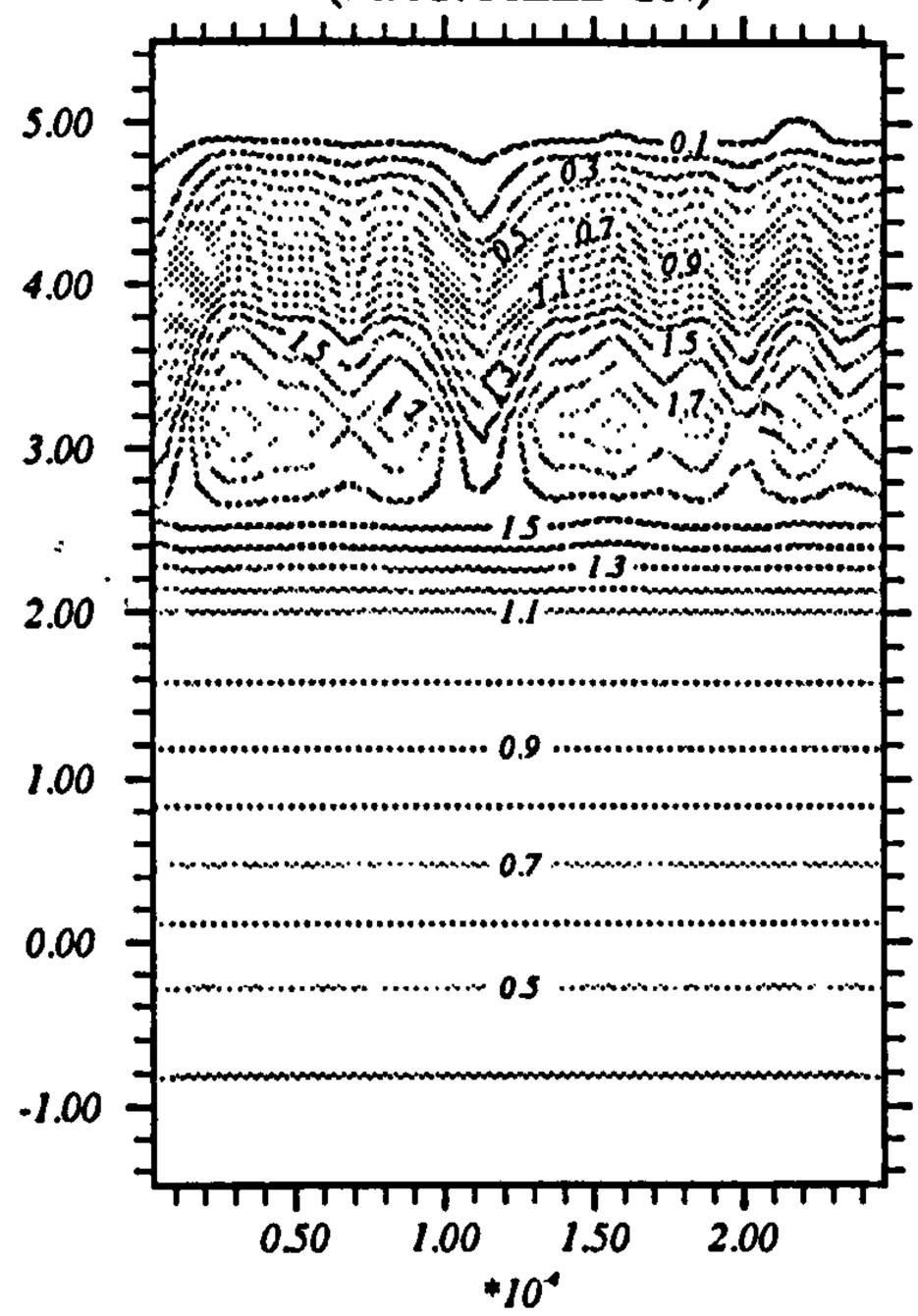

DENSITY MAP AT 250PS
(NO MAG. FIELD)

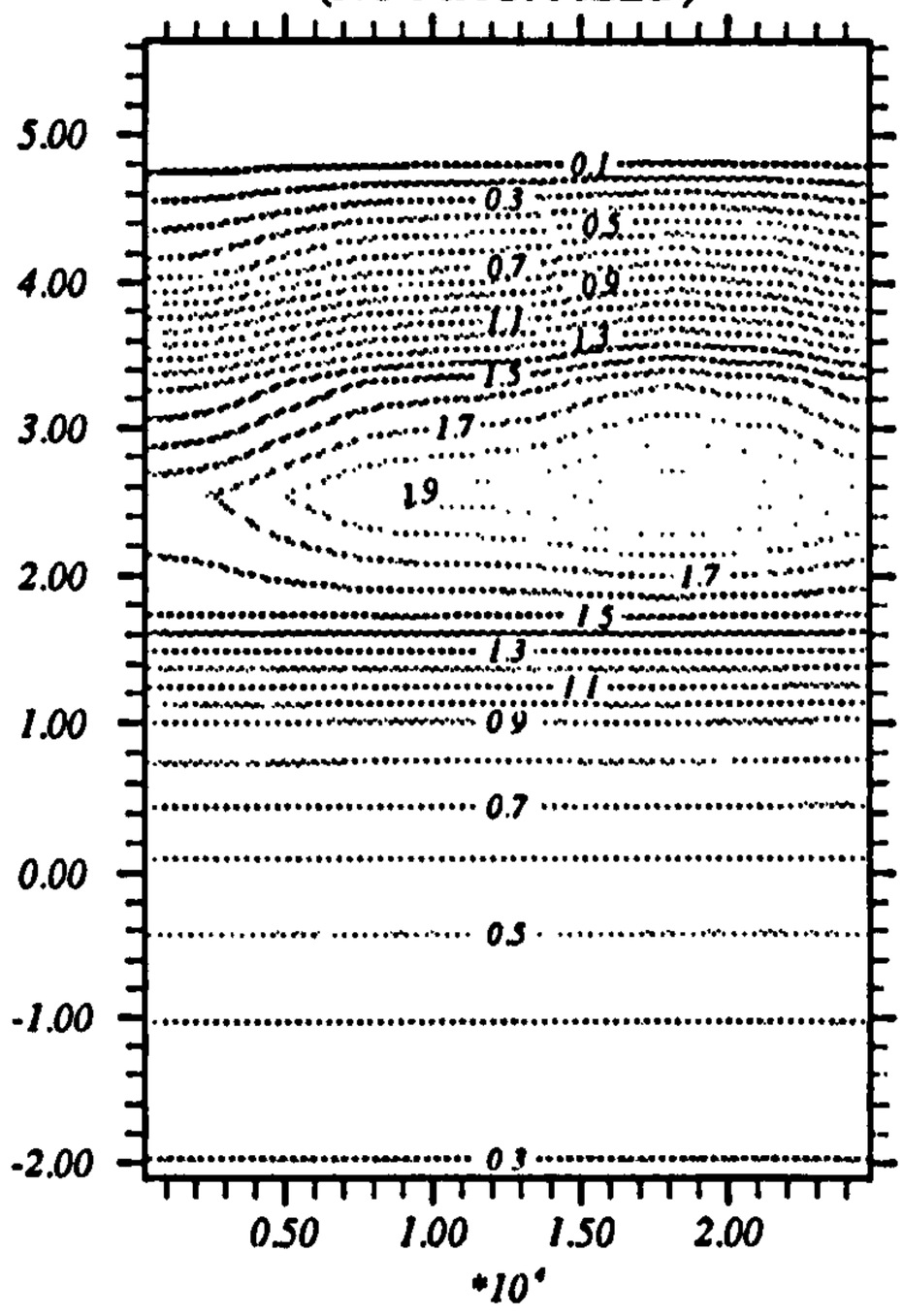

DENSITY MAP AT 250PS
(MAG. FIELD ON)

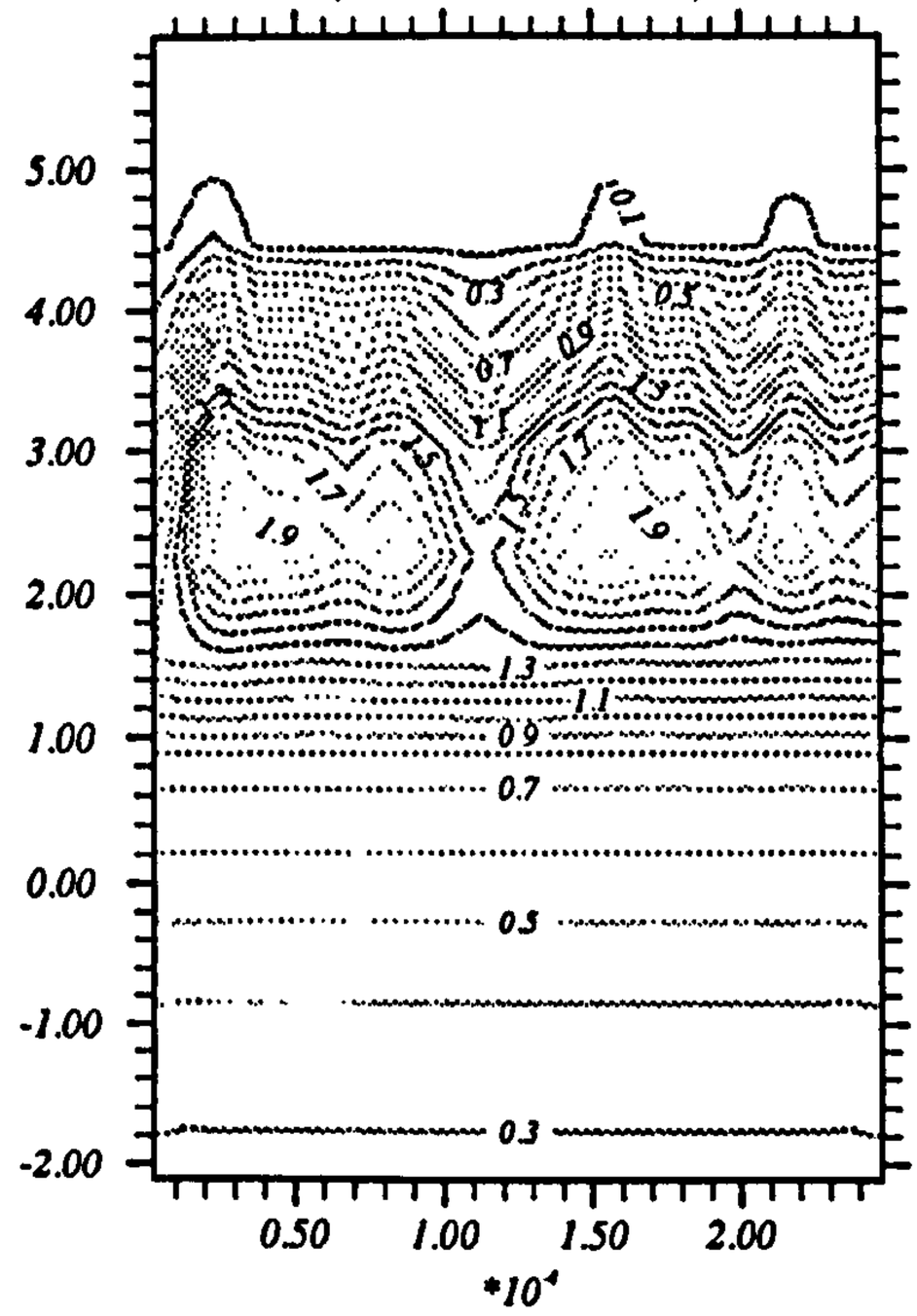

DENSITY MAP AT 300PS
(NO MAG. FIELD)

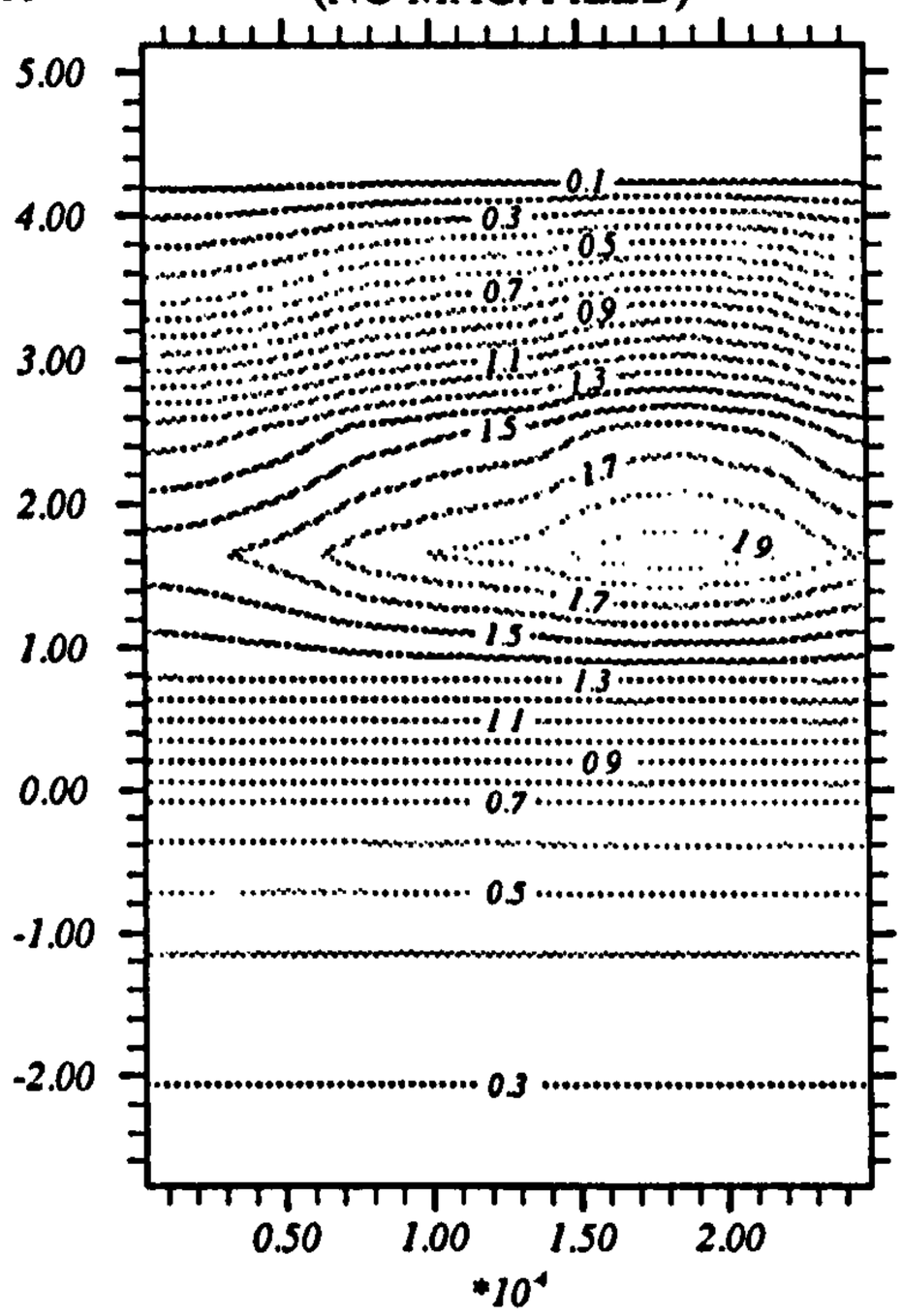

DENSITY MAP AT 300PS
(MAG. FIELD ON)

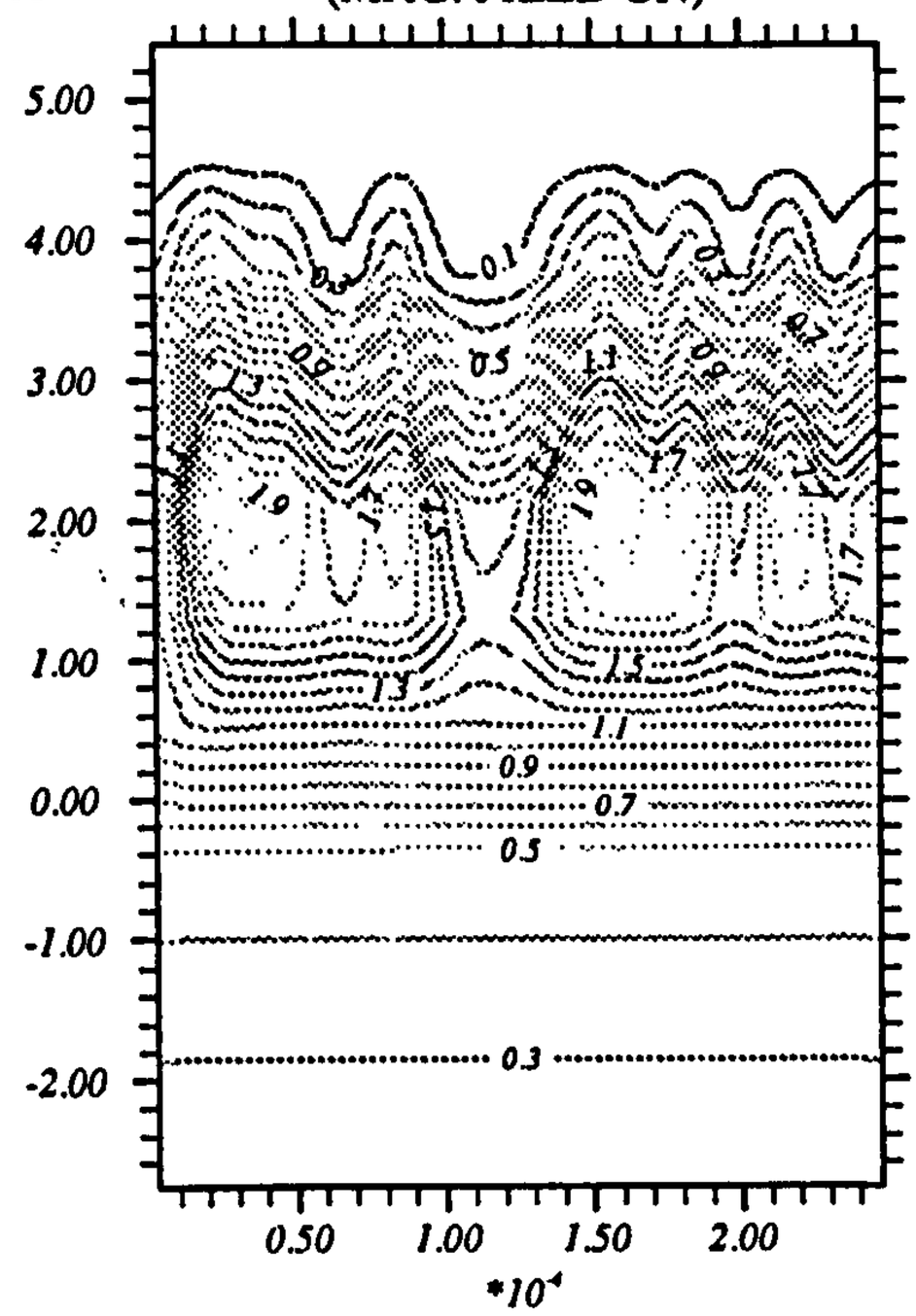

DENSITY MAP AT 350PS
(NO MAG. FIELD)

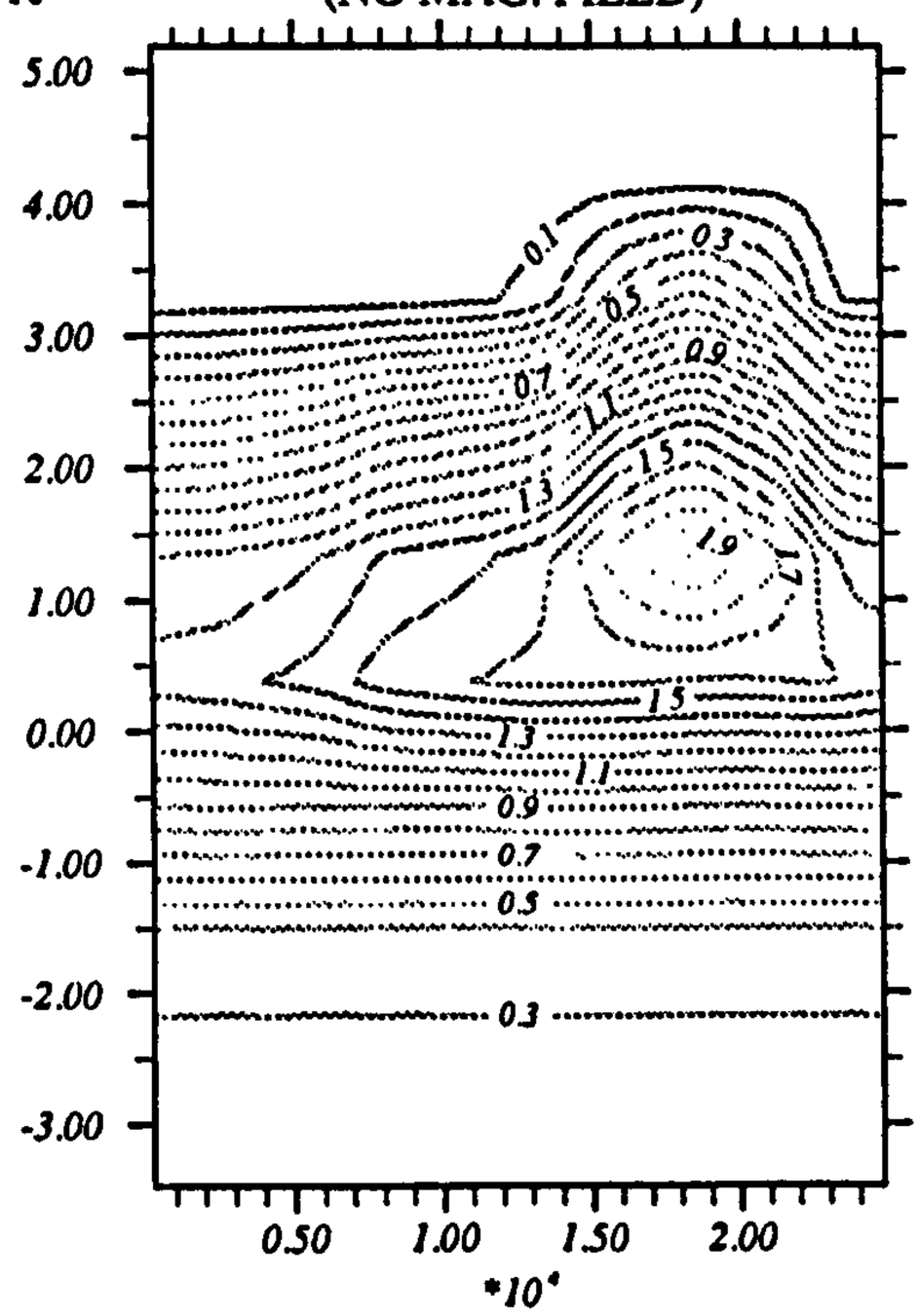

DENSITY MAP AT 350PS
(MAG. FIELD ON)

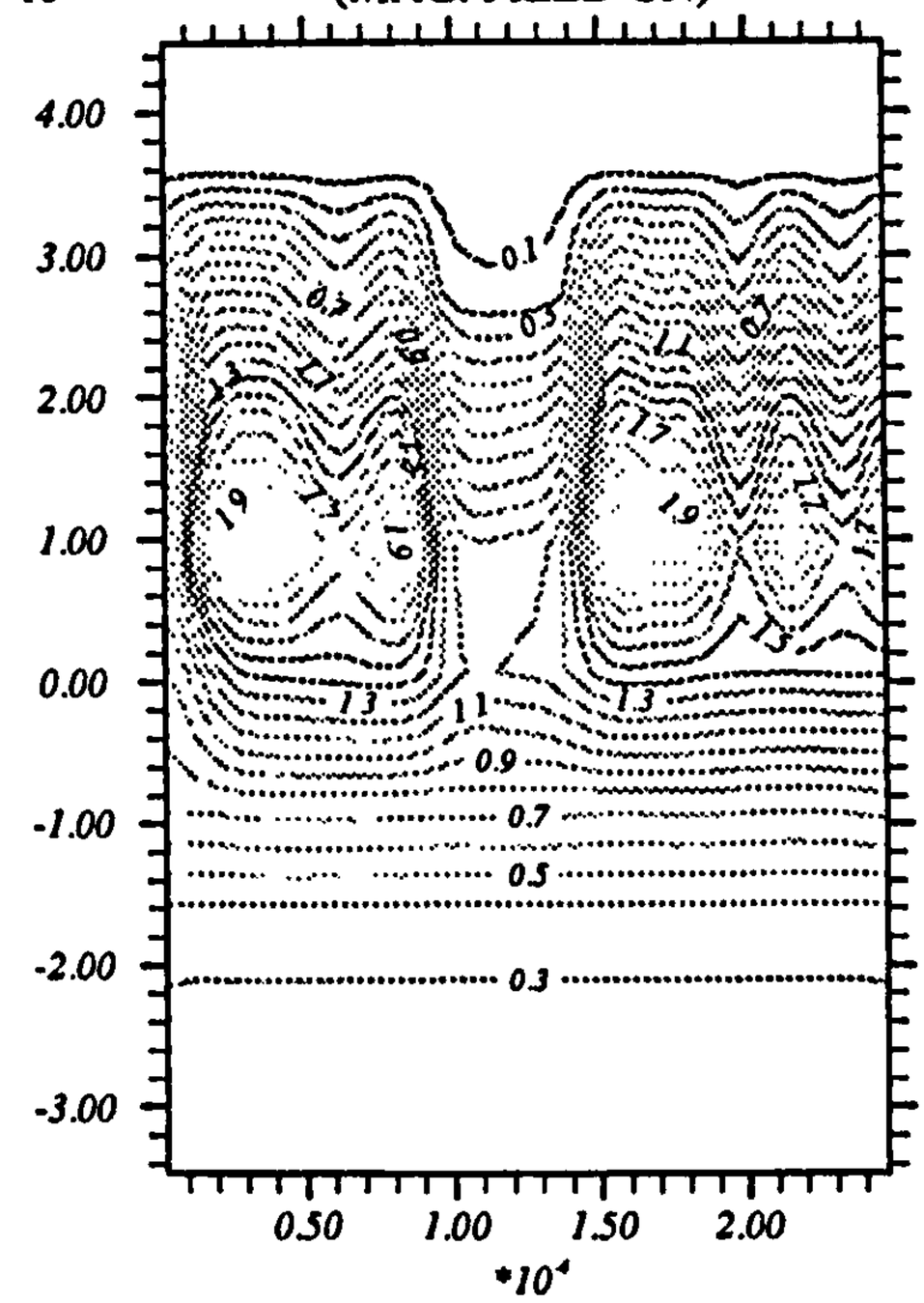

DENSITY MAP AT 400PS
(NO MAG. FIELD)

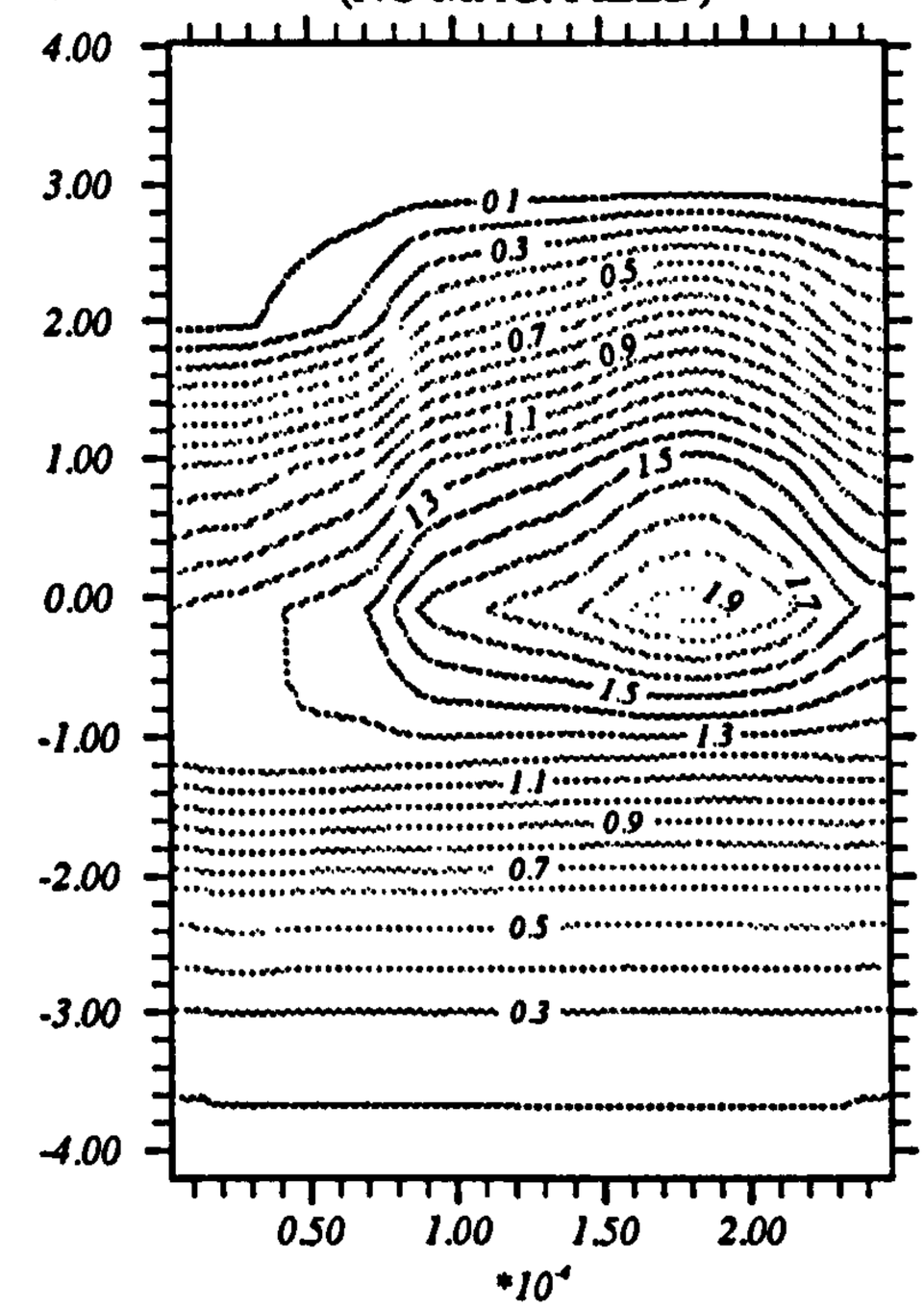

DENSITY MAP AT 400PS
(MAG. FIELD ON)

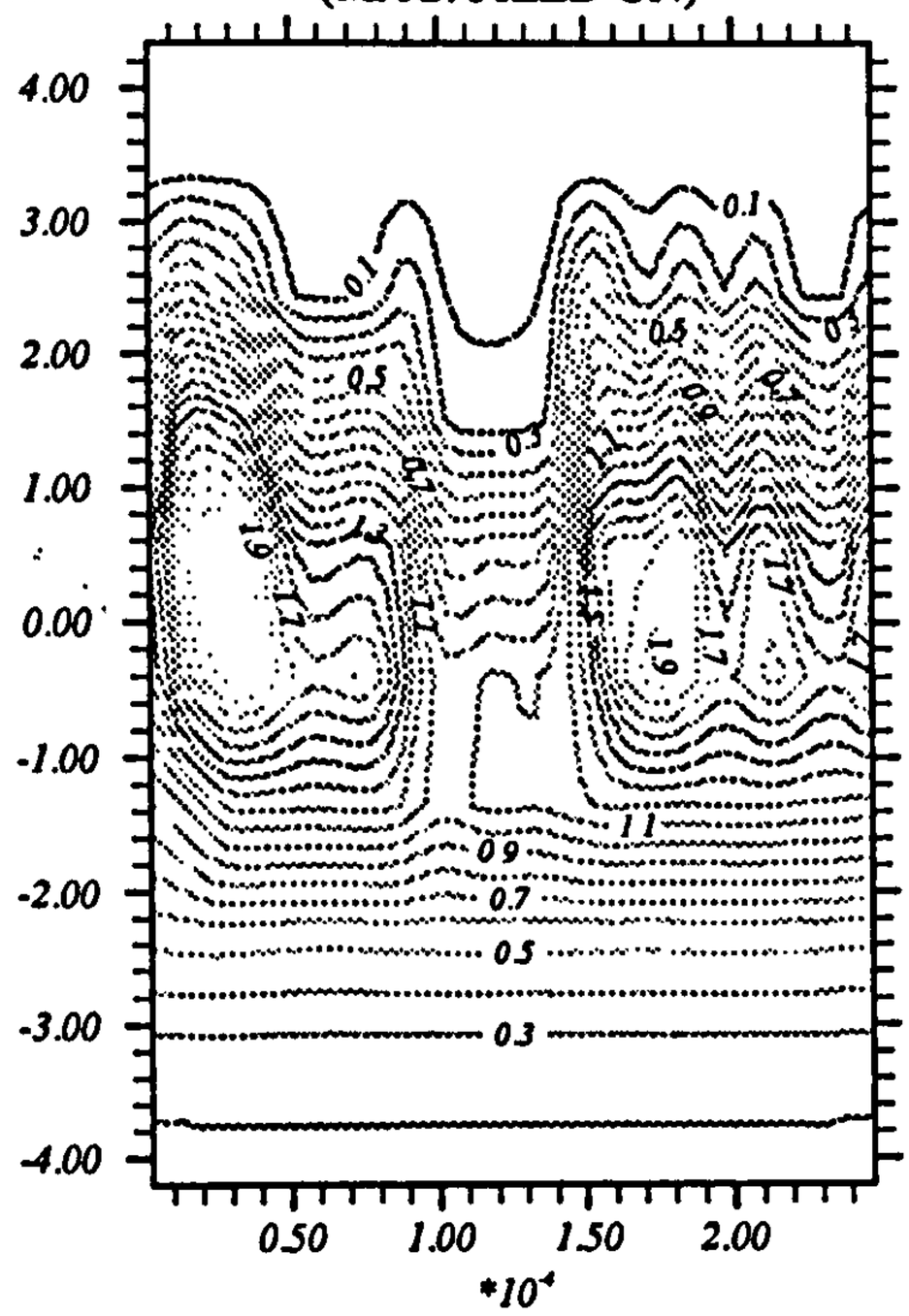

DENSITY MAP AT 450PS
(NO MAG. FIELD)

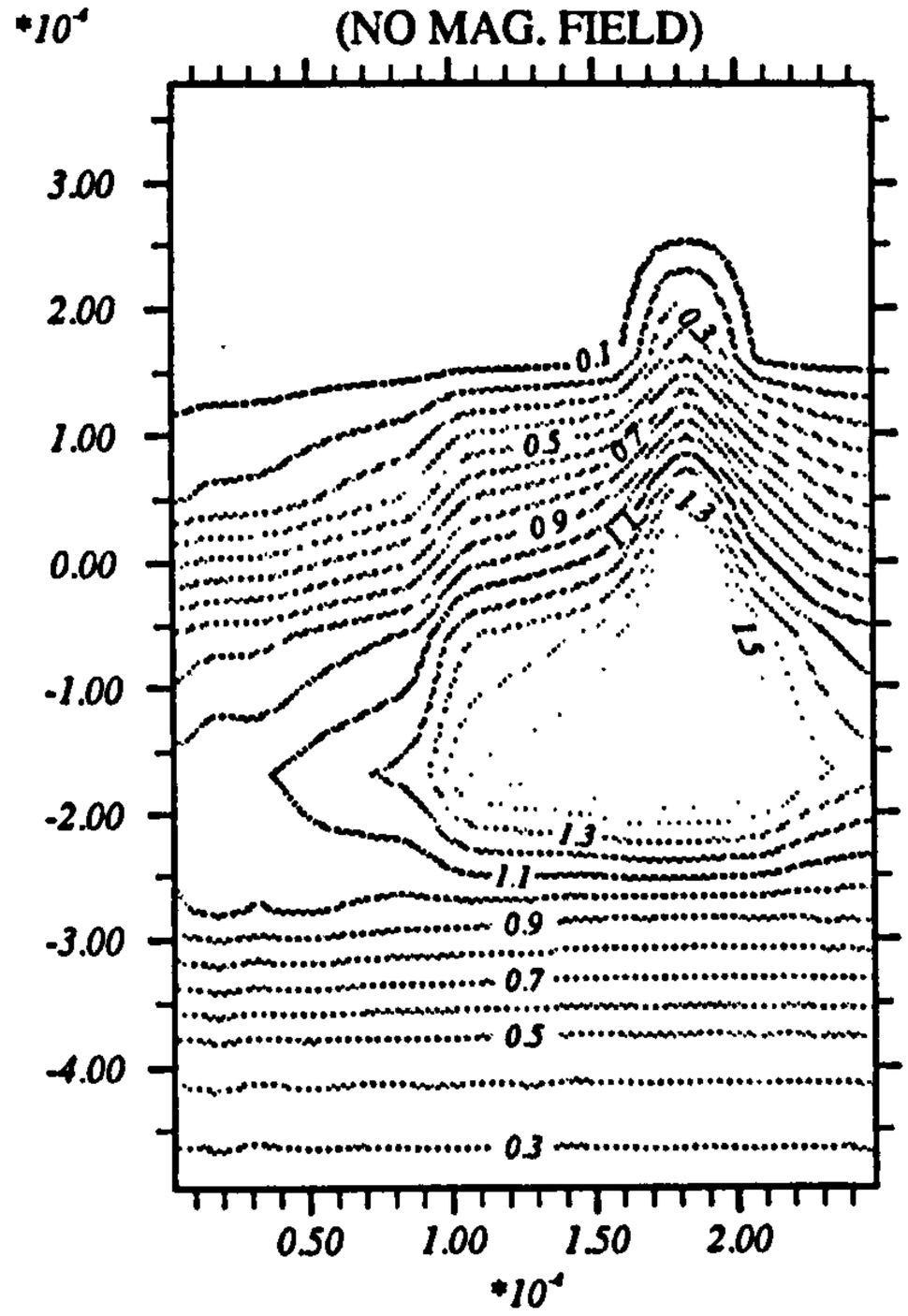

DENSITY MAP AT 450PS
(MAG. FIELD ON)

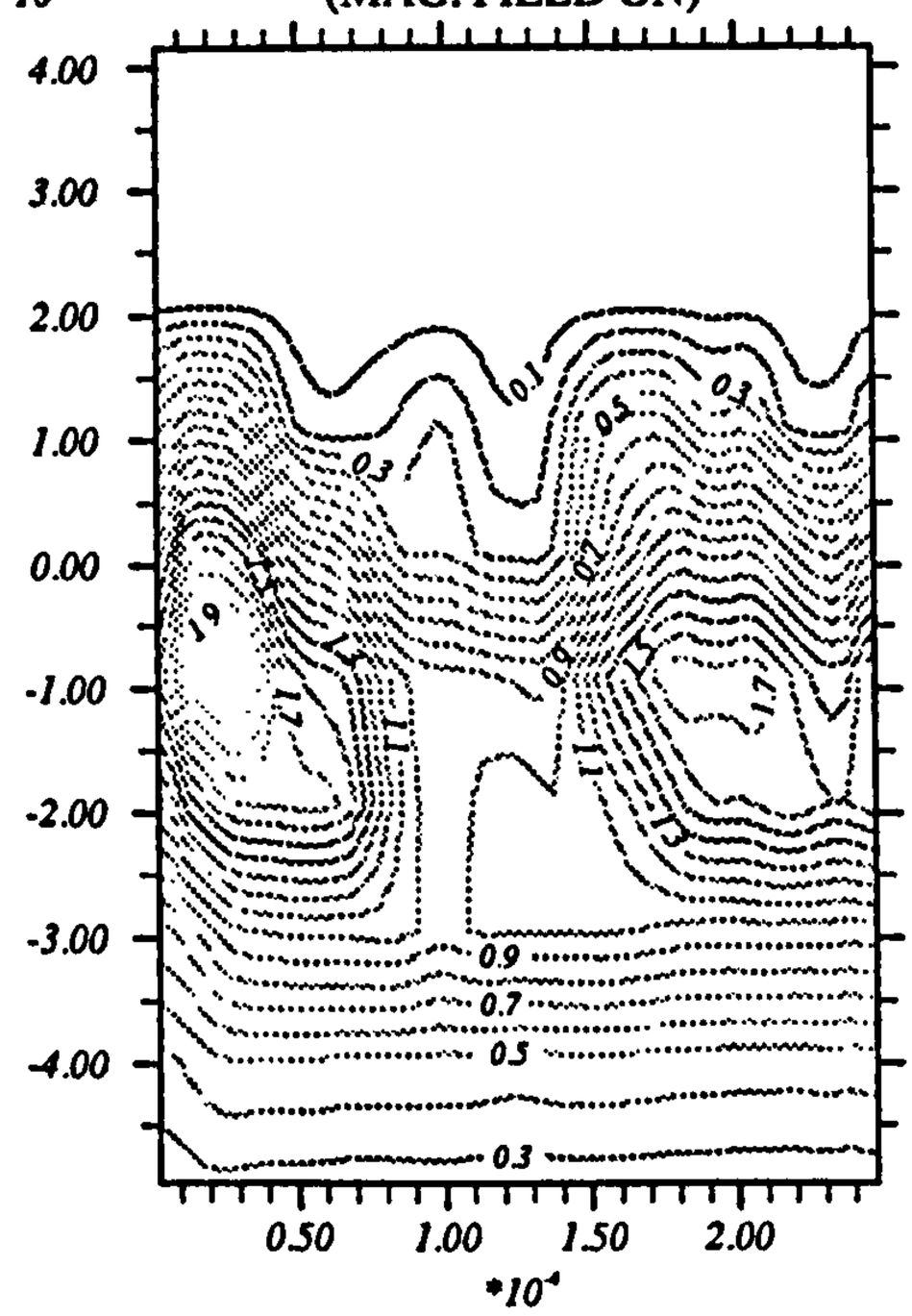

DENSITY MAP AT 500PS
(NO MAG. FIELD)

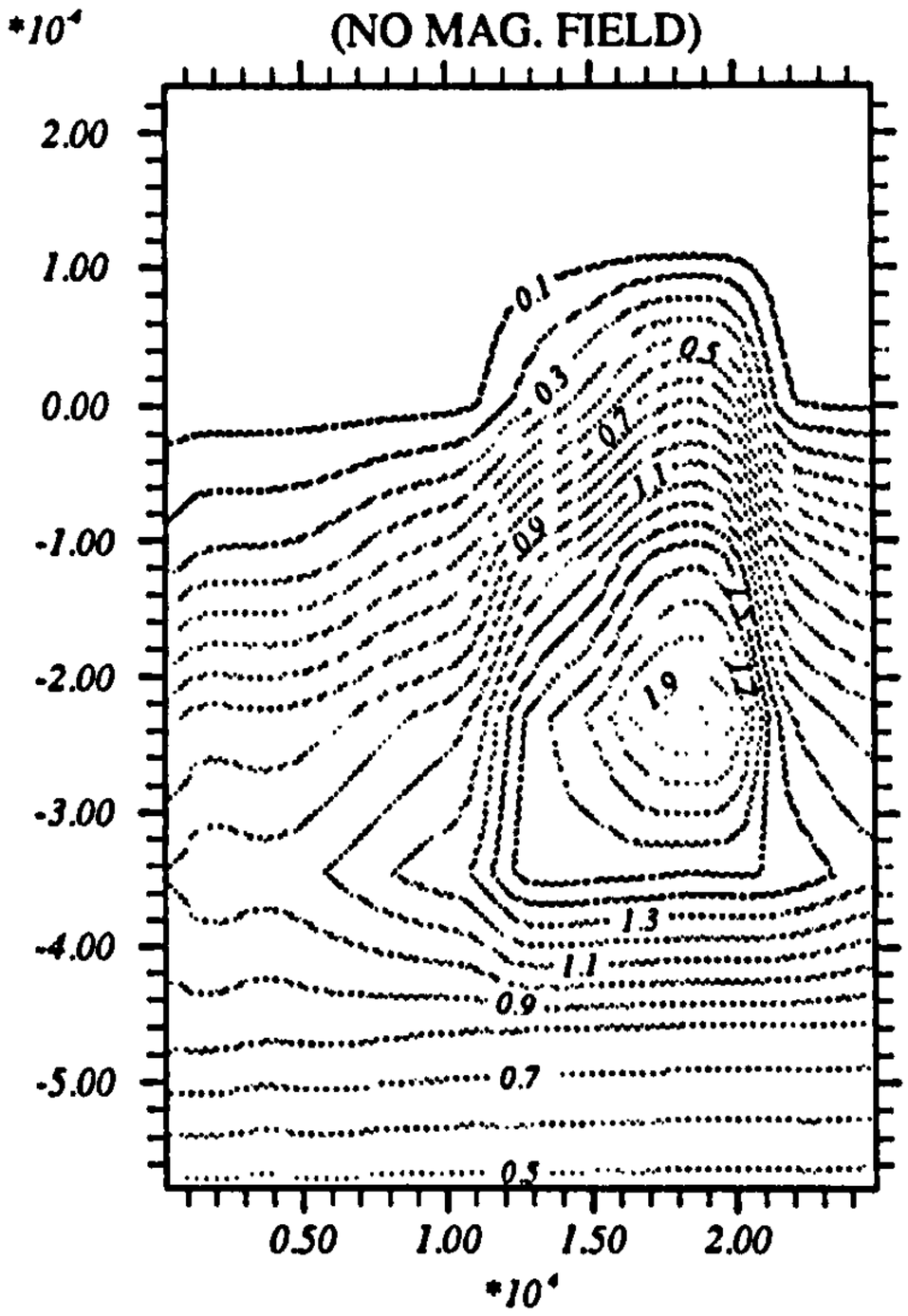

DENSITY MAP AT 500PS
(MAG. FIELD ON)

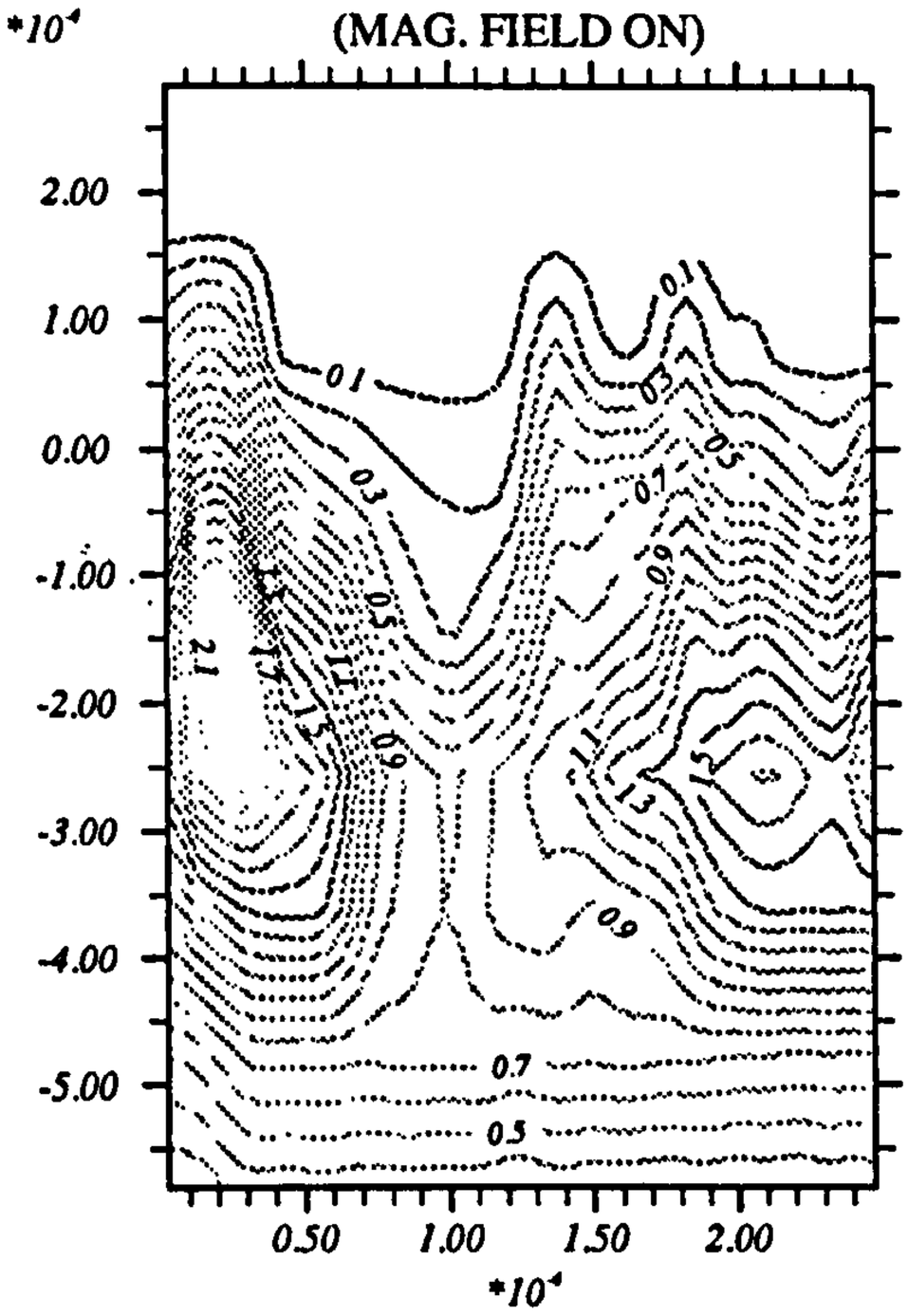

DENSITY MAP AT 550PS
(NO MAG. FIELD)

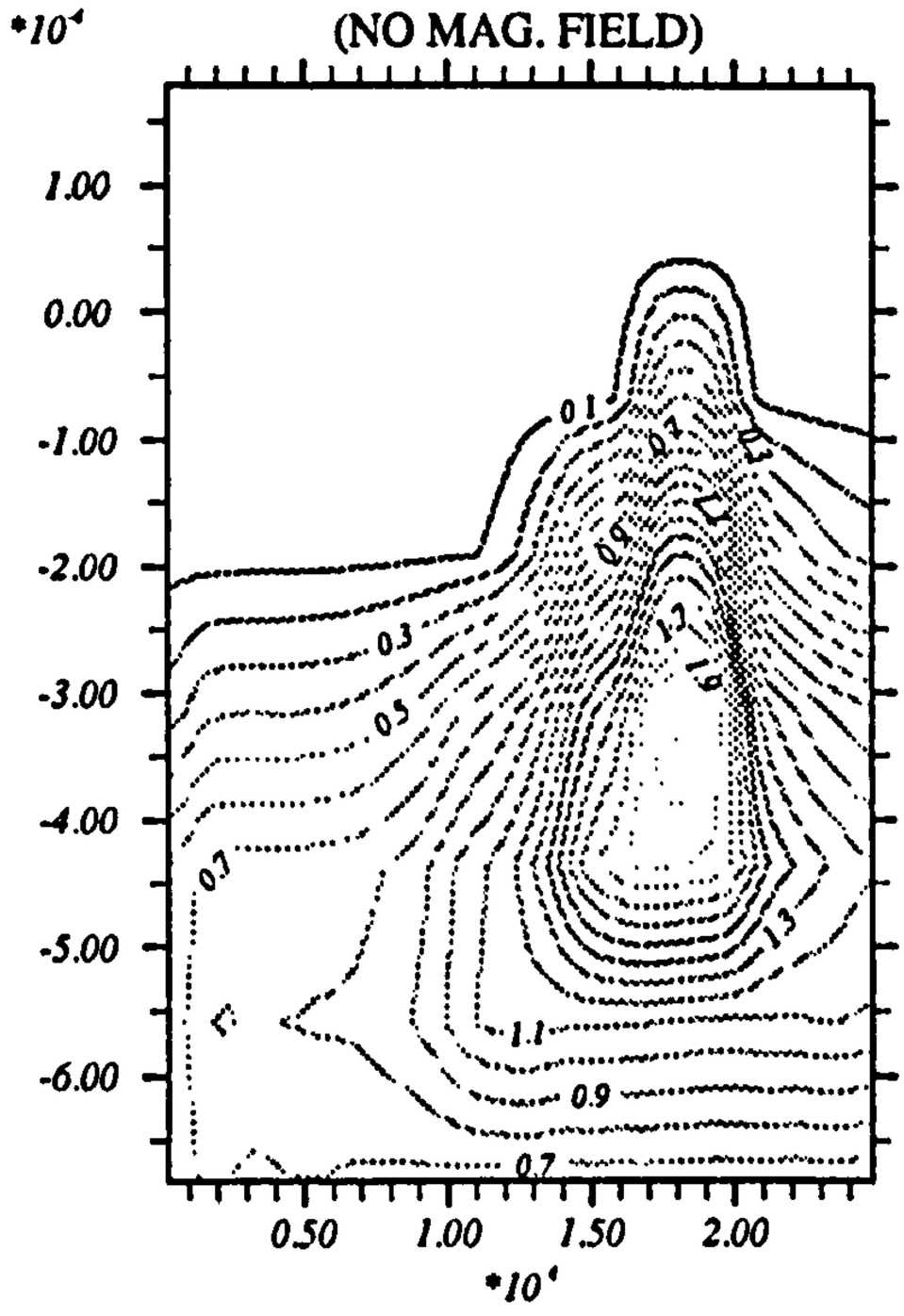

DENSITY MAP AT 550PS
(MAG. FIELD ON)

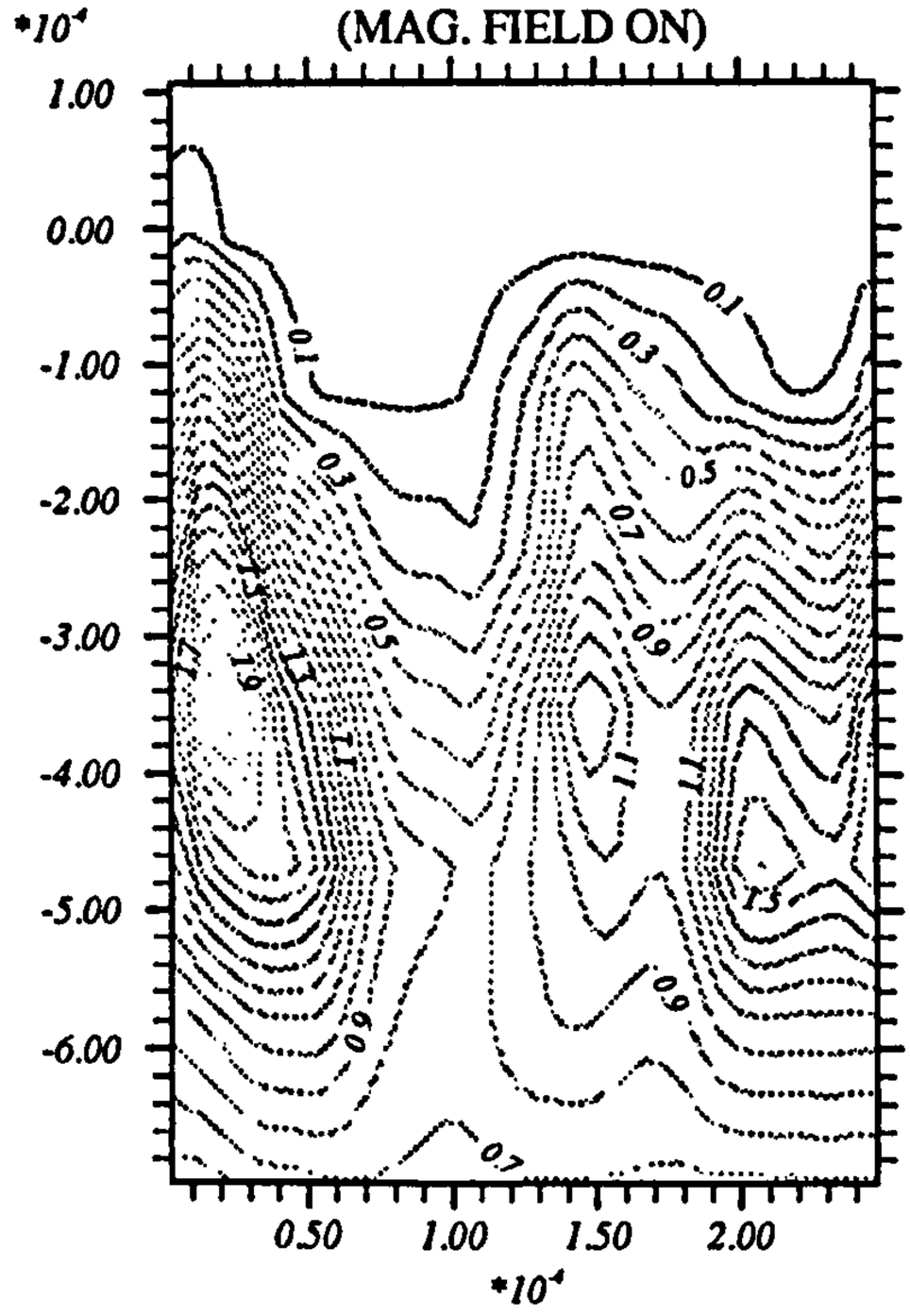

DENSITY MAP AT 600PS
(NO MAG. FIELD)

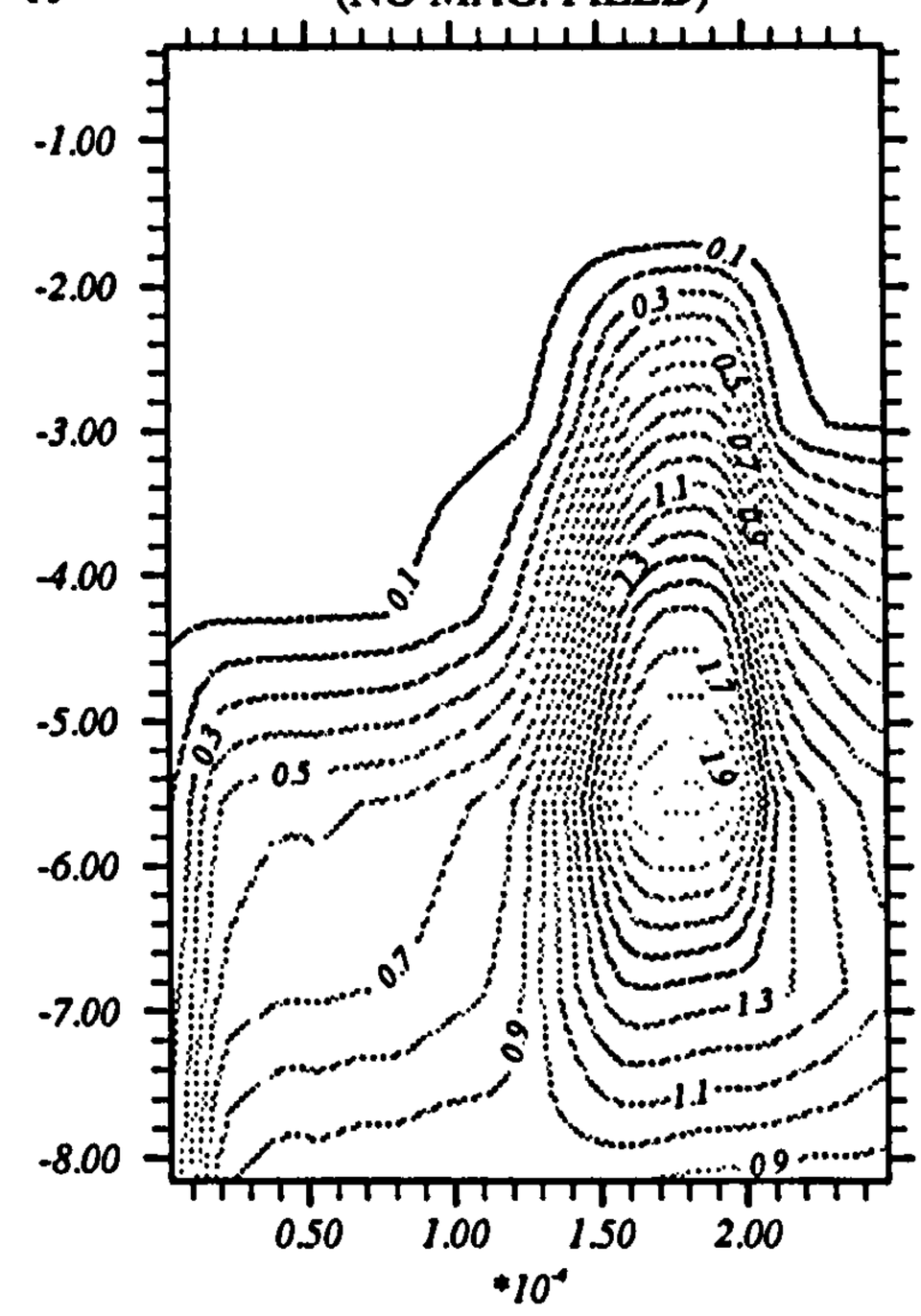

DENSITY MAP AT 600PS
(MAG. FIELD ON)

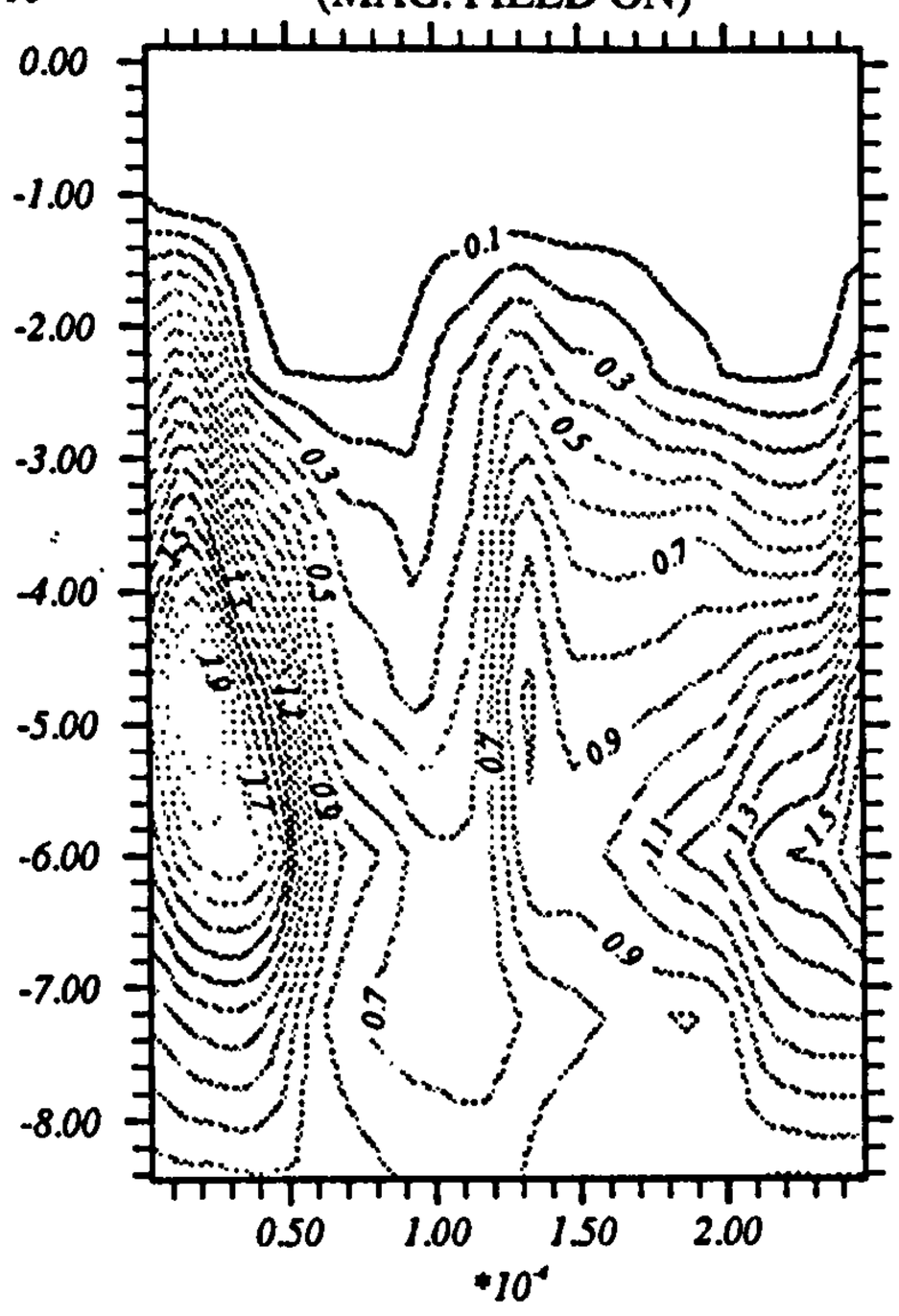

DENSITY MAP AT 650PS
(NO MAG. FIELD)

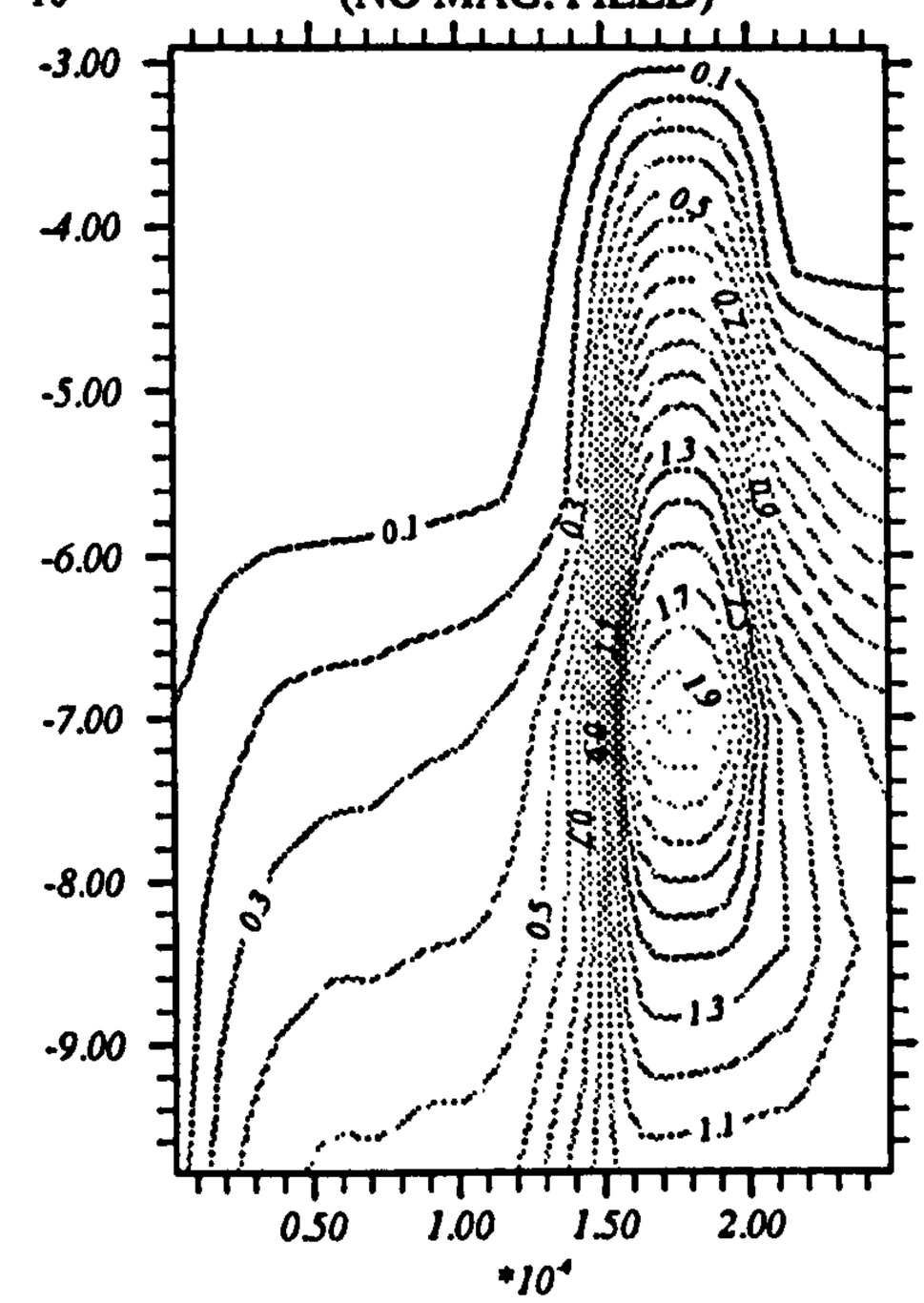

DENSITY MAP AT 650PS
(MAG. FIELD ON)

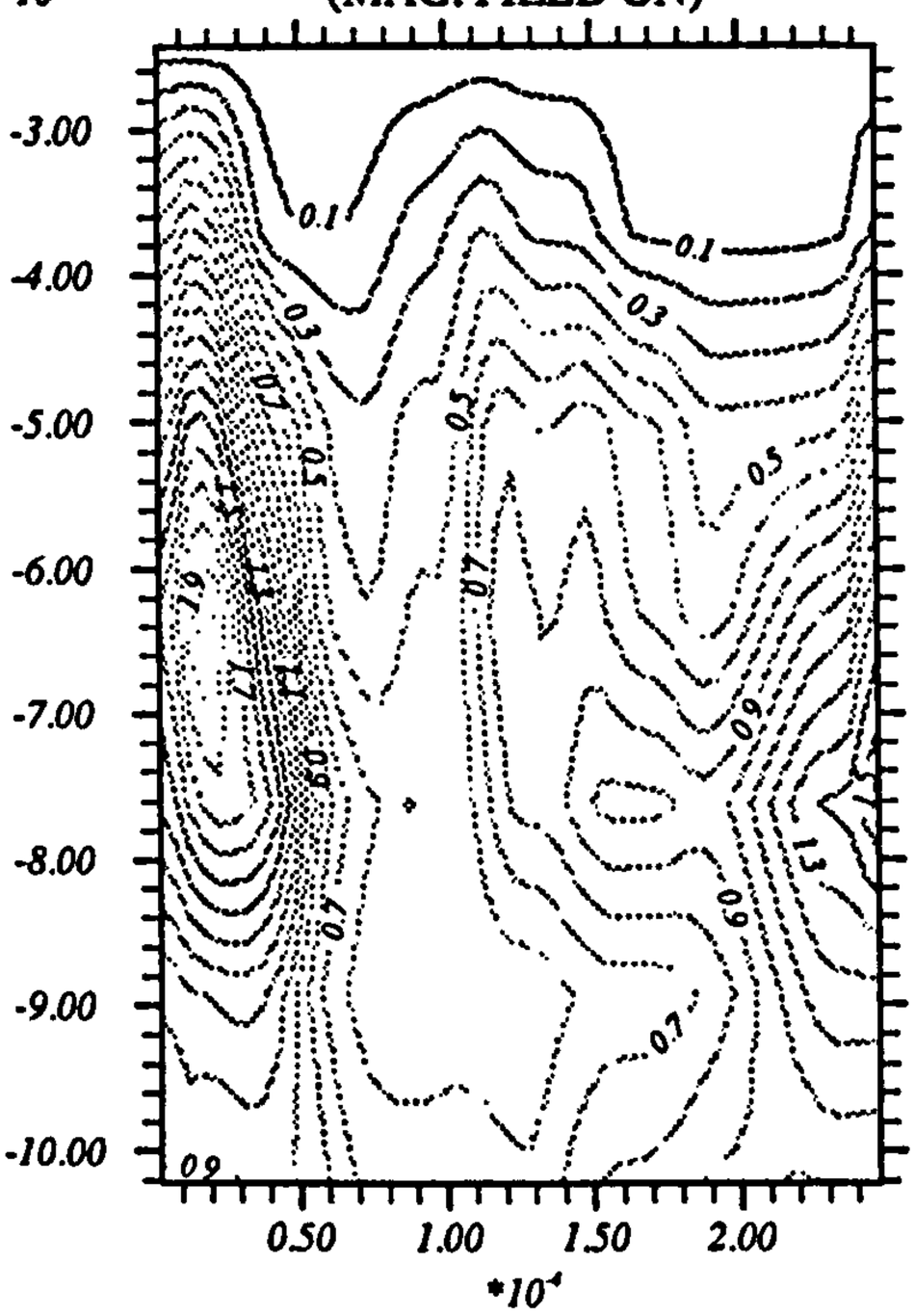

DENSITY MAP AT 700PS
(NO MAG. FIELD)

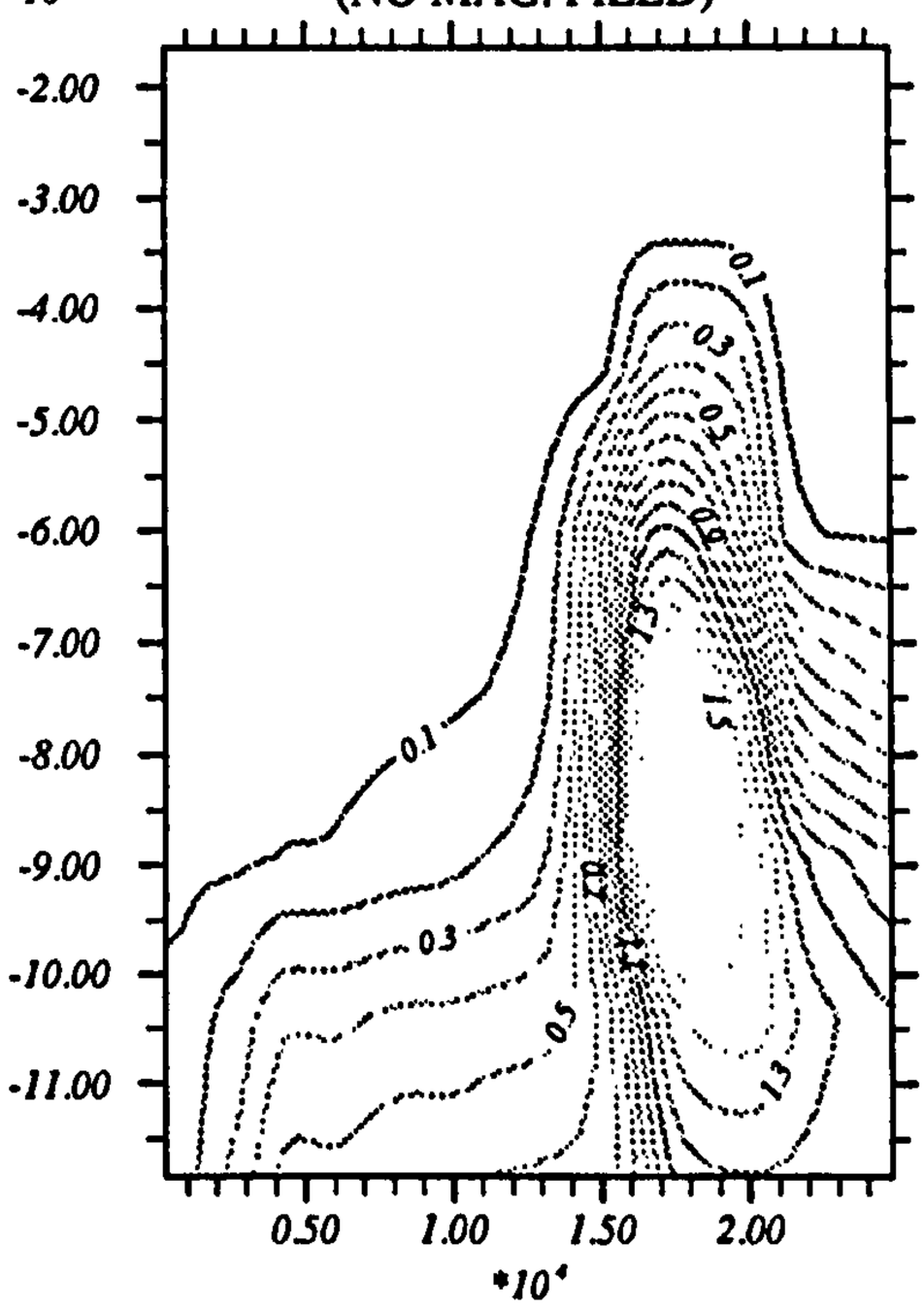

DENSITY MAP AT 700PS
(MAG. FIELD ON)

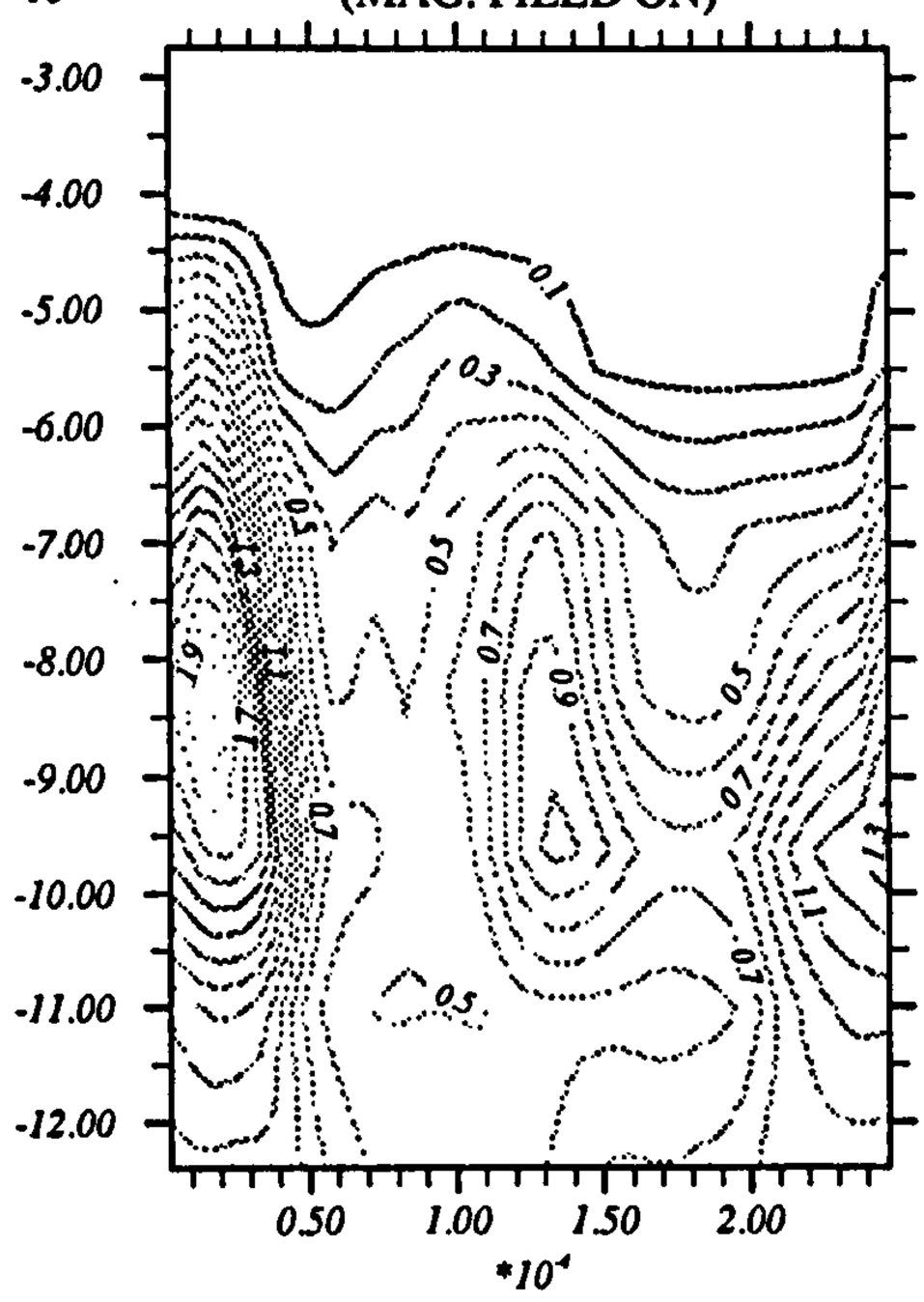

DENSITY MAP AT 750PS
(NO MAG. FIELD)

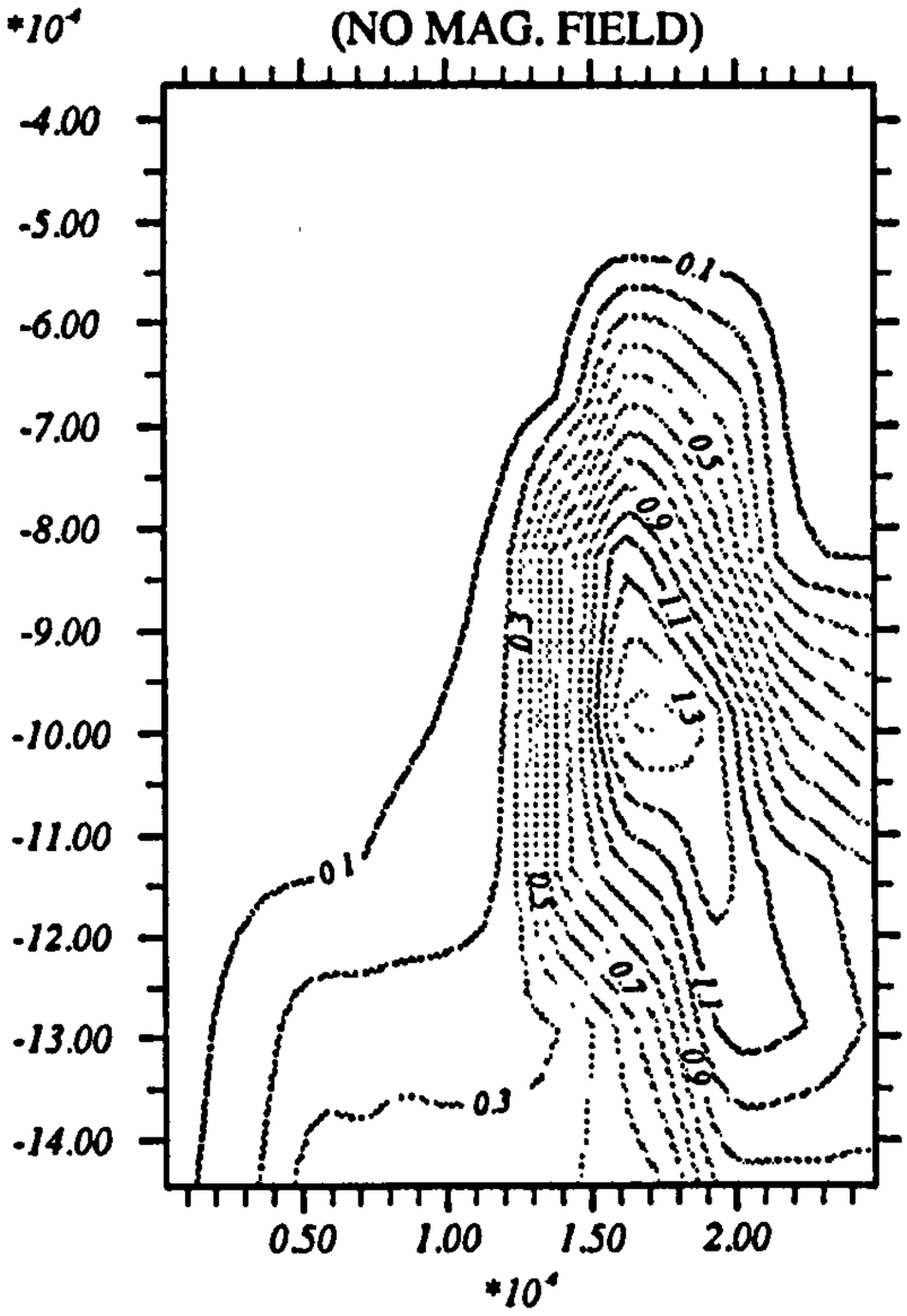

DENSITY MAP AT 750PS
(MAG. FIELD ON)

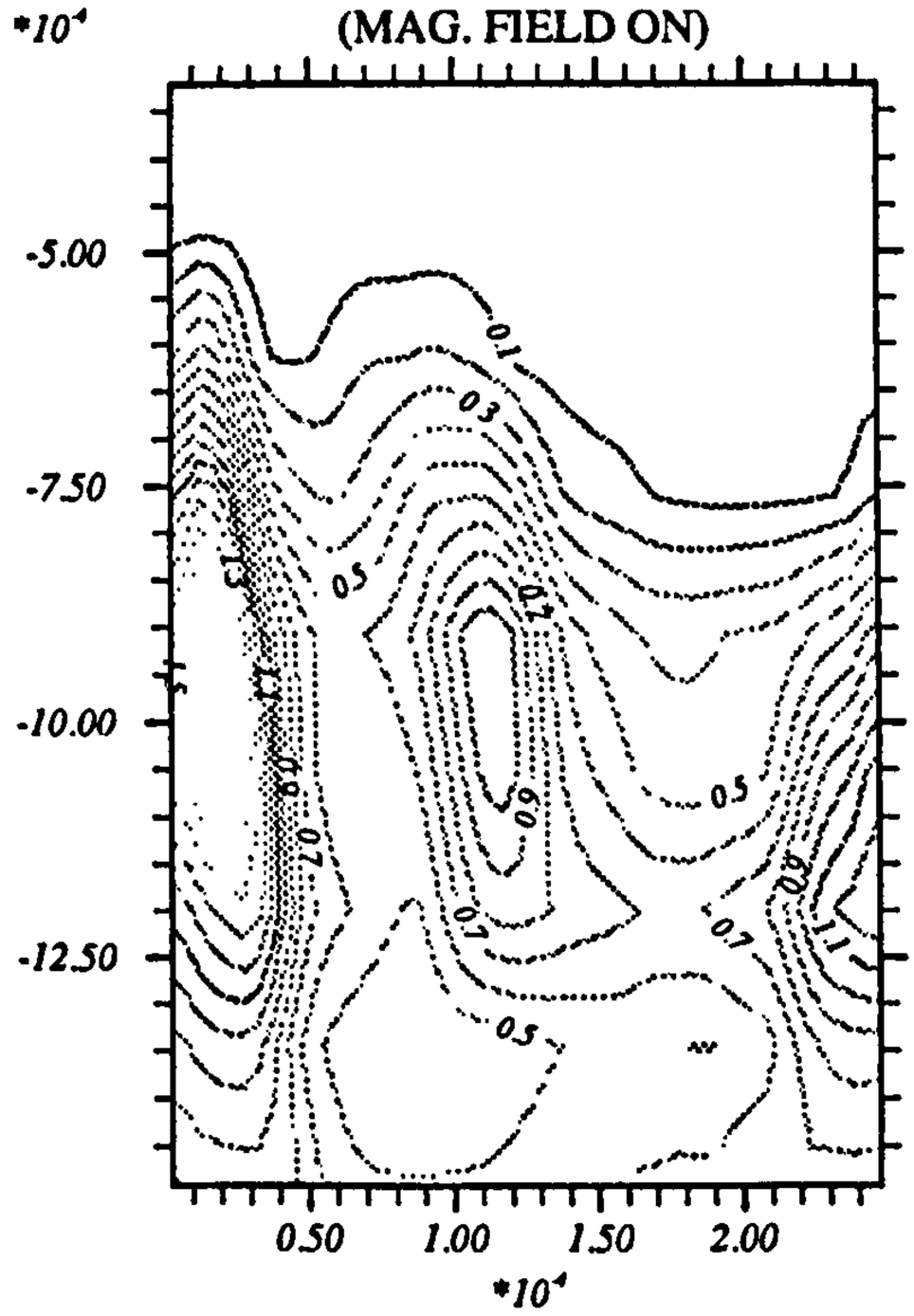

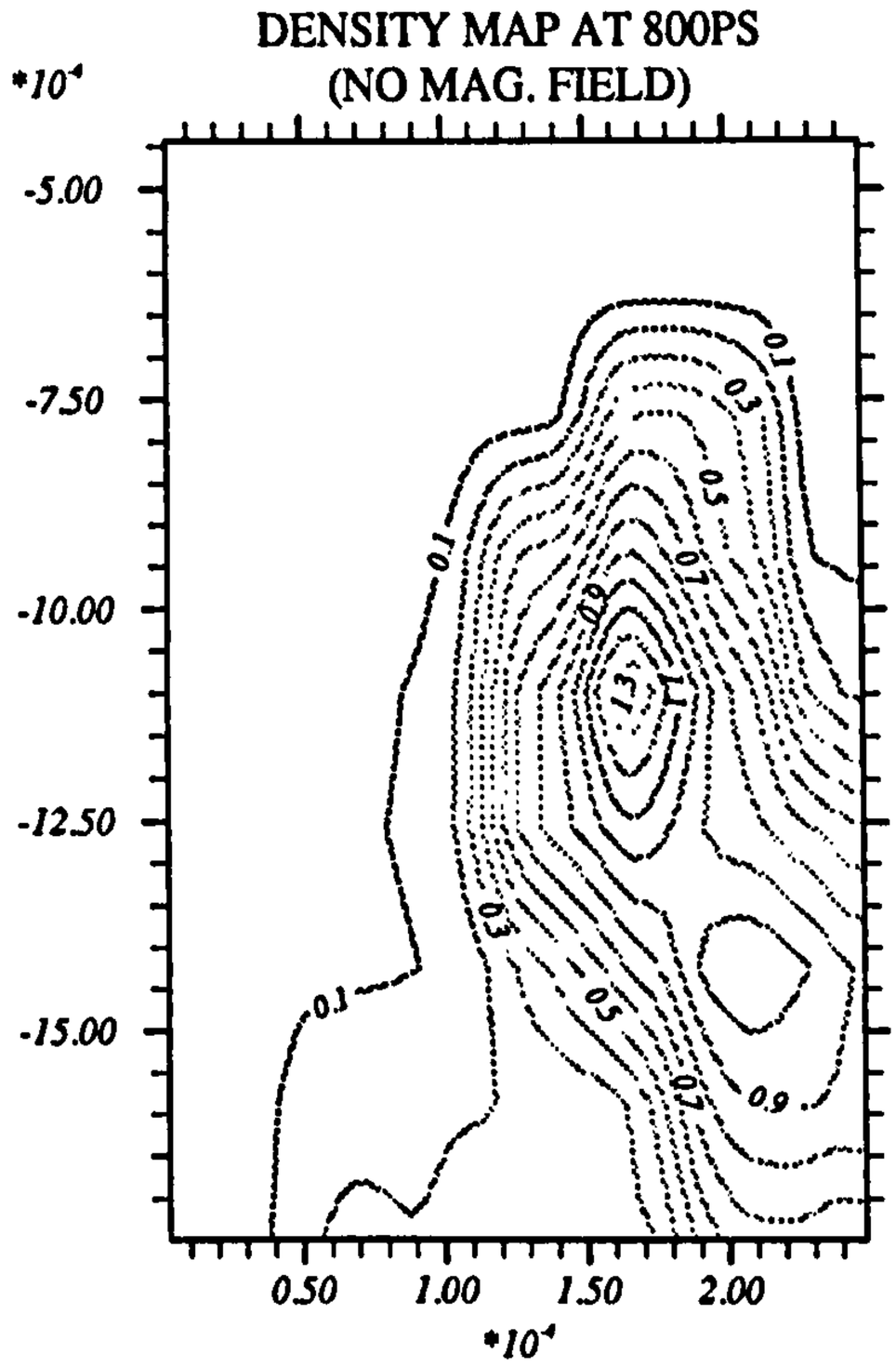
DENSITY MAP AT 800PS
(NO MAG. FIELD)
*10⁻⁴
-5.00
-7.50
-10.00
-12.50
-15.00
0.50
1.00
1.50
2.00
*10⁻⁴
0.1
0.3
0.5
0.7
0.9
1.1
1.3

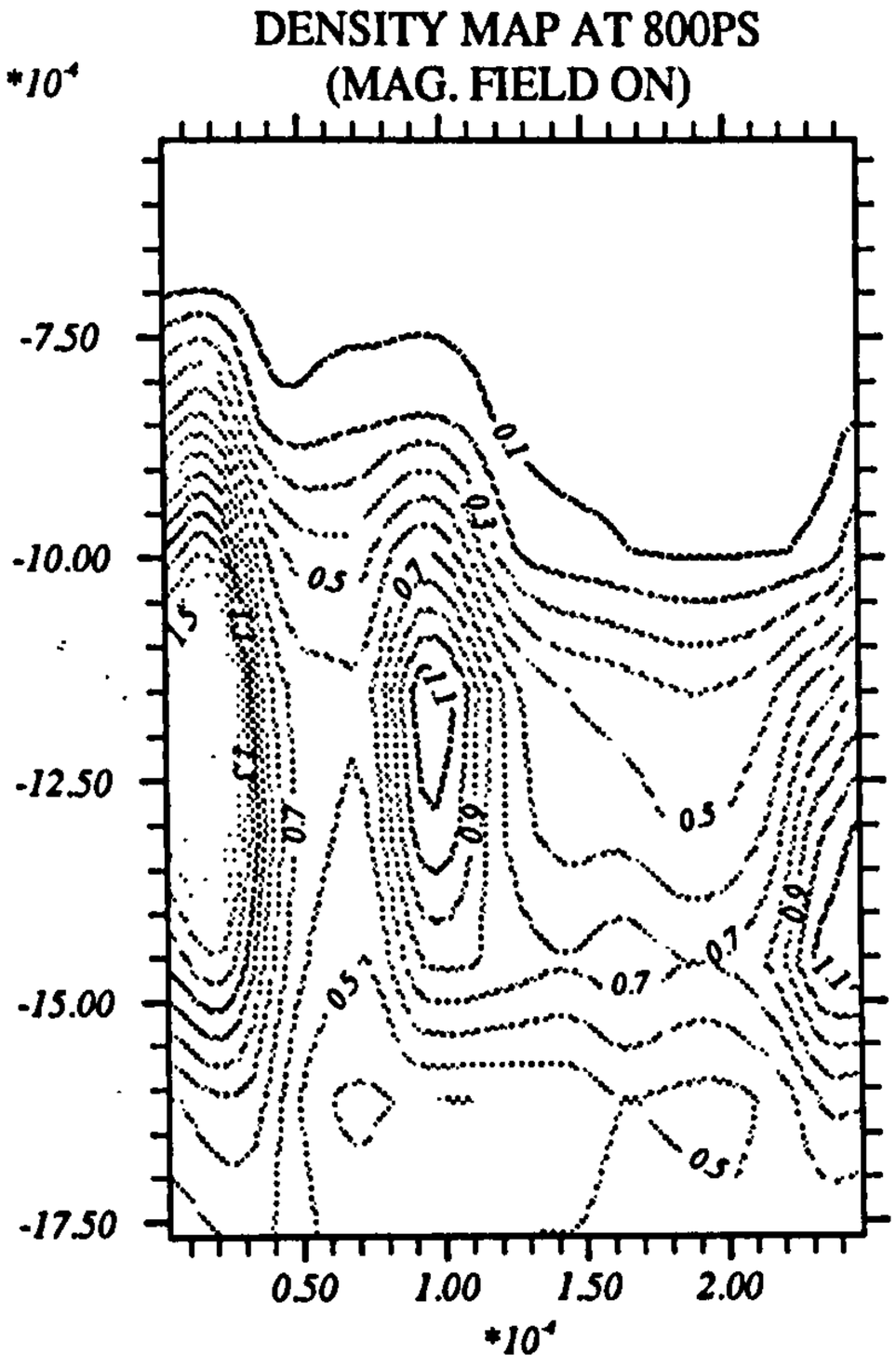
DENSITY MAP AT 800PS
(MAG. FIELD ON)
*10⁻⁴
-7.50
-10.00
-12.50
-15.00
-17.50
0.50
1.00
1.50
2.00
*10⁻⁴
0.1
0.3
0.5
0.7
0.9
1.1
1.3
1.5

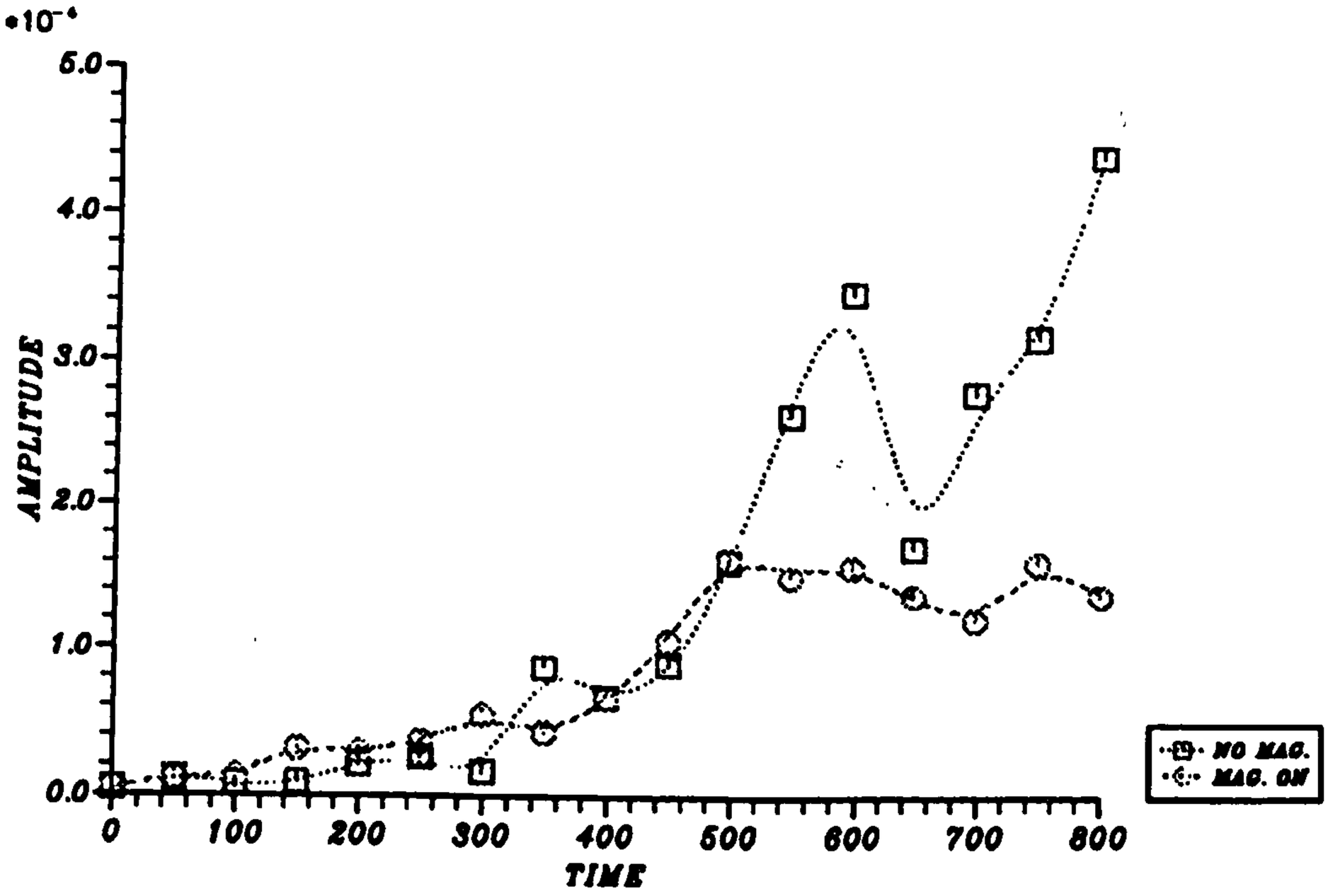

Figure 5.11: Amplitude vs time graph for the target of thickness $5 \cdot 0 \mu m$ and radius $2 \cdot 5 \mu m$

these form many loops around the axis which are the source generating shorter wavelength modes in the density contours as discussed previously. These high frequency modes enhance the growth of Rayleigh-Taylor instability in the linear phase over non-magnetic field studies.

5.5 SUMMARY OF RESULTS

The maximum field positive (directed out of the paper) and negative (directed into the paper) as a function of time are shown in figure $5 \cdot 13$ and $5 \cdot 14$ respectively. The fields are of high value in the early stages and gradually decrease until they reach to only few hundred killogauss at 800ps. A maximum of $1 \cdot 8$ MG is generated in both positive and negative directions for the target ($5 \cdot 0 \times 5 \cdot 0$) and for the other two targets this value is about $1 \cdot 6$ MG.

In the density contour maps it was observed that the magnetic fields enhance the growth of Rayleigh-Taylor instability. In that context it was necessary to investigate the size of the plasma beta, the ratio of magnetic pressure to particle

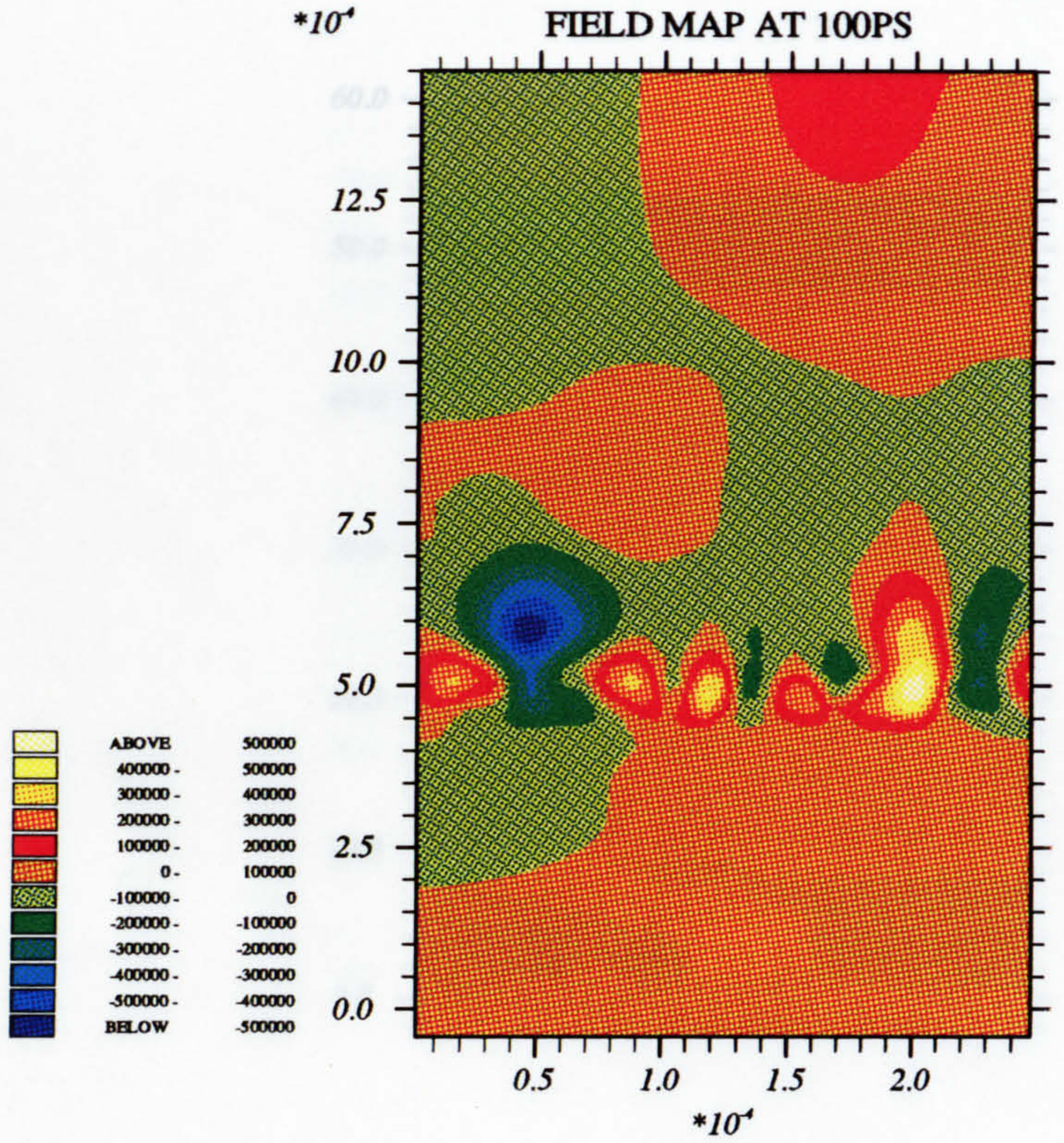

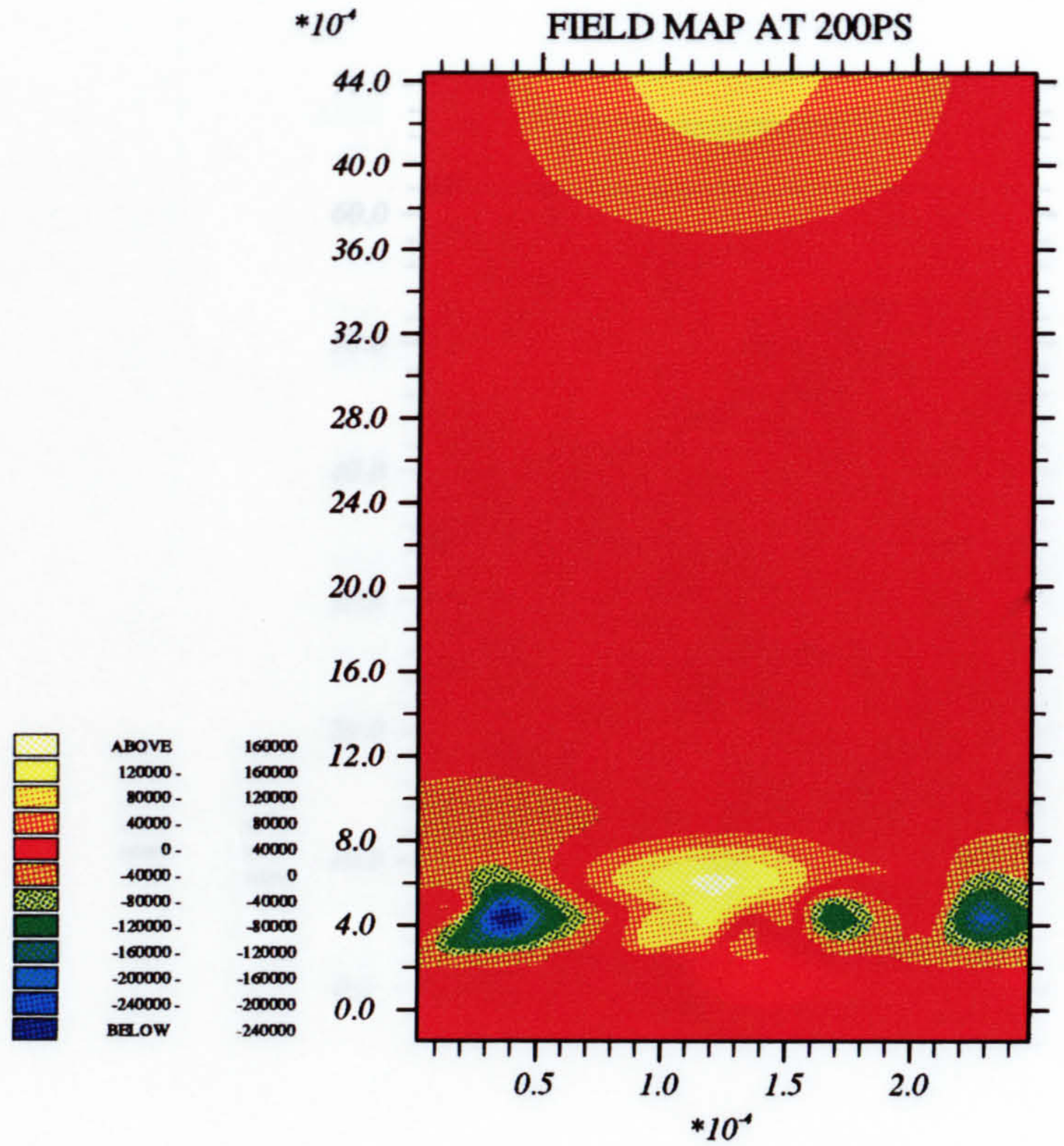

Figure 5.12: Magnetic field map for the target (5.0 μ m x 2.5 μ m) in axial and radial directions.

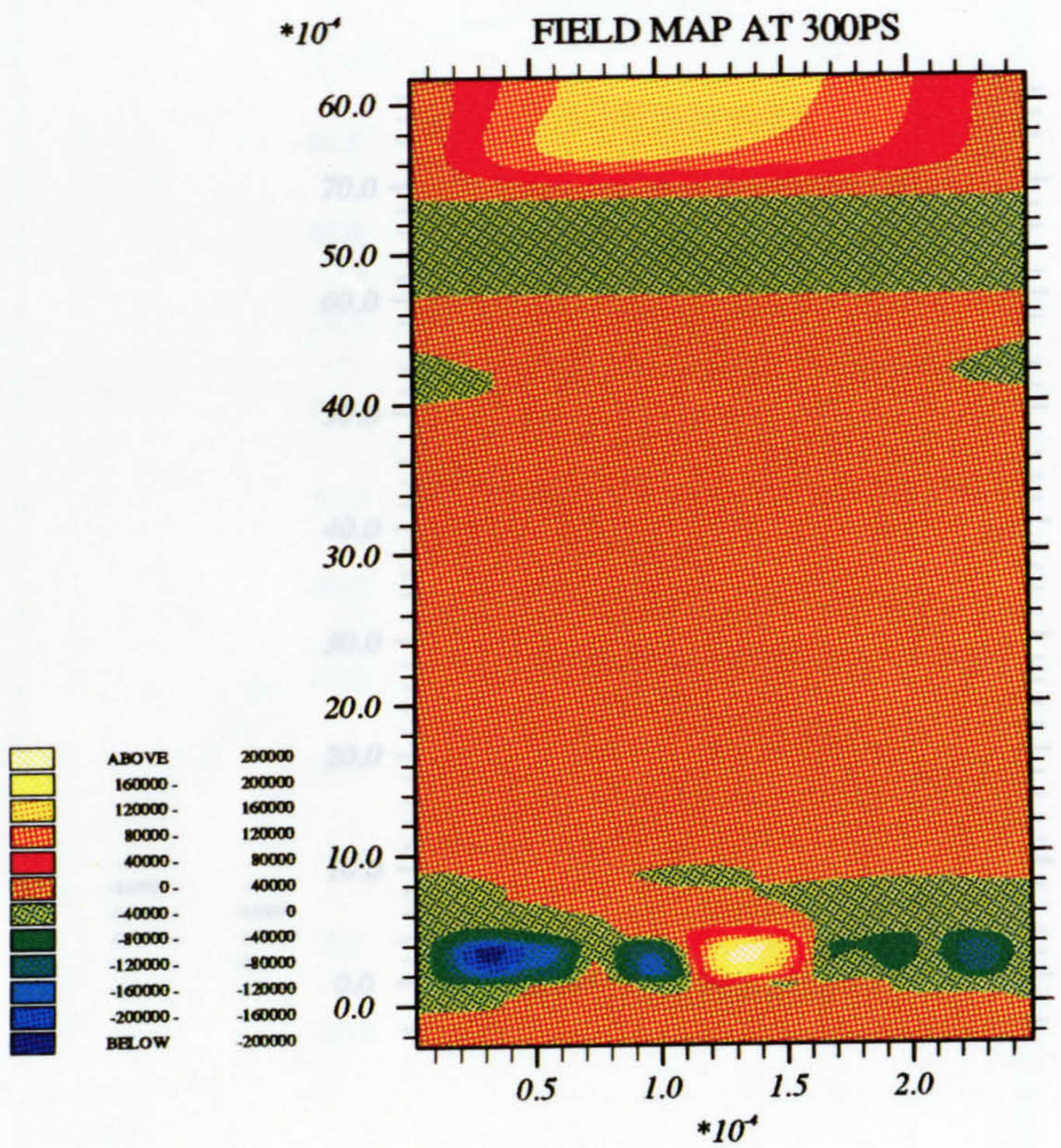
*10⁻⁴
FIELD MAP AT 300PS
60.0
50.0
40.0
30.0
20.0
10.0
0.0
0.5
1.0
1.5
2.0
*10⁻⁴
ABOVE 200000
160000 - 200000
120000 - 160000
80000 - 120000
40000 - 80000
0 - 40000
-40000 - 0
-80000 - -40000
-120000 - -80000
-160000 - -120000
-200000 - -160000
BELOW -200000

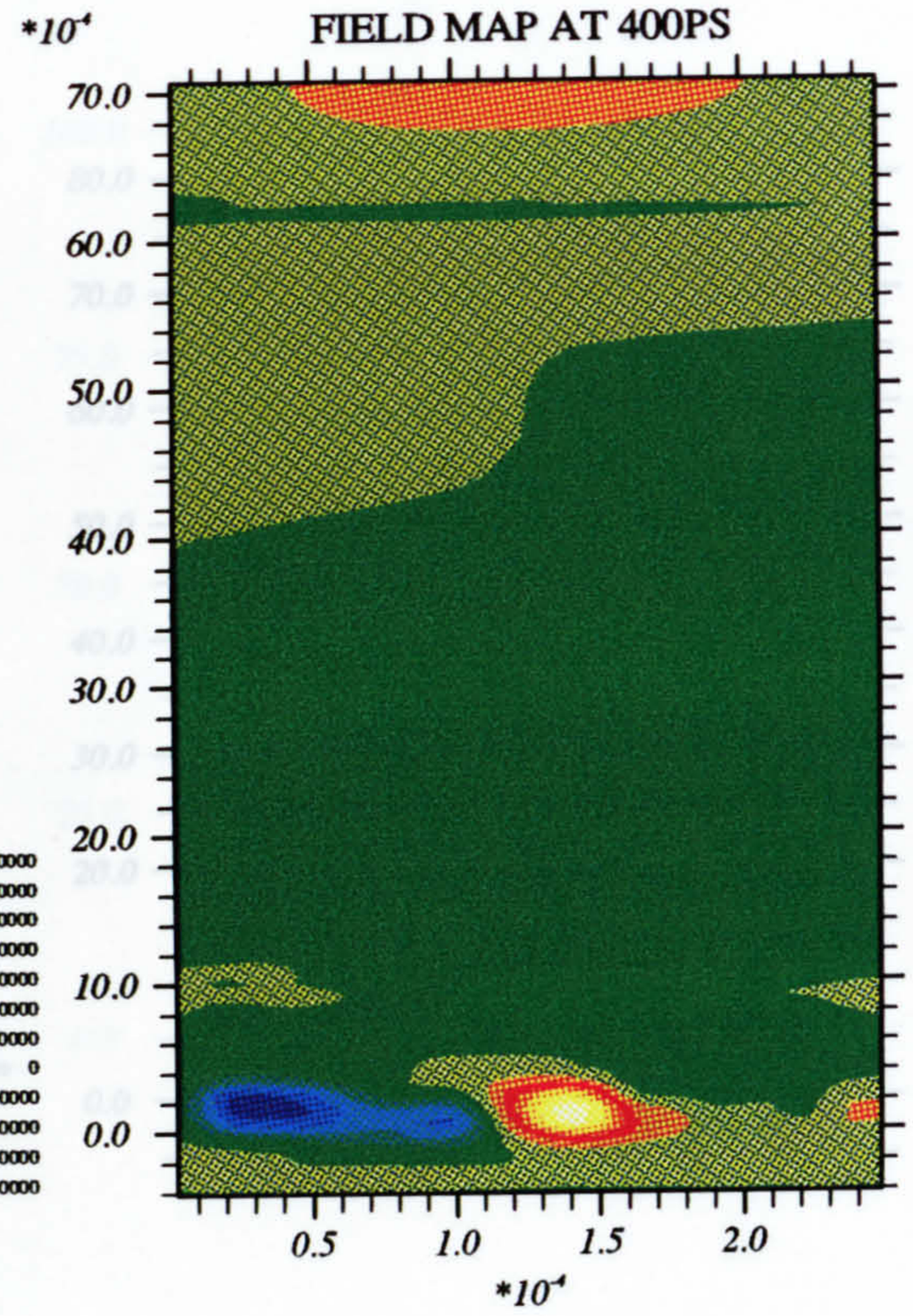
*10⁻⁴
FIELD MAP AT 400PS
70.0
60.0
50.0
40.0
30.0
20.0
10.0
0.0
0.5
1.0
1.5
2.0
*10⁻⁴
ABOVE 420000
350000 - 420000
280000 - 350000
210000 - 280000
140000 - 210000
70000 - 140000
0 - 70000
-70000 - 0
-140000 - -70000
-210000 - -140000
-280000 - -210000
BELOW -280000

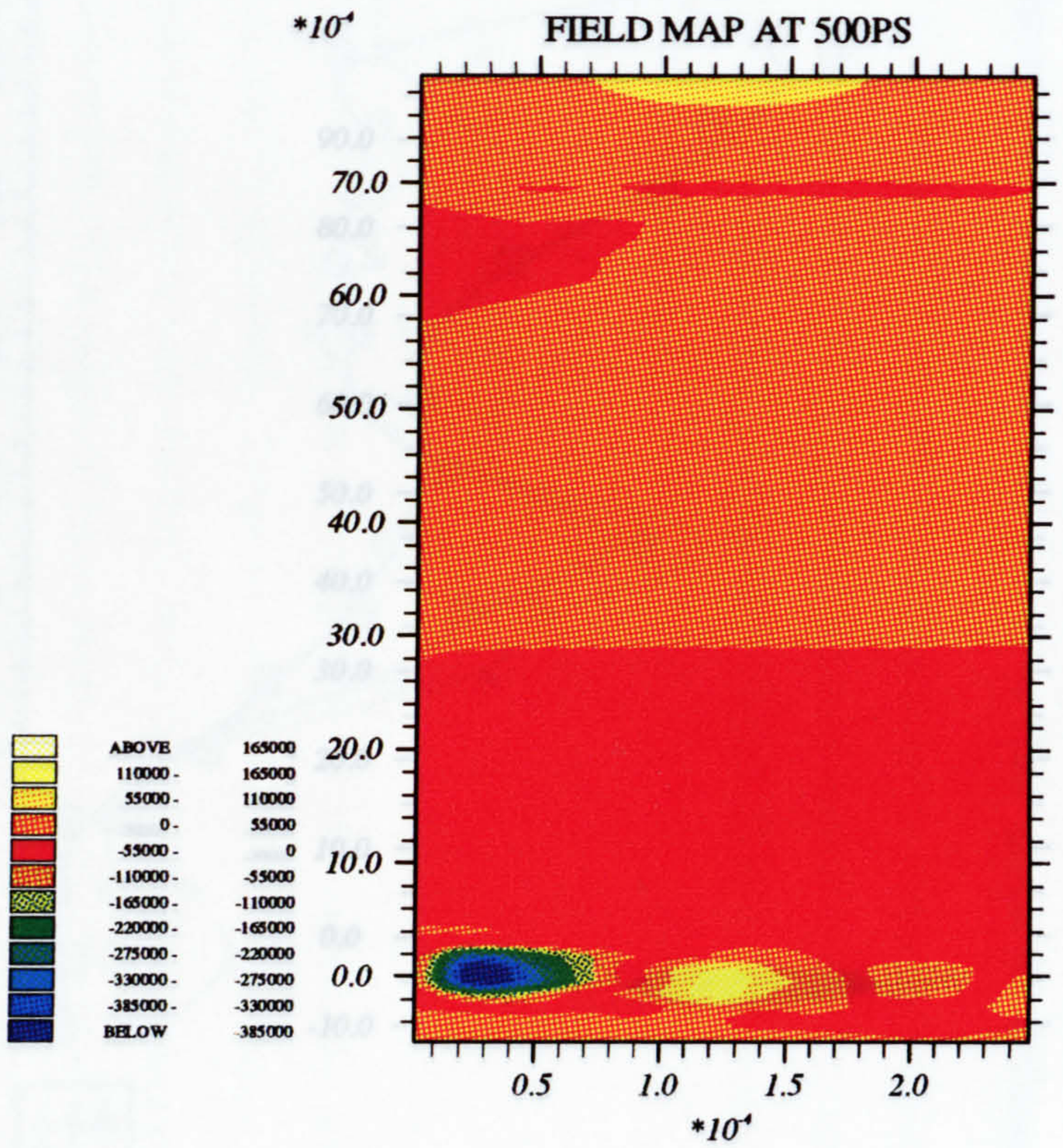
*10⁻⁴
FIELD MAP AT 500PS
70.0
60.0
50.0
40.0
30.0
20.0
10.0
0.0
0.5
1.0
1.5
2.0
*10⁻⁴
ABOVE 165000
110000 - 165000
55000 - 110000
0 - 55000
-55000 - 0
-110000 - -55000
-165000 - -110000
-220000 - -165000
-275000 - -220000
-330000 - -275000
-385000 - -330000
BELOW -385000

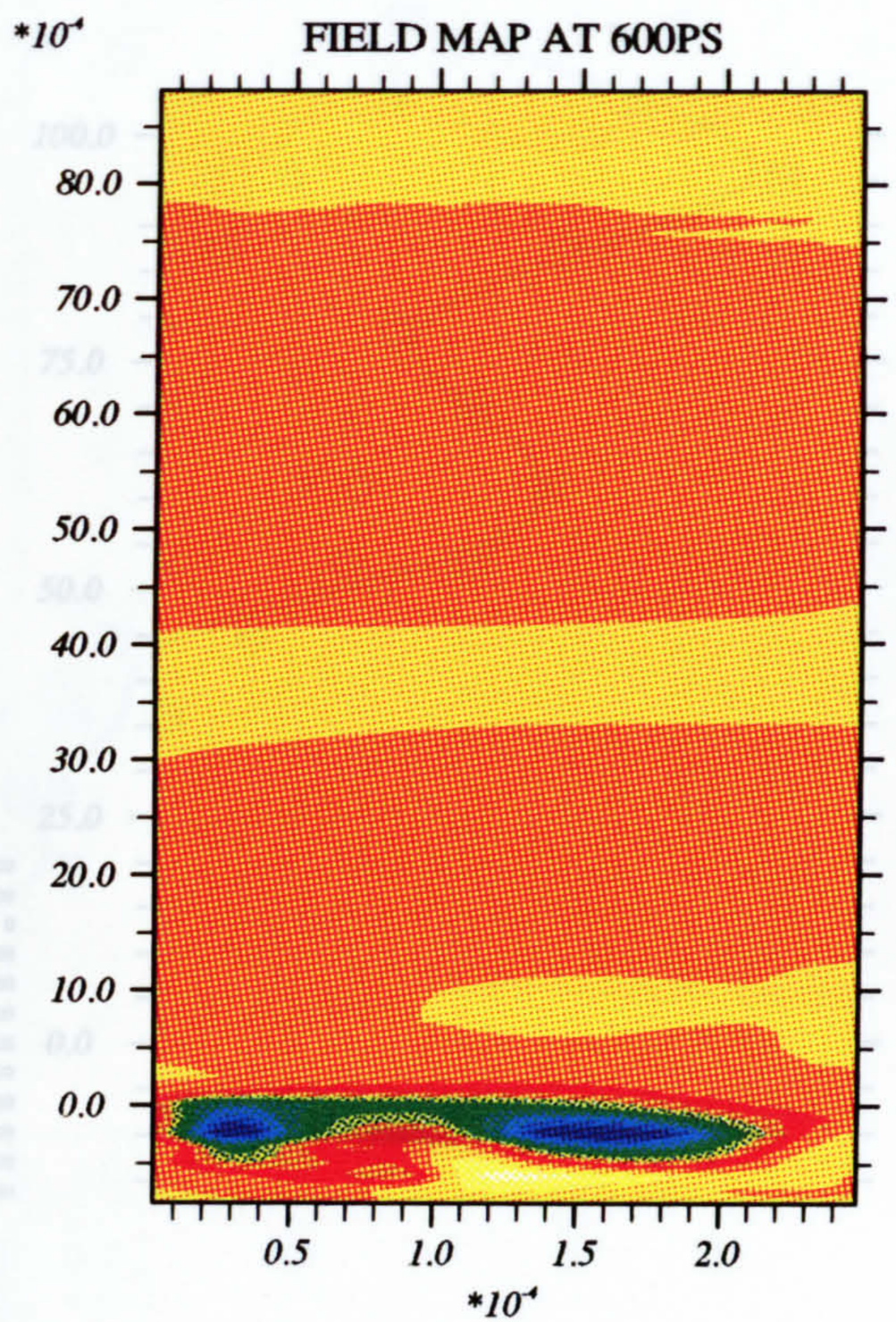
*10⁻⁴
FIELD MAP AT 600PS
80.0
70.0
60.0
50.0
40.0
30.0
20.0
10.0
0.0
0.5
1.0
1.5
2.0
*10⁻⁴
ABOVE 20000
10000 - 20000
0 - 10000
-10000 - 0
-20000 - -10000
-30000 - -20000
-40000 - -30000
-50000 - -40000
-60000 - -50000
-70000 - -60000
-80000 - -70000
BELOW -80000

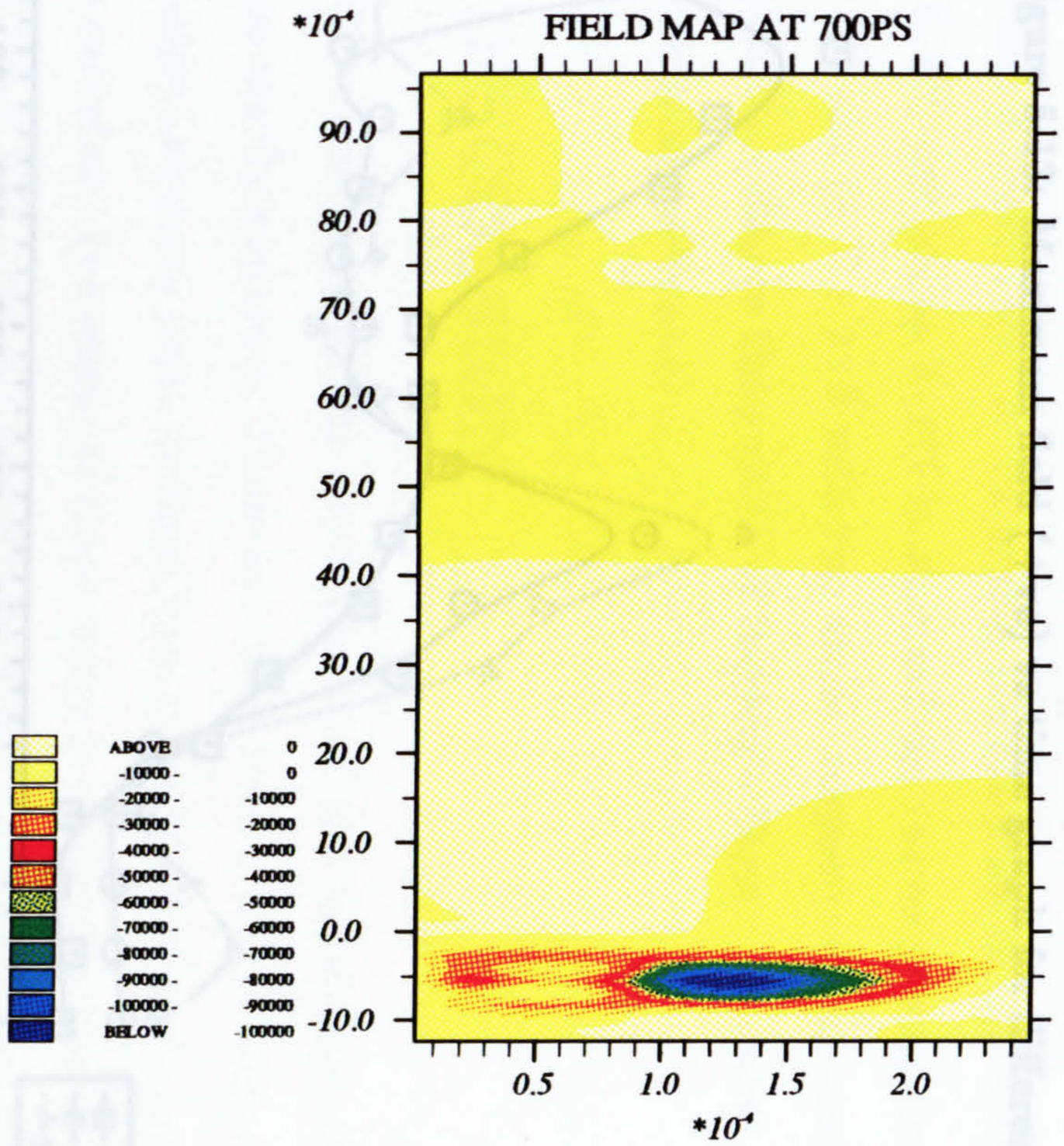
*10⁻⁴
FIELD MAP AT 700PS
90.0
80.0
70.0
60.0
50.0
40.0
30.0
20.0
10.0
0.0
-10.0
0.5
1.0
1.5
2.0
*10⁻⁴
ABOVE 0
-10000 - 0
-20000 - -10000
-30000 - -20000
-40000 - -30000
-50000 - -40000
-60000 - -50000
-70000 - -60000
-80000 - -70000
-90000 - -80000
-100000 - -90000
BELOW -100000

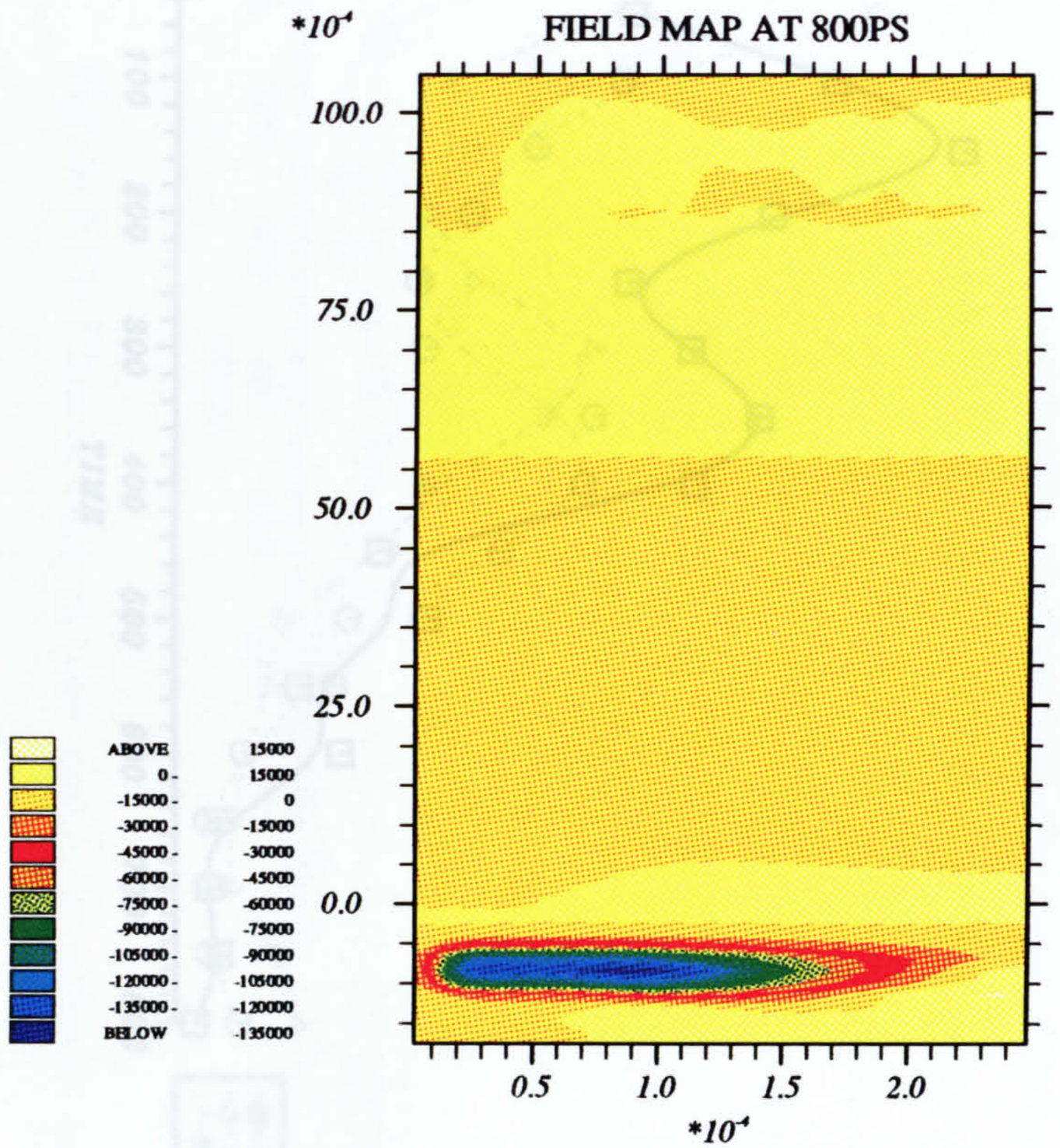
*10⁻⁴
FIELD MAP AT 800PS
100.0
75.0
50.0
25.0
0.0
0.5
1.0
1.5
2.0
*10⁻⁴
ABOVE 15000
0 - 15000
-15000 - 0
-30000 - -15000
-45000 - -30000
-60000 - -45000
-75000 - -60000
-90000 - -75000
-105000 - -90000
-120000 - -105000
-135000 - -120000
BELOW -135000

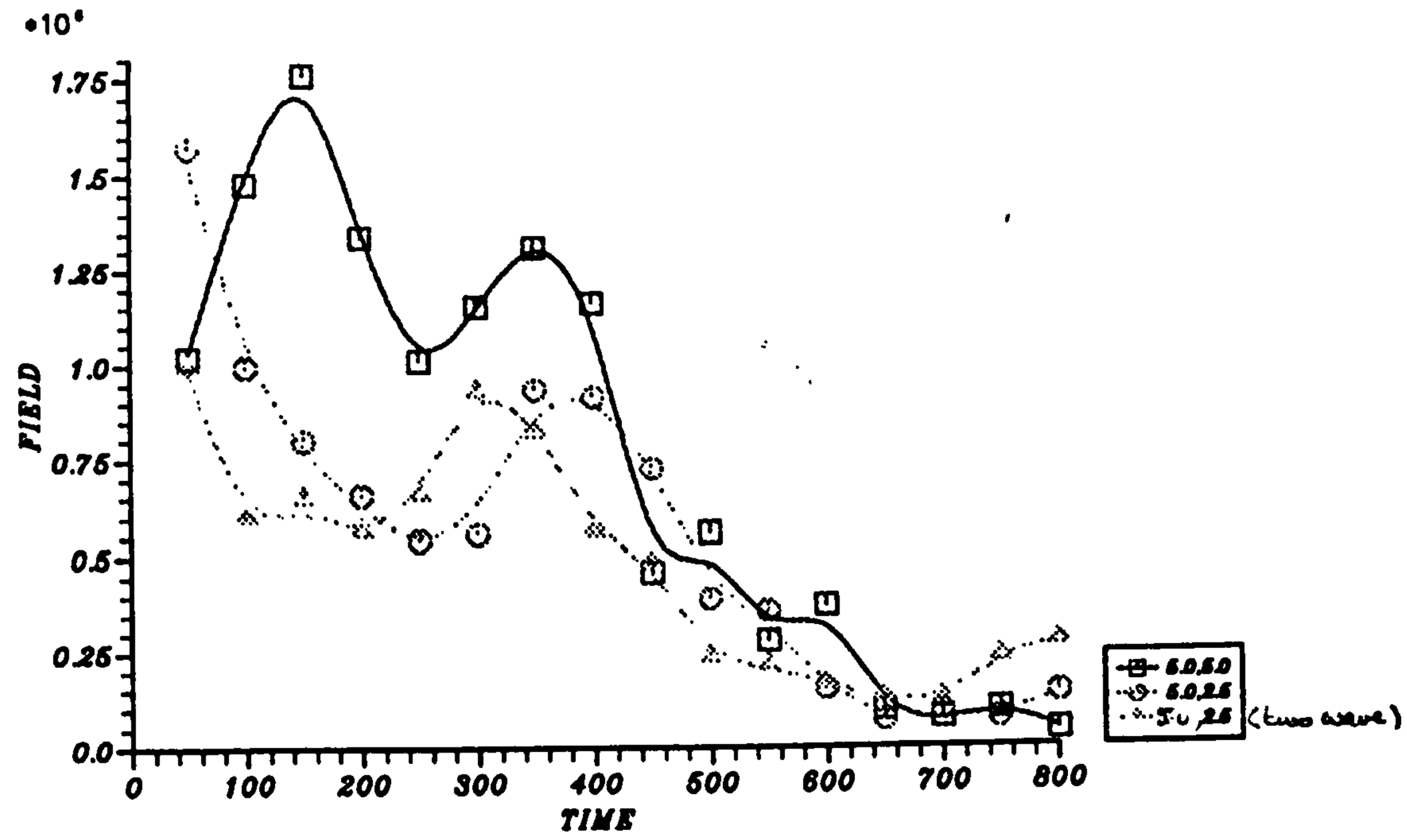

Figure 5.13: Maximum field (+ve) vs time graph for different cases

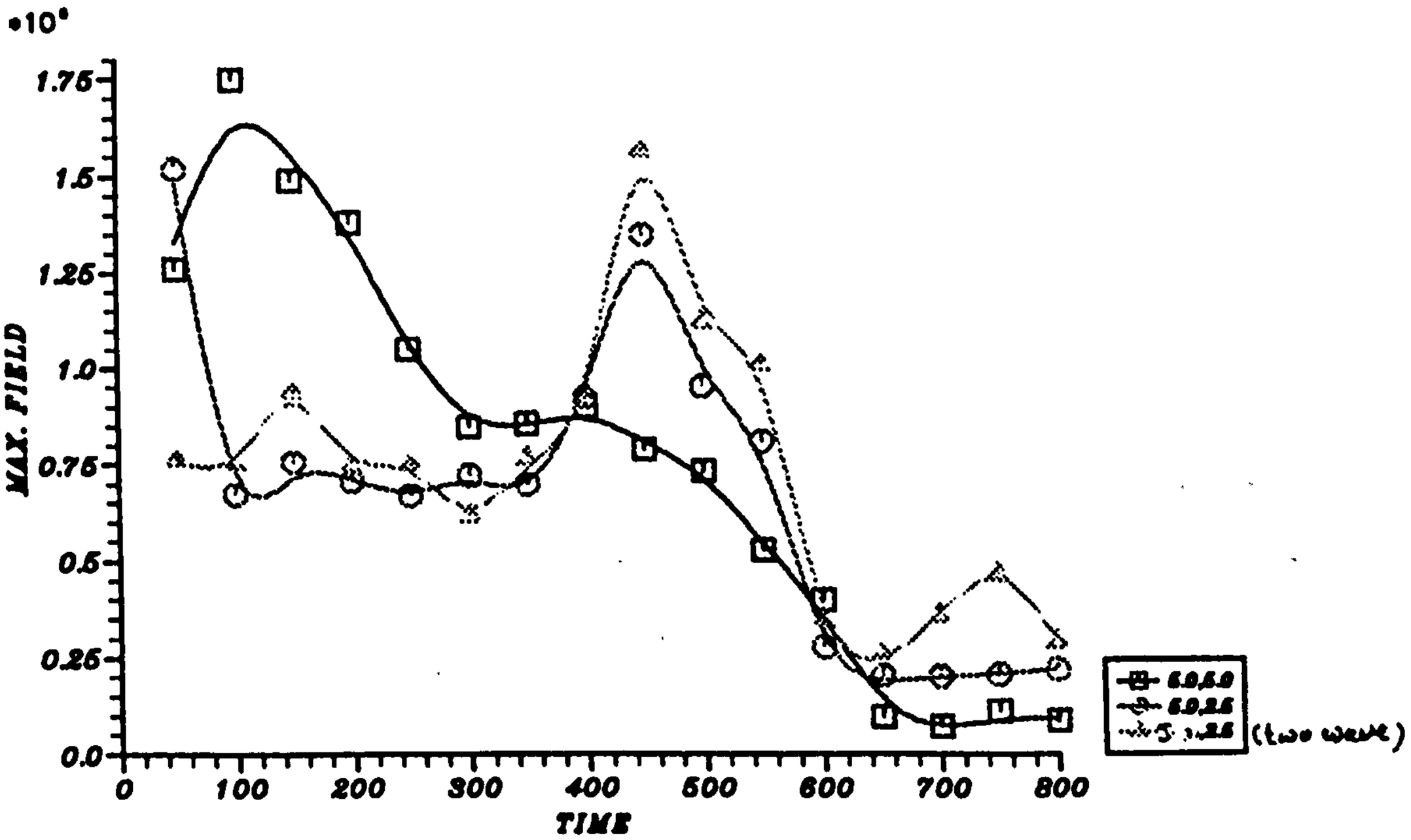

Figure 5.14: Maximum field (-ve) vs time graph for different cases

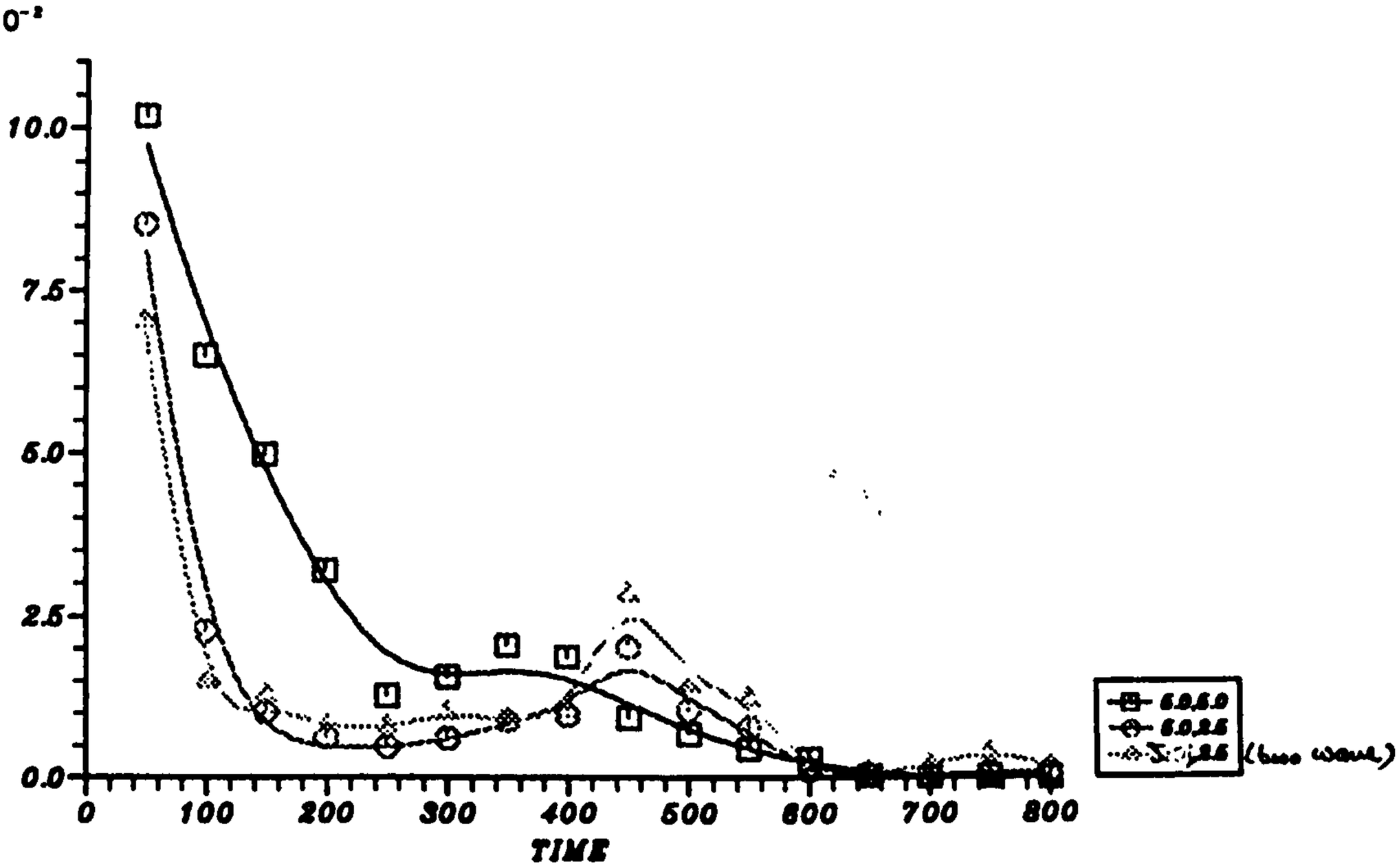

Figure 5.15: Plasma beta vs time graph for different cases

pressure. We, therefore, plotted plasma beta vs time in figure 5 · 15 for all the cases discussed previously. A maximum plasma beta in the very early stage of 10 · 2%, 8 · 5% and about 7 · 0% is observed for the targets of size (5 · 0 × 5 · 0), (5 · 0 × 2 · 5) and (5 · 0 × 2 · 5 with two waves) respectively. It seems to be a large enough value to enhance the growth of Rayleigh-Taylor instability in field studies over no magnetic field cases.

5.6 DISCUSSION

Several differences between the development of the instability when the field is present are readily apparent. These are often from a single cause, the generation of high spatial frequency perturbations from the original disturbance when the field terms are included. The origin of these terms is easily identified from the familiar cross field $\nabla n_e \times \nabla T_e$ magnetic source term which generates a field which follows the original density perturbation. Similarly relatively small variations in temperature lead to the formation of spatial harmonics in the field and thus in the magnetic pressure. Relatively small magnetic pressure variations in the region of strong

gradient lead to seeding of shorter wavelength perturbations, which grow more more rapidly hydrodynamically. The extension of this process is limited by the density gradient scale length and the grid spacing so that no more than about eight wavelengths are observed. The origin of this effect in the magnetic pressure rather than in Hall phenomena is clearly seen by examining the spatial distribution of the plasma β which has significant values $\sim 10\%$ in the region of strong instability growth. In comparison the Hall parameter $\omega\tau$ only has appreciable size in the low density corona.

The higher growth rate of these short wavelengths is reflected in a faster growth rate in the magnetic field case. Although they saturate earlier than the fundamental typically about 150ps, in comparison to 250ps in these simulations and are then smeared out, the flow retains small scale structures which reappear in the strong mixing phase at about 600ps.

Another feature resulting from the short wavelength features is the difference in the later time three dimensional flow on axis. Without magnetic field a bubble develops, whereas with the field a less damaging spike occurs. The origin of this behaviour is of interest. The initial perturbation should give rise to a spike, however Richtmyer-Meshkov instability following the initial shock leads to a bubble on axis by about 60ps. The development of the small scale terms leads to the generation of a dense region near the axis in the non-linear phase and fills the bubble. The final stages with the field on are characterised by fine scale mixing, whereas without the field a deep cavity is formed, which eventually penetrates the foil.

The initially faster growth with the field is reduced when the instability saturates, and the growth occurs at approximately the same rate in the two cases during the non-linear phase.

The magnetic field shows two peaks in time. The first at about 100ps is due to the fine scale field development, and is approximately equal in both polarities. The second peak associated with the strong gradients in the non-linear phase occurs a different time for the two polarities. This reflects the fact that density is much less structured at this time.

Chapter 6

COMPUTER SIMULATION OF RAYLEIGH-TAYLOR INSTABILITY THROUGH INTENSITY PERTURBATION

6.1 INTRODUCTION

The simulation results presented in this chapter are carried out using the same code MAGT2LD as discussed in Chapter 4. The target material, geometry and the dimensions are kept the same as in the previous Chapter. We have also used the same laser wavelength, power and the pulse shape. However instead of applying the perturbation through mass, it is seeded through the laser intensity. The applied perturbation is sinusoidal in its form although the perturbation wavelength may vary in different simulations.

6.2 TARGET SIZE ($2 \cdot 5\mu m \times 2 \cdot 5\mu m$)

A polythene target of thickness $2{\cdot}5\mu m$ and radius of $2{\cdot}5\mu m$ is uniformly accelerated by a $0 \cdot 53\mu m$ laser. The incoming beam is parallel to the axial direction and the laser has the peak rise time of 300ps. This time the perturbation is applied through the laser itself in contrast to the previous Chapter. The emphasis is to find out

whether changing the applied perturbation affects the growth of Rayleigh-Taylor instability. The applied perturbation is two wavelengths with its perturbation amplitude 5% of the intensity. The code is run twice with magnetic field terms included and excluded. All the necessary laser and target parameters are given in Table 6 · 1. The time history of density contour maps is shown in figure 6 · 1. with an interval of 50ps up to 800ps, where the simulations are stopped as most of the target material is burnt through and strong mixing takes place. At 50ps the behaviour for both magnetic field switched on/off is the same apart from some high frequency modes with small amplitude in the field included. The reason of these high frequency modes generation is the same as explained in the previous Chapter. These high frequency modes remain until 300ps and enhance the growth of the instability. There is no significant growth of Rayleigh-Taylor instability observed until 250ps when the magnetic field effects are not switched on. With the field on, the high frequency modes dominate from 150ps and the amplitude of these modes increases with time. At the later time 300ps, these high frequency modes are overtaken by the original applied perturbation. The Rayleigh-Taylor instability only starts growing with no magnetic field at 300ps whereas at the same time the mixing starts taking place when the field routines are included. At 500ps fine spikes are formed with the field switched off in contrast the back edge of the target start breaking through with field on. At 600ps most the target material is burnt through in both field on/off cases and strong mixing has taken place.

The amplitude as a function of time graph is shown in figure 6 · 2. This graph shows clearly the difference in the growth of the instability when the field is included or excluded. In these simulations for targets of this size and perturbation wavelength, the growth rate of the instability is much higher for the field included case than in no magnetic field simulations. Later at about 300ps the instability growth starts damping for the field on simulations because the outer side of the target starts mixing and it becomes difficult to measure the exact value of the mix region. The graph represents data only up to 450ps for the reason that after this time most of the target material is burnt through.

The magnetic field contour maps at intervals of 100ps are shown in figure 6 · 3. The intention is not to show the size of the field strength but how the field affects

TARGET PARAMETERS	
Target thickness	$2 \cdot 5 \mu m$
Target Radius	$2 \cdot 5 \mu m$
Geometry	Cylindrical
Material	Polythene $(CH_2)_n$
Solid Density	$1 \cdot 2 g/cm^3$
Mass No. (F)	$4 \cdot 67$
Charge No.(Z)	$2 \cdot 67$
Ratio of Specific heat	$1 \cdot 667$
Initial Temperature	$10^4 K°$
LASER PARAMETERS	
Peak Power on Axis	$1 \cdot 0 \times 10^{14} W/cm^2$
Focal Radius	$1 \cdot 0 \times 10^4 cm$
Laser wavelength	$0 \cdot 53 \mu m$
Laser Rise Time	300ps
Total Duration of Laser Pulse	2ns
Total Run Time	800ps
Perturbation Wavelength	$1 \cdot 25 \mu m$
Perturbation Amplitude	5%
Reflection Coefficient	$0 \cdot 8$
TRANSPORT PARAMETERS	
Flux limit Factor (f)	$0 \cdot 1$
Diffusion	Classical

Table 6.1: Input data for the target $(2 \cdot 5 \mu m \times 2 \cdot 5 \mu m)$ in both directions.

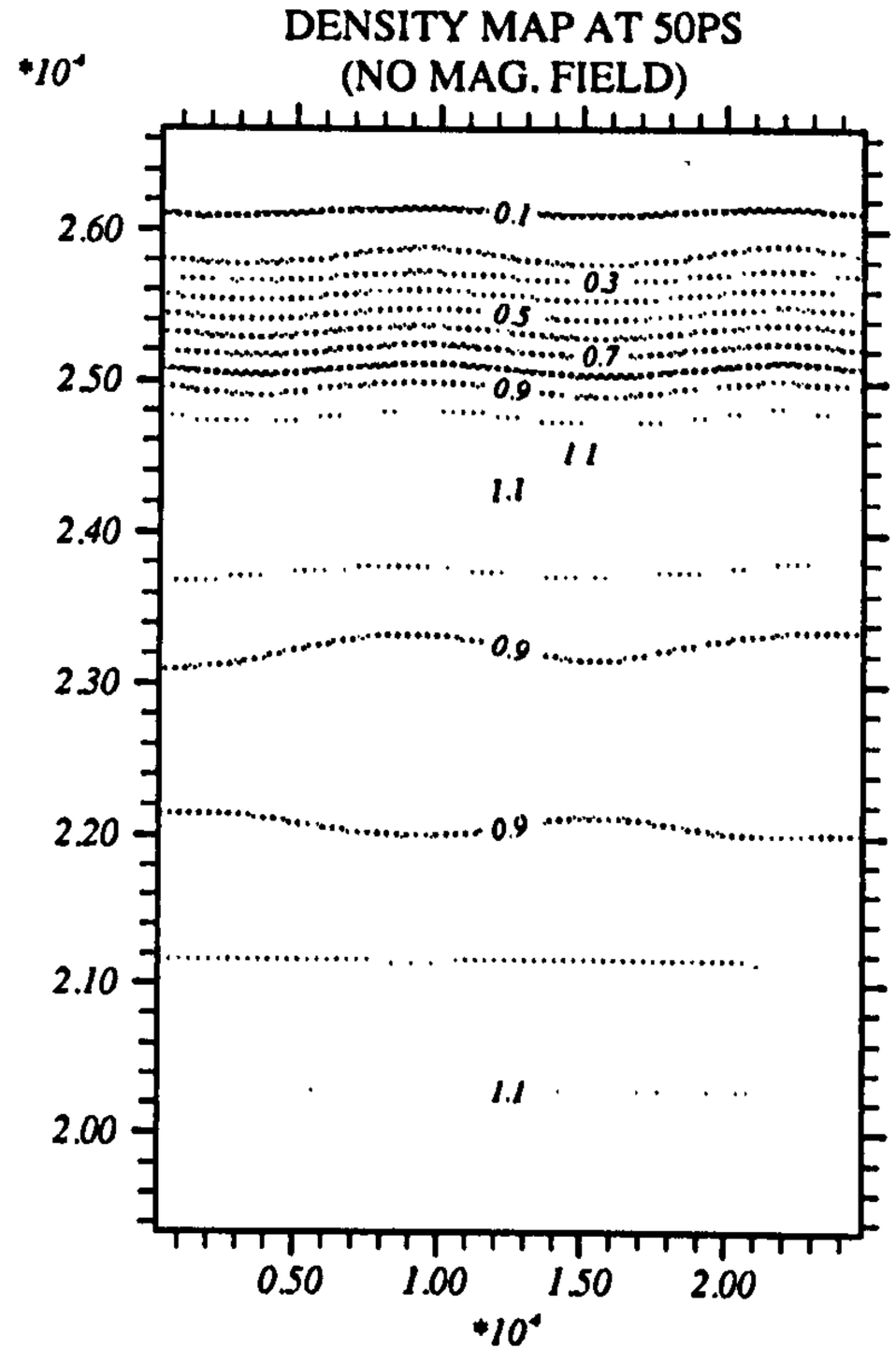

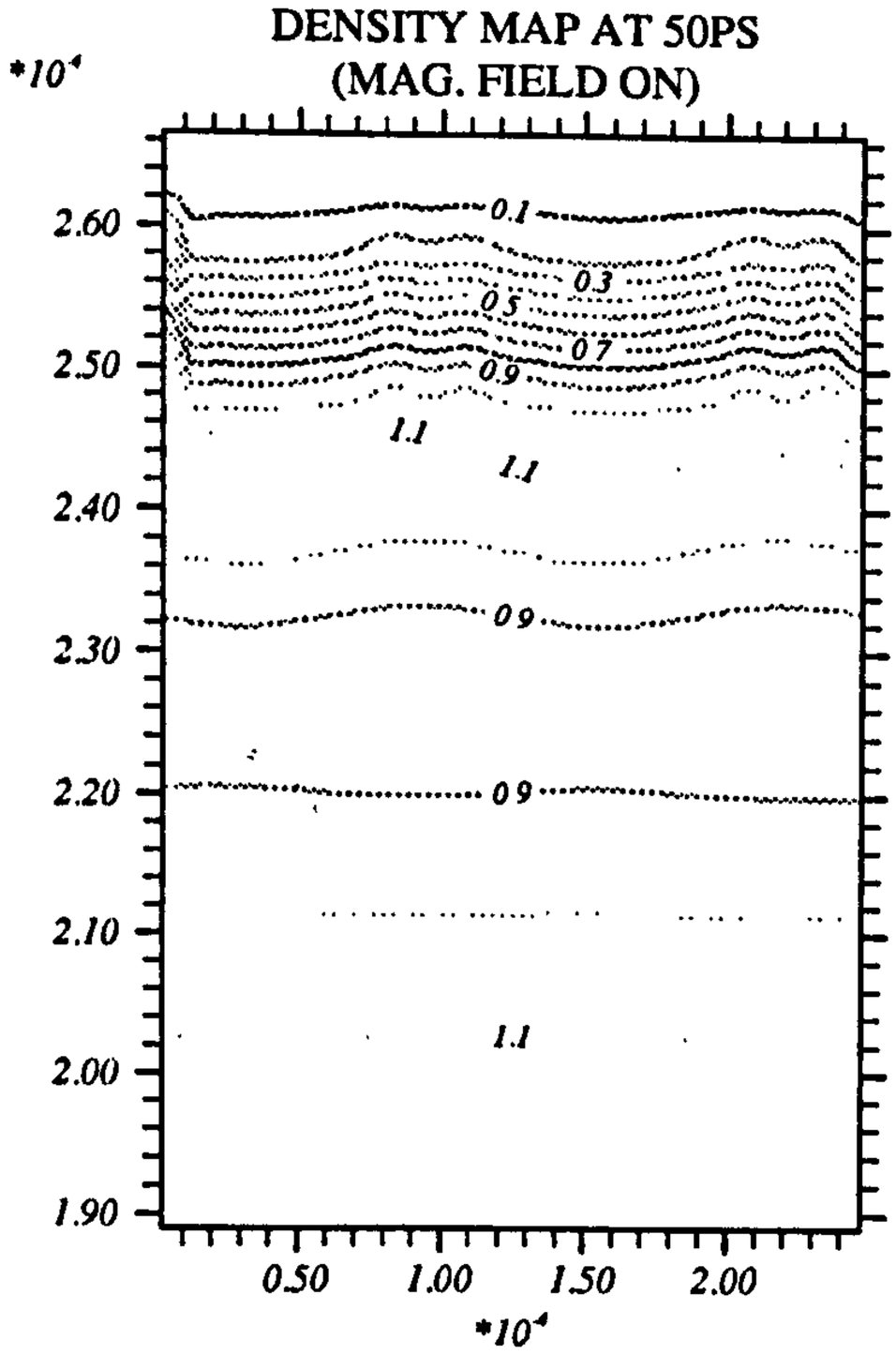

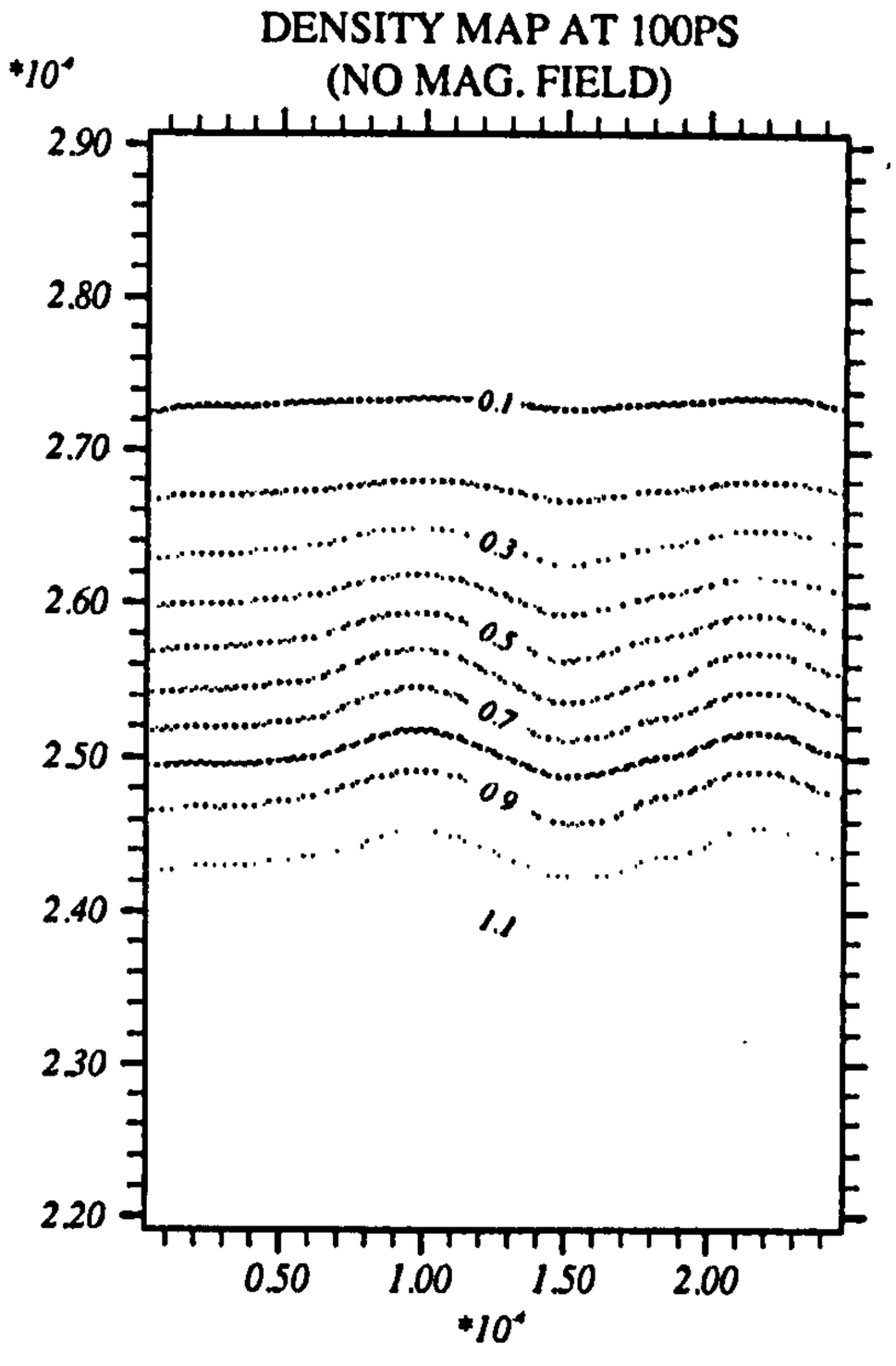

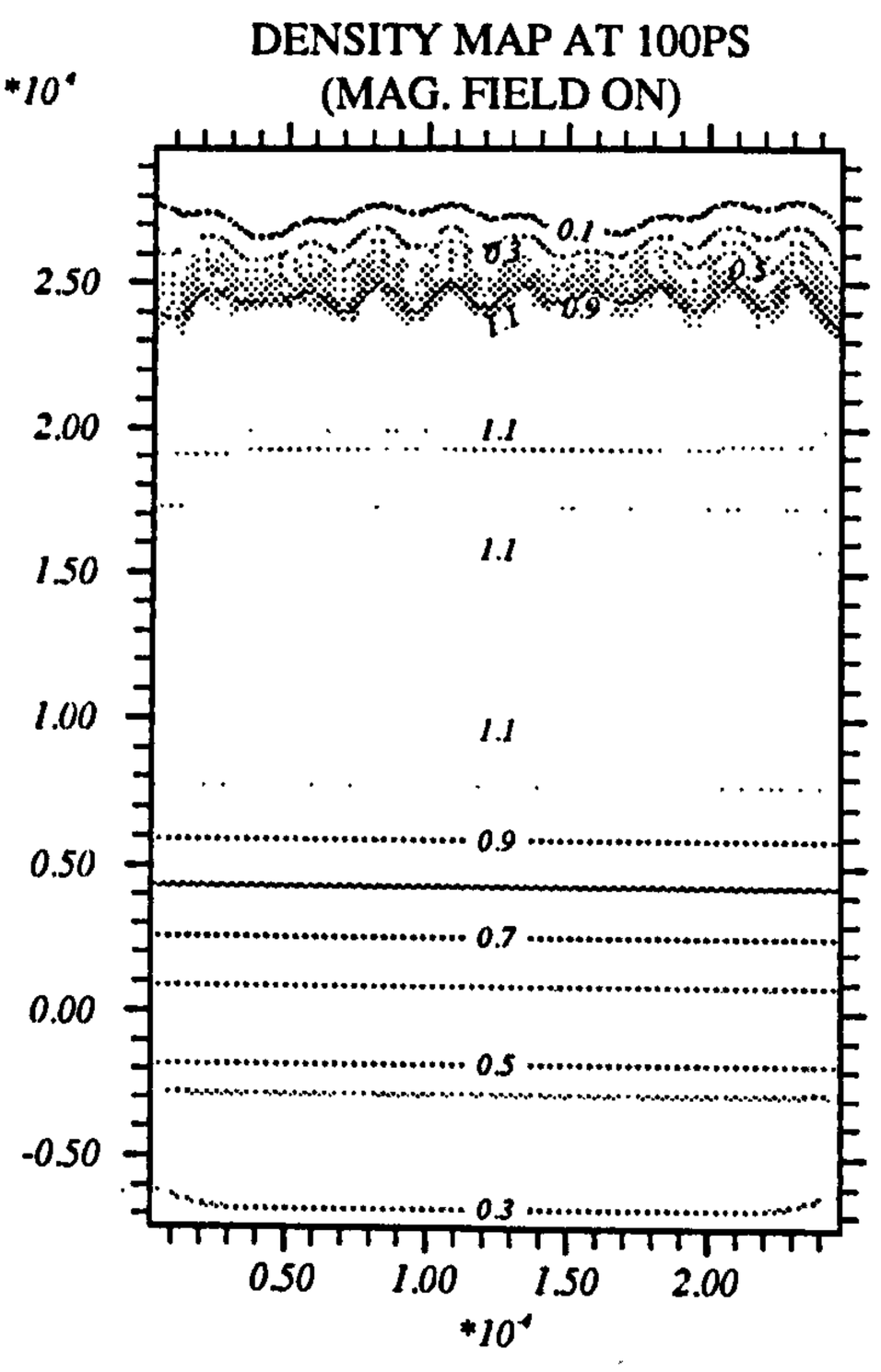

Figure 6.1: Density contour map for $(2 \cdot 5\mu m \times 2 \cdot 5\mu m)$ with the two perturbation wavelength.

DENSITY MAP AT 150PS
(NO MAG. FIELD)

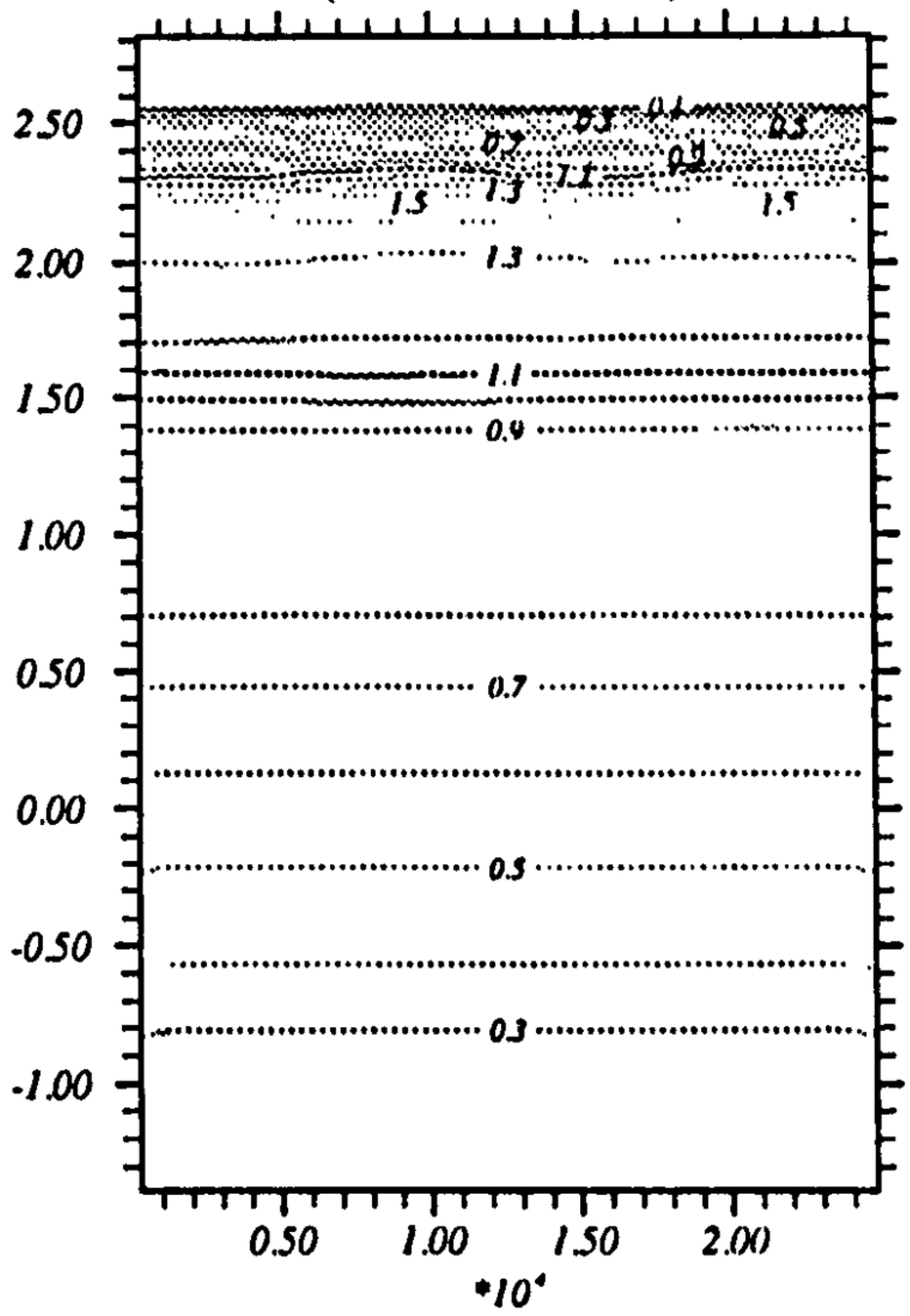

DENSITY MAP AT 150PS
(MAG. FIELD ON)

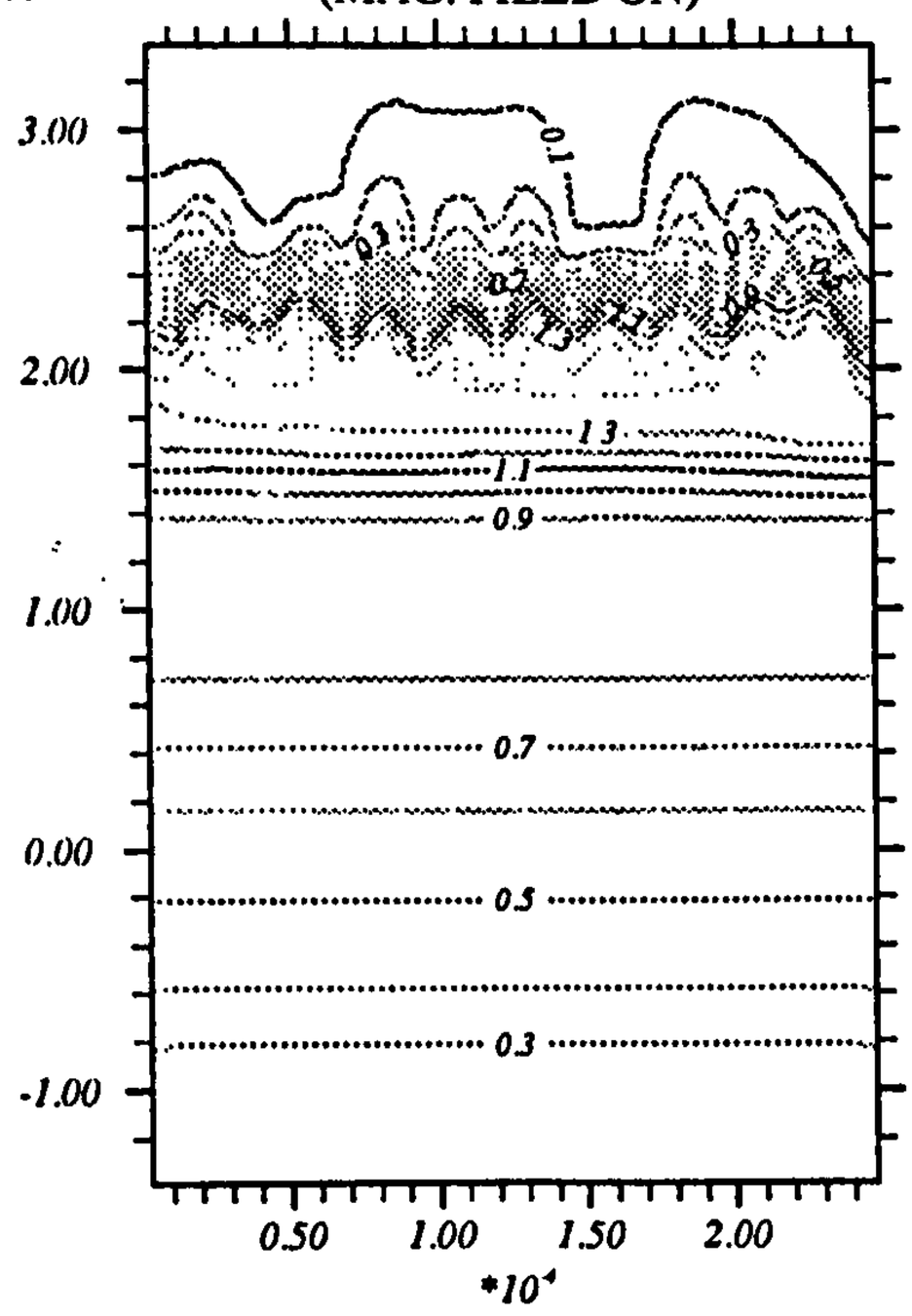

DENSITY MAP AT 200PS
(NO MAG. FIELD)

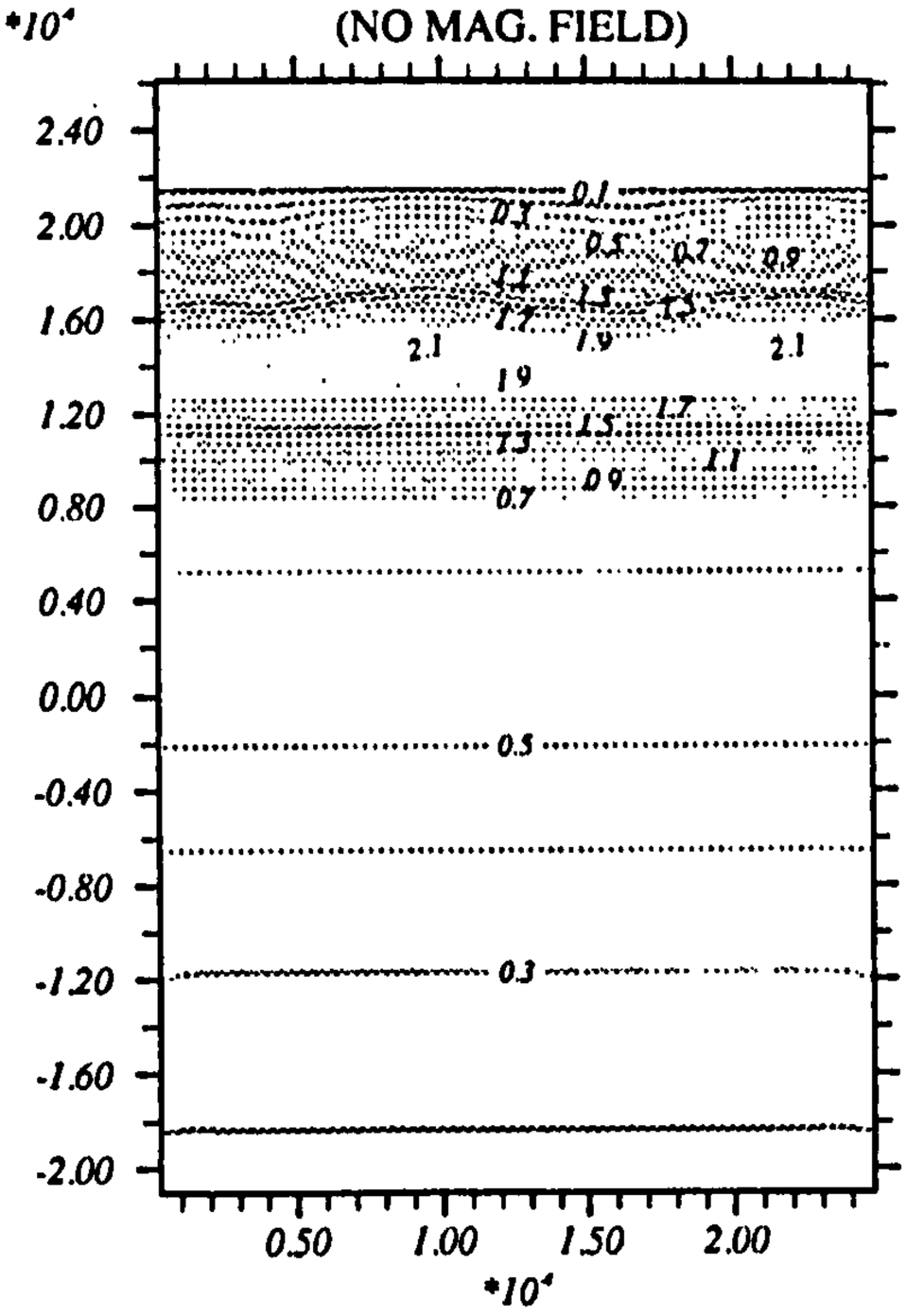

DENSITY MAP AT 200PS
(MAG. FIELD ON)

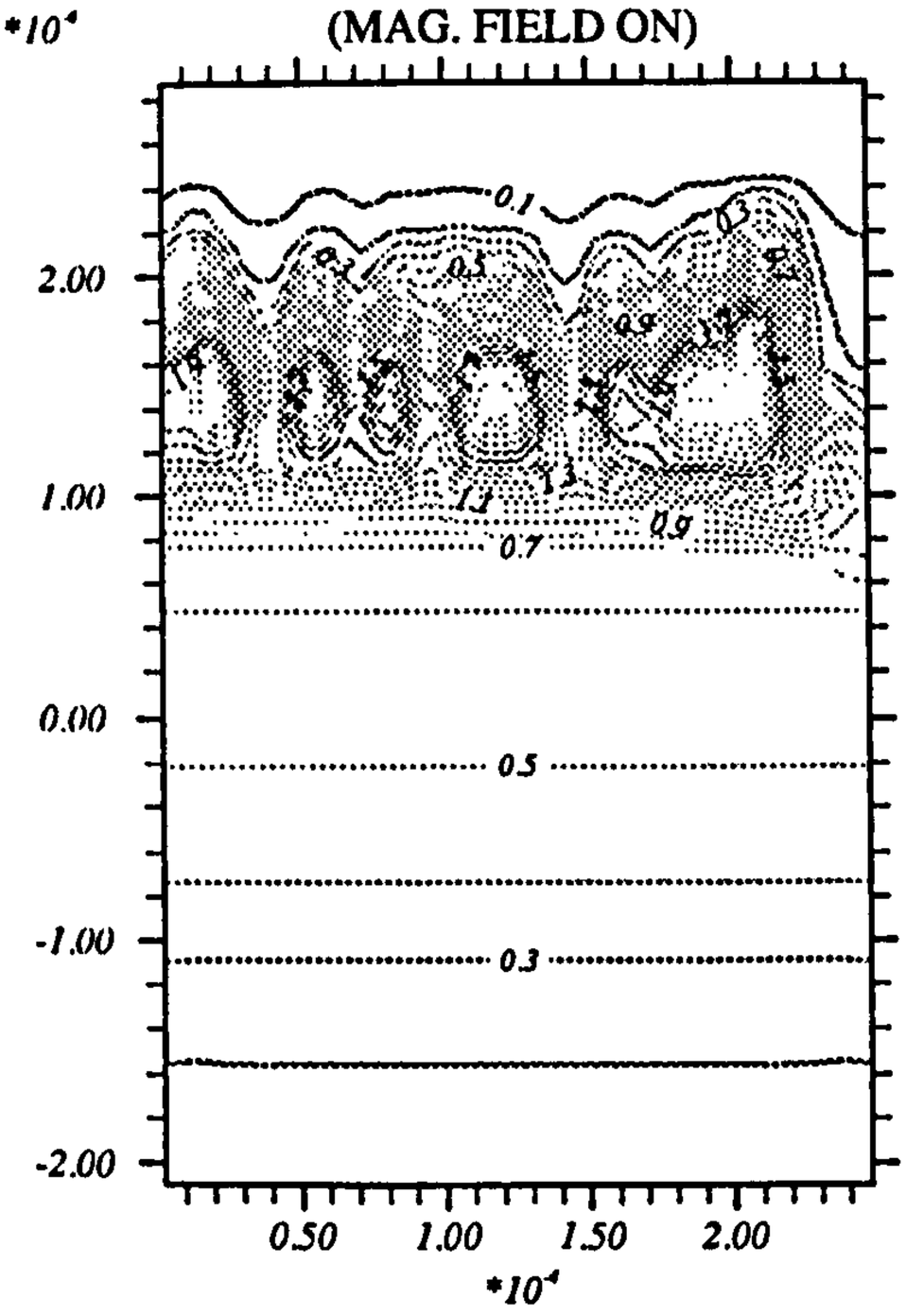

DENSITY MAP AT 250PS
(NO MAG. FIELD)

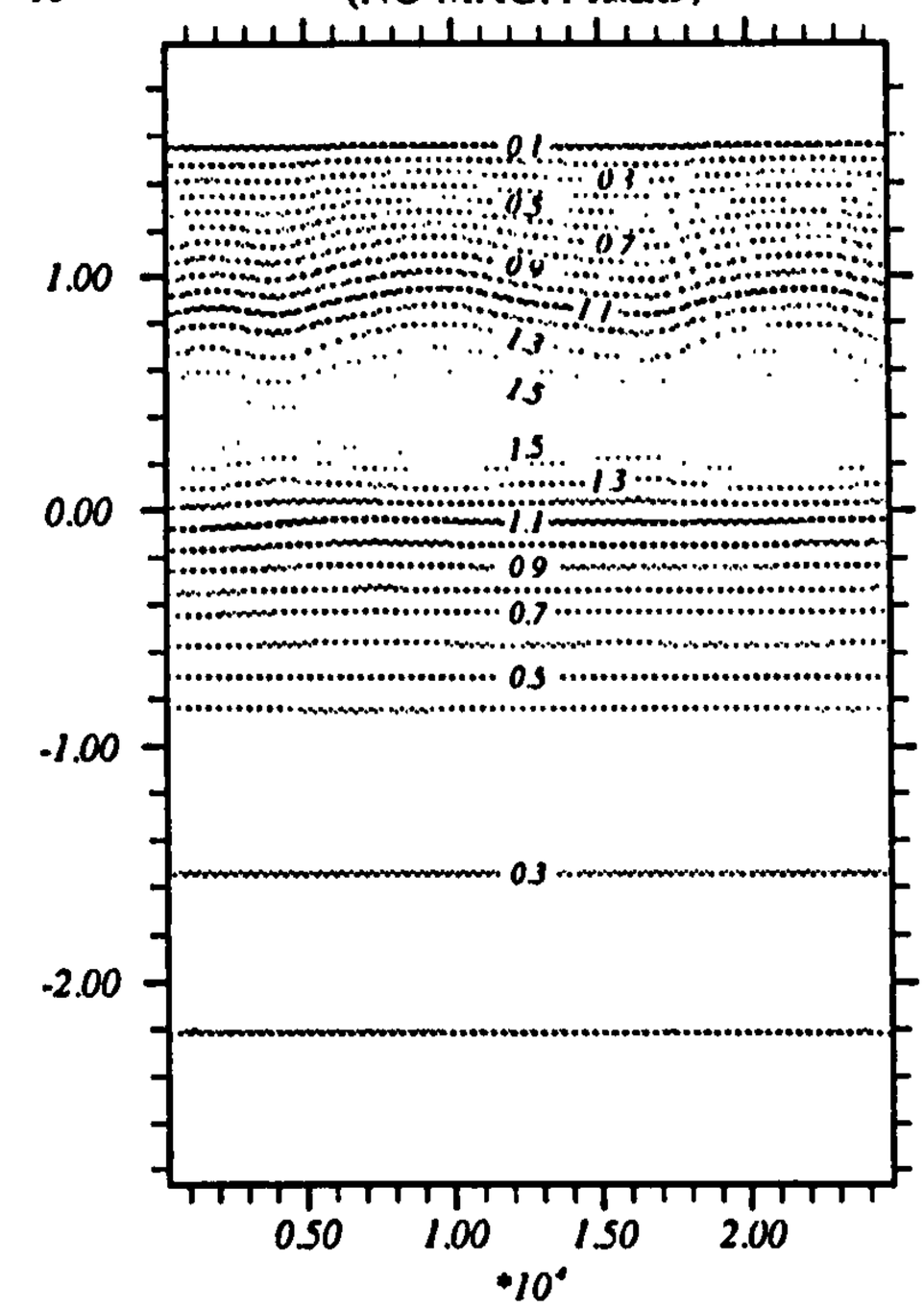

DENSITY MAP AT 250PS
(MAG. FIELD ON)

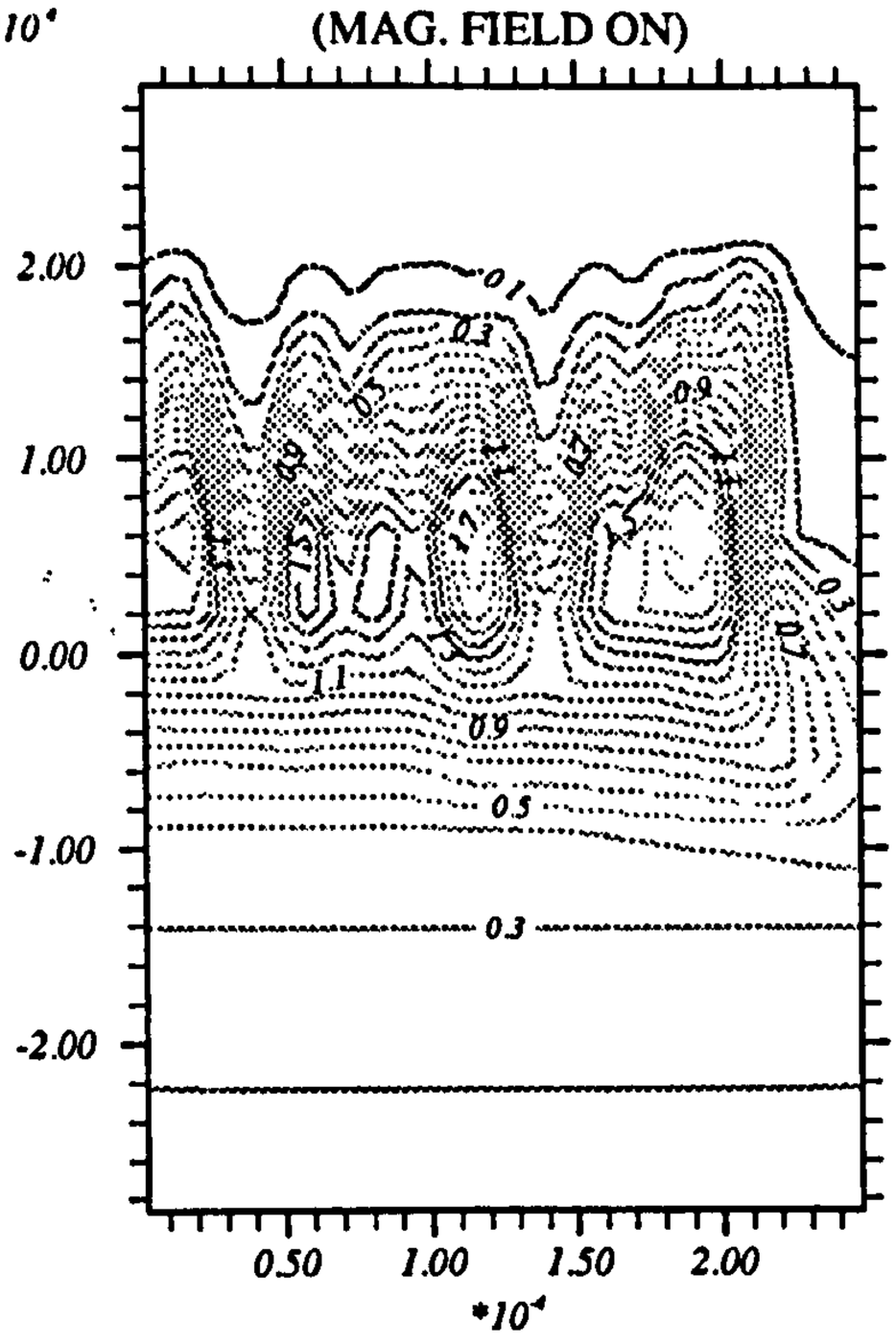

DENSITY MAP AT 300PS
(NO MAG. FIELD)

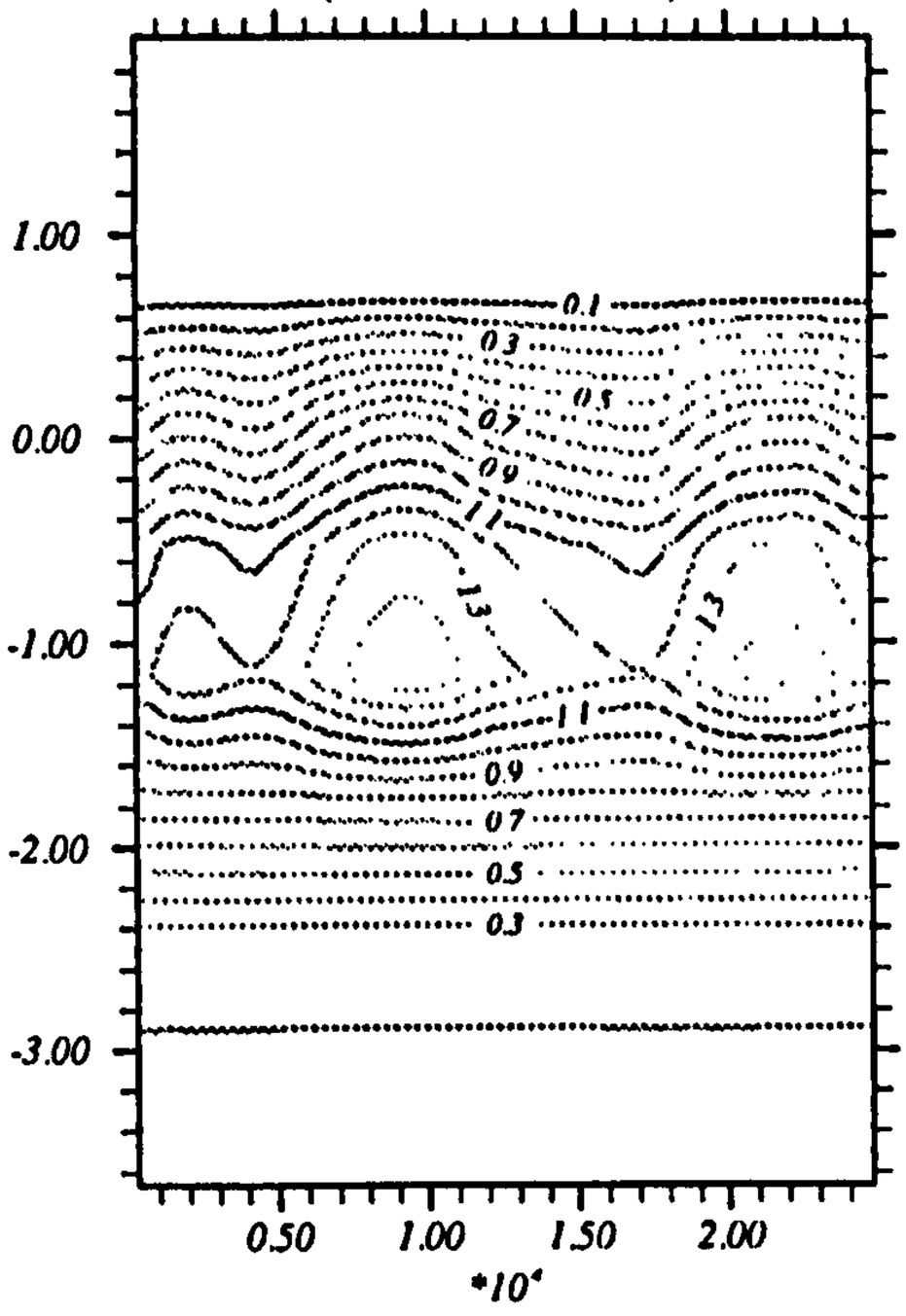

DENSITY MAP AT 300PS
(MAG. FIELD ON)

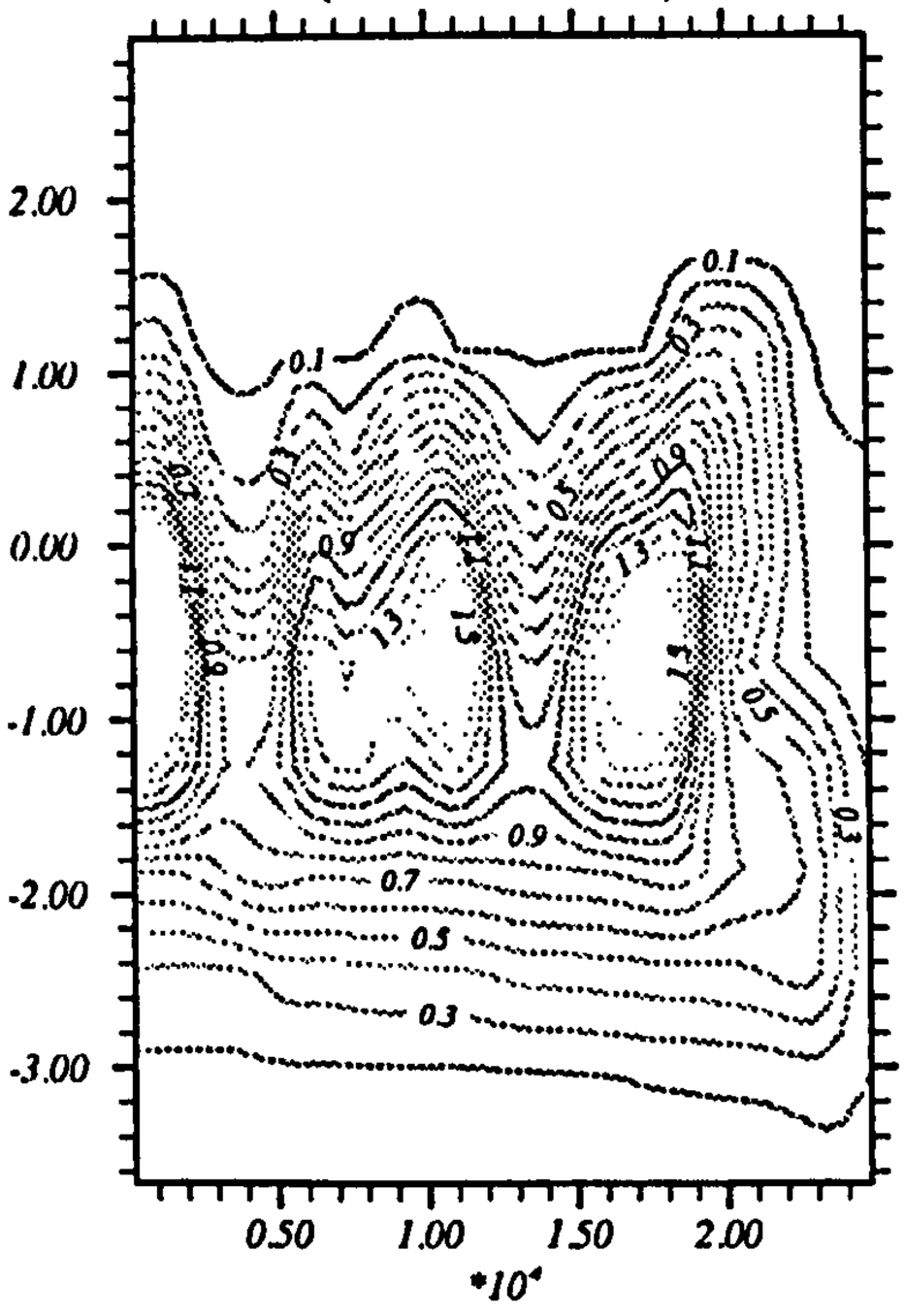

DENSITY MAP AT 350PS
(NO MAG. FIELD)

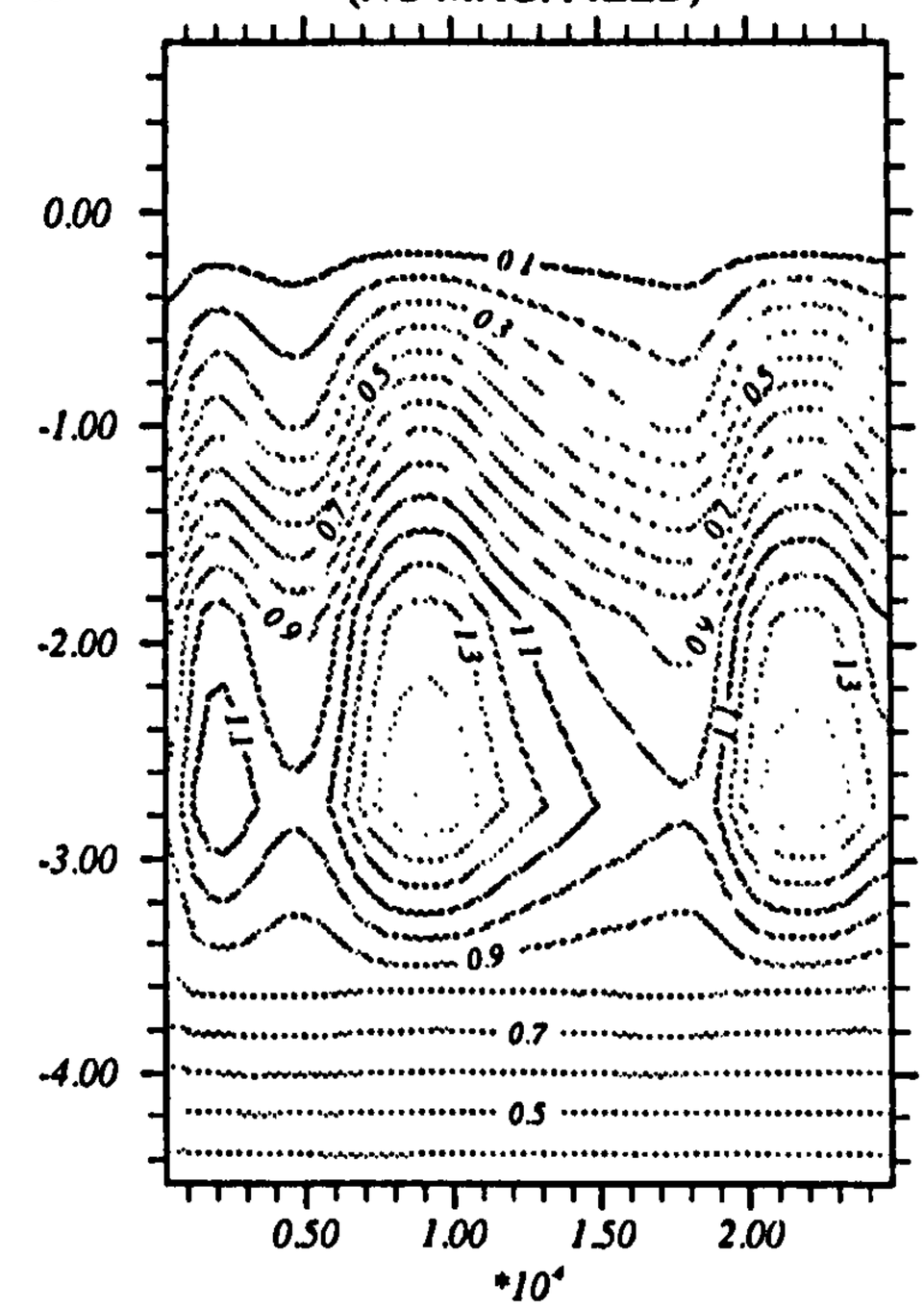

DENSITY MAP AT 350PS
(MAG. FIELD ON)

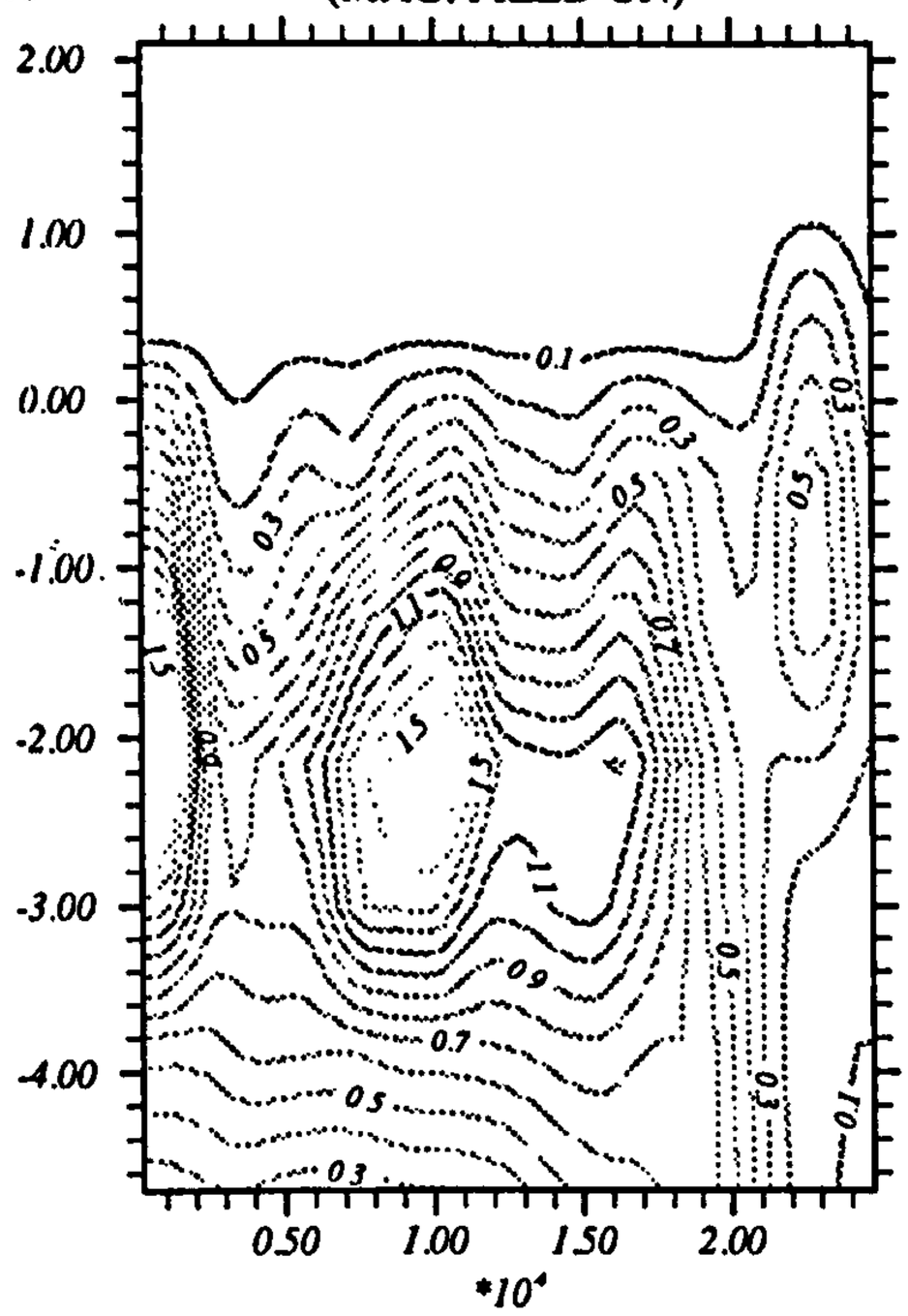

DENSITY MAP AT 400PS
(NO MAG. FIELD)

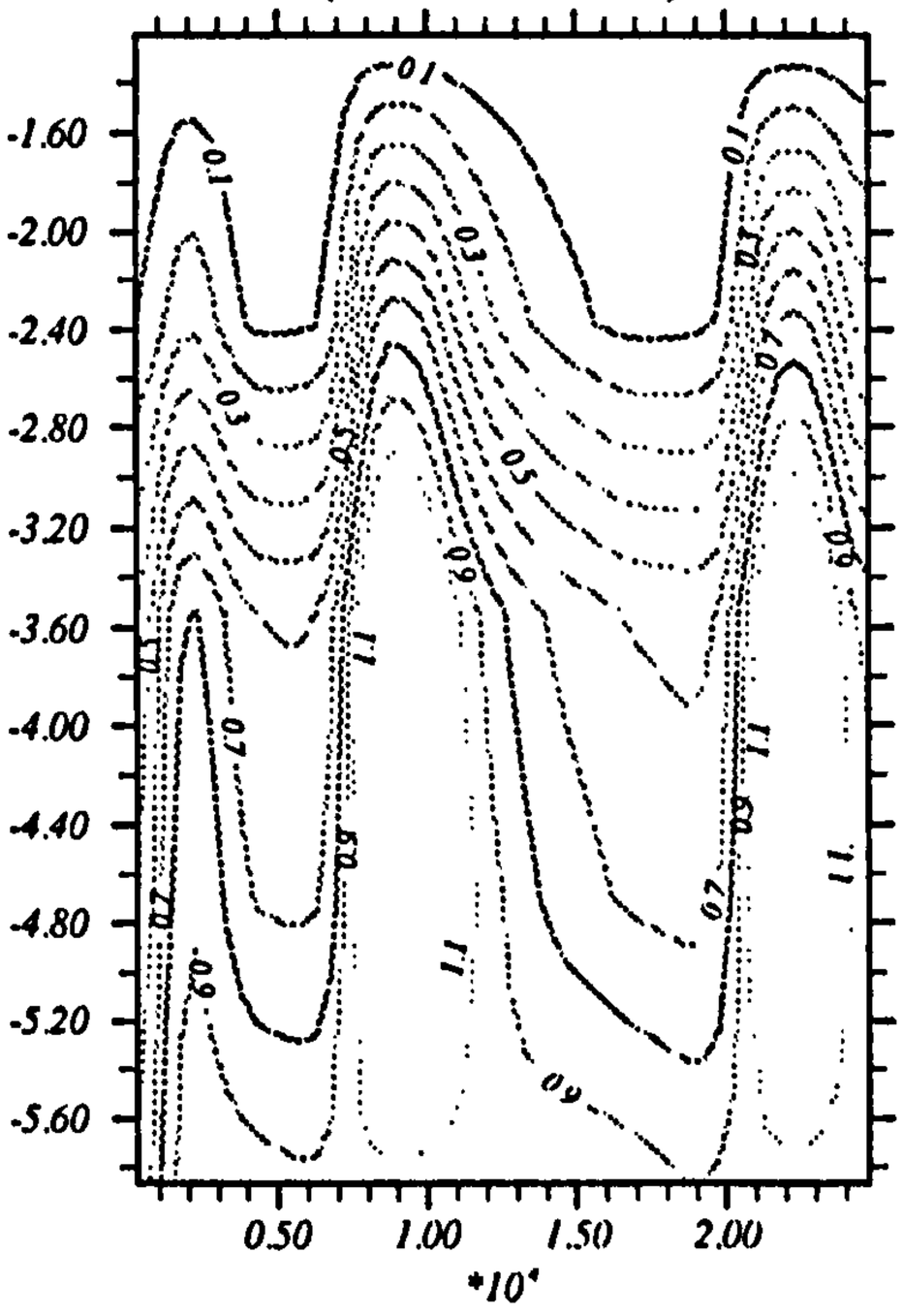

DENSITY MAP AT 400PS
(MAG. FIELD ON)

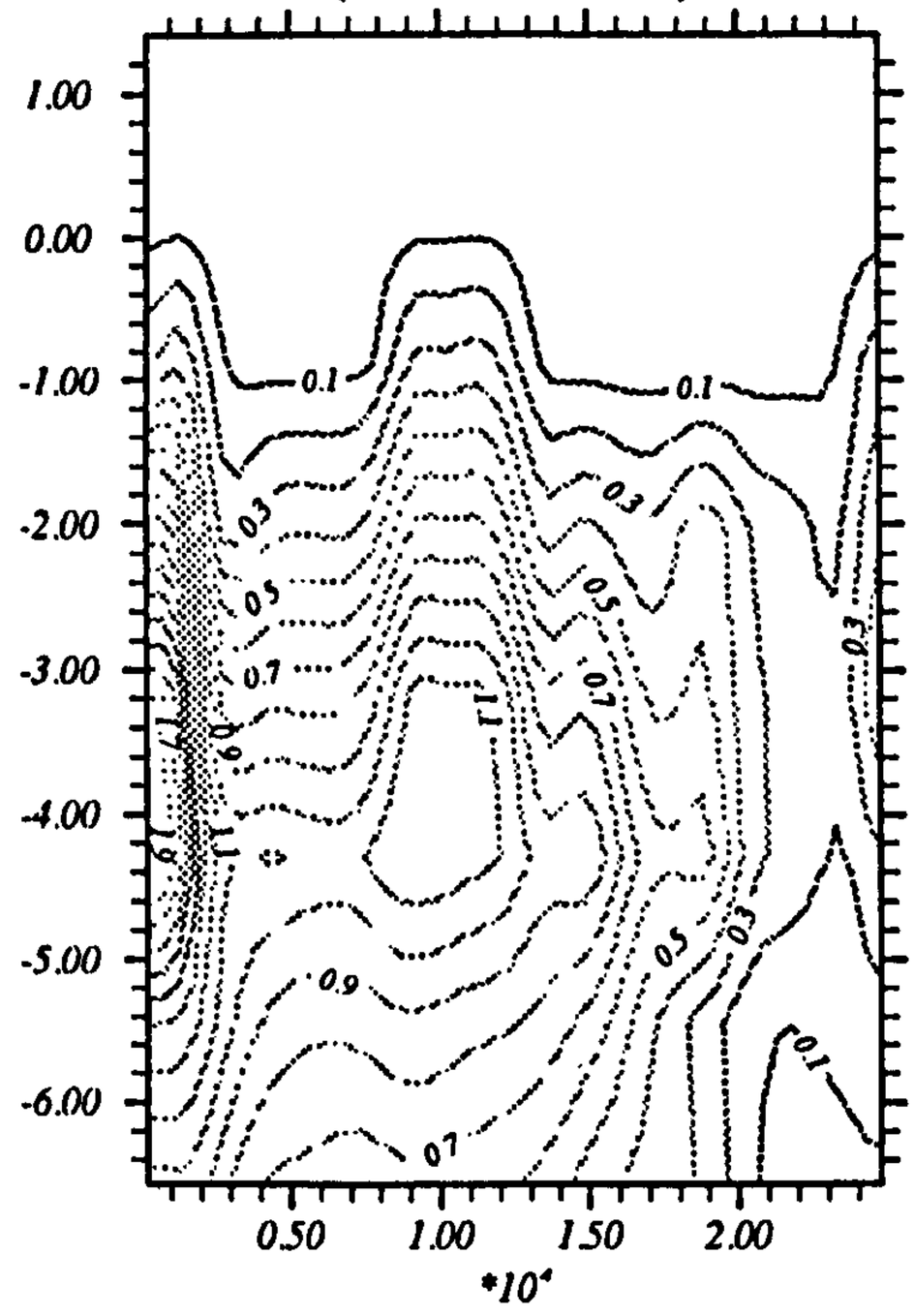

DENSITY MAP AT 450PS
(NO MAG. FIELD)

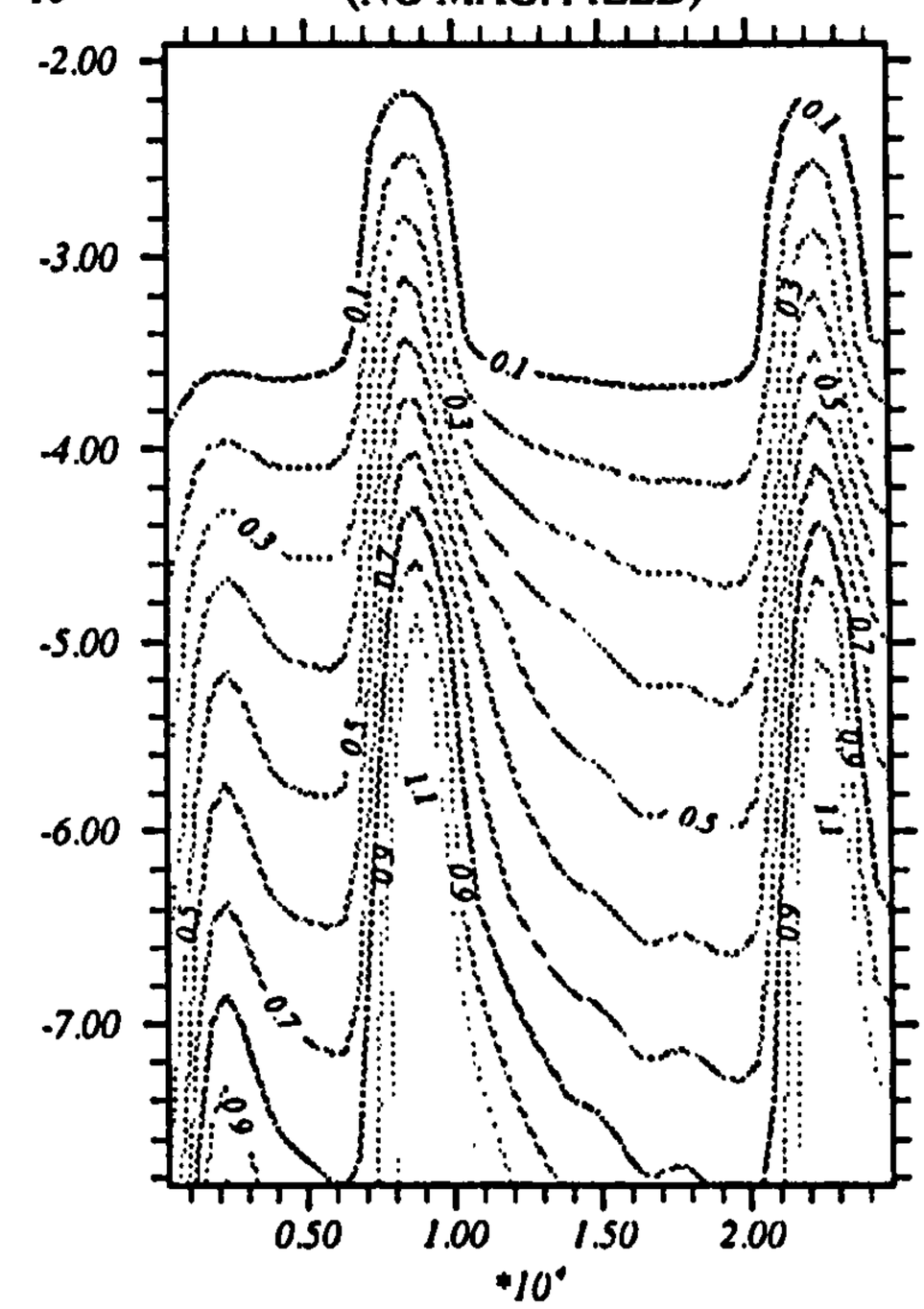

DENSITY MAP AT 450PS
(MAG. FIELD ON)

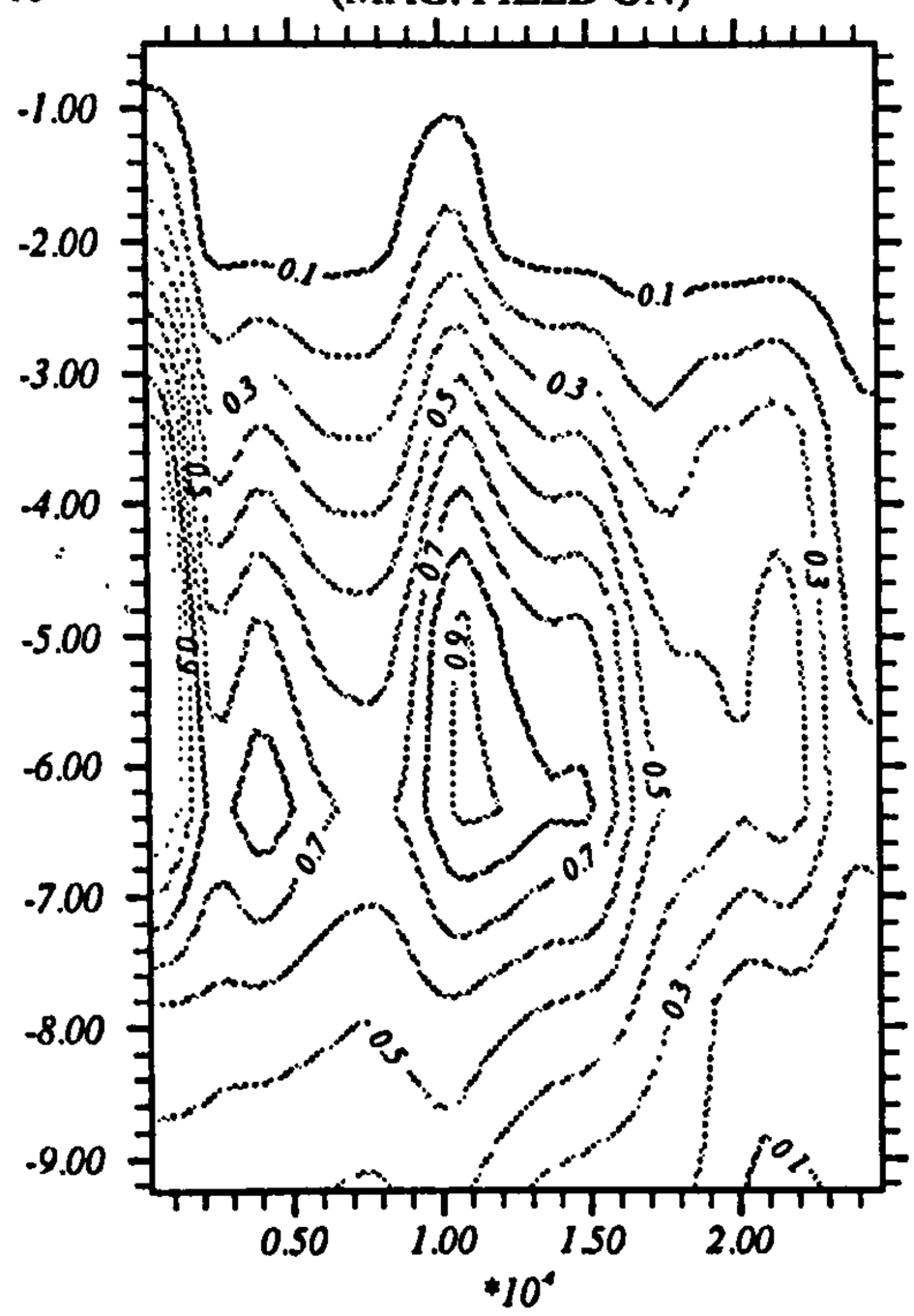

DENSITY MAP AT 500PS
(NO MAG. FIELD)

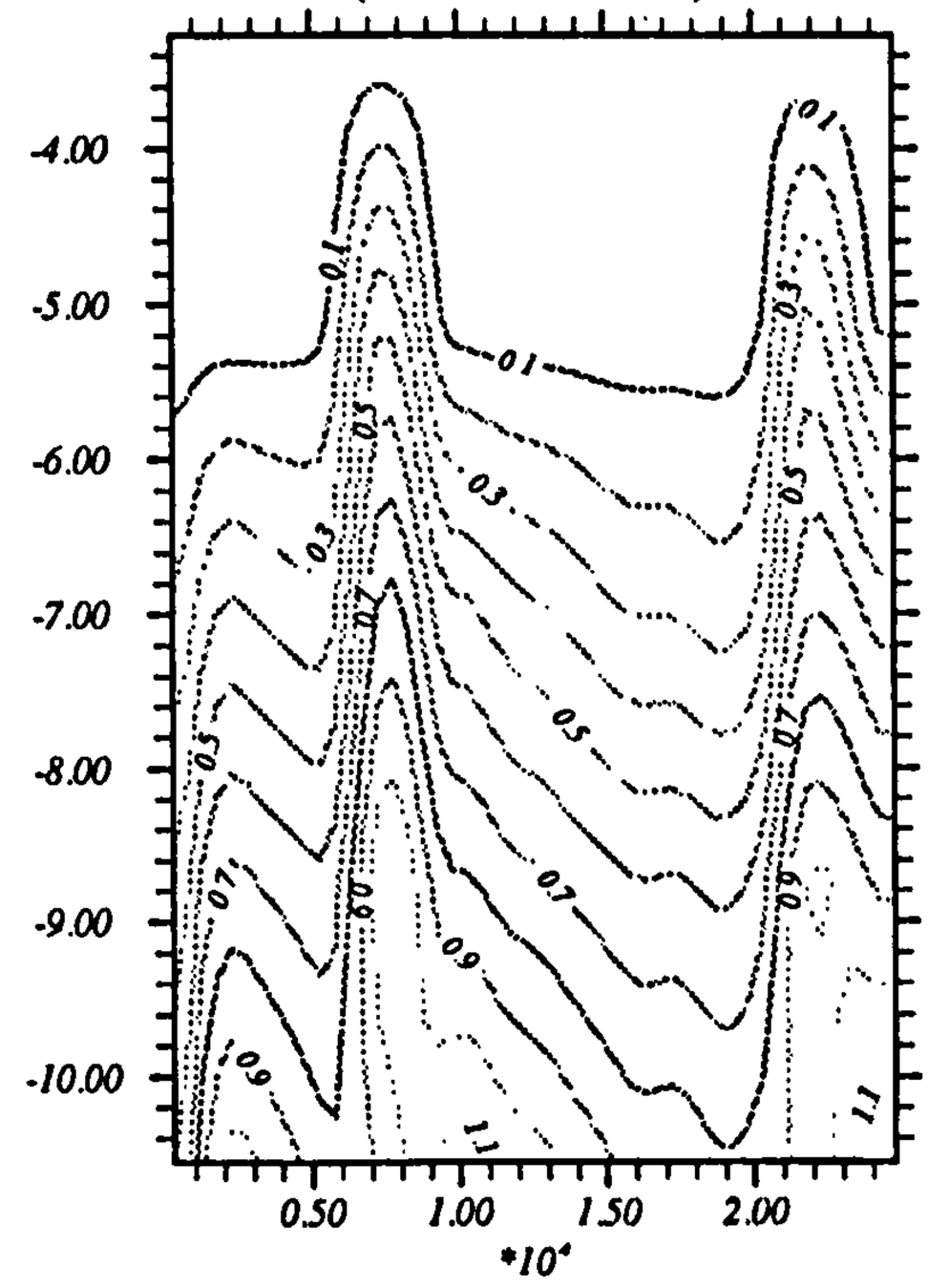

DENSITY MAP AT 500PS
(MAG. FIELD ON)

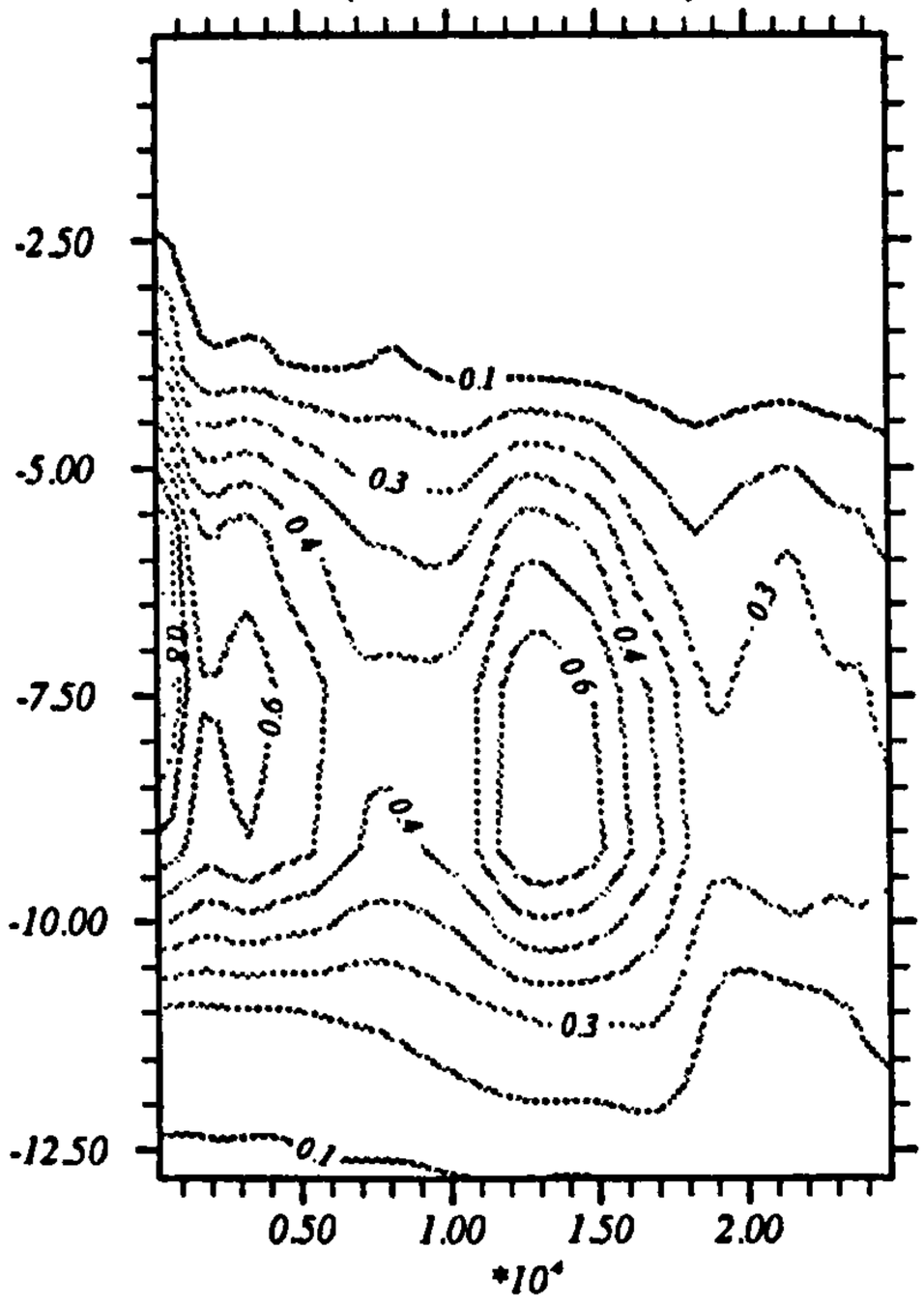

DENSITY MAP AT 550PS
(NO MAG. FIELD)

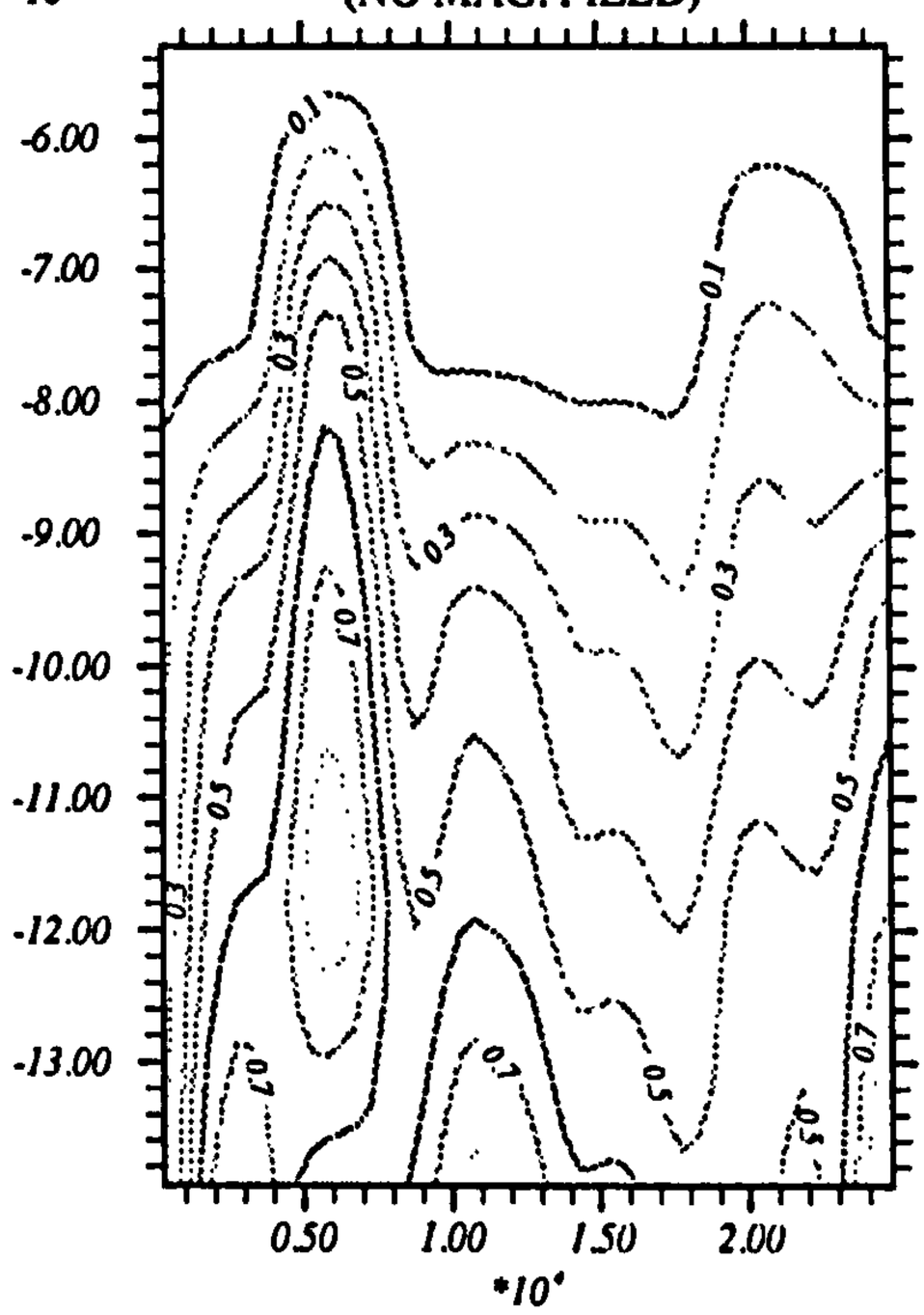

DENSITY MAP AT 550PS
(MAG. FIELD ON)

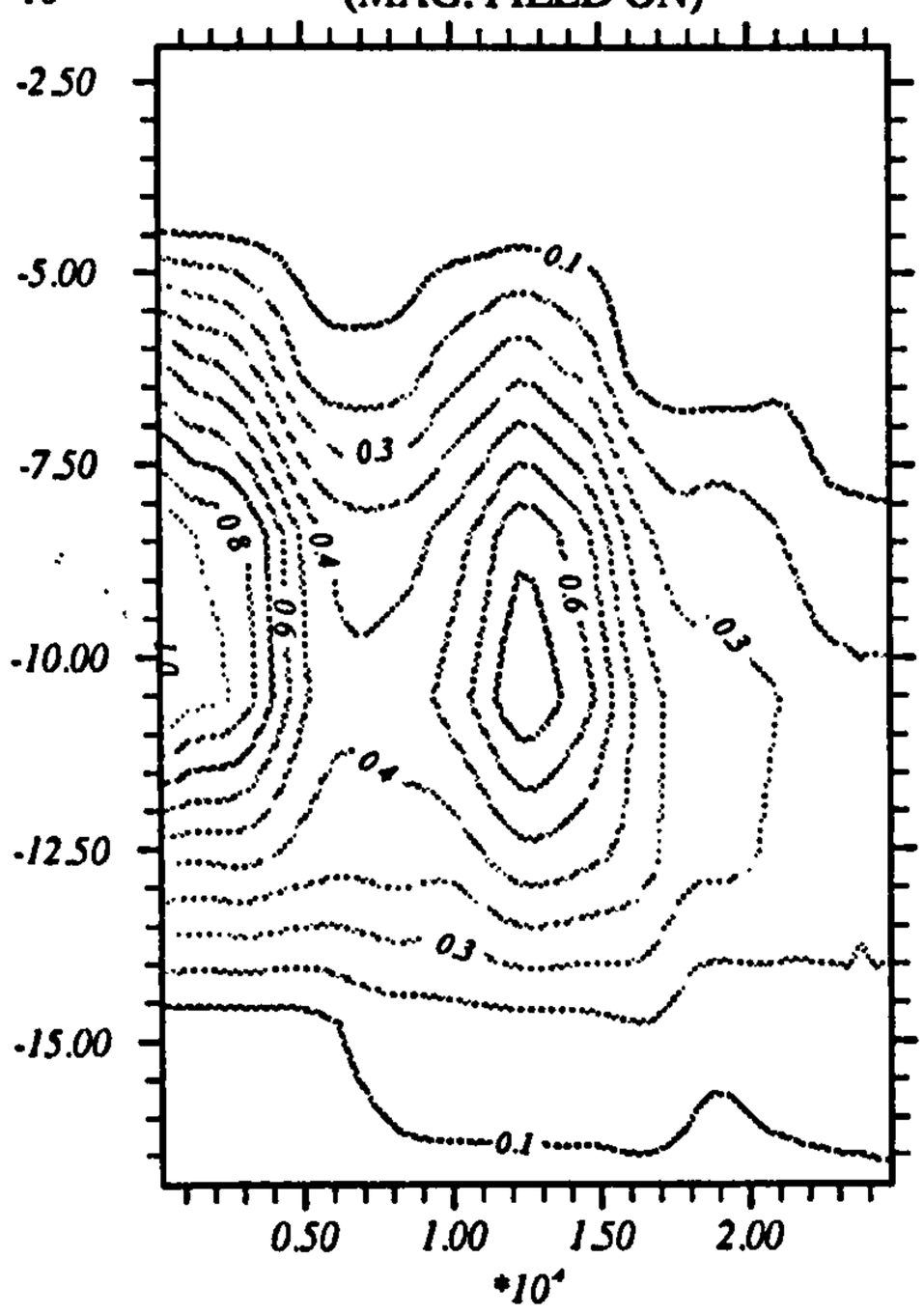

DENSITY MAP AT 600PS
(NO MAG. FIELD)

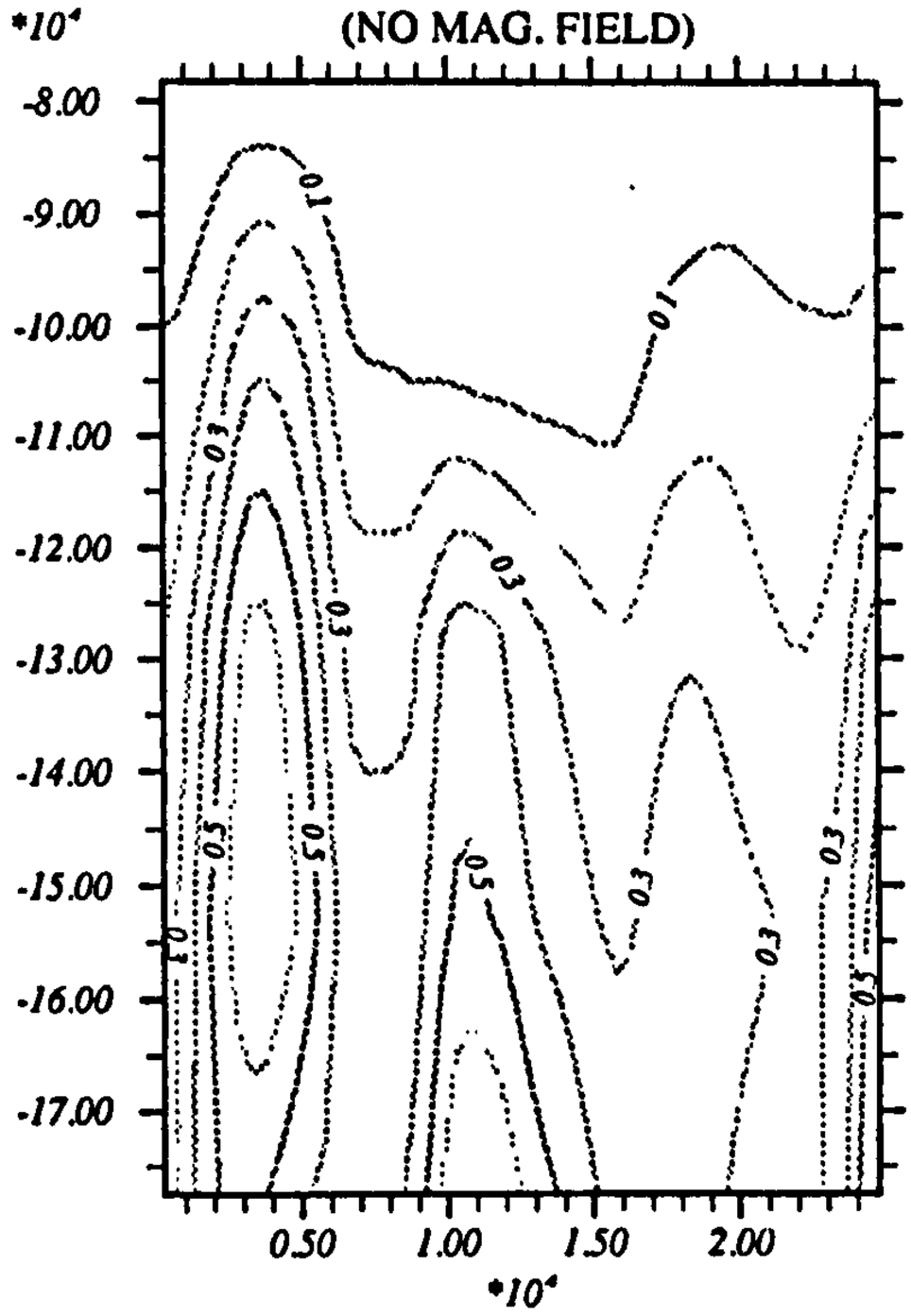

DENSITY MAP AT 600PS
(MAG. FIELD ON)

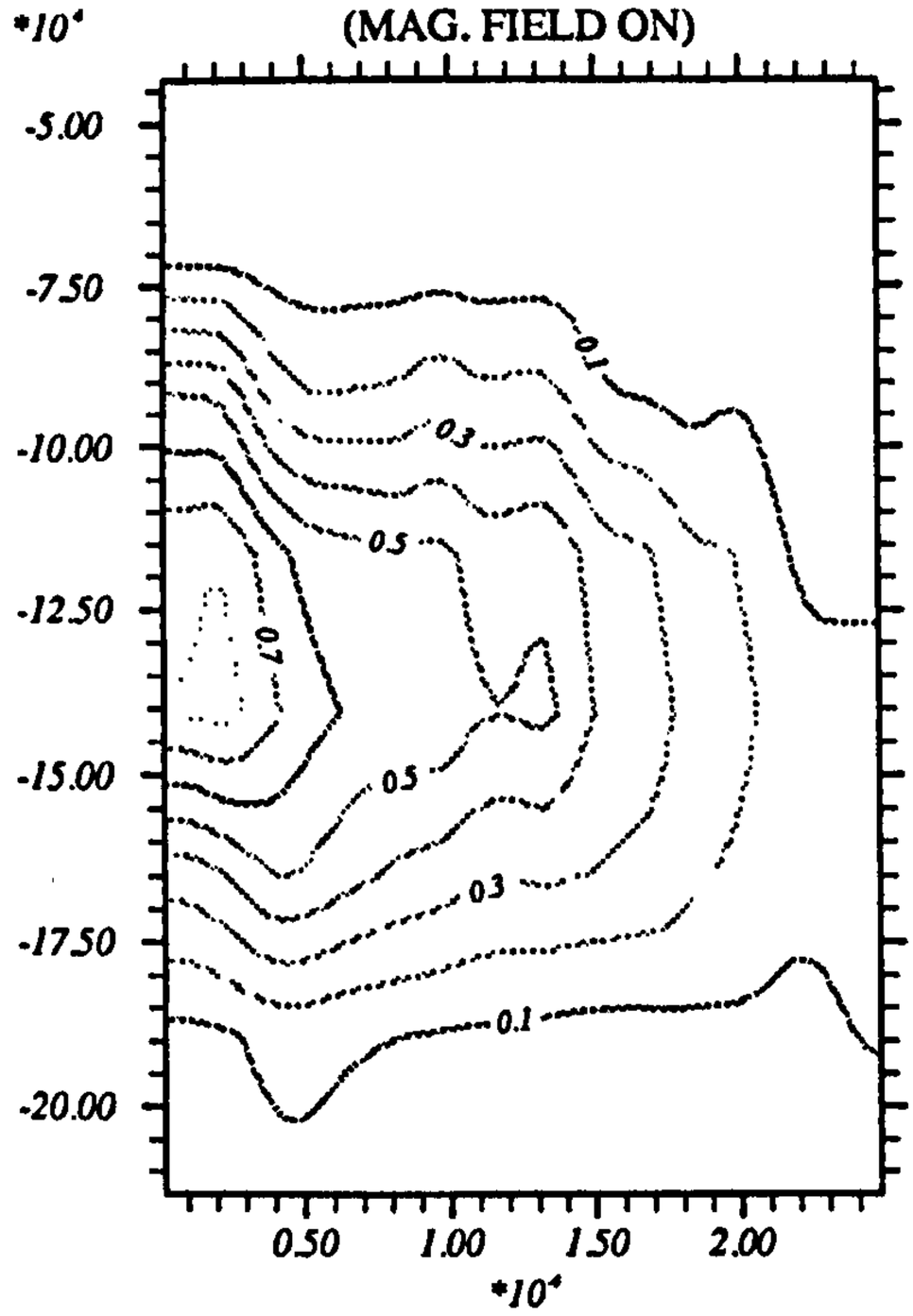

DENSITY MAP AT 650PS
(NO MAG. FIELD)

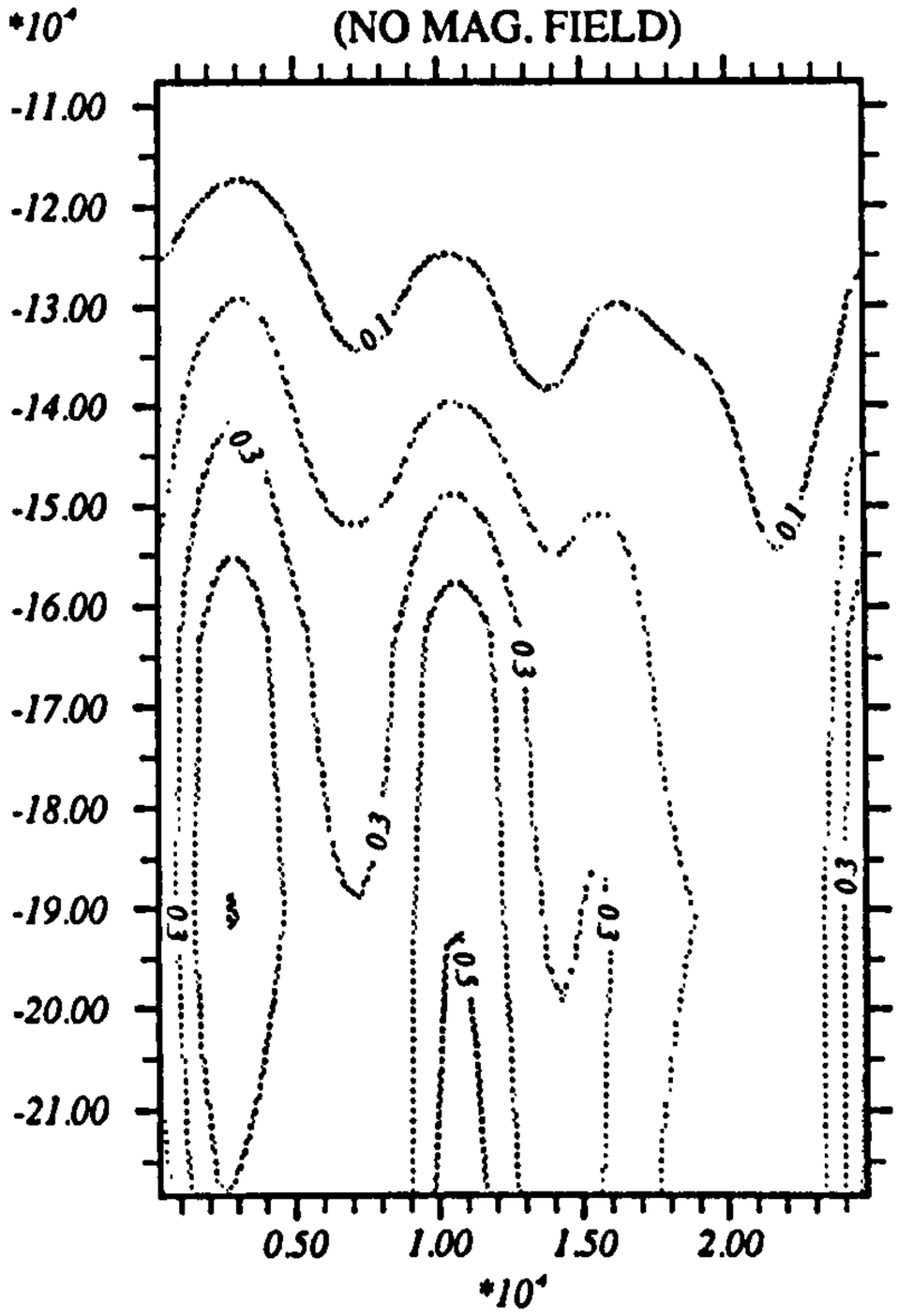

DENSITY MAP AT 650PS
(MAG. FIELD ON)

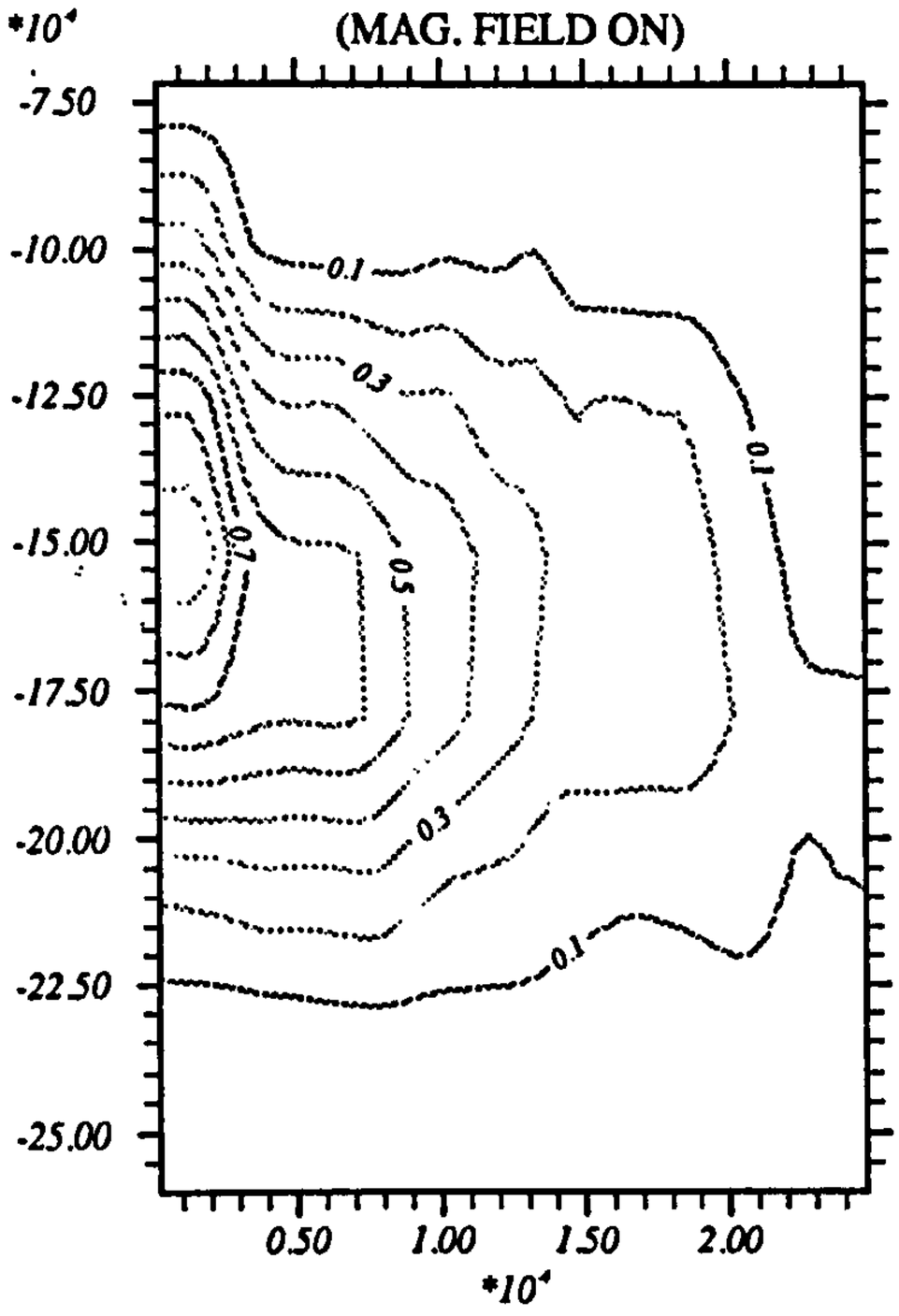

DENSITY MAP AT 700PS
(NO MAG. FIELD)

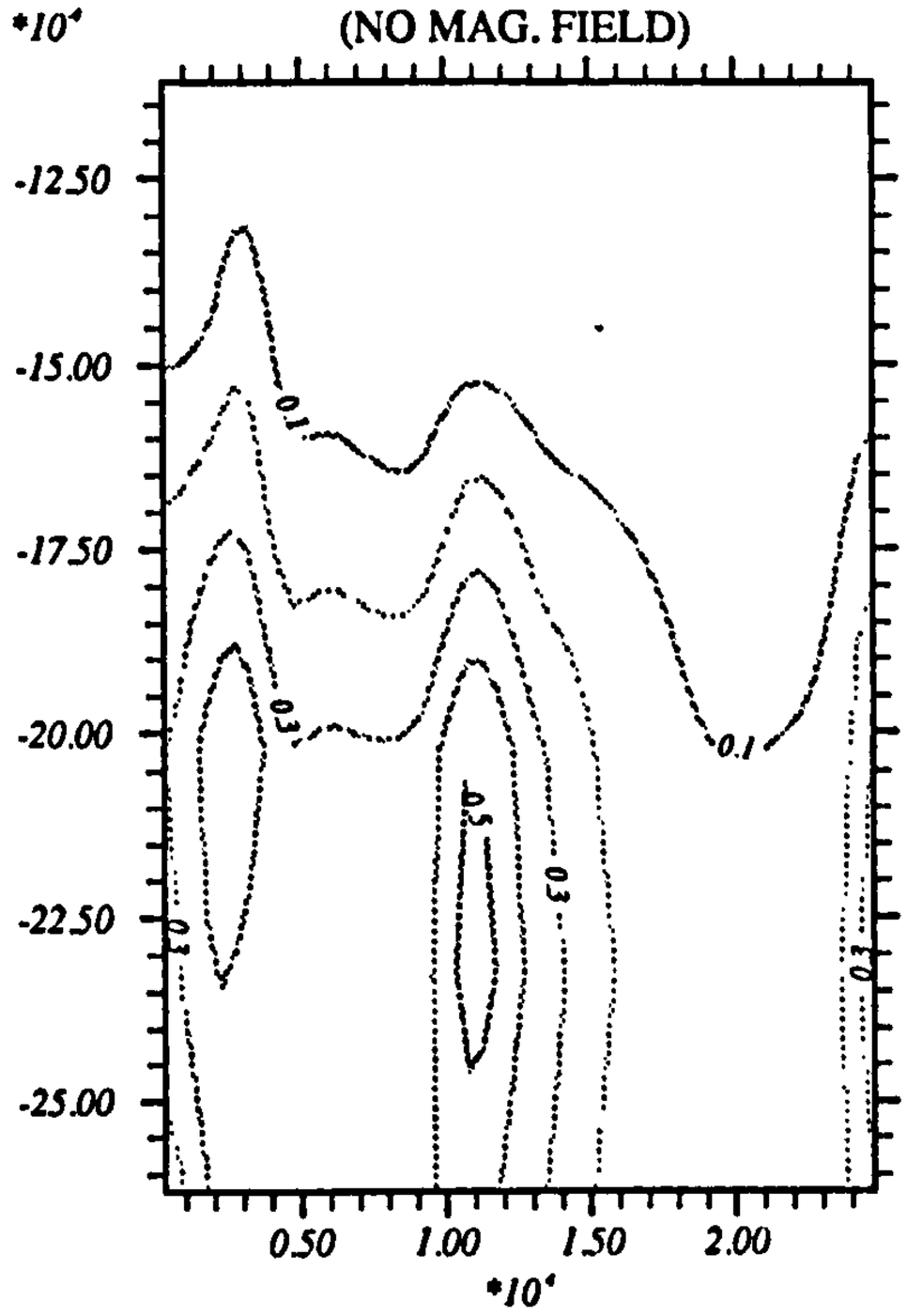

DENSITY MAP AT 700PS
(MAG. FIELD ON)

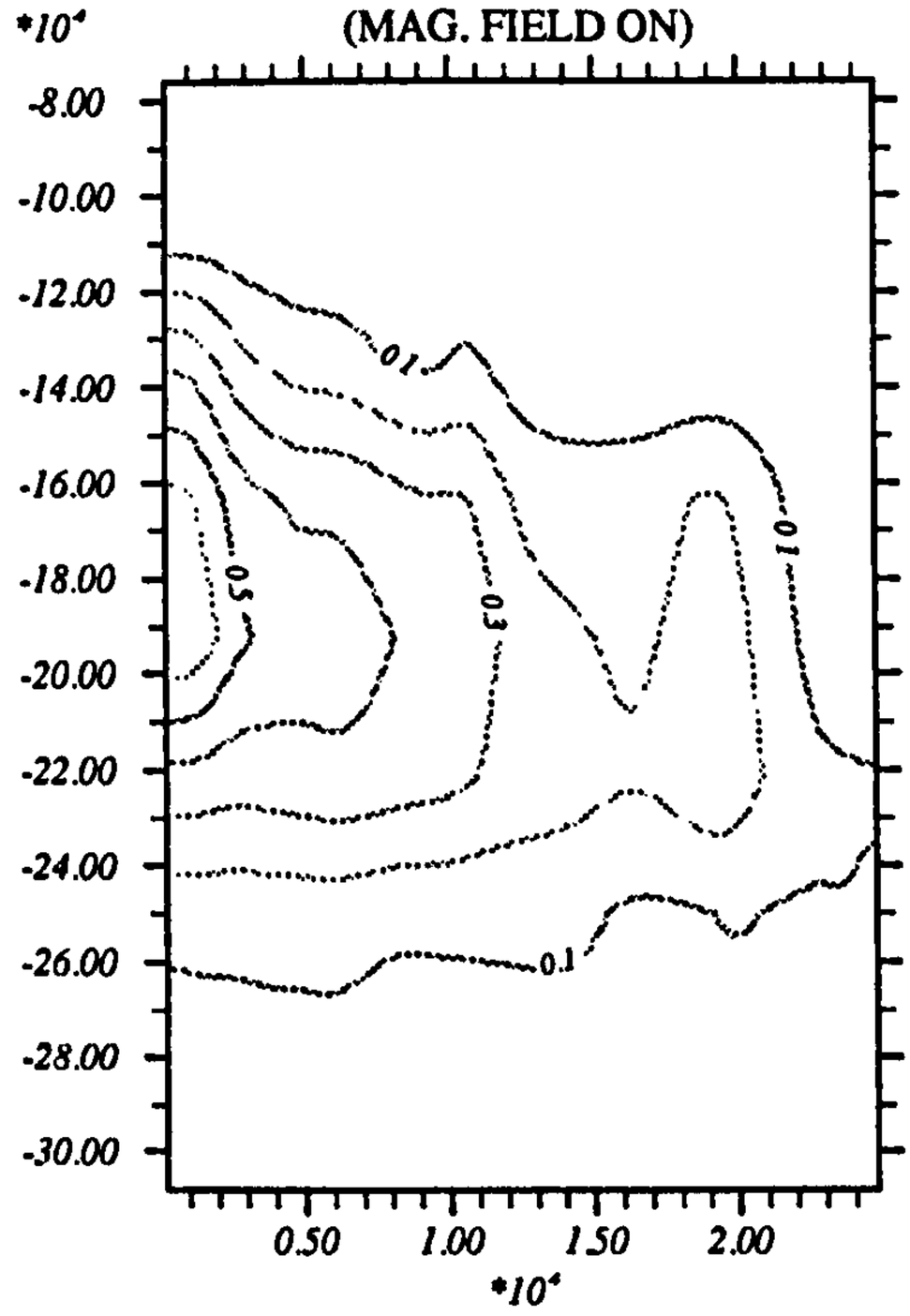

DENSITY MAP AT 750PS
(NO MAG. FIELD)

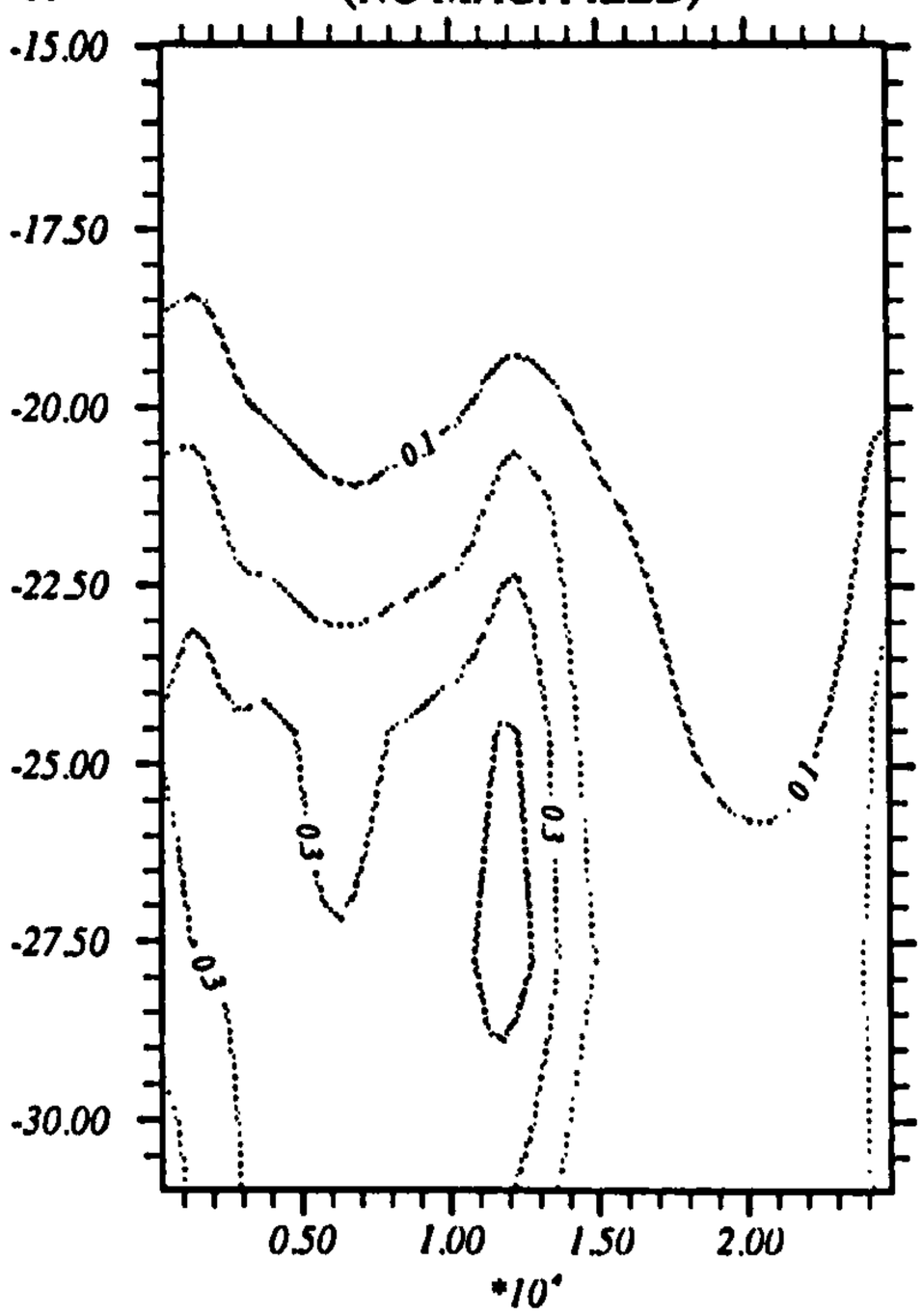

DENSITY MAP AT 750PS
(MAG. FIELD ON)

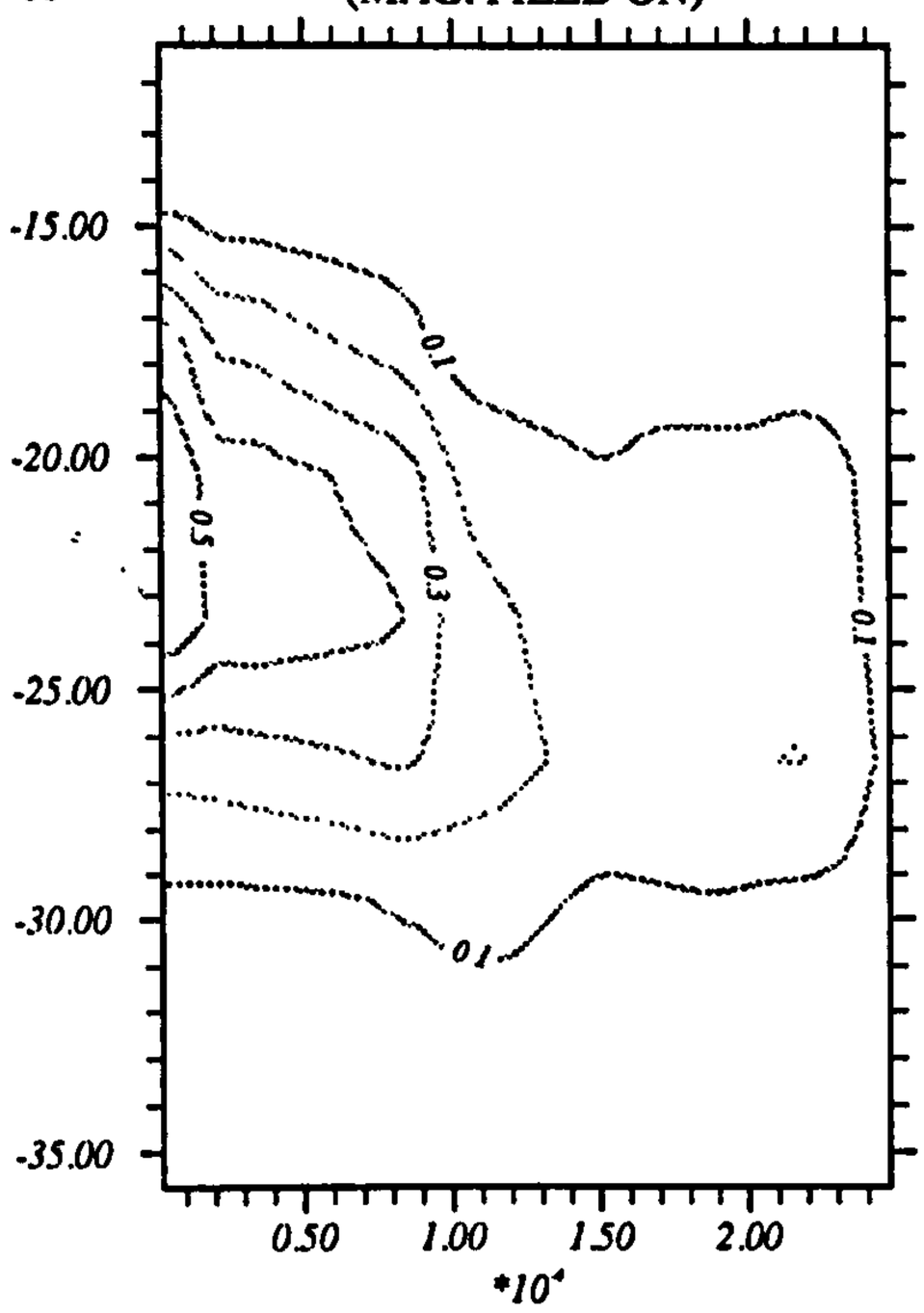

DENSITY MAP AT 800PS
(NO MAG. FIELD)

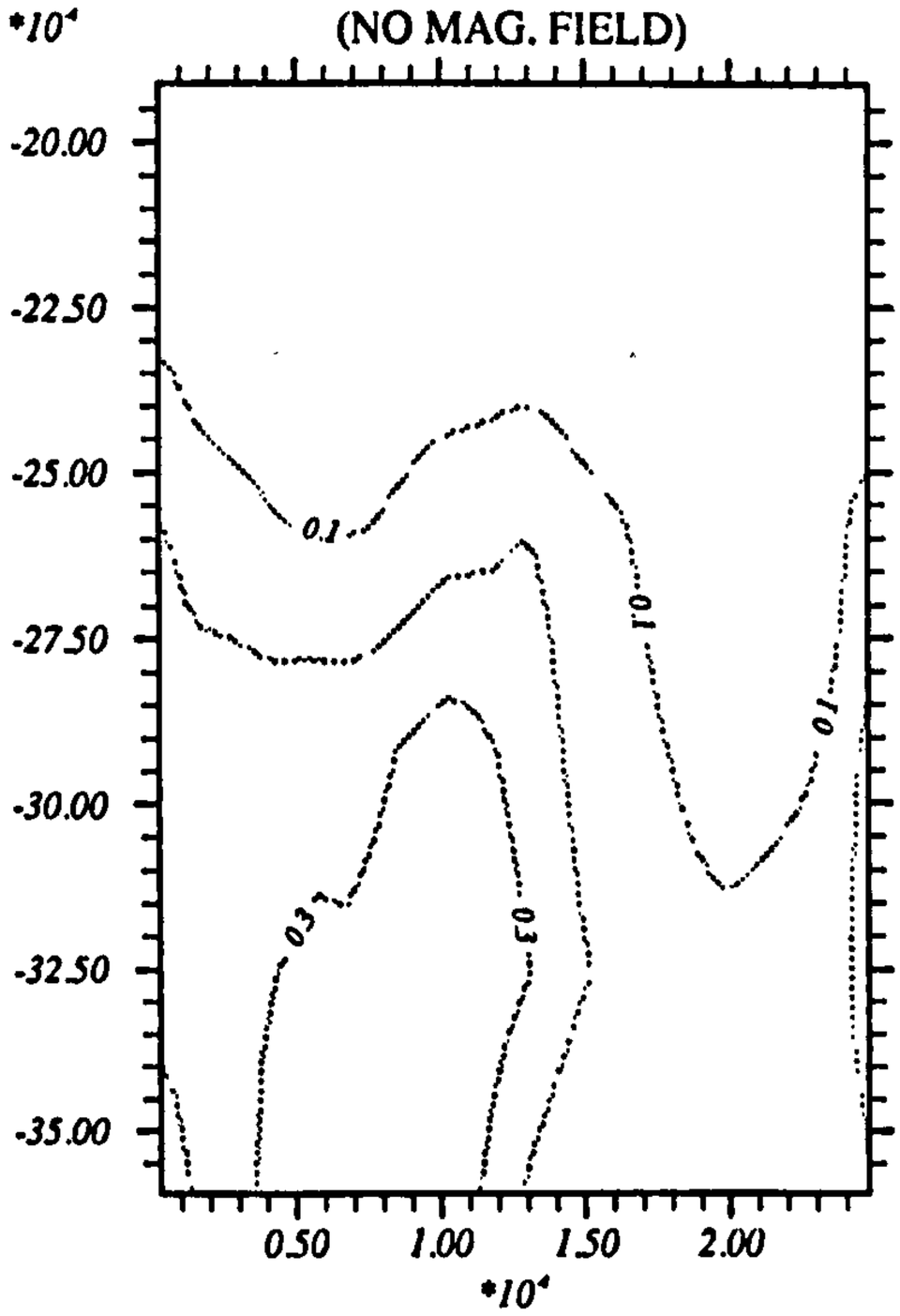

DENSITY MAP AT 800PS
(MAG. FIELD ON)

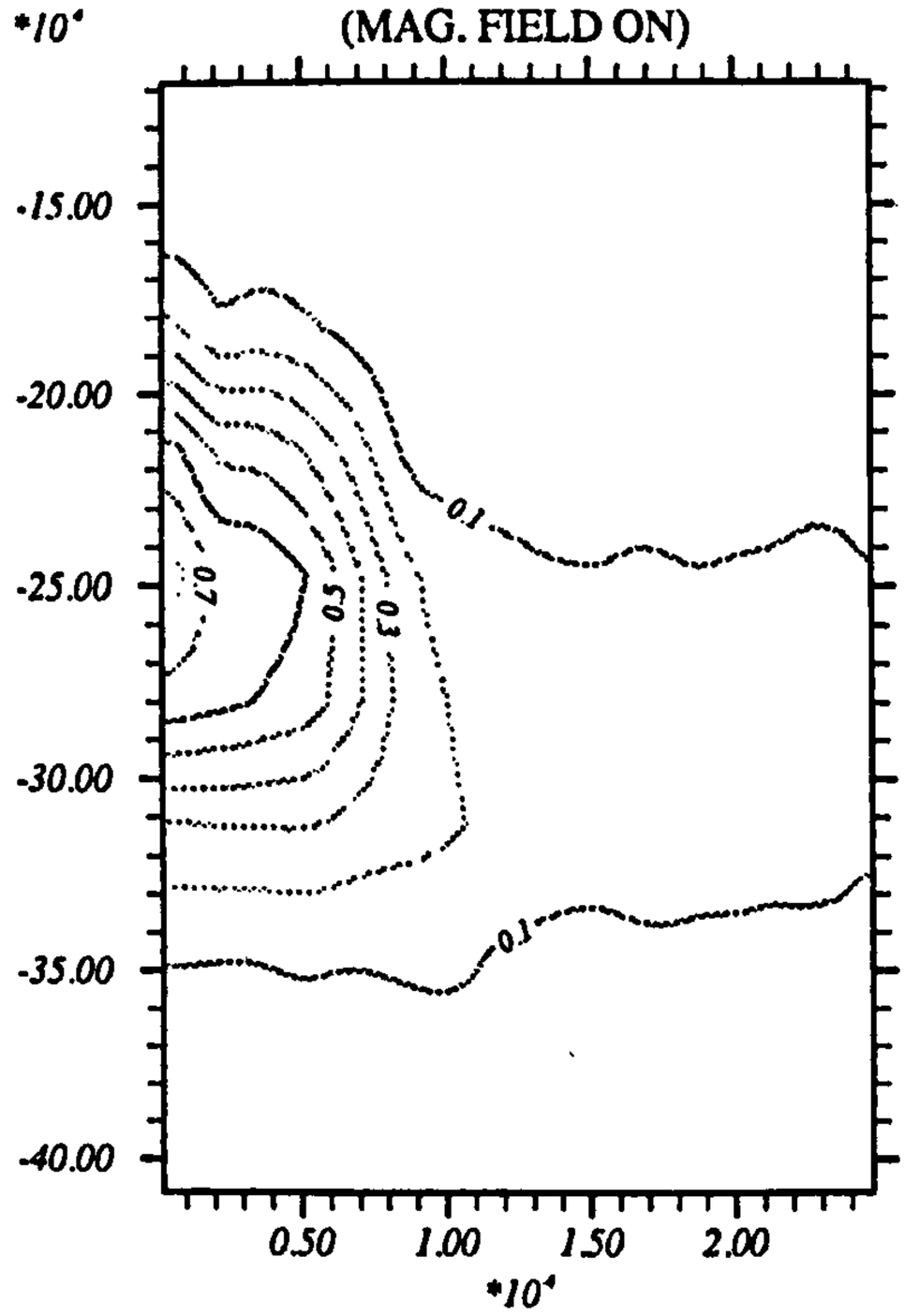

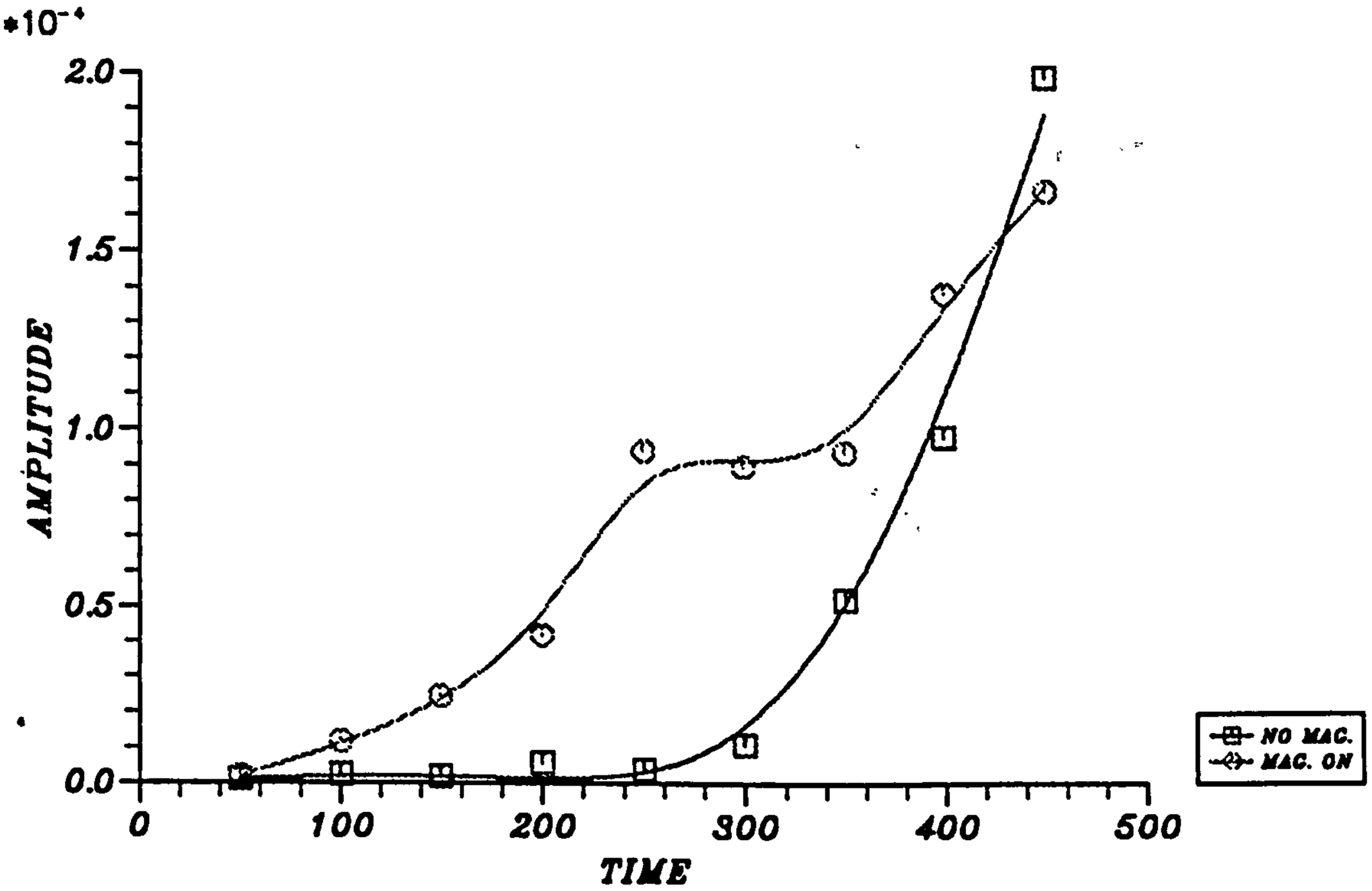

Figure 6.2: Amplitude as a function of time graph for the target ($2{\cdot}5\mu m \times 2{\cdot}5\mu m$).

the instability growth. The positive field lines come out of the paper and the negative go in to the paper. In a real situation these field lines form loops around the principal axis of the cylinder. It is observed from these contour maps that the additional field lines present at 100ps are the source which generates the high frequency modes in the density contour map. These high frequency modes enhance the instability growth over no field simulations.

6.3 TARGET SIZE ($5 \cdot 0\mu m \times 5 \cdot 0\mu m$)

The target used in these simulations is $5 \cdot 0\mu m$ in both axial and radial directions. The perturbation applied through the intensity has a wavelength of $2{\cdot}5\mu m$, whereas the initial applied perturbation amplitude is $5 \cdot 0\%$ of the intensity. The target and laser input parameters are given in Table $6 \cdot 2$.

The density contour maps for both magnetic field included and excluded are shown in figure $6 \cdot 4$ for the comparison of the growth of the instability. The density profile is similar for both cases until 150ps. The high frequency modes have a delayed start at about 200ps and these last until 500ps; thereby enhancing

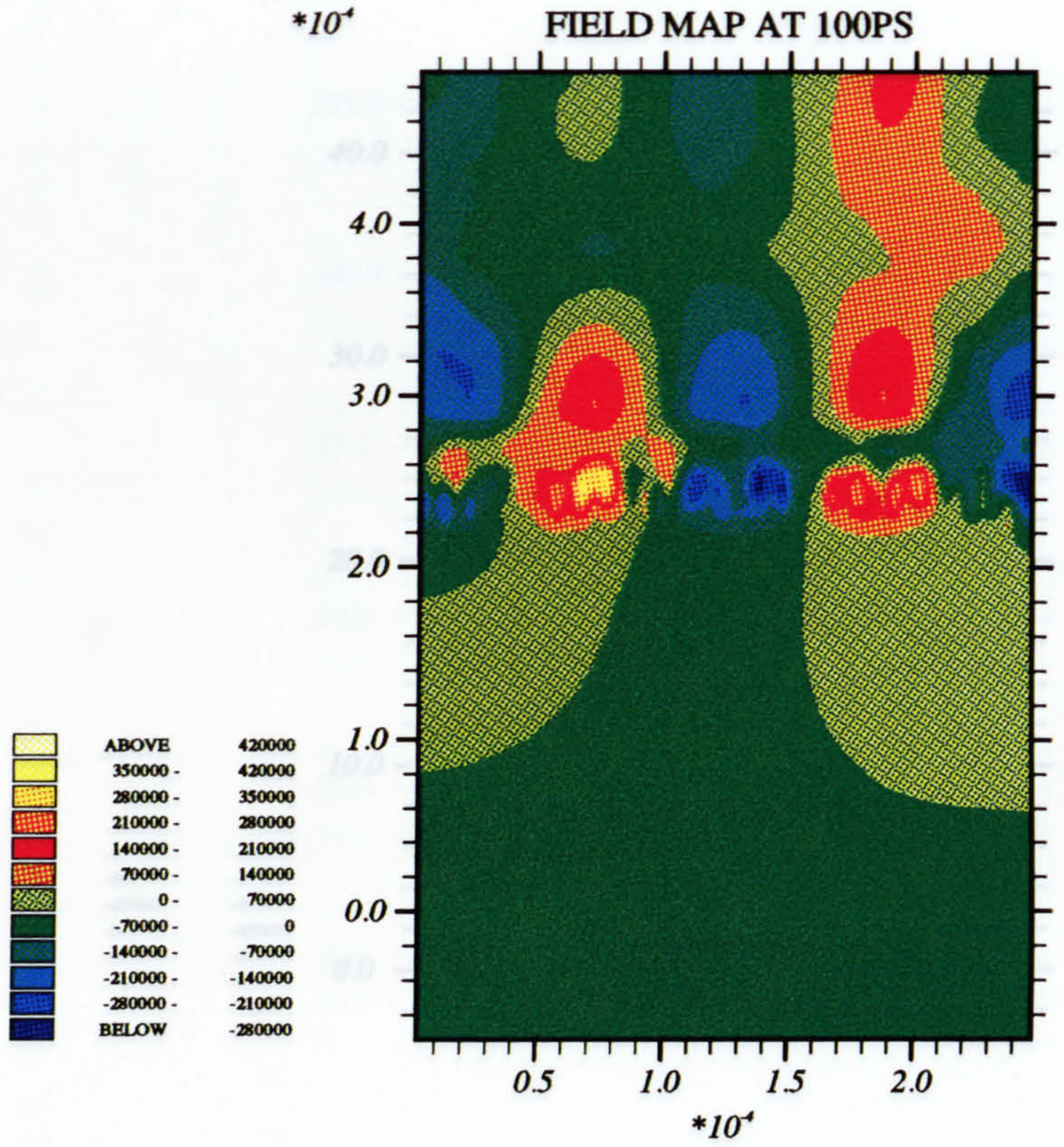

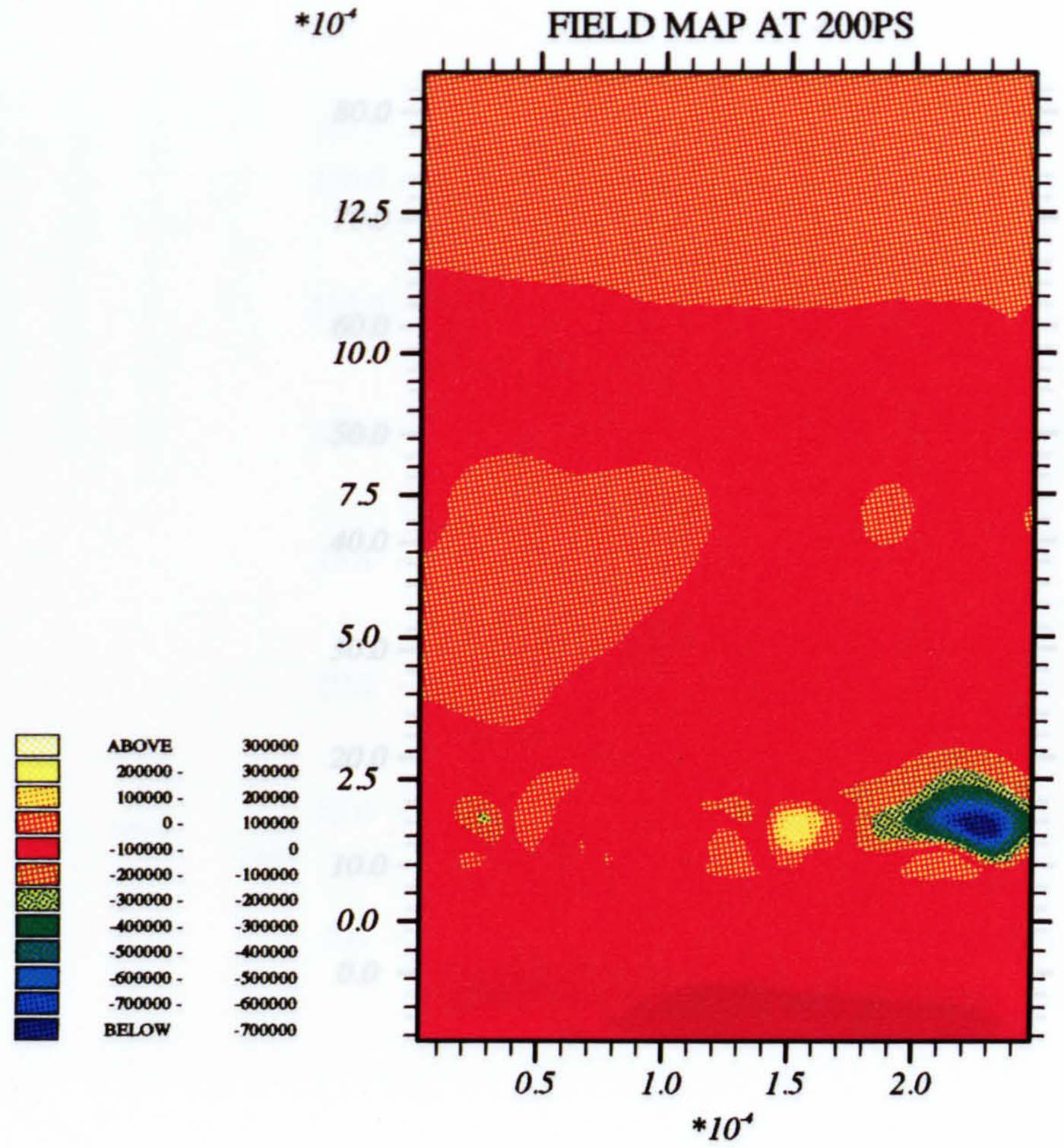

Figure 6.3: Magnetic field contour map for the target (2.5 μ m x 2.5 μ m) with perturbation applied through laser intensity.

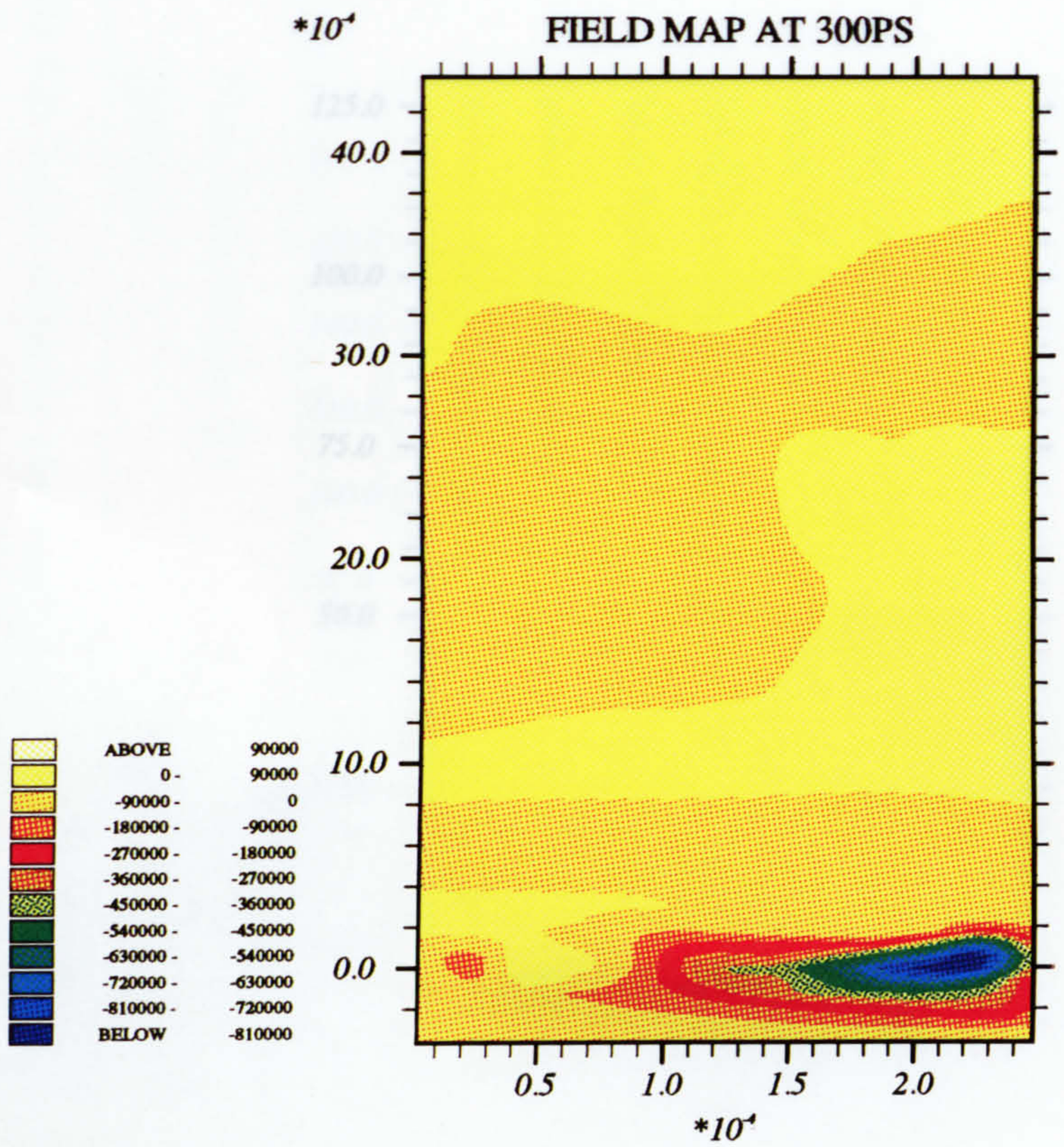
*10⁻⁴
FIELD MAP AT 300PS
40.0
30.0
20.0
10.0
0.0
0.5
1.0
1.5
2.0
*10⁻⁴
ABOVE 90000
0 - 90000
-90000 - 0
-180000 - -90000
-270000 - -180000
-360000 - -270000
-450000 - -360000
-540000 - -450000
-630000 - -540000
-720000 - -630000
-810000 - -720000
BELOW -810000

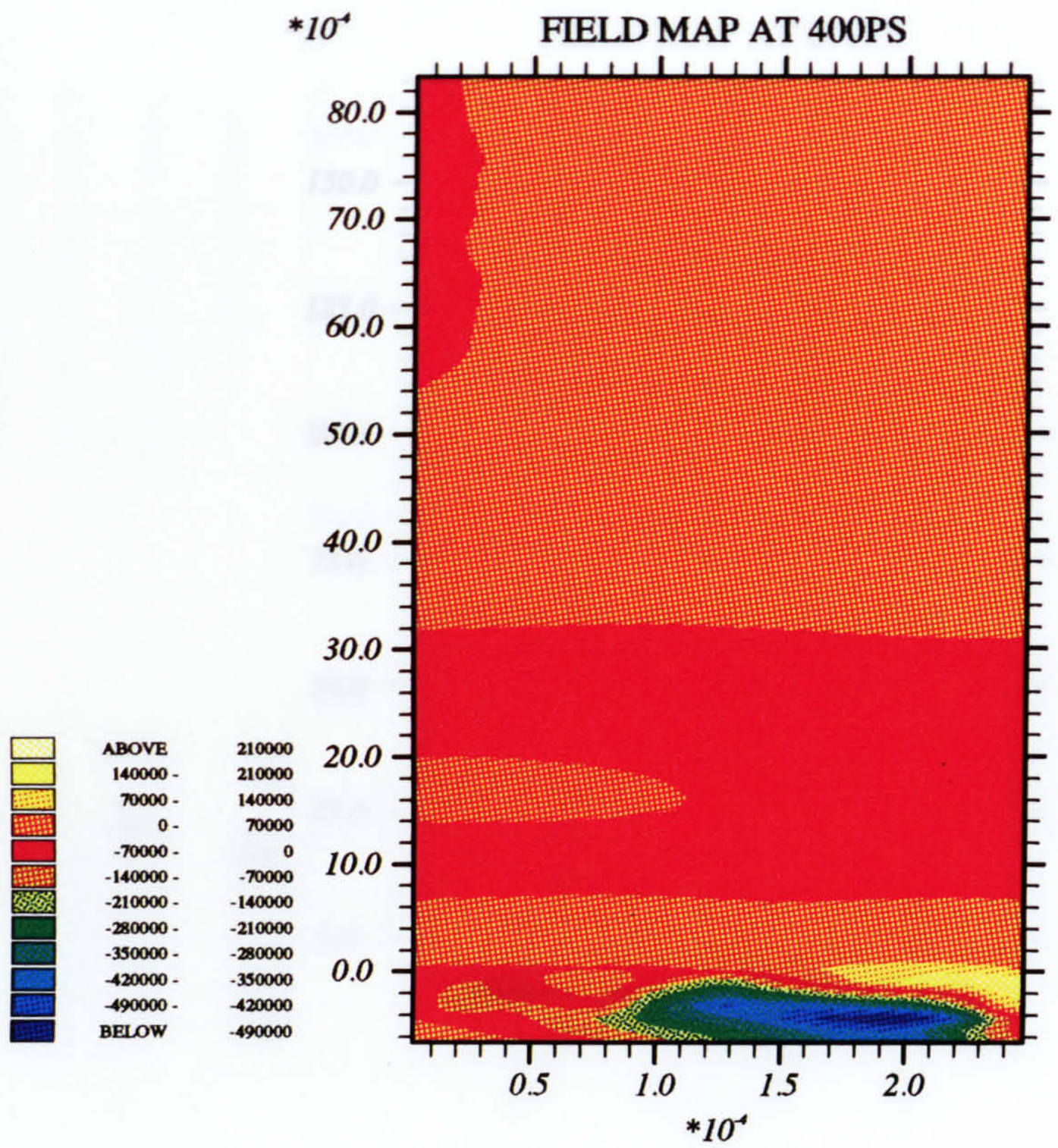
*10⁻⁴
FIELD MAP AT 400PS
80.0
70.0
60.0
50.0
40.0
30.0
20.0
10.0
0.0
0.5
1.0
1.5
2.0
*10⁻⁴
ABOVE 210000
140000 - 210000
70000 - 140000
0 - 70000
-70000 - 0
-140000 - -70000
-210000 - -140000
-280000 - -210000
-350000 - -280000
-420000 - -350000
-490000 - -420000
BELOW -490000

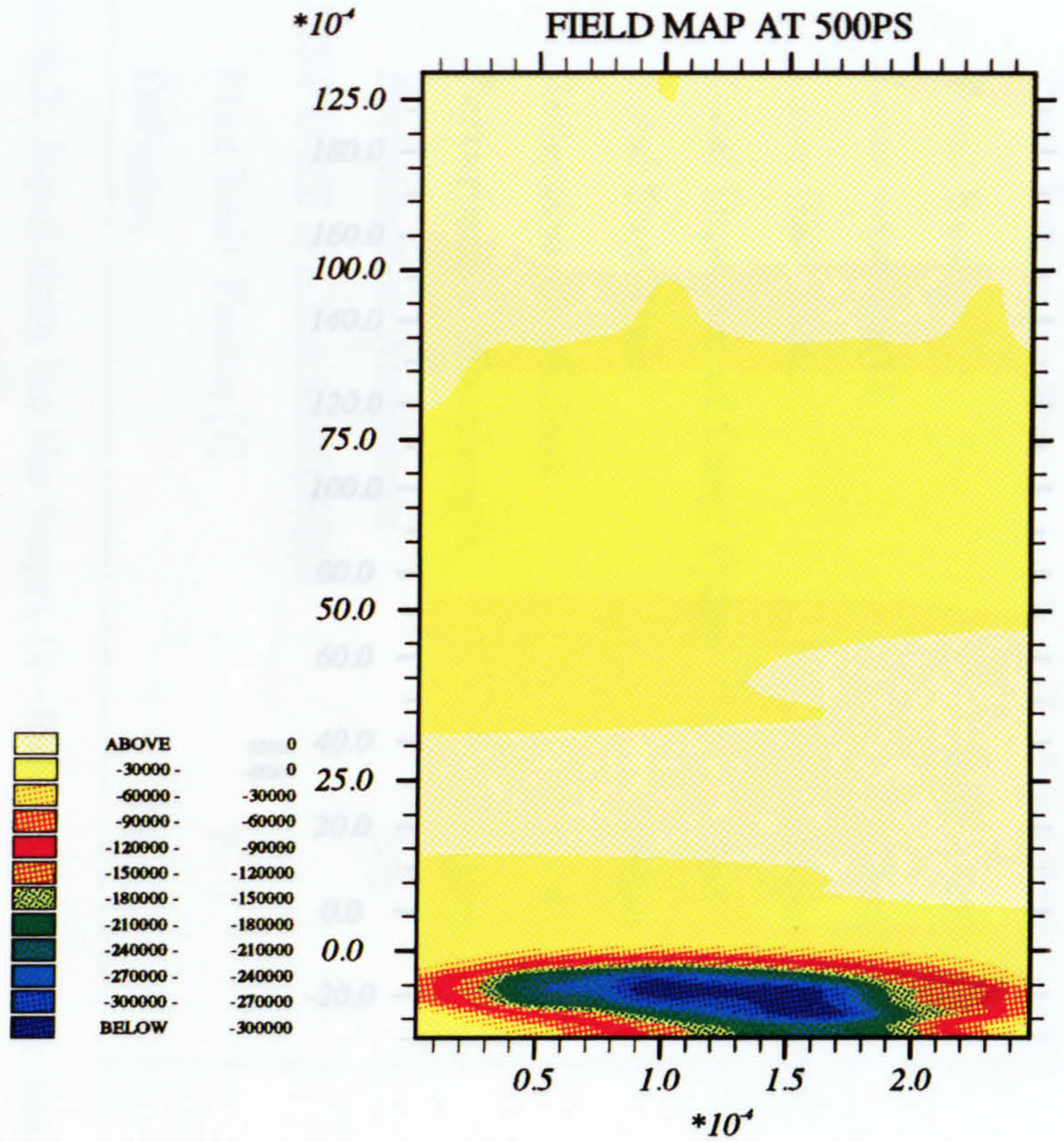
FIELD MAP AT 500PS
*10⁻⁴
125.0
100.0
75.0
50.0
25.0
0.0
0.5
1.0
1.5
2.0
*10⁻⁴
ABOVE 0
-30000 - 0
-60000 - -30000
-90000 - -60000
-120000 - -90000
-150000 - -120000
-180000 - -150000
-210000 - -180000
-240000 - -210000
-270000 - -240000
-300000 - -270000
BELOW -300000

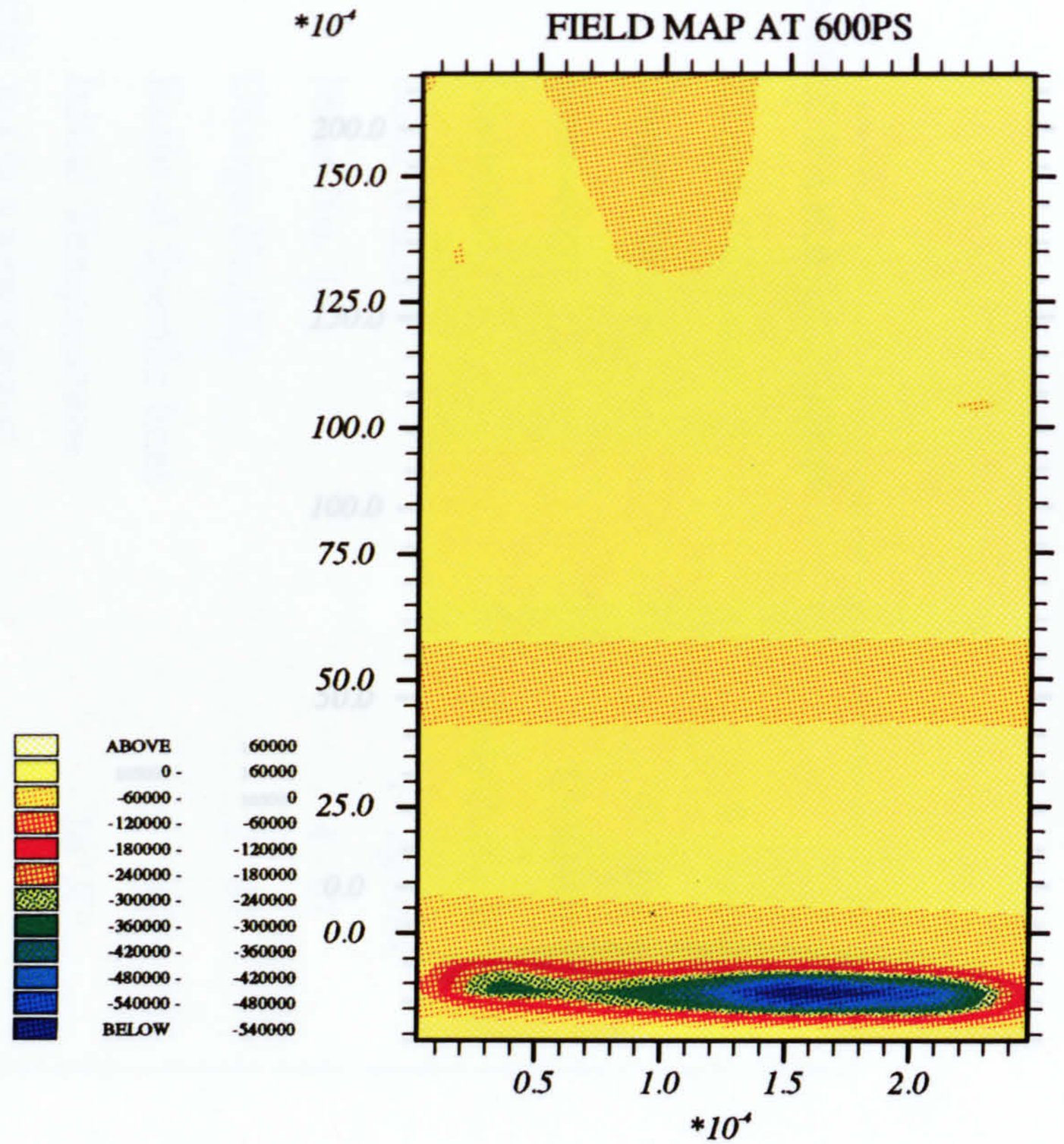
FIELD MAP AT 600PS
*10⁻⁴
150.0
125.0
100.0
75.0
50.0
25.0
0.0
0.5
1.0
1.5
2.0
*10⁻⁴
ABOVE 60000
0 - 60000
-60000 - 0
-120000 - -60000
-180000 - -120000
-240000 - -180000
-300000 - -240000
-360000 - -300000
-420000 - -360000
-480000 - -420000
-540000 - -480000
BELOW -540000

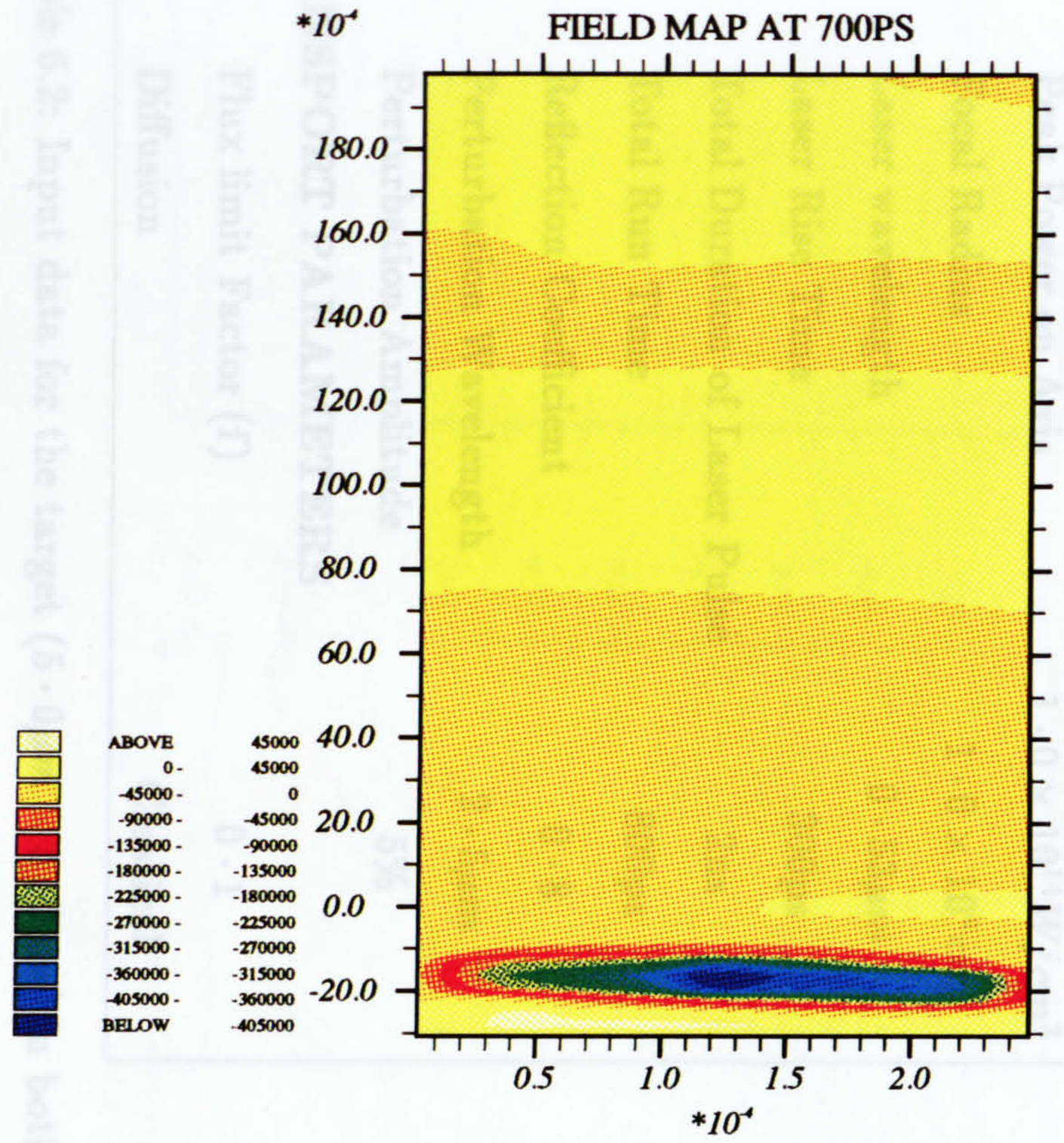
*10⁻⁴
FIELD MAP AT 700PS
180.0
160.0
140.0
120.0
100.0
80.0
60.0
40.0
20.0
0.0
-20.0
0.5
1.0
1.5
2.0
*10⁻⁴
ABOVE 45000
0 - 45000
-45000 - 0
-90000 - -45000
-135000 - -90000
-180000 - -135000
-225000 - -180000
-270000 - -225000
-315000 - -270000
-360000 - -315000
-405000 - -360000
BELOW -405000

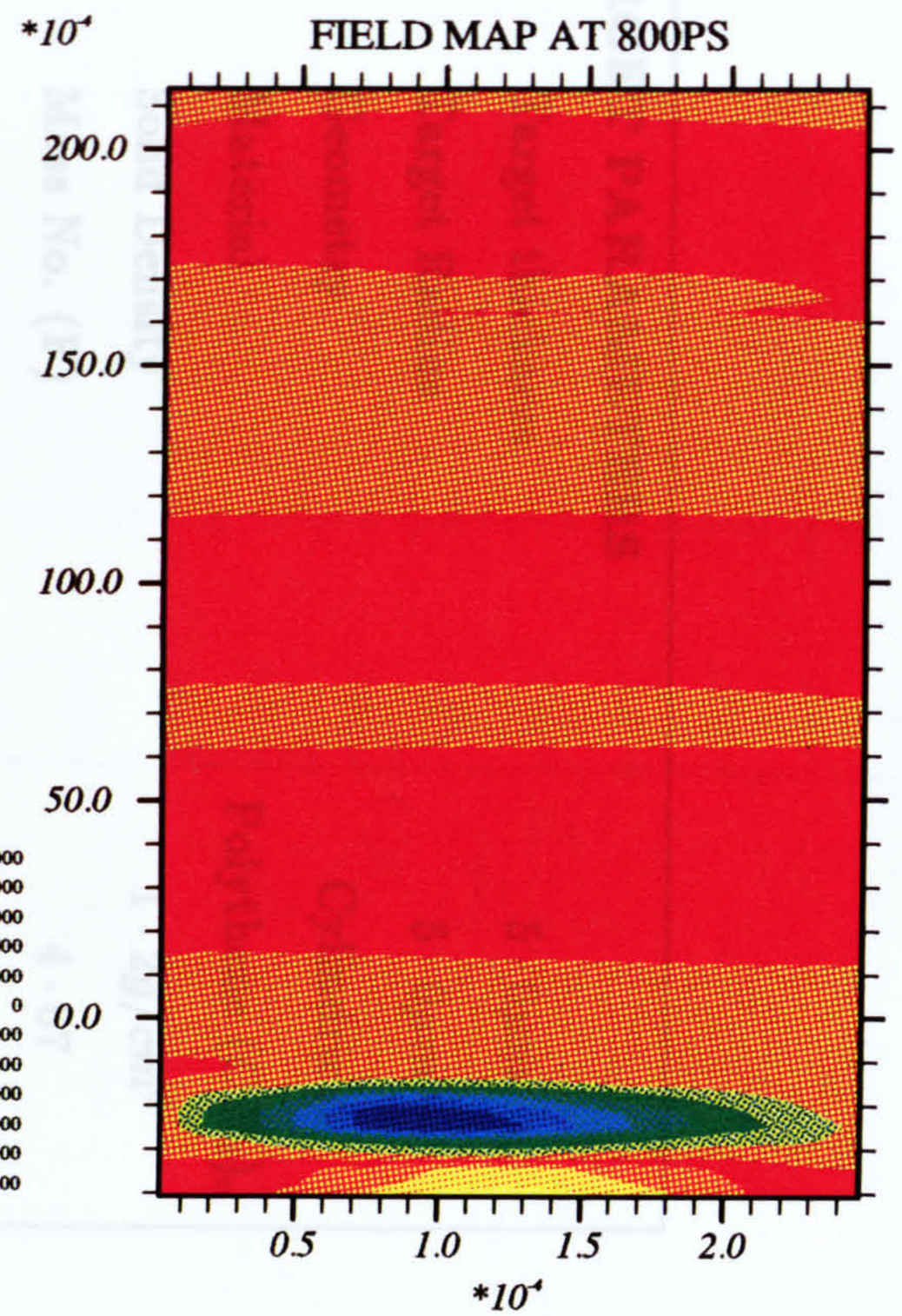
*10⁻⁴
FIELD MAP AT 800PS
200.0
150.0
100.0
50.0
0.0
0.5
1.0
1.5
2.0
*10⁻⁴
ABOVE 140000
105000 - 140000
70000 - 105000
35000 - 70000
0 - 35000
-35000 - 0
-70000 - -35000
-105000 - -70000
-140000 - -105000
-175000 - -140000
-210000 - -175000
BELOW -210000

TARGET PARAMETERS	
Target thickness	$5 \cdot 0 \mu m$
Target Radius	$5 \cdot 0 \mu m$
Geometry	Cylindrical
Material	Polythene $(CH_2)_n$
Solid Density	$1 \cdot 2 g/cm^3$
Mass No. (F)	$4 \cdot 67$
Charge No.(Z)	$2 \cdot 67$
Ratio of Specific heat	$1 \cdot 667$
Initial Temperature	$10^4 K°$
LASER PARAMETERS	
Peak Power on Axis	$1 \cdot 0 \times 10^{14} W/cm^2$
Focal Radius	$1 \cdot 0 \times 10^4 cm$
Laser wavelength	$0 \cdot 53 \mu m$
Laser Rise Time	300ps
Total Duration of Laser Pulse	2ns
Total Run Time	800ps
Reflection Coefficient	$0 \cdot 8$
Perturbation Wavelength	$2 \cdot 5 \mu m$
Perturbation Amplitude	5%
TRANSPORT PARAMETERS	
Flux limit Factor (f)	$0 \cdot 1$
Diffusion	Classical

Table 6.2: Input data for the target $(5 \cdot 0 \mu m \times 5 \cdot 0 \mu m)$ in both directions.

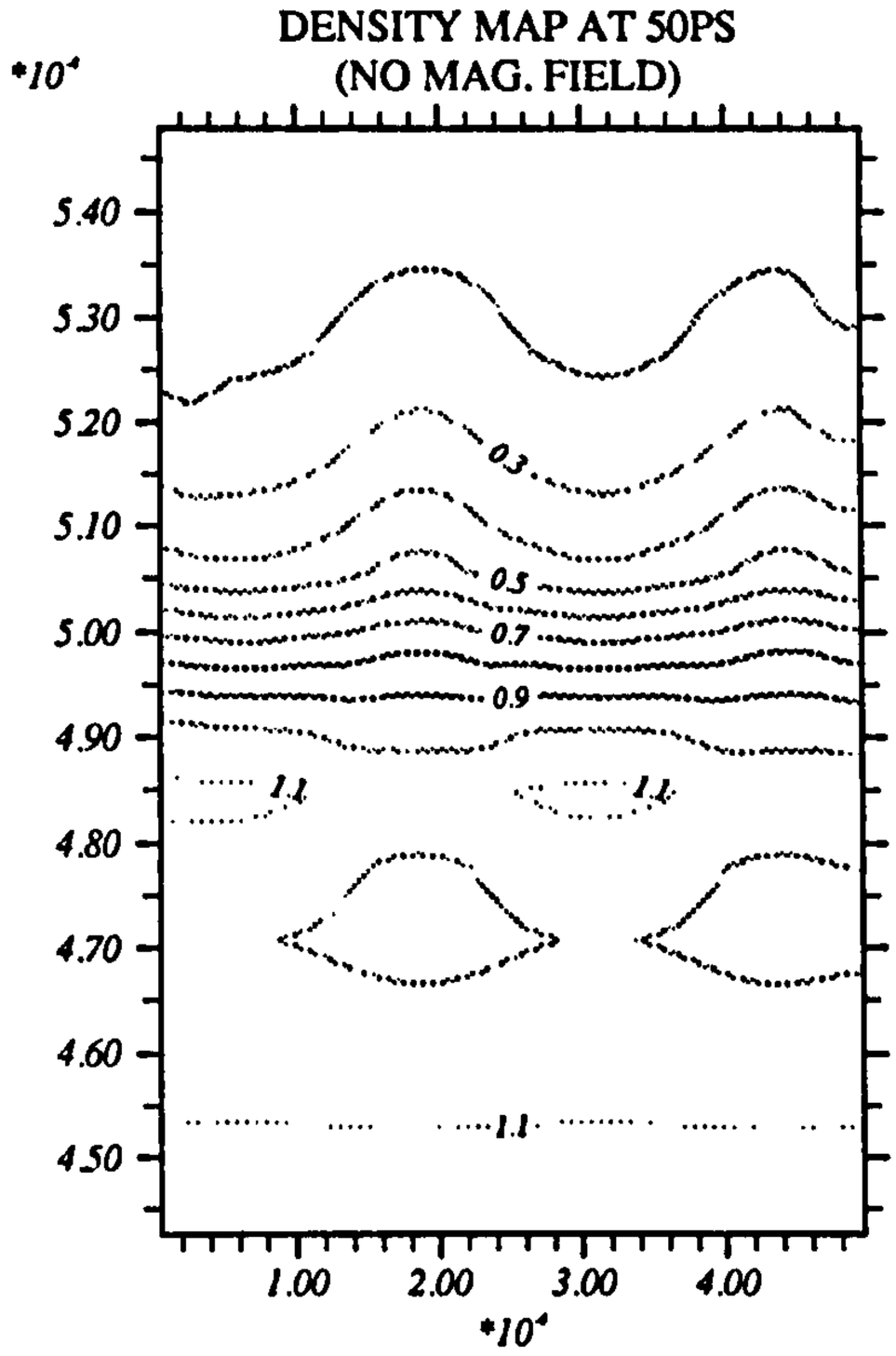

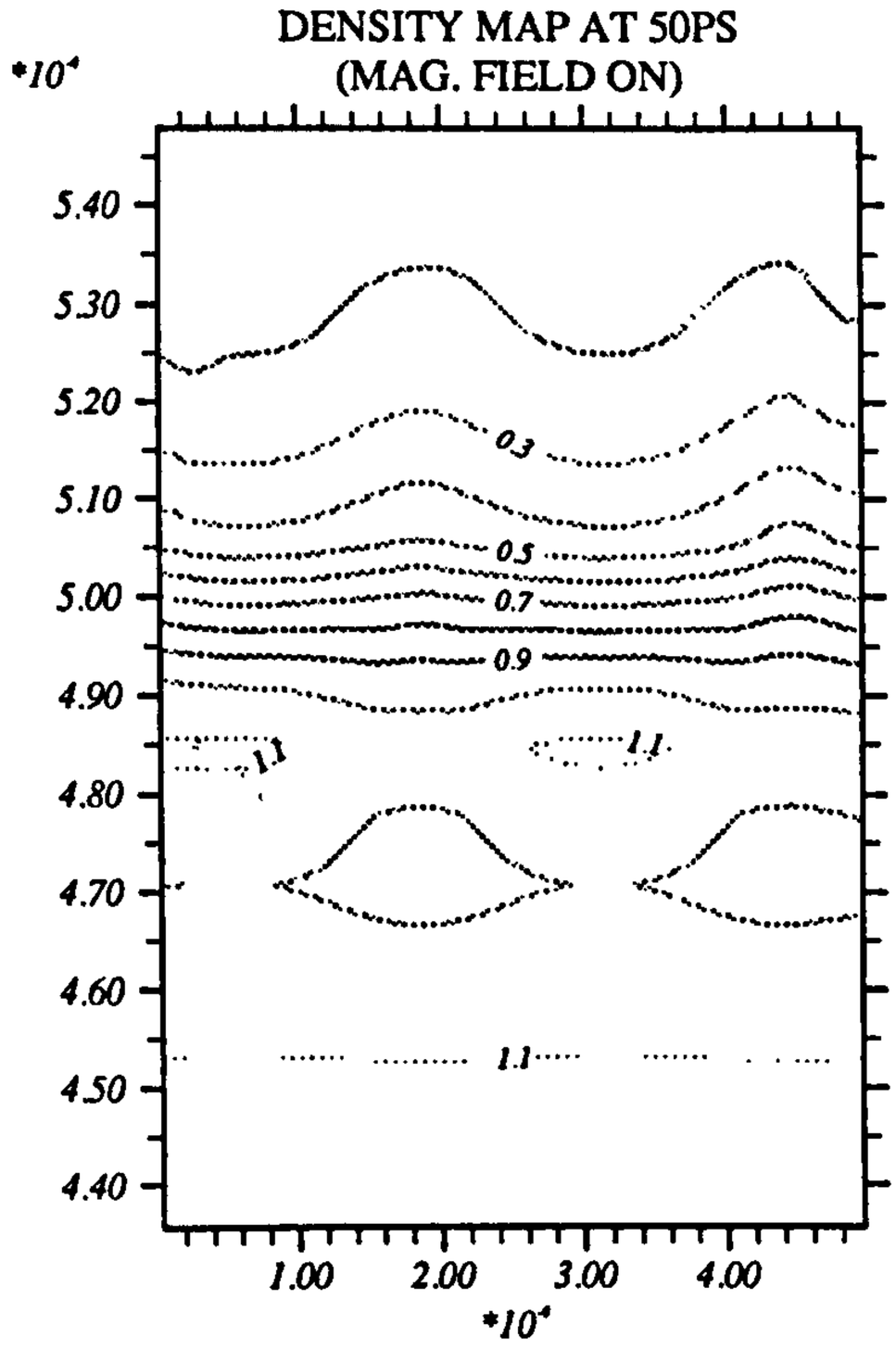

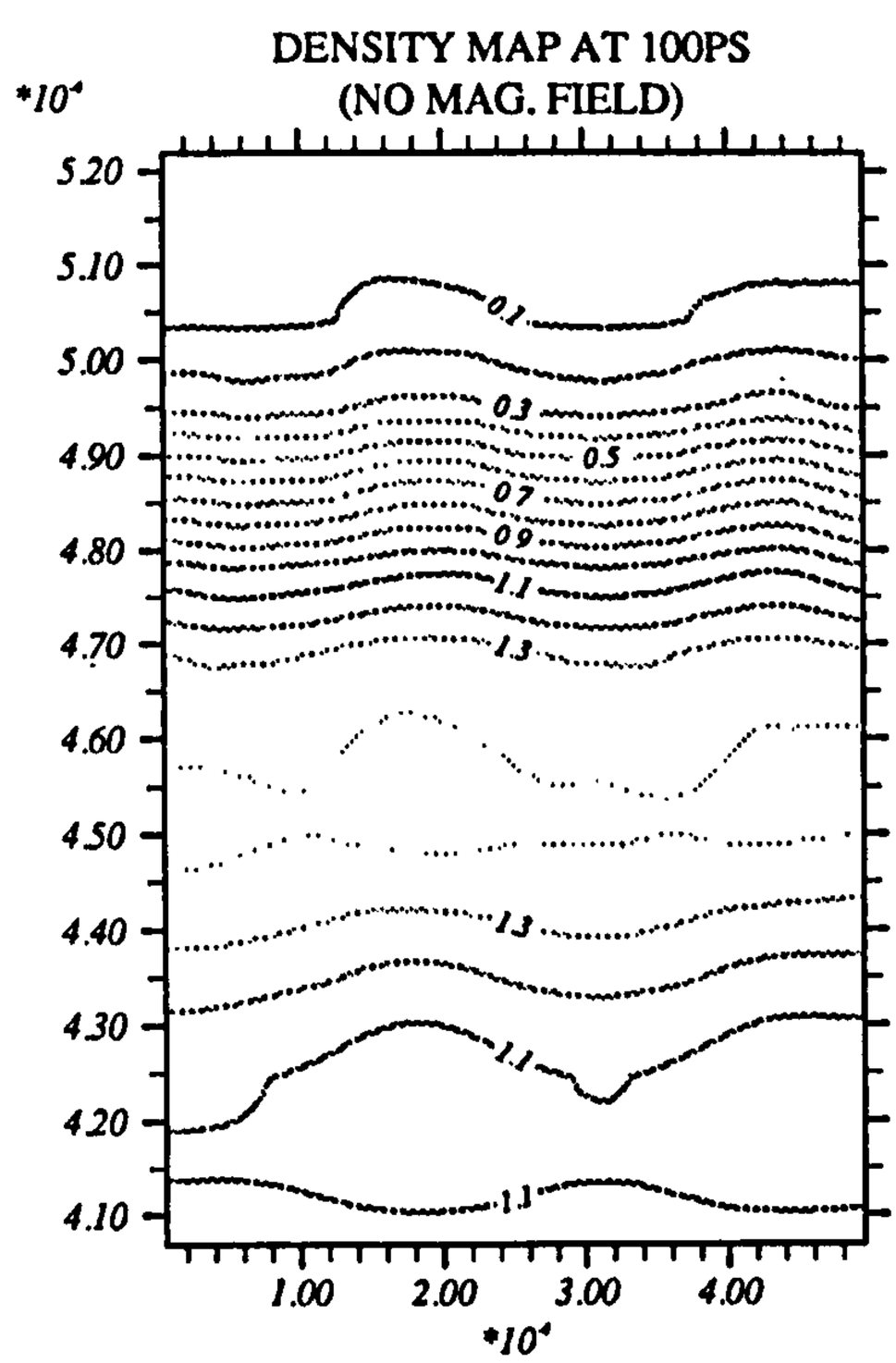

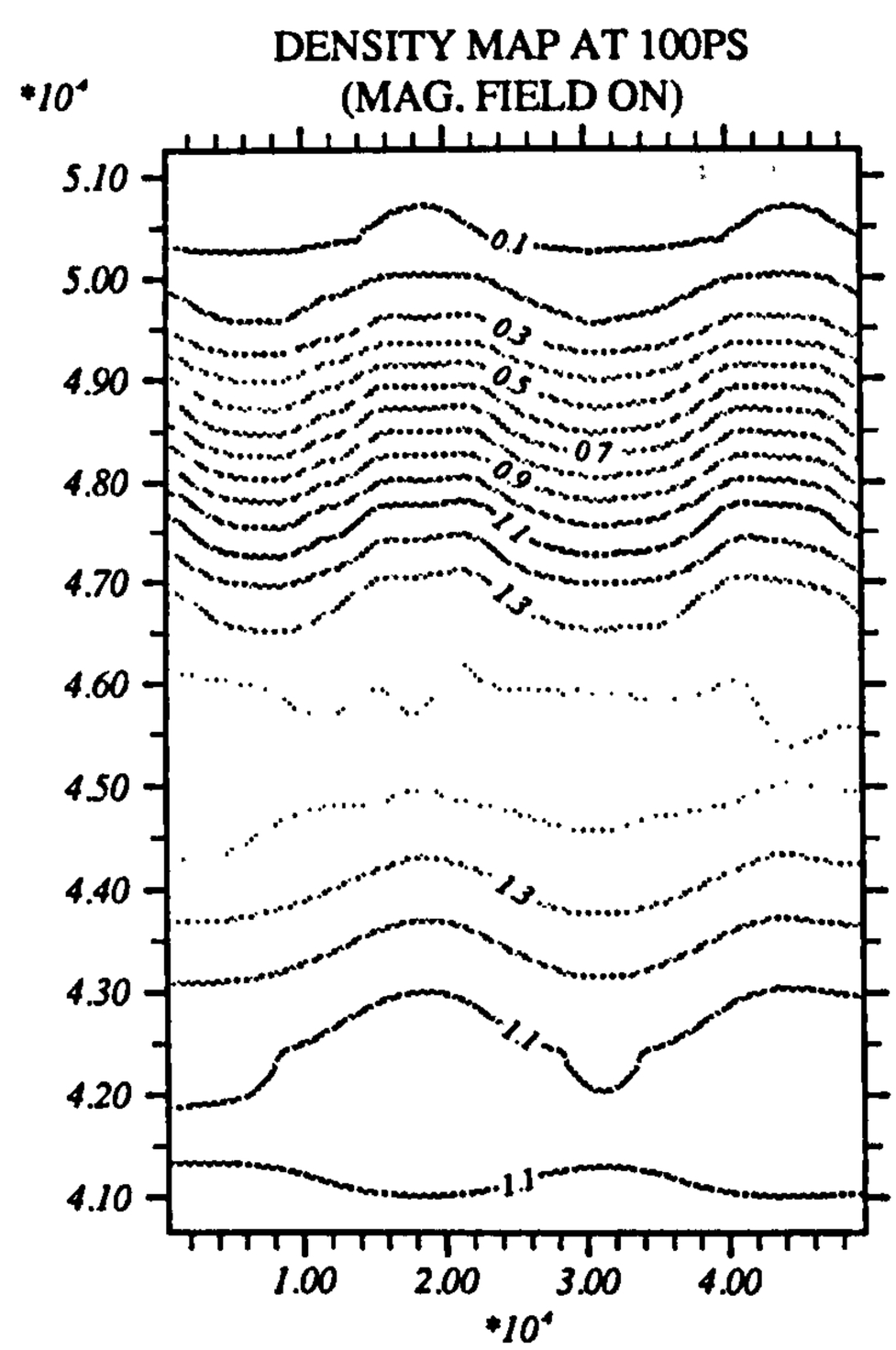

Figure 6.4: Density contour map for the target ($5{\cdot}0\mu m \times 5{\cdot}0\mu m$) with perturbation applied through laser intensity

DENSITY MAP AT 150PS
(NO MAG. FIELD)

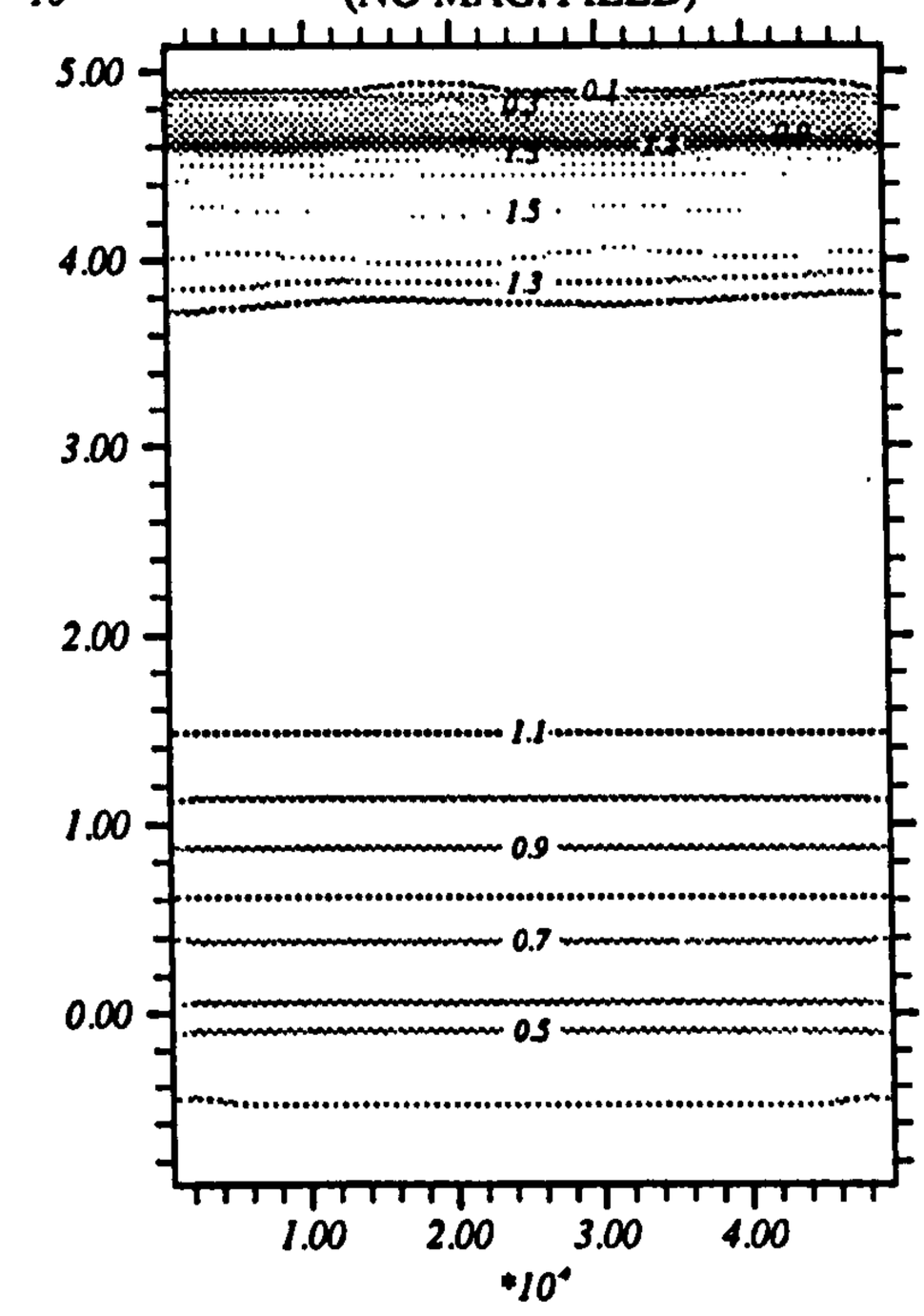

DENSITY MAP AT 150PS
(MAG. FIELD ON)

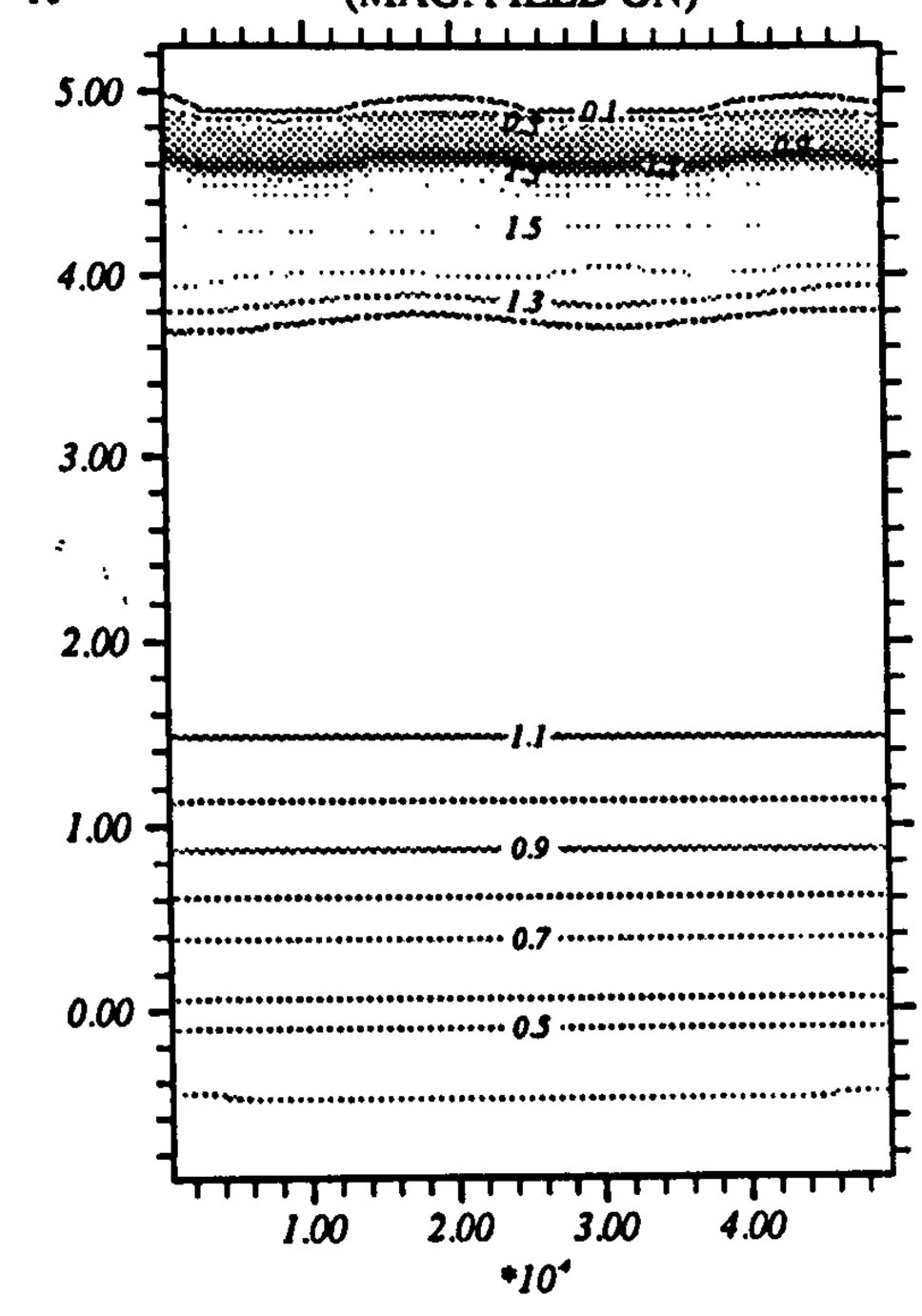

DENSITY MAP AT 200PS
(NO MAG. FIELD)

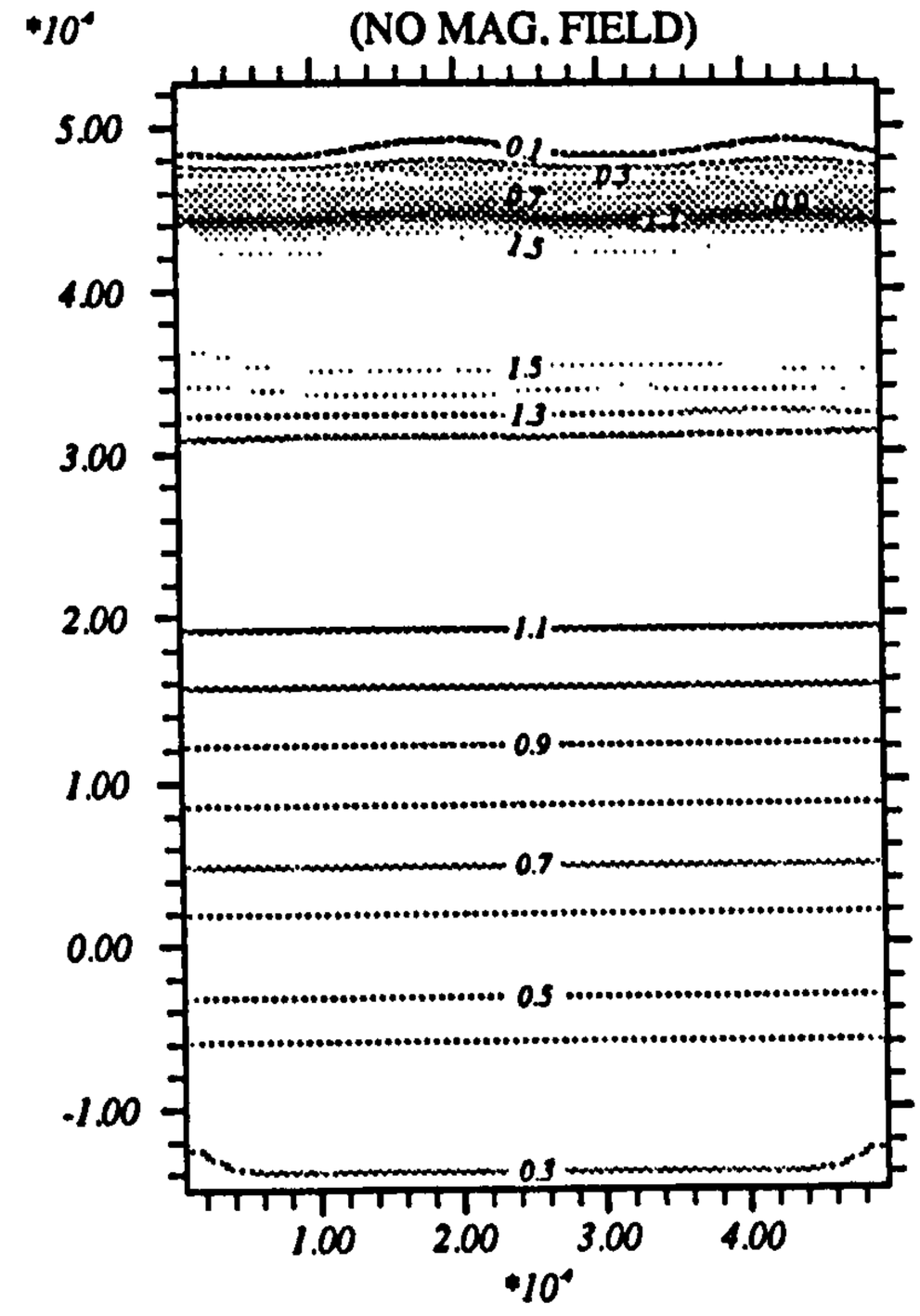

DENSITY MAP AT 200PS
(MAG. FIELD ON)

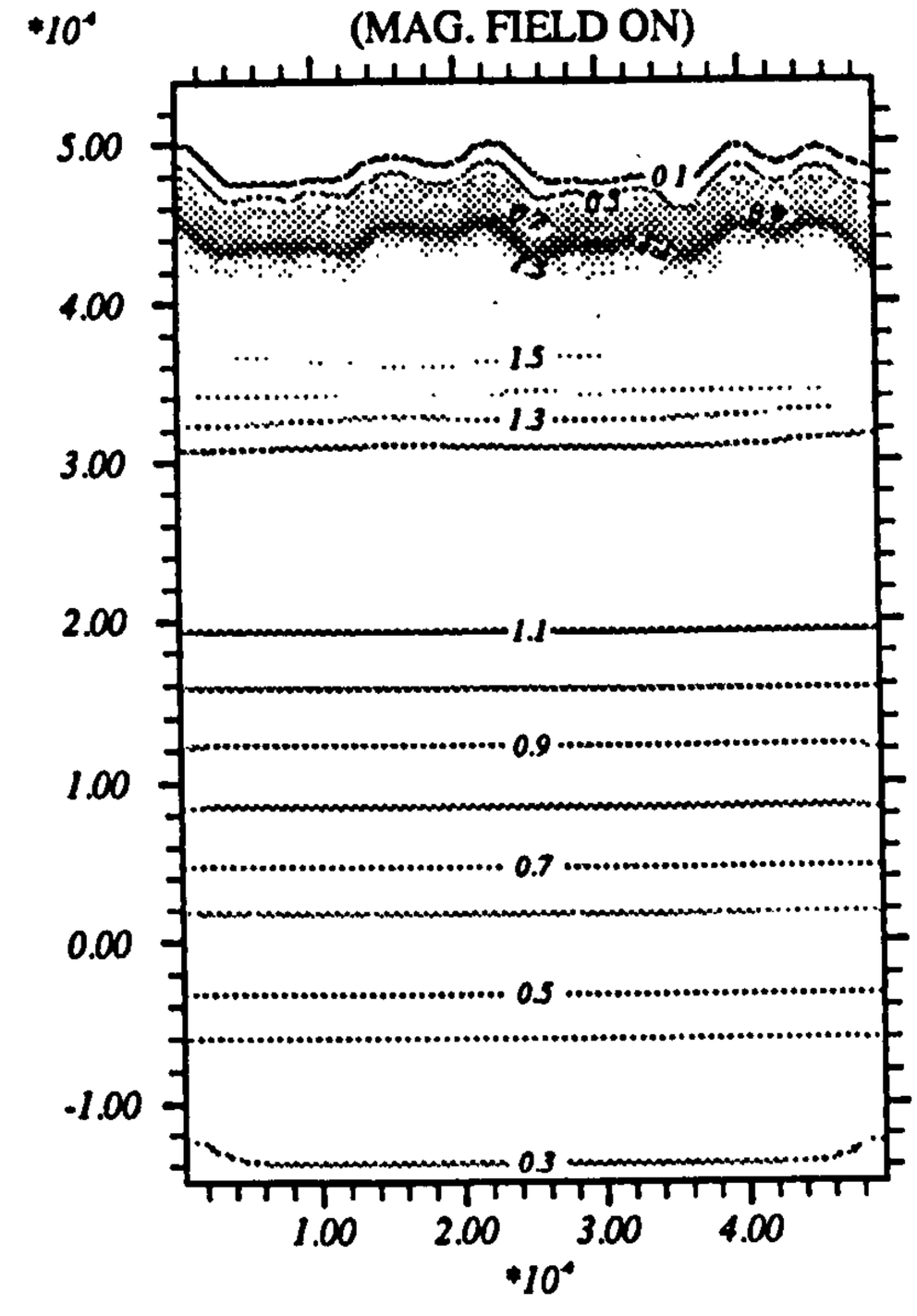

DENSITY MAP AT 250PS
(NO MAG. FIELD)

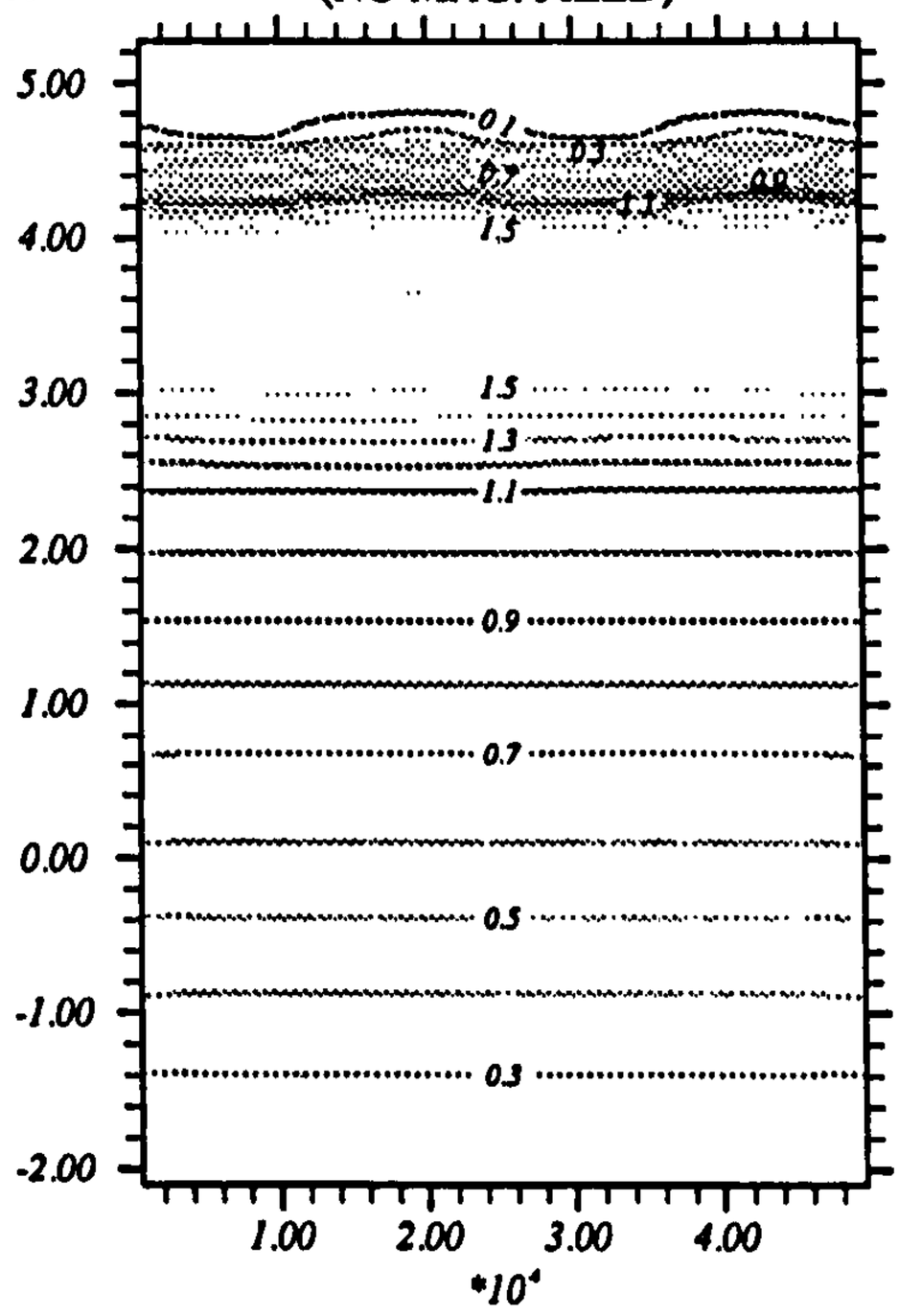

DENSITY MAP AT 250PS
(MAG. FIELD ON)

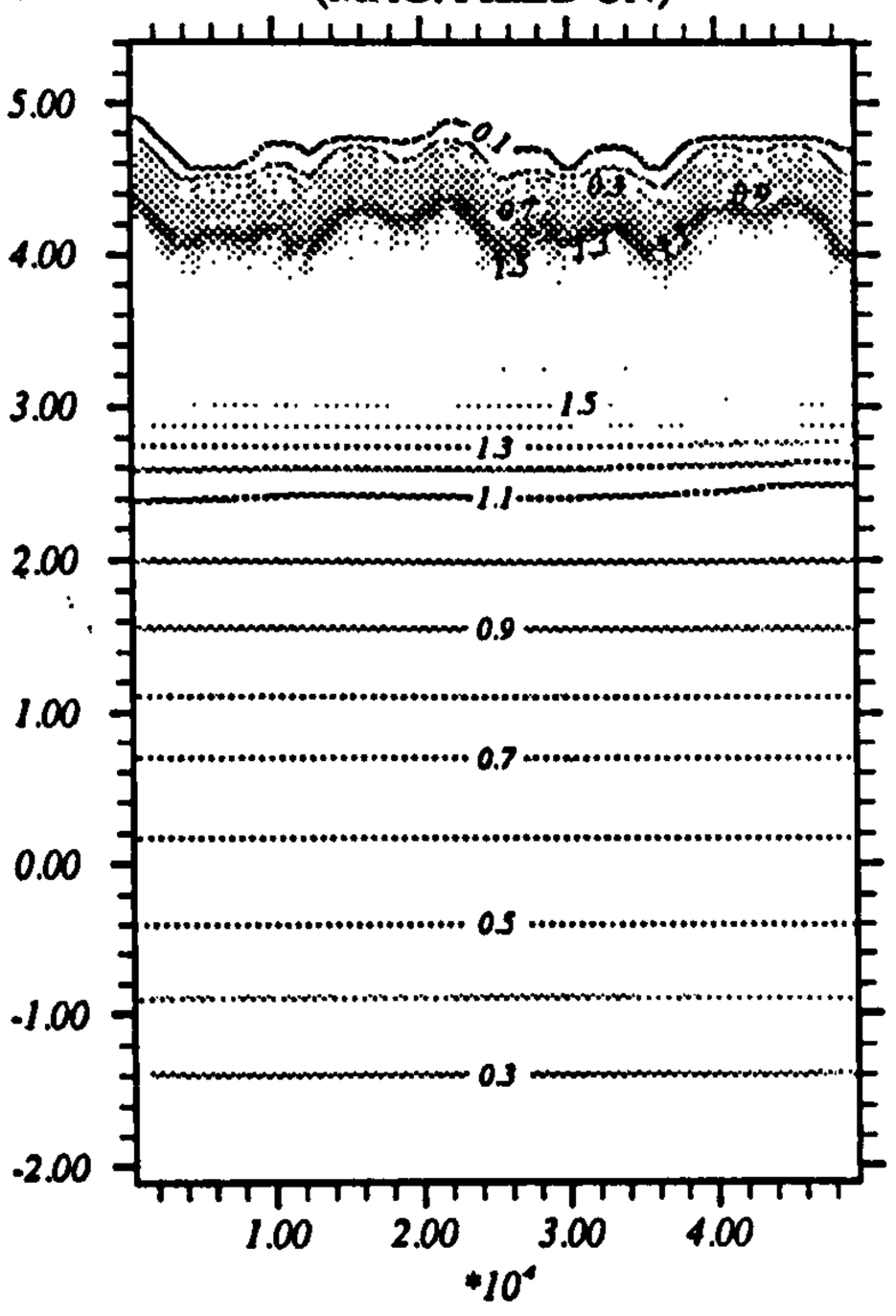

DENSITY MAP AT 300PS
(NO MAG. FIELD)

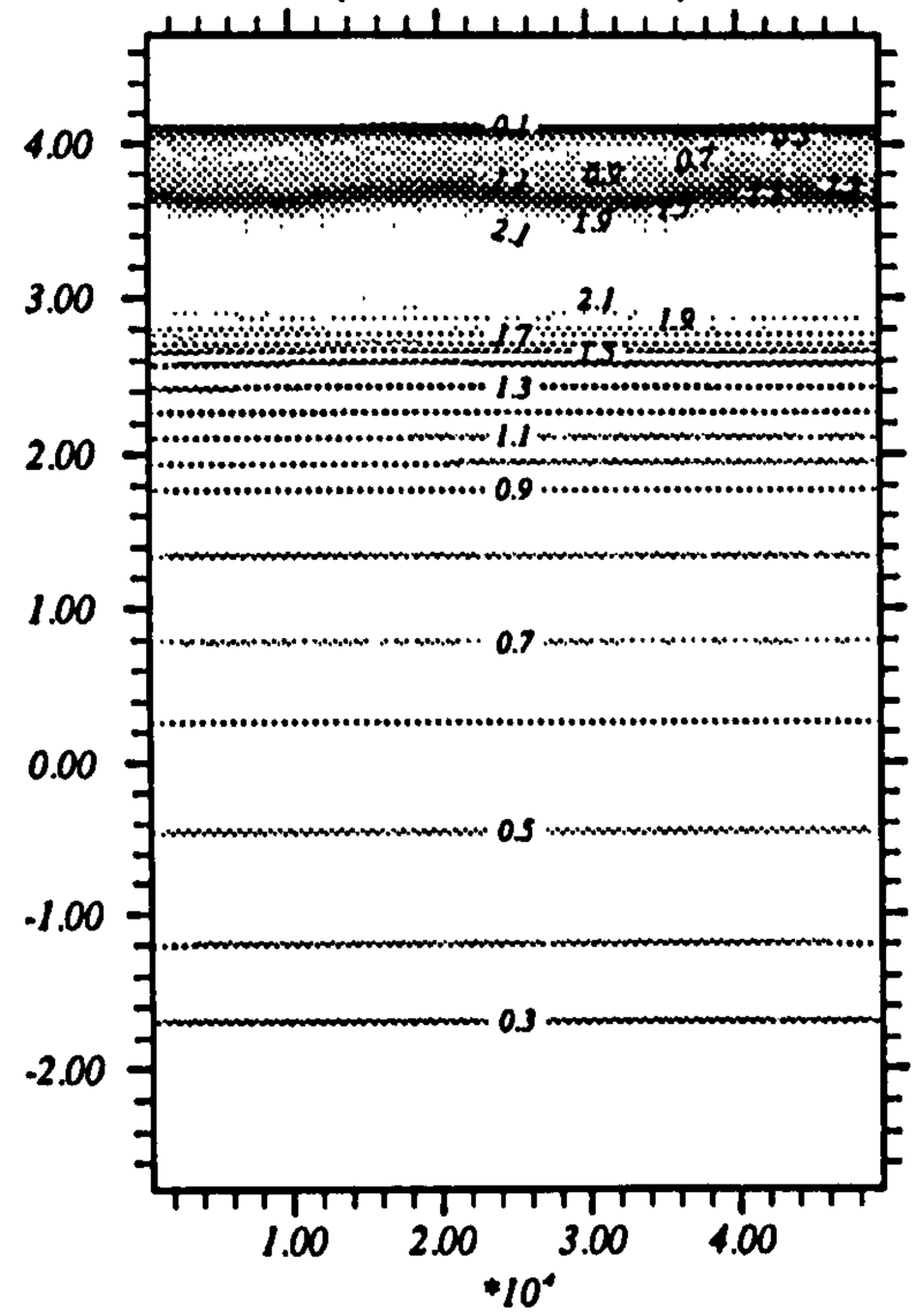

DENSITY MAP AT 300PS
(MAG. FIELD ON)

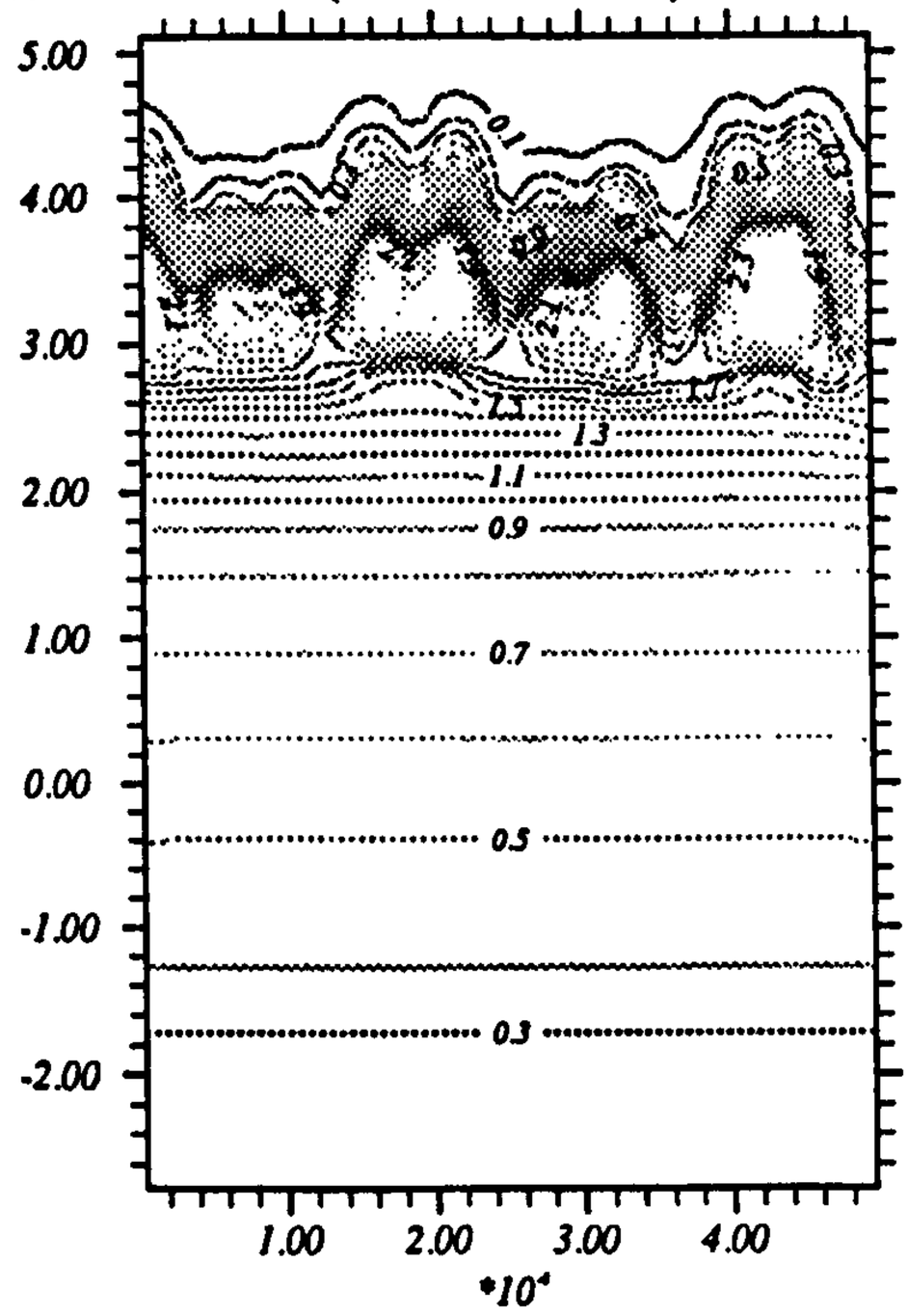

DENSITY MAP AT 350PS
(NO MAG. FIELD)

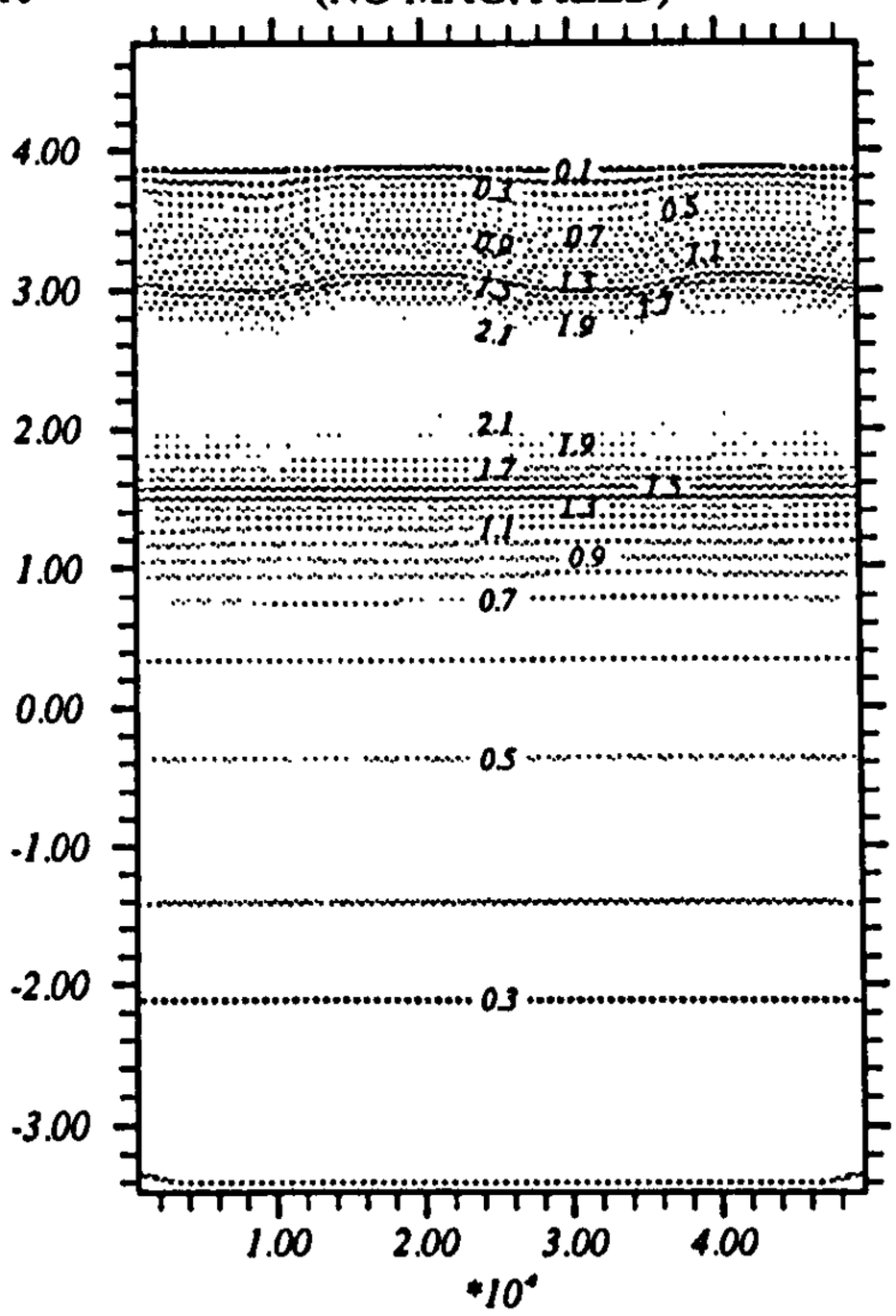

DENSITY MAP AT 350PS
(MAG. FIELD ON)

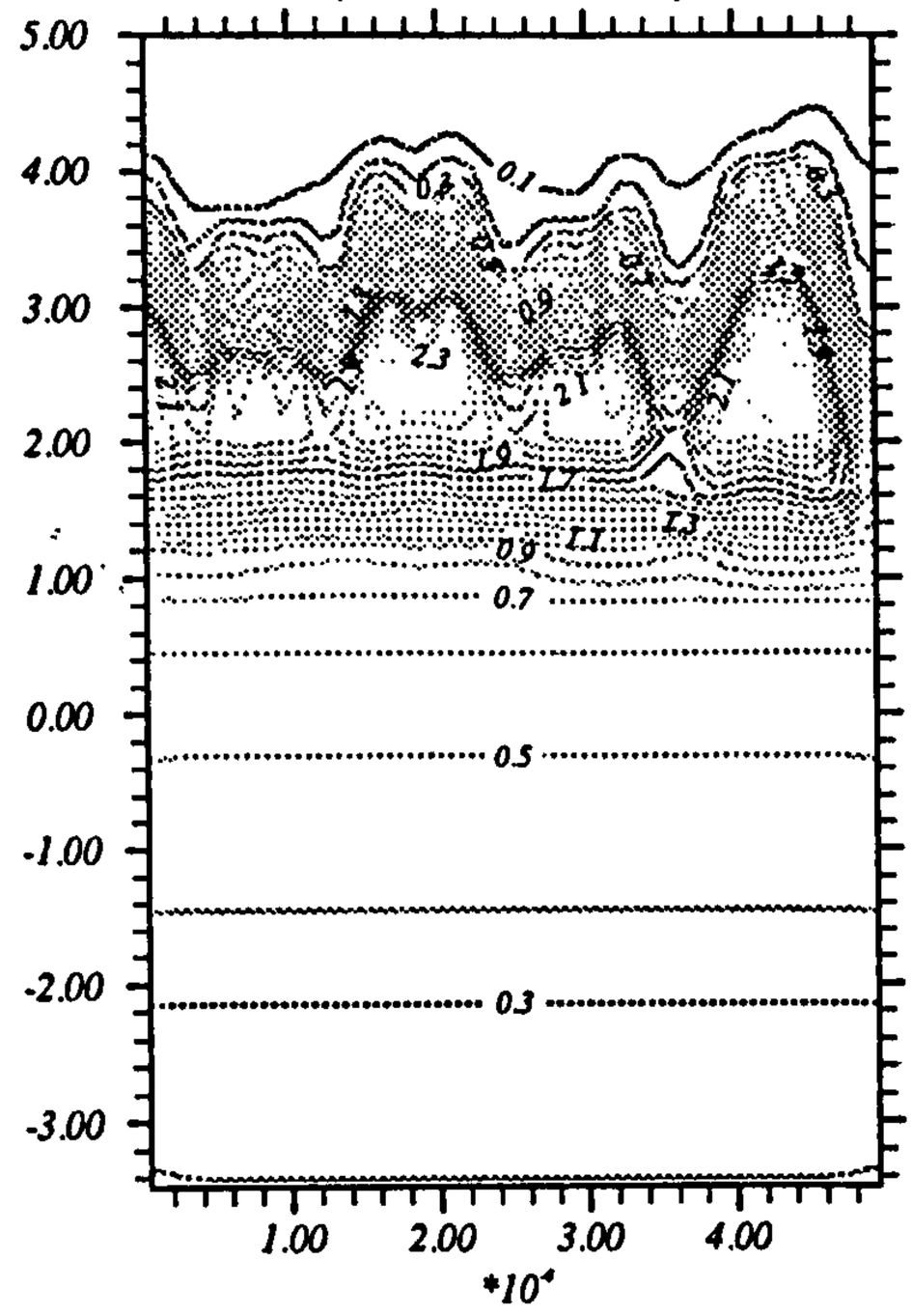

DENSITY MAP AT 400PS
(NO MAG. FIELD)

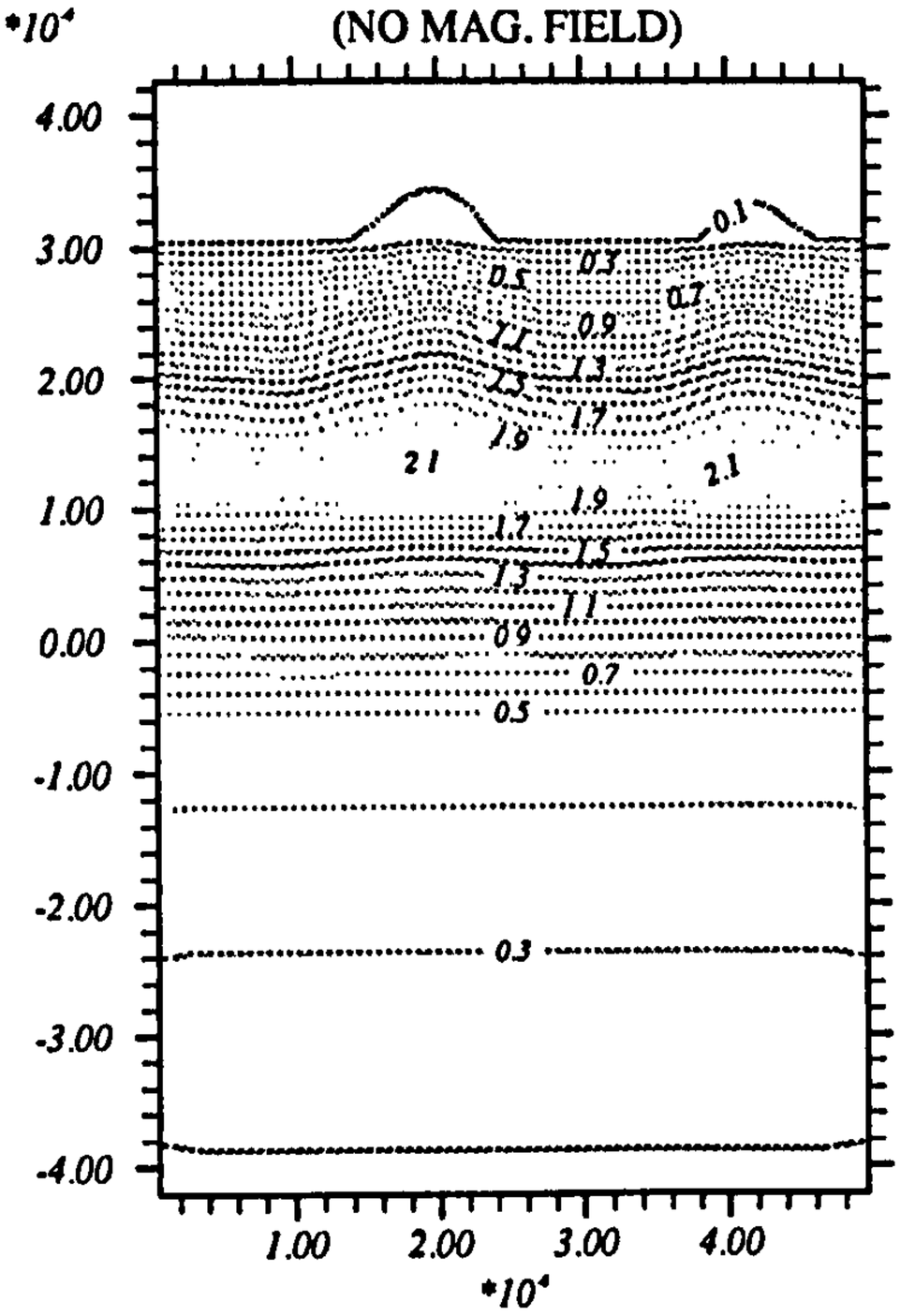

DENSITY MAP AT 400PS
(MAG. FIELD ON)

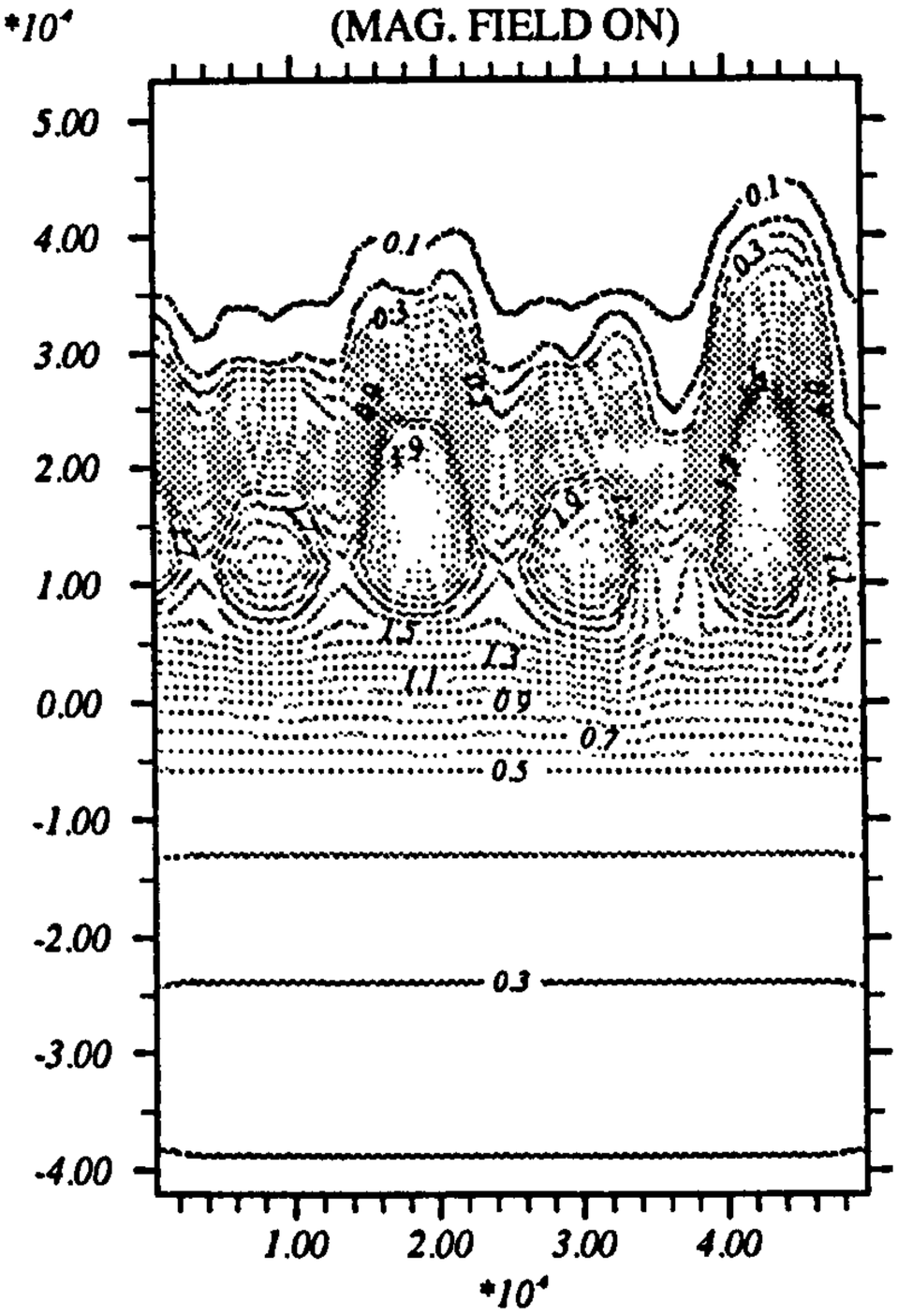

DENSITY MAP AT 450PS
(NO MAG. FIELD)

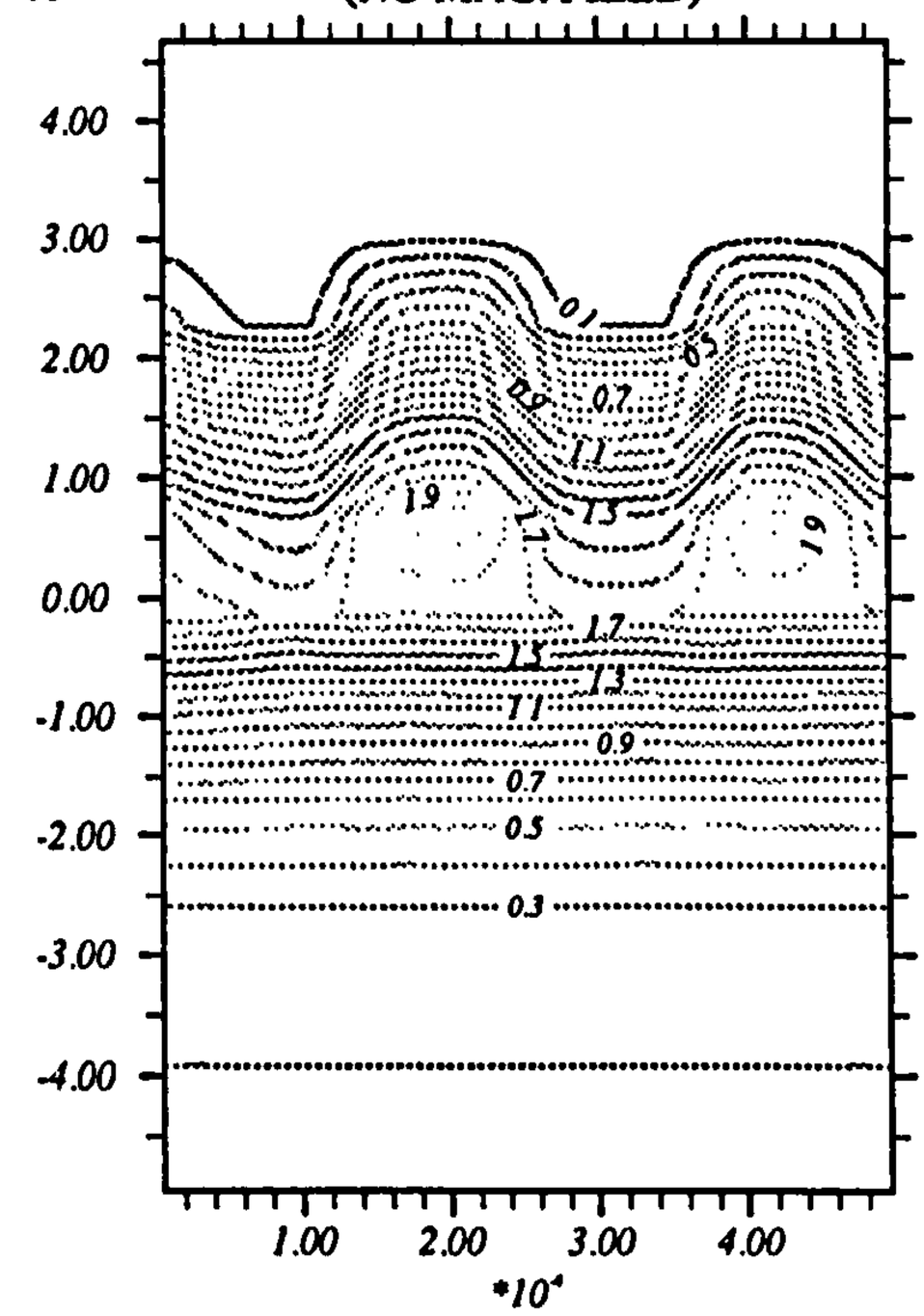

DENSITY MAP AT 450PS
(MAG. FIELD ON)

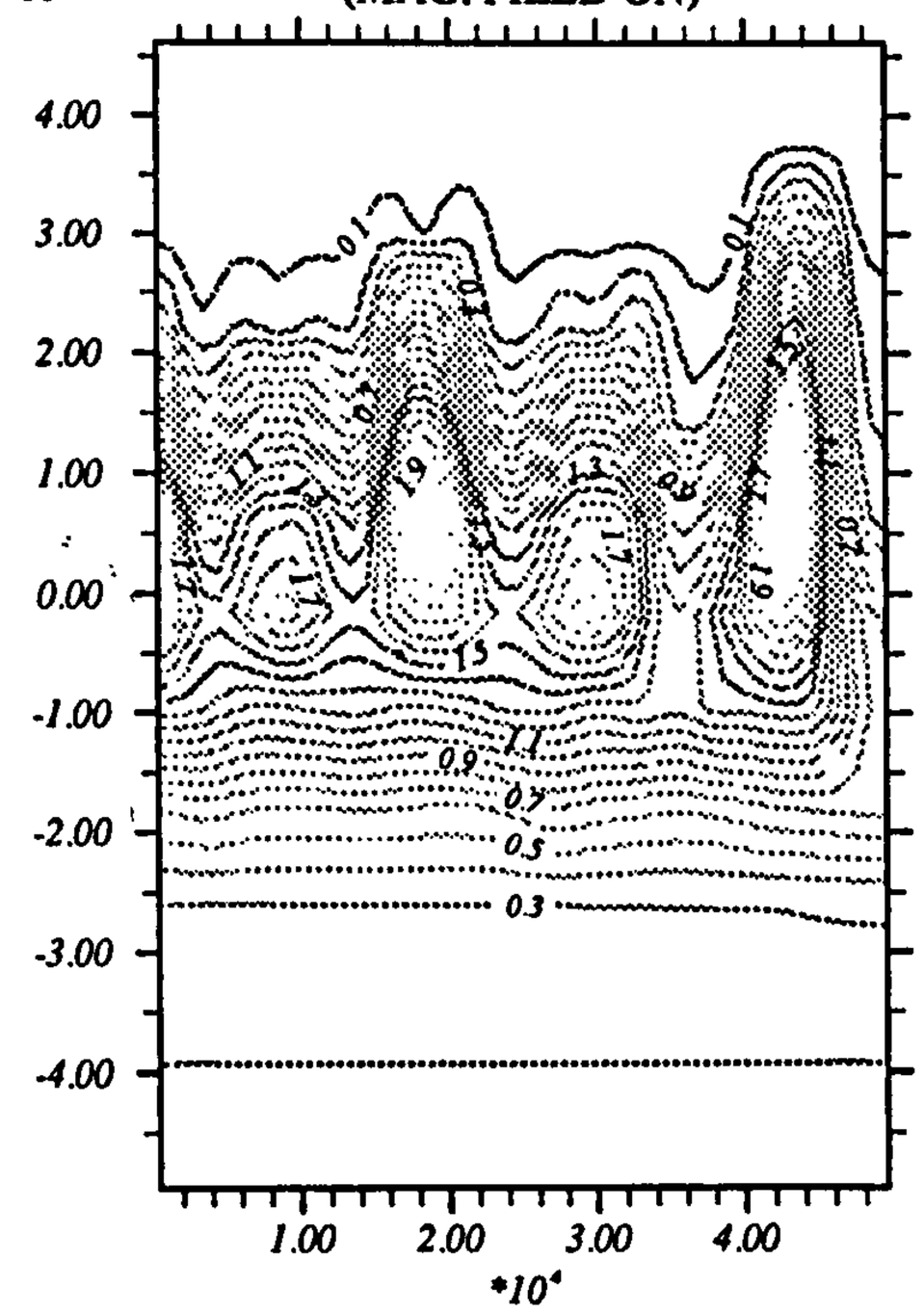

DENSITY MAP AT 500PS
(NO MAG. FIELD)

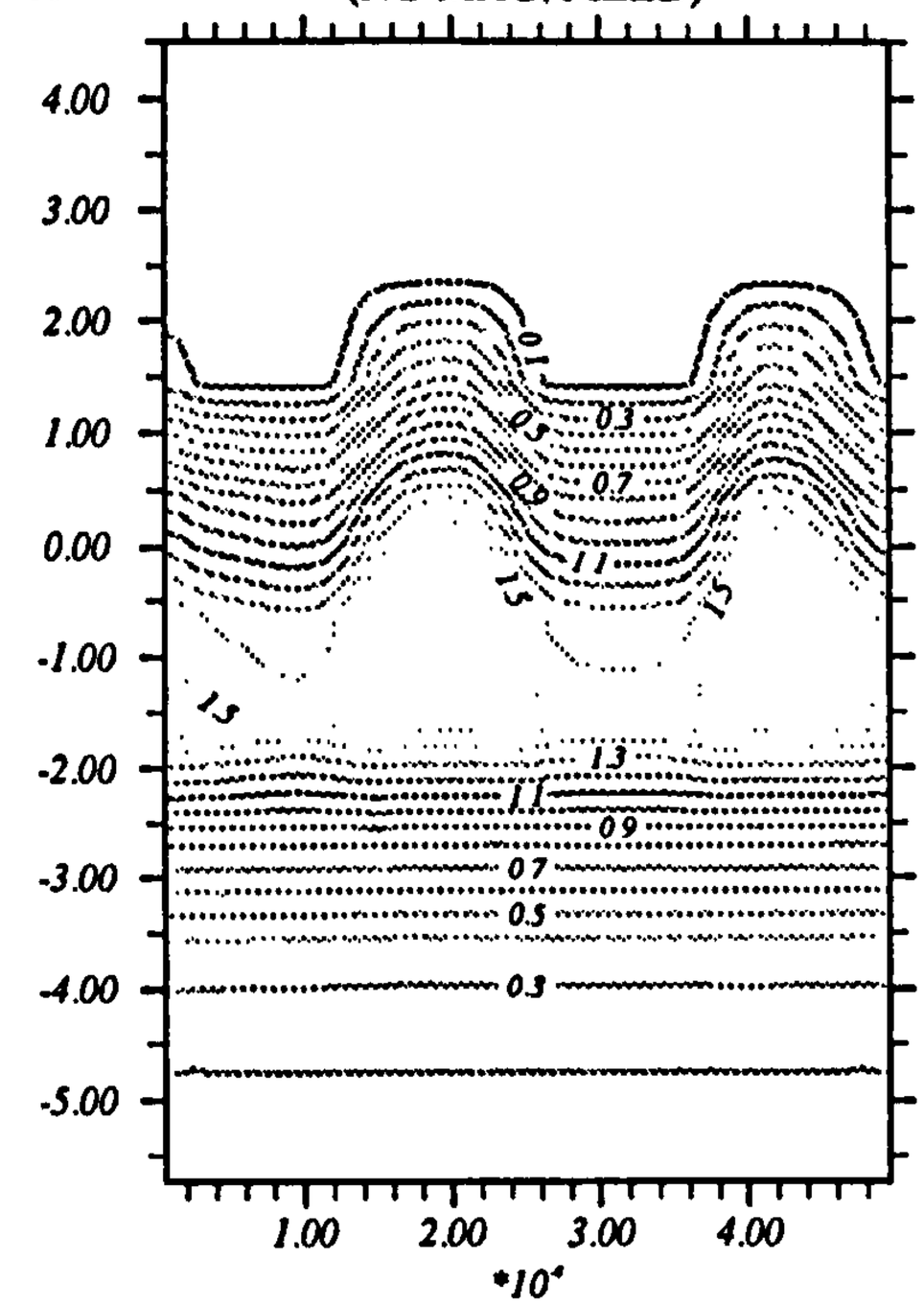

DENSITY MAP AT 500PS
(MAG. FIELD ON)

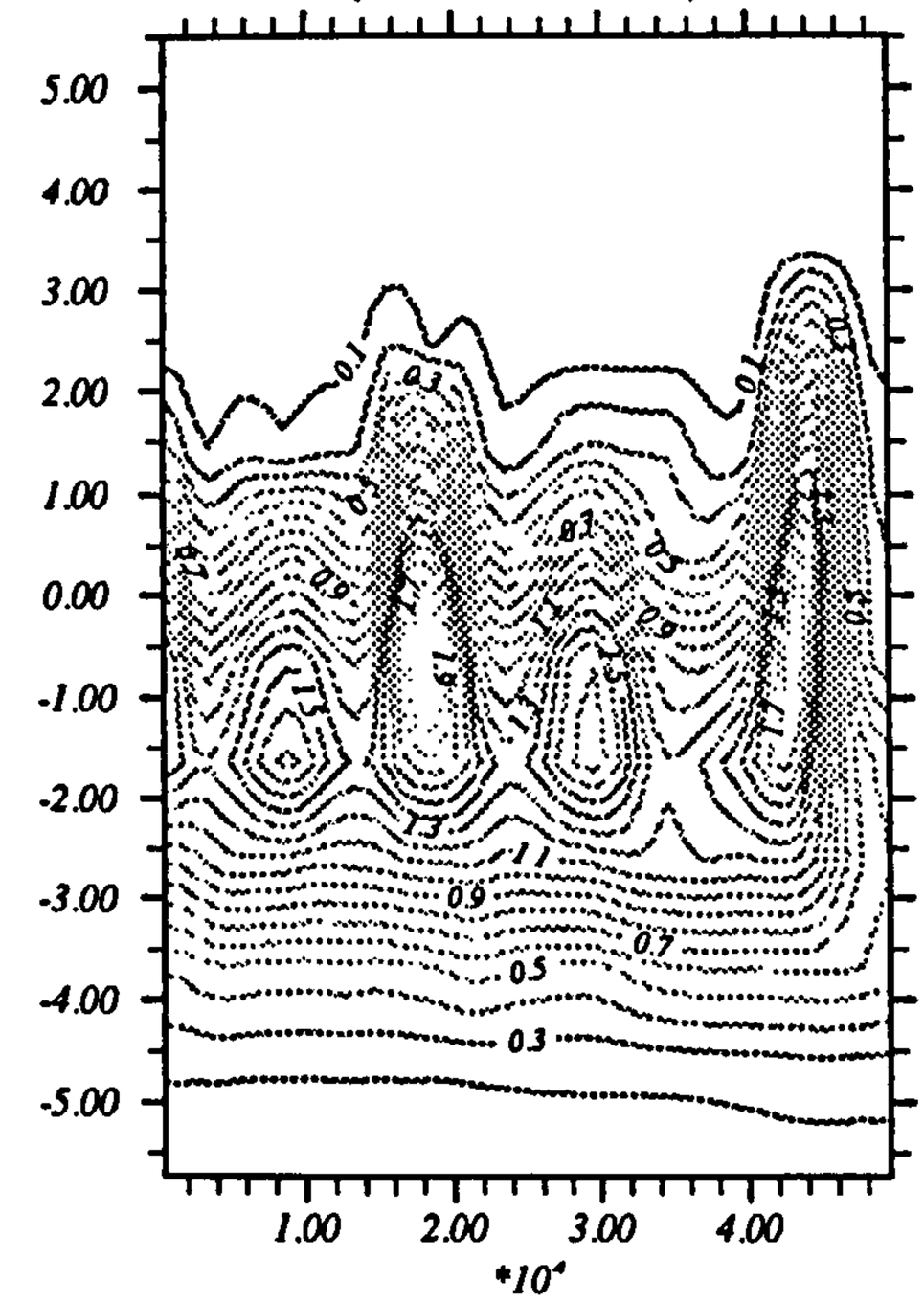

DENSITY MAP AT 550PS
(NO MAG. FIELD)

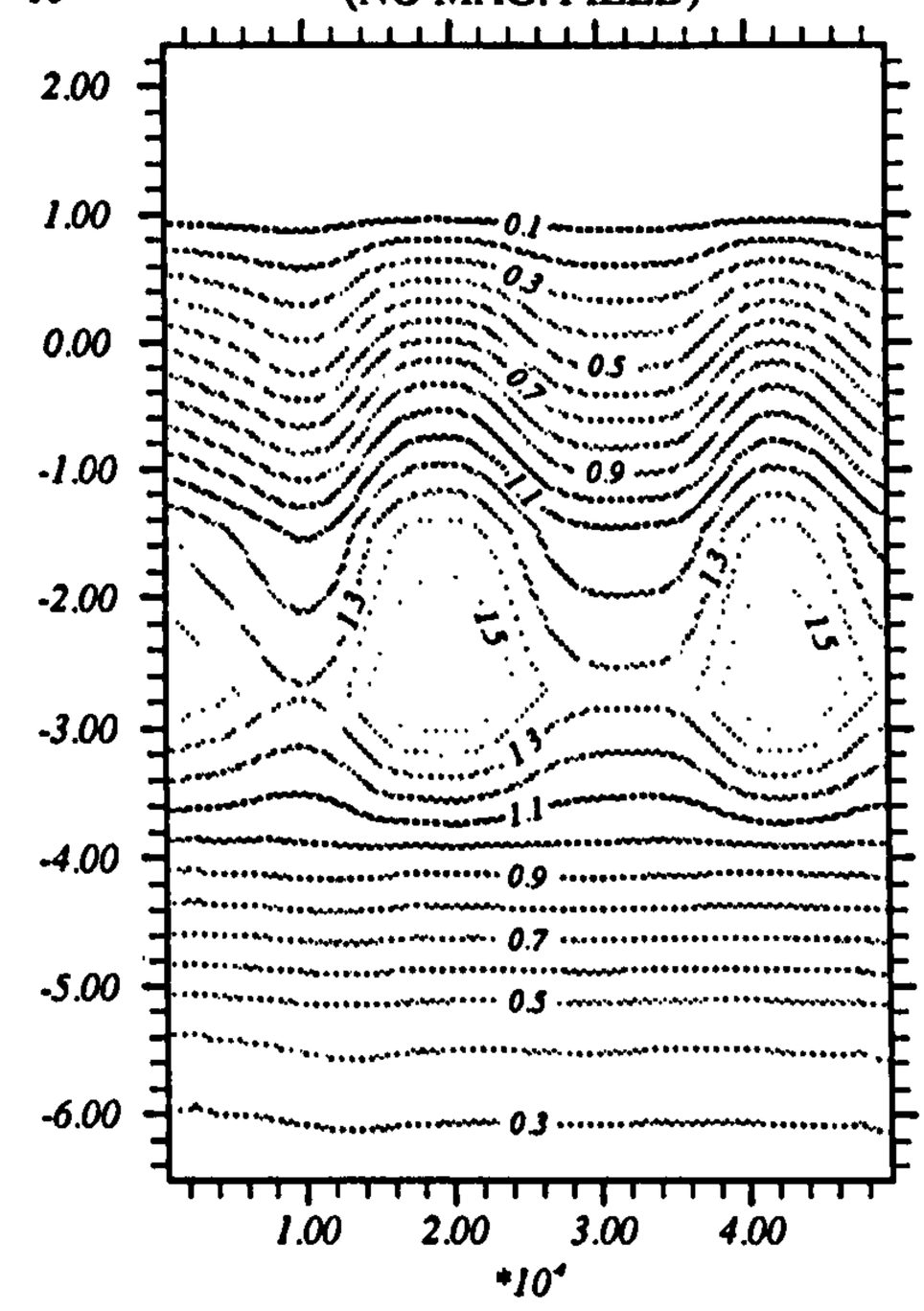

DENSITY MAP AR 550PS
(MAG. FIELD ON)

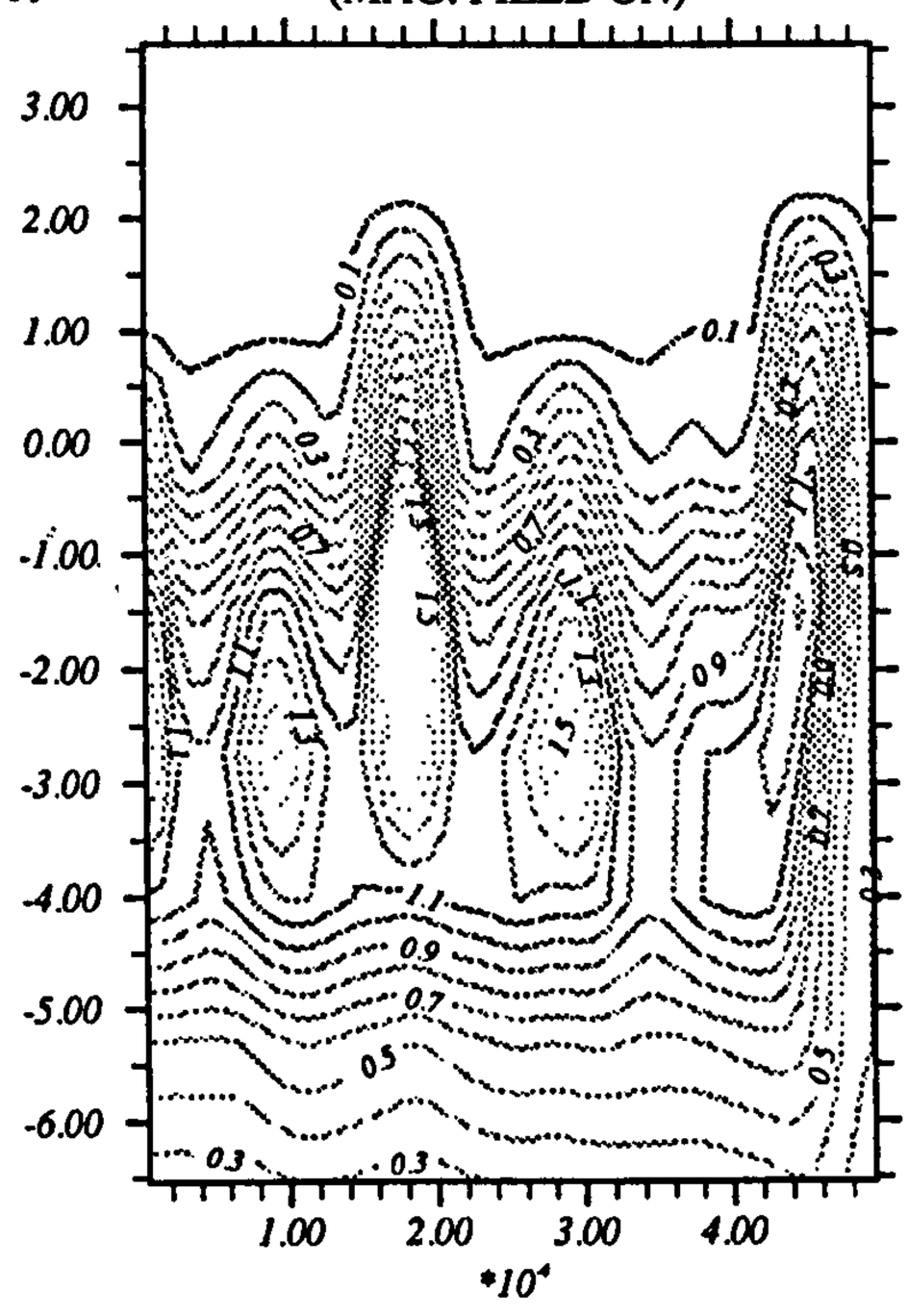

DENSITY MAP AT 600PS
(NO MAG. FIELD)

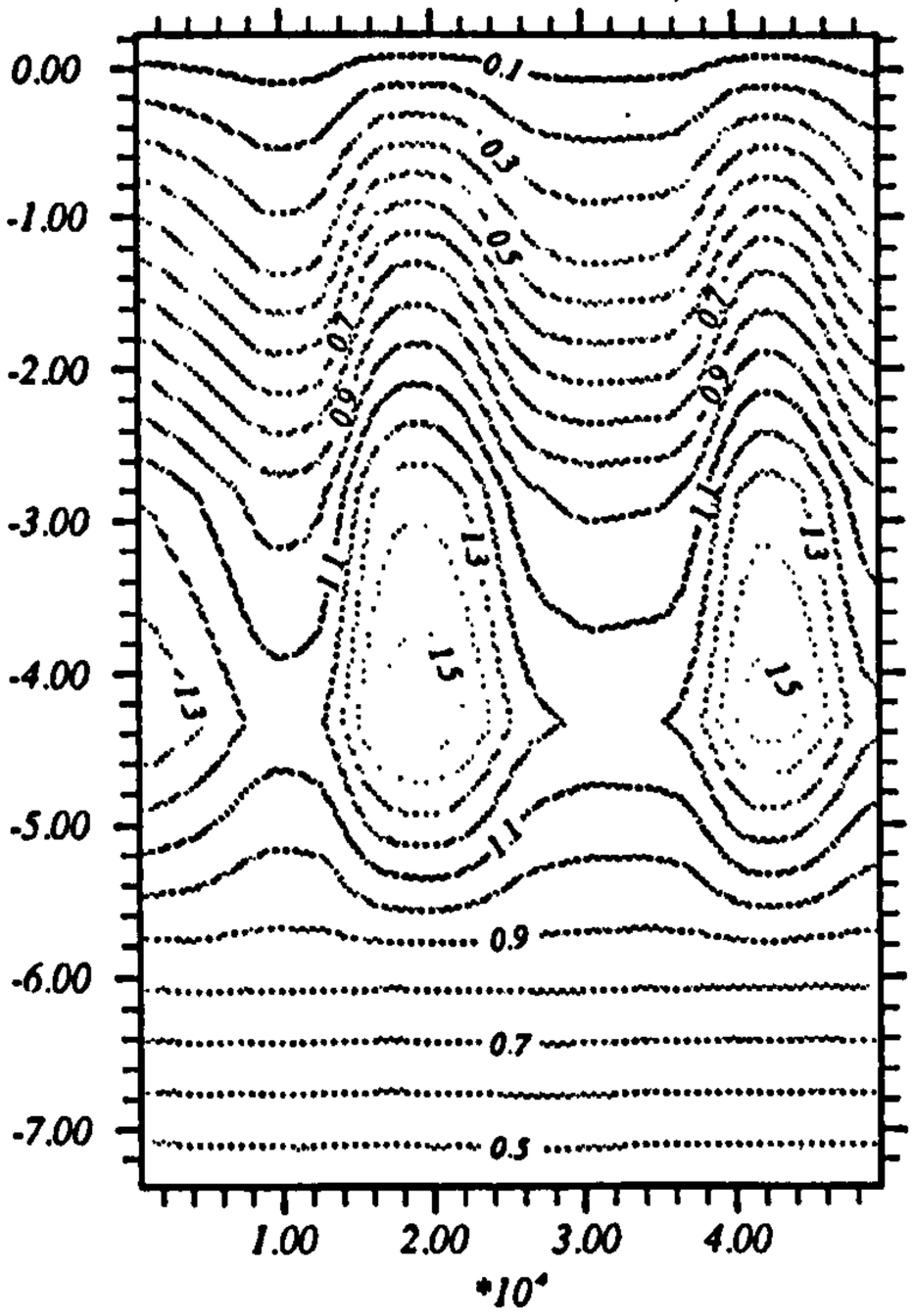

DENSITY MAP AT 600PS
(MAG. FIELD ON)

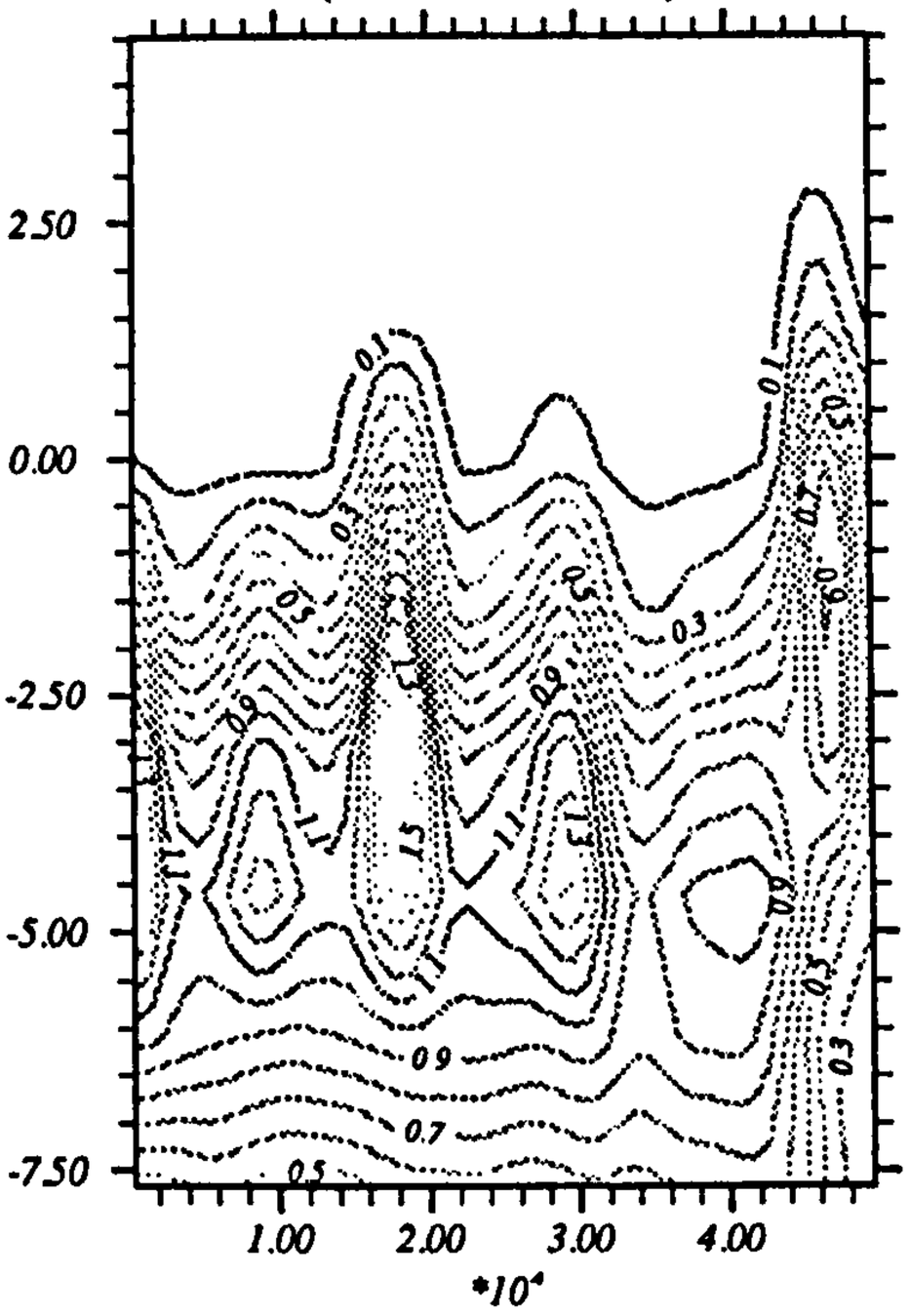

DENSITY MAP AT 650PS
(NO MAG. FIELD)

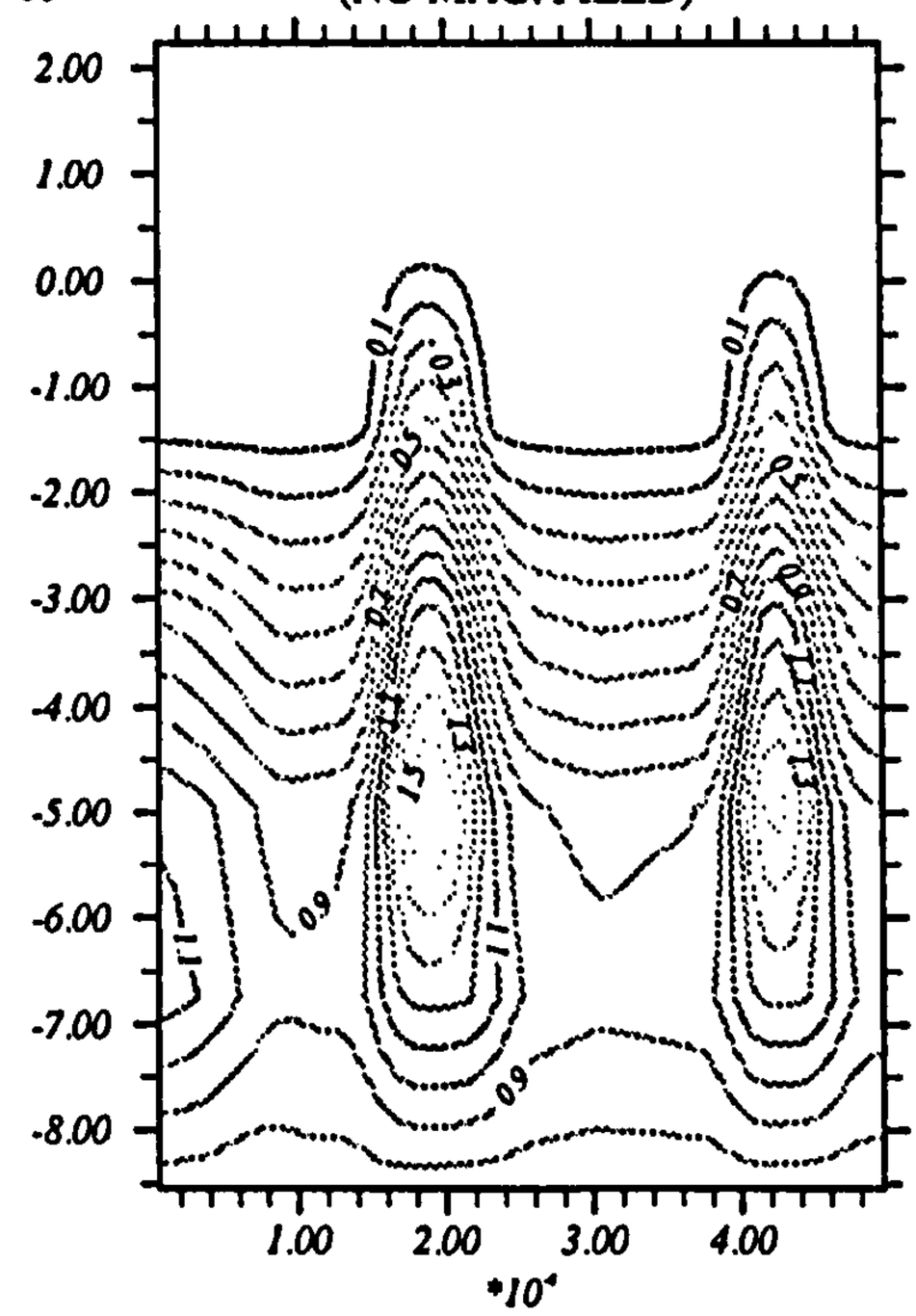

DENSITY MAP AT 650PS
(MAG. FIELD ON)

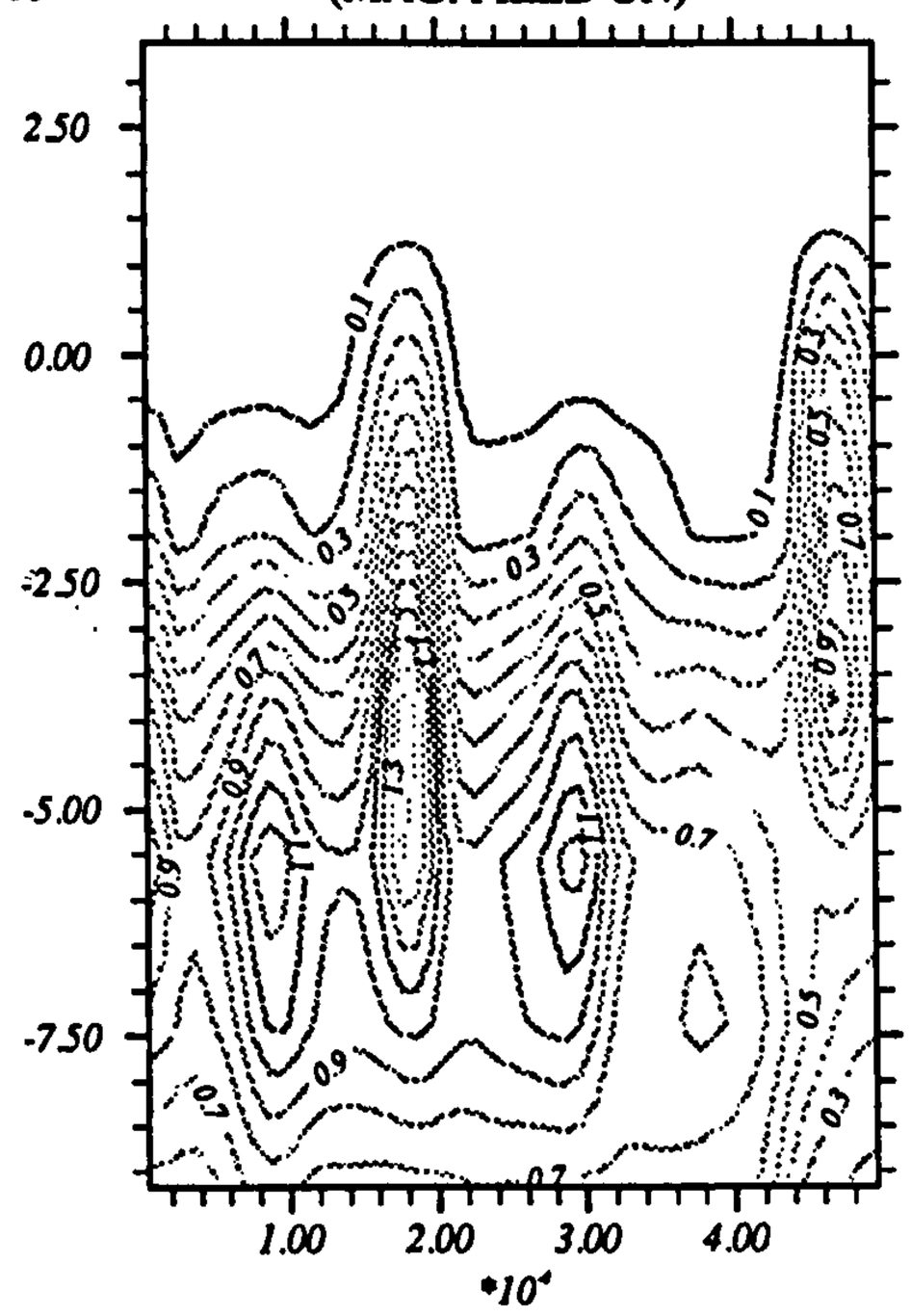

DENSITY MAP AT 700PS
(NO MAG. FIELD)

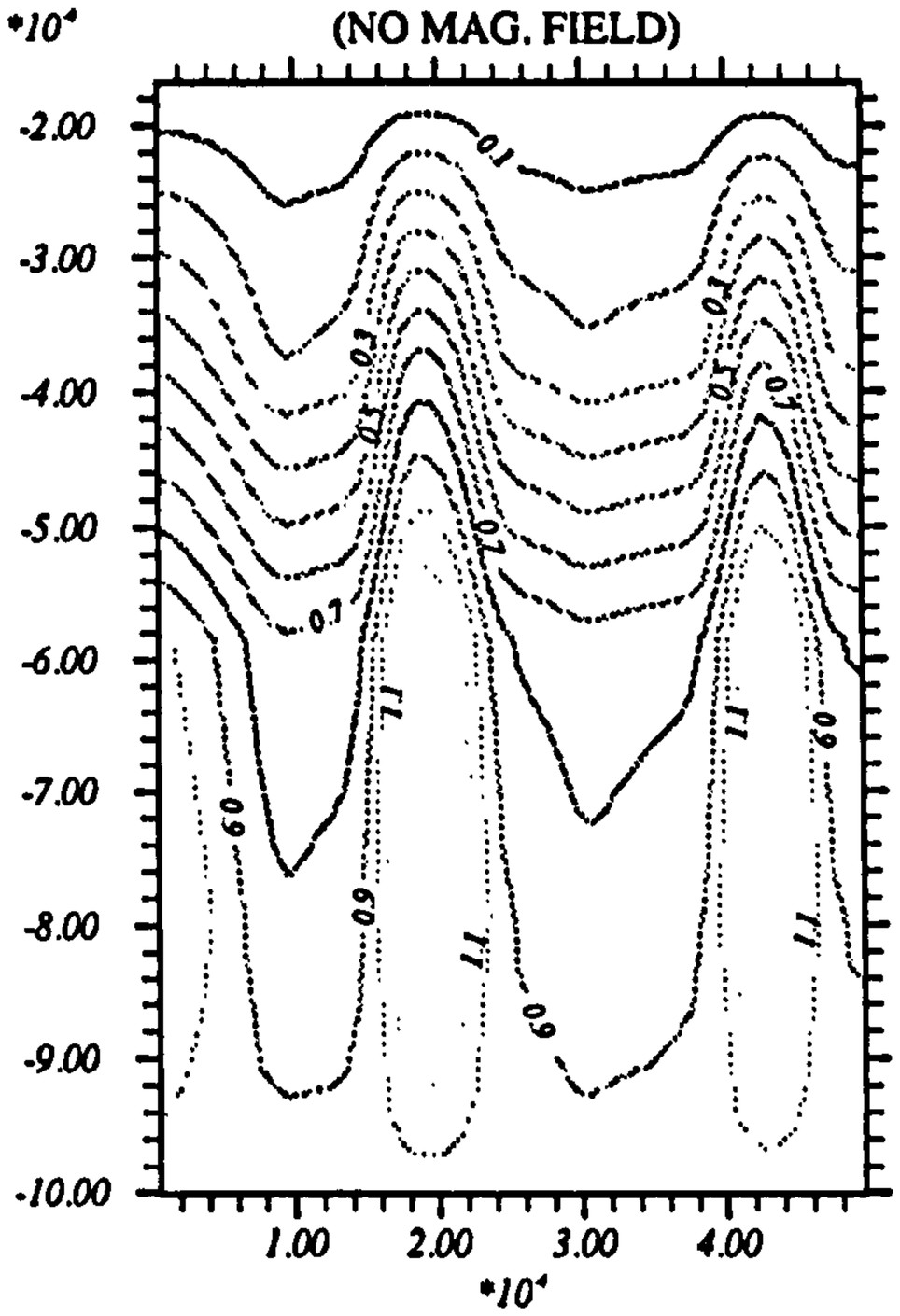

DENSITY MAP AT 700PS
(MAG. FIELD ON)

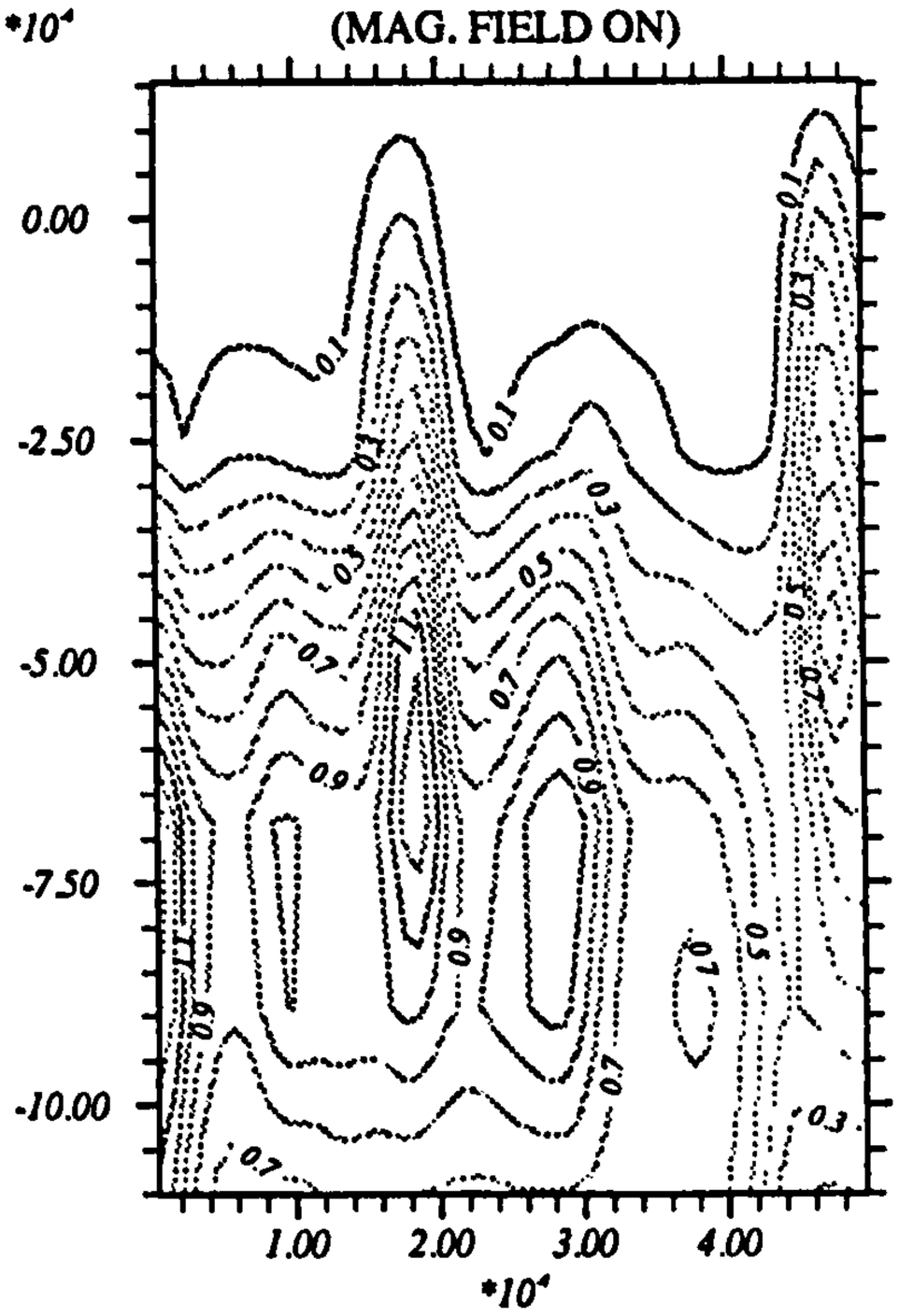

DENSITY MAP AT 750PS
(NO MAG. FIELD)

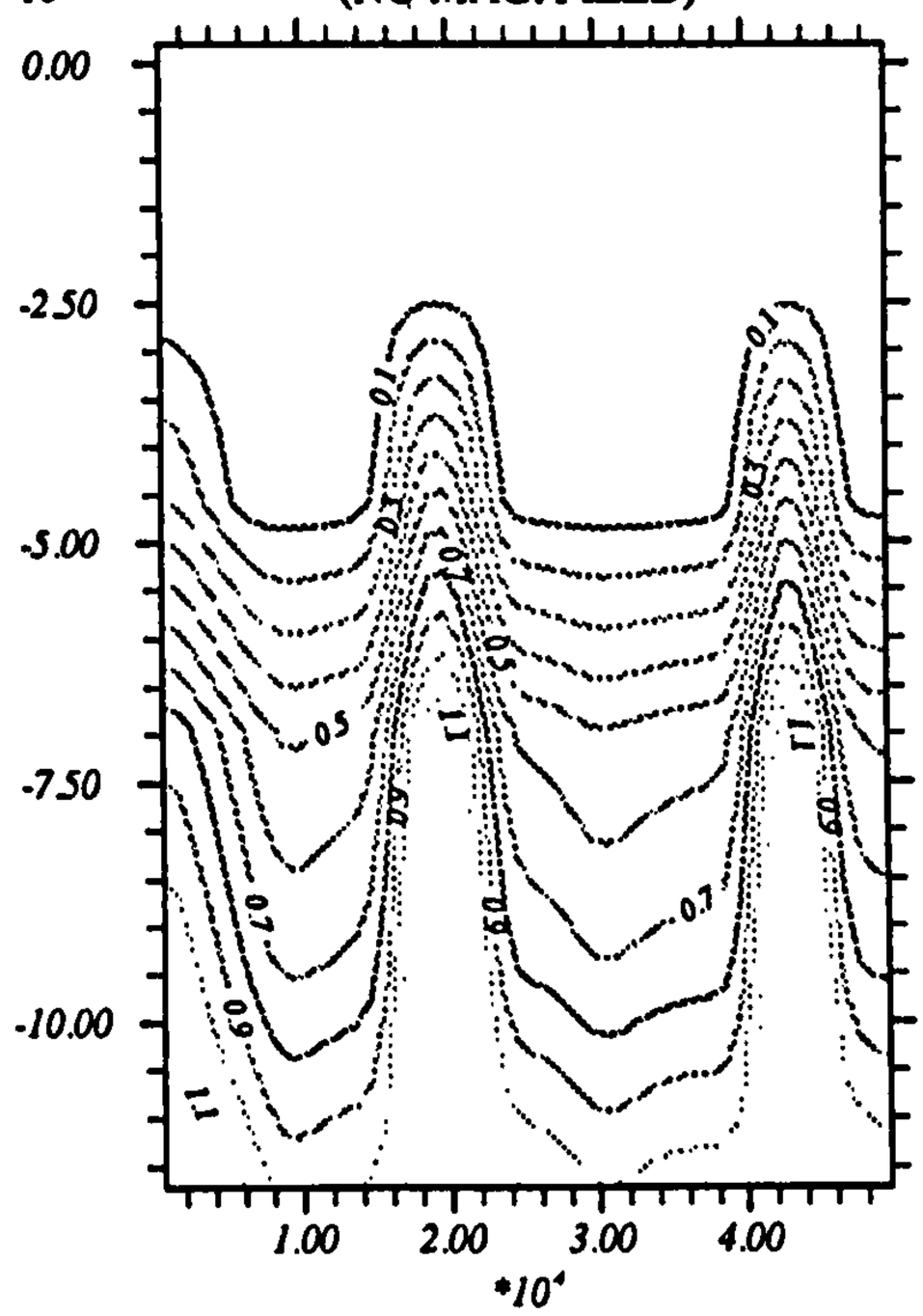

DENSITY MAP AT 750PS
(MAG. FIELD ON)

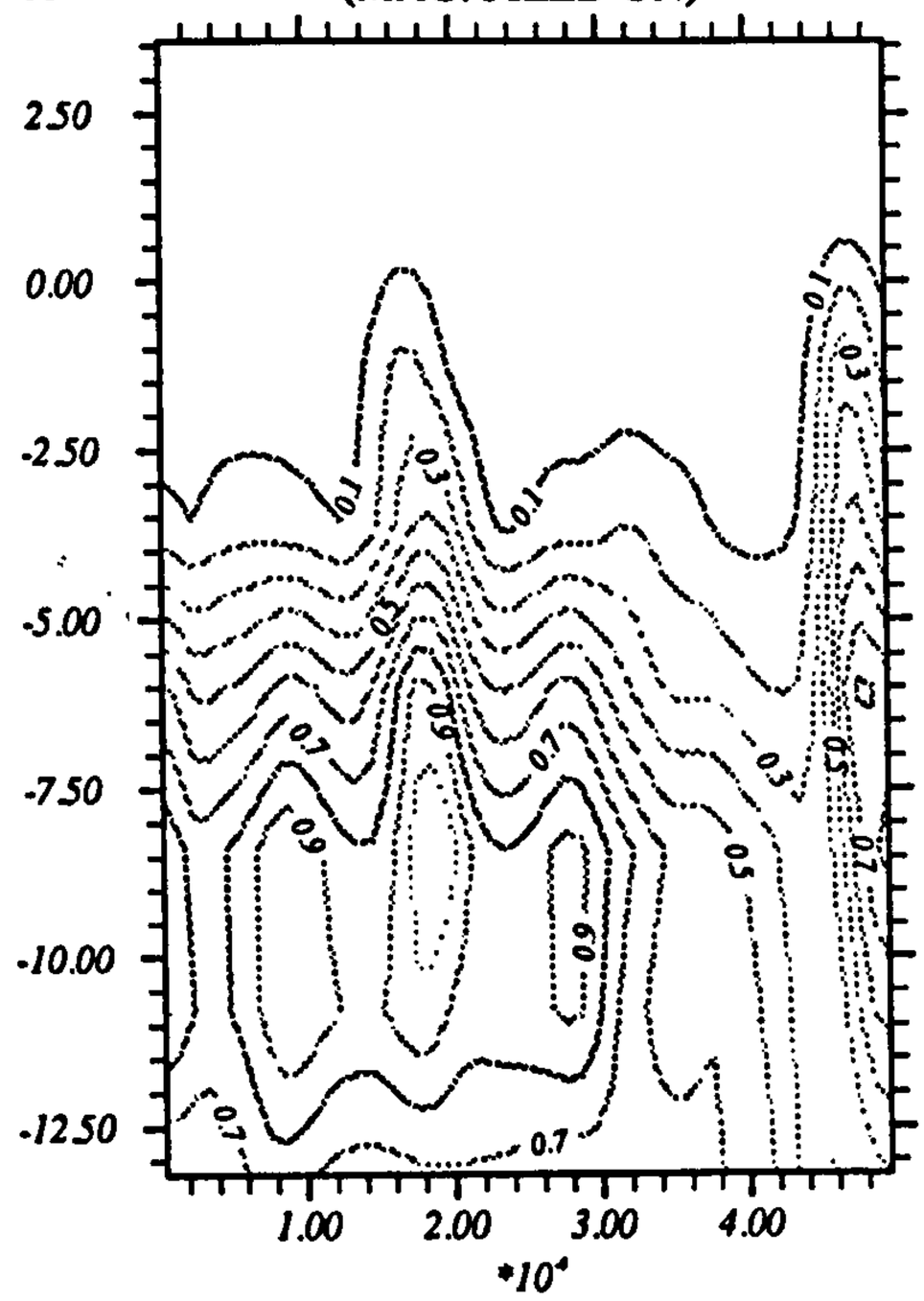

DENSITY MAP AT 800PS
(NO MAG. FIELD)

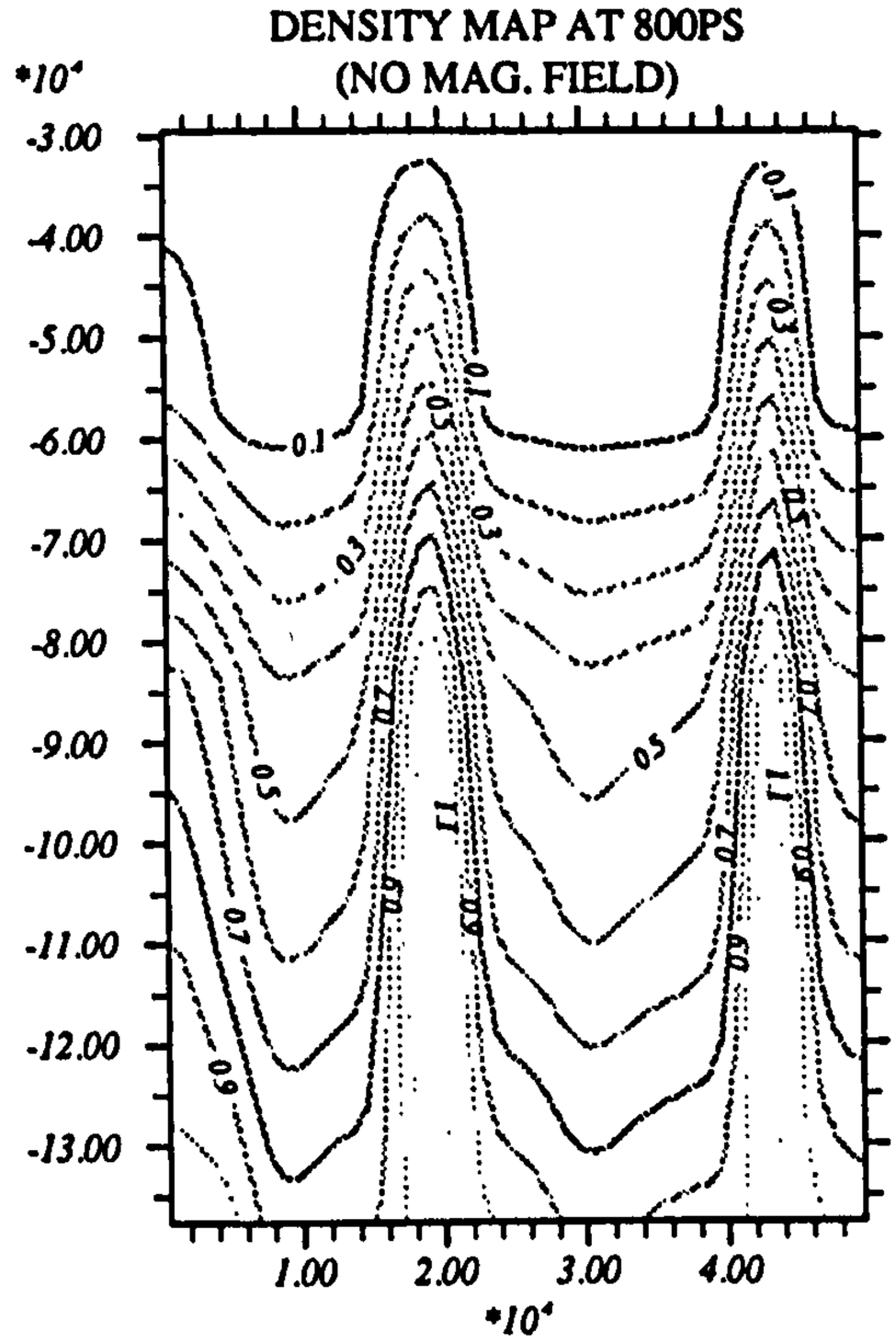

DENSITY MAP AT 800PS
(MAG. FIELD ON)

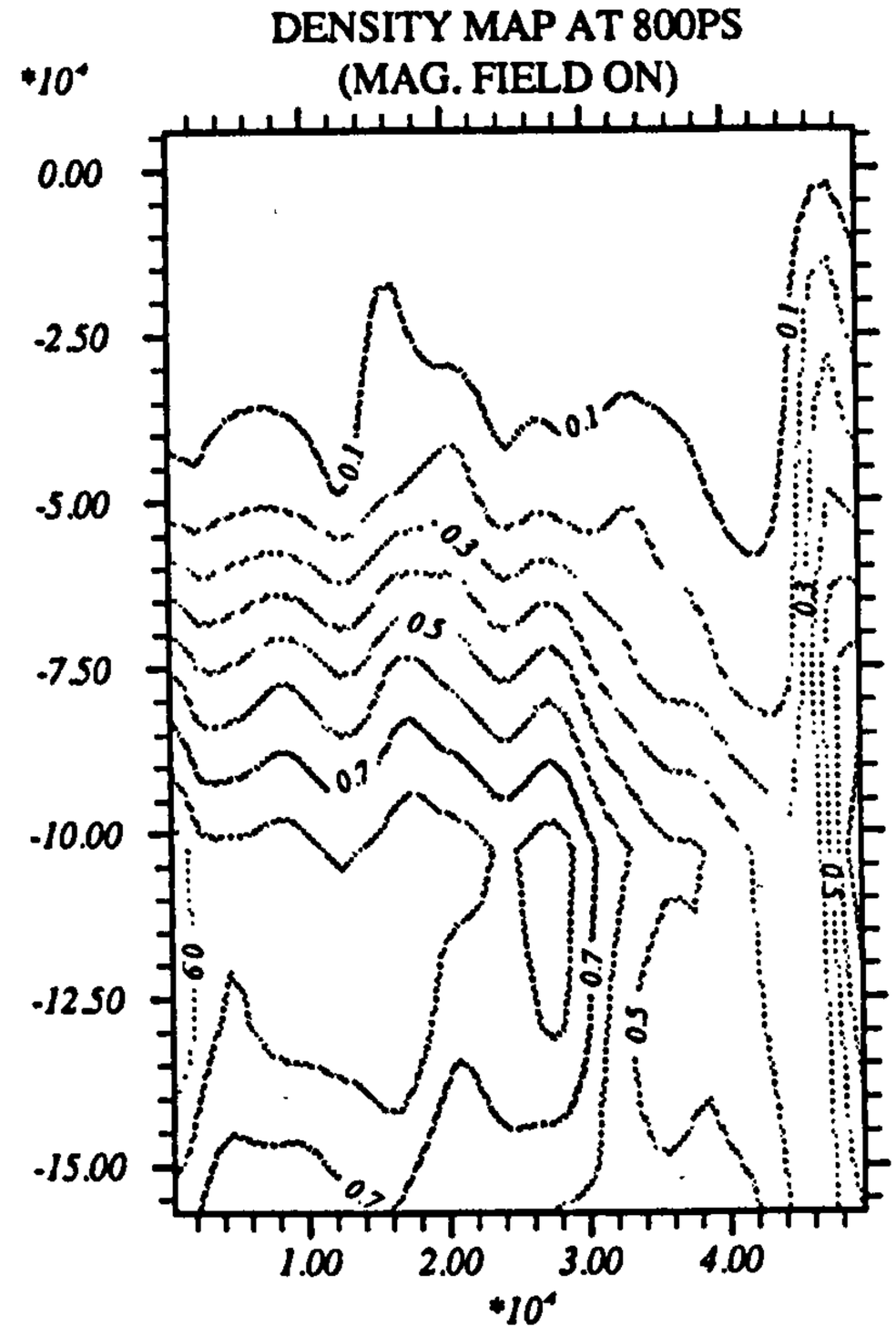

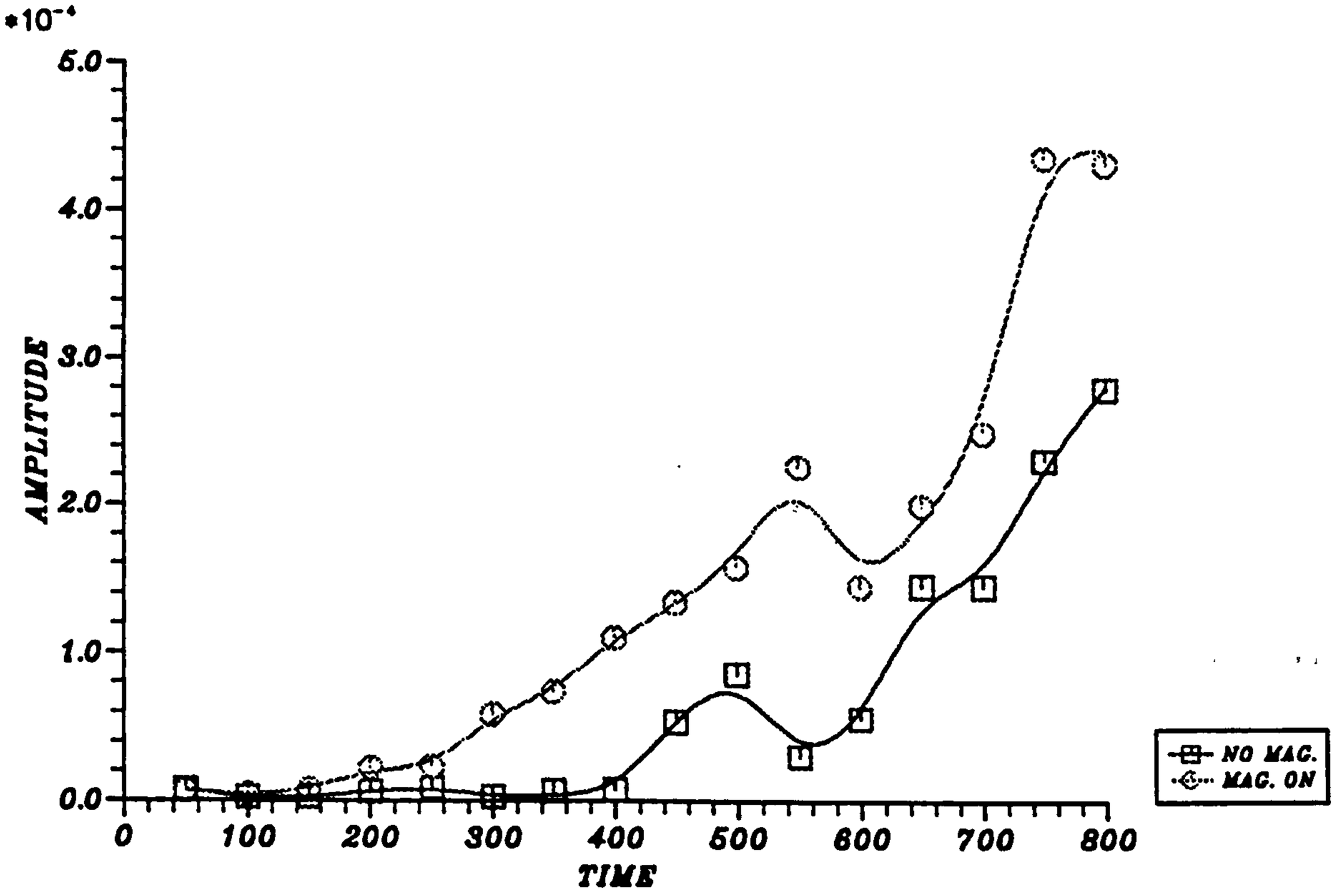

Figure 6.5: Amplitude-time graph for target $(5 \cdot 0\mu m \times 5 \cdot 0\mu m)$.

the growth of instability compared with the no field case. The reason for the delayed start of the high frequency modes is not very well understood, but could be because of large target size and small density gradients reduces the growth of the magnetic field. The relatively low field strength could also be another factor for the delayed start of the non-linear generation of high frequency modes. In contrast to this growth is negligible until 400ps with no field simulations. The instability structures are very clear at 450ps when the field terms are off, whereas at the same time in the other simulations with the field on the high frequency modes are still present. The mixing takes place after 500ps with the field on and it has a delayed start until 650ps in no field simulations. At 700ps most of the target material is burnt through in both cases.

The amplitude vs time graph is plotted in figure $6 \cdot 5$. In these simulations the amplitude of instability is always longer for magnetic field included simulations compared to no field simulations. The behaviour of growth of the instability is almost linear in both field included and excluded.

The field contour maps are shown in figure $6 \cdot 6$. In these simulations it is observed that the additional field contour lines are generated late, which are the

source to generate delayed high frequency modes in density contour maps.

6.4 TARGET SIZE ($5 \cdot 0\mu m \times 2 \cdot 5\mu m$)

The target in these simulations is $5 \cdot 0\mu m$ thick with a radius of $2 \cdot 5\mu m$. The perturbation is applied through the laser intensity. The applied perturbation wavelength is $1 \cdot 25\mu m$ with its perturbation amplitude the same as in the previous simulations. The complete target and laser input parameters are given in Table $6 \cdot 3$. Time history of density through contour maps at the interval of 50ps are shown in figure $6 \cdot 7$. The density profile is similar for both magnetic field included and excluded at 50ps. There is not any substantial growth in the instability up to 450ps in the absence of the magnetic field. The high frequency modes start at 150ps and are overtaken by the initial perturbation at about 350ps because at this time the variation in electron temperature contour maps disappear. This is the source generating these high frequency modes. Target penetration and mixing starts at 500ps with the field on, where it becomes difficult to measure the growth amplitude exactly as the outer edge of the target is burnt through. The late growth in the case of no field is possibly because hydrodynamic effects have only started at late times.

The amplitude-time is shown in figure $6 \cdot 8$. We again observe here that when the magnetic field effects are included the instability growth is significantly larger over the no field simulations all the times until 500ps. We are unable to observe after this time as the mixing starts earlier when the magnetic field routines are included in the simulations.

The field contour maps at the interval of 100ps are shown in figure $6 \cdot 9$. It is observed that at 200ps some extra positive and negative contour lines loops are generated which again produce a delayed high frequency modes in density maps which eventually are damped.

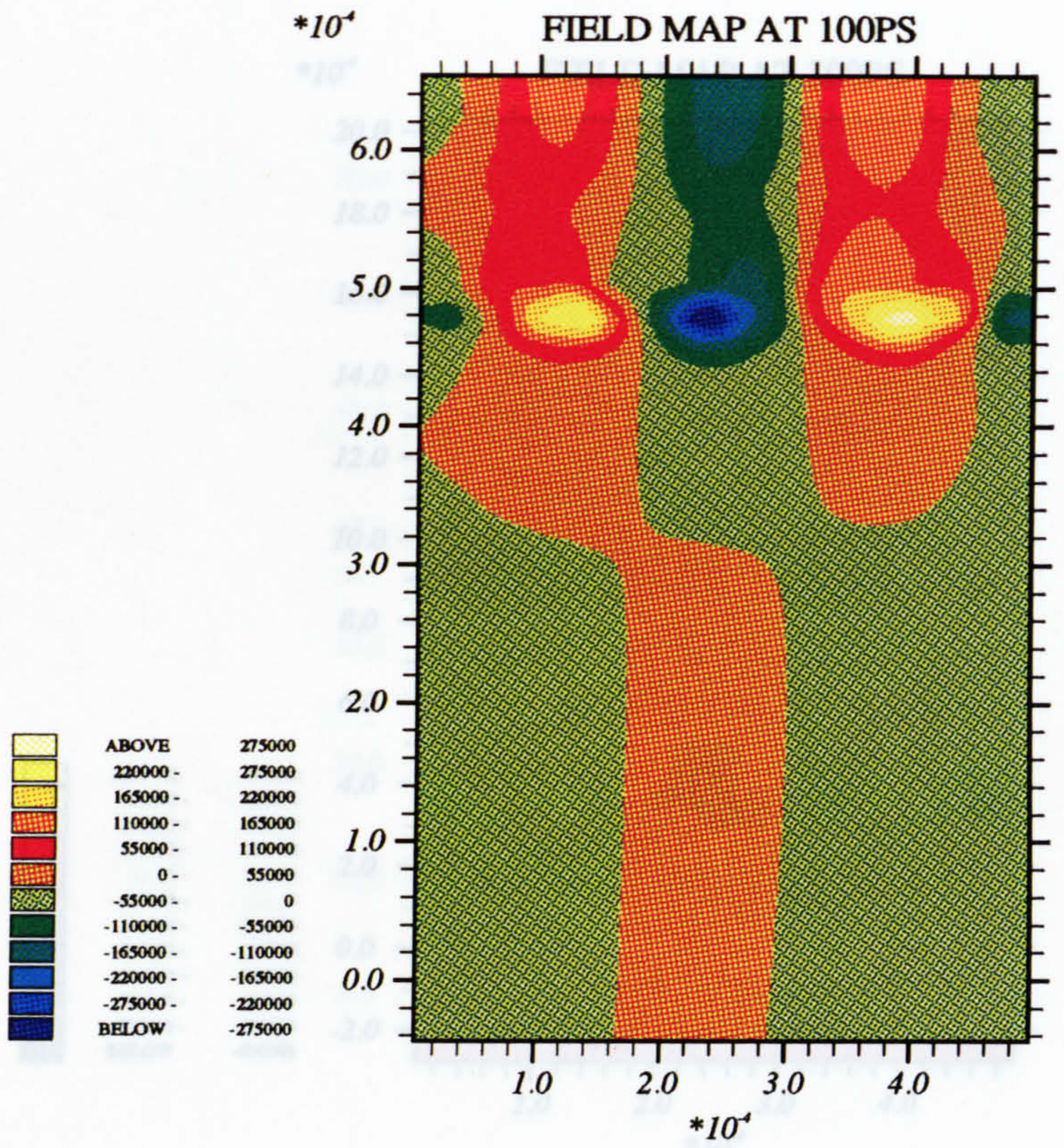

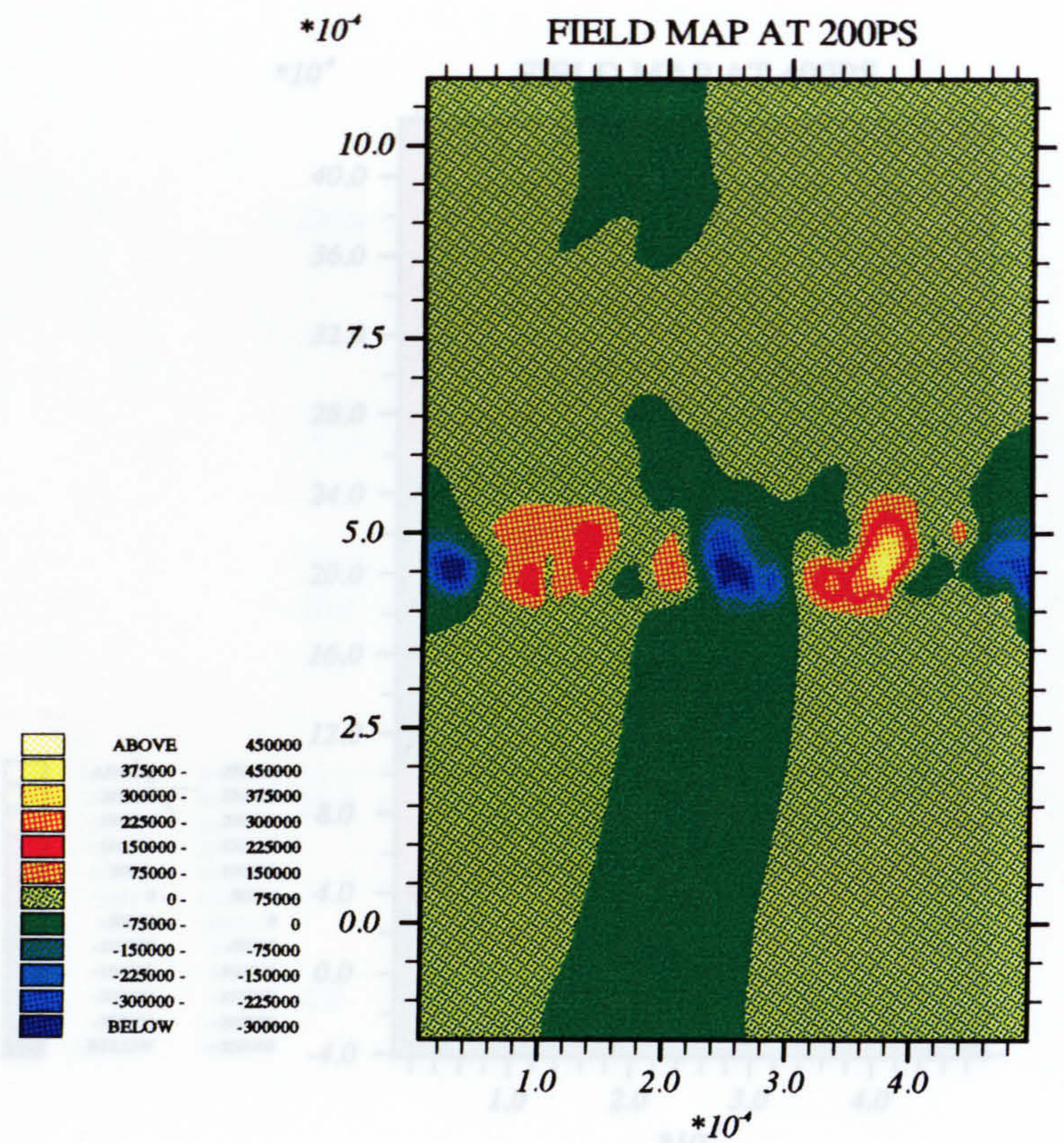

Figure 6.6: Magnetic field contour map for the target (5.0 μ m x 5.0 μ m) with perturbation applied through laser intensity.

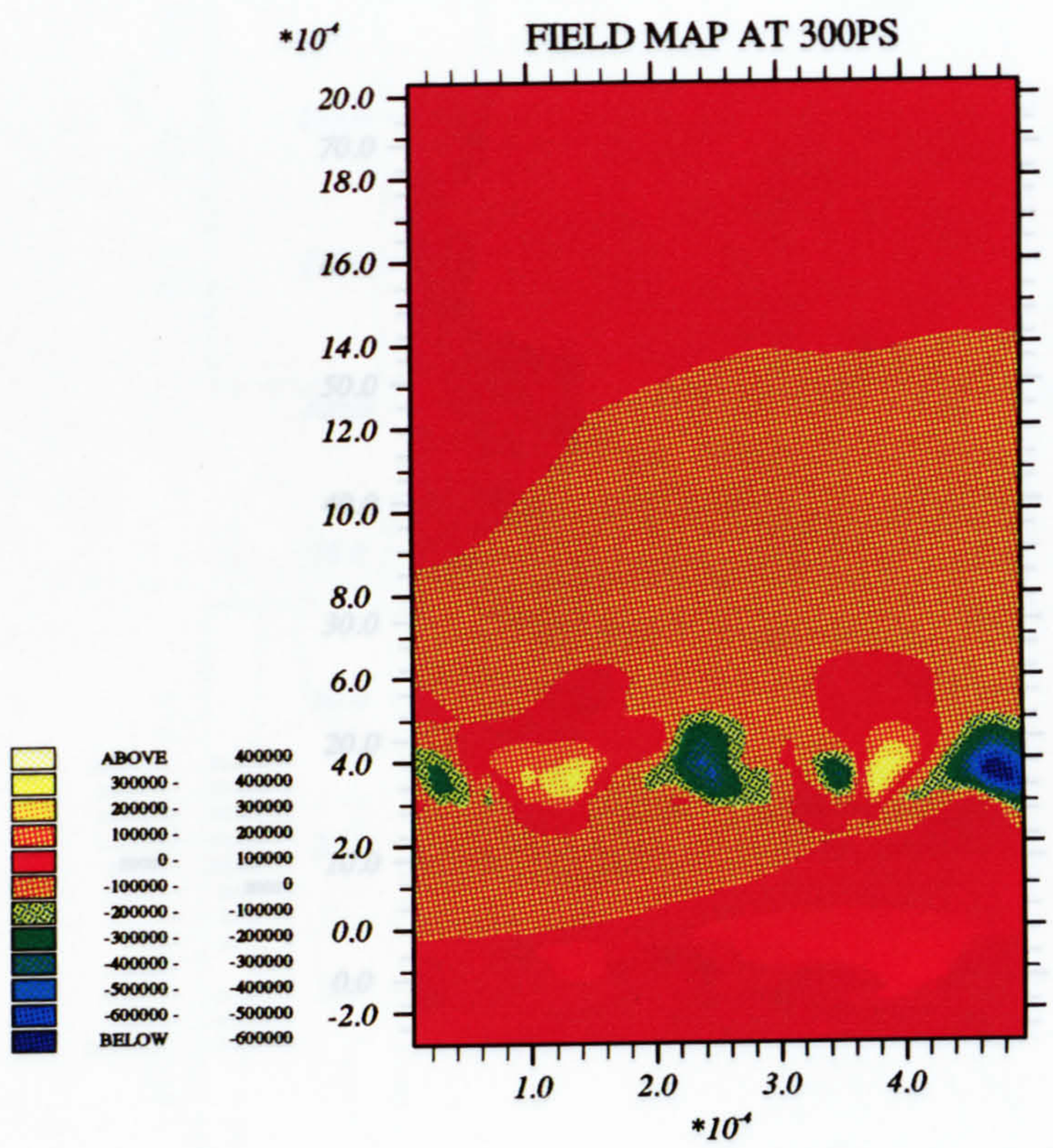
FIELD MAP AT 300PS
*10⁻⁴
20.0
18.0
16.0
14.0
12.0
10.0
8.0
6.0
4.0
2.0
0.0
-2.0
1.0
2.0
3.0
4.0
*10⁻⁴
ABOVE 400000
300000 - 400000
200000 - 300000
100000 - 200000
0 - 100000
-100000 - 0
-200000 - -100000
-300000 - -200000
-400000 - -300000
-500000 - -400000
-600000 - -500000
BELOW -600000

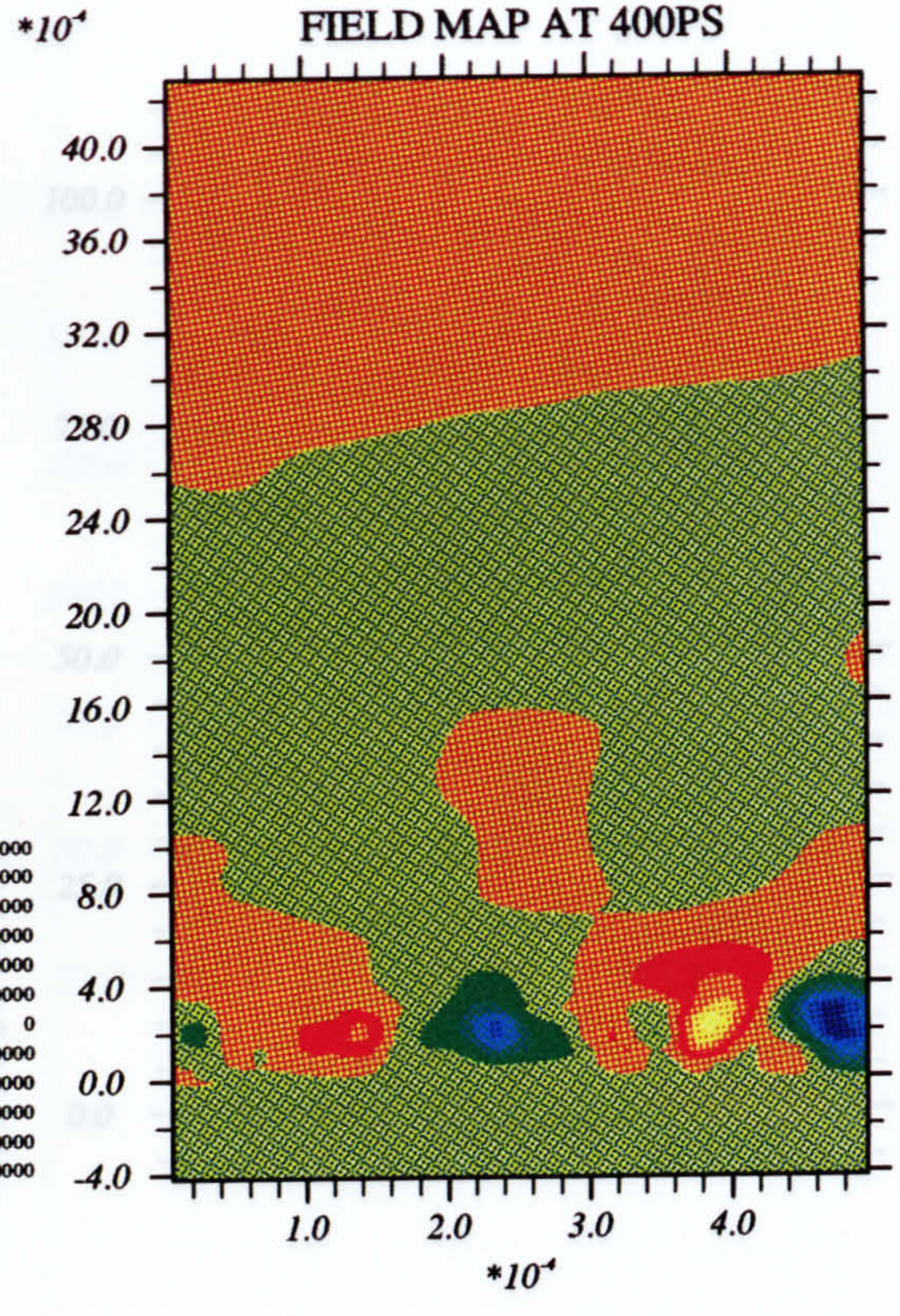
FIELD MAP AT 400PS
*10⁻⁴
40.0
36.0
32.0
28.0
24.0
20.0
16.0
12.0
8.0
4.0
0.0
-4.0
1.0
2.0
3.0
4.0
*10⁻⁴
ABOVE 250000
200000 - 250000
150000 - 200000
100000 - 150000
50000 - 100000
0 - 50000
-50000 - 0
-100000 - -50000
-150000 - -100000
-200000 - -150000
-250000 - -200000
BELOW -250000

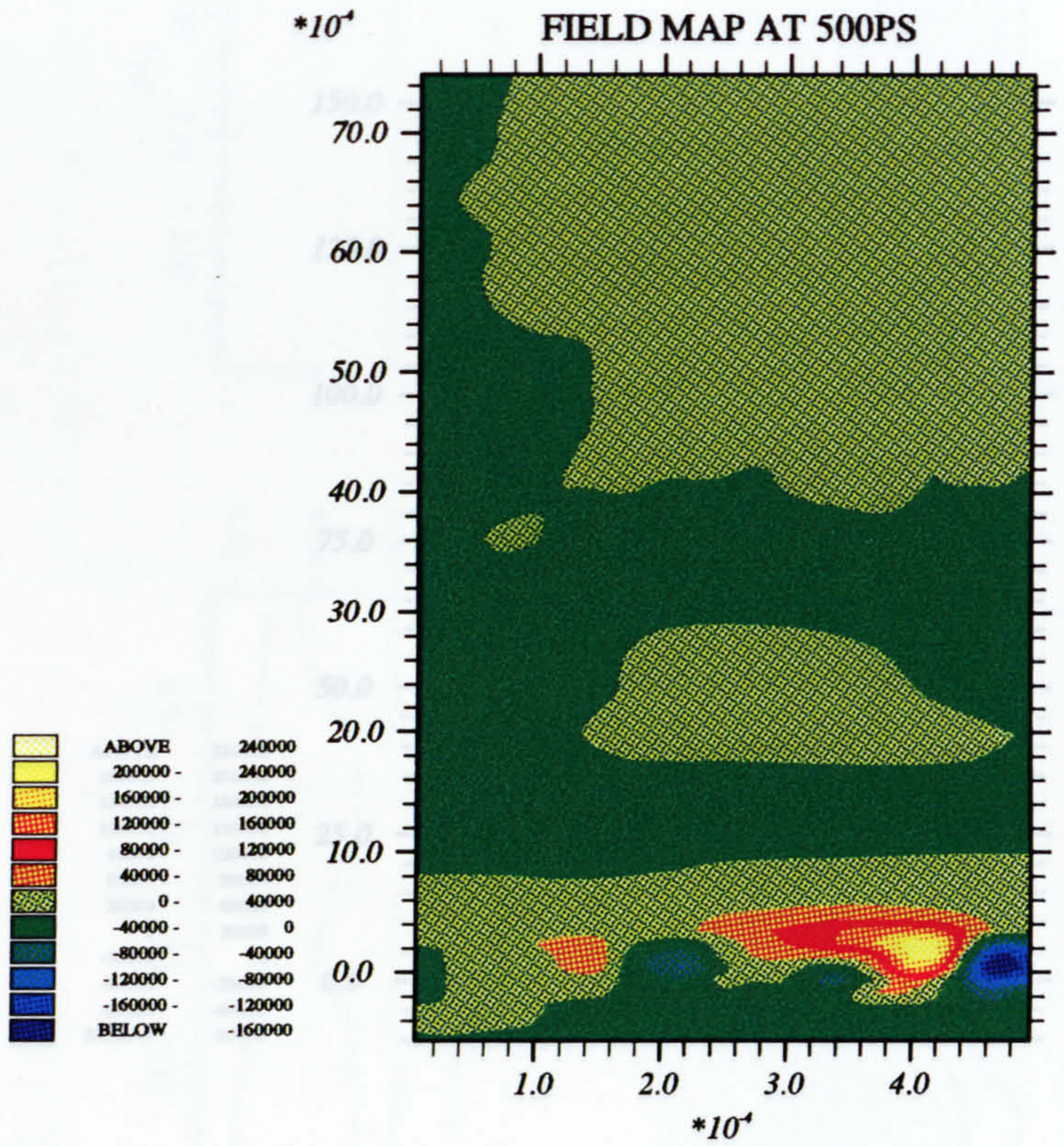
FIELD MAP AT 500PS
*10⁻⁴
70.0
60.0
50.0
40.0
30.0
20.0
10.0
0.0
1.0
2.0
3.0
4.0
*10⁻⁴
ABOVE 240000
200000 - 240000
160000 - 200000
120000 - 160000
80000 - 120000
40000 - 80000
0 - 40000
-40000 - 0
-80000 - -40000
-120000 - -80000
-160000 - -120000
BELOW -160000

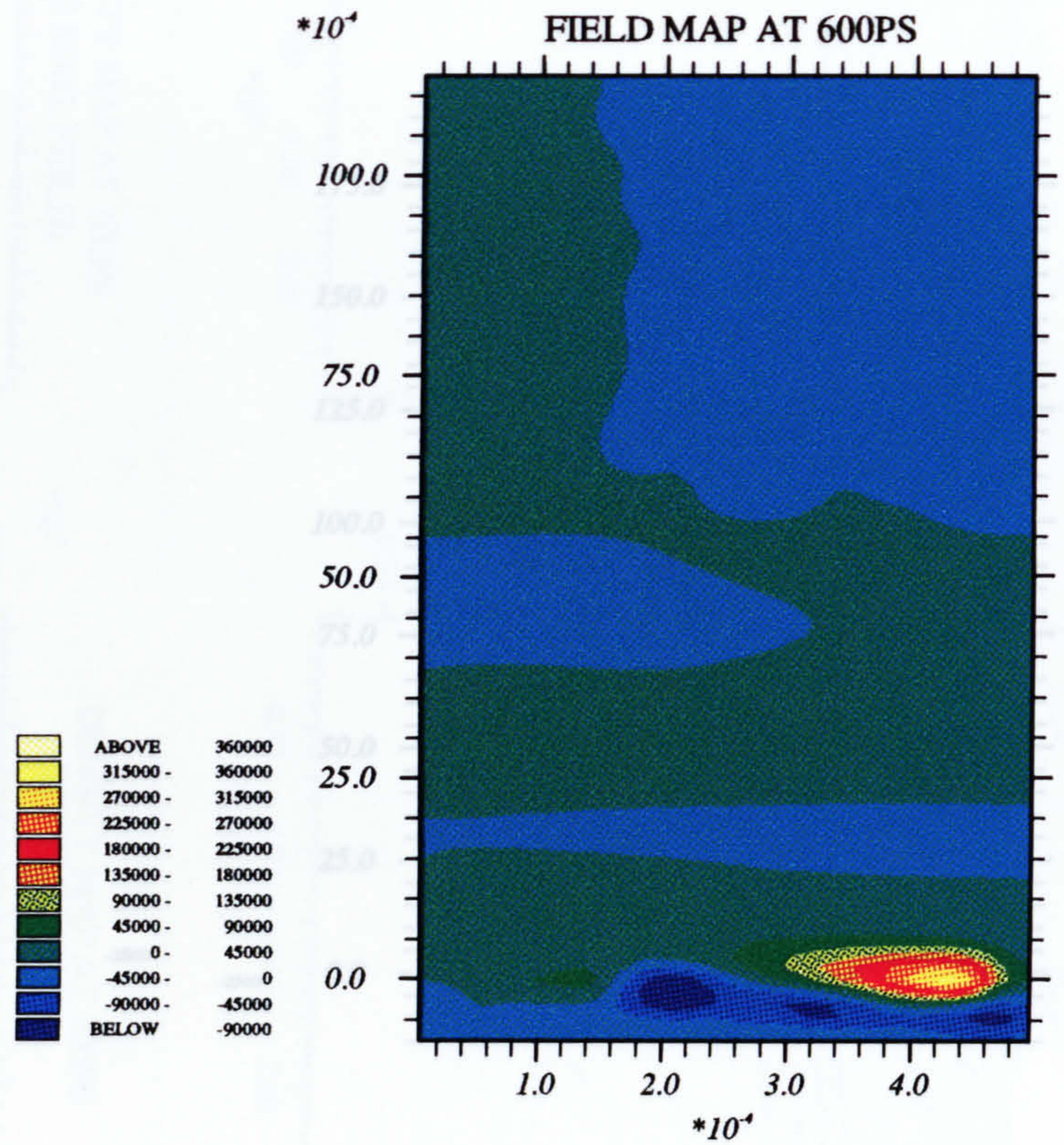
FIELD MAP AT 600PS
*10⁻⁴
100.0
75.0
50.0
25.0
0.0
1.0
2.0
3.0
4.0
*10⁻⁴
ABOVE 360000
315000 - 360000
270000 - 315000
225000 - 270000
180000 - 225000
135000 - 180000
90000 - 135000
45000 - 90000
0 - 45000
-45000 - 0
-90000 - -45000
BELOW -90000

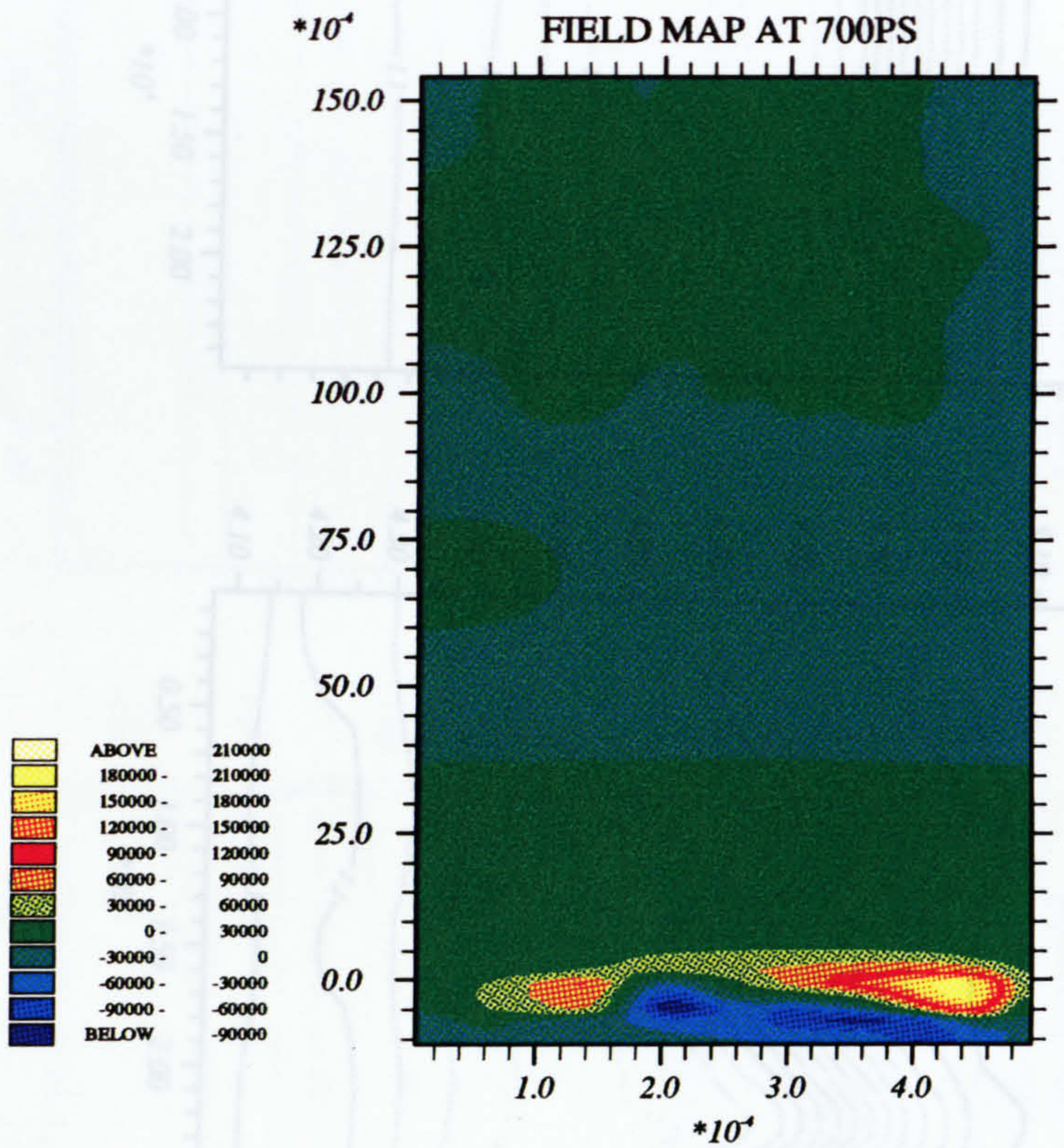
*10⁻⁴
FIELD MAP AT 700PS
150.0
125.0
100.0
75.0
50.0
25.0
0.0
1.0
2.0
3.0
4.0
*10⁻⁴
ABOVE 210000
180000 - 210000
150000 - 180000
120000 - 150000
90000 - 120000
60000 - 90000
30000 - 60000
0 - 30000
-30000 - 0
-60000 - -30000
-90000 - -60000
BELOW -90000

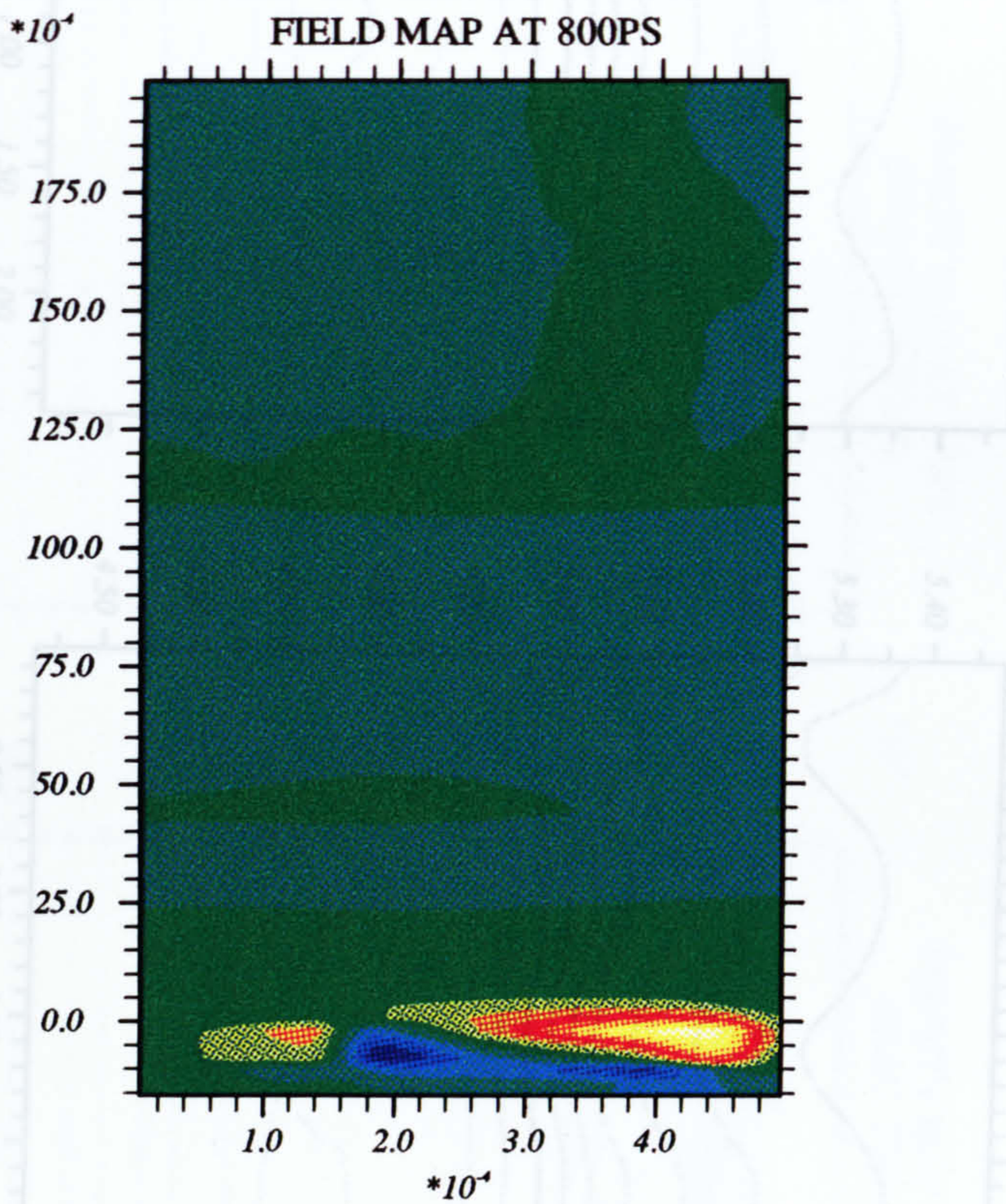
*10⁻⁴
FIELD MAP AT 800PS
175.0
150.0
125.0
100.0
75.0
50.0
25.0
0.0
1.0
2.0
3.0
4.0
*10⁻⁴
ABOVE 175000
150000 - 175000
125000 - 150000
100000 - 125000
75000 - 100000
50000 - 75000
25000 - 50000
0 - 25000
-25000 - 0
-50000 - -25000
-75000 - -50000
BELOW -75000

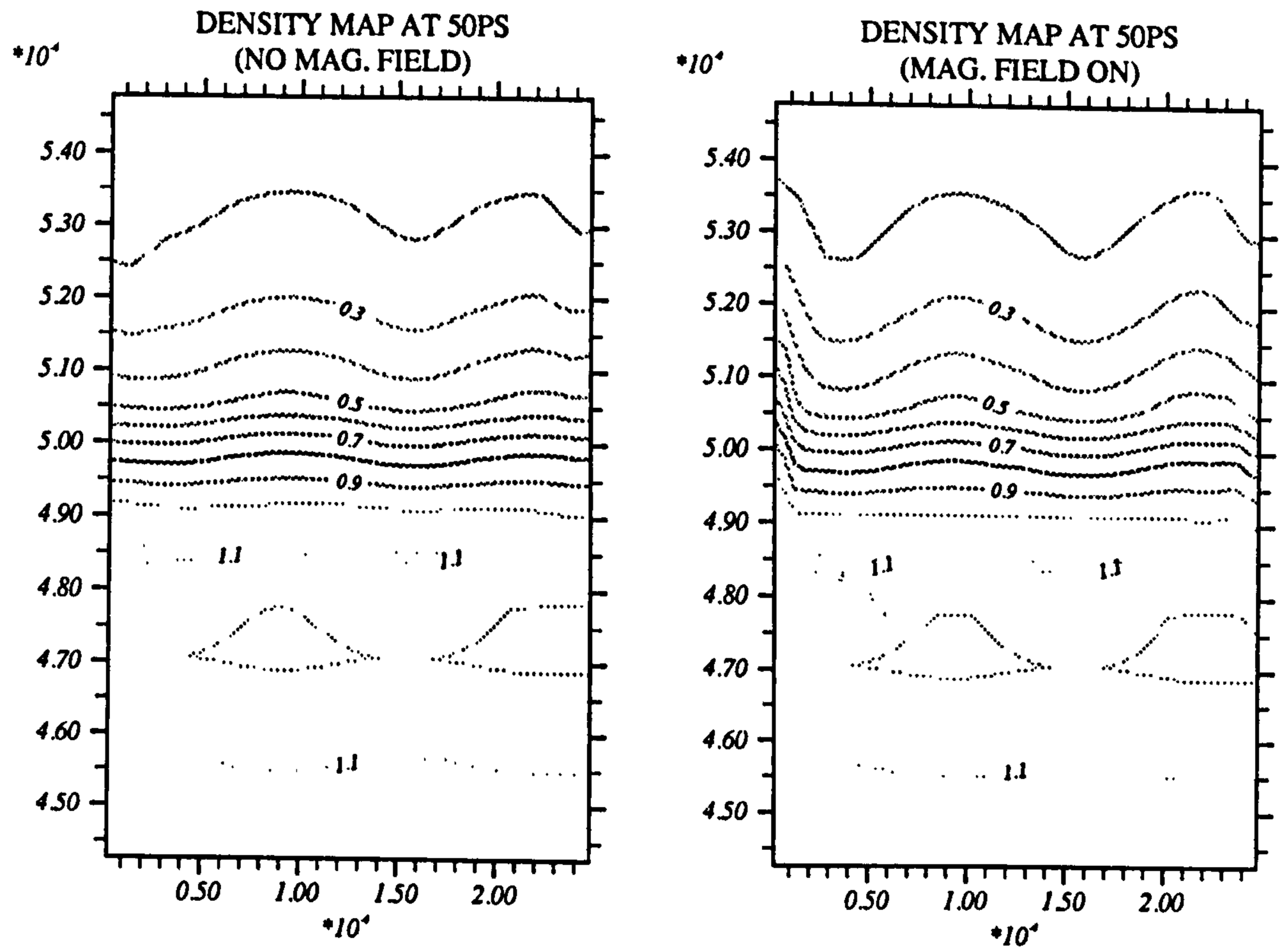

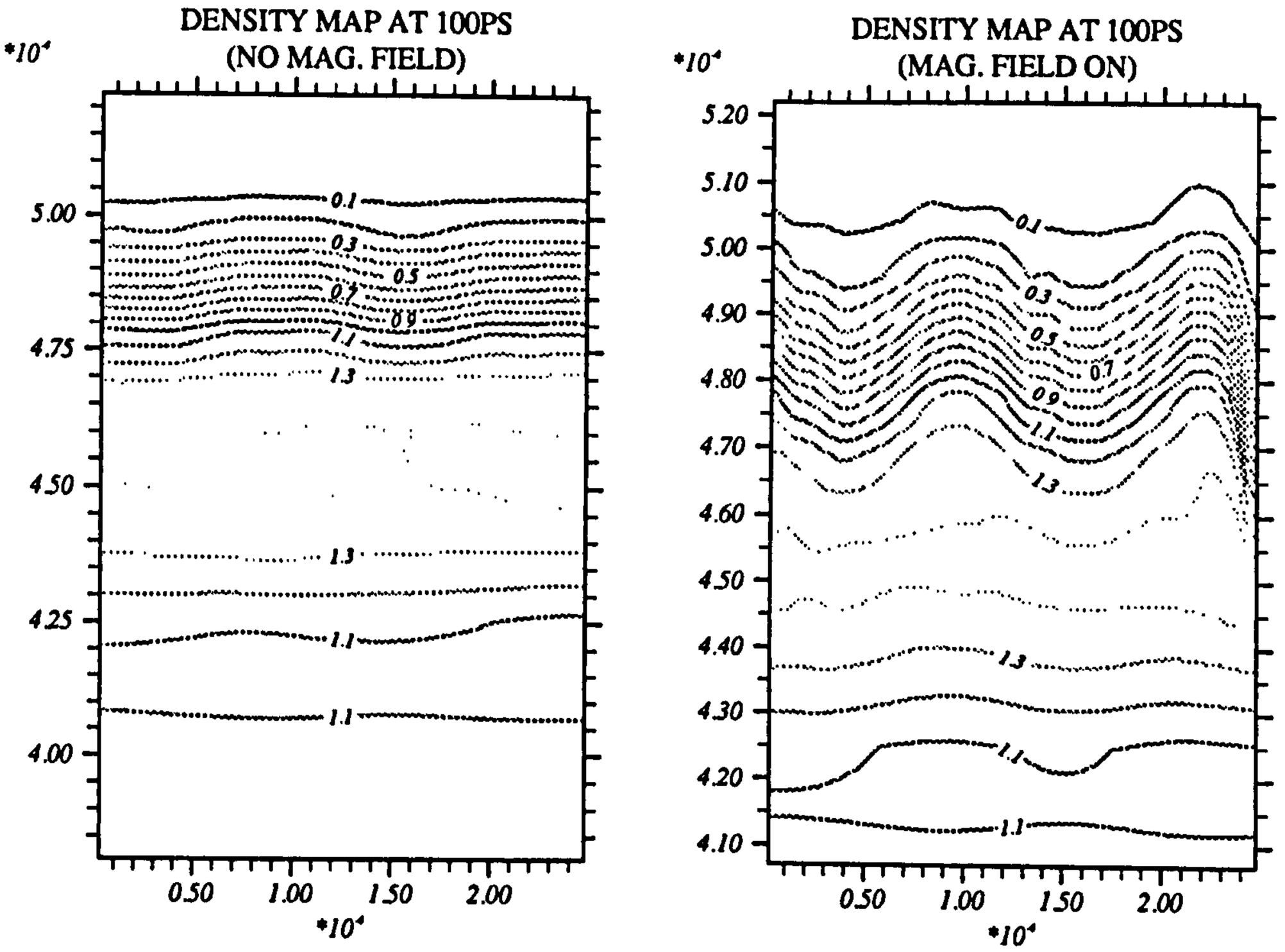

Figure 6.7: Density contour map for the target ($5{\cdot}0\mu m \times 2{\cdot}5\mu m$) with perturbation applied through laser intensity

DENSITY MAP AT 150PS
(NO MAG. FIELD)

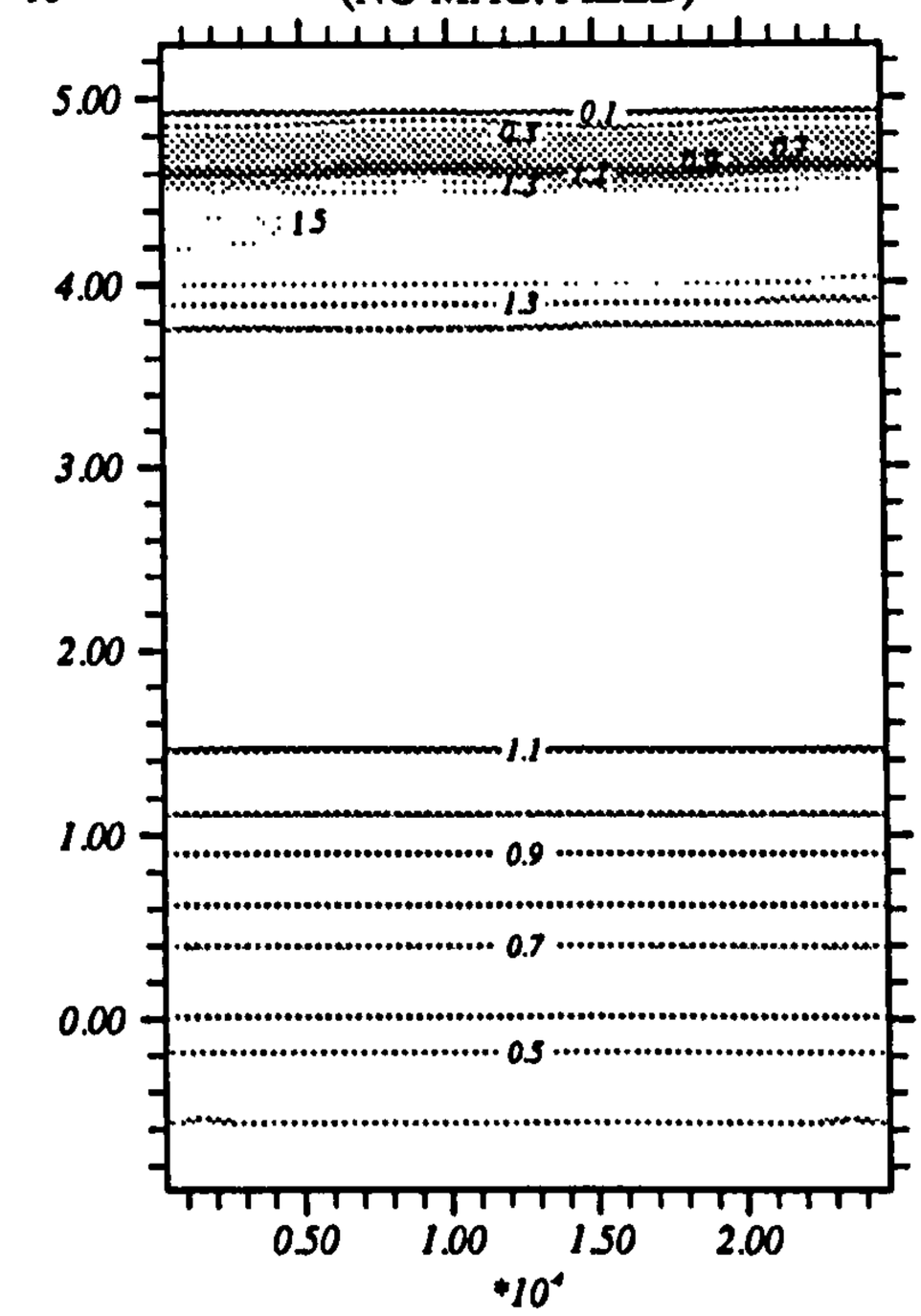

DENSITY MAP AT 150PS
(MAG. FIELD ON)

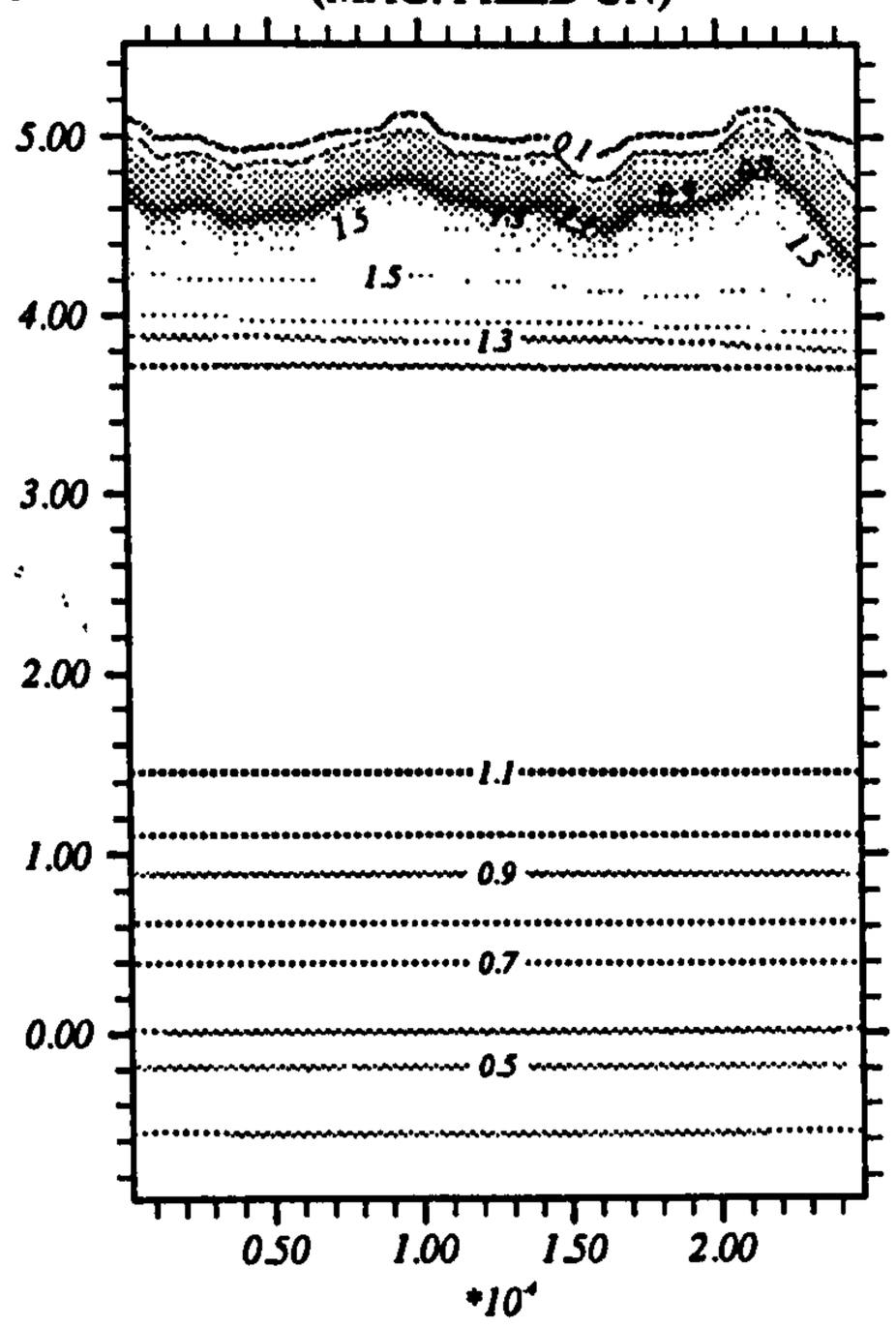

DENSITY MAP AT 200PS
(NO MAG. FIELD)

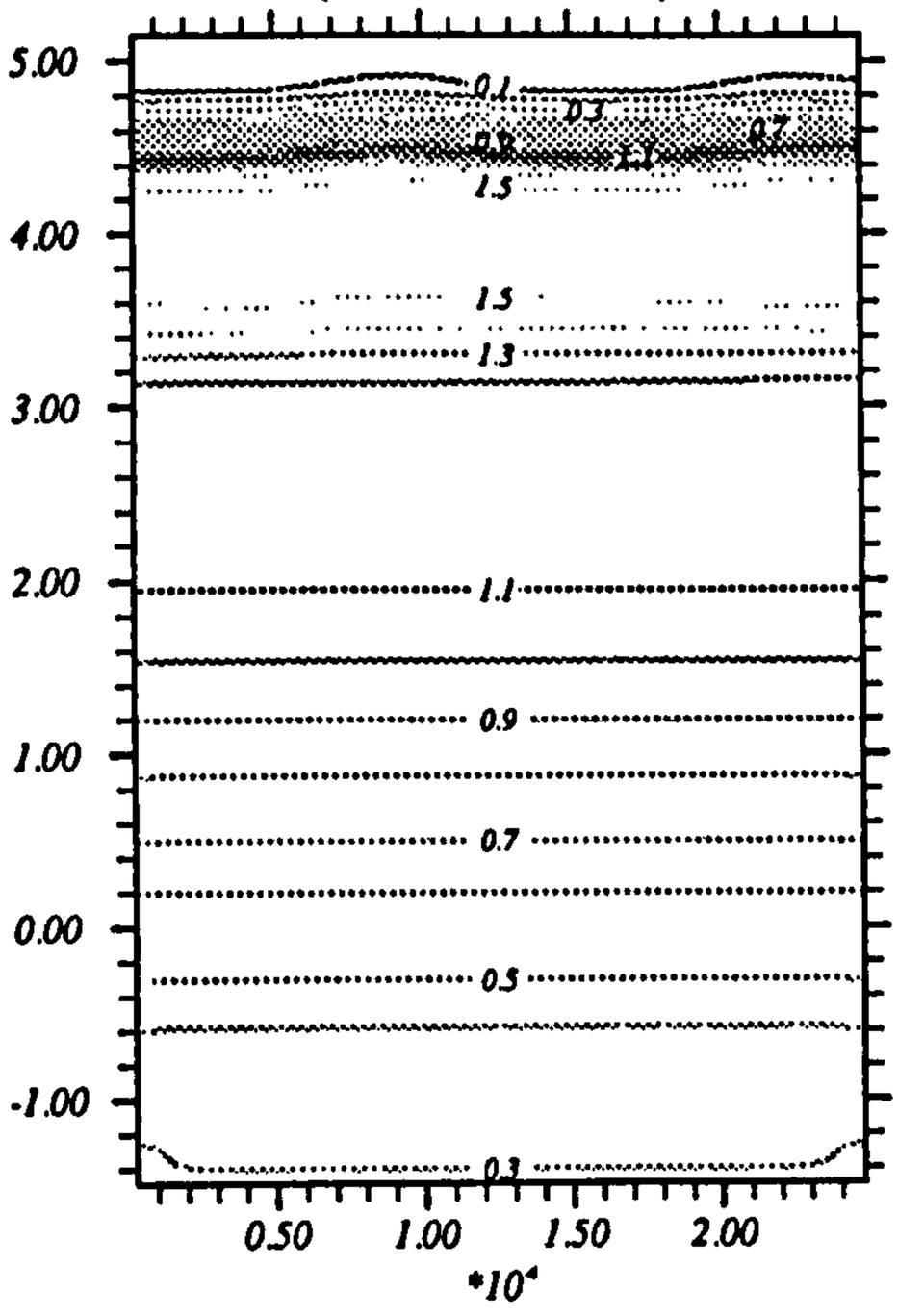

DENSITY MAP AT 200PS
(MAG. FIELD ON)

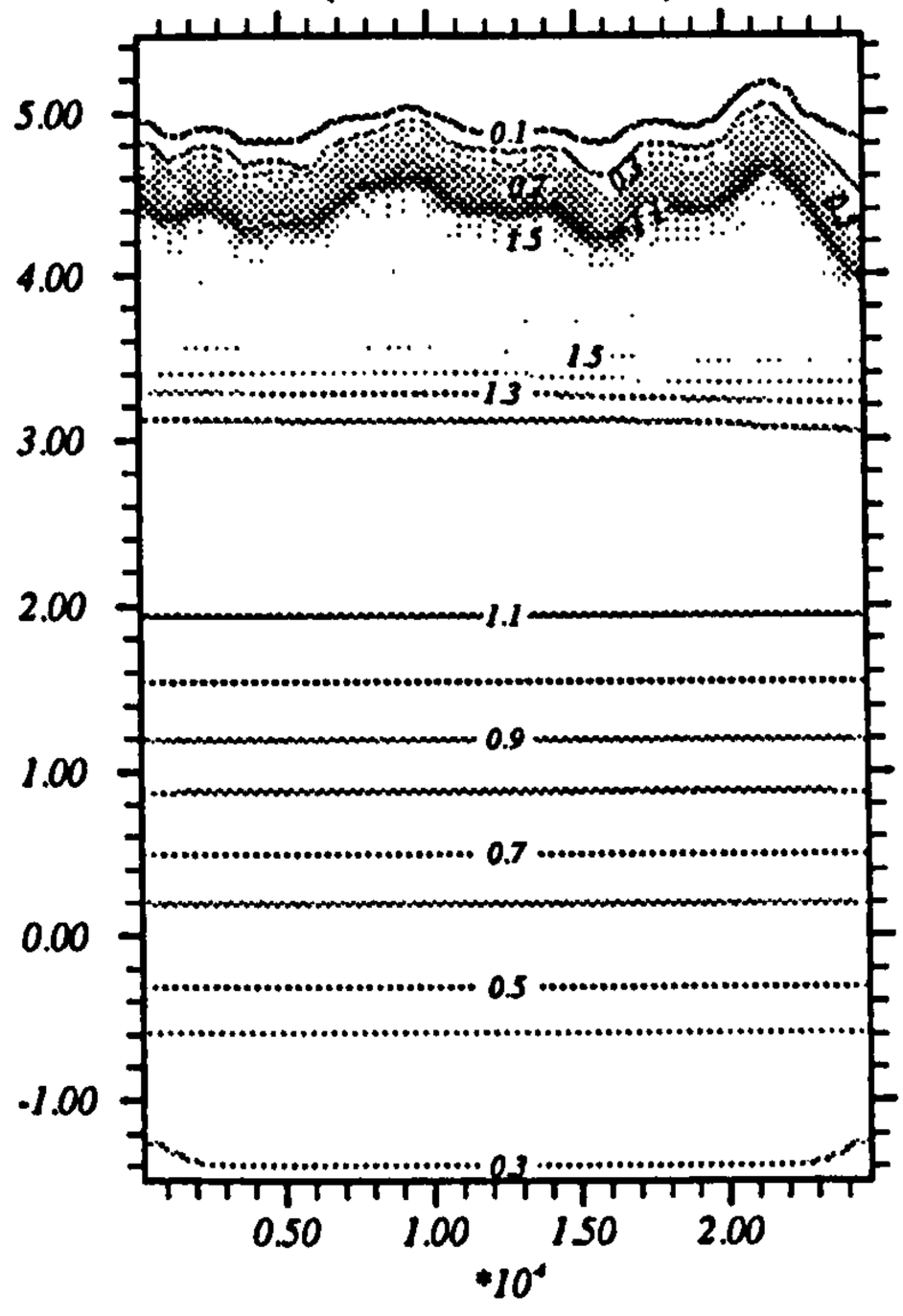

DENSITY MAP AT 250PS
(NO MAG. FIELD)

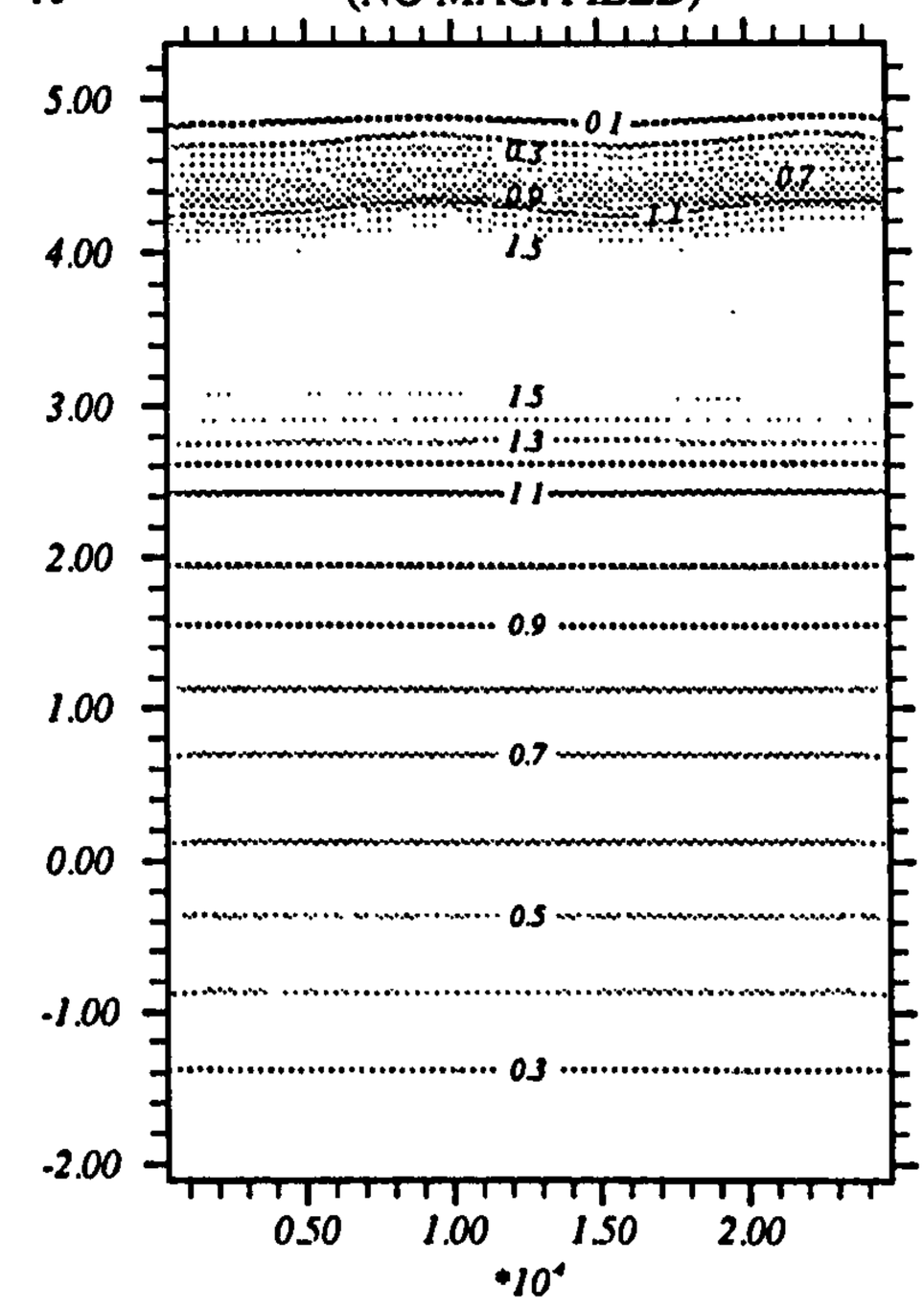

DENSITY MAP AT 250PS
(MAG. FIELD ON)

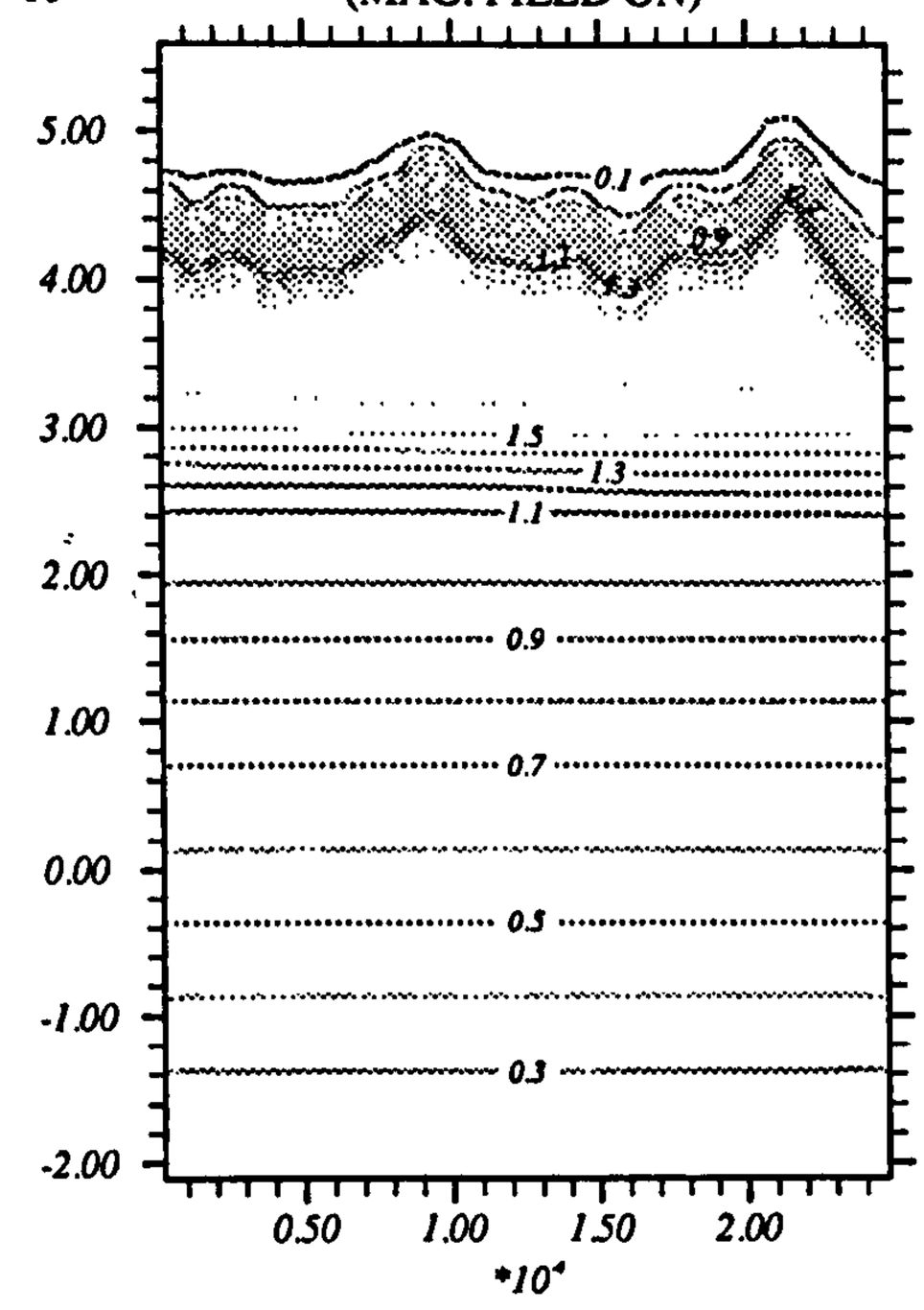

DENSITY MAP AT 300PS
(NO MAG. FIELD)

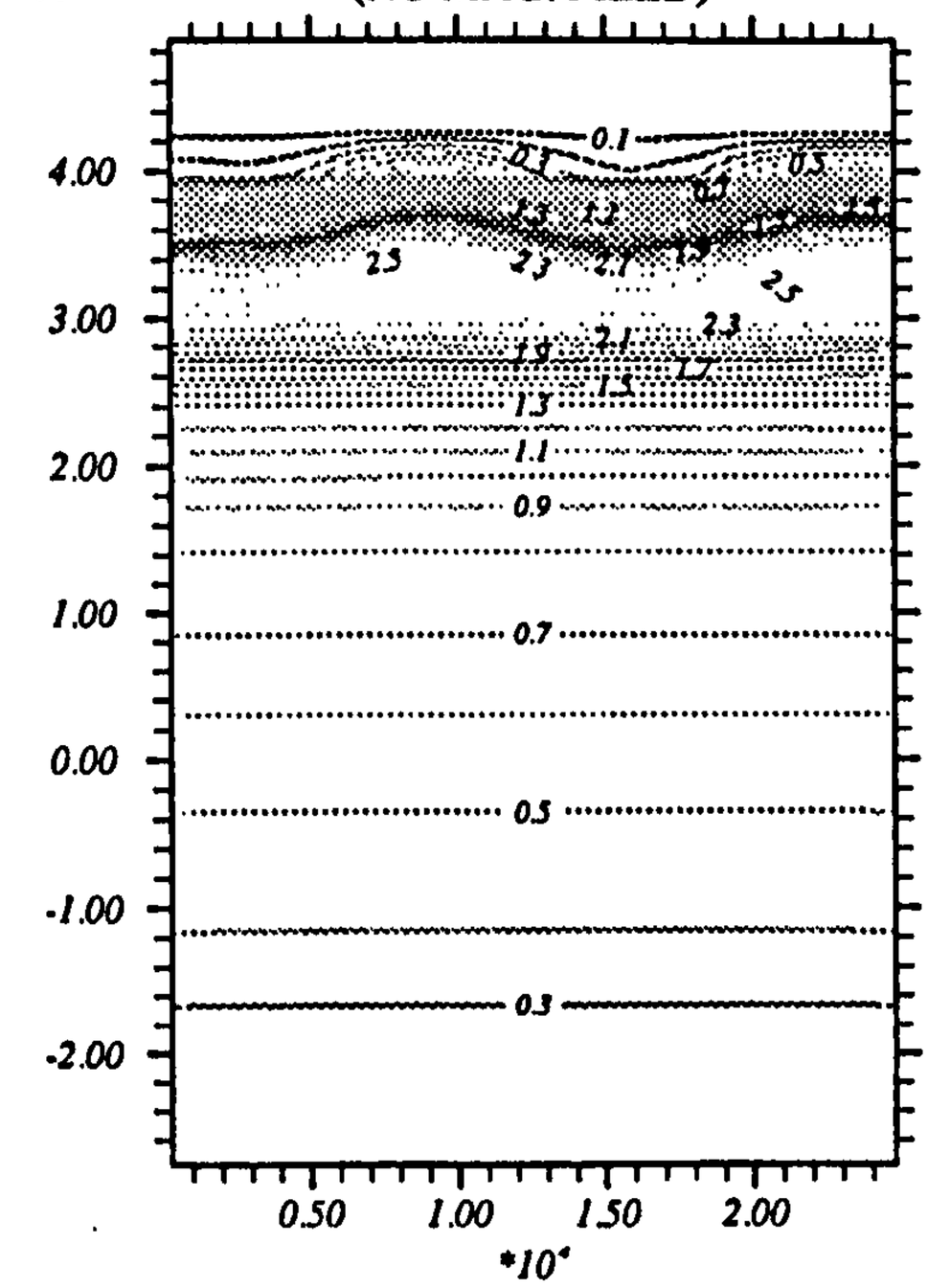

DENSITY MAP AT 300PS
(MAG. FIELD ON)

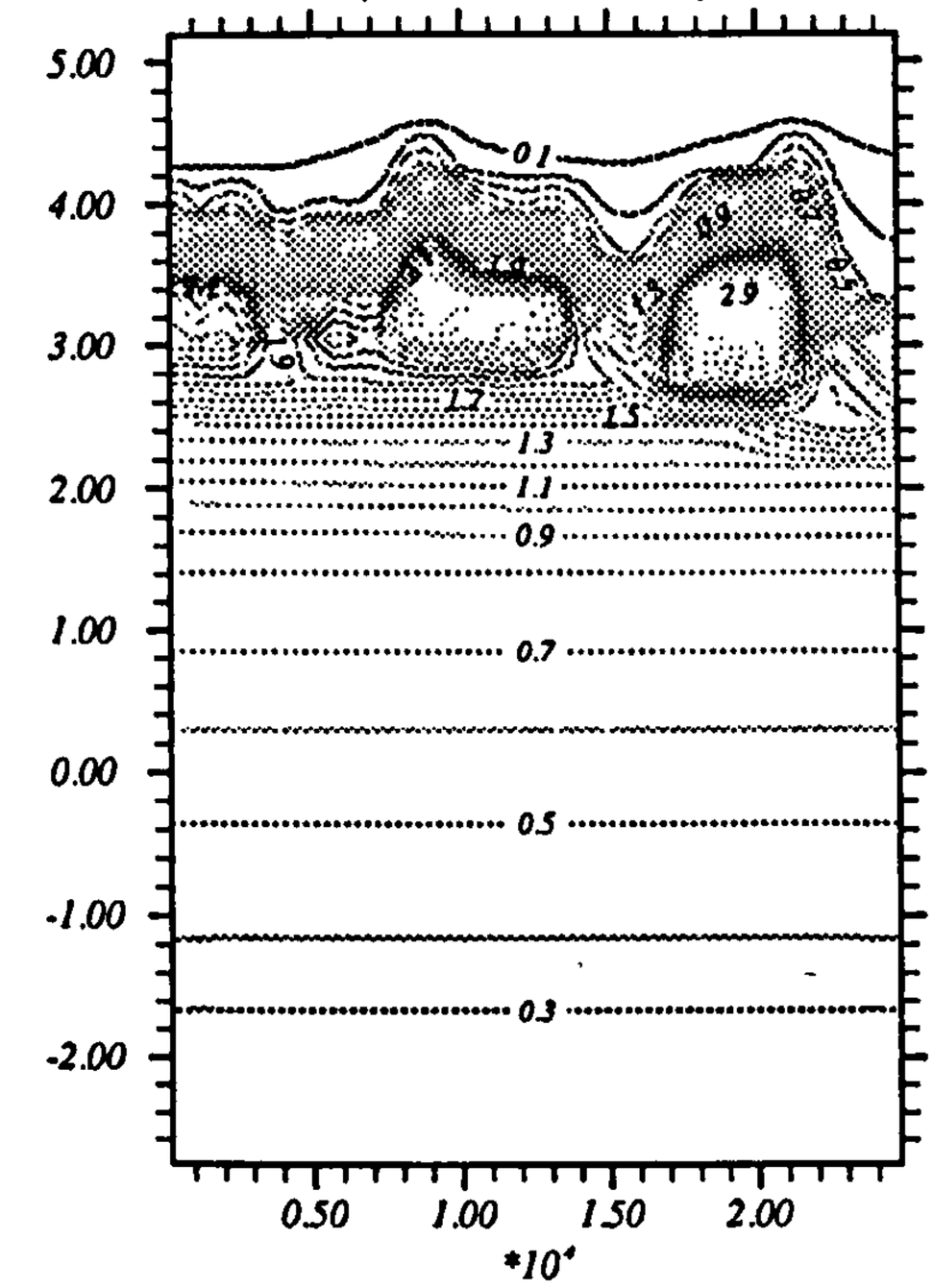

DENSITY MAP AT 350PS
(NO MAG. FIELD)

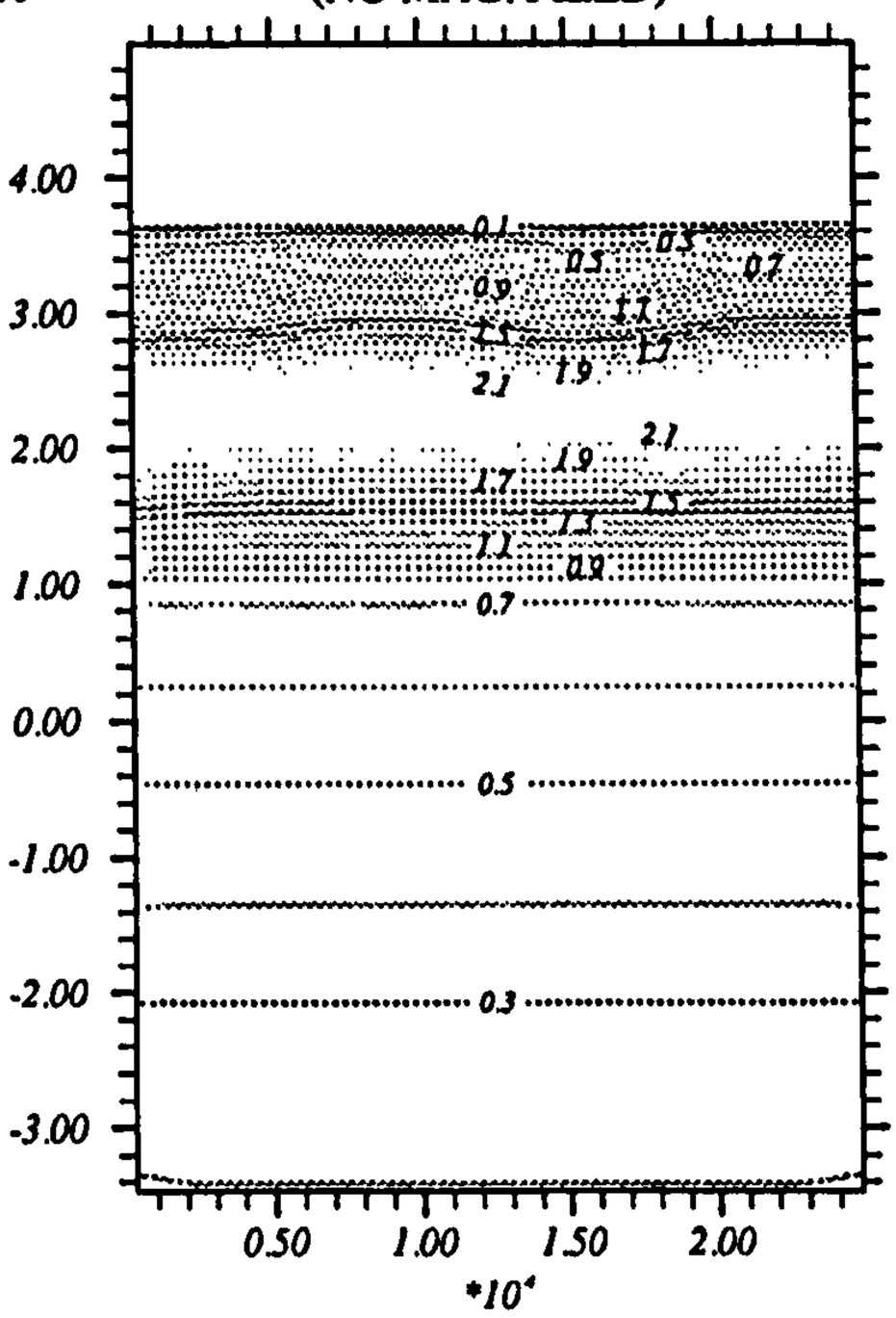

DENSITY MAP AT 350PS
(MAG. FIELD ON)

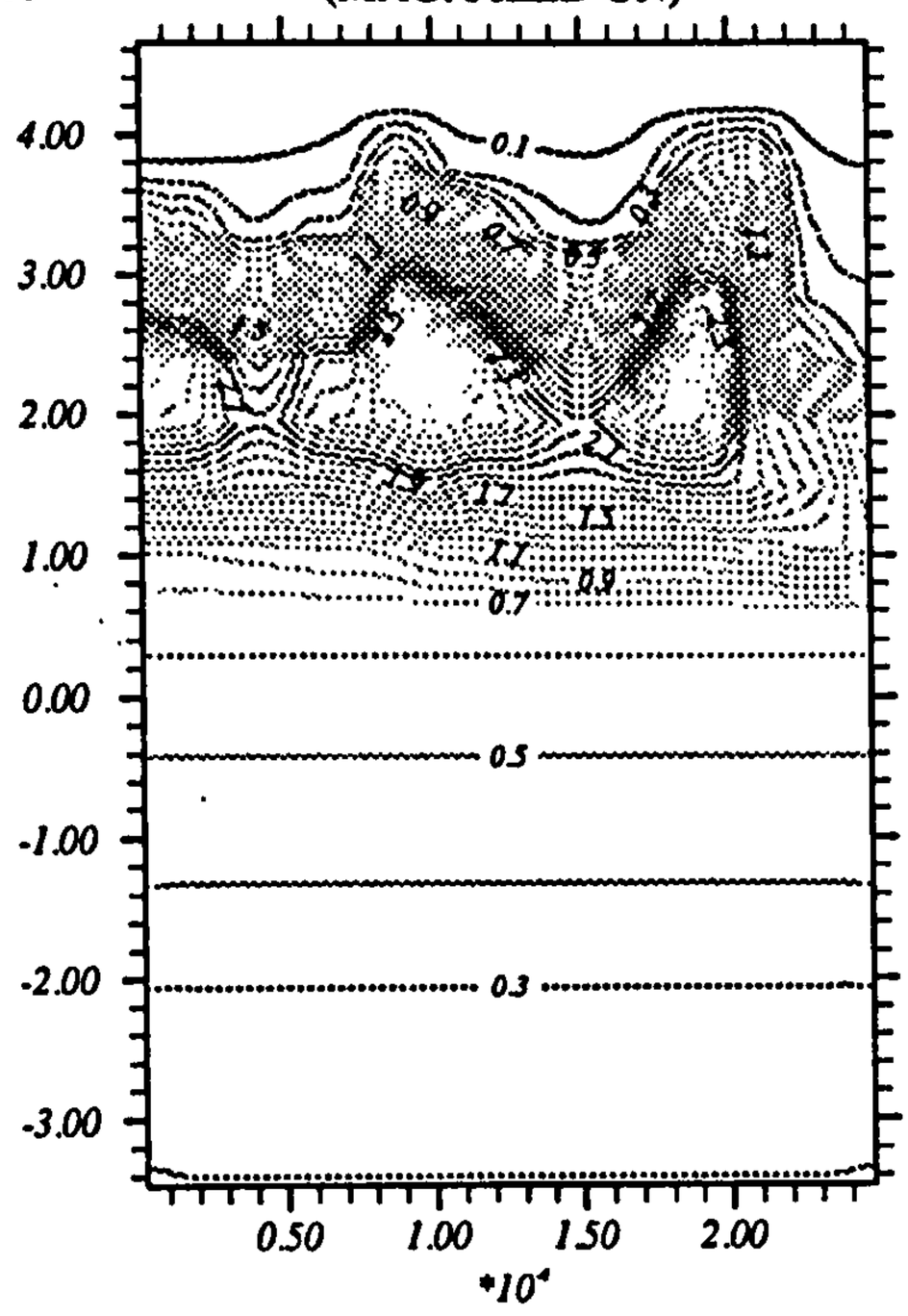

DENSITY MAP AT 400PS
(NO MAG. FIELD)

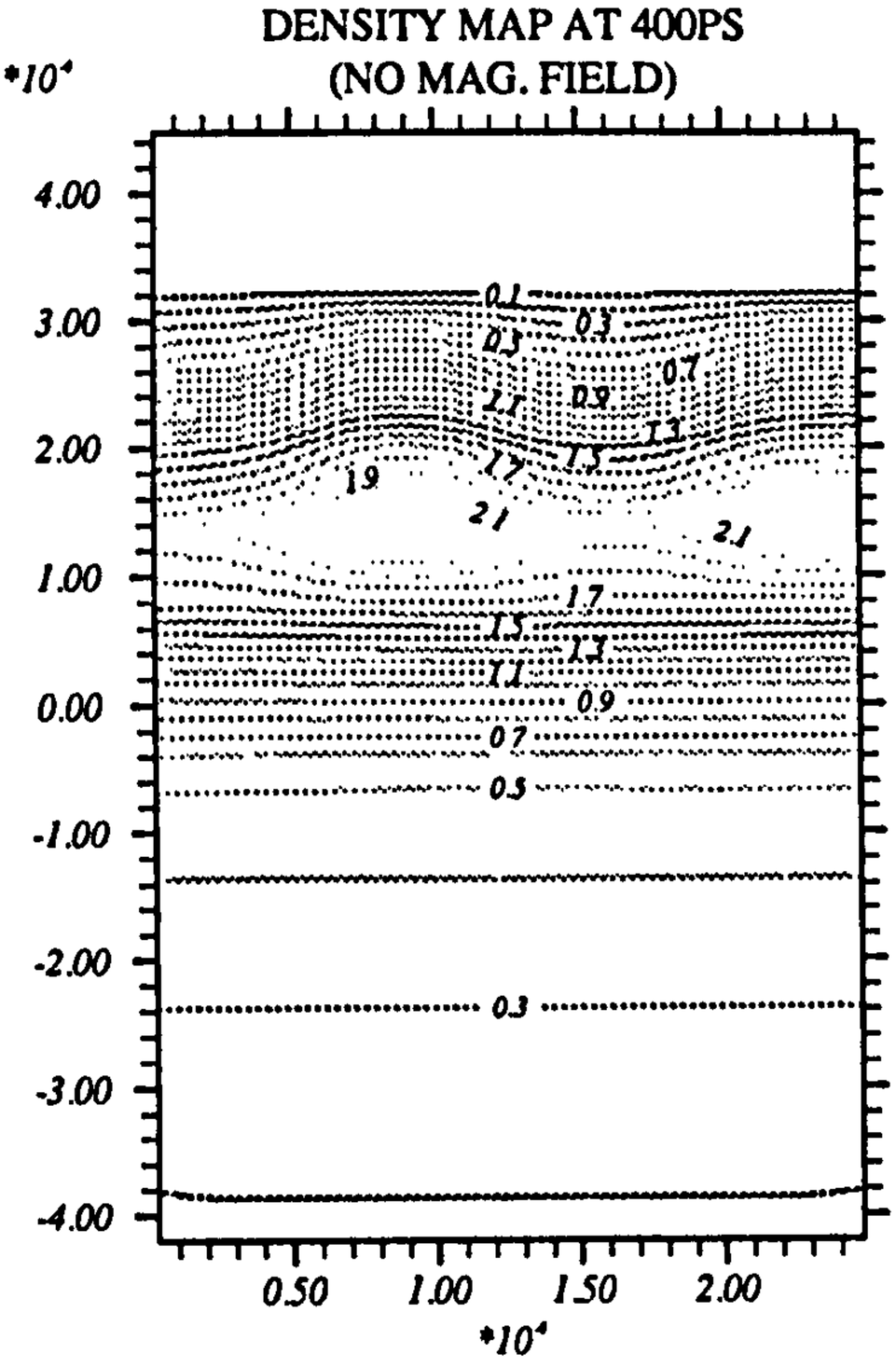

DENSITY MAP AT 400PS
(MAG. FIELD ON)

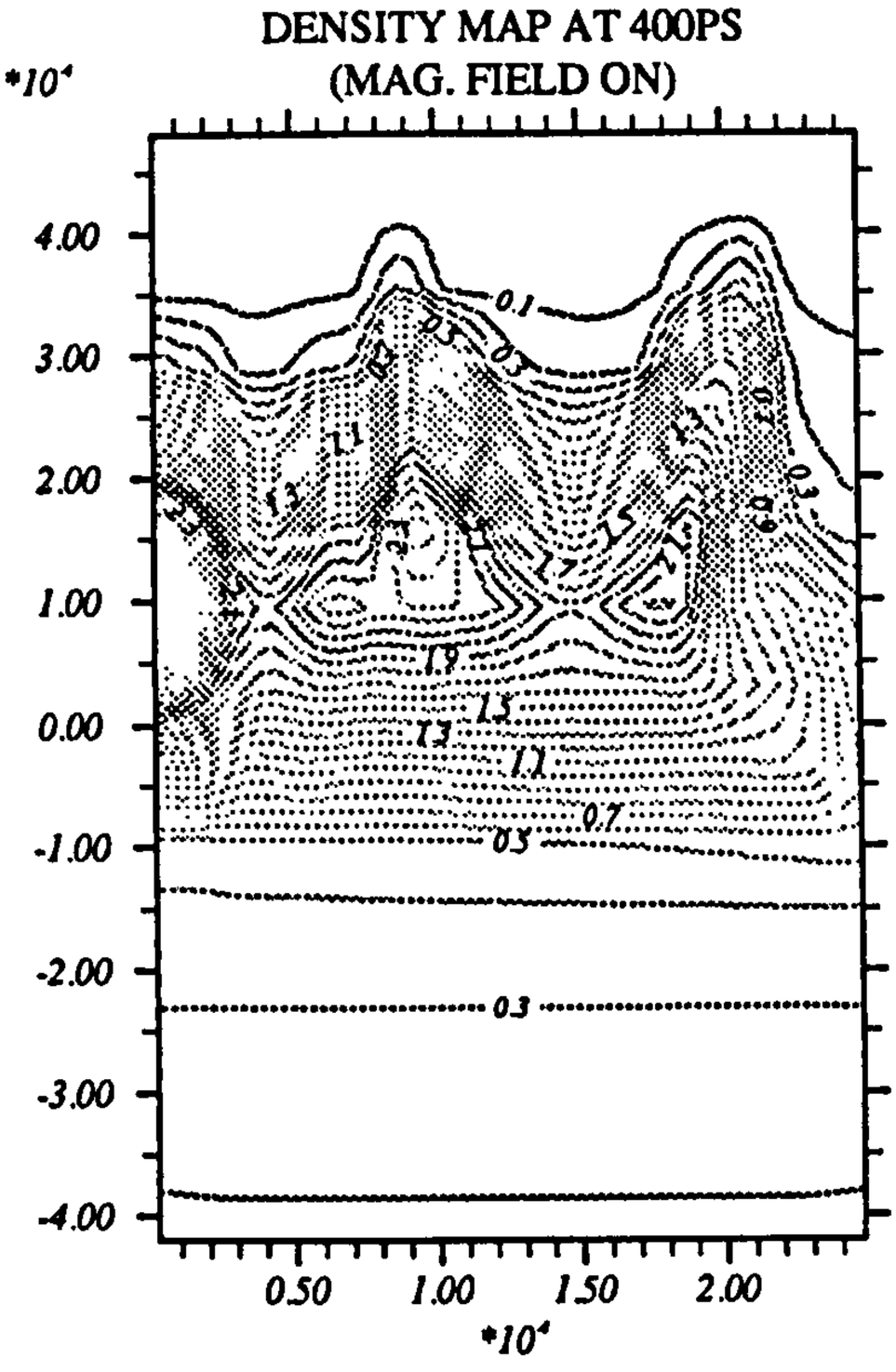

DENSITY MAP AT 450PS
(NO MAG. FIELD)

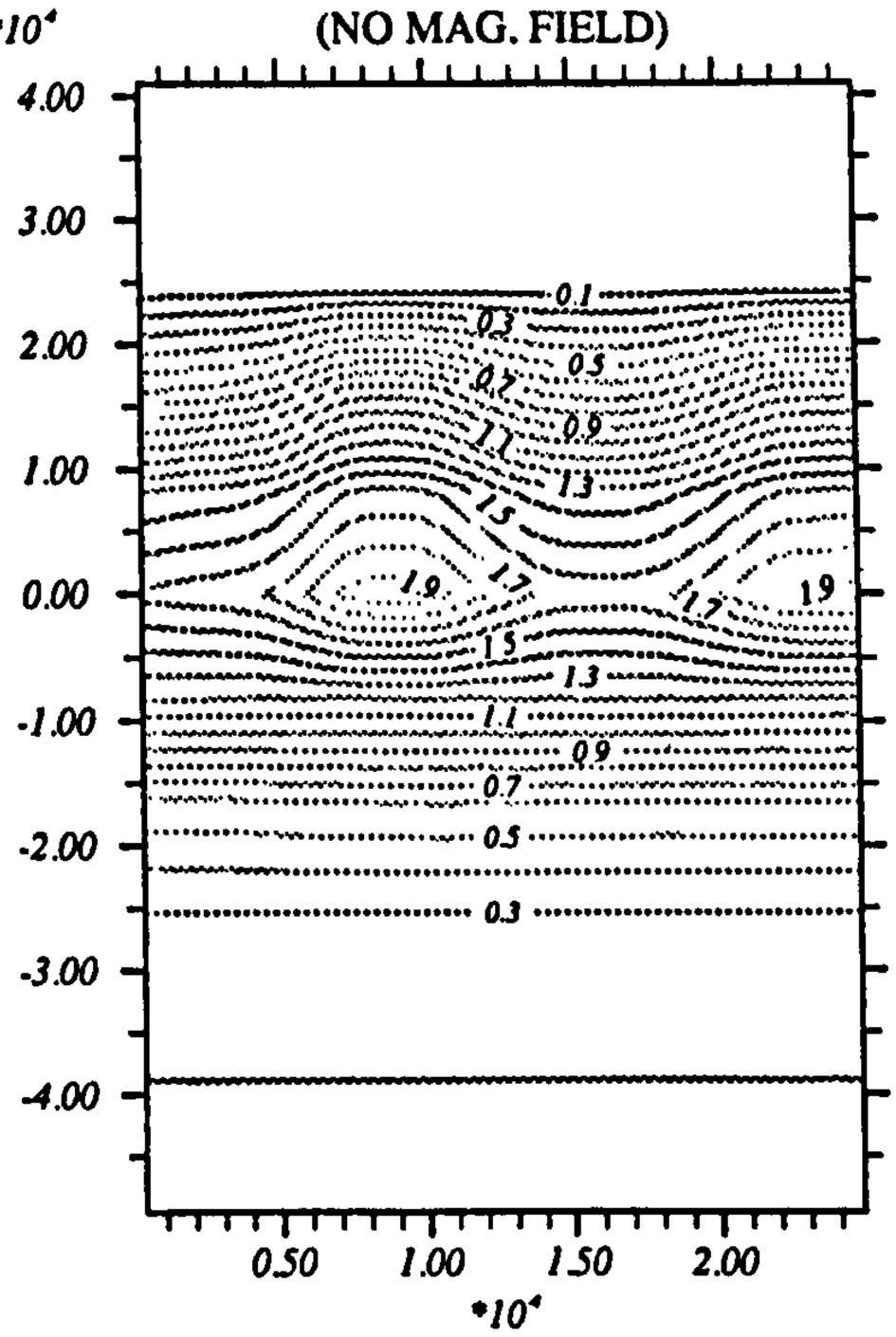

DENSITY MAP AT 450PS
(MAG. FIELD ON)

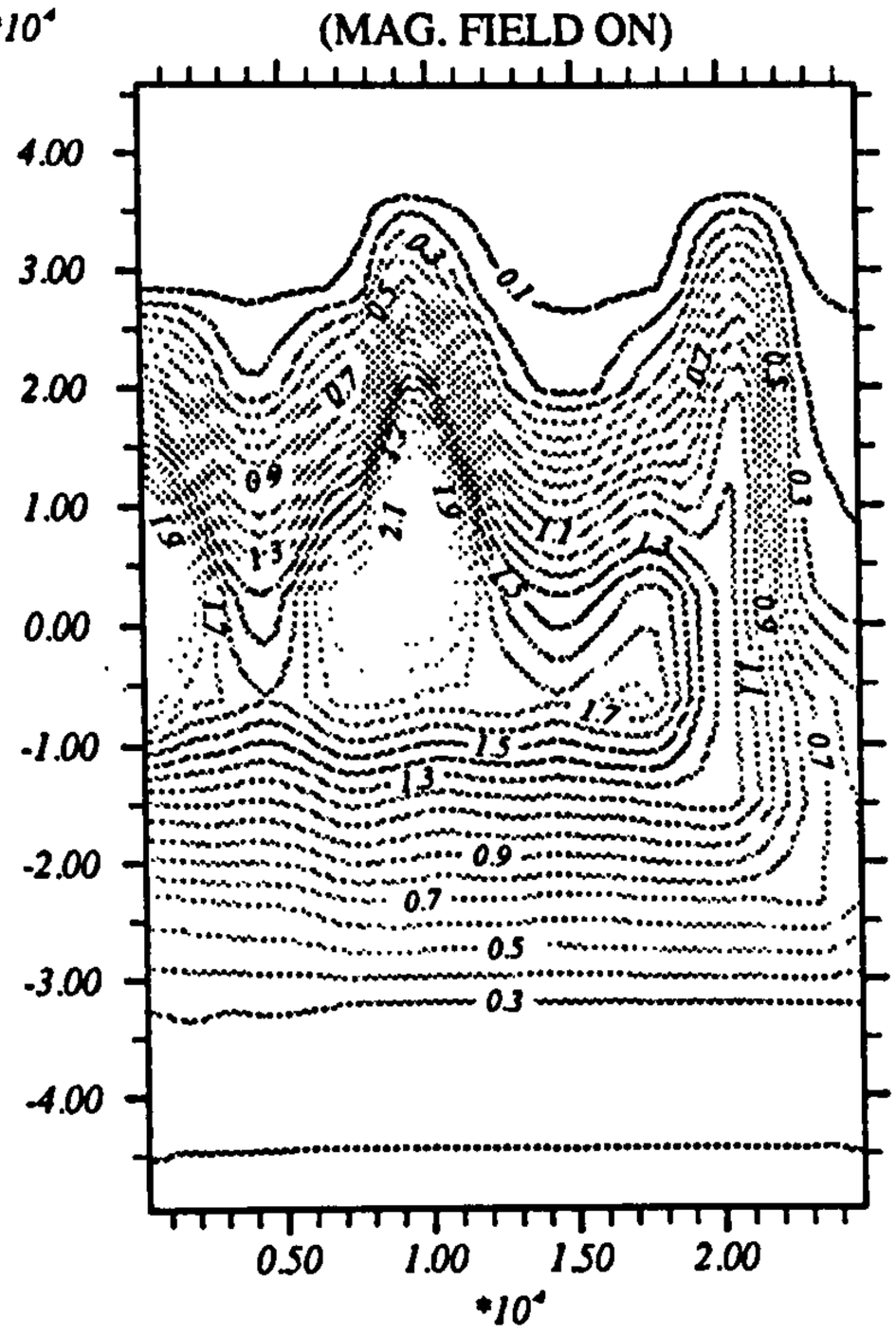

DENSITY MAP AT 500PS
(NO MAG. FIELD)

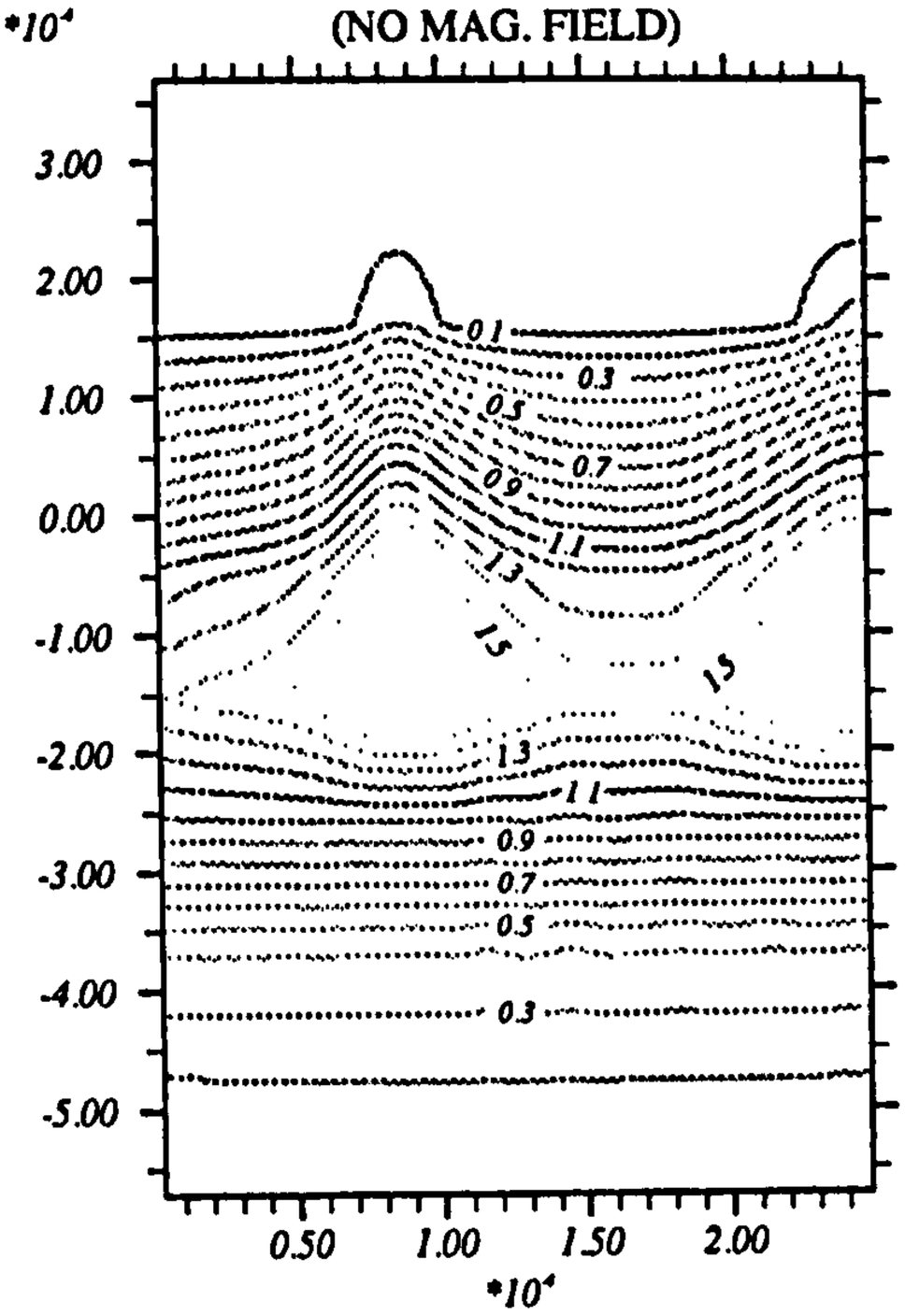

DENSITY MAP AT 500PS
(MAG. FIELD ON)

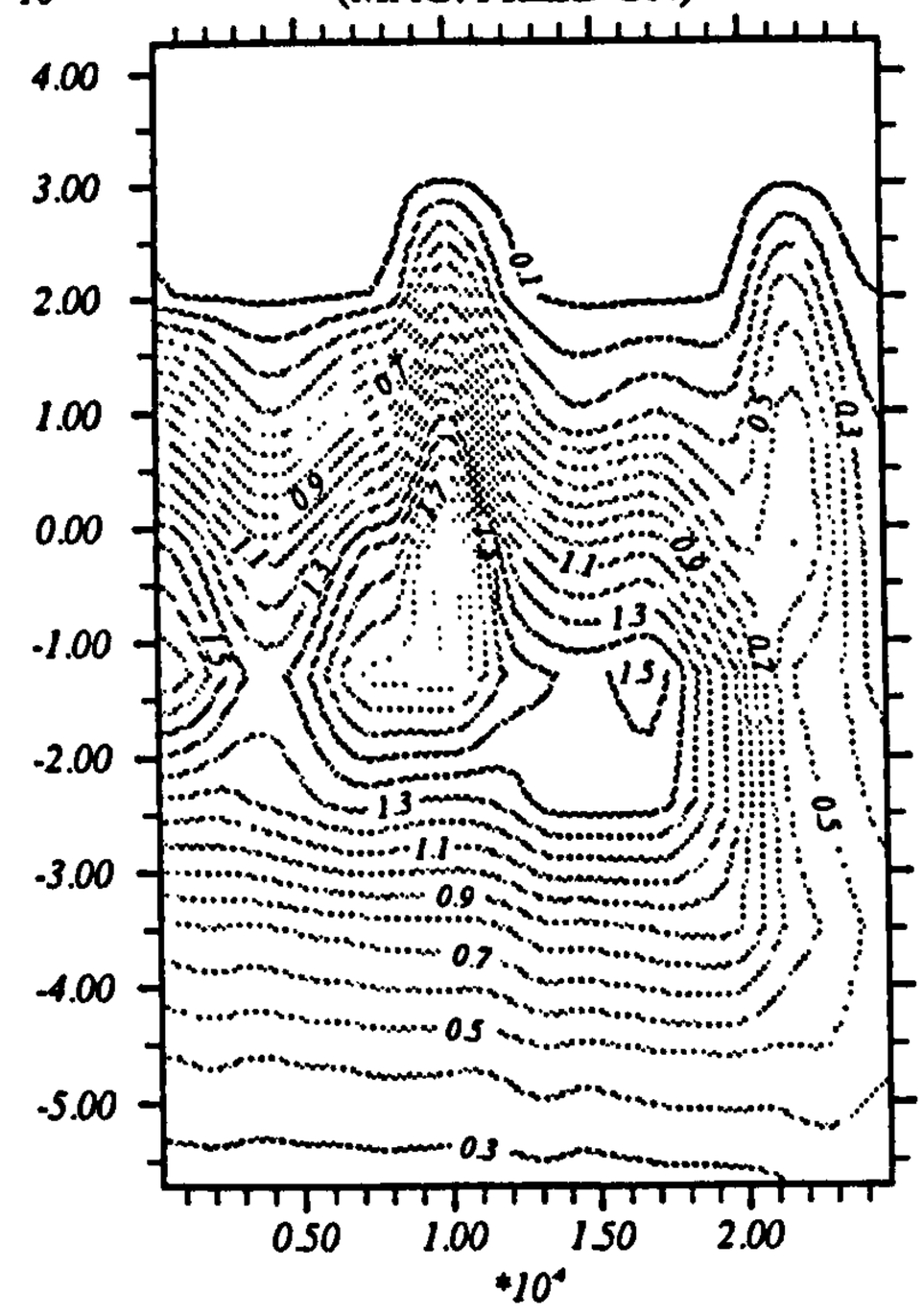

DENSITY MAP AT 550PS
(NO MAG. FIELD)

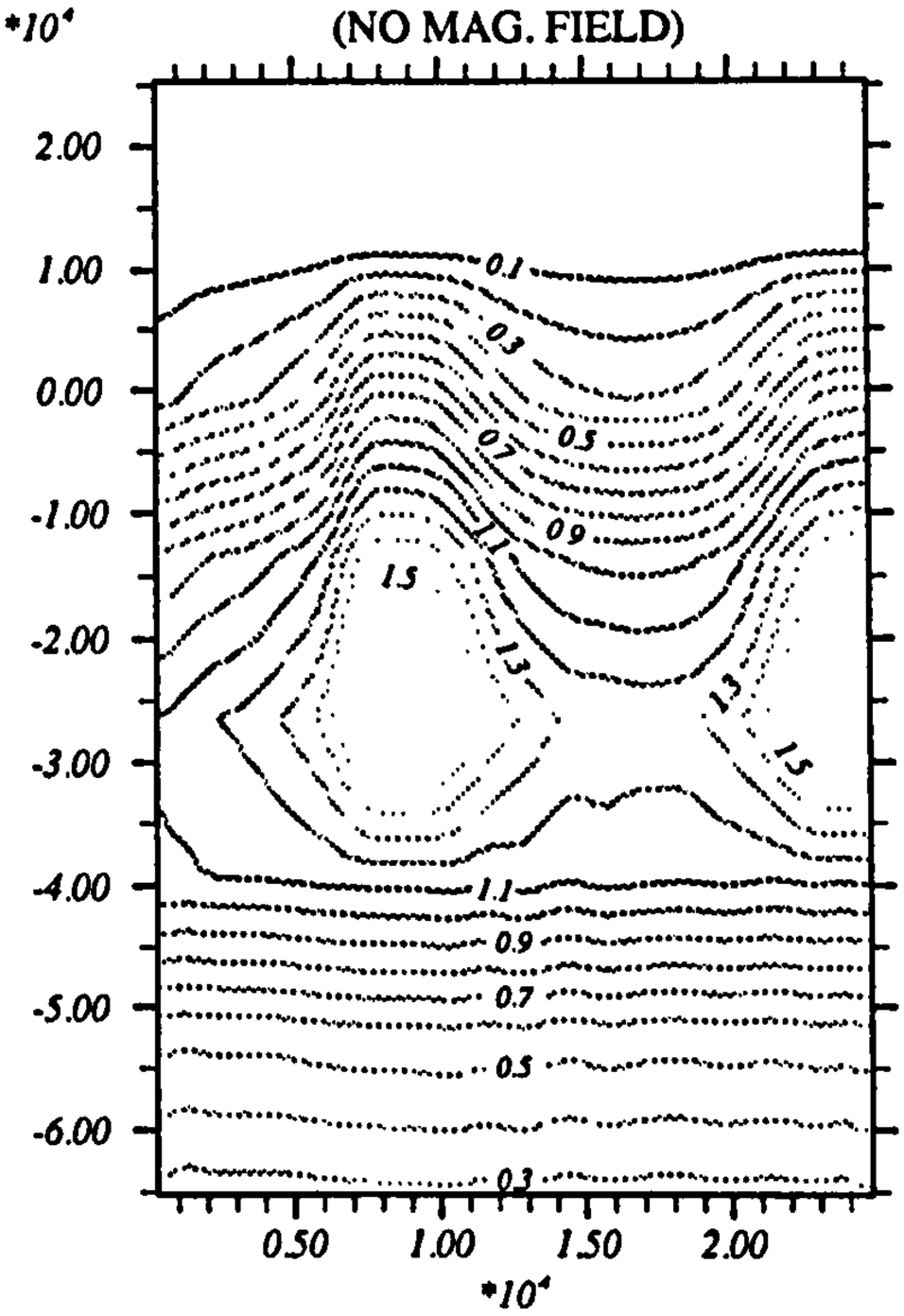

DENSITY MAP AT 550PS
(MAG. FIELD ON)

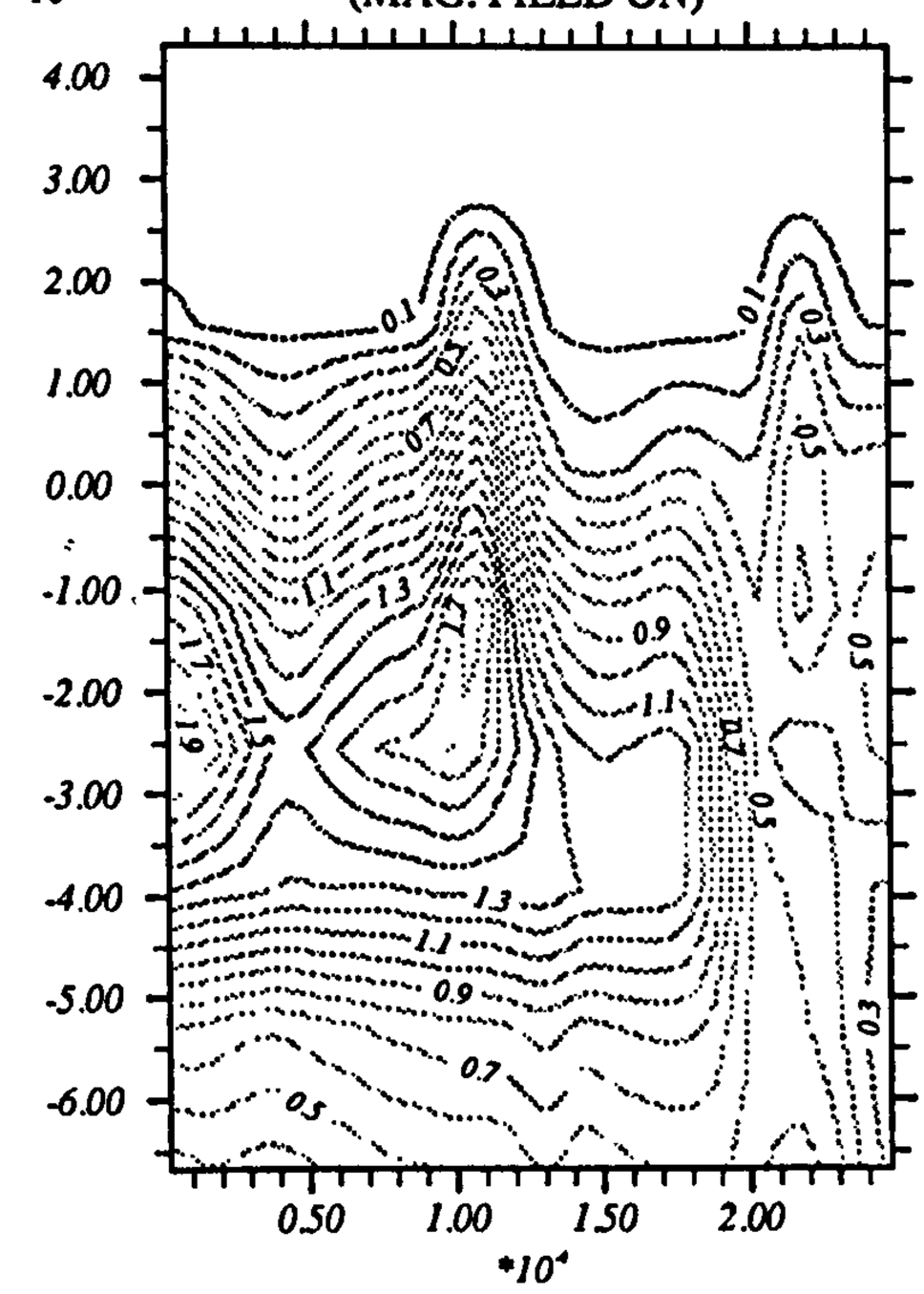

DENSITY MAP AT 600PS
(NO MAG. FIELD)

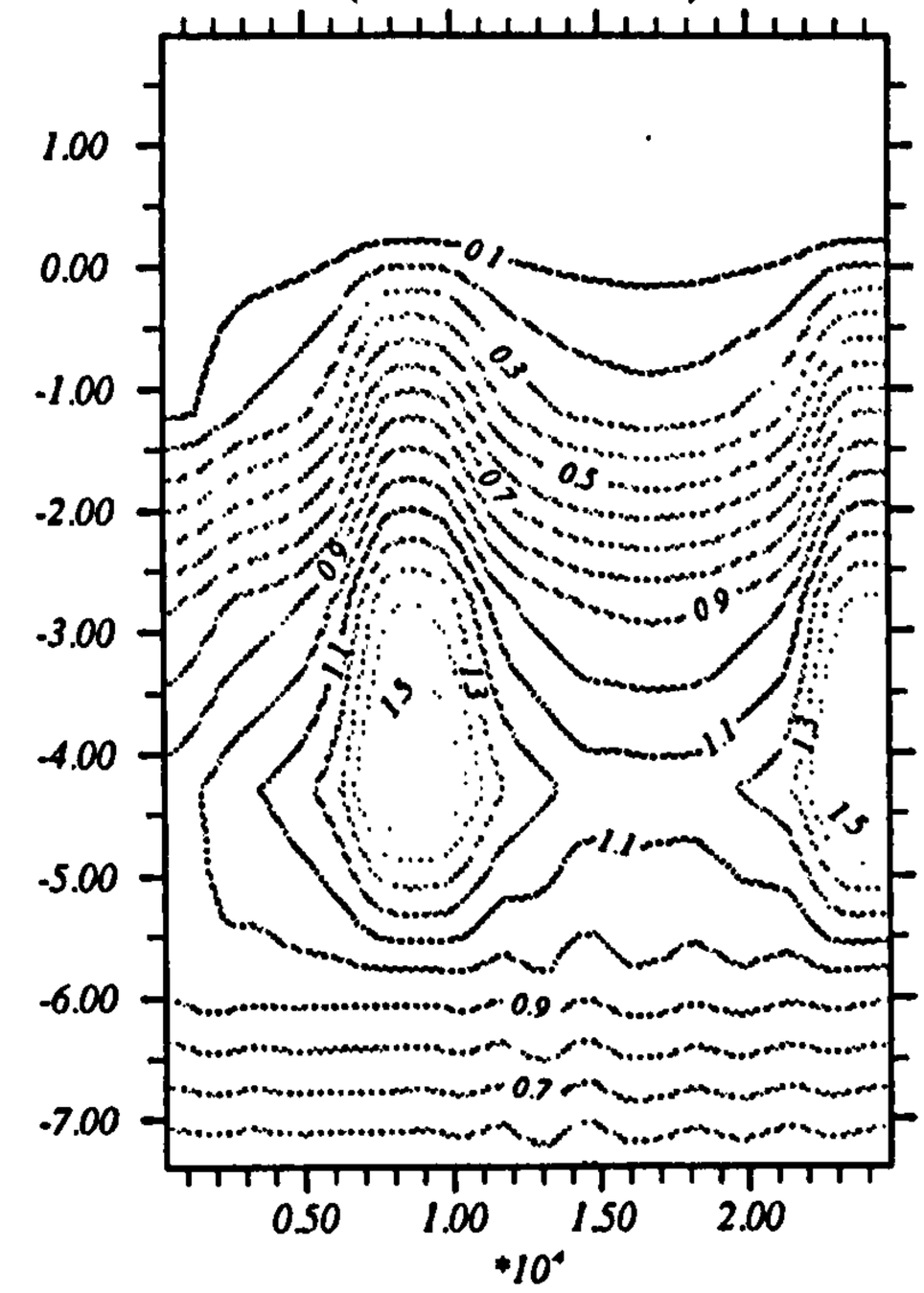

DENSITY MAP AT 600PS
(MAG. FIELD ON)

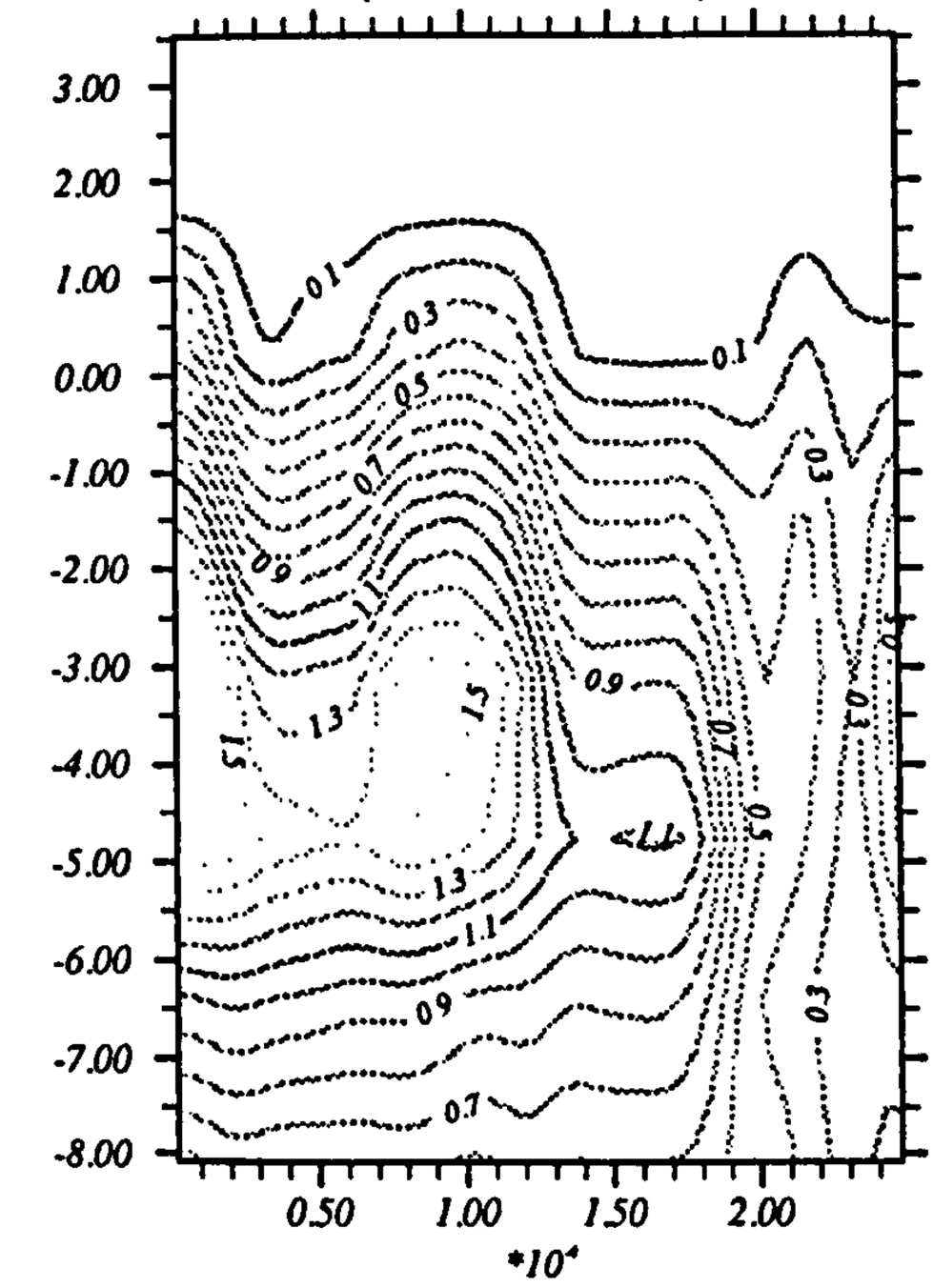

DENSITY MAP AT 650PS
(NO MAG. FIELD)

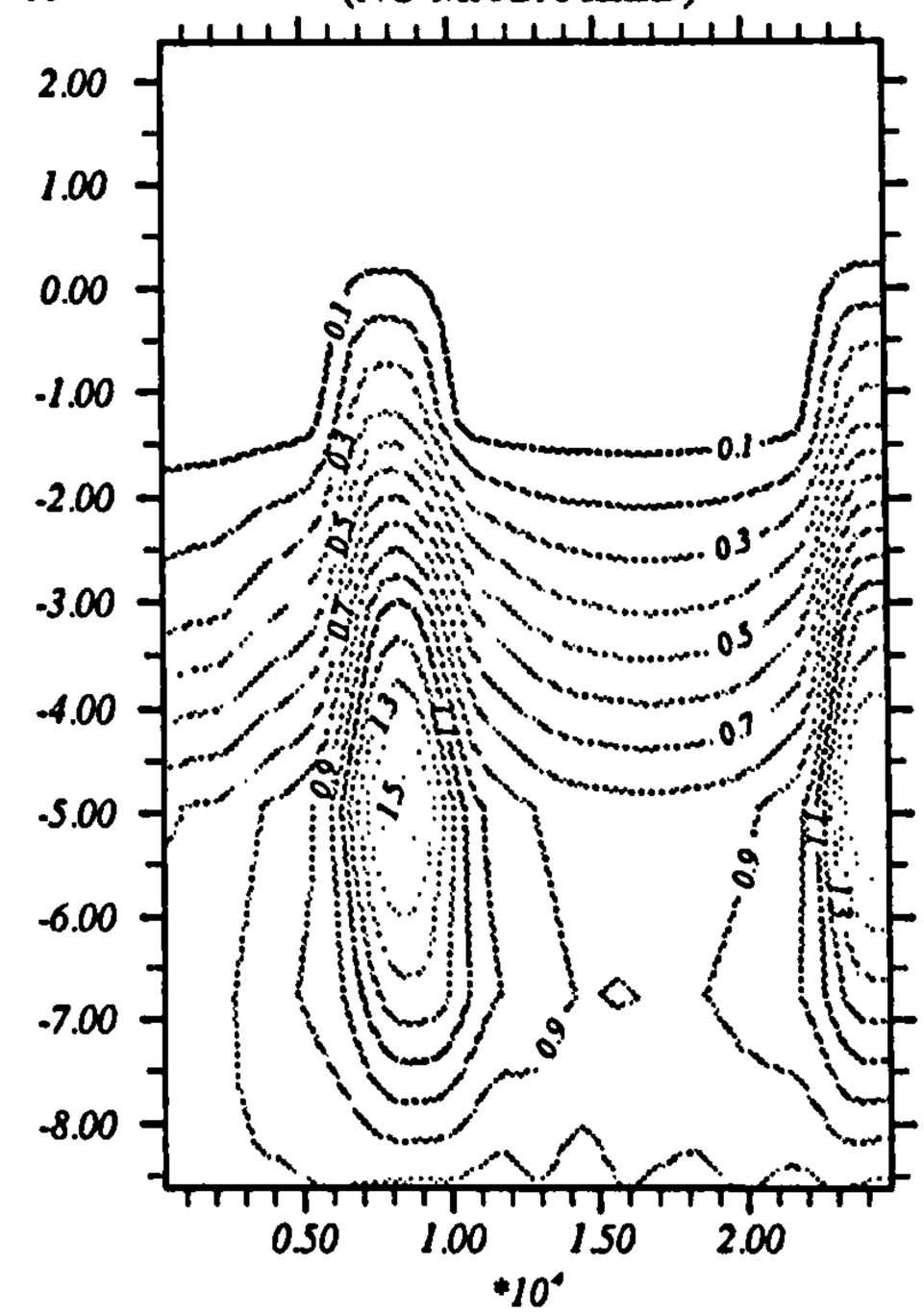

DENSITY MAP AT 650PS
(MAG. FIELD ON)

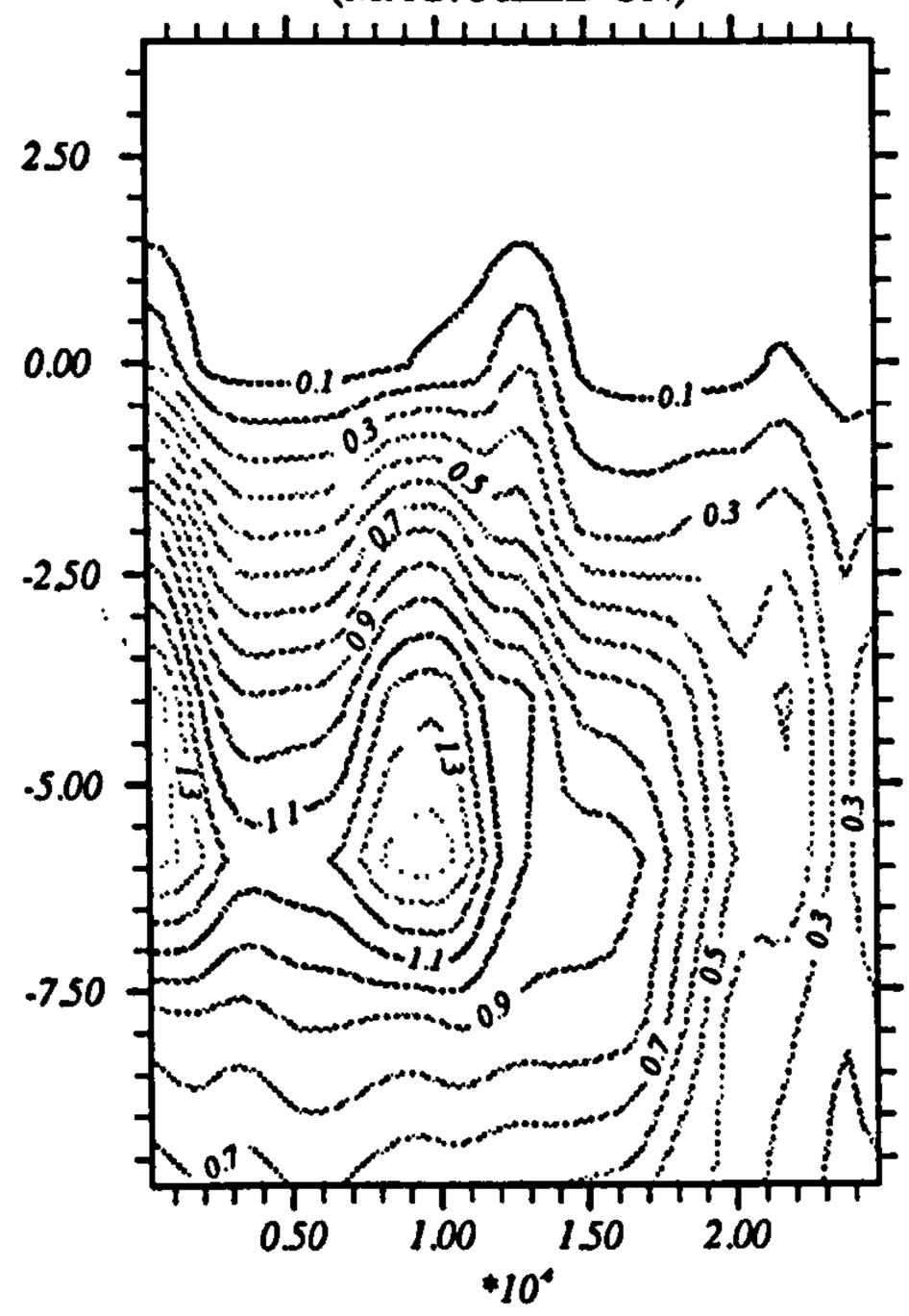

DENSITY MAP AT 700PS
(NO MAG. FIELD)

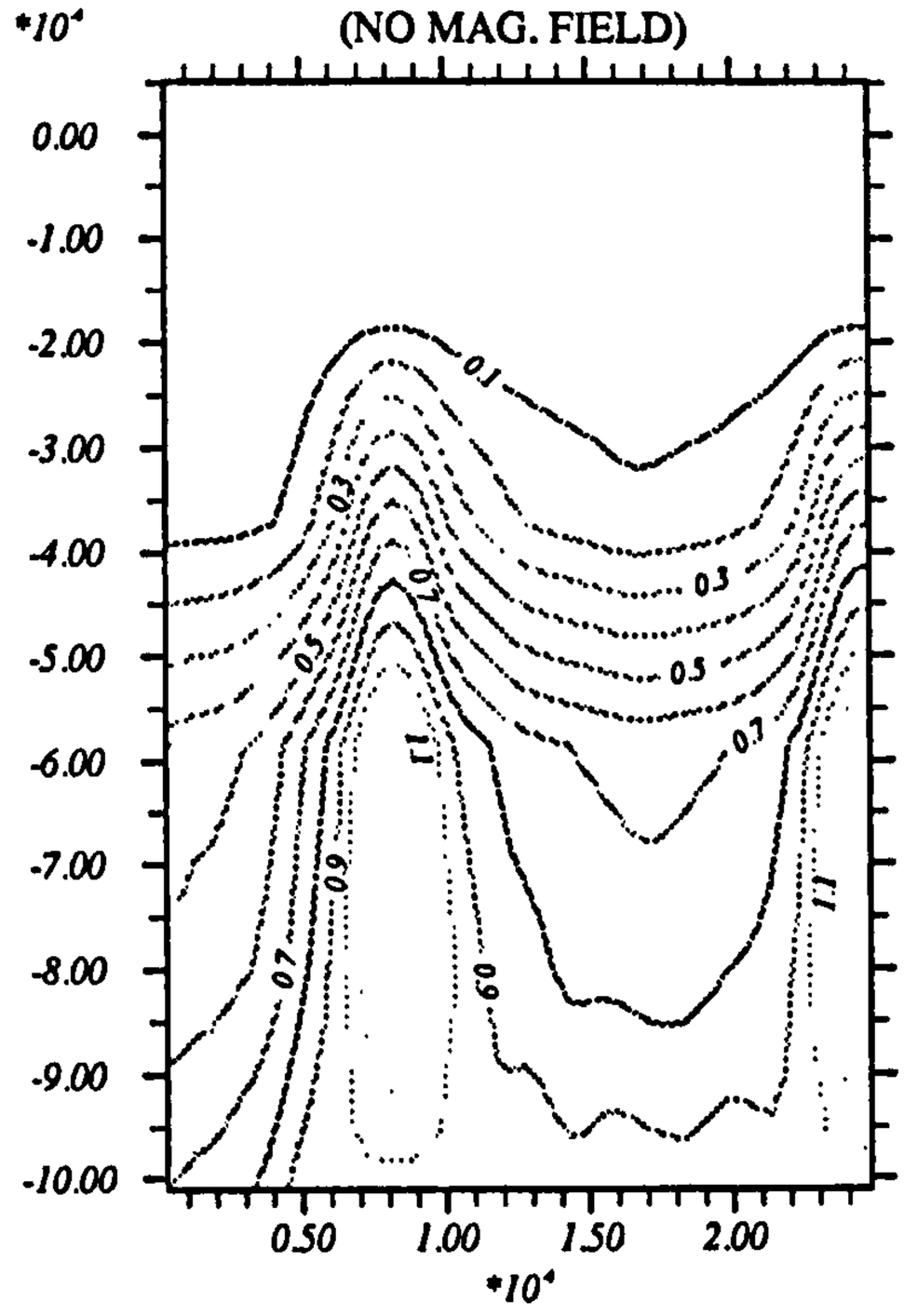

DENSITY MAP AT 700PS
(MAG. FIELD ON)

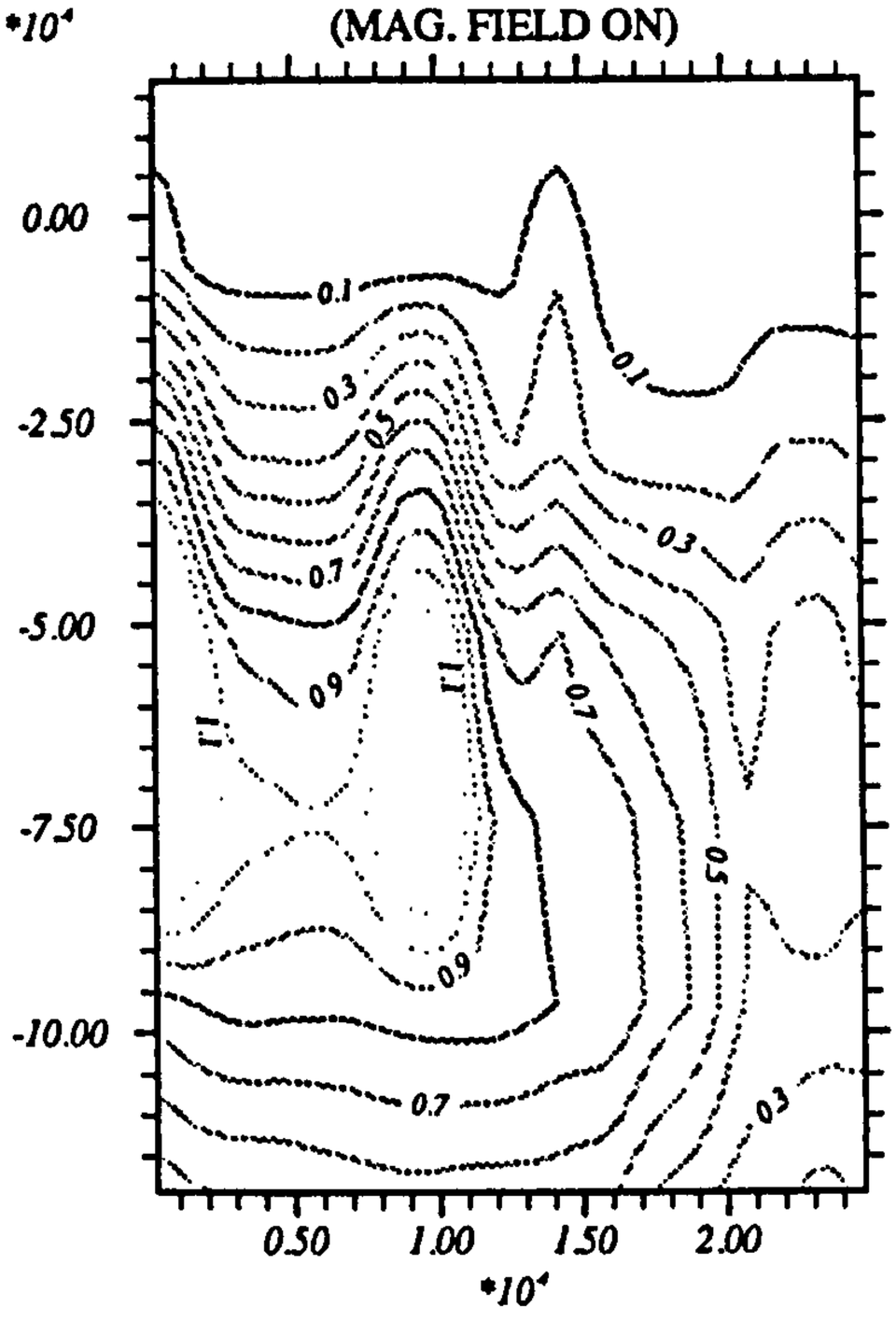

DENSITY MAP AT 750PS
(NO MAG. FIELD)

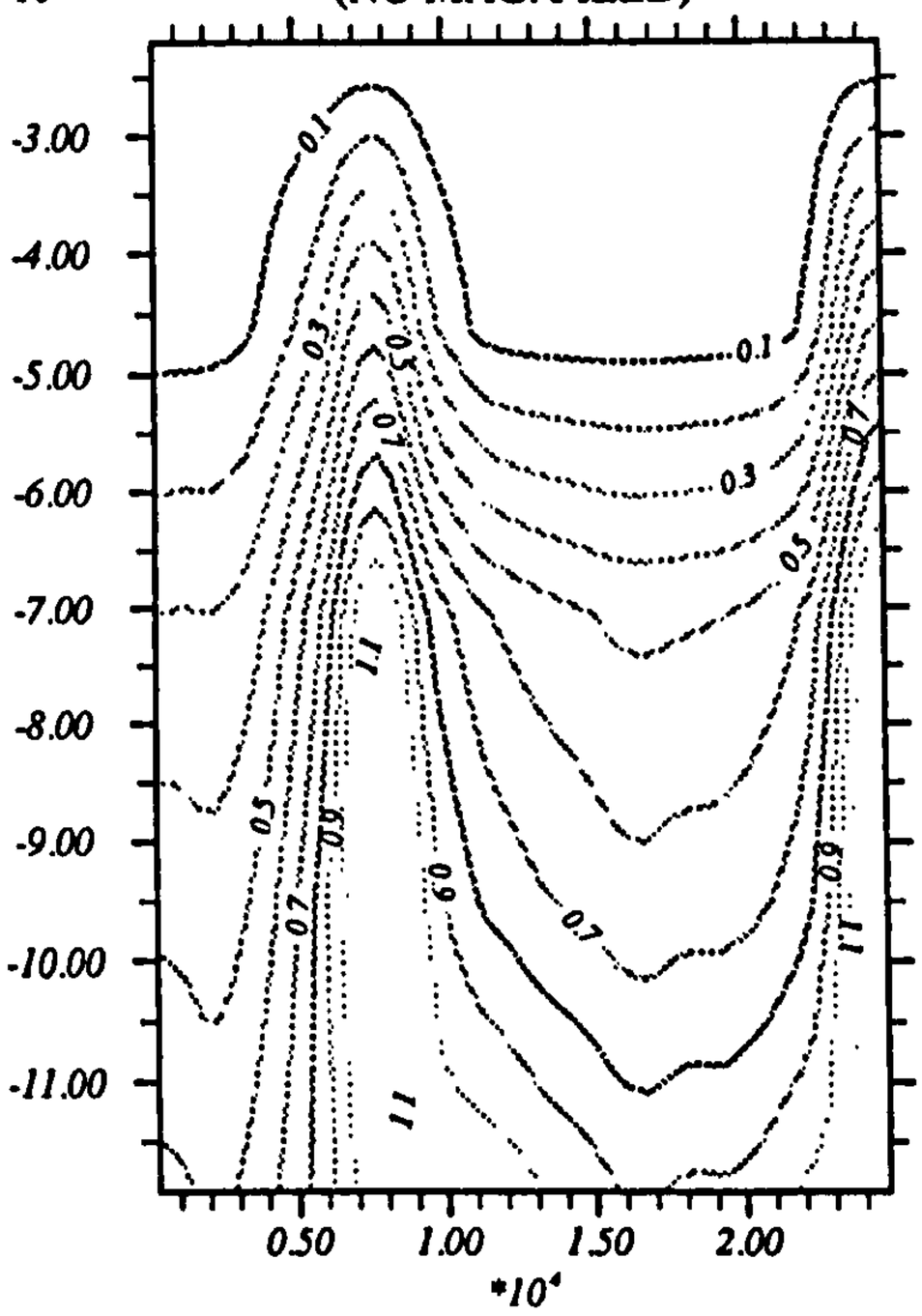

DENSITY MAP AT 750PS
(MAG. FIELD ON)

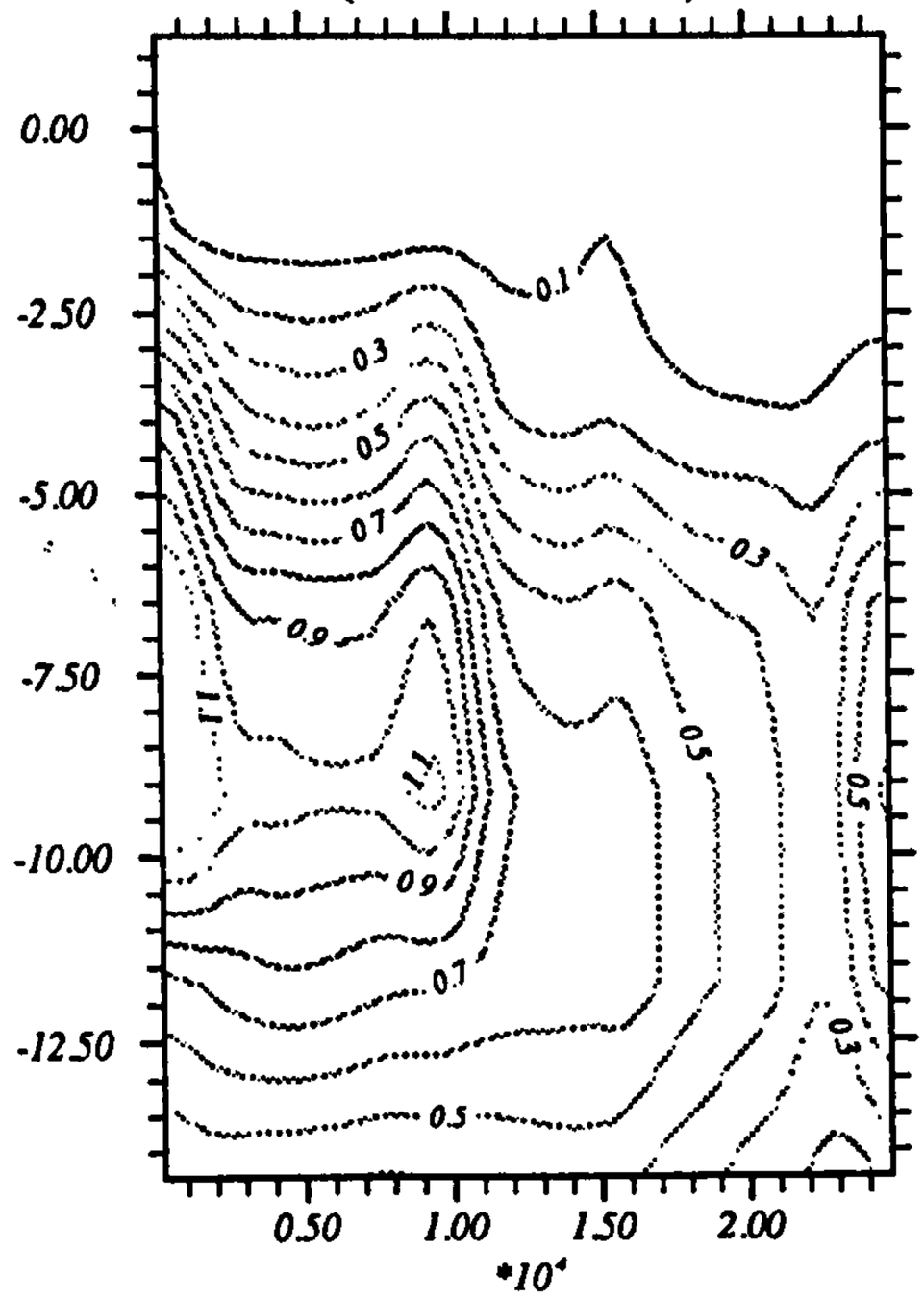

DENSITY MAP AT 800PS
(NO MAG. FIELD)

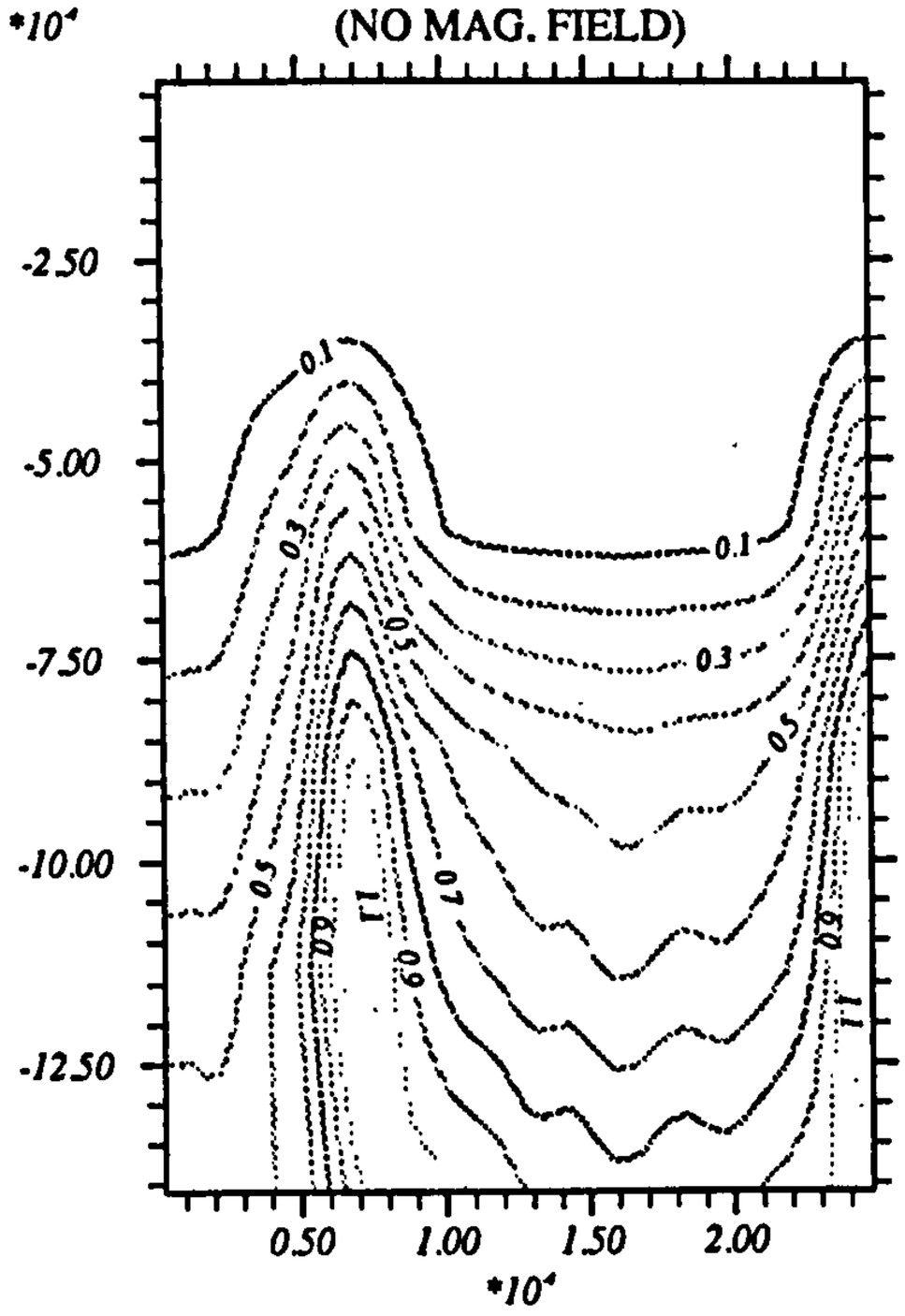

DENSITY MAP AT 800PS
(MAG. FIELD ON)

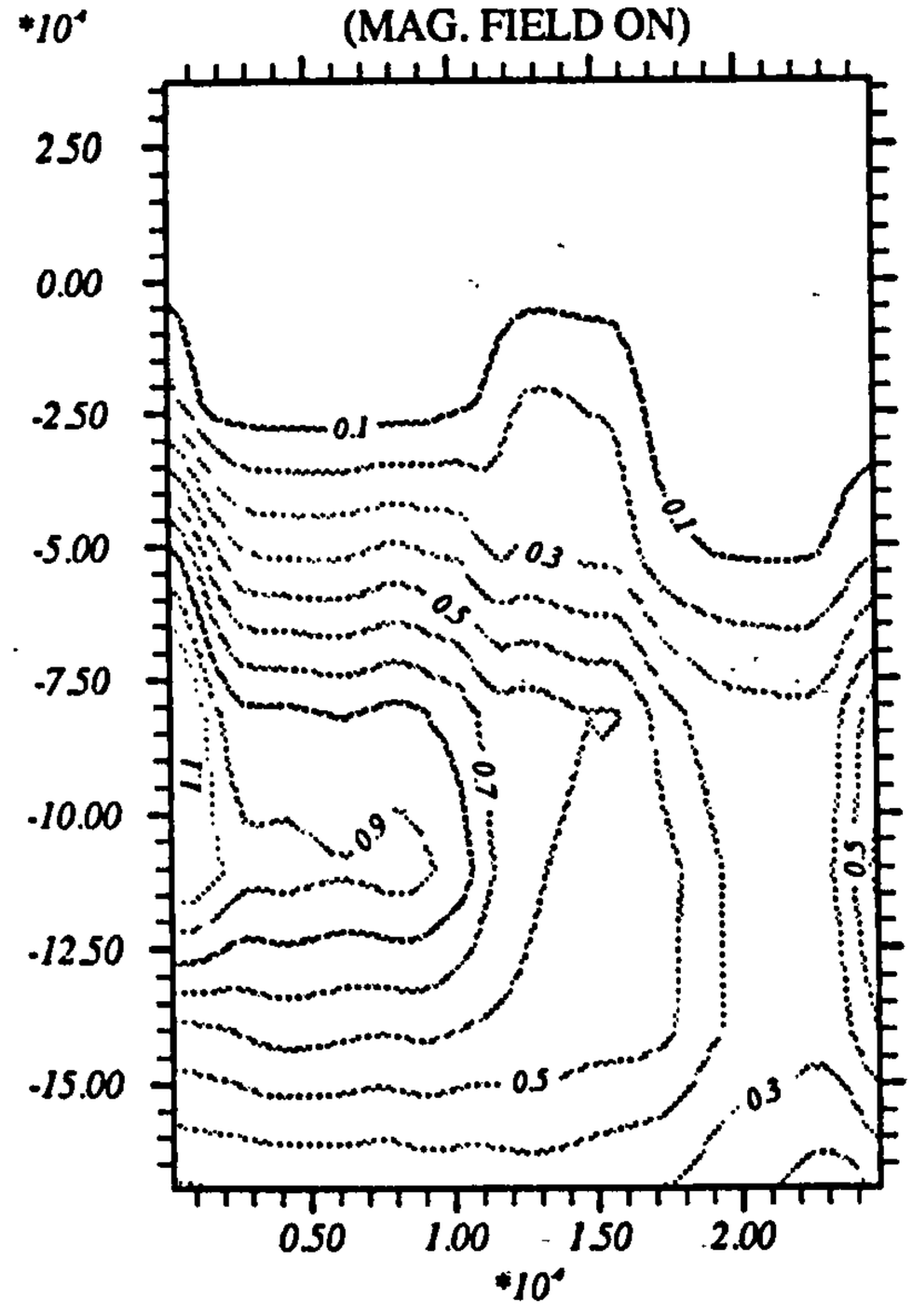

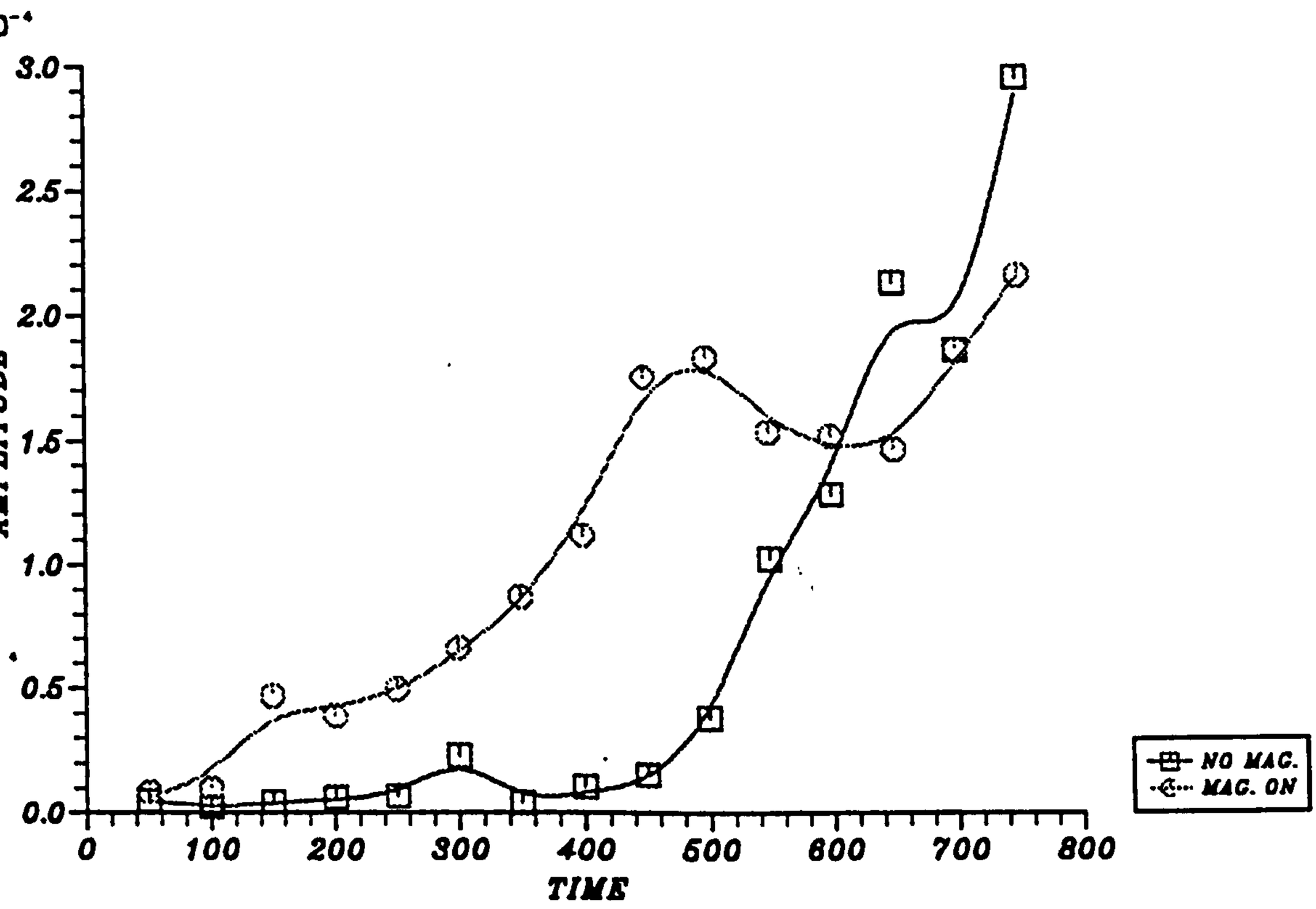

Figure 6.8: Amplitude-time graph for target $(5 \cdot 0\mu m \times 2 \cdot 5\mu m)$.

6.5 SUMMARY

The maximum field (+ve) as a function of time is plotted in figure $6 \cdot 10$. For the target of size $(5 \cdot 0 \times 5 \cdot 0)$ the field reaches to a peak value of $1 \cdot 85$ MG at 300ps and then slowly falls and for the other two targets it does not attain the same maximum value but reaches a value less that $1 \cdot 3$ MG. The maximum field (-ve) - time graph is also plotted in figure $6 \cdot 11$ for all the cases considered and attains a maximum value of about $1 \cdot 8$ MG in each case. The maximum plasma beta vs time graph is shown in figure $6 \cdot 12$ for all the simulations carried out with intensity perturbations. This attains a maximum of $7 \cdot 5\%$ for the target of size $(2 \cdot 5 \times 2 \cdot 5)$ and for the other two cases it approaches a value slightly higher than 5%. This shows that there is sufficient pressure to affect the growth of Rayleigh-Taylor instability through the magnetic pressure.

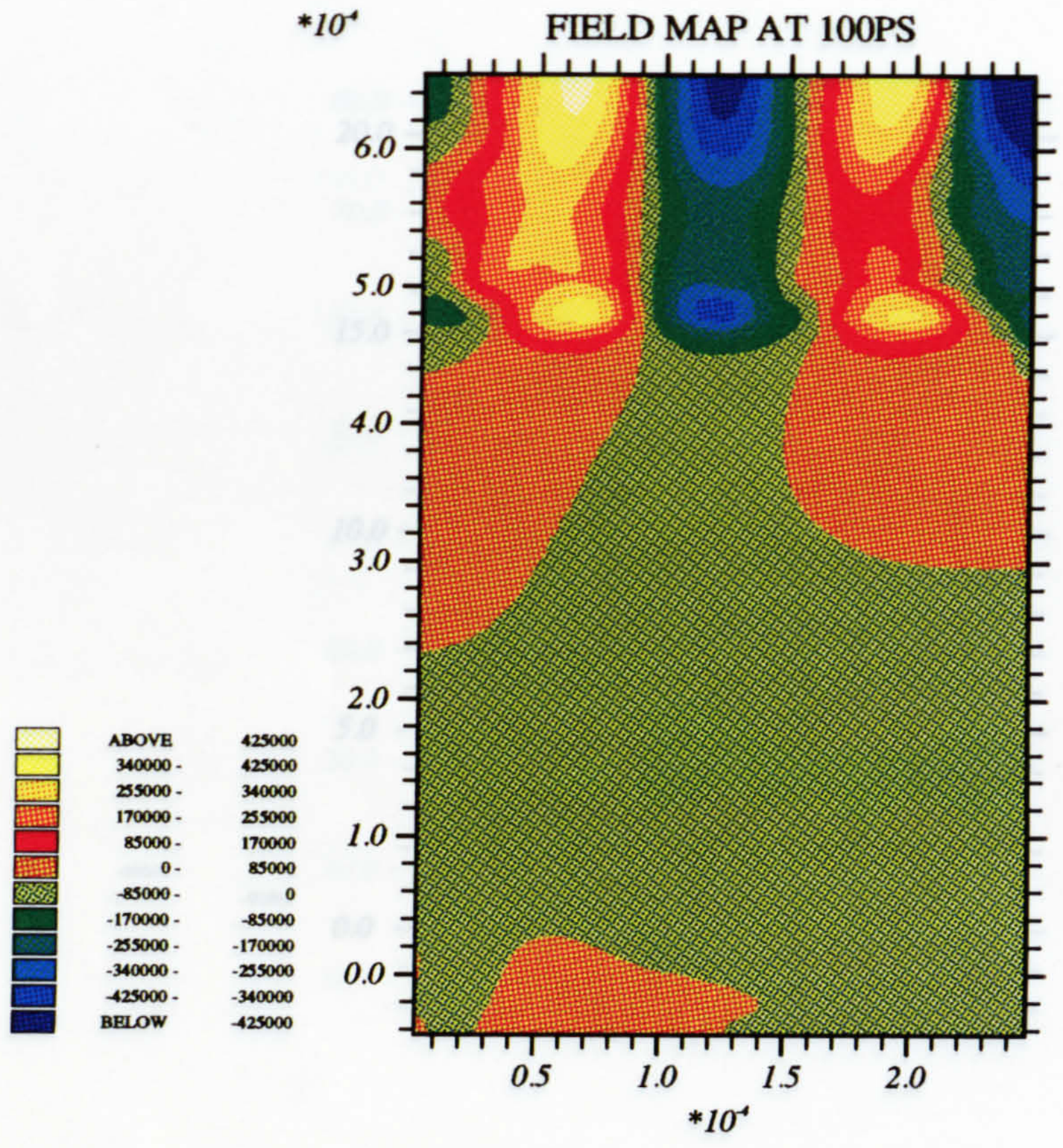

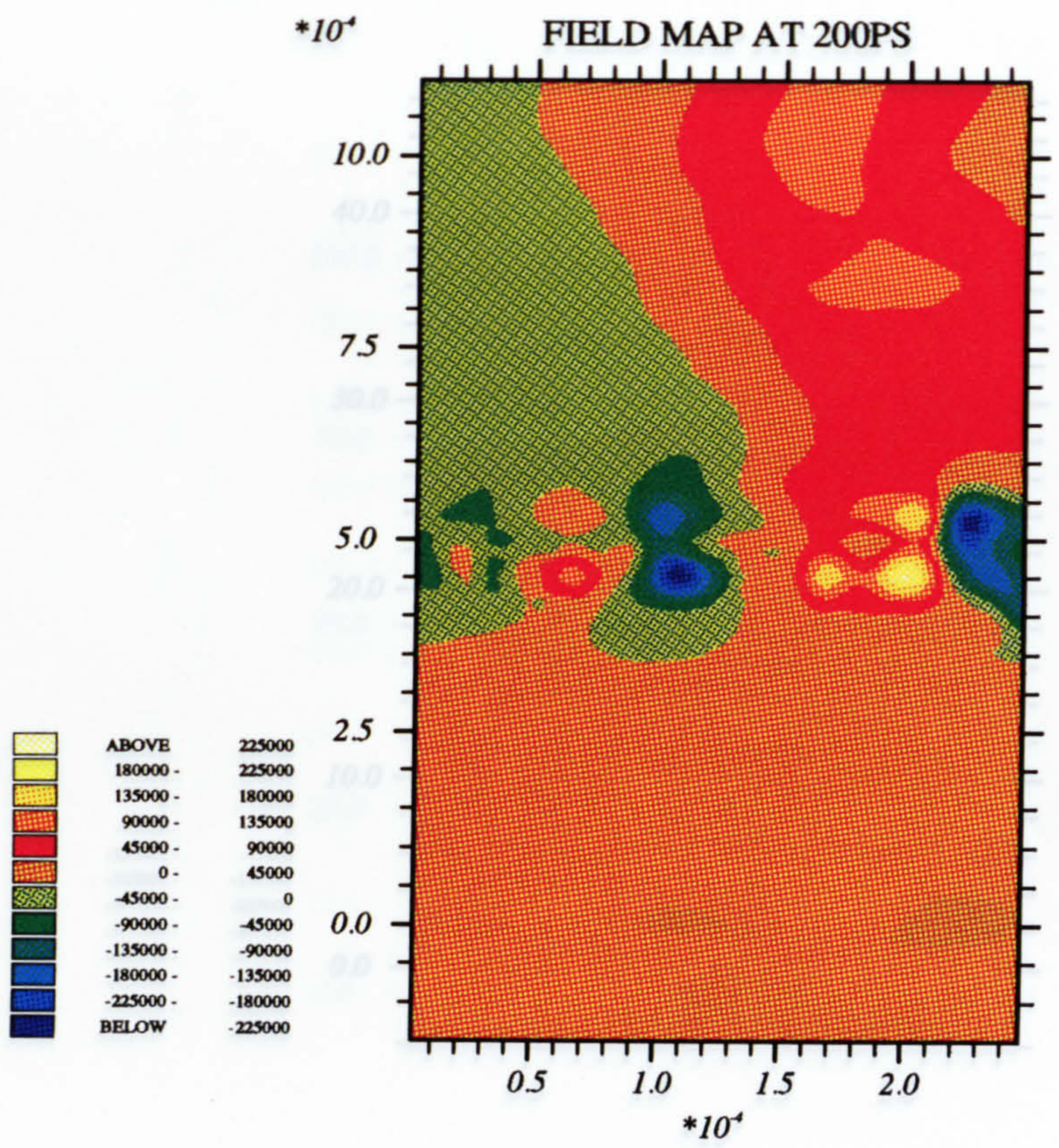

Figure 6.9: Magnetic field contour map for the target (5.0 μ m x 2.5 μ m) with perturbation applied through laser intensity.

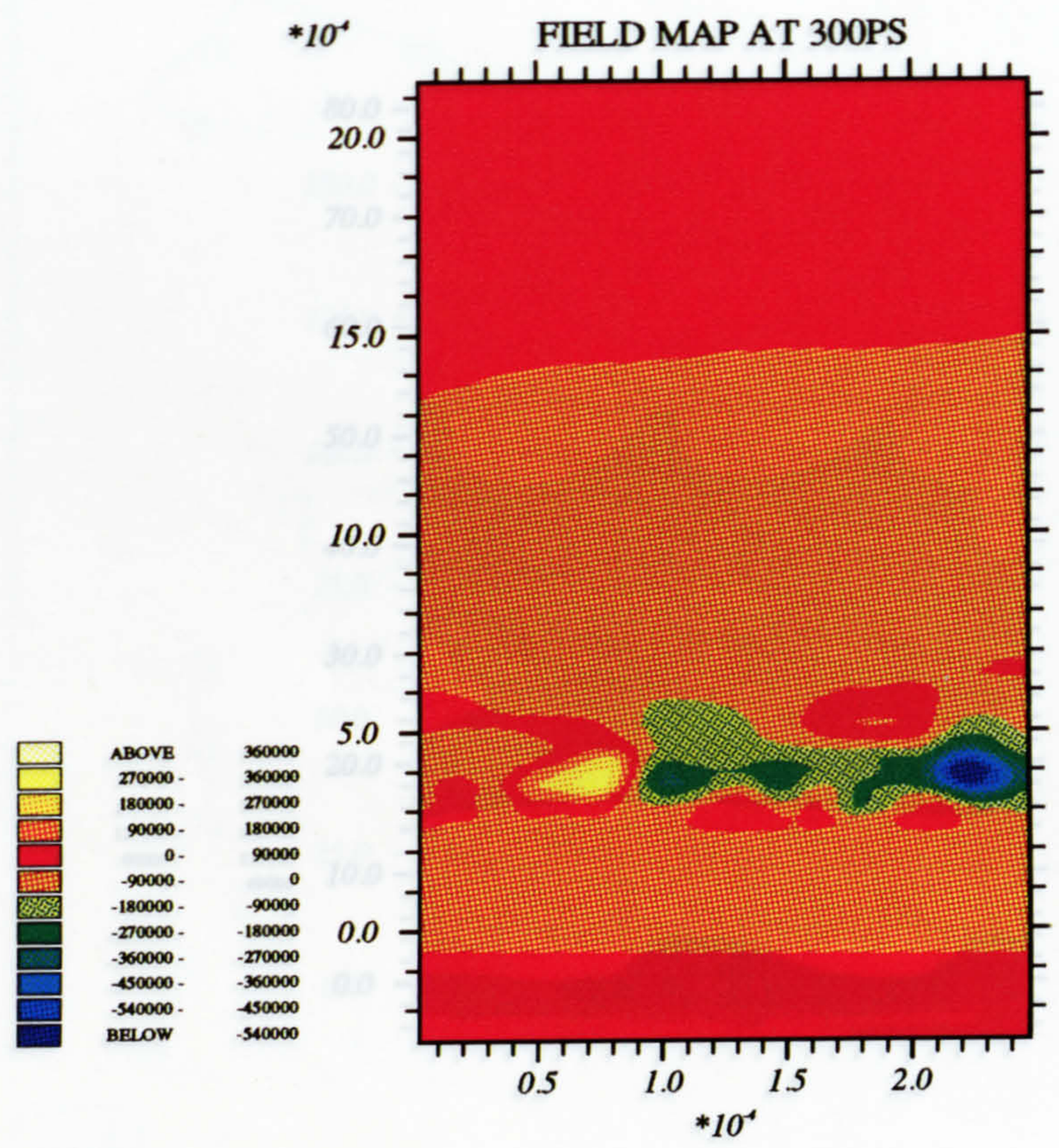
*10⁻⁴
FIELD MAP AT 300PS
20.0
15.0
10.0
5.0
0.0
0.5
1.0
1.5
2.0
*10⁻⁴
ABOVE 360000
270000 - 360000
180000 - 270000
90000 - 180000
0 - 90000
-90000 - 0
-180000 - -90000
-270000 - -180000
-360000 - -270000
-450000 - -360000
-540000 - -450000
BELOW -540000

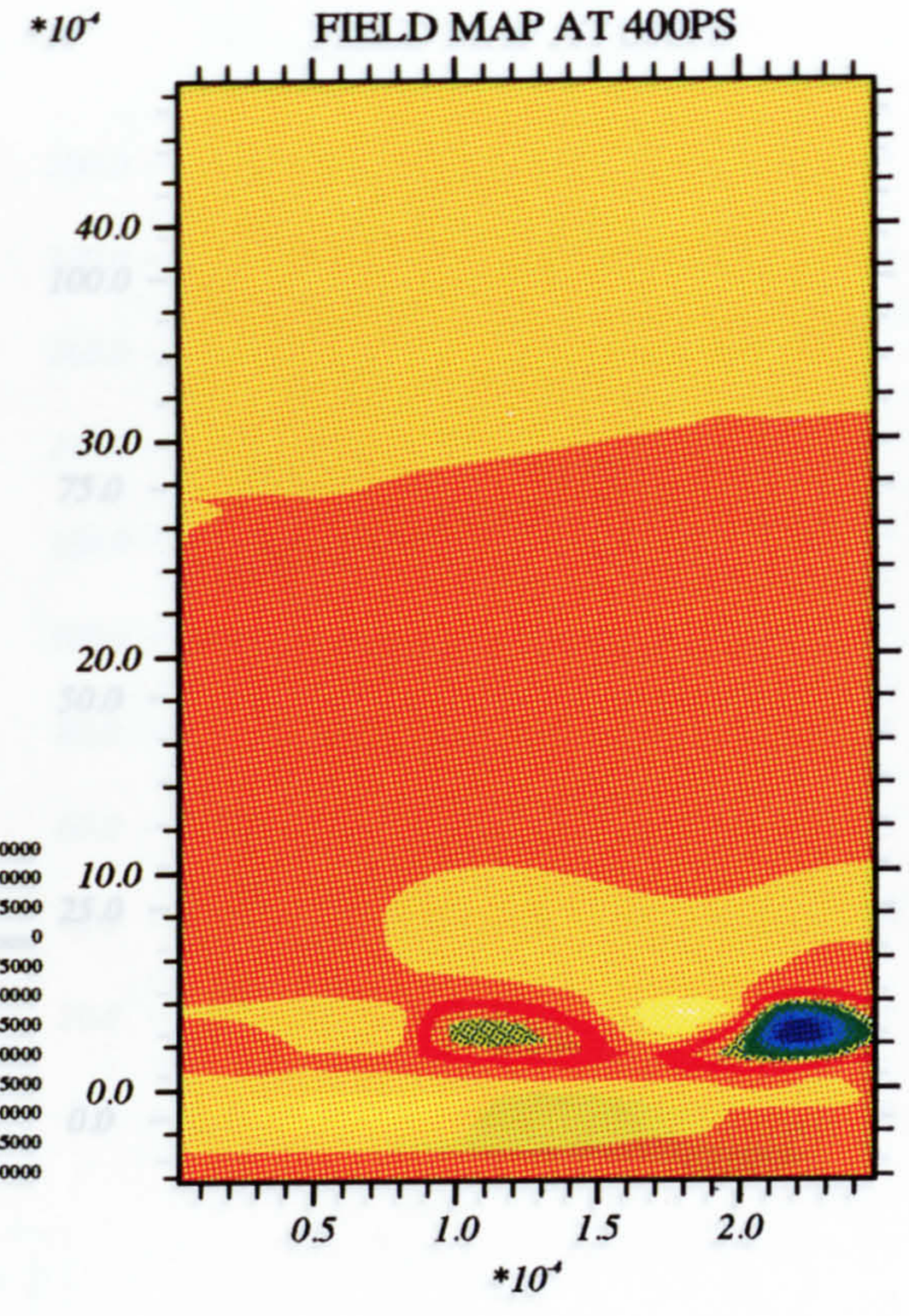
*10⁻⁴
FIELD MAP AT 400PS
40.0
30.0
20.0
10.0
0.0
0.5
1.0
1.5
2.0
*10⁻⁴
ABOVE 150000
75000 - 150000
0 - 75000
-75000 - 0
-150000 - -75000
-225000 - -150000
-300000 - -225000
-375000 - -300000
-450000 - -375000
-525000 - -450000
-600000 - -525000
BELOW -600000

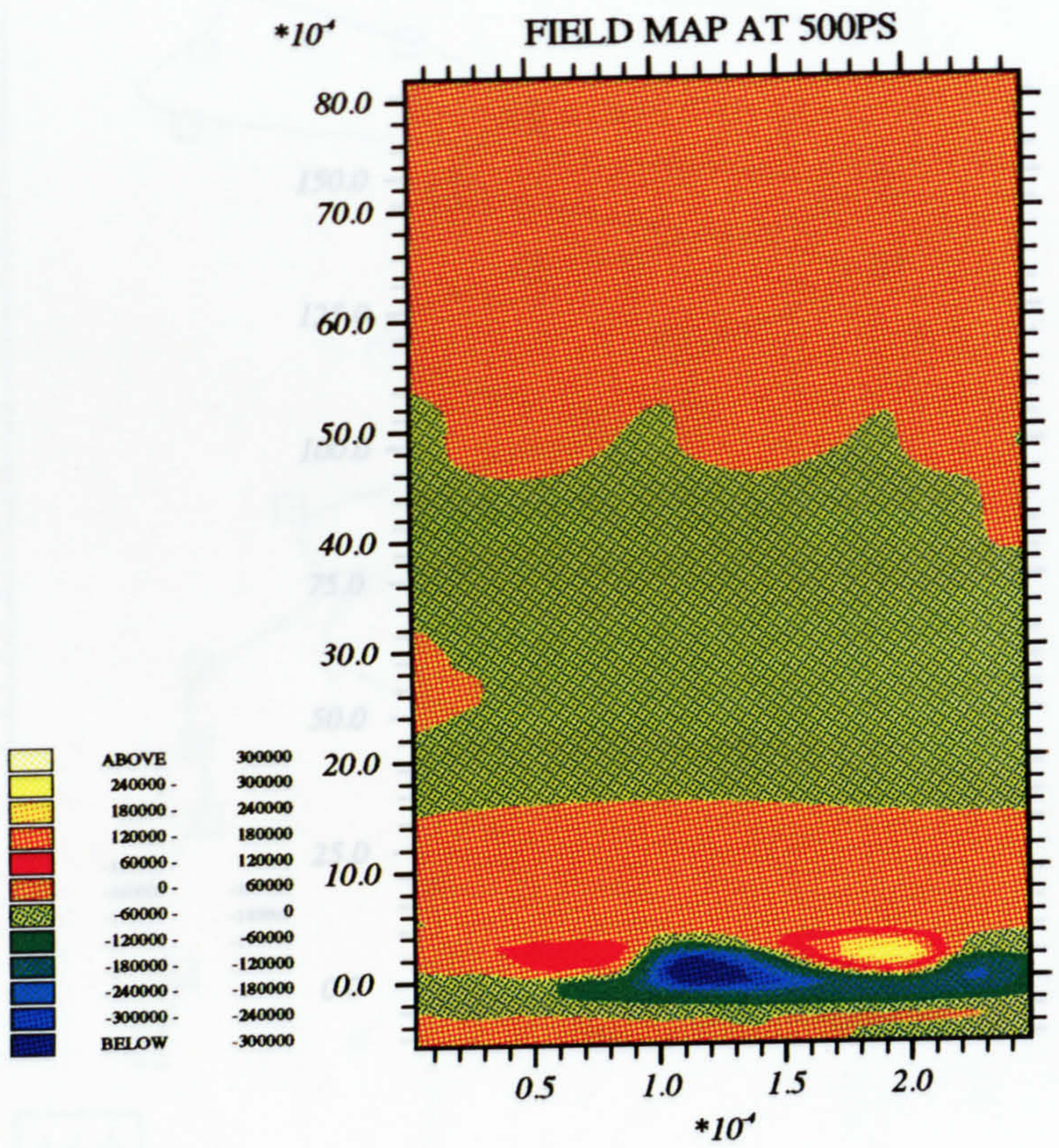
FIELD MAP AT 500PS
*10⁴
80.0
70.0
60.0
50.0
40.0
30.0
20.0
10.0
0.0
0.5
1.0
1.5
2.0
*10⁴
ABOVE 300000
240000 - 300000
180000 - 240000
120000 - 180000
60000 - 120000
0 - 60000
-60000 - 0
-120000 - -60000
-180000 - -120000
-240000 - -180000
-300000 - -240000
BELOW -300000

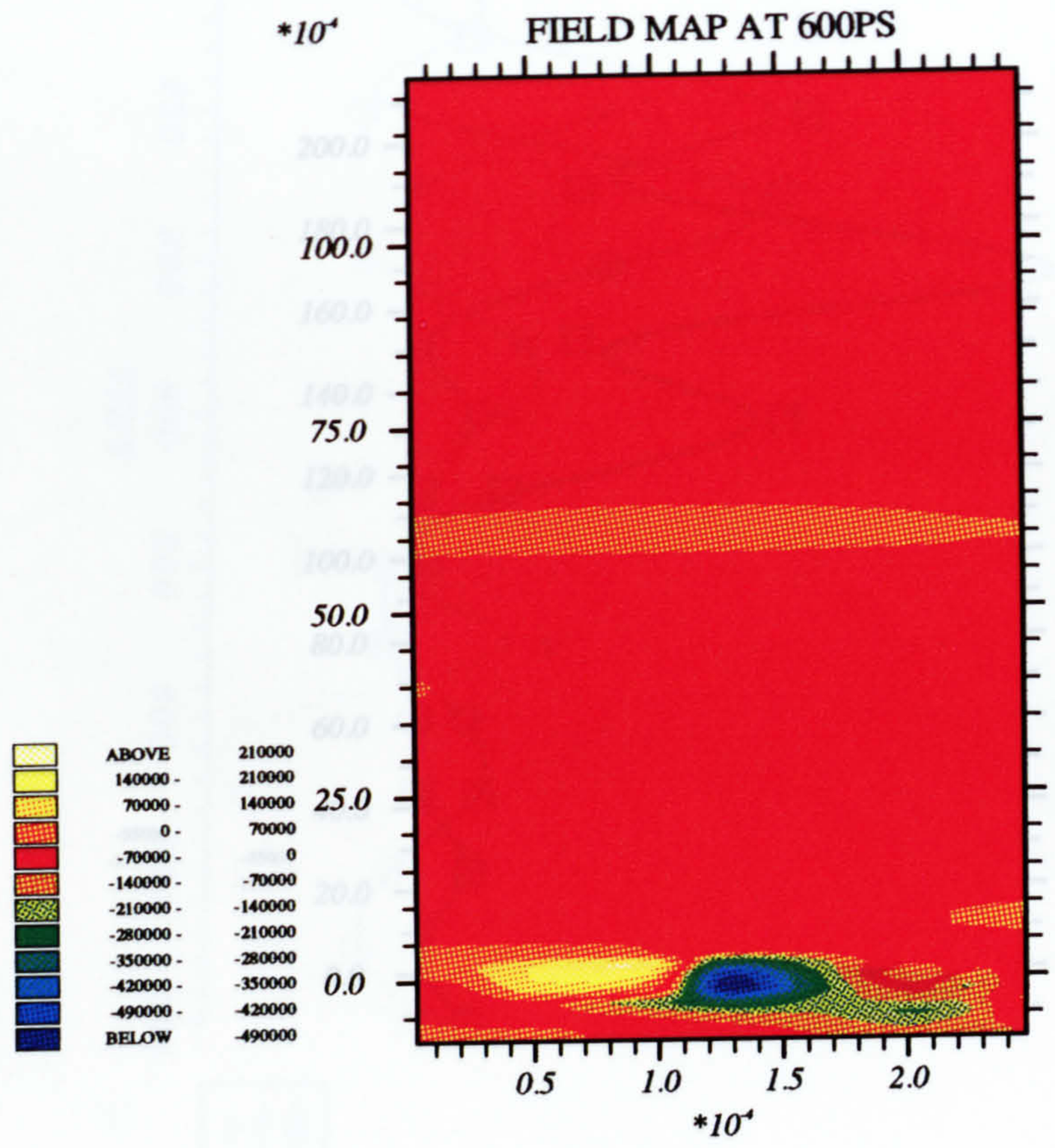
FIELD MAP AT 600PS
*10⁴
100.0
75.0
50.0
25.0
0.0
0.5
1.0
1.5
2.0
*10⁴
ABOVE 210000
140000 - 210000
70000 - 140000
0 - 70000
-70000 - 0
-140000 - -70000
-210000 - -140000
-280000 - -210000
-350000 - -280000
-420000 - -350000
-490000 - -420000
BELOW -490000

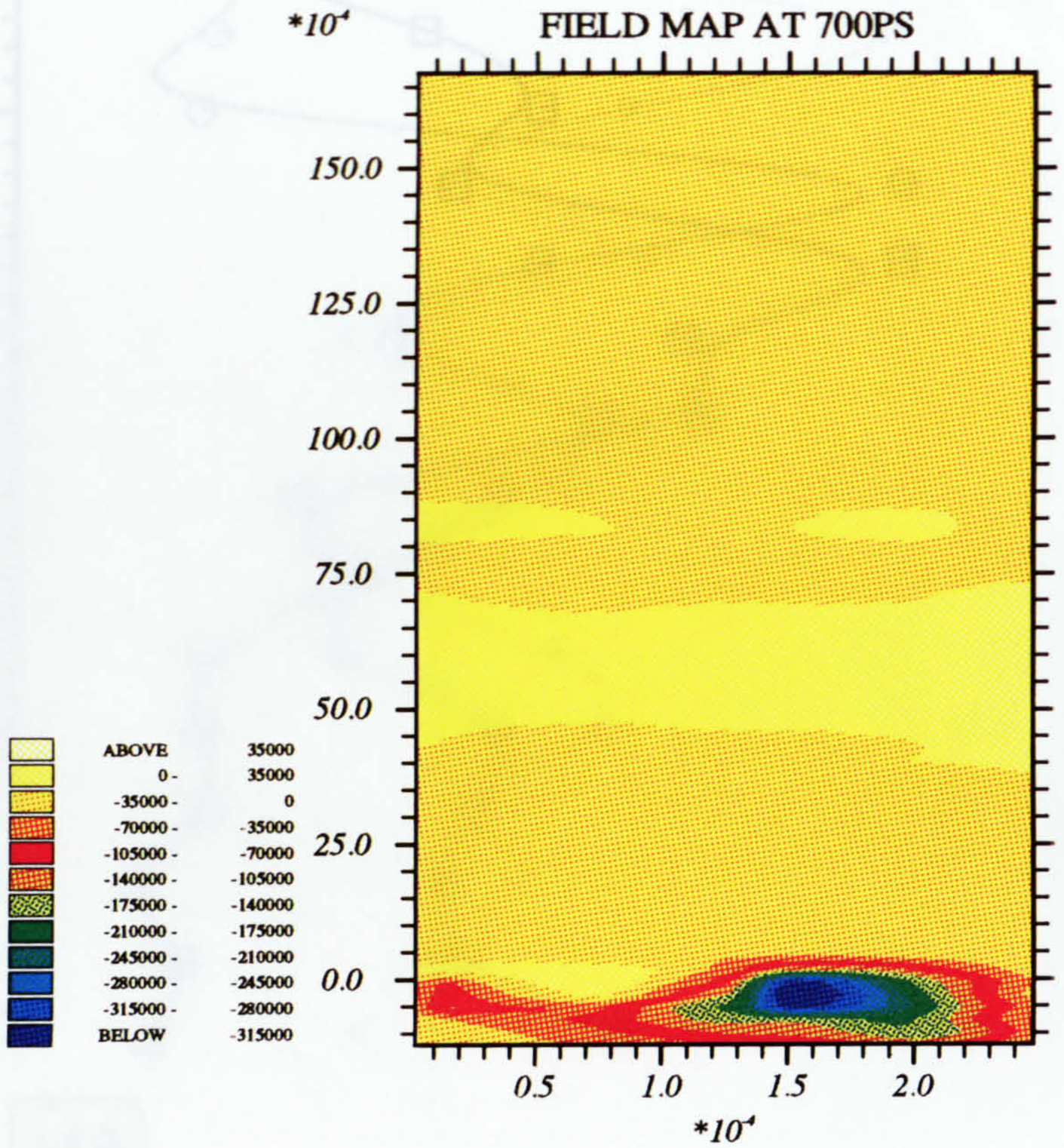
FIELD MAP AT 700PS
*10⁻⁴
150.0
125.0
100.0
75.0
50.0
25.0
0.0
0.5
1.0
1.5
2.0
*10⁻⁴
ABOVE 35000
0 - 35000
-35000 - 0
-70000 - -35000
-105000 - -70000
-140000 - -105000
-175000 - -140000
-210000 - -175000
-245000 - -210000
-280000 - -245000
-315000 - -280000
BELOW -315000

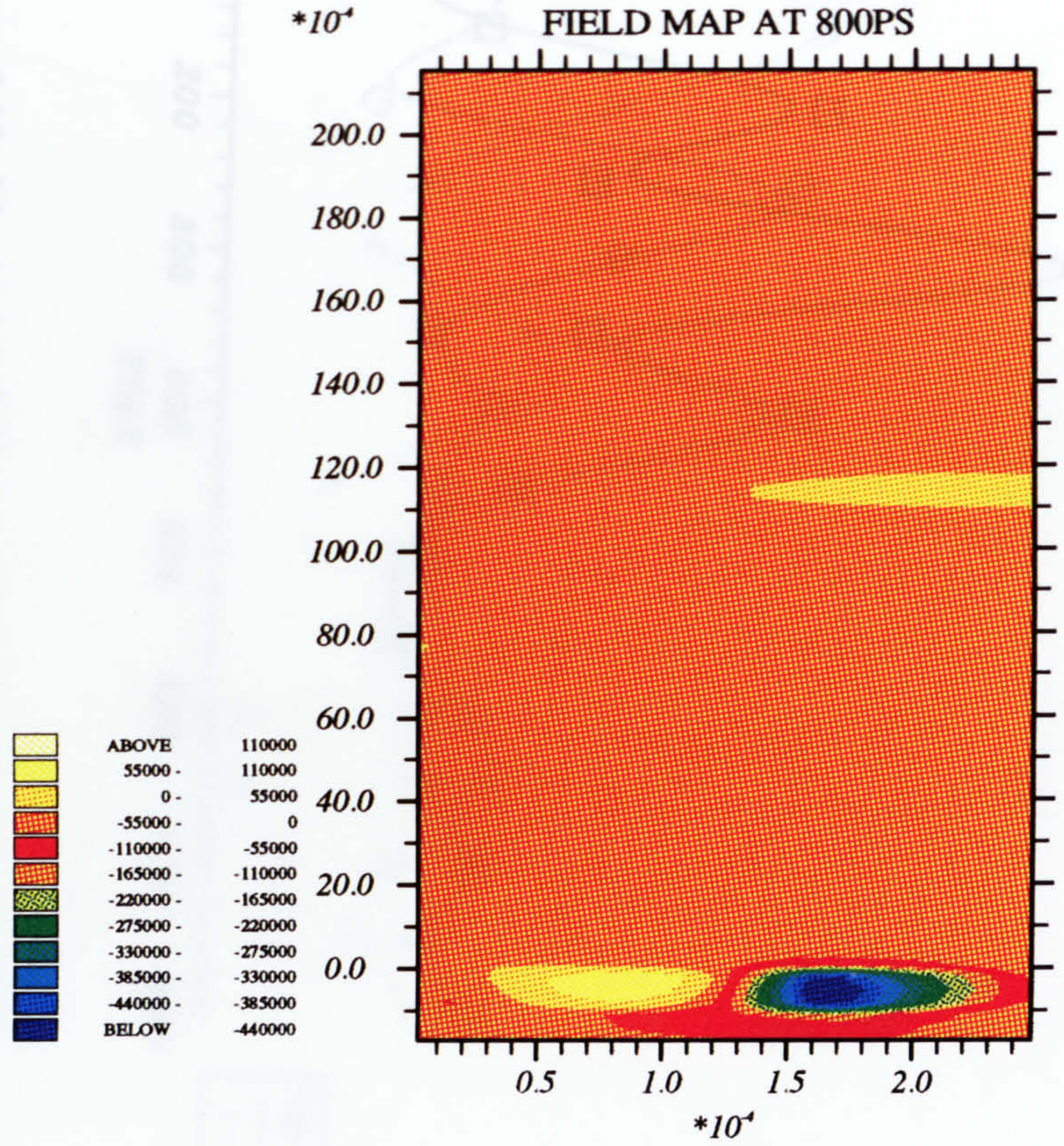
FIELD MAP AT 800PS
*10⁻⁴
200.0
180.0
160.0
140.0
120.0
100.0
80.0
60.0
40.0
20.0
0.0
0.5
1.0
1.5
2.0
*10⁻⁴
ABOVE 110000
55000 - 110000
0 - 55000
-55000 - 0
-110000 - -55000
-165000 - -110000
-220000 - -165000
-275000 - -220000
-330000 - -275000
-385000 - -330000
-440000 - -385000
BELOW -440000

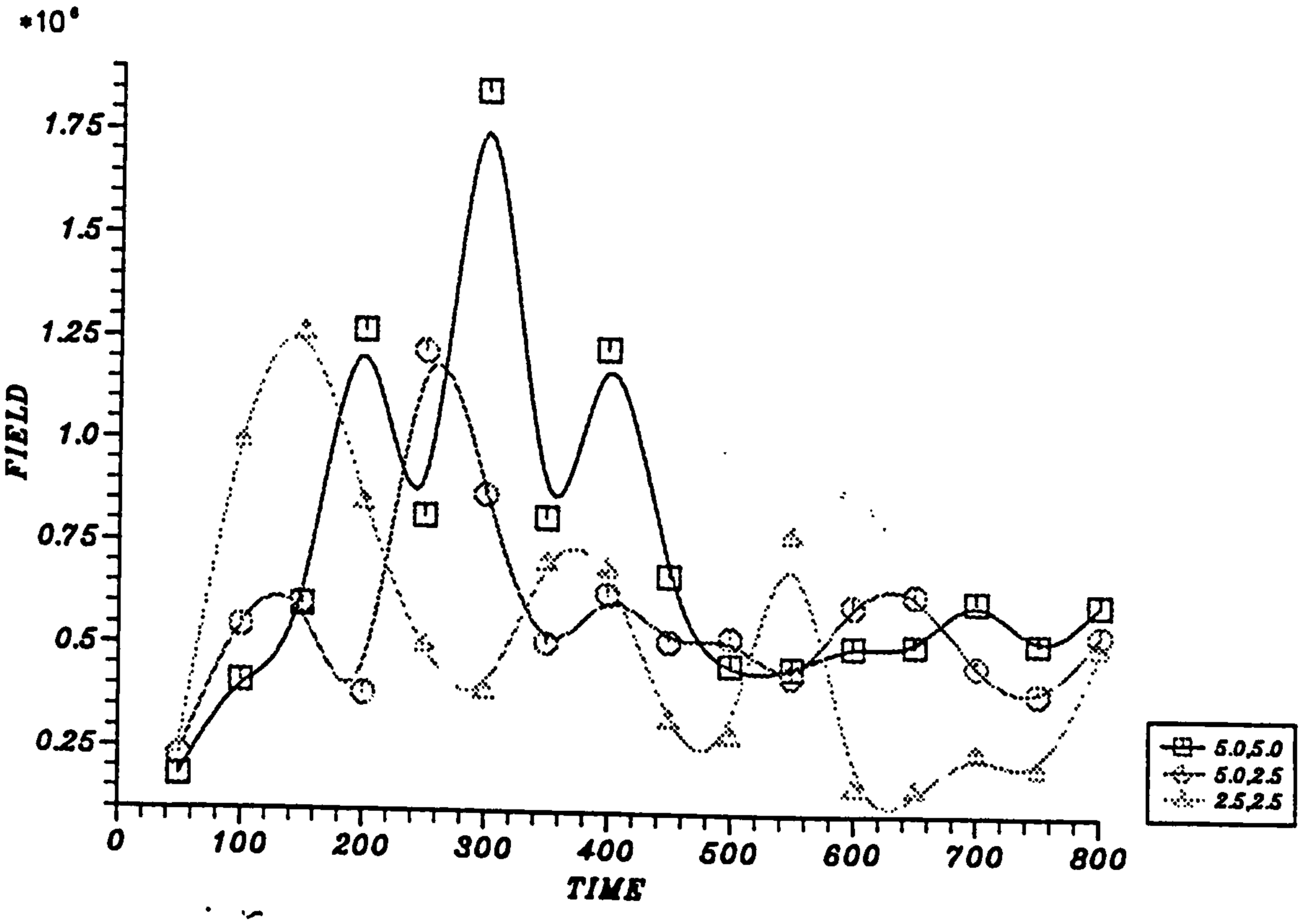

Figure 6.10: Maximum field (+ve) vs time graph for different simulations

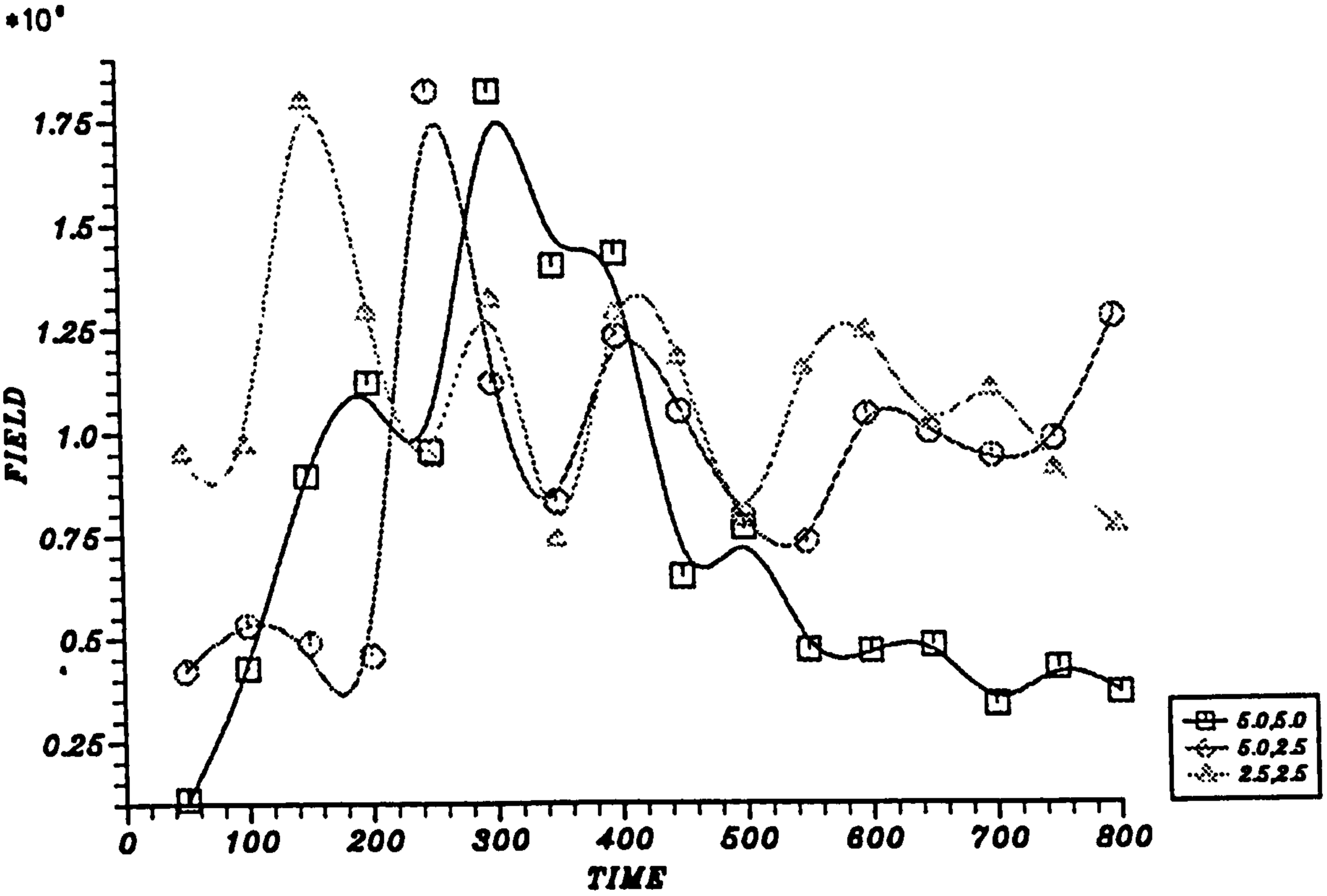

Figure 6.11: Maximum field (-ve) vs time graph for different simulations

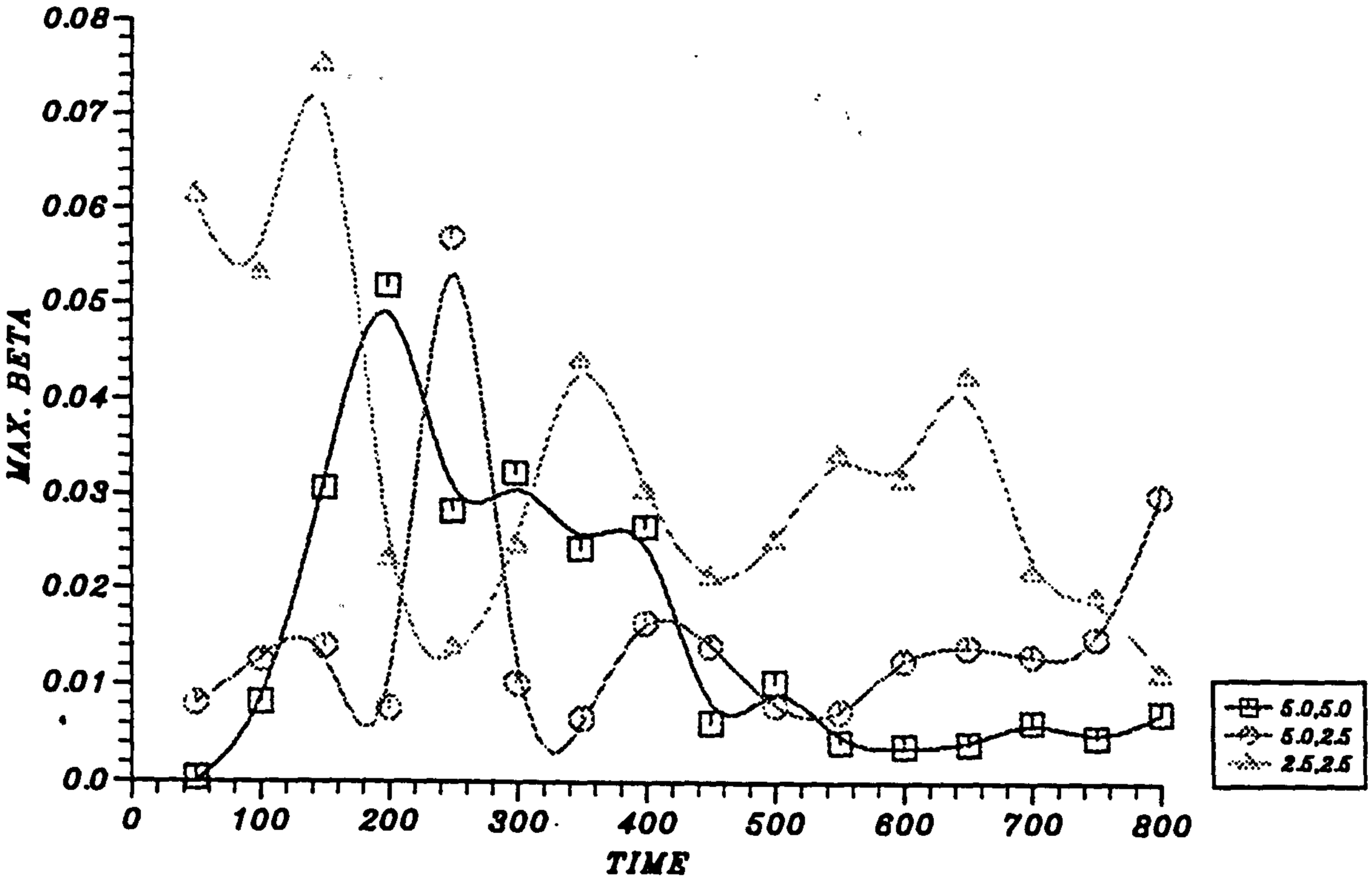

Figure 6.12: Plasma beta-time graph for different simulations

TARGET PARAMETERS	
Target thickness	$5 \cdot 0 \mu m$
Target Radius	$2 \cdot 5 \mu m$
Geometry	Cylindrical
Material	Polythene $(CH_2)_n$
Solid Density	$1 \cdot 2 g/cm^3$
Mass No. (F)	$4 \cdot 67$
Charge No.(Z)	$2 \cdot 67$
Ratio of Specific heat	$1 \cdot 667$
Initial Temperature	$10^4 K°$
LASER PARAMETERS	
Peak Power on Axis	$1 \cdot 0 \times 10^{14} W/cm^2$
Focal Radius	$1 \cdot 0 \times 10^4 cm$
Laser wavelength	$0 \cdot 53 \mu m$
Laser Rise Time	300ps
Total Duration of Laser Pulse	2ns
Total Run Time	800ps
Reflection Coefficient	$0 \cdot 8$
Perturbation Wavelength	$1 \cdot 25 \mu m$
Perturbation Amplitude	5%
TRANSPORT PARAMETERS	
Flux limit Factor (f)	$0 \cdot 1$
Diffusion	Classical

Table 6.3: Input data for the target $(5 \cdot 0 \mu m \times 2 \cdot 5 \mu m)$ in axial and radial directions.

Chapter 7

COMPARISON OF SIMULATIONS

7.1 INTRODUCTION

The object of this Chapter is to investigate some of the effects observed in the growth of Rayleigh-Taylor instability in Chapters 5 and 6. We have run the code for the target of the size ($5 \cdot 0\mu m \times 5 \cdot 0\mu m$) inverting the applied perturbation for one simulation to understand the possible reason for hole generation on the target axis in section 5.3 and whether this helps us in solving this problem. The simulations are also performed using plane geometry for the same type of target to study, with the field on, the drift of high density nodes towards the axis. We have, also, performed simulations using the additional thermo-electric transport terms of Braginskii to see if this affects the growth of Rayleigh-Taylor instability. Furthermore, we have performed simulations using less power but all other parameters same as in the first run performed in Chapter 6.

7.2 PLANE GEOMETRY

The target used in these simulations is $5 \cdot 0\mu m$ in both axial and radial directions. The simulations in this particular test problem are carried out only for the case with magnetic field switched on. In this problem instead of using cylindrical geometry as usual we used plane geometry with all other parameters exactly the same

as used in section 5 · 2.

We noted there the drift of material towards the axis of the target, and pointed out some possibilities which could generate this type of drift towards the axis. In this study we have not run the code up to 800ps but stopped the simulations at 600ps as our intention was only to find out the source which generates this drift. The density maps with an interval of 50ps are shown in figure 7 · 1. The analysis of the maps shows no such drift towards the axis. The high density nodes remain at the position where these were generated. It is, therefore, concluded from these results that the drift of high density nodes towards the axis is a geometrical effect. We note also in this run the bubble merging effect in the non-linear phase discussed by Henshaw [67].

7.3 PERTURBATION INVERTED SIMULATIONS

It was observed in section 5 · 2 that a hole was created at the axis of the target in the density contour maps for the simulations excluding magnetic field effects. It was important to find the possible reasons for this hole. We, therefore, performed simulations using all the target parameters same as used in those simulations except that we reversed the applied perturbation.

The density contour maps for this case are shown in figure 7 · 2 to compare the instability behaviour with section 5 · 2. We observe here the instability growth is slow as compared to section 5 · 2. At later stage in that section a hole started developing at 550ps which later on developed to a complete hole. In these simulations a spike rather than a bubble develops on axis, and the hole is not formed. This problem is explained by inverting the applied perturbation.

7.4 EFFECT OF POWER VARIATION

There are many factors such as laser power and wavelength, the wavelength and the amplitude of applied perturbation, target size and geometry and the applied perturbation source etc., which can influence the growth of Rayleigh-Taylor insta-

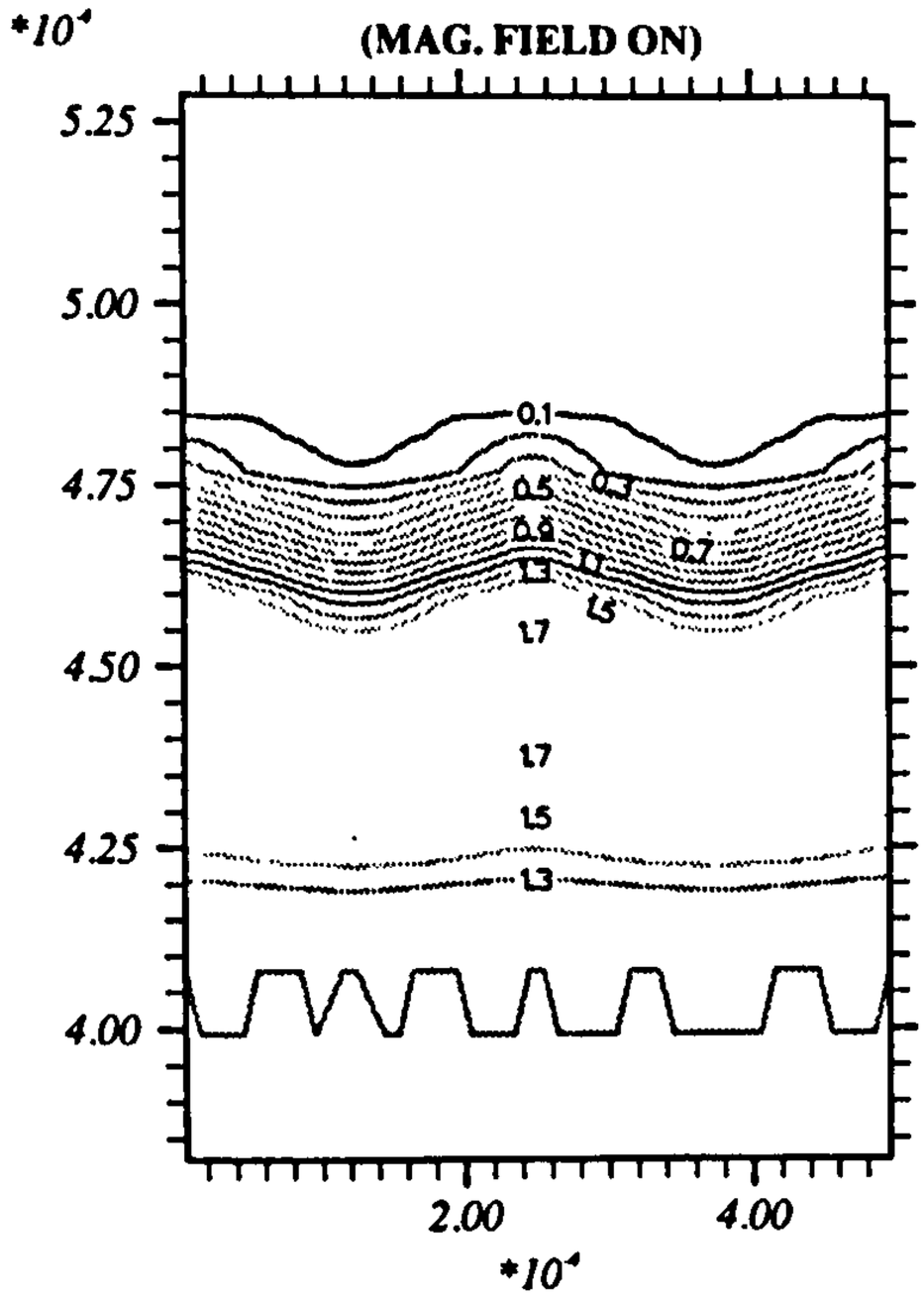

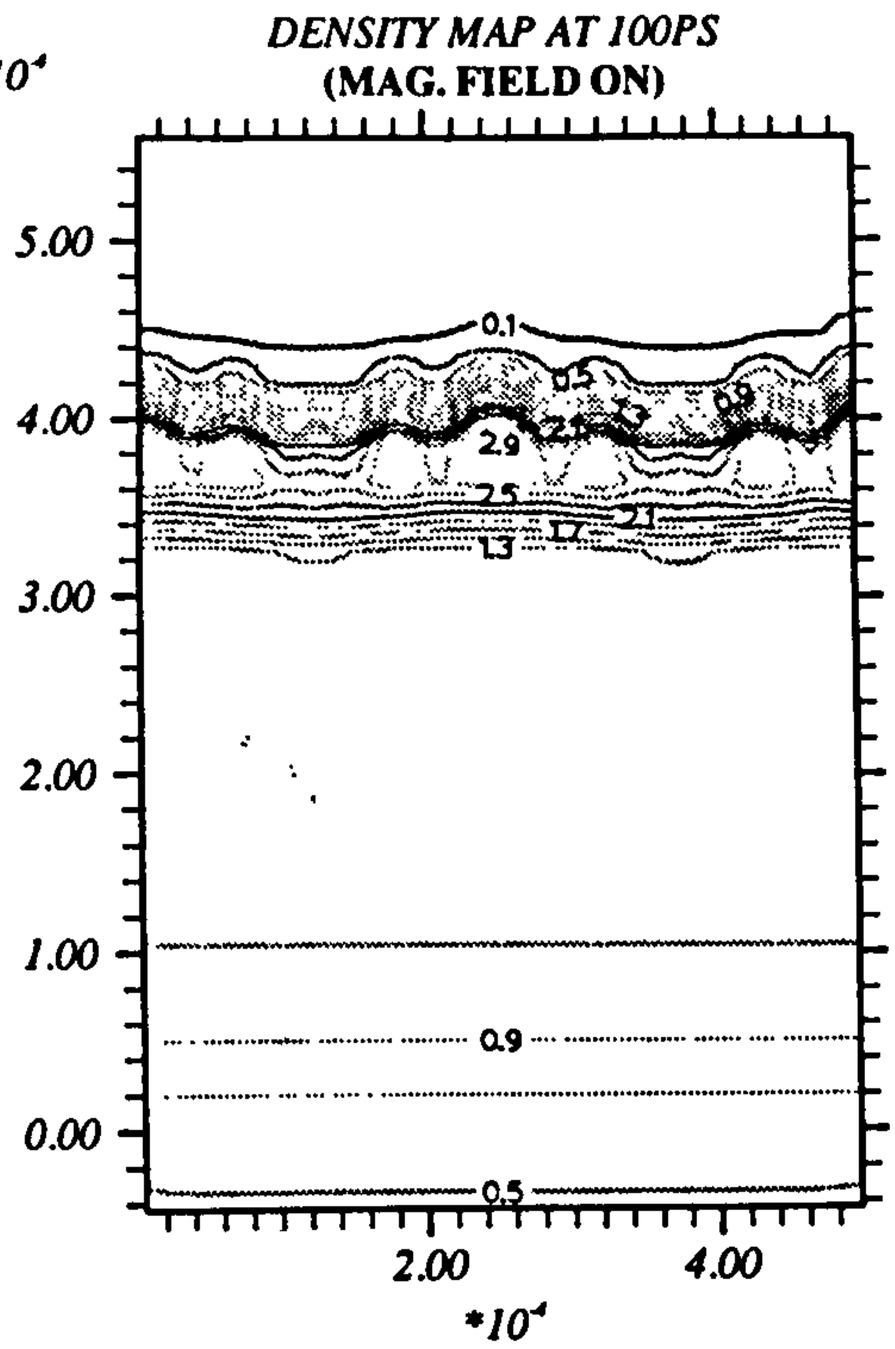

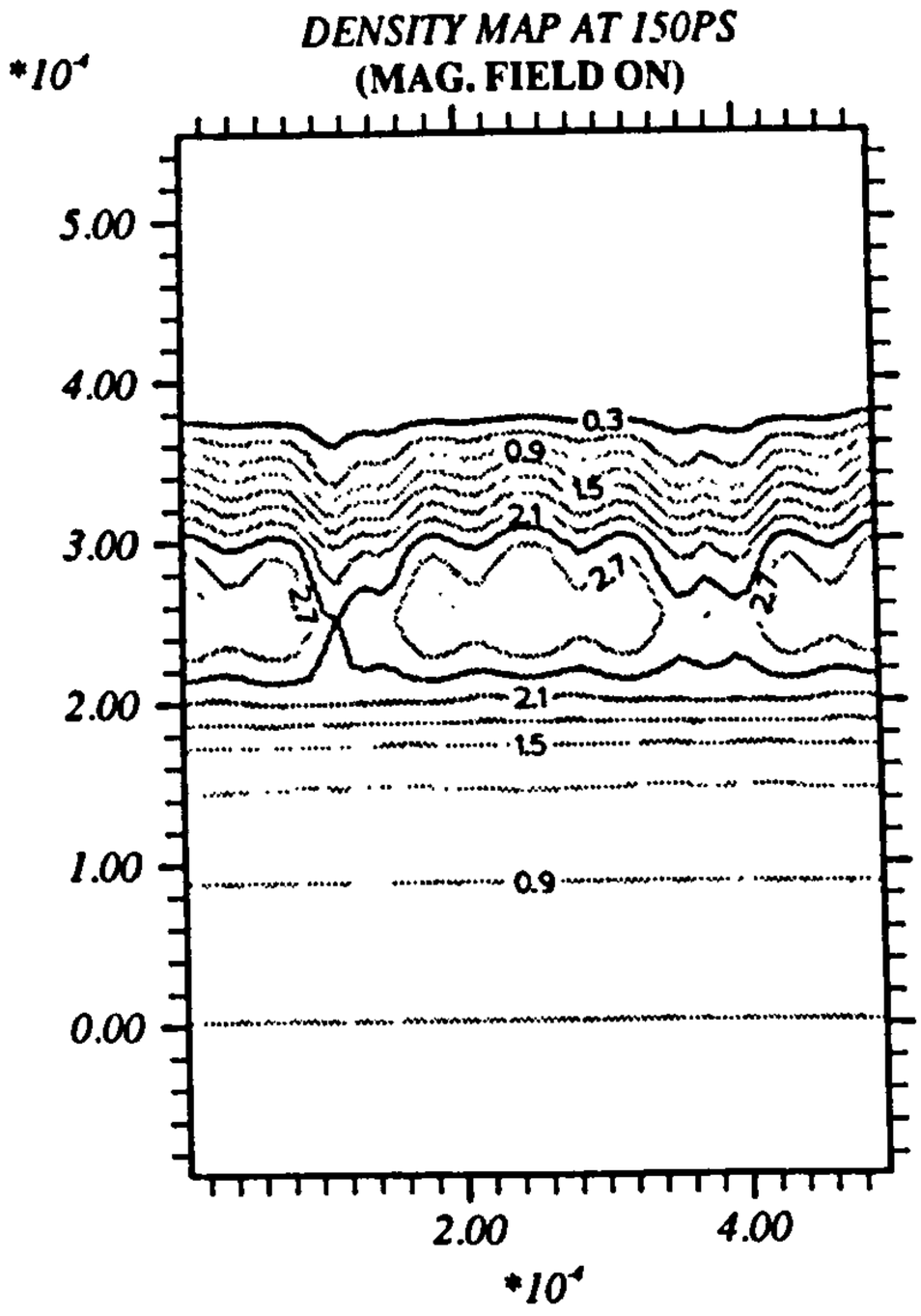

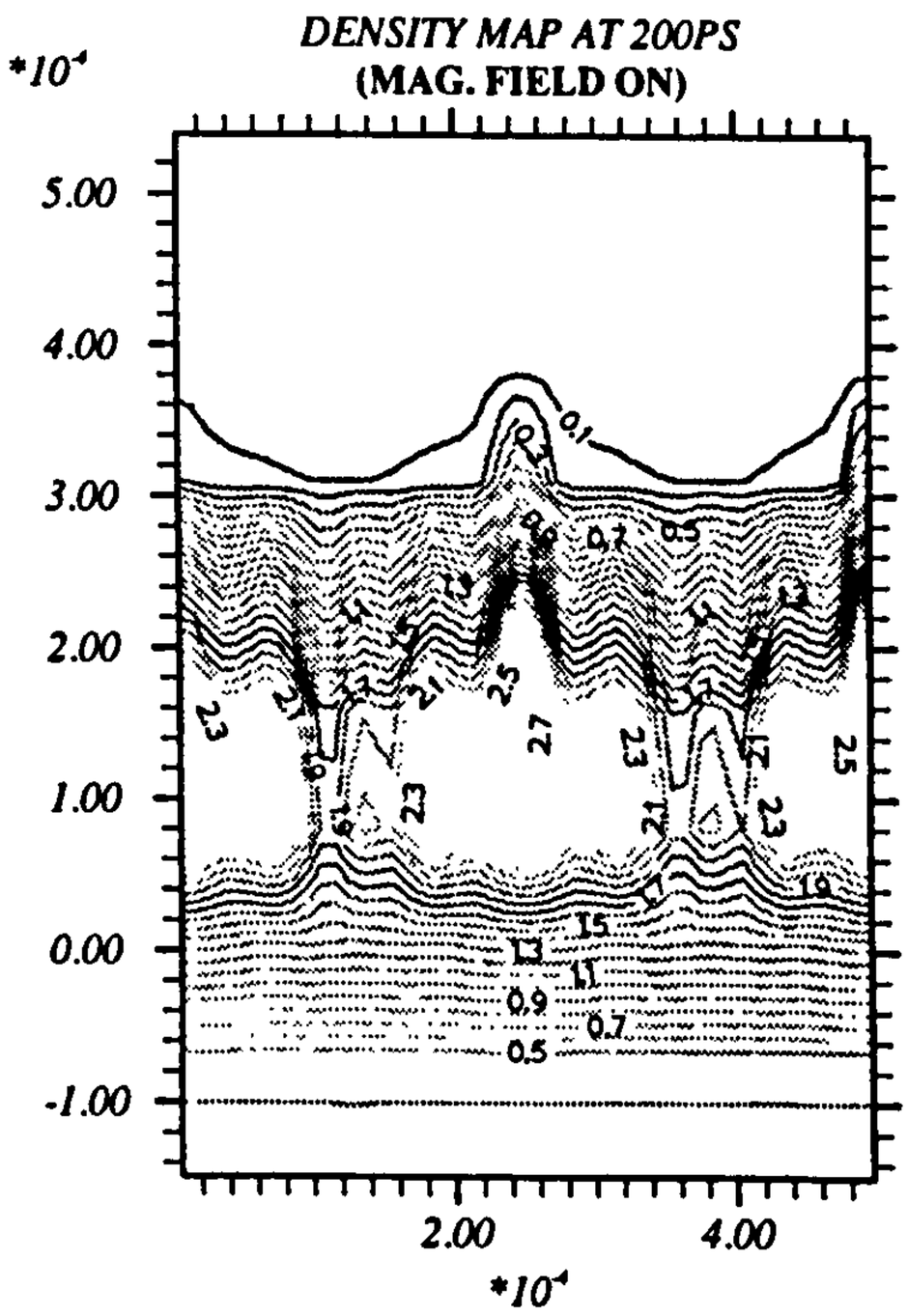

Figure 7.1: Density contour maps for the target of $(5 \cdot 0\mu m \times 5 \cdot 0\mu m)$ in plane geometry.

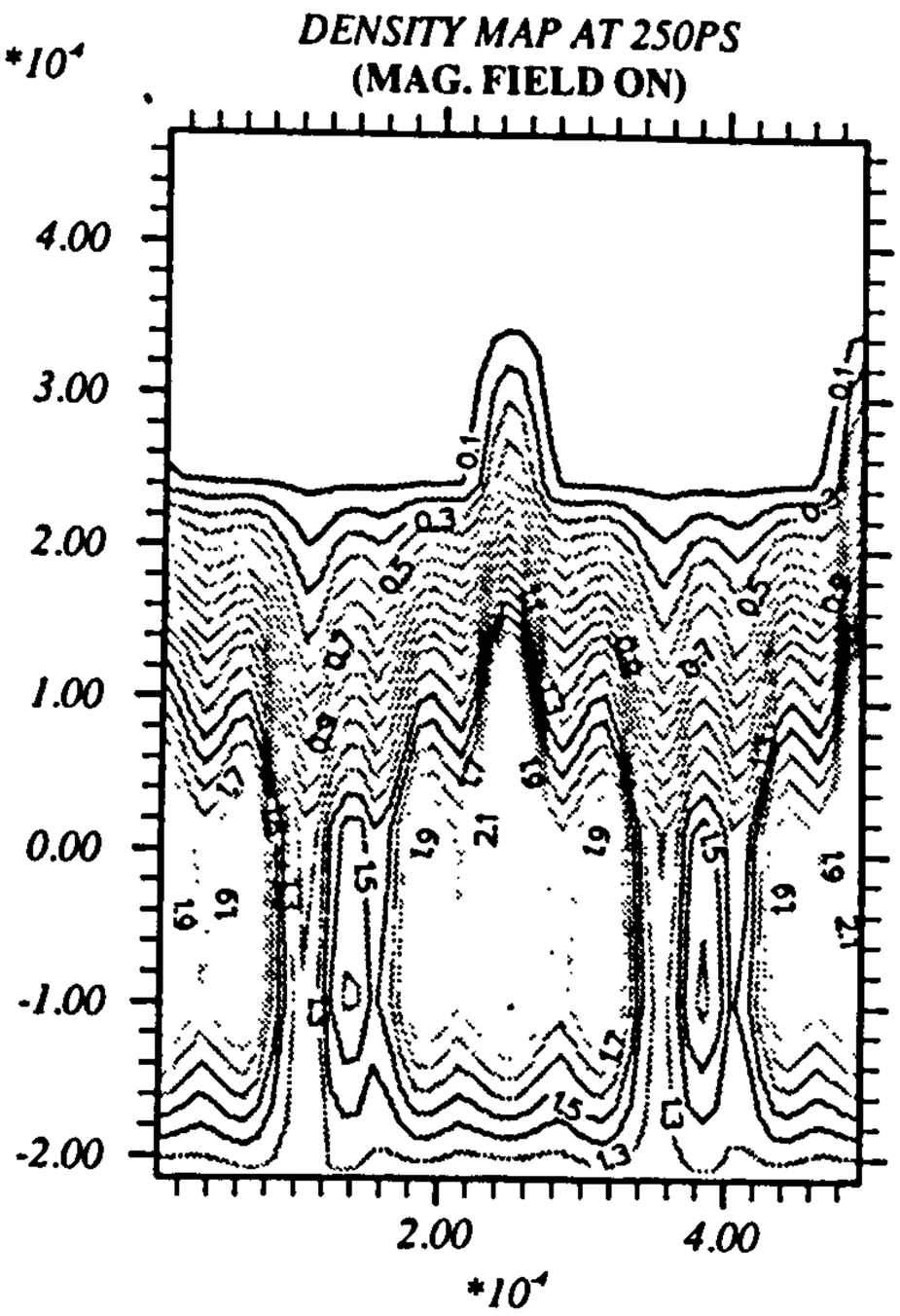
DENSITY MAP AT 250PS
(MAG. FIELD ON)
*10⁻⁴
4.00
3.00
2.00
1.00
0.00
-1.00
-2.00
2.00
4.00
*10⁻⁴

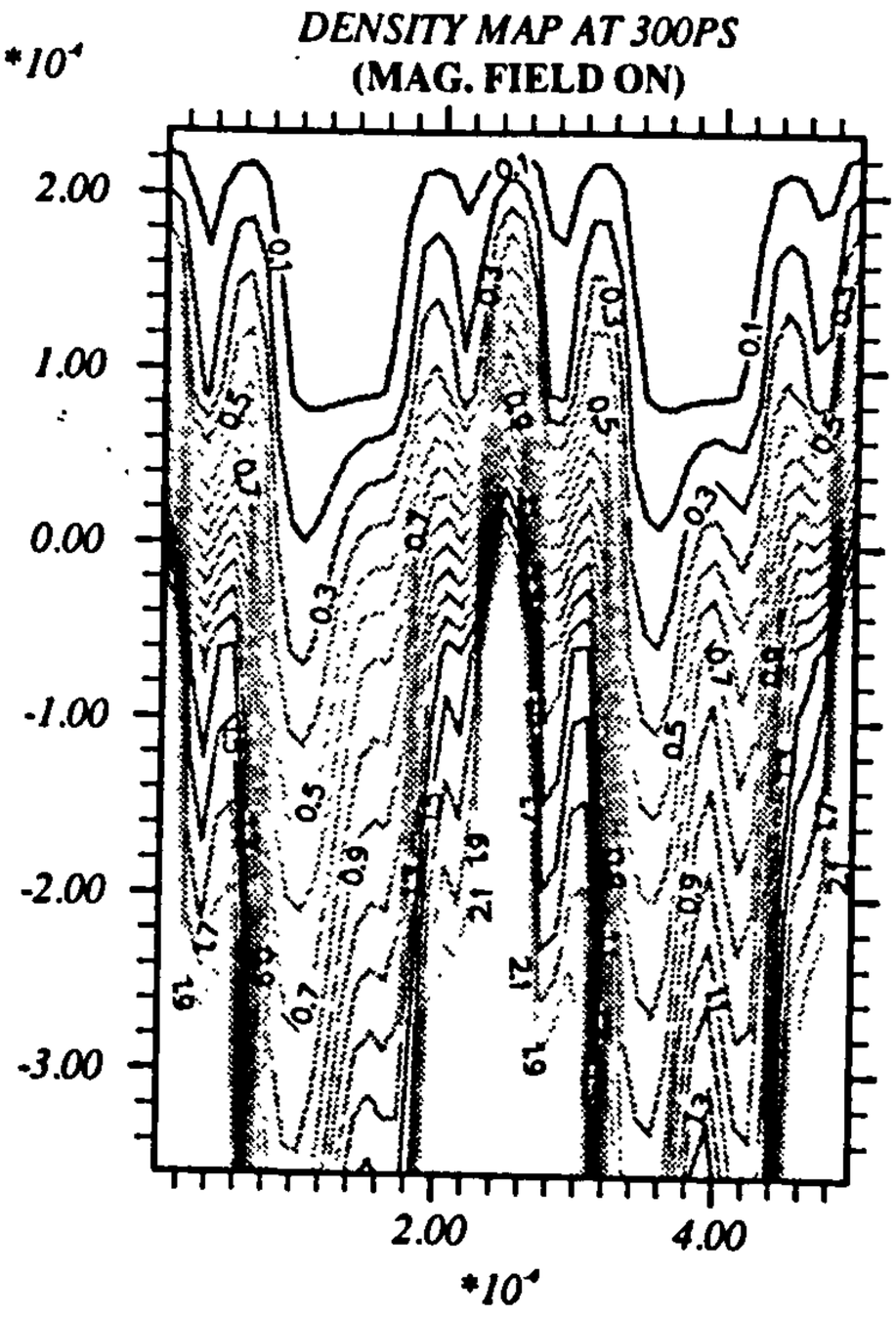
DENSITY MAP AT 300PS
(MAG. FIELD ON)
*10⁻⁴
2.00
1.00
0.00
-1.00
-2.00
-3.00
2.00
4.00
*10⁻⁴

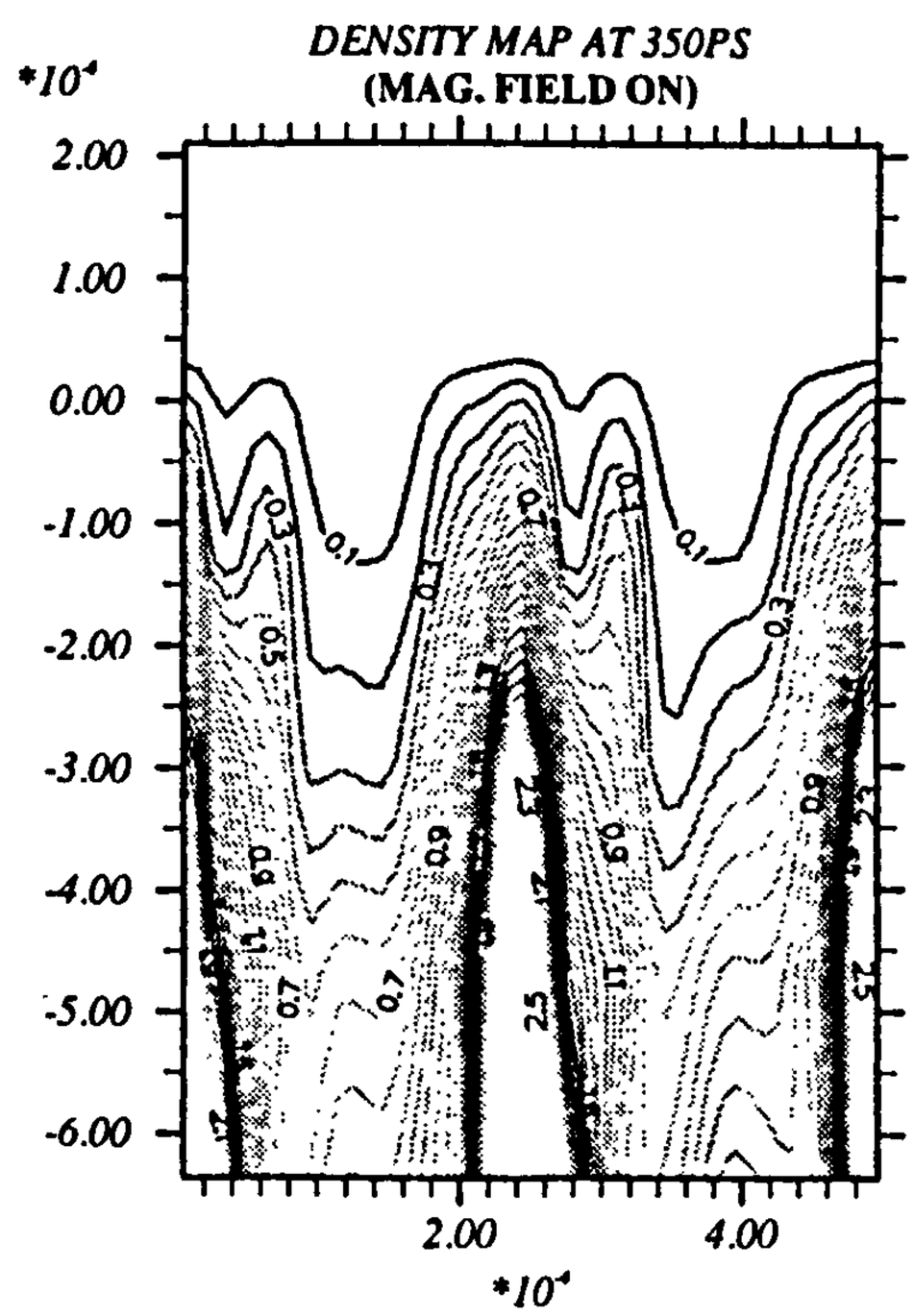
DENSITY MAP AT 350PS
(MAG. FIELD ON)
*10⁻⁴
2.00
1.00
0.00
-1.00
-2.00
-3.00
-4.00
-5.00
-6.00
2.00
4.00
*10⁻⁴

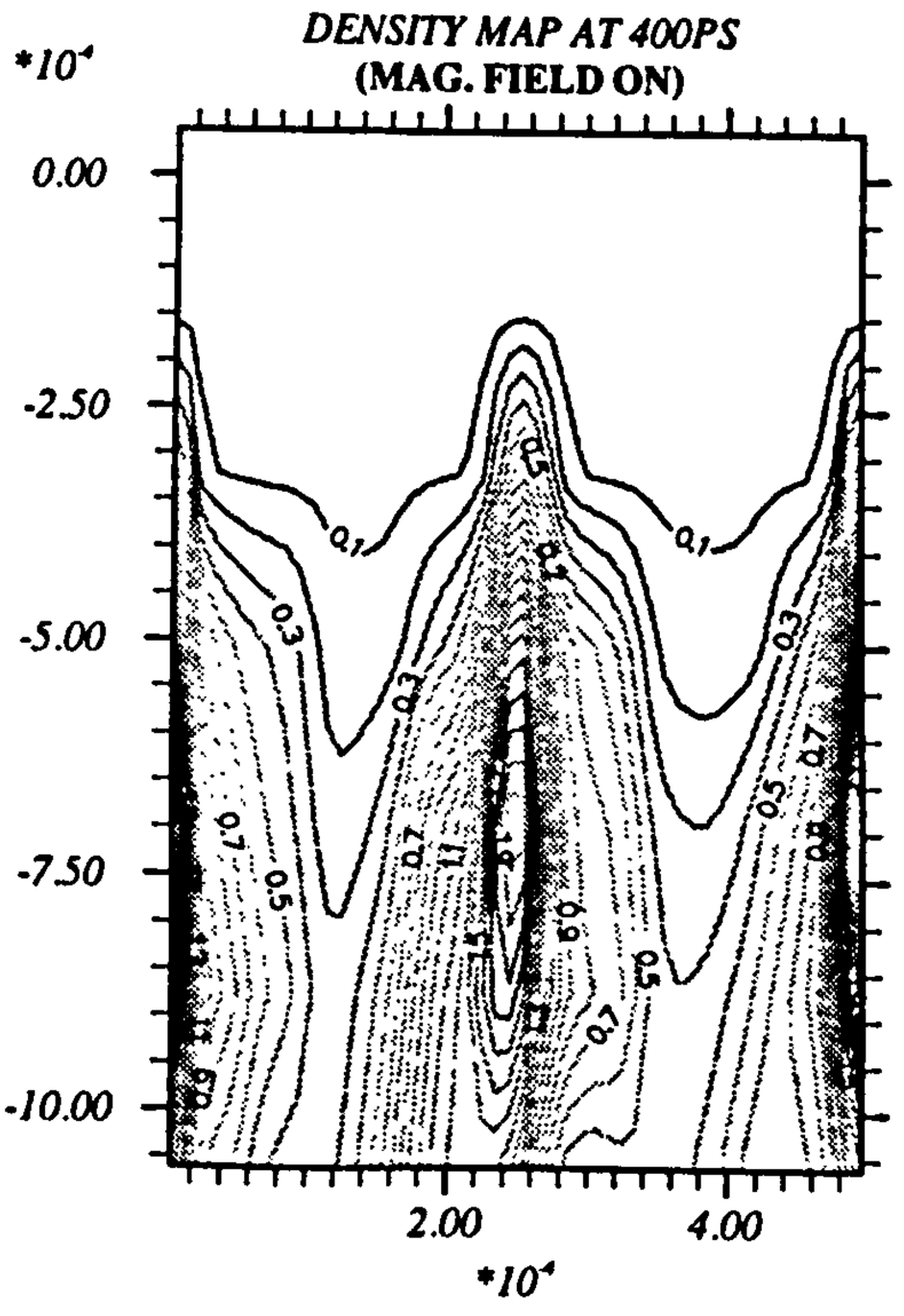
DENSITY MAP AT 400PS
(MAG. FIELD ON)
*10⁻⁴
0.00
-2.50
-5.00
-7.50
-10.00
2.00
4.00
*10⁻⁴

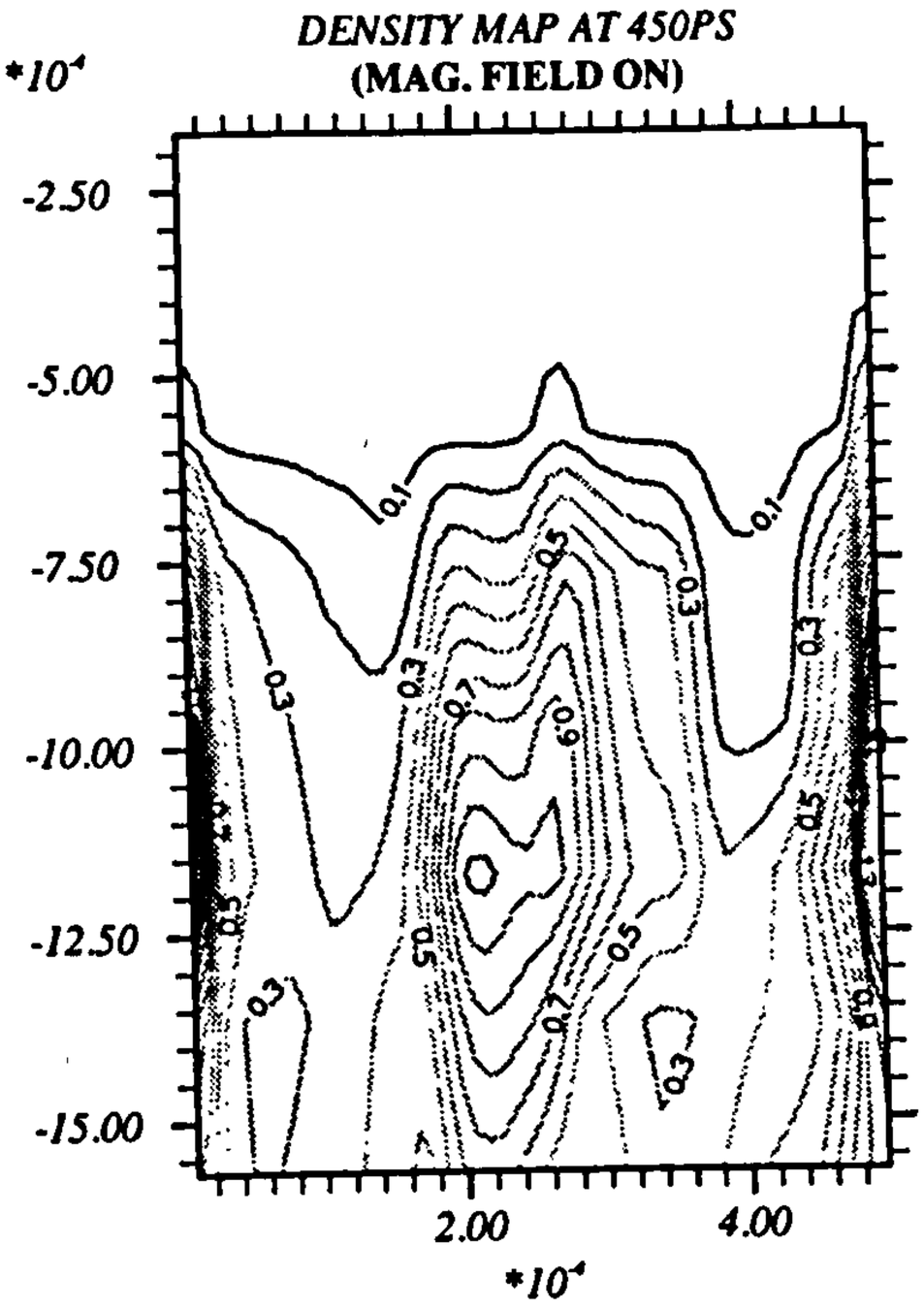
DENSITY MAP AT 450PS
(MAG. FIELD ON)
*10⁻⁴
-2.50
-5.00
-7.50
-10.00
-12.50
-15.00
2.00
4.00
*10⁻⁴
0.1
0.3
0.5
0.7
0.9

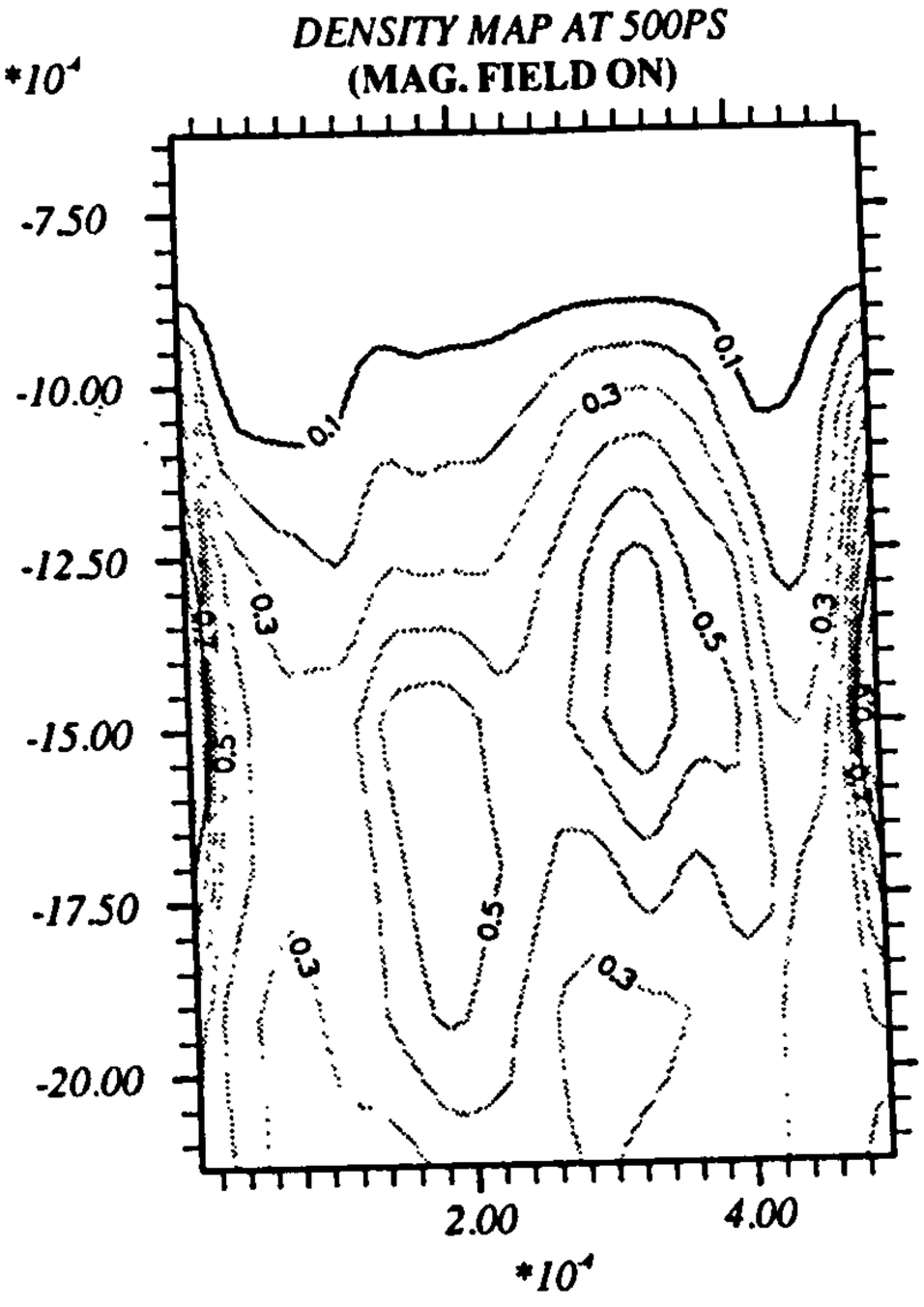
DENSITY MAP AT 500PS
(MAG. FIELD ON)
*10⁻⁴
-7.50
-10.00
-12.50
-15.00
-17.50
-20.00
2.00
4.00
*10⁻⁴
0.1
0.3
0.5
0.7

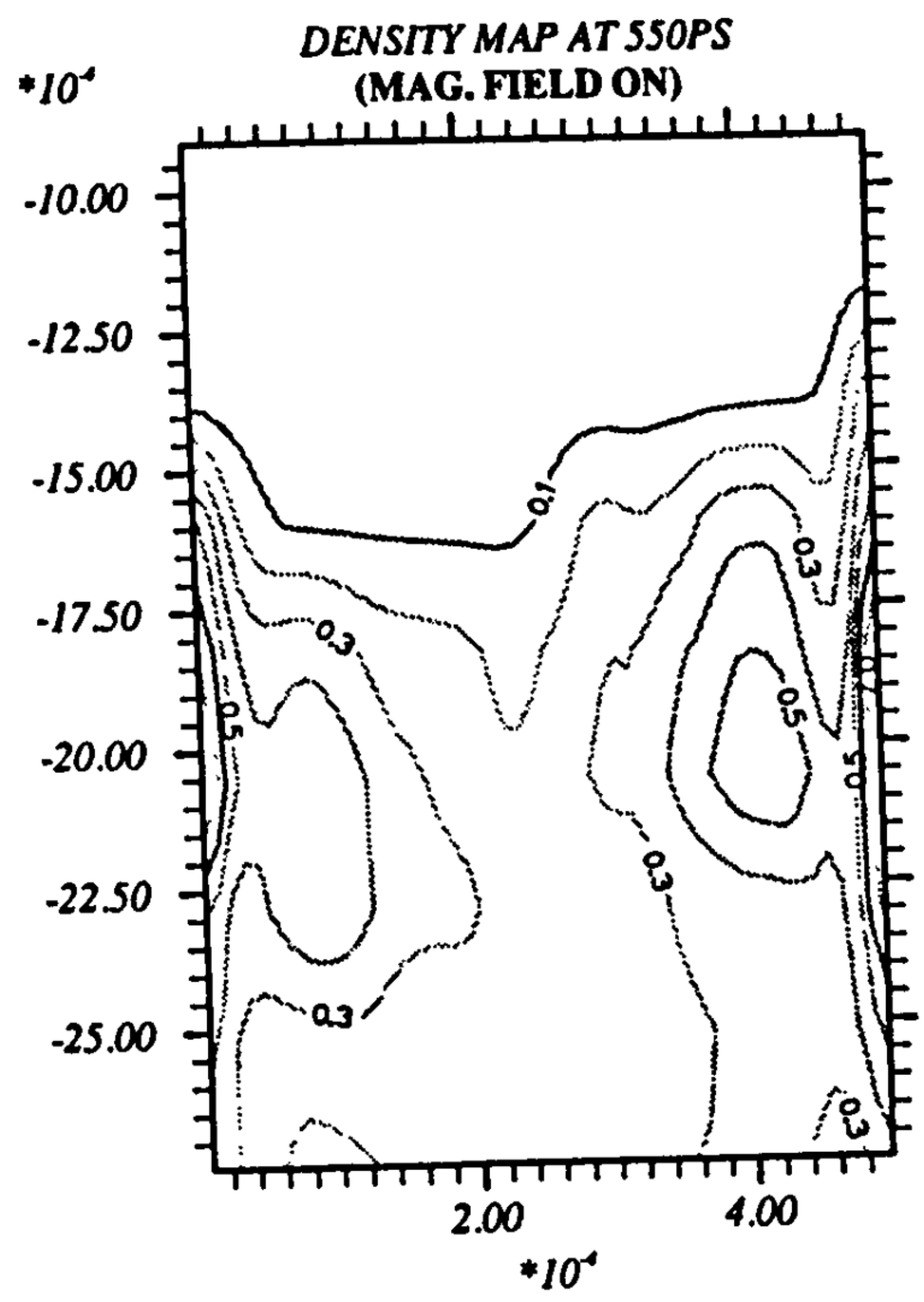
DENSITY MAP AT 550PS
(MAG. FIELD ON)
*10⁻⁴
-10.00
-12.50
-15.00
-17.50
-20.00
-22.50
-25.00
2.00
4.00
*10⁻⁴
0.1
0.3
0.5

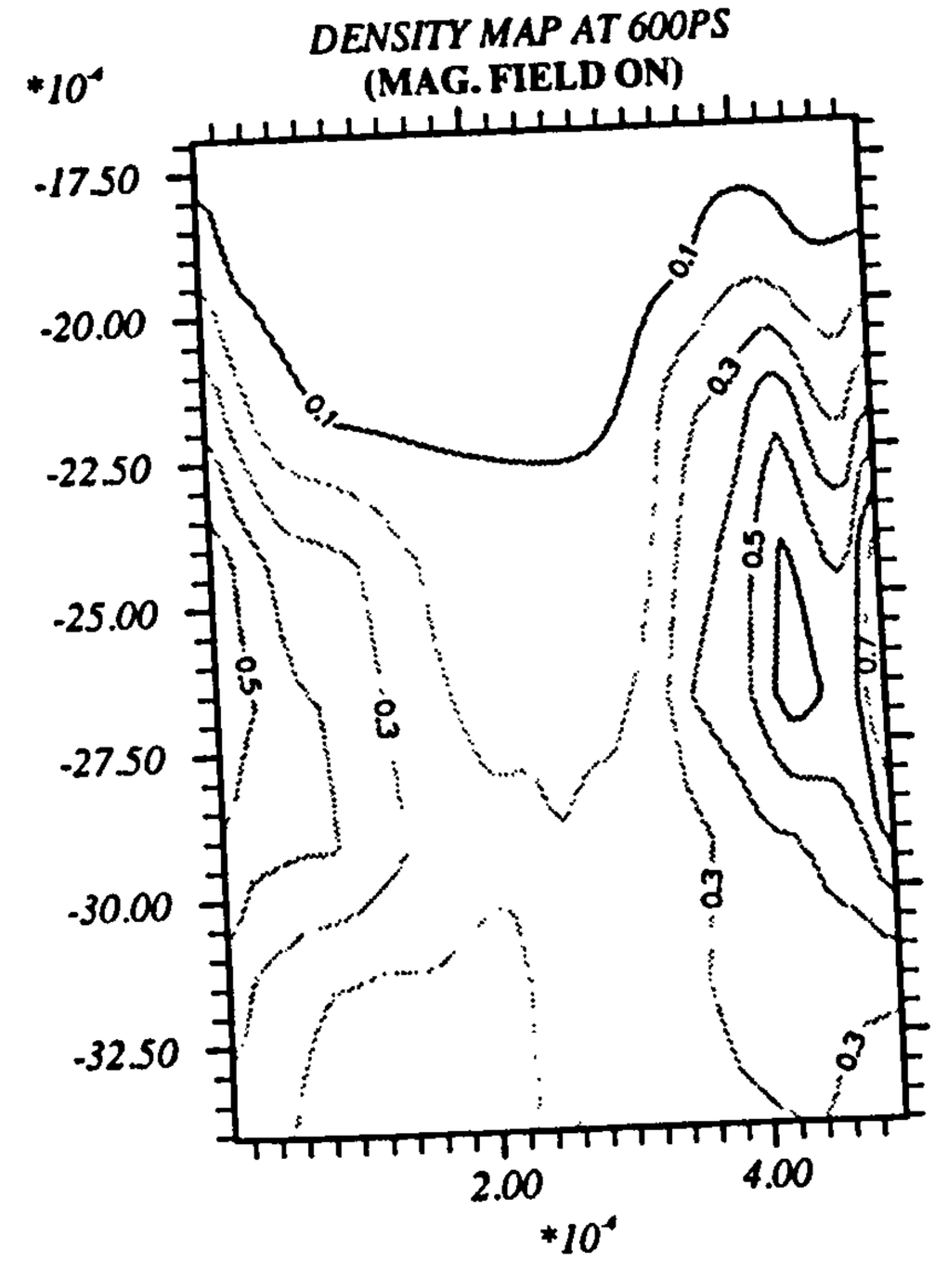
DENSITY MAP AT 600PS
(MAG. FIELD ON)
*10⁻⁴
-17.50
-20.00
-22.50
-25.00
-27.50
-30.00
-32.50
2.00
4.00
*10⁻⁴
0.1
0.3
0.5

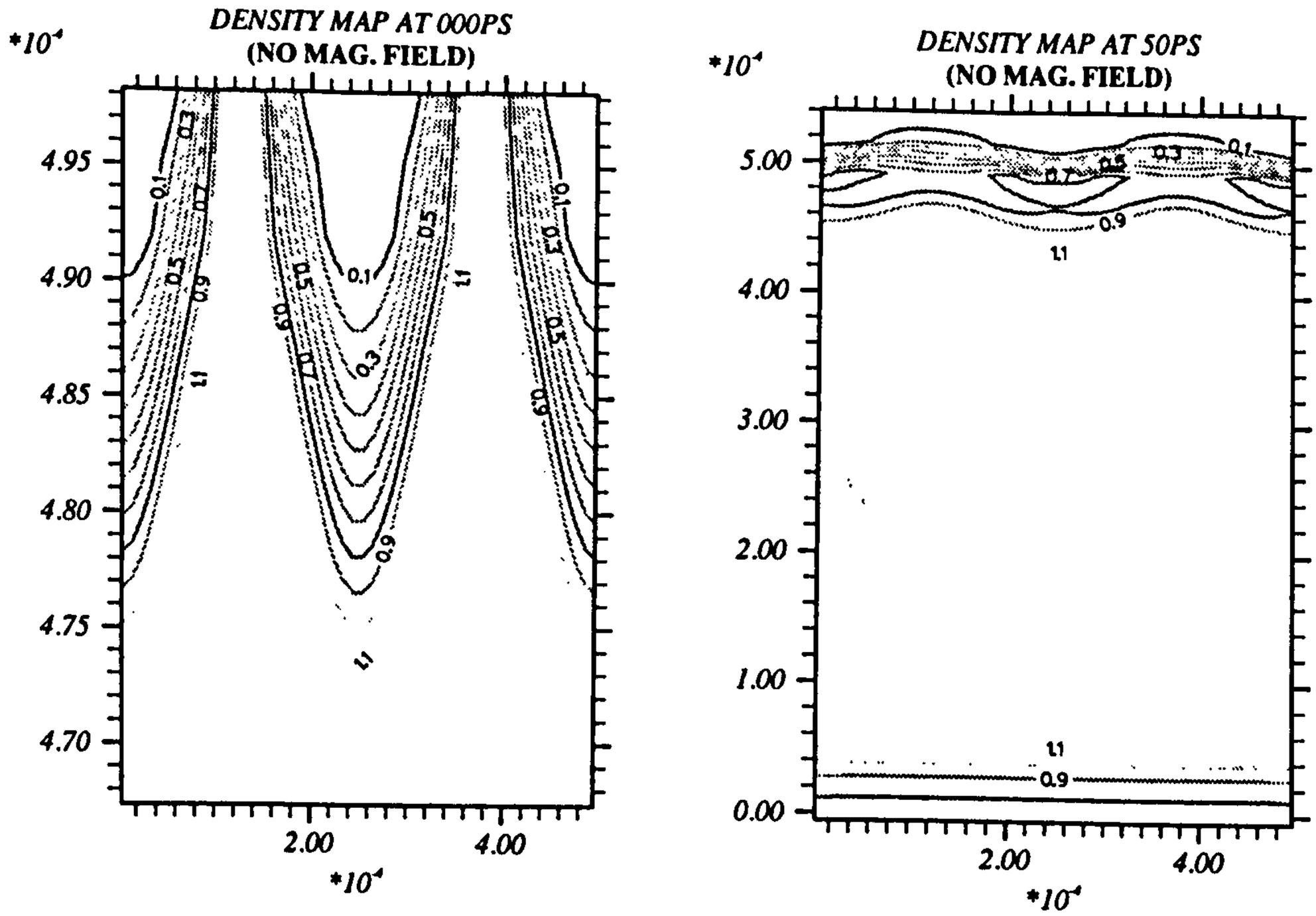

Figure 7.2: Density contour map for the target of $(5 \cdot 0\mu m \times 5 \cdot 0\mu m)$ with perturbation inverted

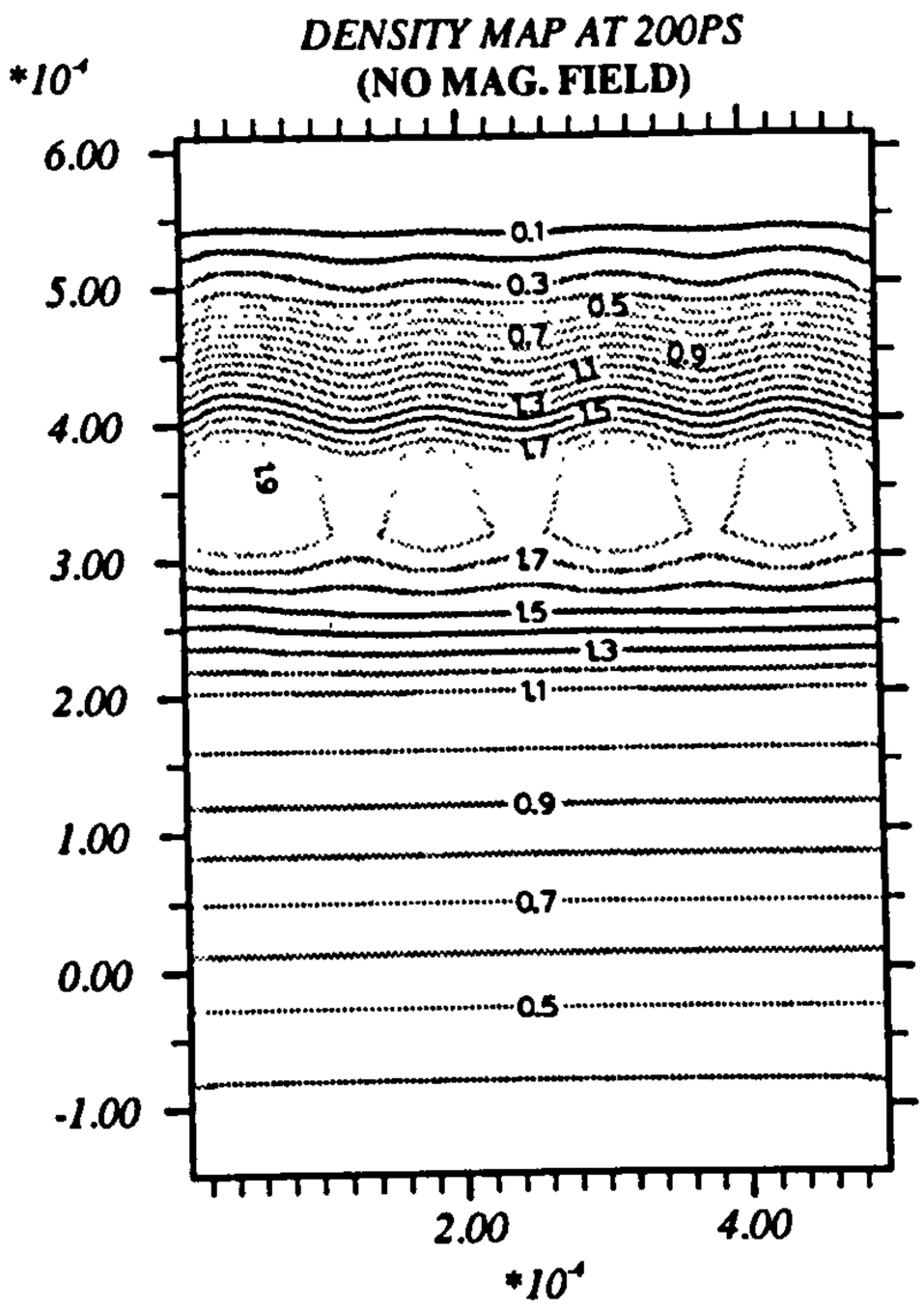
DENSITY MAP AT 200PS
(NO MAG. FIELD)
*10⁻⁴
6.00
5.00
4.00
3.00
2.00
1.00
0.00
-1.00
2.00
4.00
*10⁻⁴
0.1
0.3
0.5
0.7
0.9
1.1
1.3
1.5
1.7

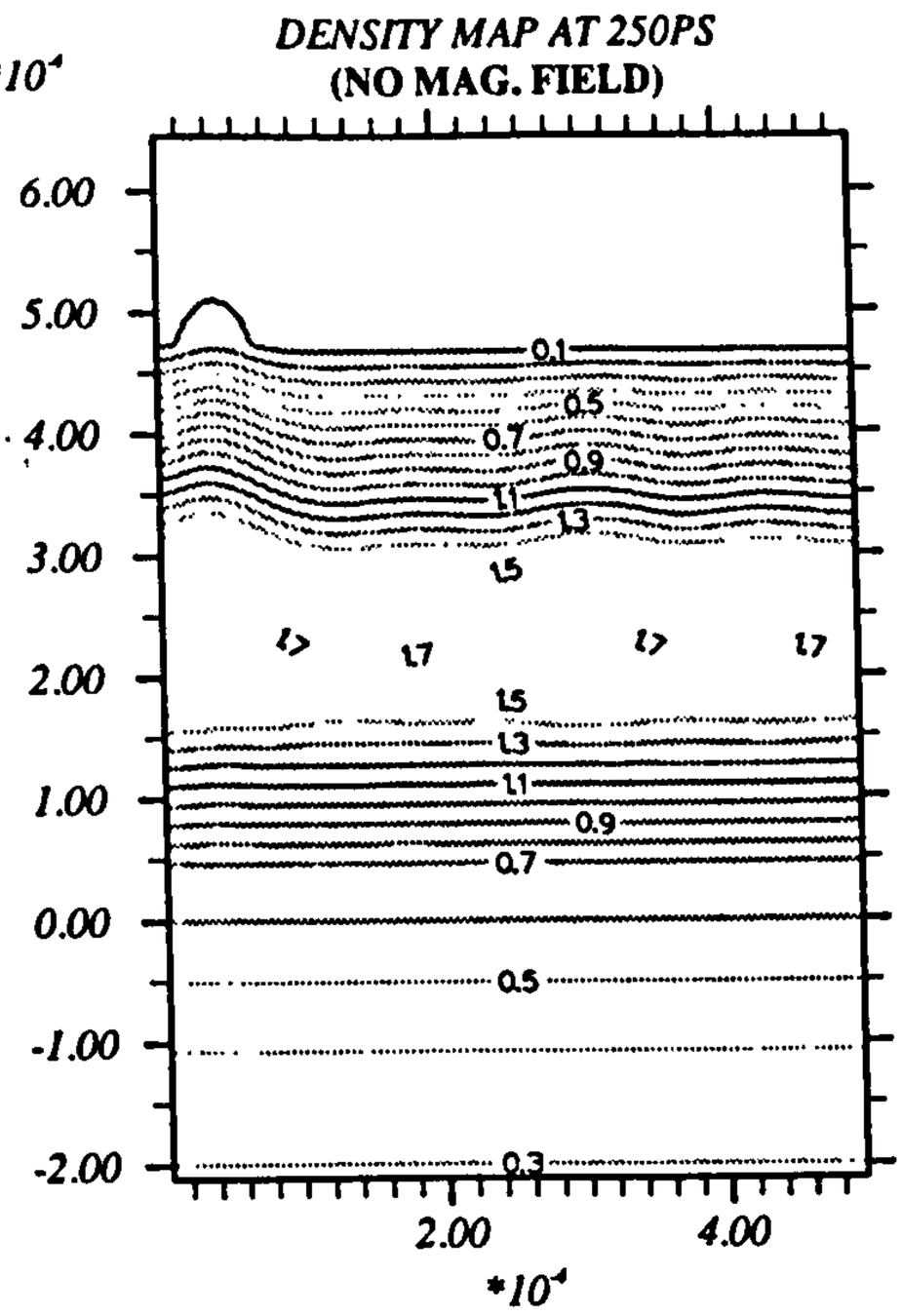
DENSITY MAP AT 250PS
(NO MAG. FIELD)
*10⁻⁴
6.00
5.00
4.00
3.00
2.00
1.00
0.00
-1.00
-2.00
2.00
4.00
*10⁻⁴
0.1
0.3
0.5
0.7
0.9
1.1
1.3
1.5
1.7

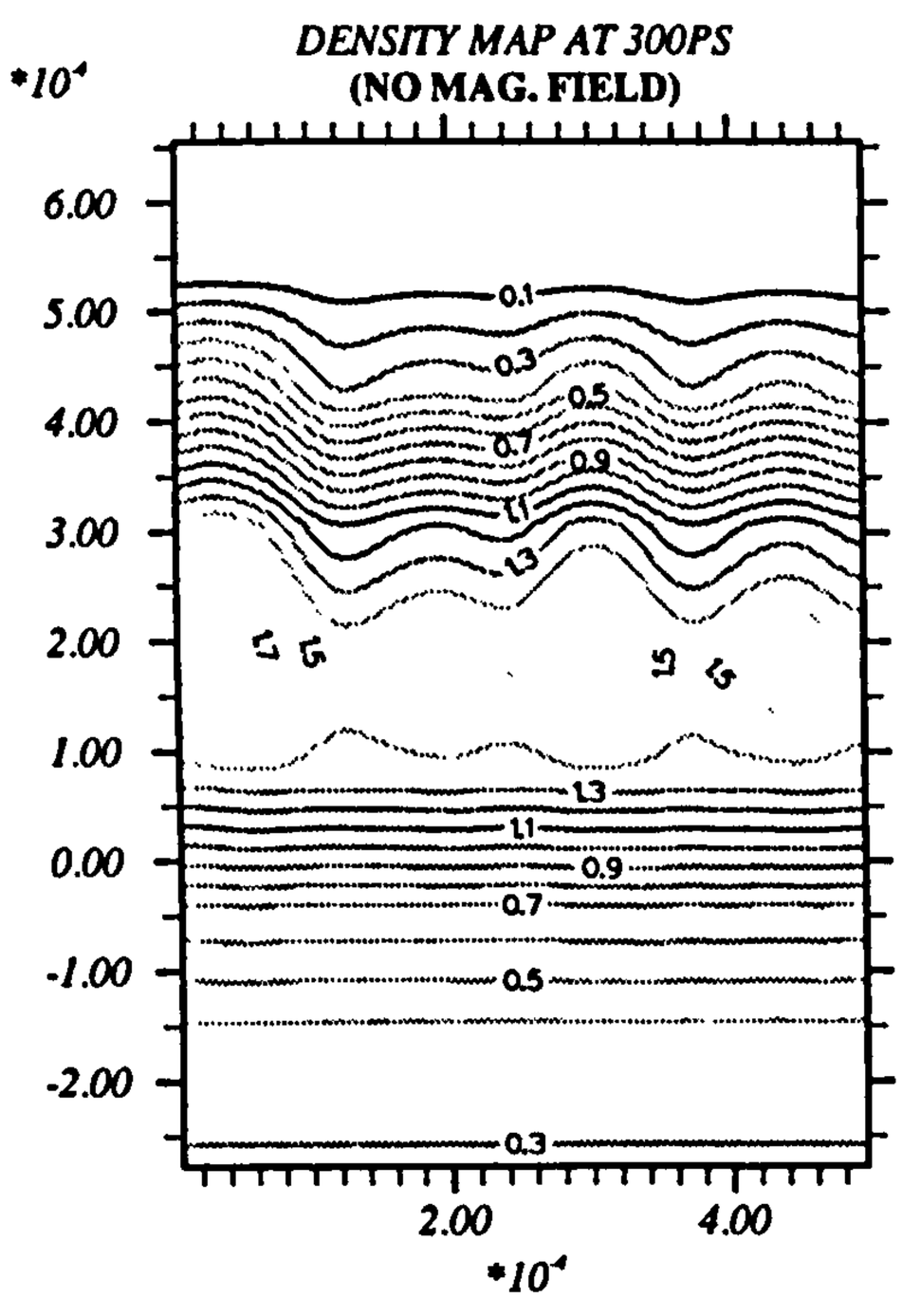
DENSITY MAP AT 300PS
(NO MAG. FIELD)
*10⁻⁴
6.00
5.00
4.00
3.00
2.00
1.00
0.00
-1.00
-2.00
2.00
4.00
*10⁻⁴
0.1
0.3
0.5
0.7
0.9
1.1
1.3
1.5
1.7

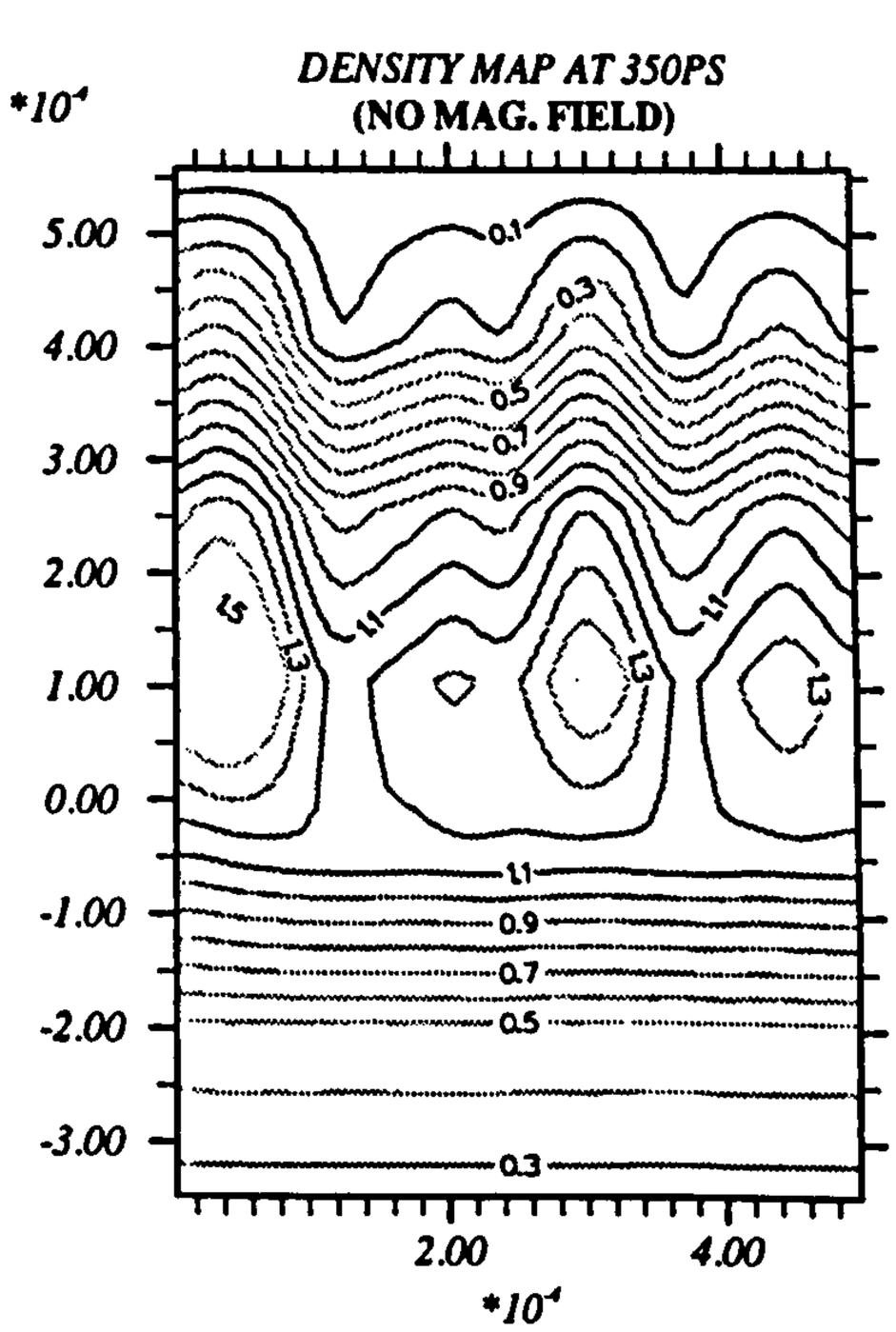
DENSITY MAP AT 350PS
(NO MAG. FIELD)
*10⁻⁴
5.00
4.00
3.00
2.00
1.00
0.00
-1.00
-2.00
-3.00
2.00
4.00
*10⁻⁴
0.1
0.3
0.5
0.7
0.9
1.1
1.3
1.5

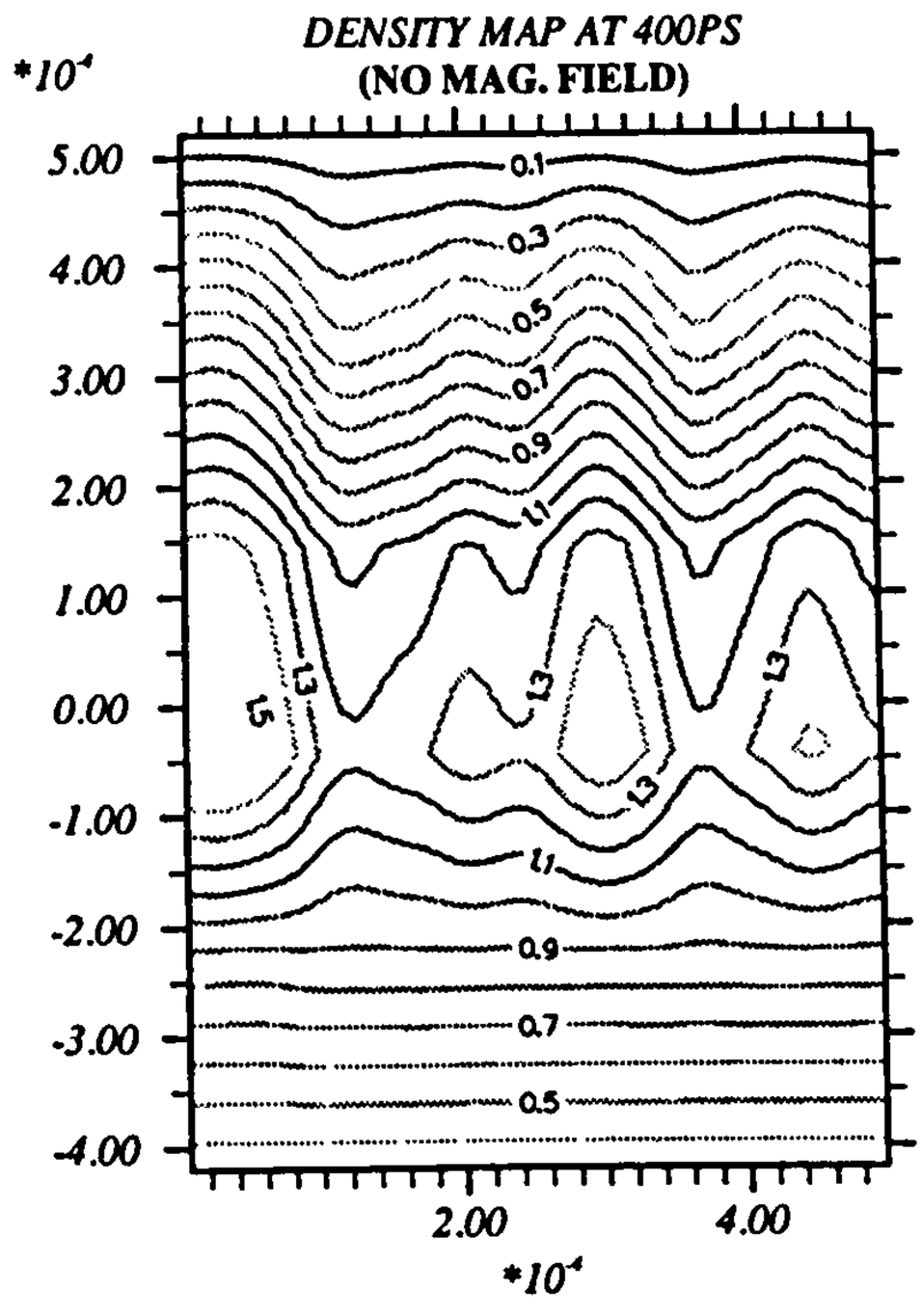
DENSITY MAP AT 400PS
(NO MAG. FIELD)
*10⁻⁴
5.00
4.00
3.00
2.00
1.00
0.00
-1.00
-2.00
-3.00
-4.00
2.00
4.00
*10⁻⁴
0.1
0.3
0.5
0.7
0.9
1.1
1.3
1.5

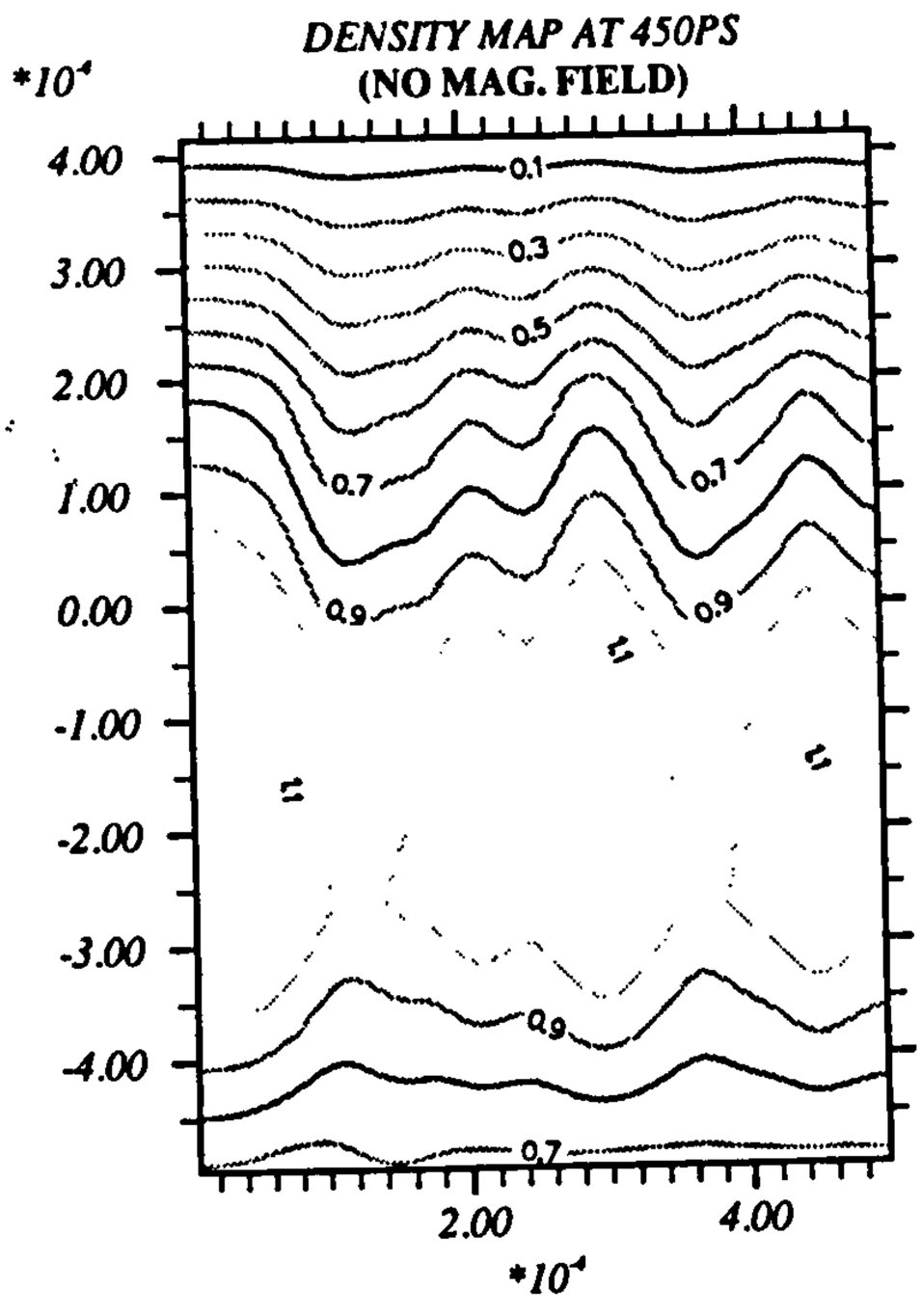
DENSITY MAP AT 450PS
(NO MAG. FIELD)
*10⁻⁴
4.00
3.00
2.00
1.00
0.00
-1.00
-2.00
-3.00
-4.00
2.00
4.00
*10⁻⁴
0.1
0.3
0.5
0.7
0.9
1.1

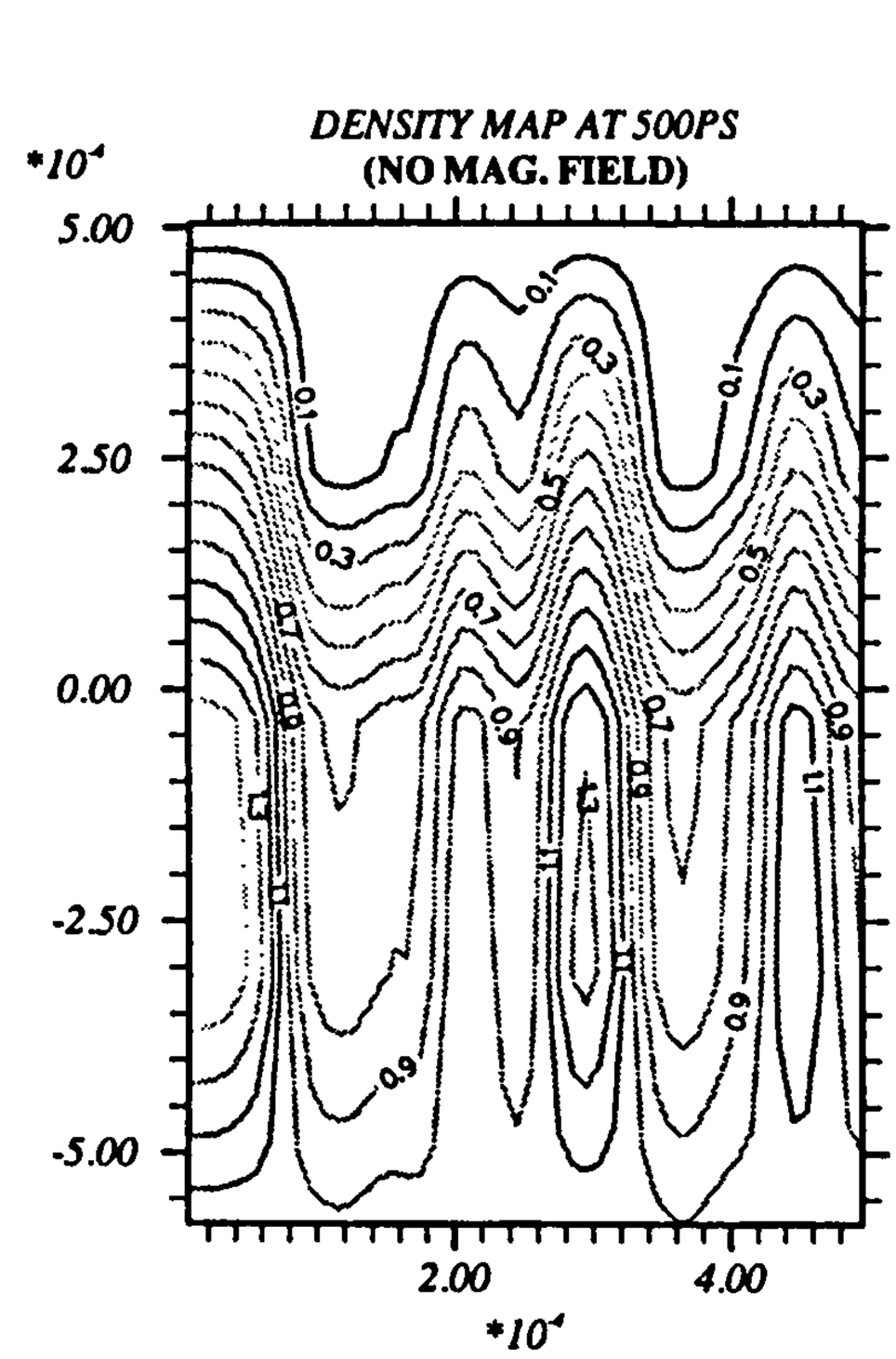
DENSITY MAP AT 500PS
(NO MAG. FIELD)
*10⁻⁴
5.00
2.50
0.00
-2.50
-5.00
2.00
4.00
*10⁻⁴
0.1
0.3
0.5
0.7
0.9
1.1
1.3

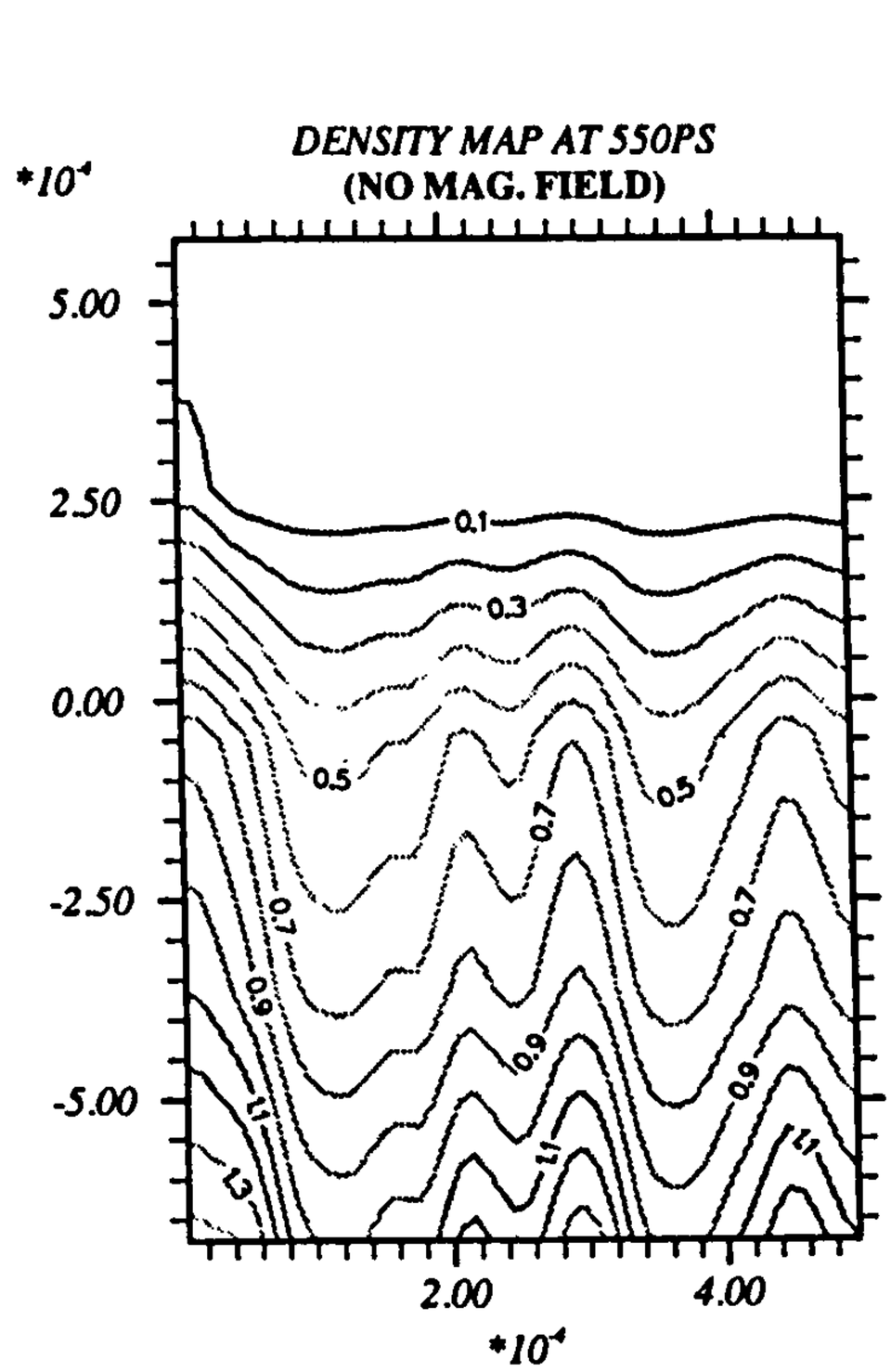
DENSITY MAP AT 550PS
(NO MAG. FIELD)
*10⁻⁴
5.00
2.50
0.00
-2.50
-5.00
2.00
4.00
*10⁻⁴
0.1
0.3
0.5
0.7
0.9
1.1
1.3

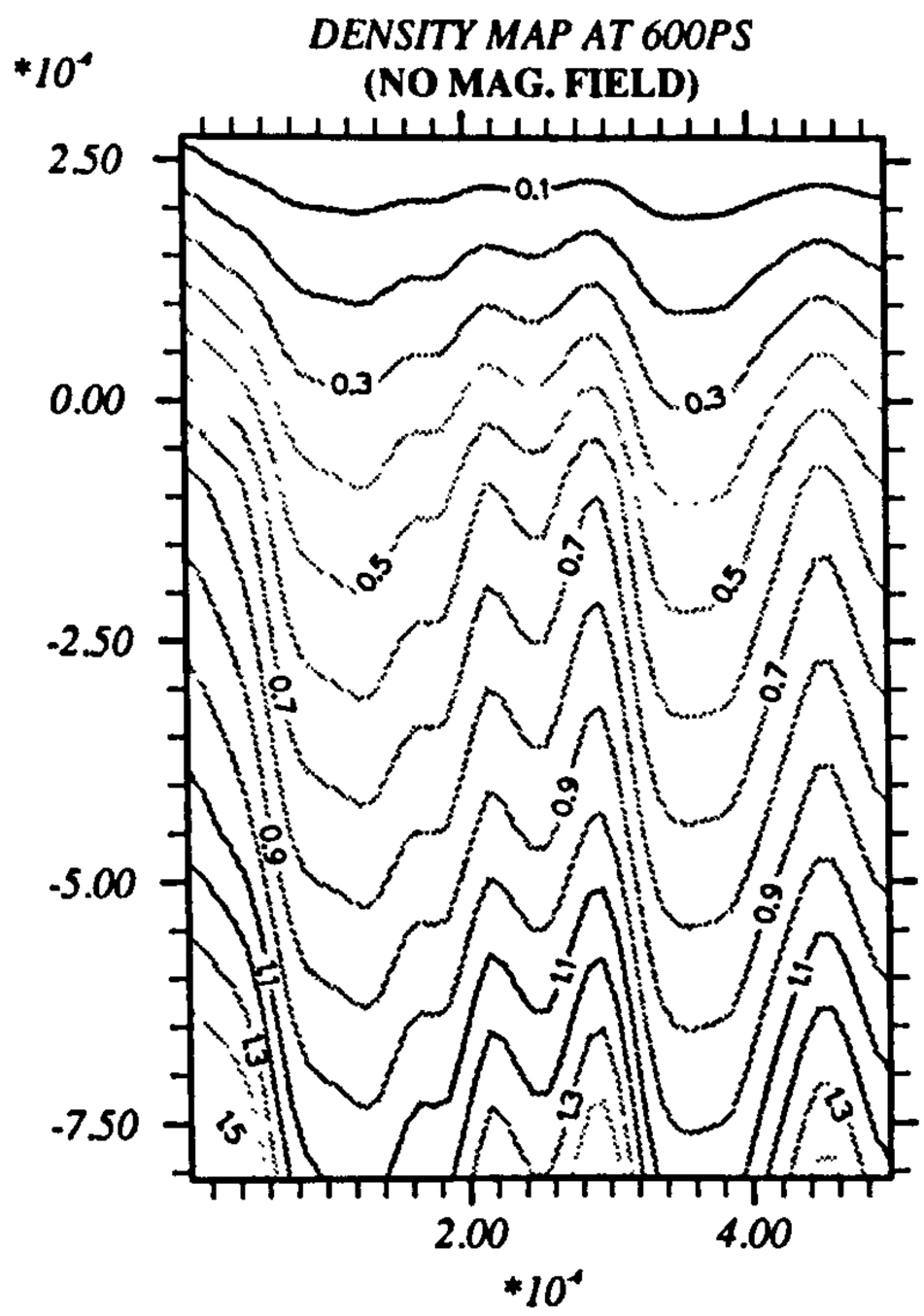
DENSITY MAP AT 600PS
(NO MAG. FIELD)
*10⁻⁴
2.50
0.00
-2.50
-5.00
-7.50
2.00
4.00
*10⁻⁴
0.1
0.3
0.5
0.7
0.9
1.1
1.3
1.5

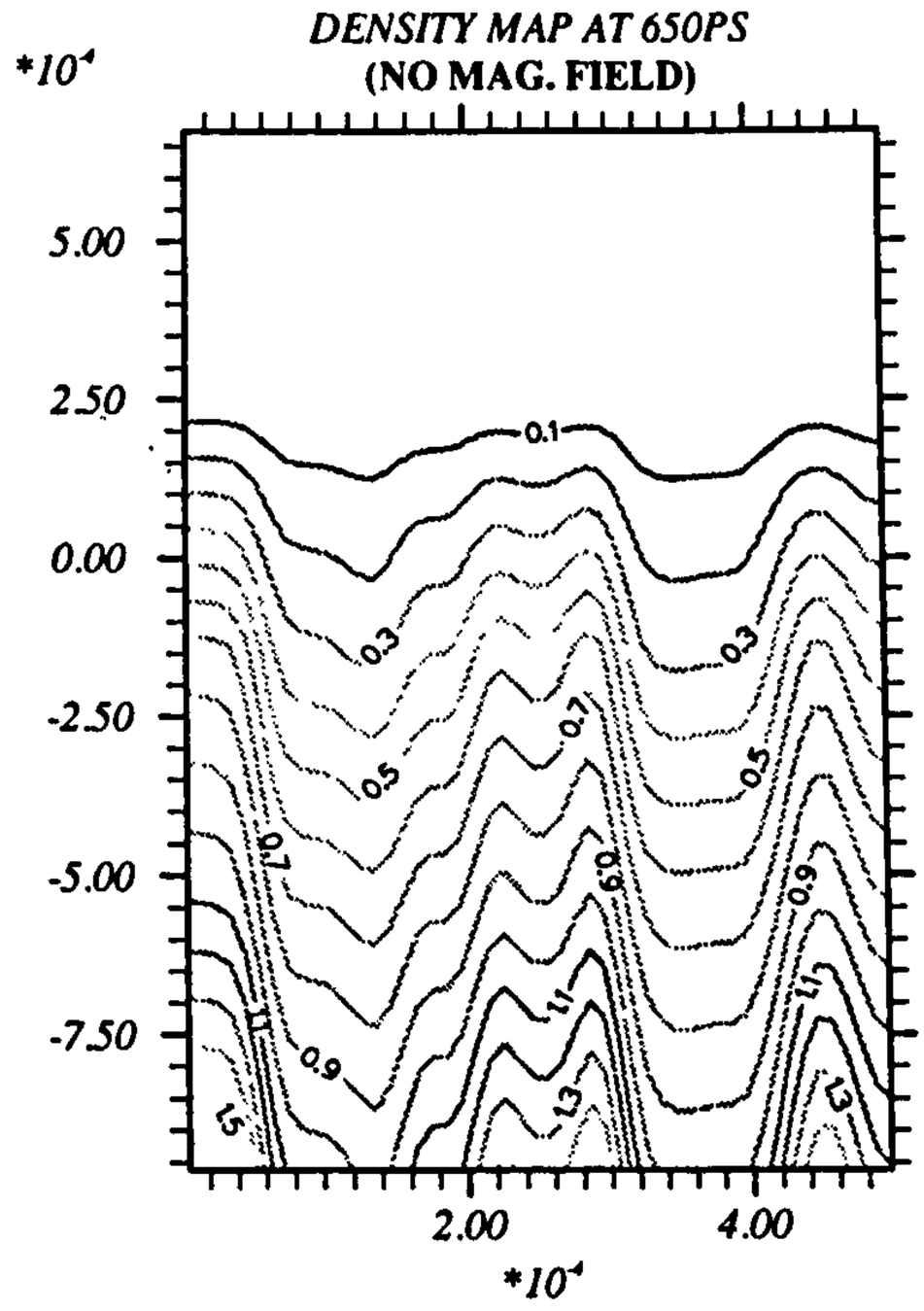
DENSITY MAP AT 650PS
(NO MAG. FIELD)
*10⁻⁴
5.00
2.50
0.00
-2.50
-5.00
-7.50
2.00
4.00
*10⁻⁴
0.1
0.3
0.5
0.7
0.9
1.1
1.3
1.5

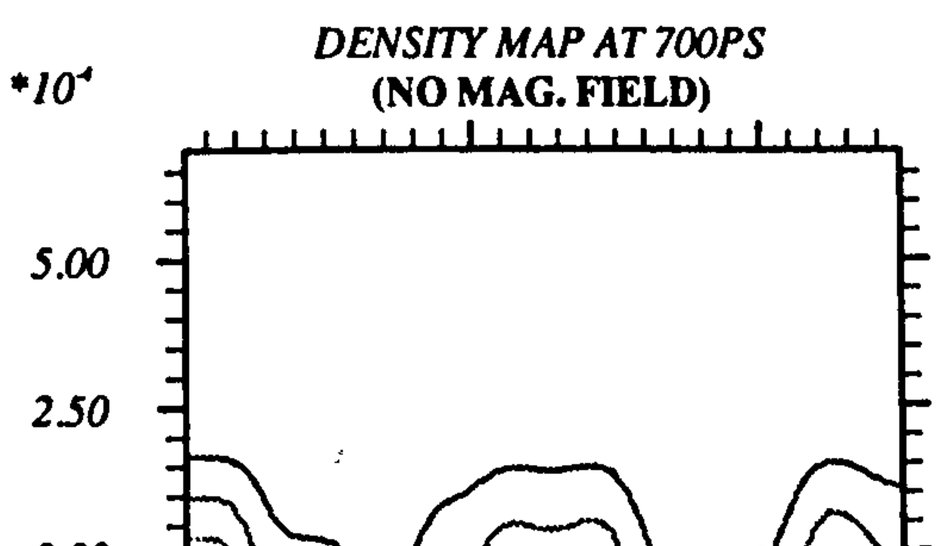
DENSITY MAP AT 700PS
(NO MAG. FIELD)
*10⁻⁴
5.00
2.50
0.00
-2.50
-5.00
-7.50
-10.00
2.00
4.00
*10⁻⁴
0.1
0.3
0.5
0.7
0.9
1.1
1.3
1.5

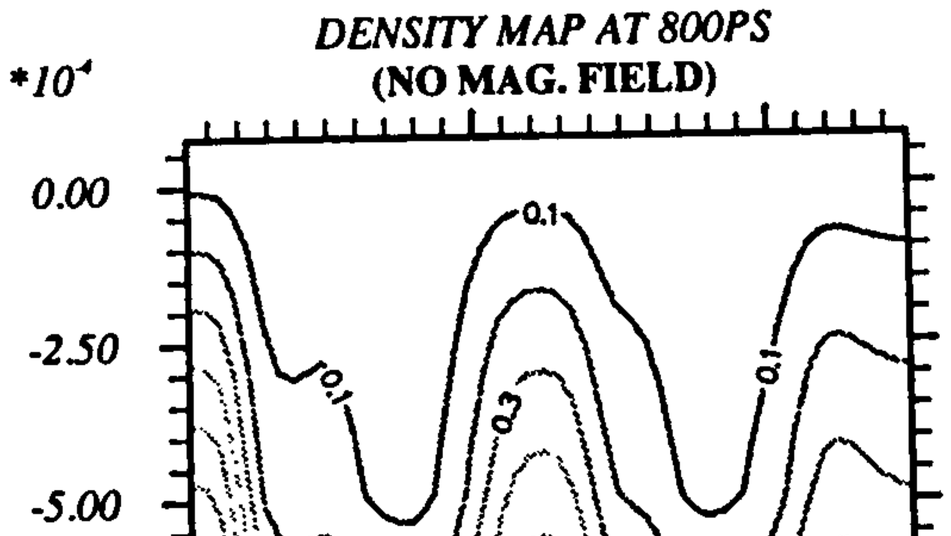
DENSITY MAP AT 800PS
(NO MAG. FIELD)
*10⁻⁴
0.00
-2.50
-5.00
-7.50
-10.00
-12.50
-15.00
2.00
4.00
*10⁻⁴
0.1
0.3
0.5
0.7
0.9
1.1
1.3
1.5

bility. Keeping in mind all these possibilities it was decided to lower the input laser power to see the effect on the instability growth.

We applied this case to a target of size $2 \cdot 5\mu m$ in both directions and the perturbation applied through laser intensity. The simulations are performed with both magnetic field included and excluded with input power of $3 \cdot 0 \times 10^{13} W/cm^2$ leaving all the other parameters exactly the same as in section $6 \cdot 1$.

The density contour maps are shown in figure $7 \cdot 3$ for magnetic field included and excluded on the same page with an interval of 50ps. Neglecting the magnetic field, it is observed from these results that until 400ps the instability growth is not significant. But for the field on simulations the growth is very fast and until reaching 400ps the instability has grown up to a level where the laser has penetrated into the target on the outer edge of the target. As time progresses further breaking and mixing of the target continues and at 600ps most of the target material is burnt through. In the no field case the target burn is approximately at the same level as for the field included simulations but the Rayleigh-Taylor instability does not start dominating until 500ps and long spike and bubbles are formed at 700ps whereas at the same time for field on simulations target is completely broken through.

The amplitude time graph is shown in figure $7 \cdot 4$. It is observed that with no field simulations the amplitude growth is very slow until 400ps and after that it increases very rapidly and for the field on case the instability grows very quickly until 300ps and after that it is not easy to measure the exact growth amplitude as the target mixing start taking place. Comparing these results with figure $6 \cdot 2$, it is observed that the pattern of the growth of instability is similar in both cases. The difference between these is that with less power the growth is slower compared to the results in section 6.1 as expected as the acceleration is less. The maximum field vs time and maximum plasma beta -time graphs are shown in figures $7 \cdot 5$ and $7 \cdot 6$ to show how these vary with time.

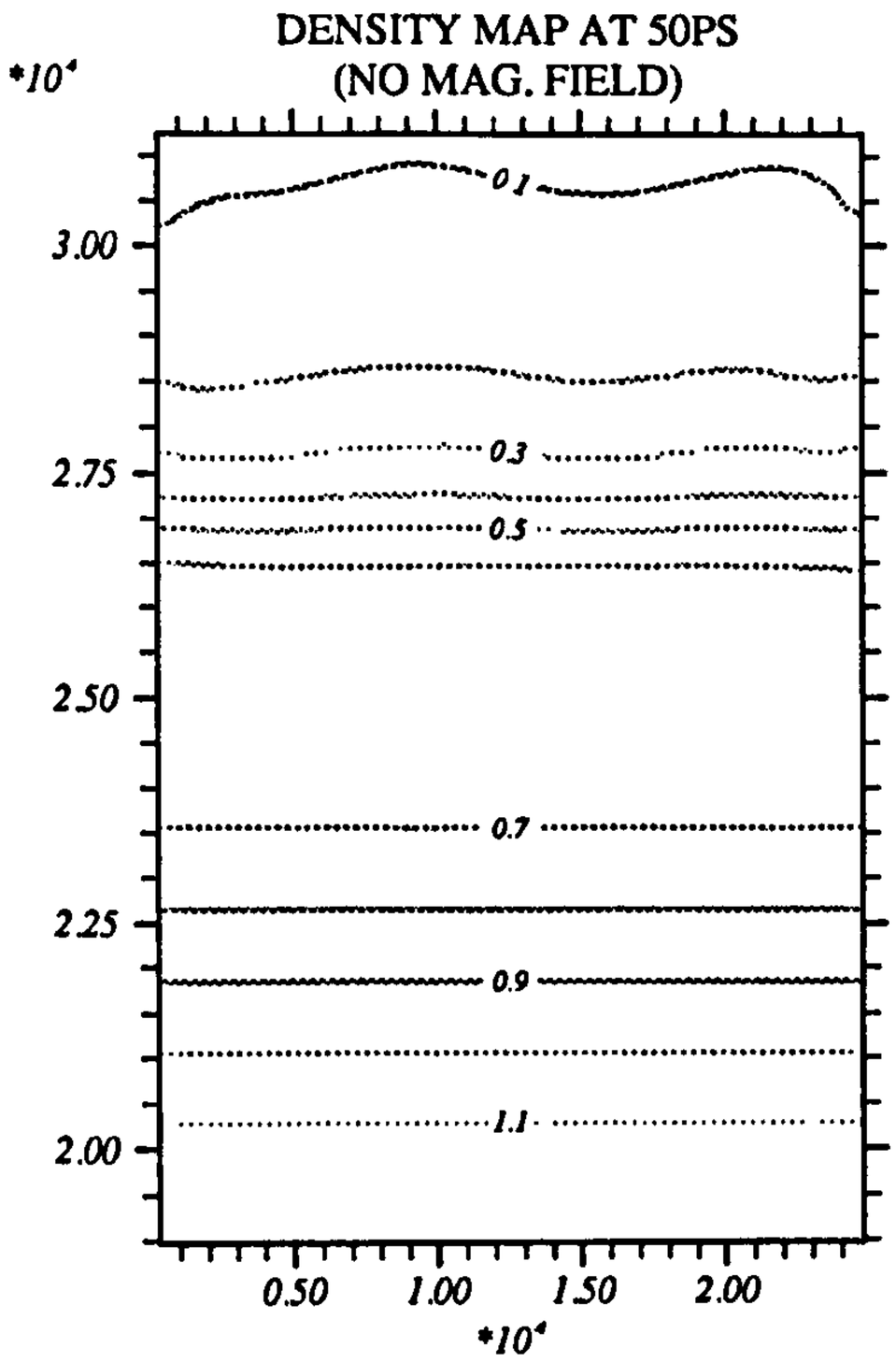

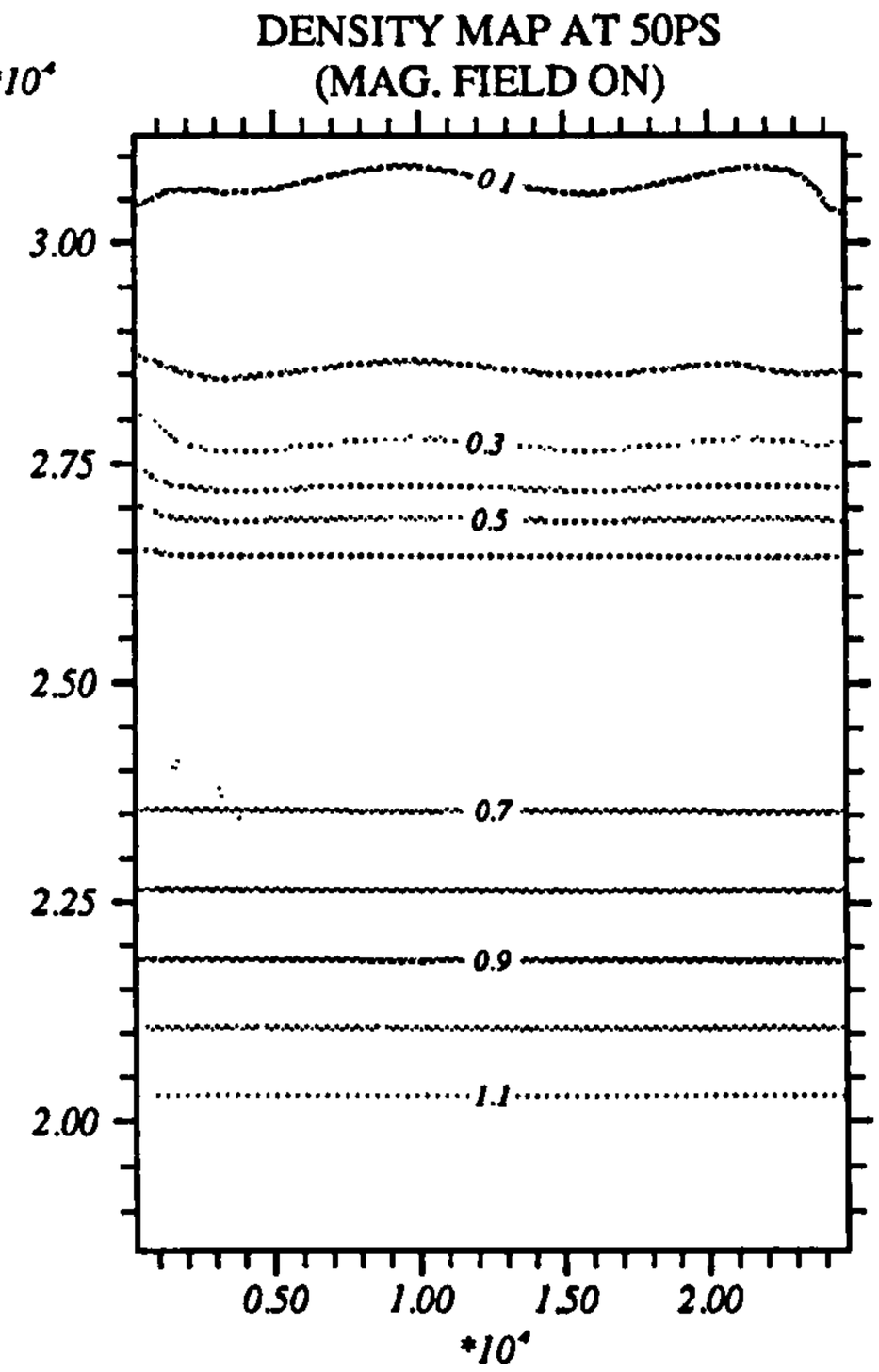

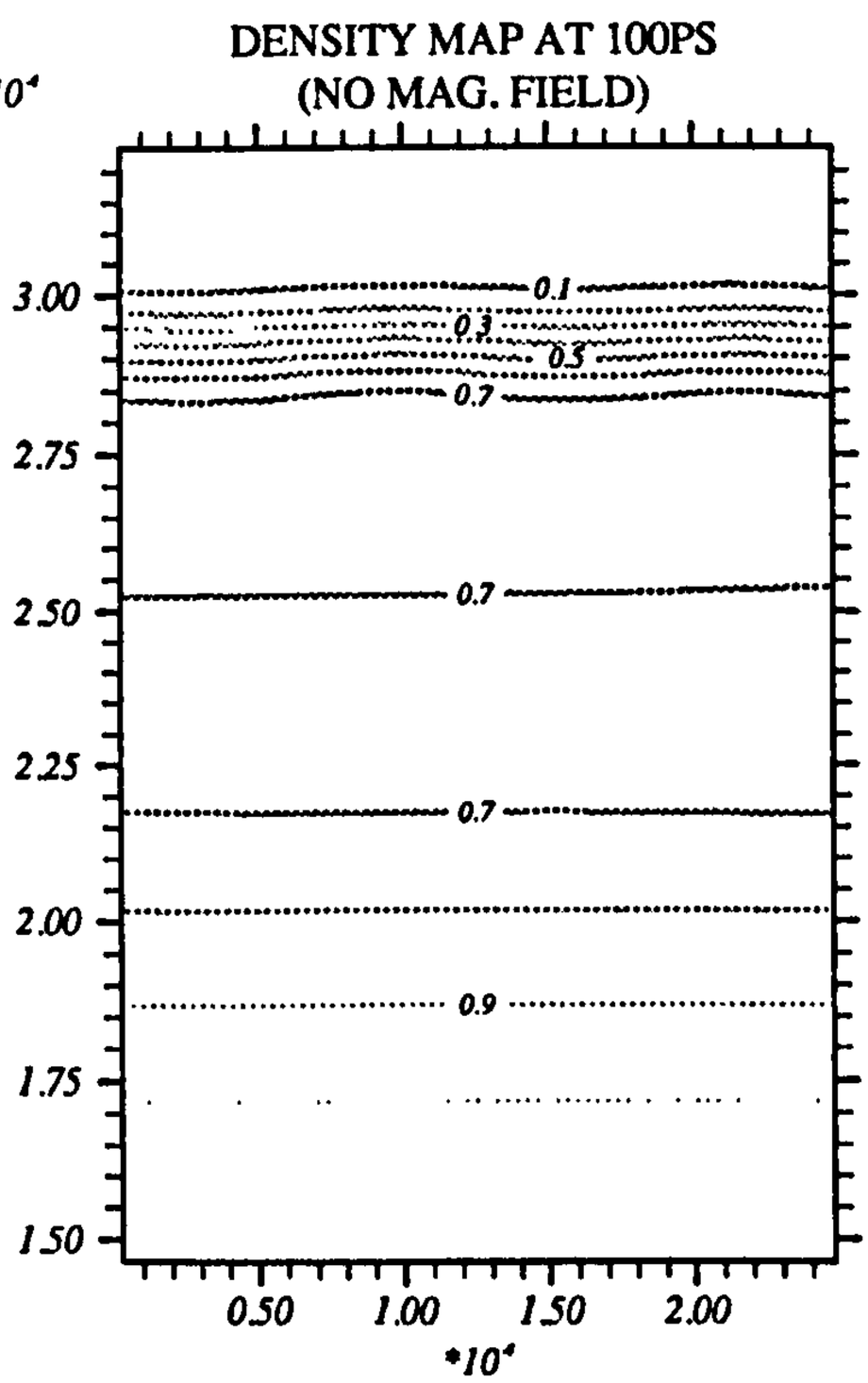

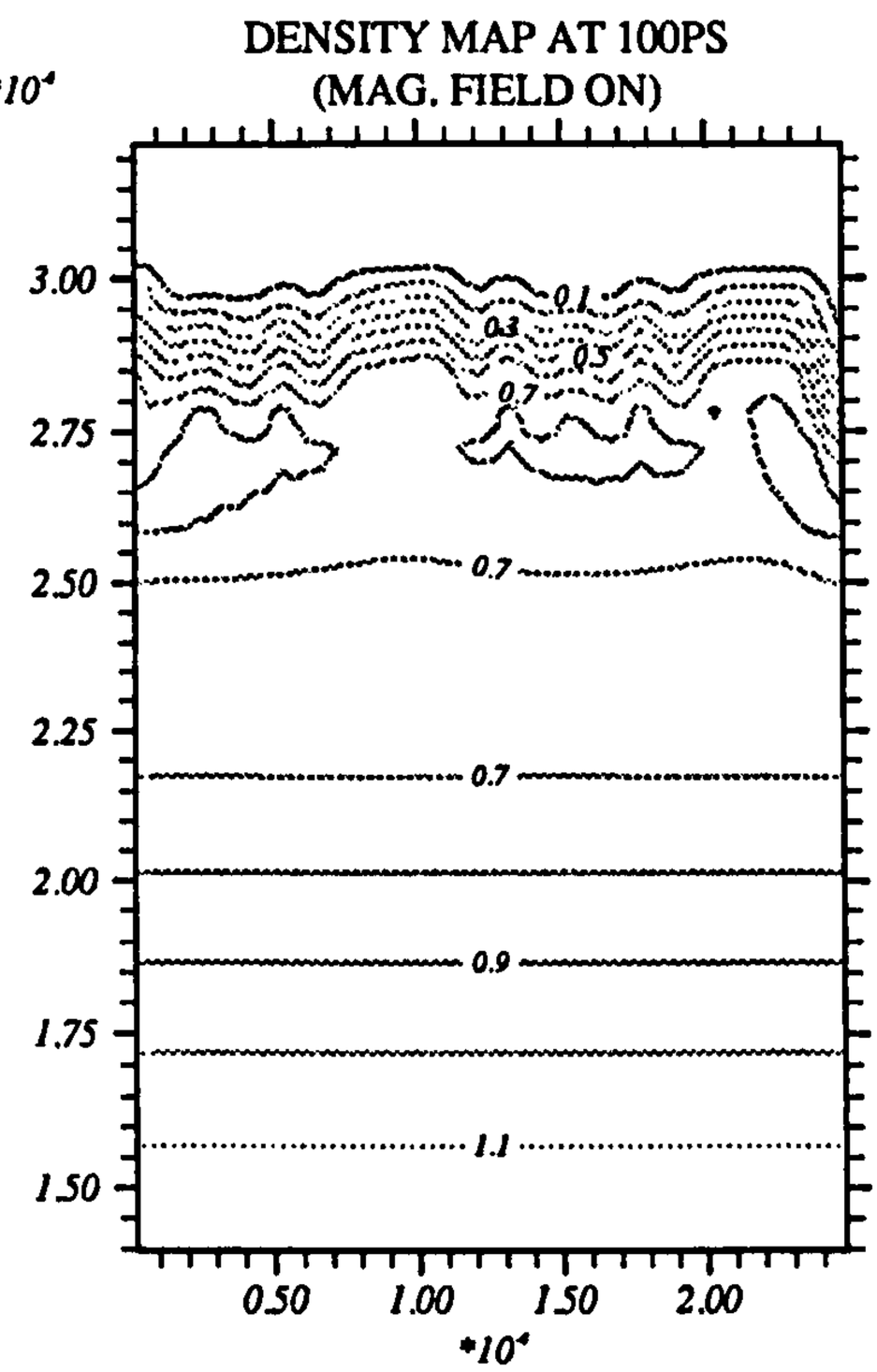

Figure 7.3: Density contour map for the target of $(2 \cdot 5\mu m \times 2 \cdot 5\mu m)$ with the laser power $3 \cdot 0 \times 10^{13} W/cm^2$.

DENSITY MAP AT 150PS
(NO MAG. FIELD)

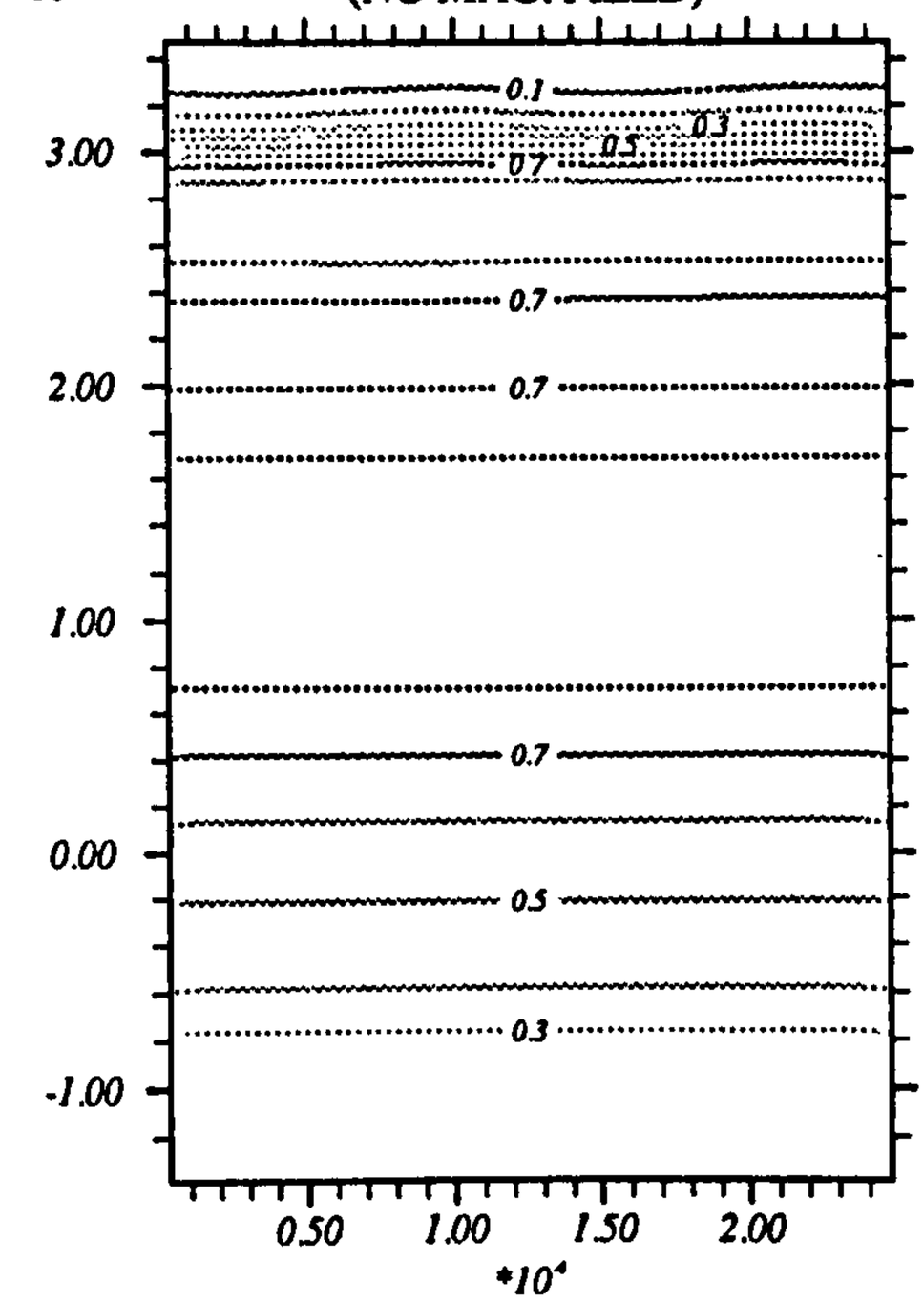

DENSITY MAP AT 150PS
(MAG. FIELD ON)

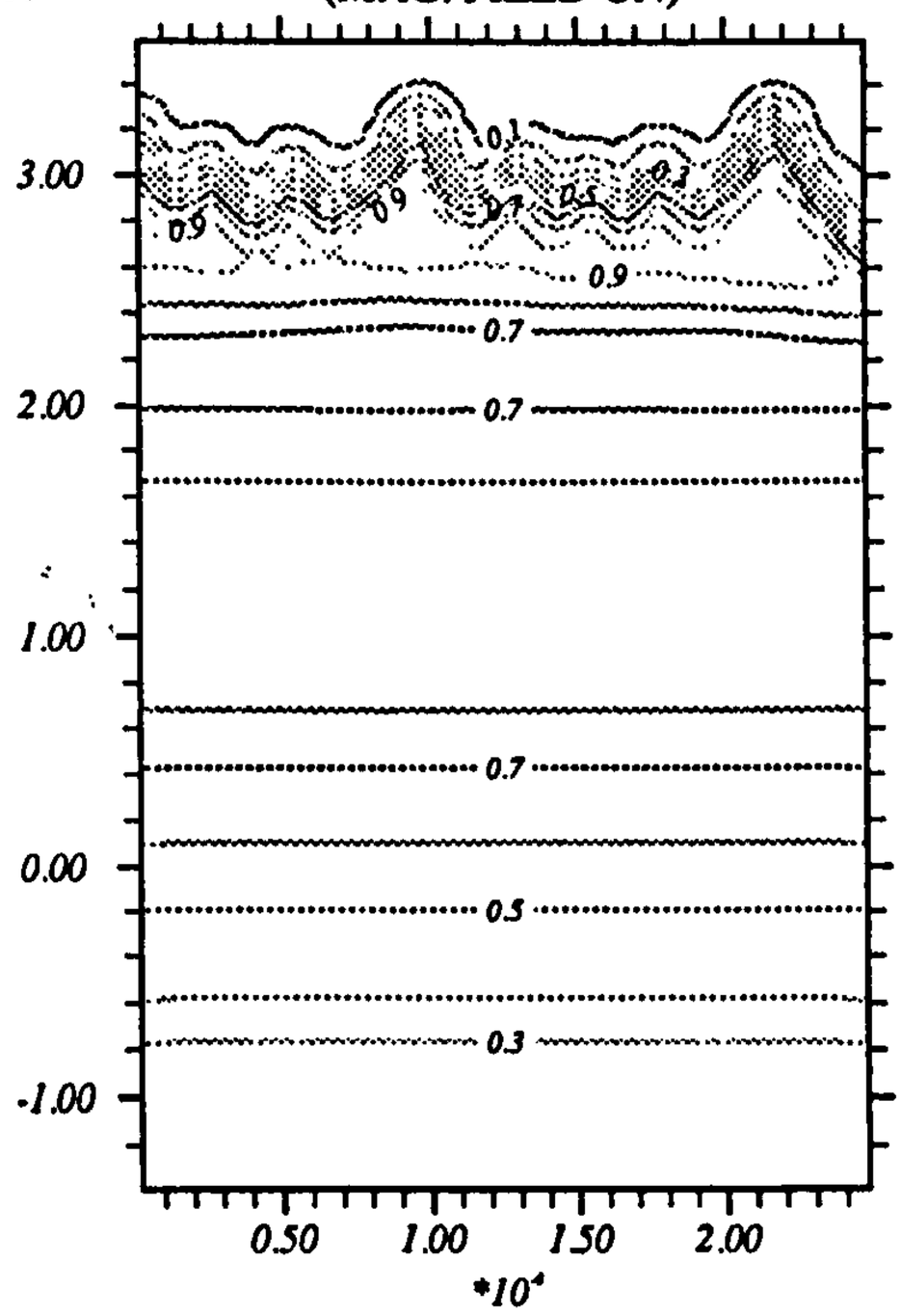

DENSITY MAP AT 200PS
(NO MAG. FIELD)

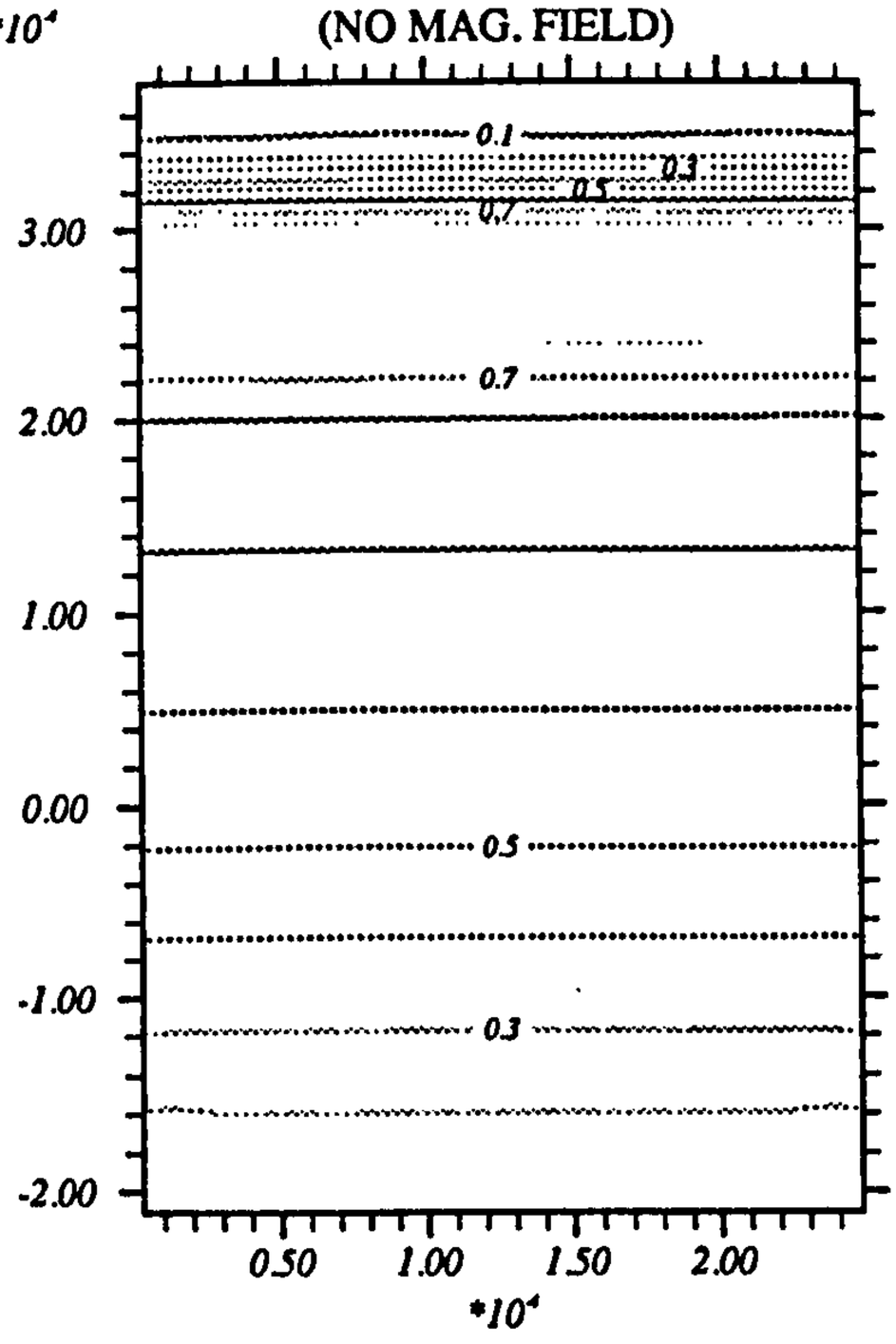

DENSITY MAP AT 200PS
(MAG. FIELD ON)

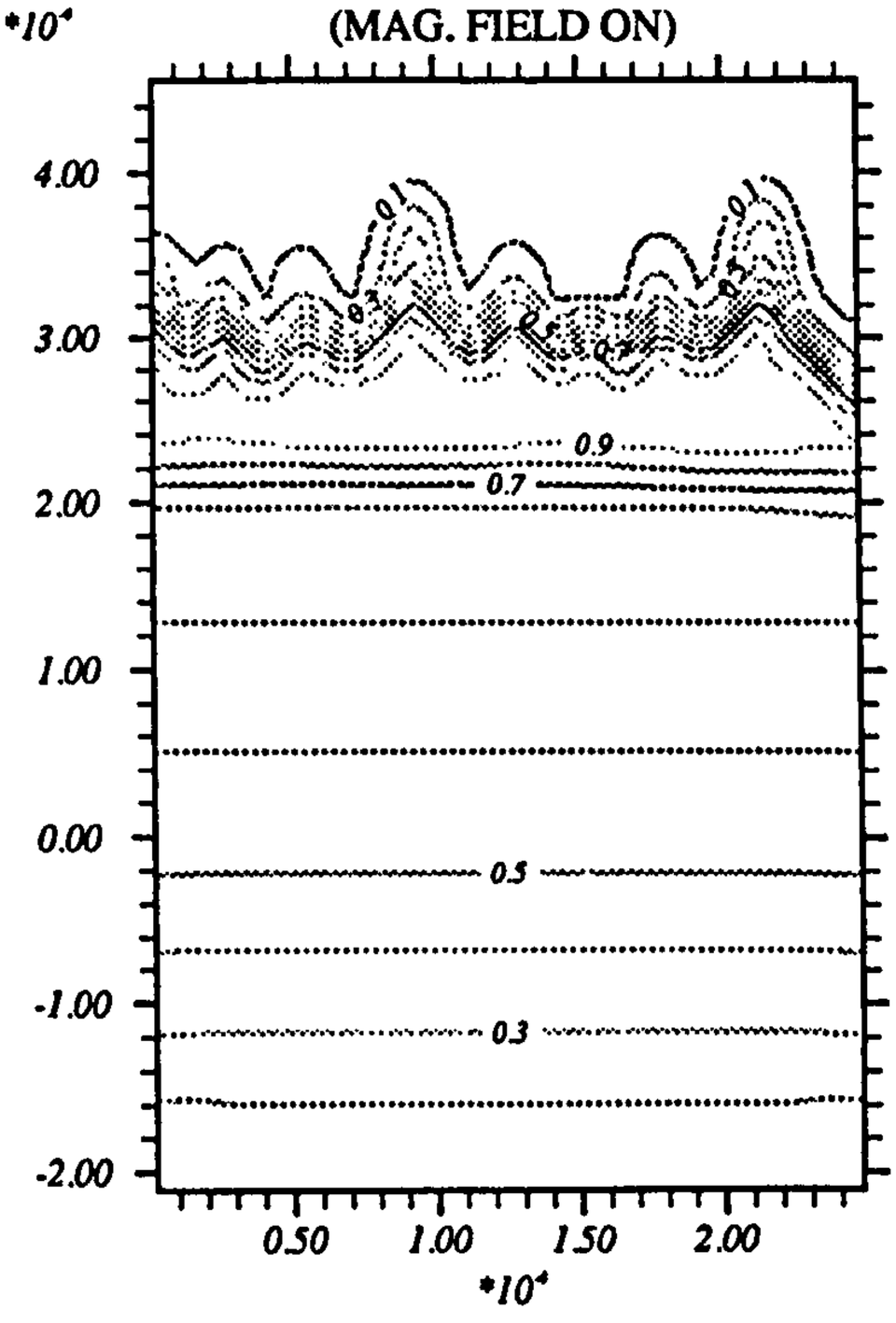

DENSITY MAP AT 250PS
(NO MAG. FIELD)

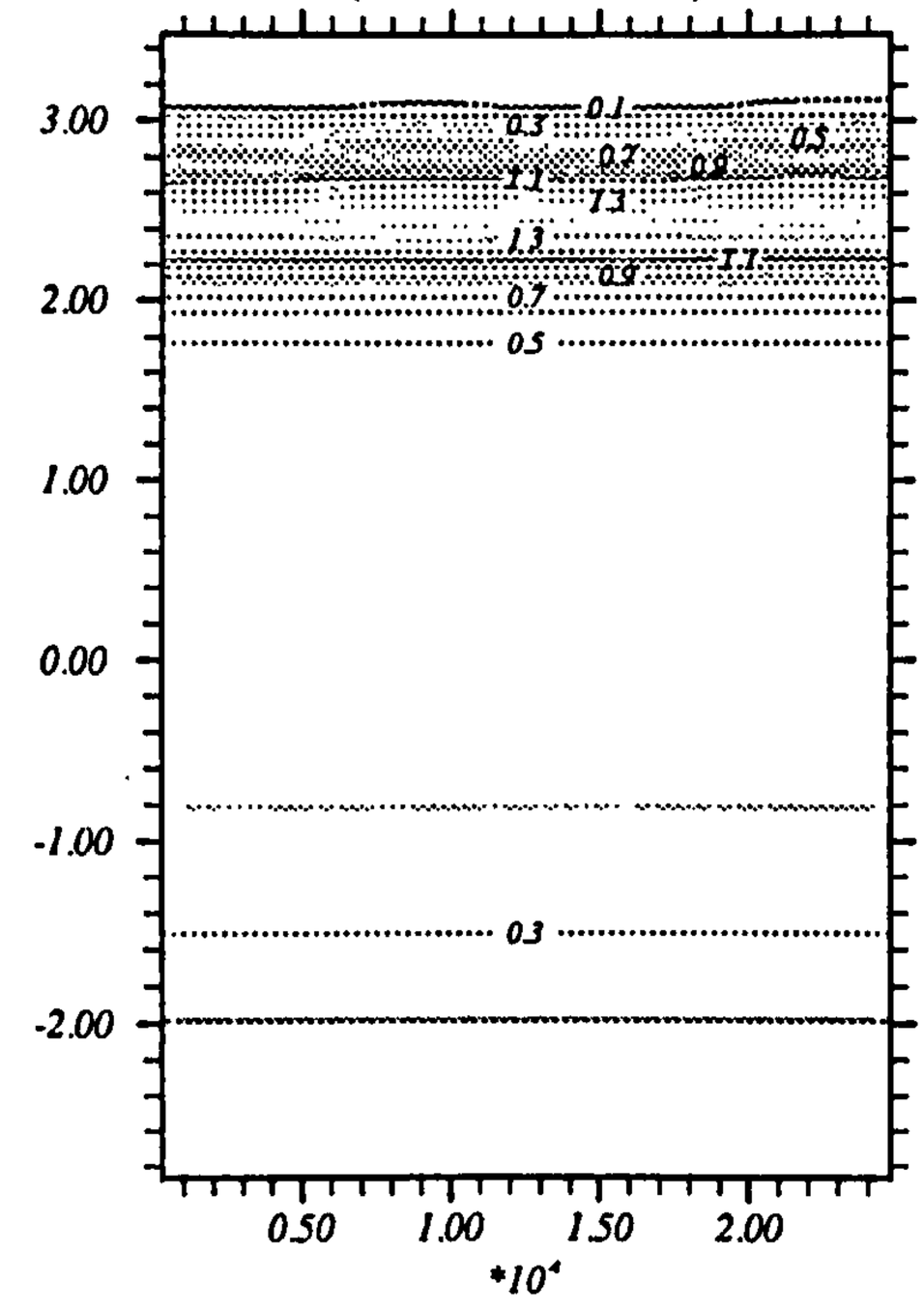

DENSITY MAP AT 250PS
(MAG. FIELD ON)

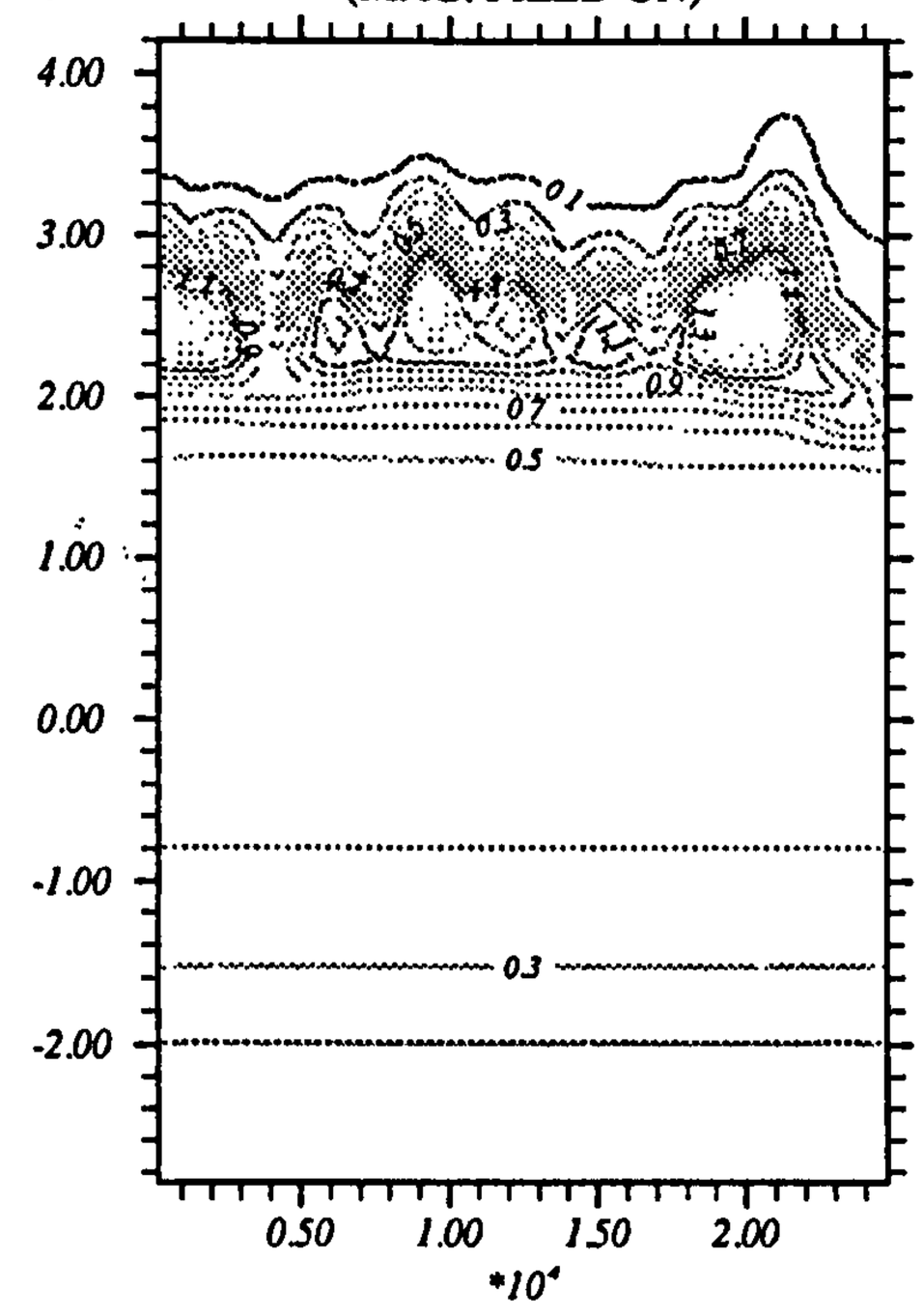

DENSITY MAP AT 300PS
(NO MAG. FIELD)

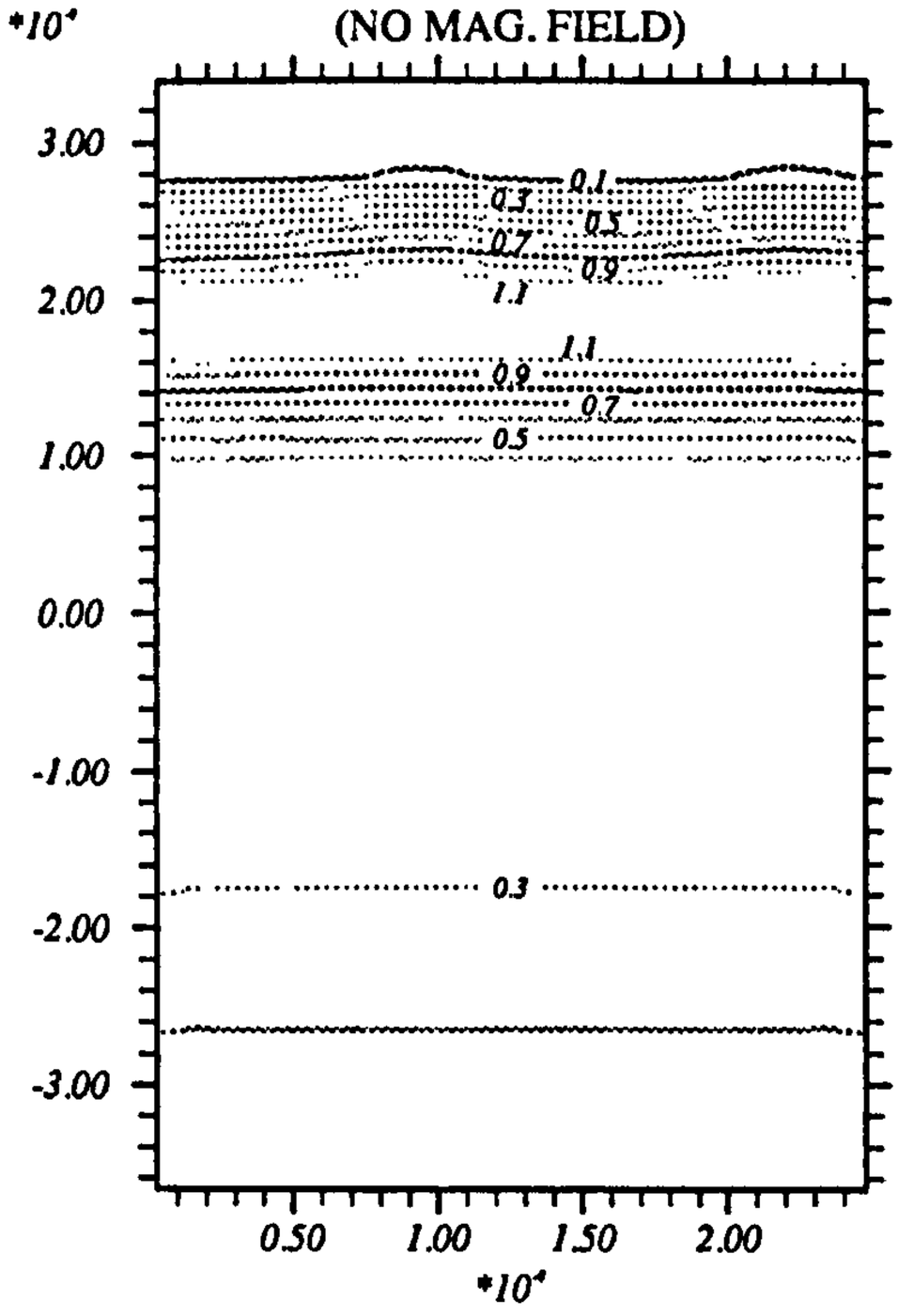

DENSITY MAP AT 300PS
(MAG. FIELD ON)

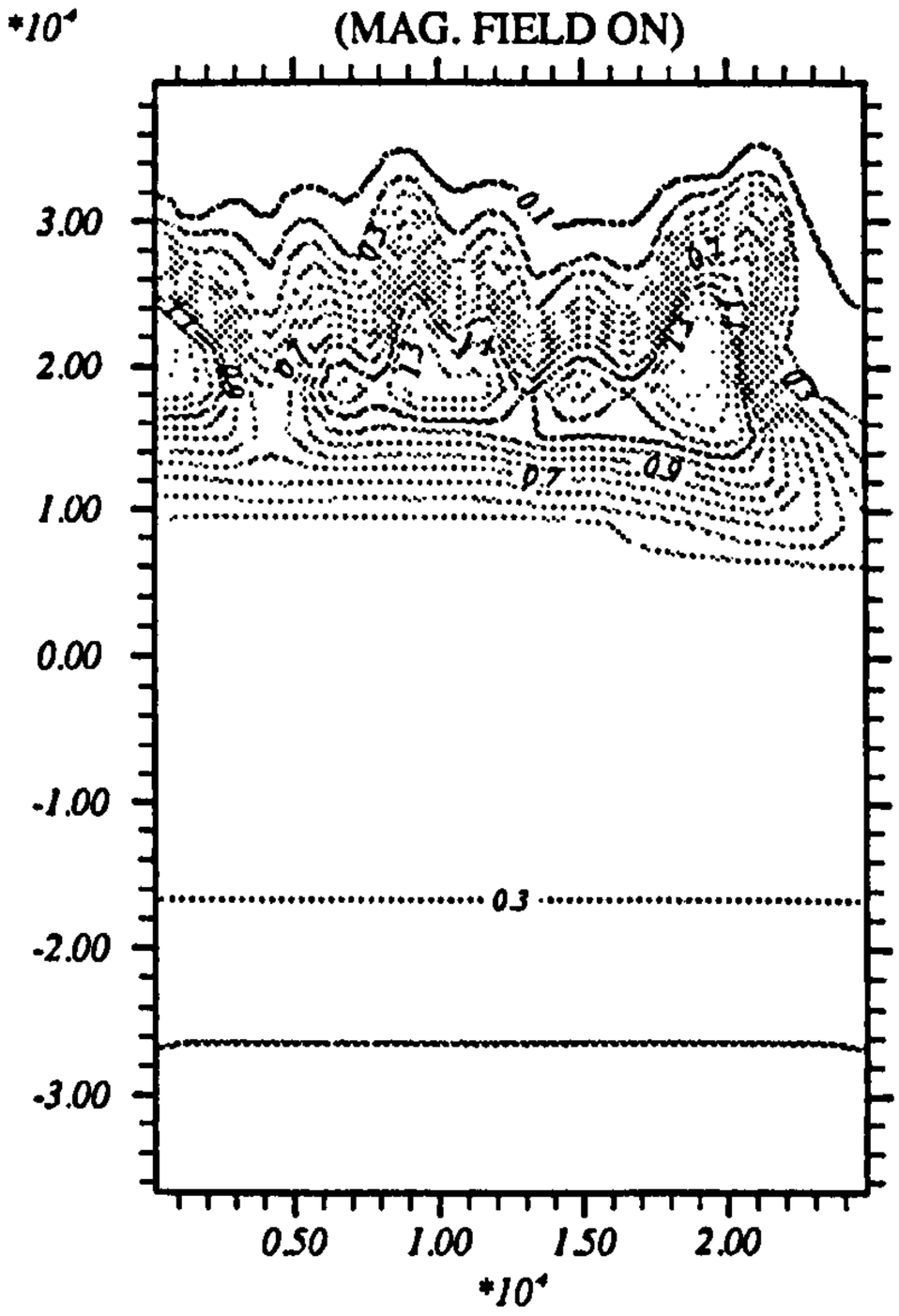

DENSITY MAP AT 350PS
(NO MAG. FIELD)

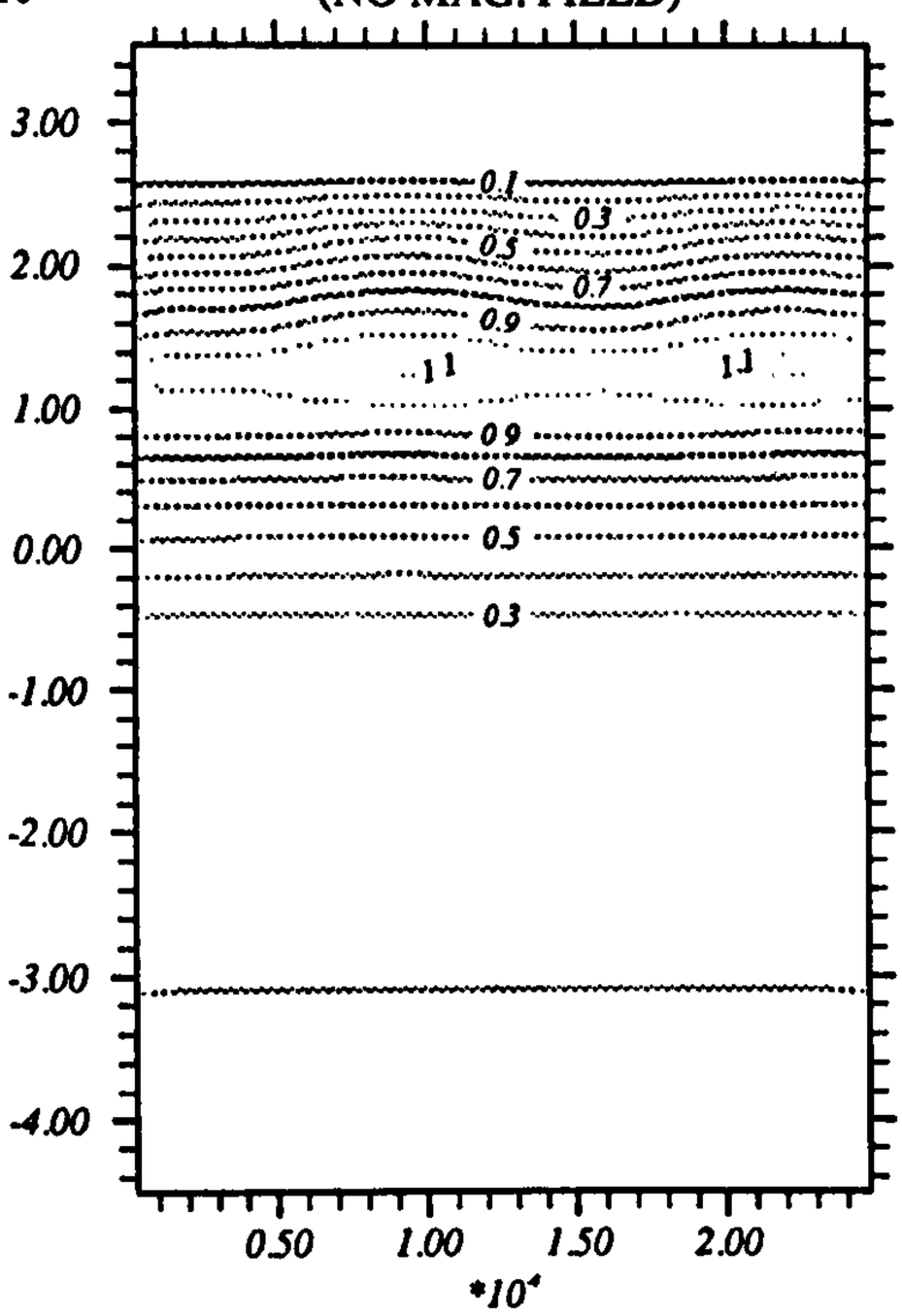

DENSITY MAP AT 350PS
(MAG. FIELD ON)

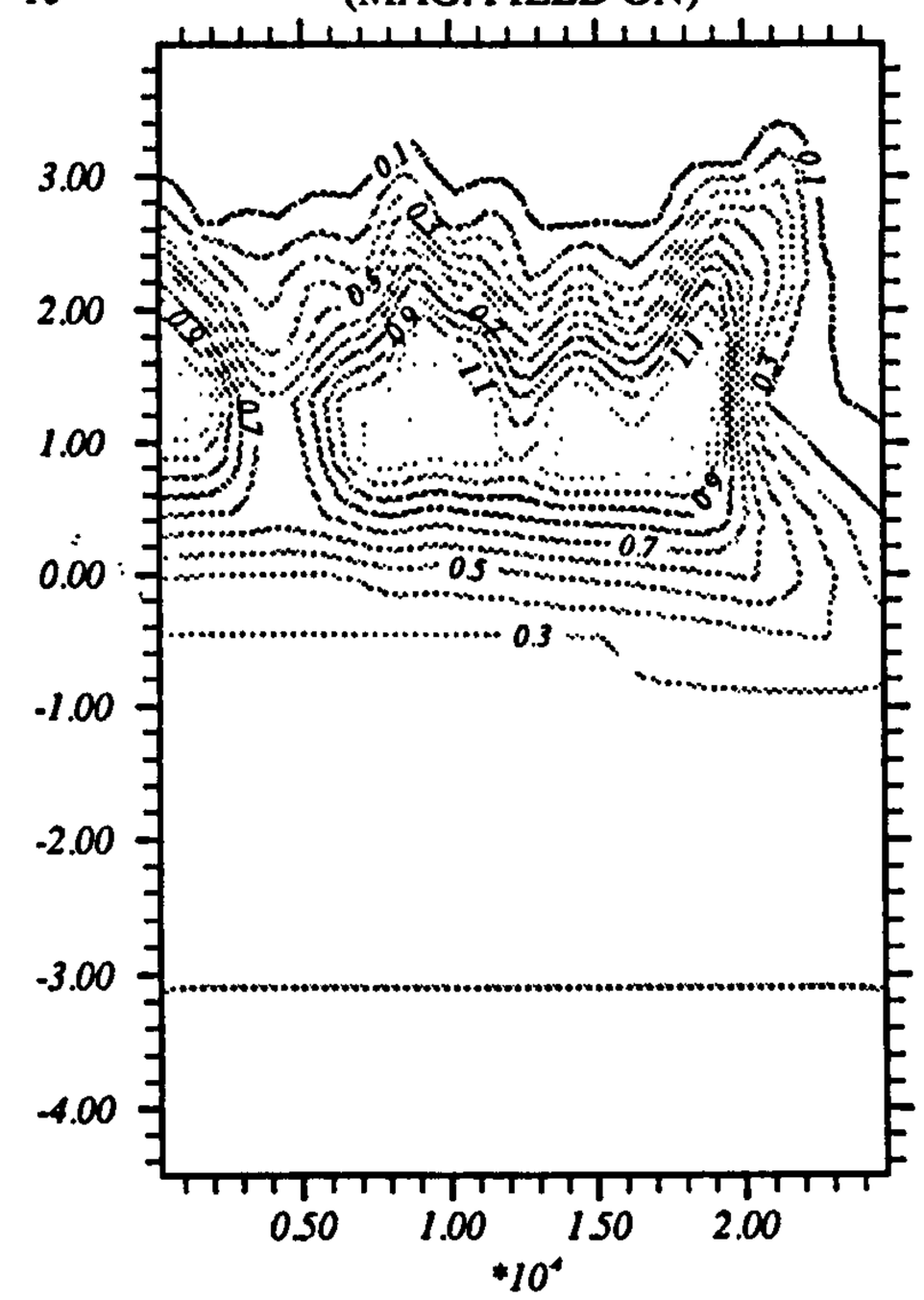

DENSITY MAP AT 400PS
(NO MAG. FIELD)

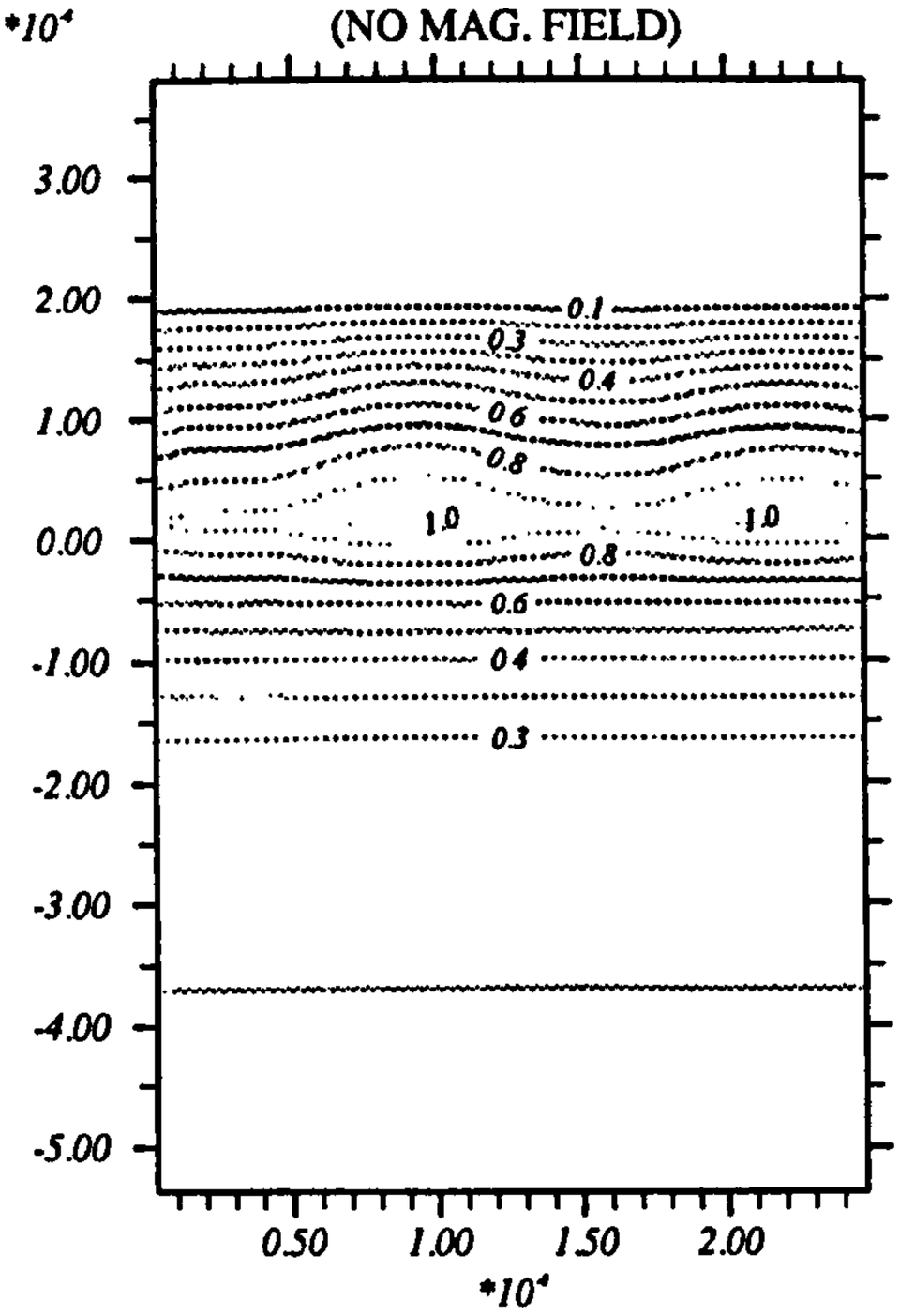

DENSITY MAP AT 400PS
(MAG. FIELD ON)

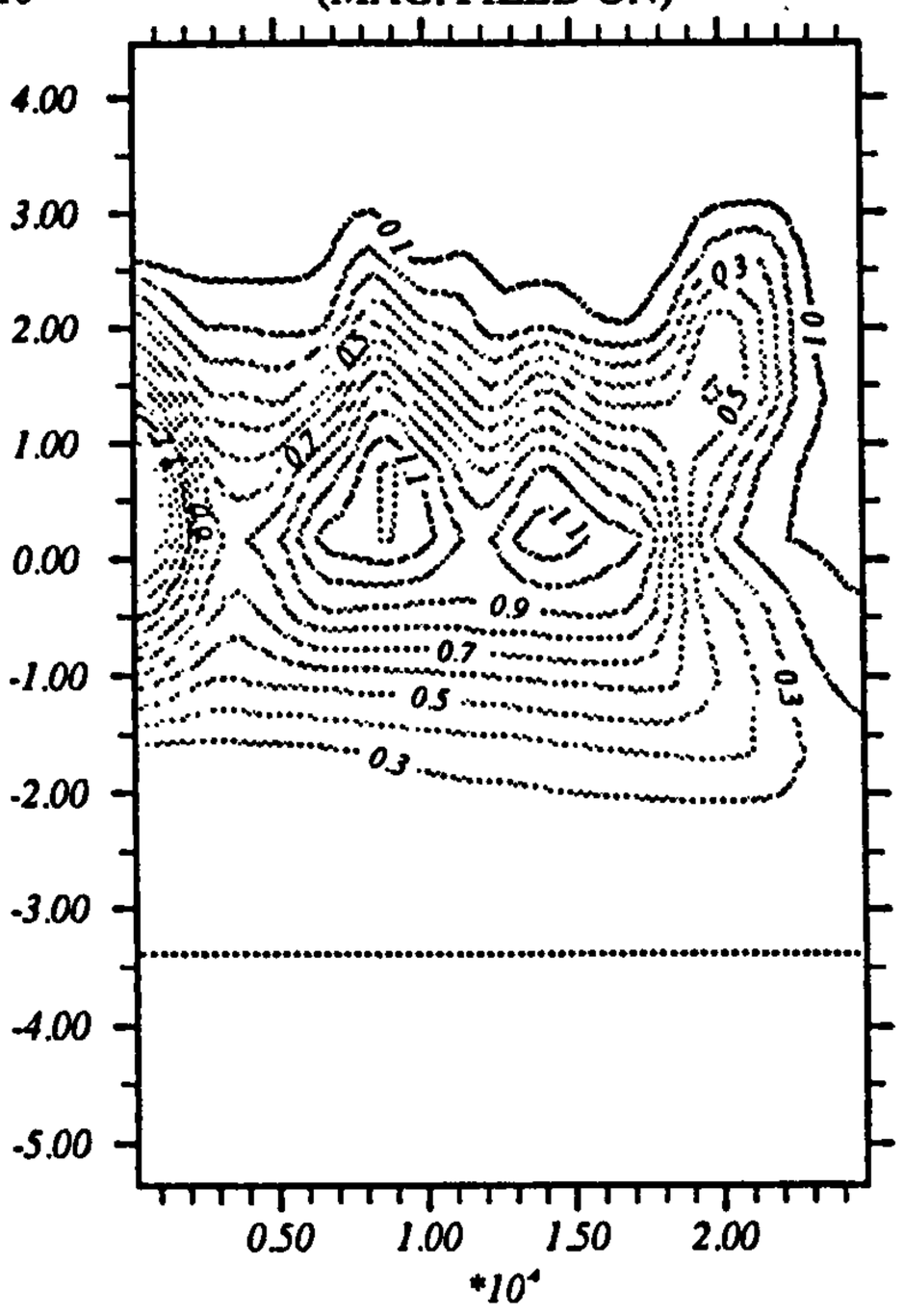

DENSITY MAP AT 450PS
(NO MAG. FIELD)

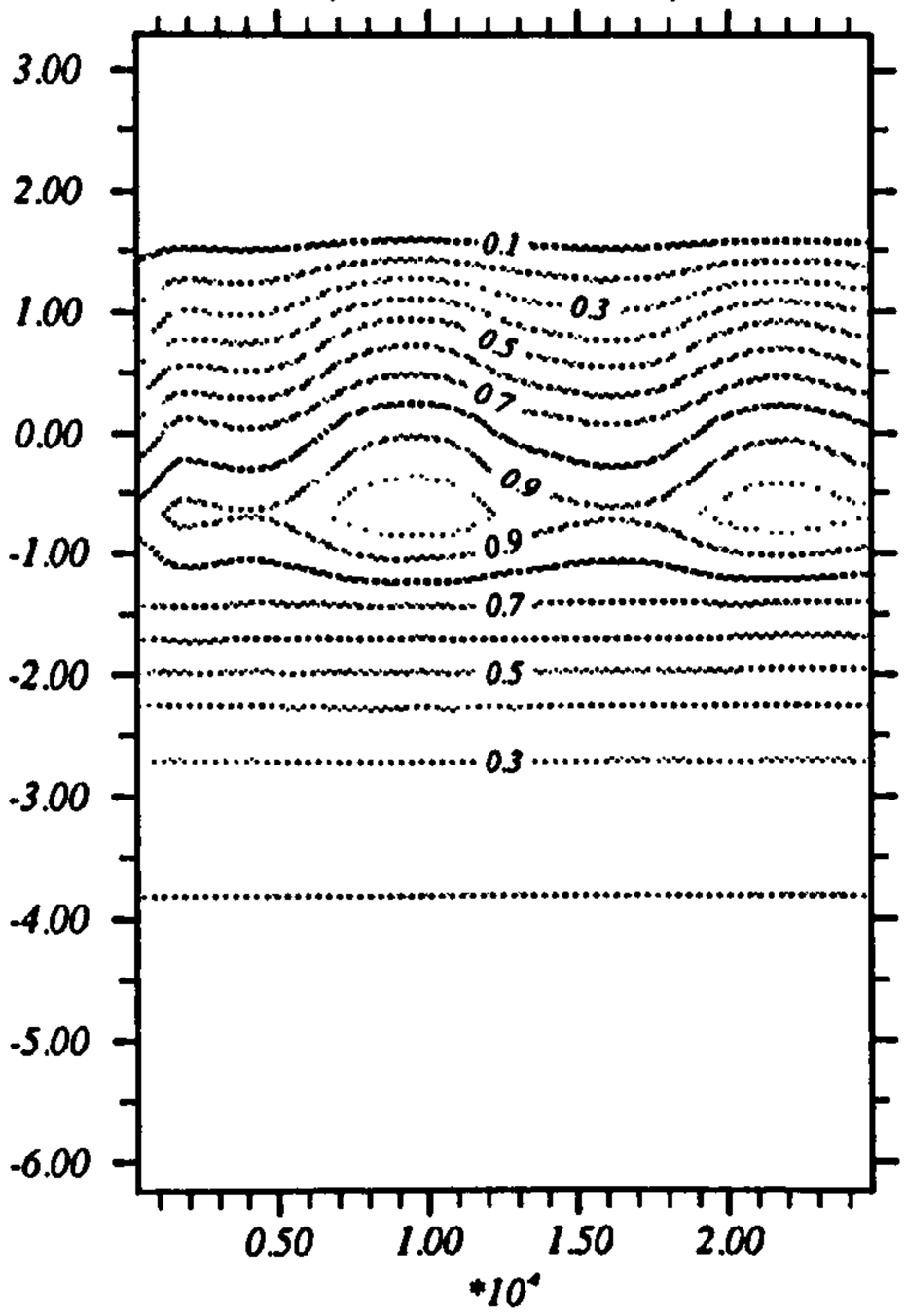

DENSITY MAP AT 450PS
(MAG. FIELD ON)

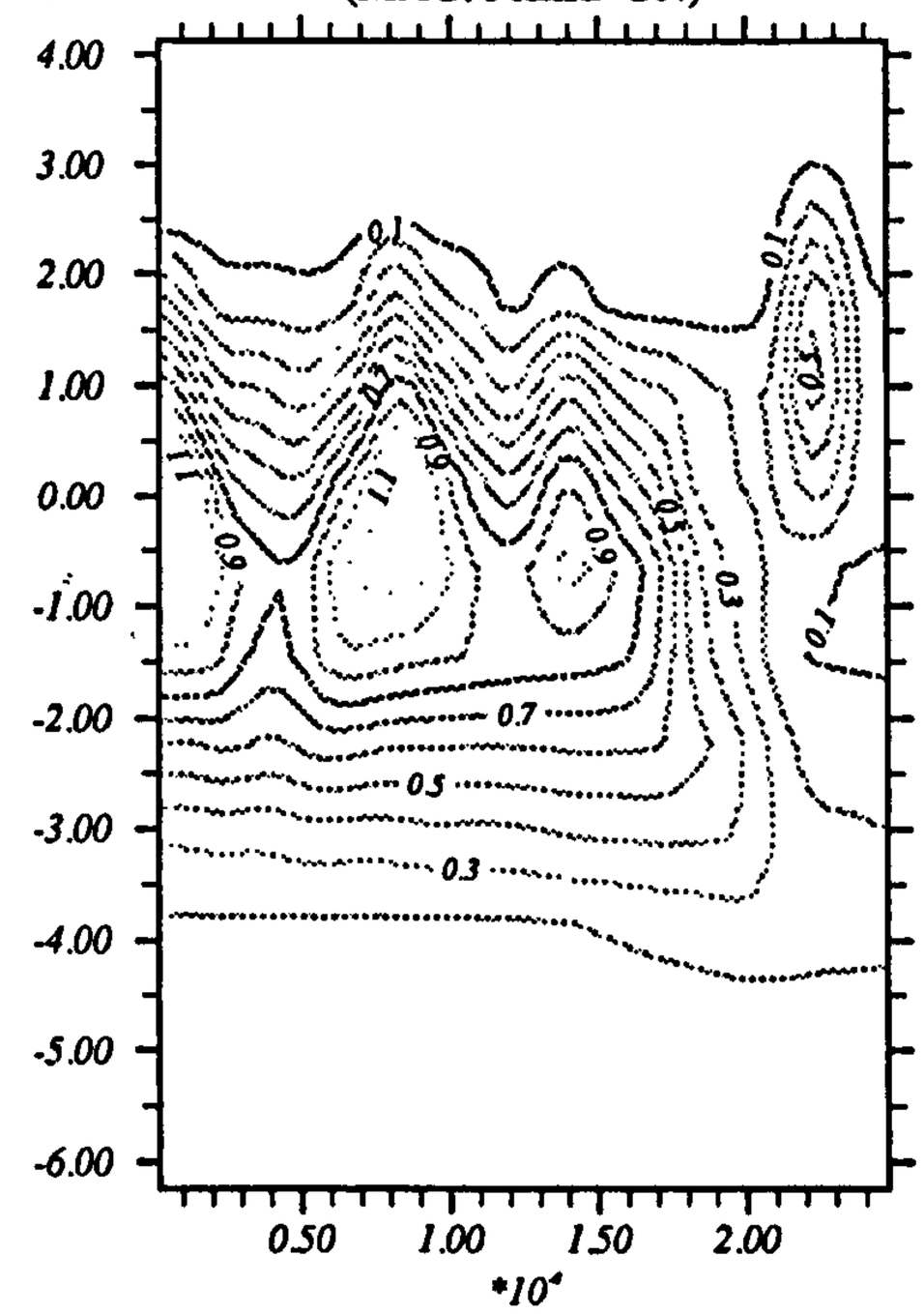

DENSITY MAP AT 500PS
(NO MAG. FIELD)

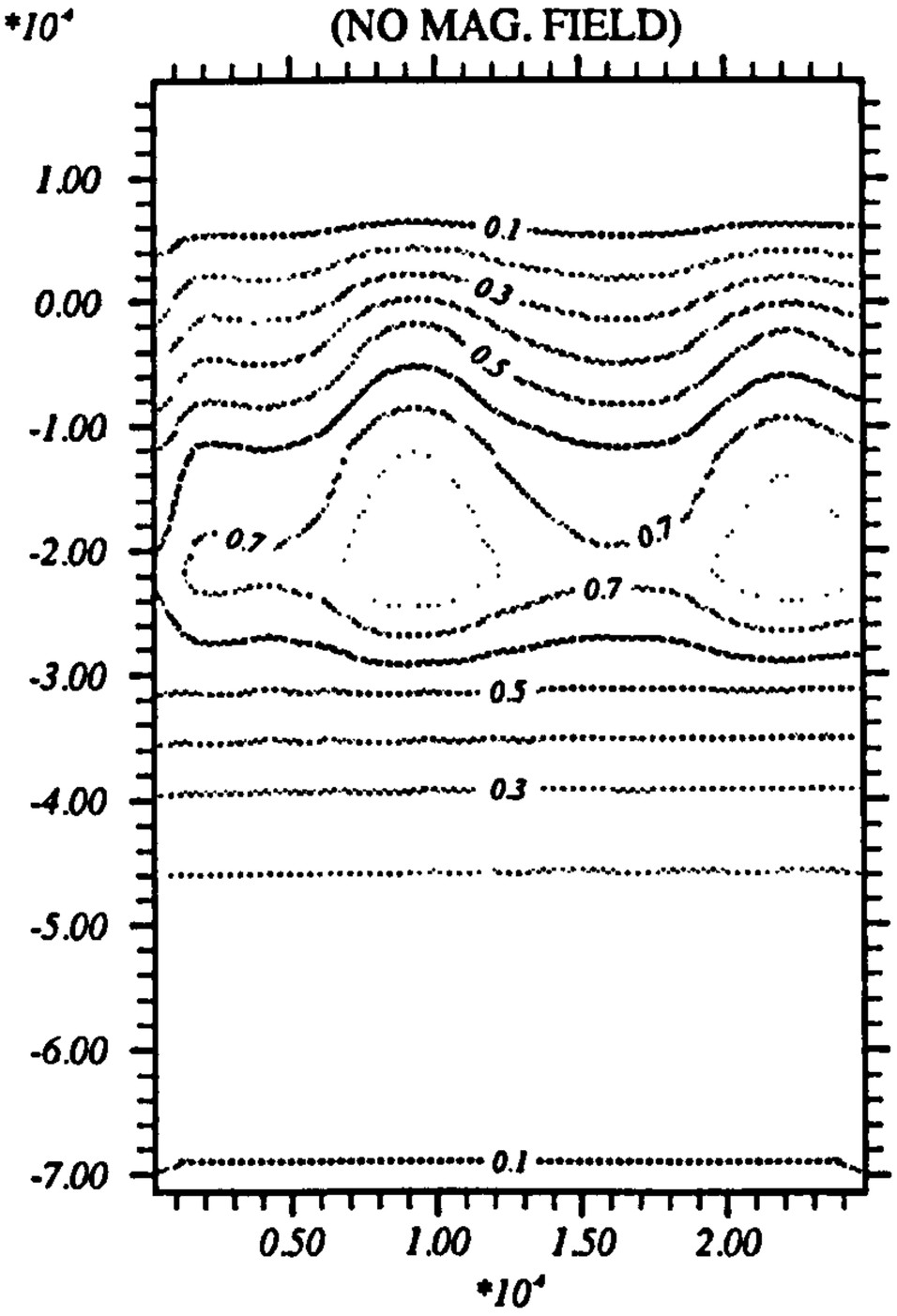

DENSITY MAP AT 500PS
(MAG. FIELD ON)

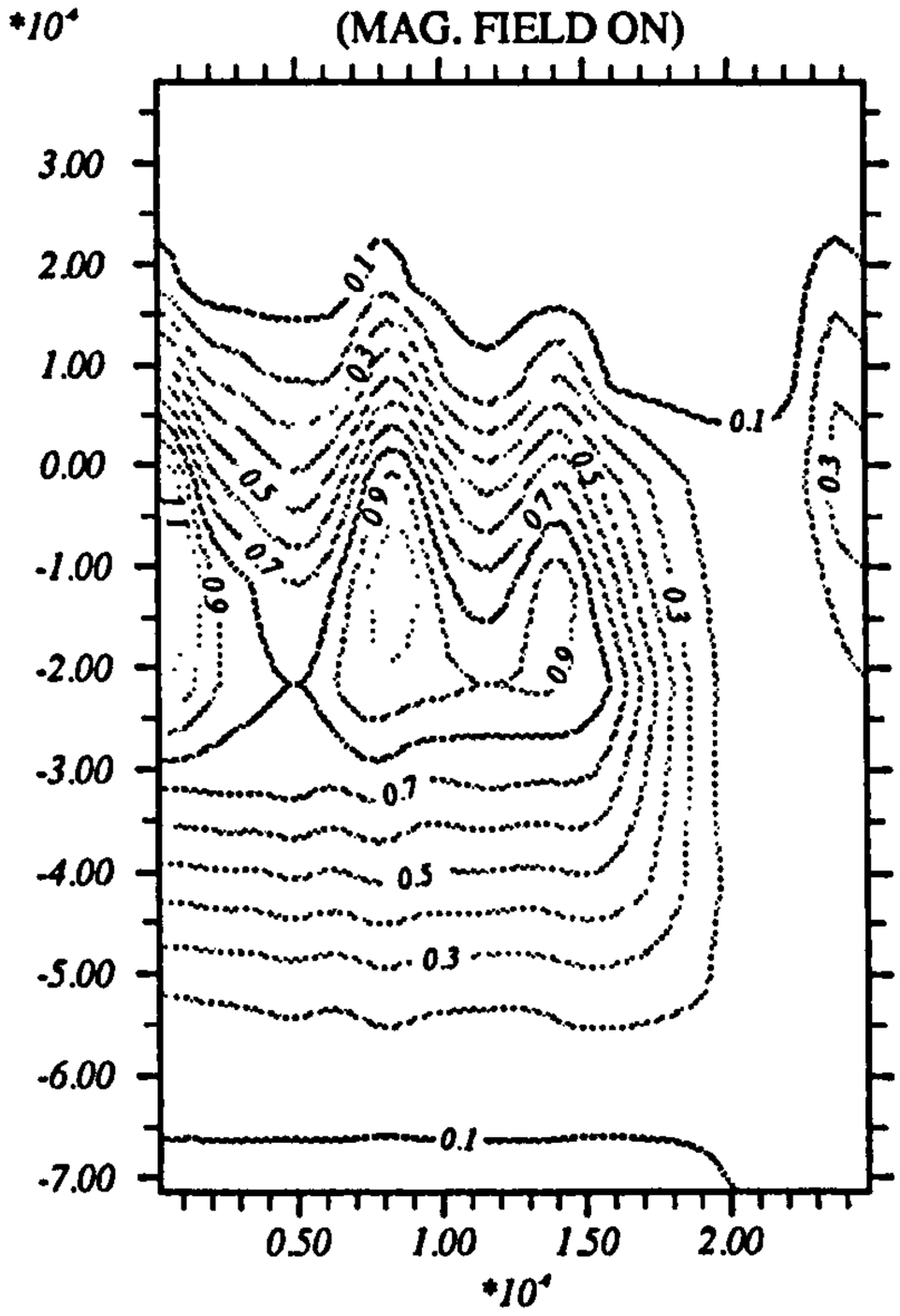

DENSITY MAP AT 550PS
(NO MAG. FIELD)

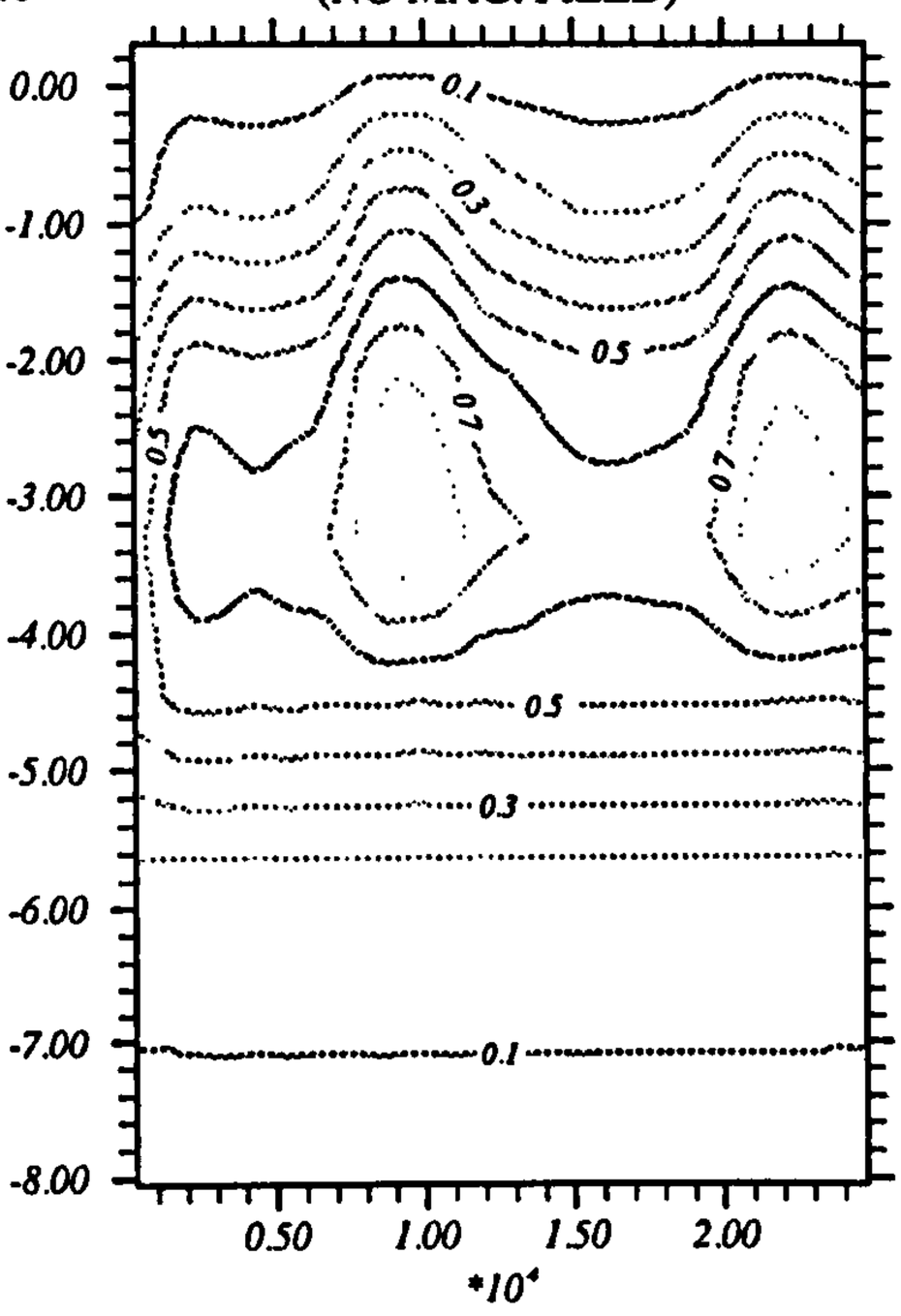

DENSITY MAP AT 550PS
(MAG. FIELD ON)

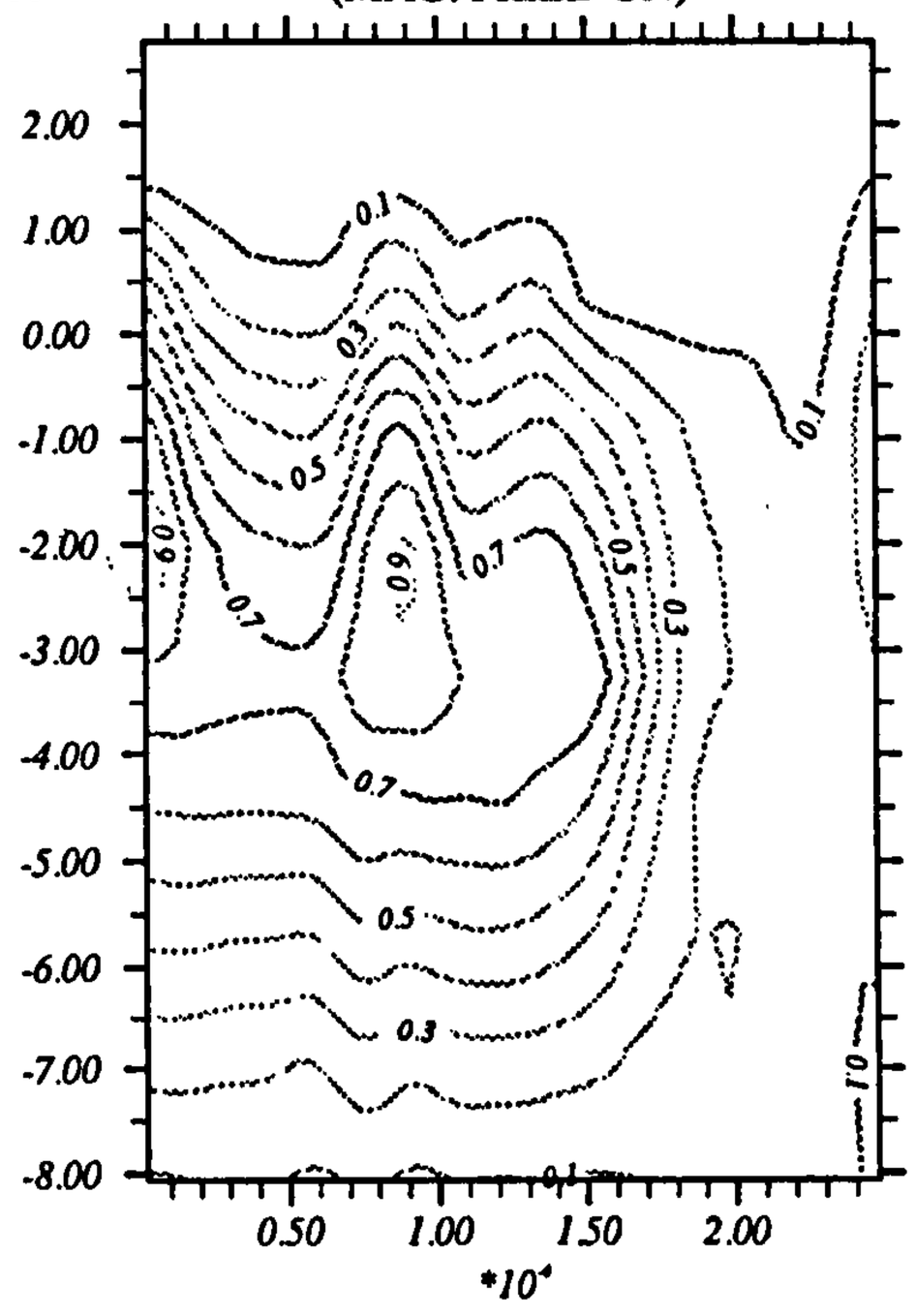

DENSITY MAP AT 600PS
(NO MAG. FIELD)

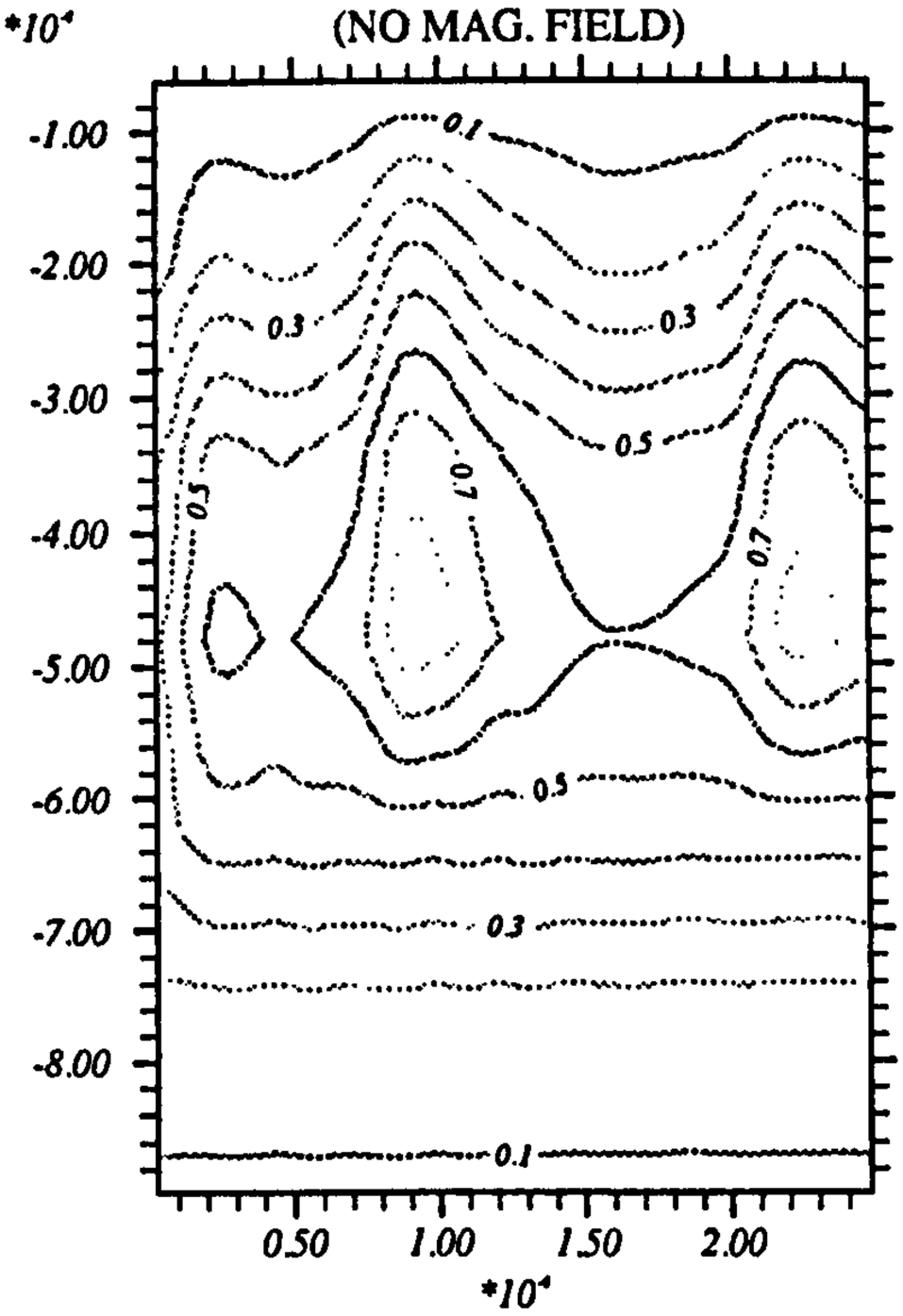

DENSITY MAP AT 600PS
(MAG. FIELD ON)

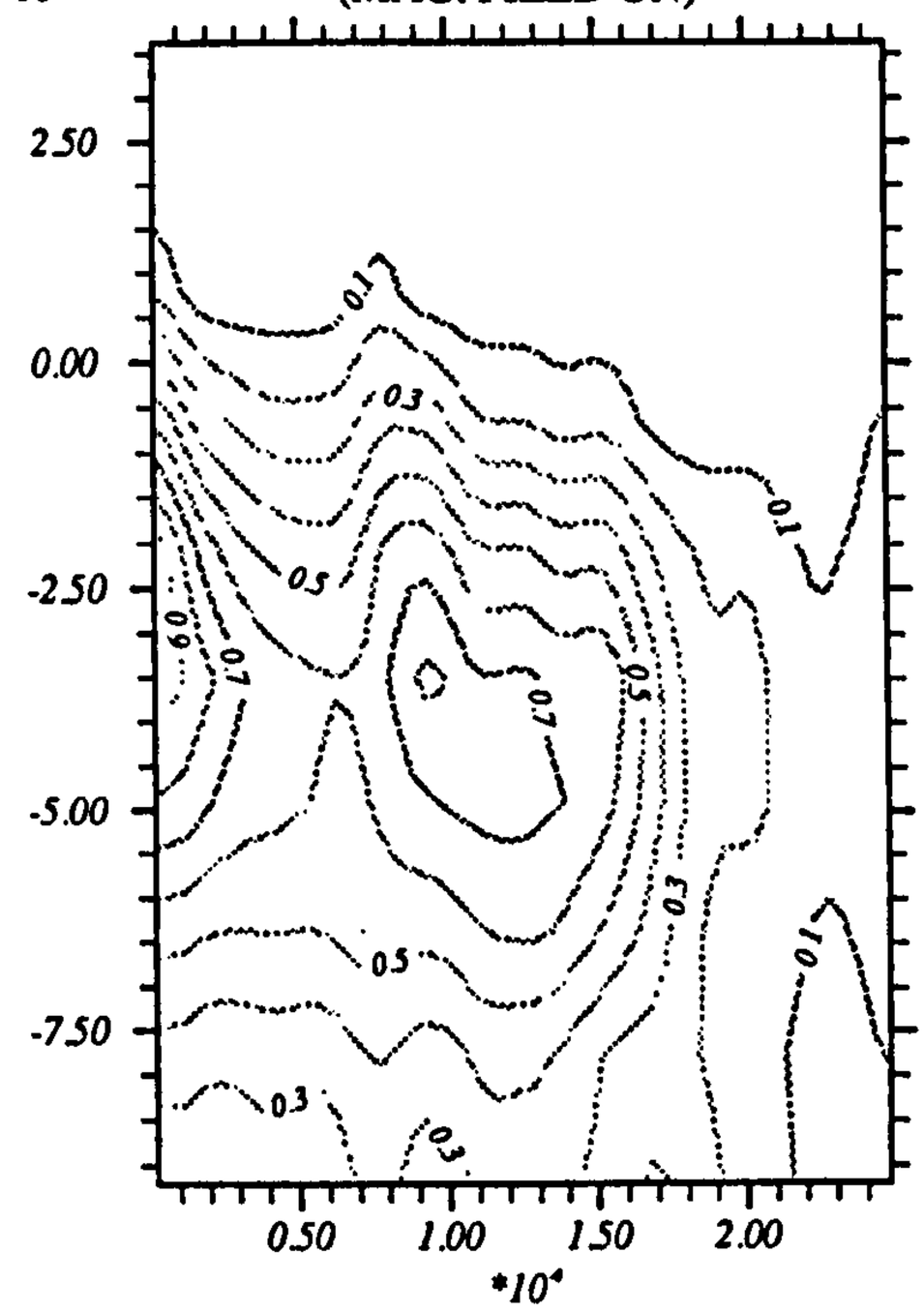

DENSITY MAP AT 650PS
(NO MAG. FIELD)

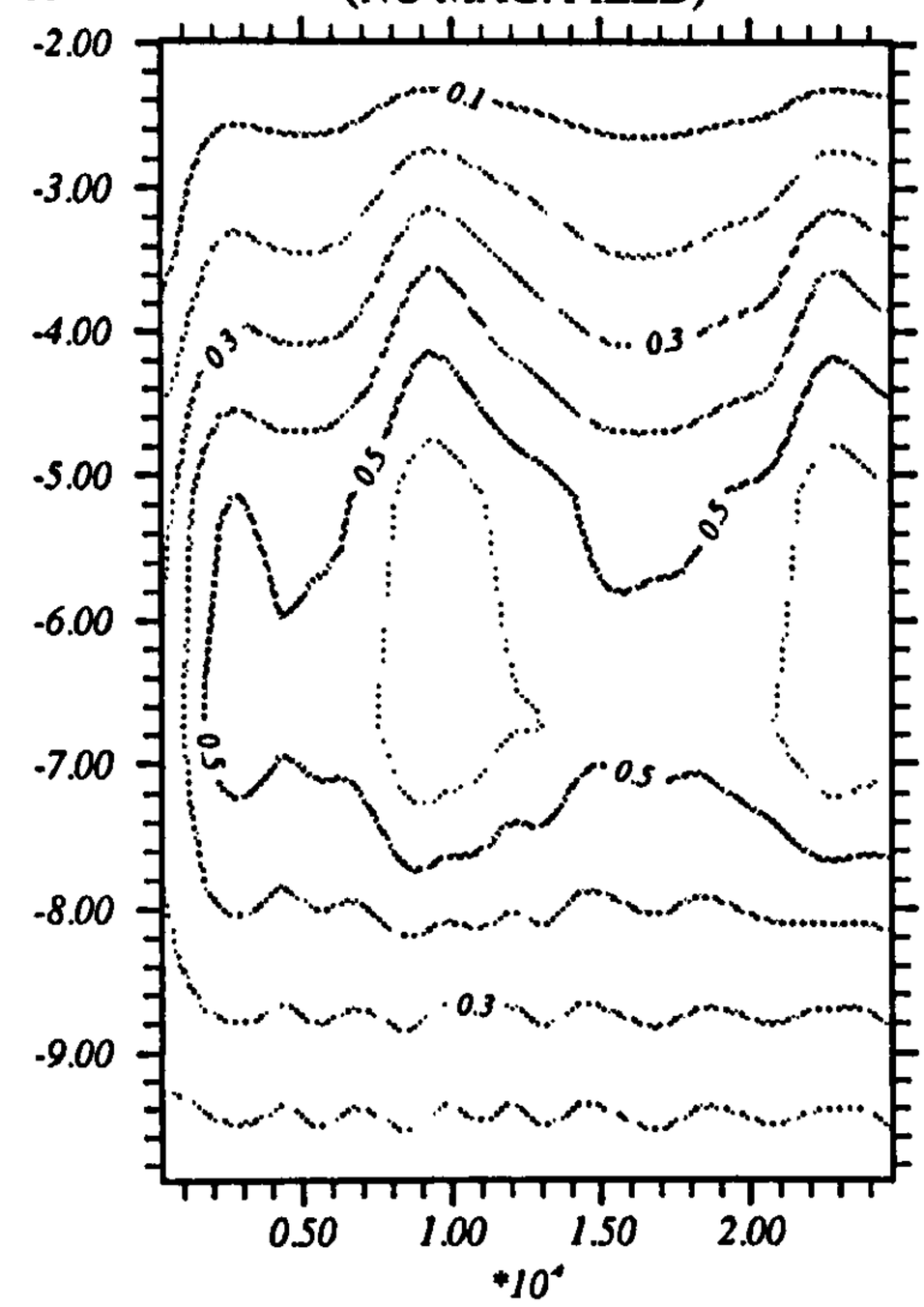

DENSITY MAP AT 650PS
(MAG. FIELD ON)

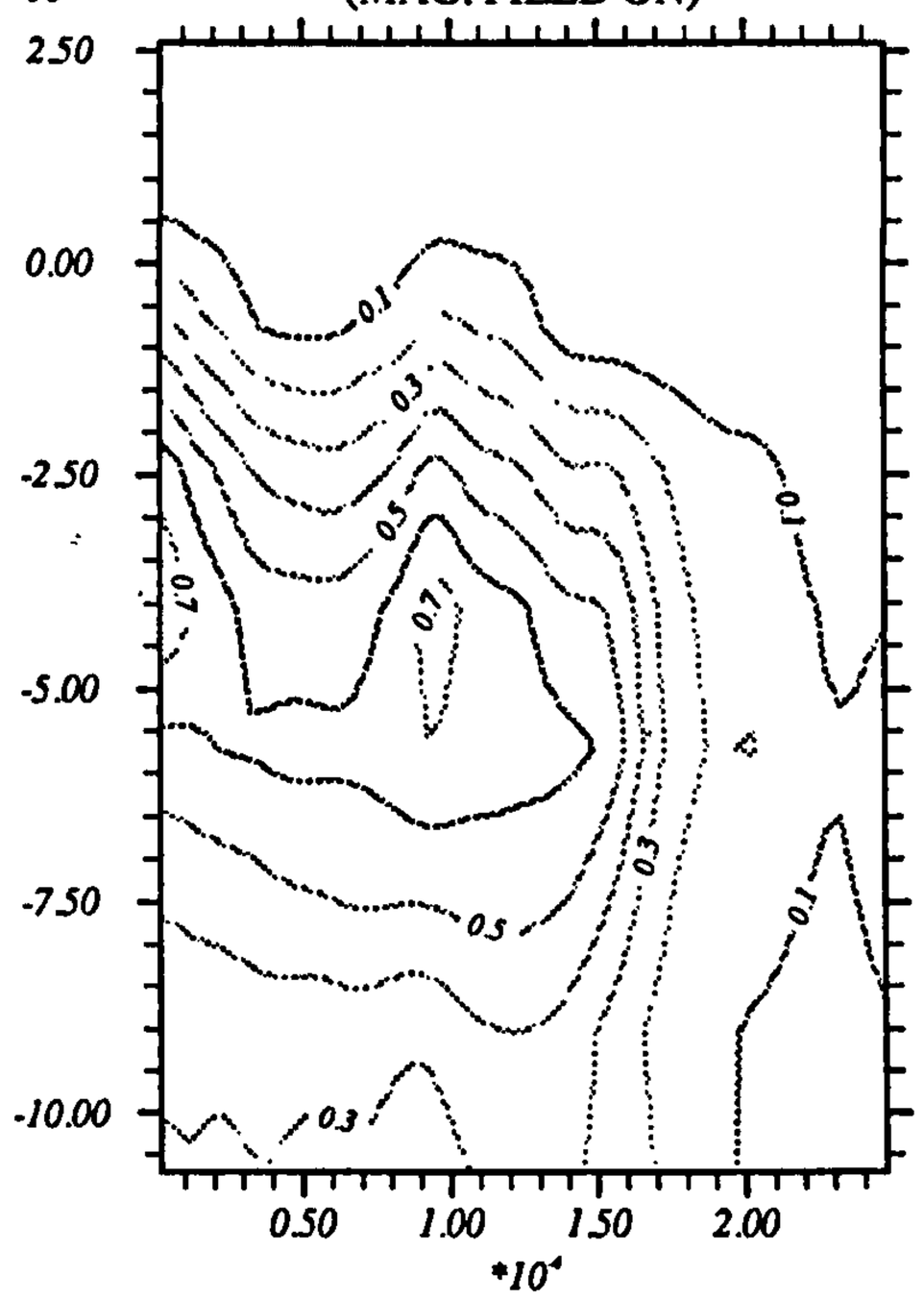

DENSITY MAP AT 700PS
(NO MAG. FIELD)

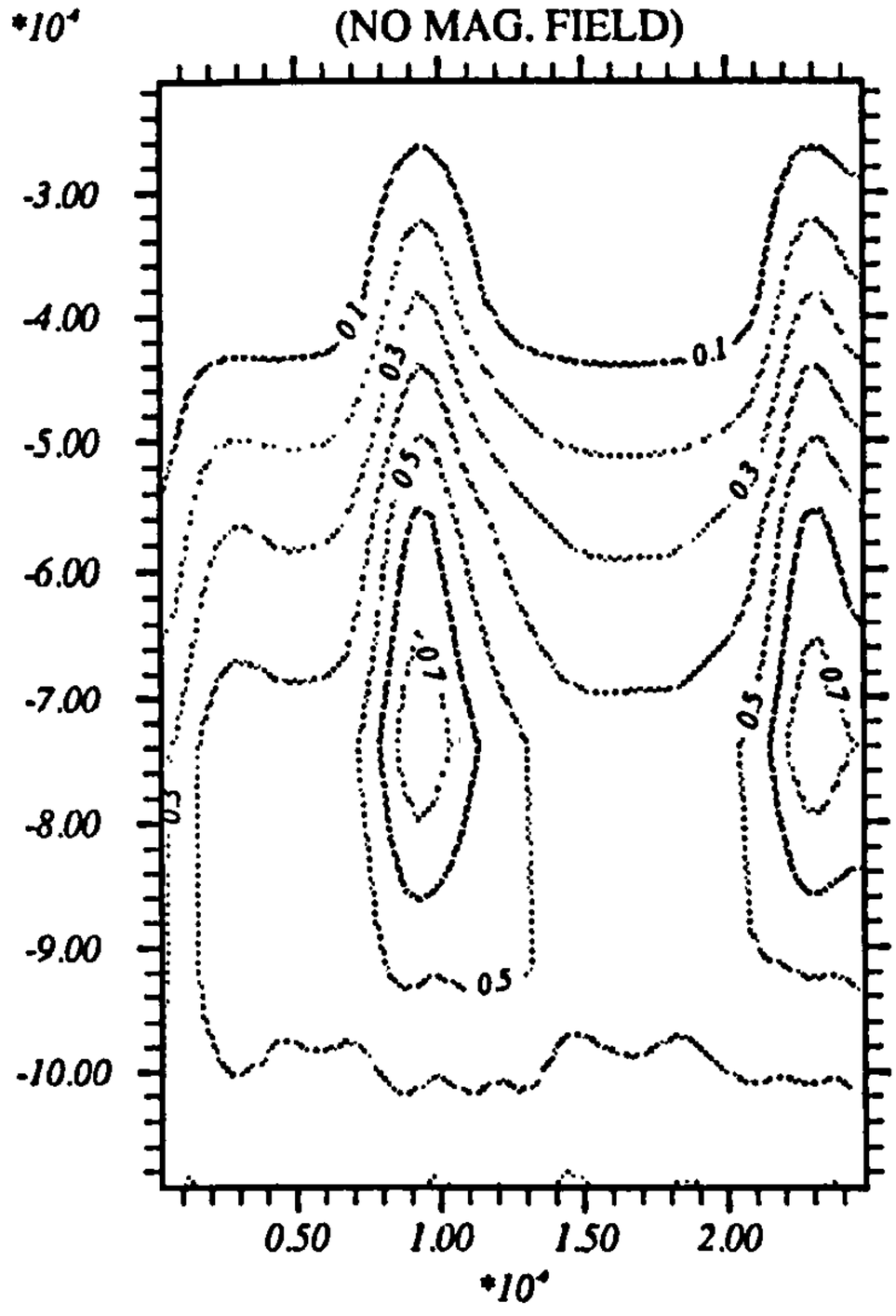

DENSITY MAP AT 700PS
(MAG. FIELD ON)

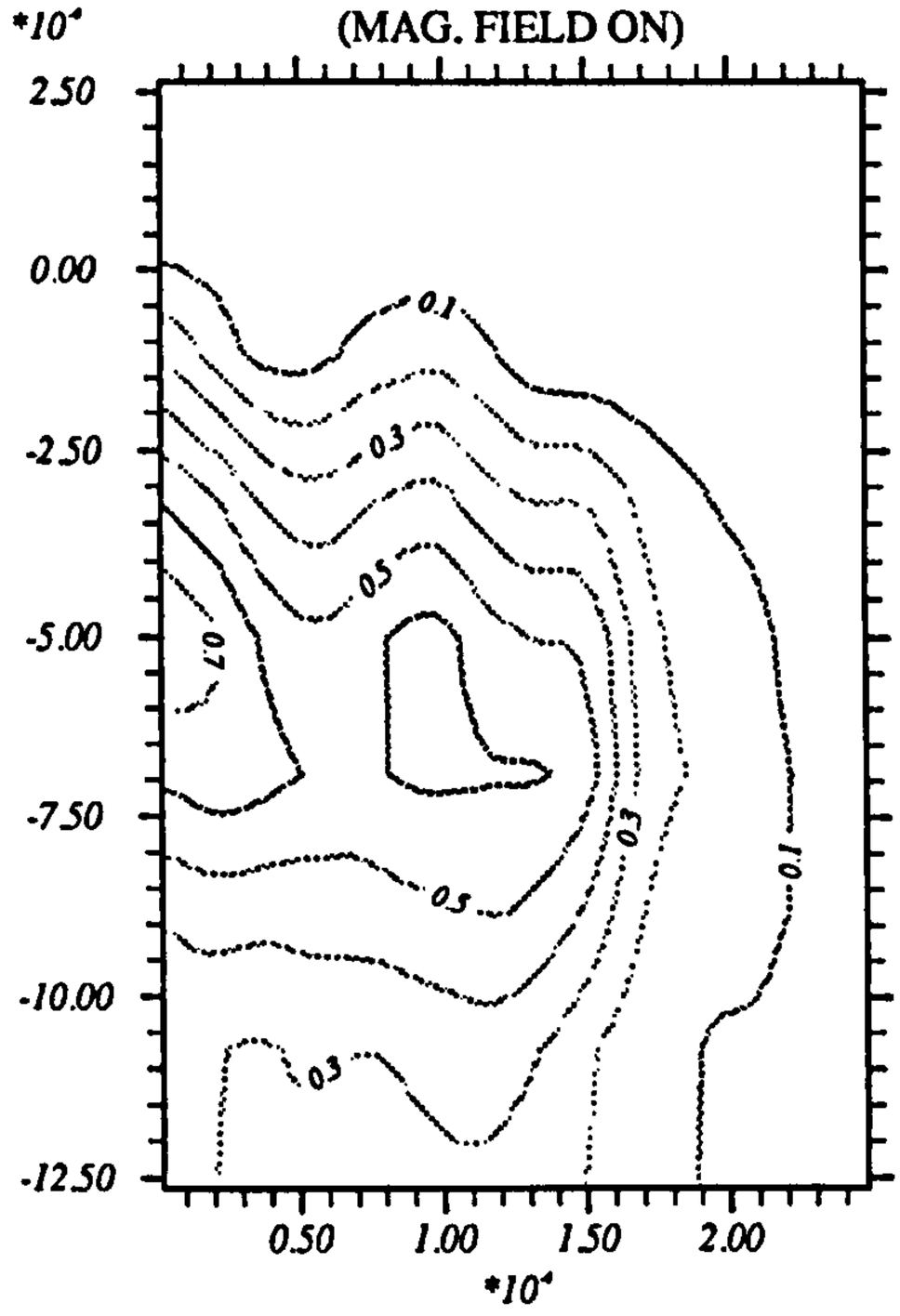

DENSITY MAP AT 750PS
(NO MAG. FIELD)

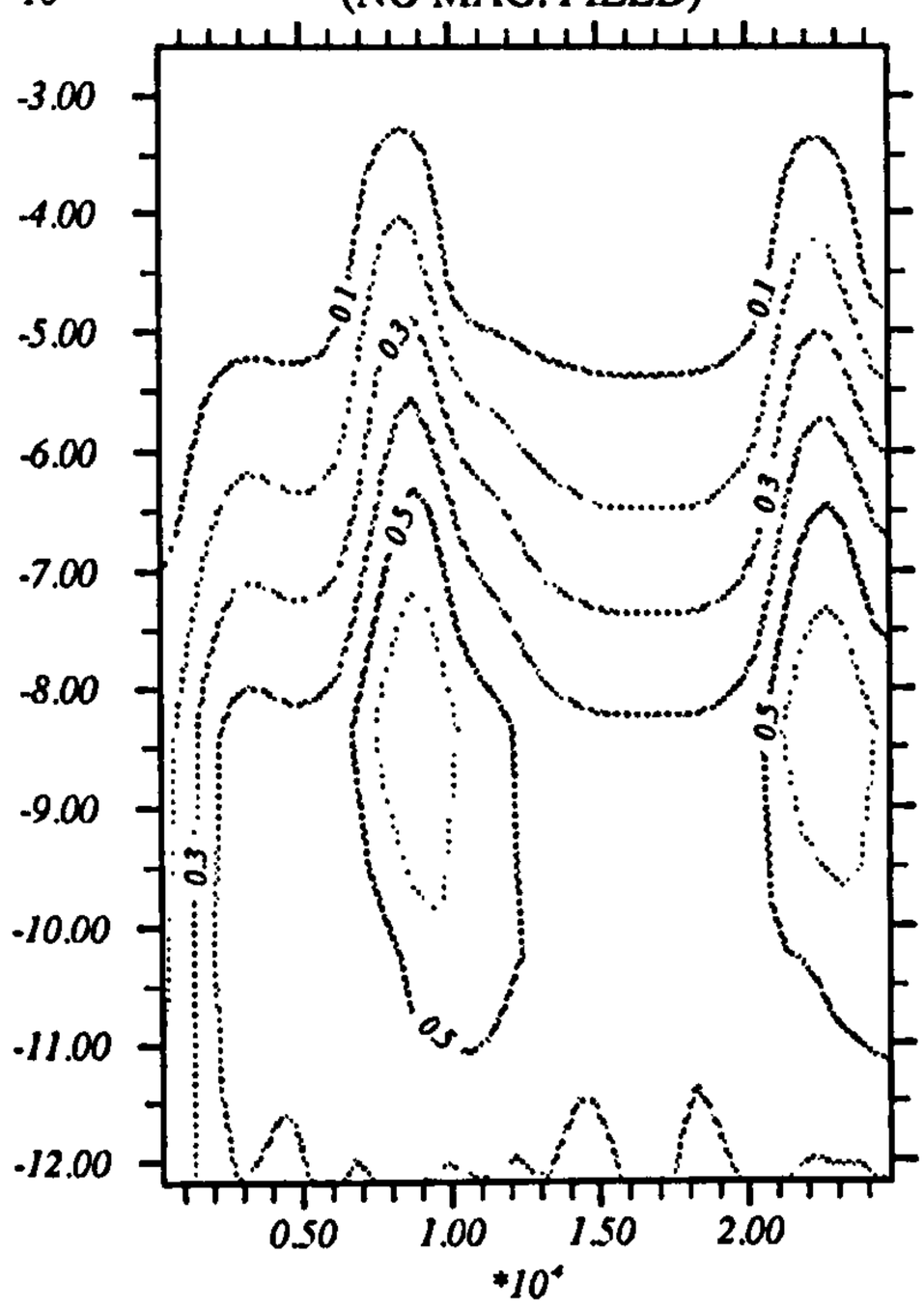

DENSITY MAP AT 750PS
(MAG. FIELD ON)

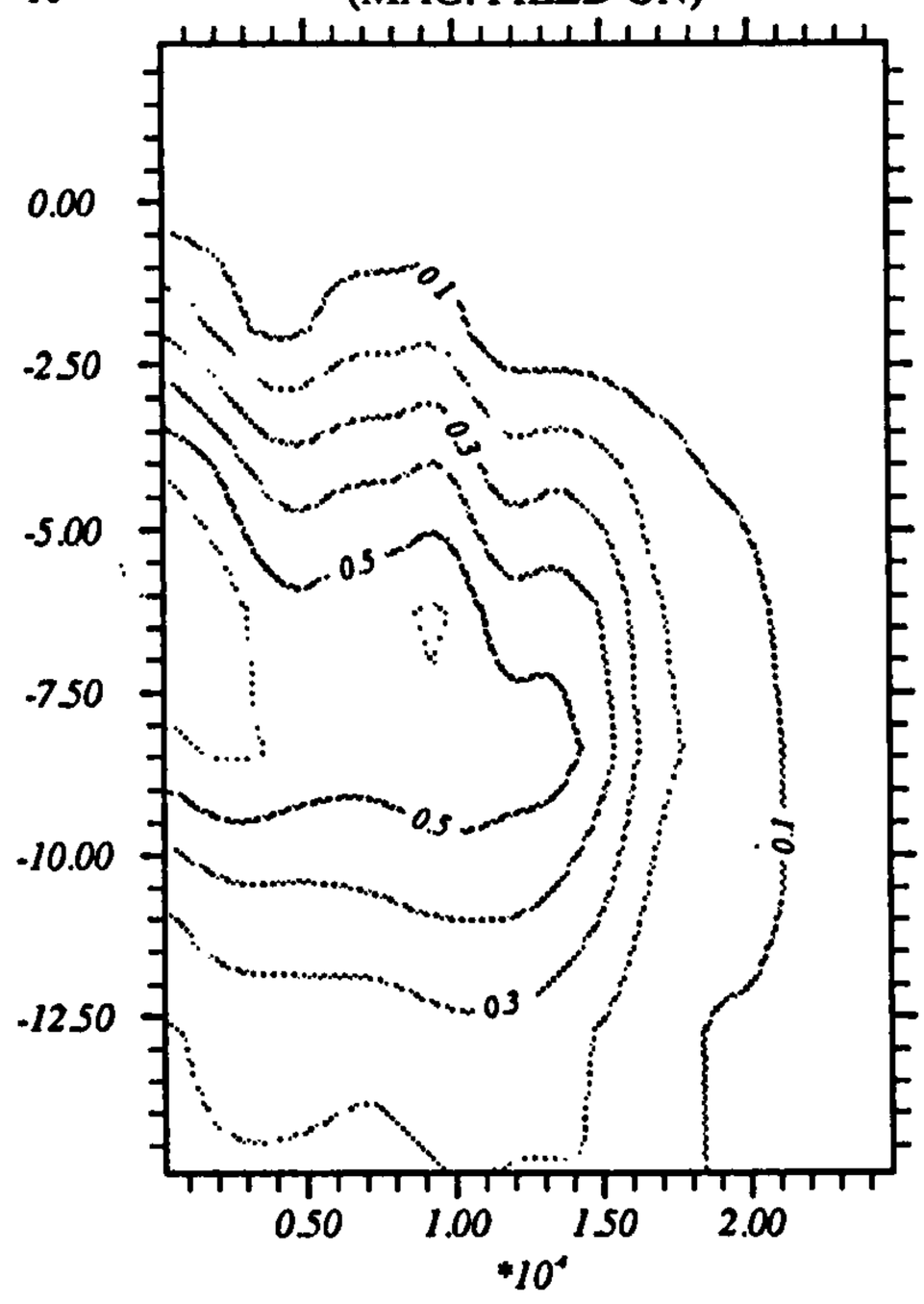

DENSITY MAP AT 800PS
(NO MAG. FIELD)

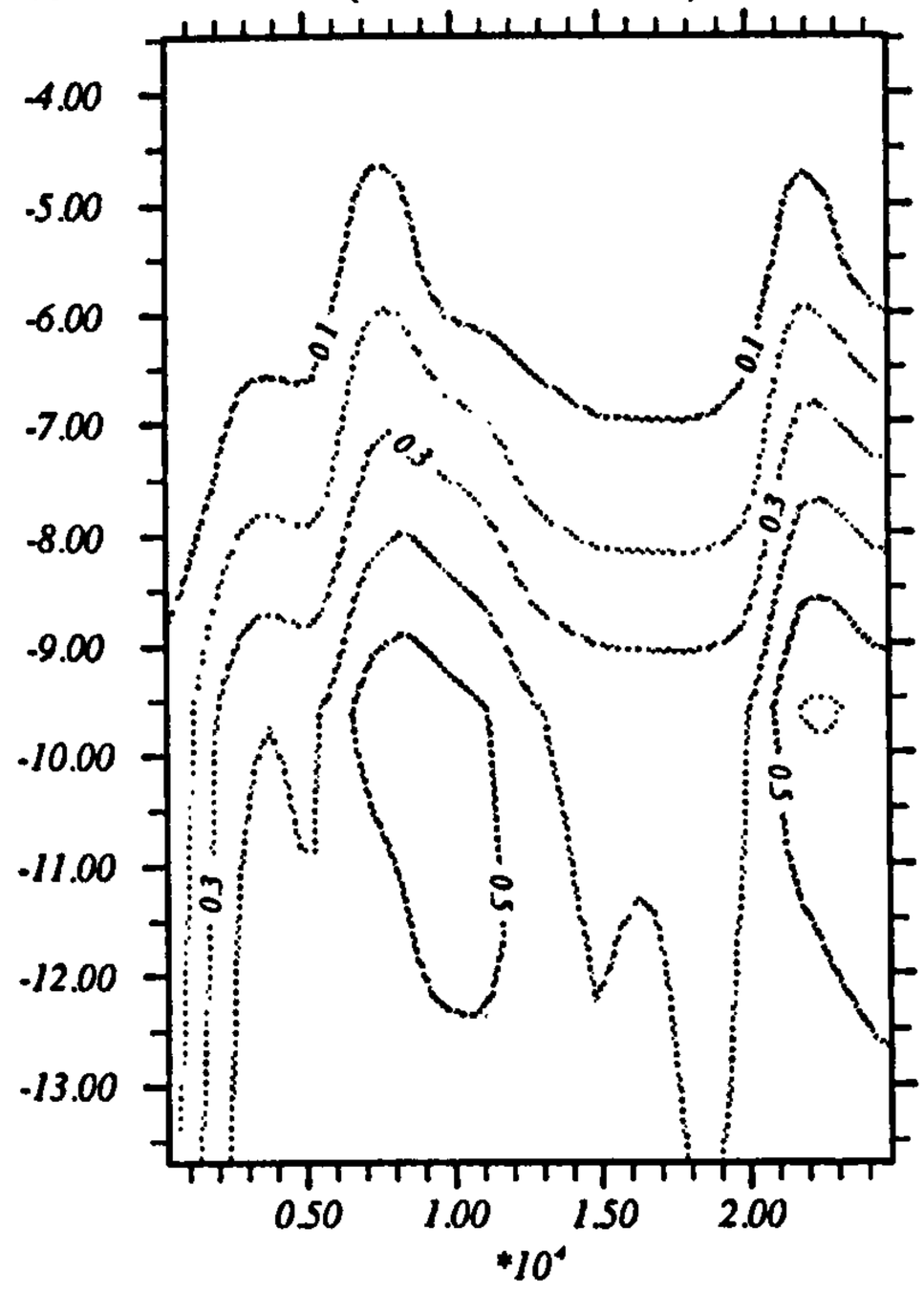

DENSITY MAP AT 800PS
(MAG. FIELD ON)

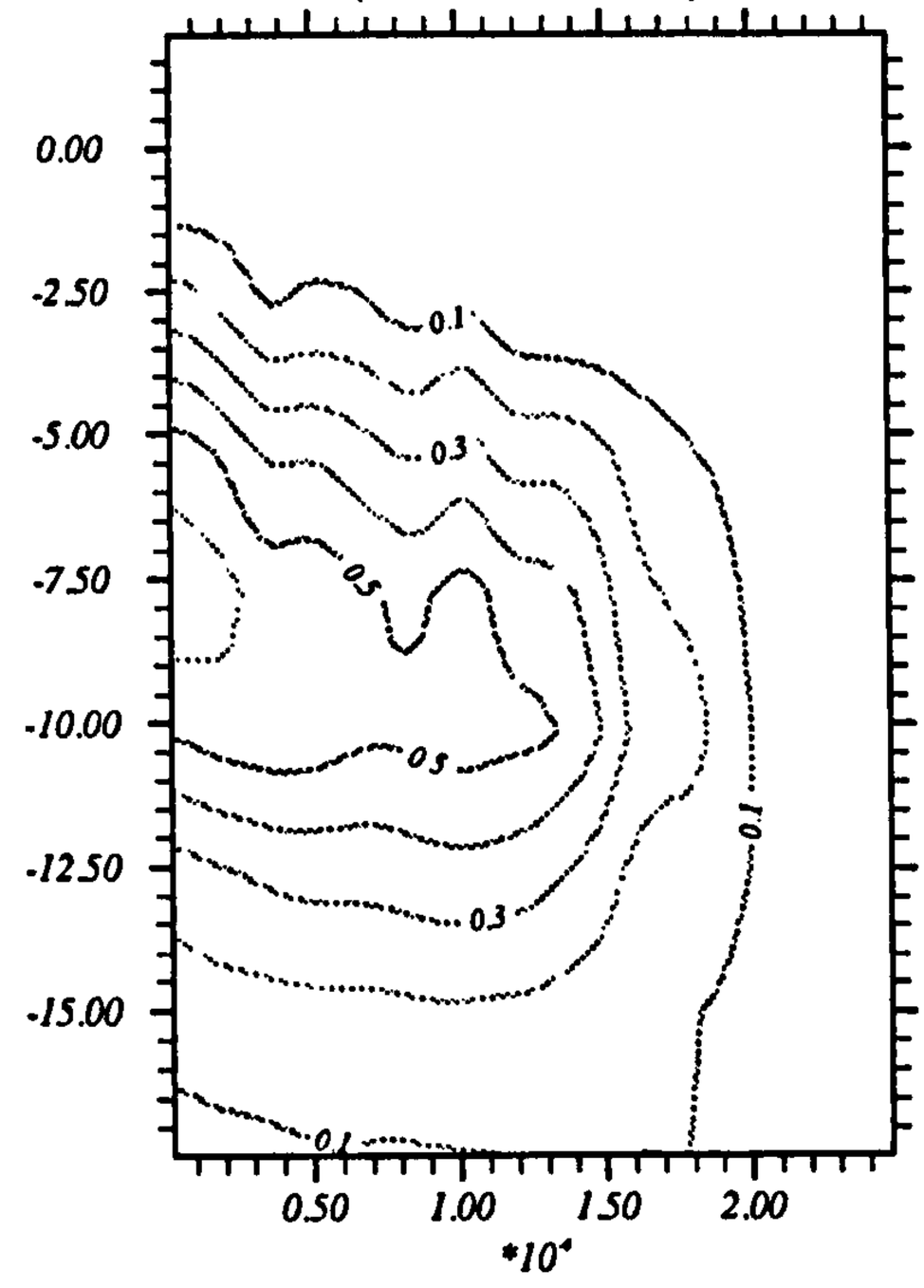

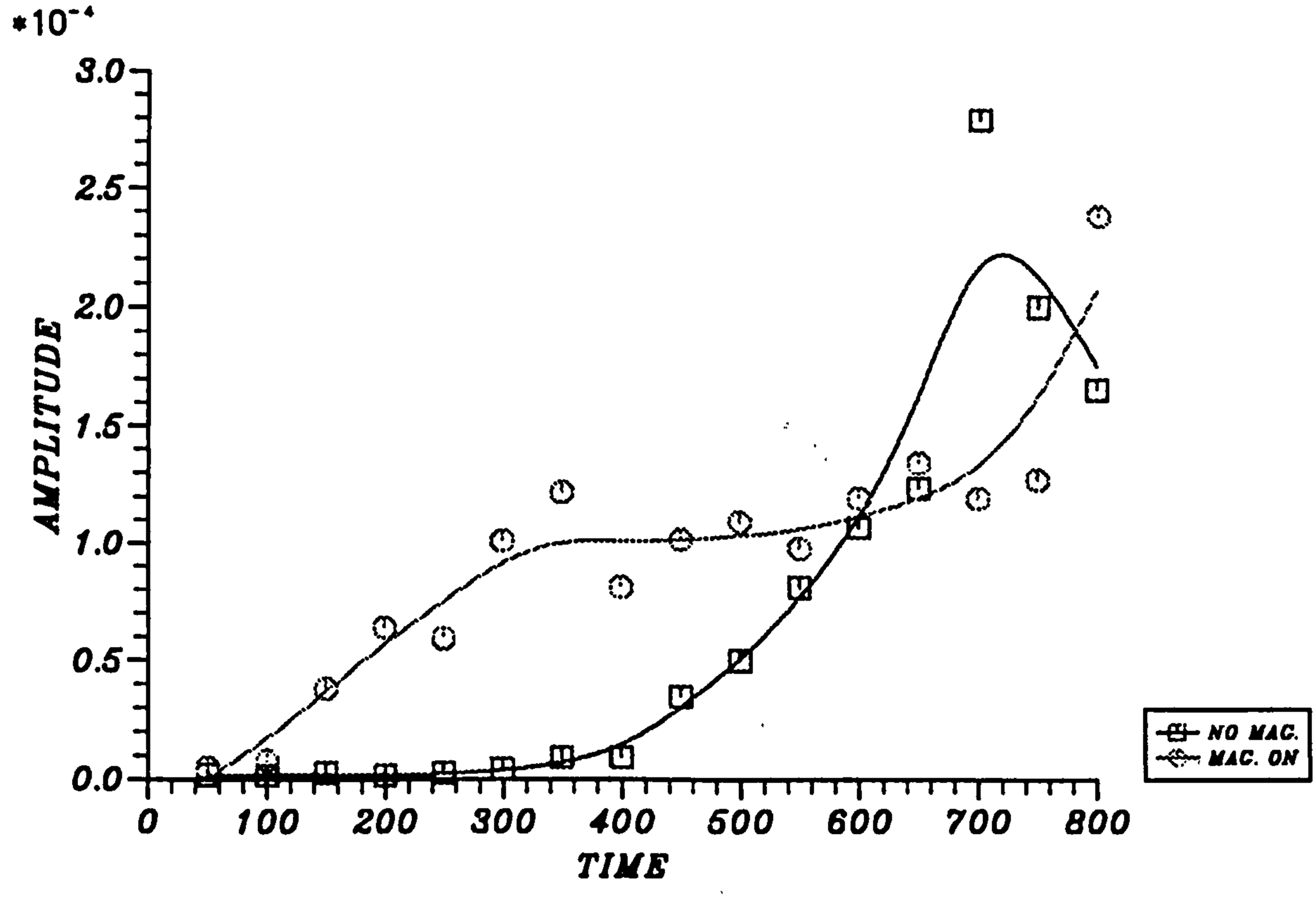

Figure 7.4: Amplitude time graph for lower power

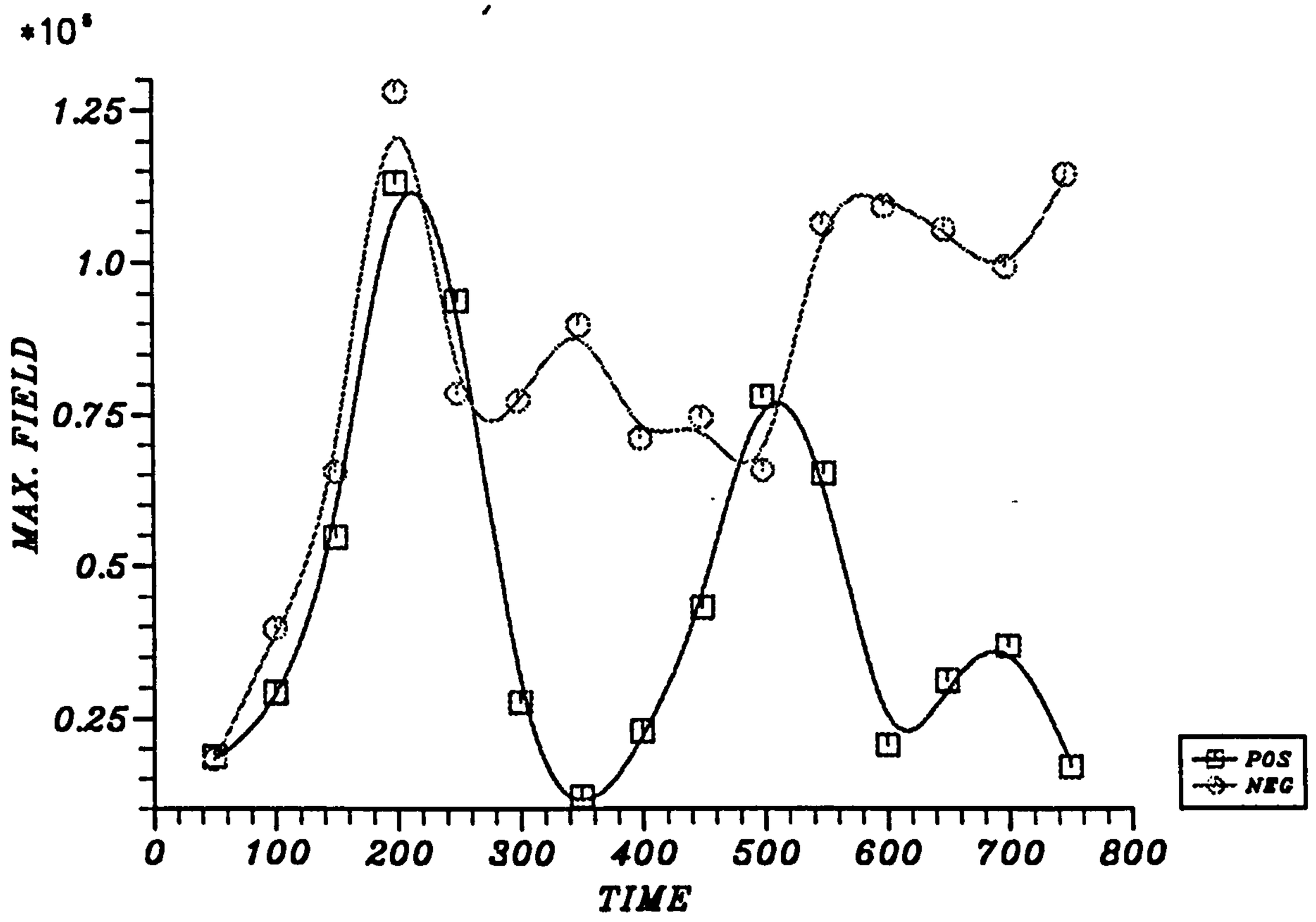

Figure 7.5: Maximum field vs time

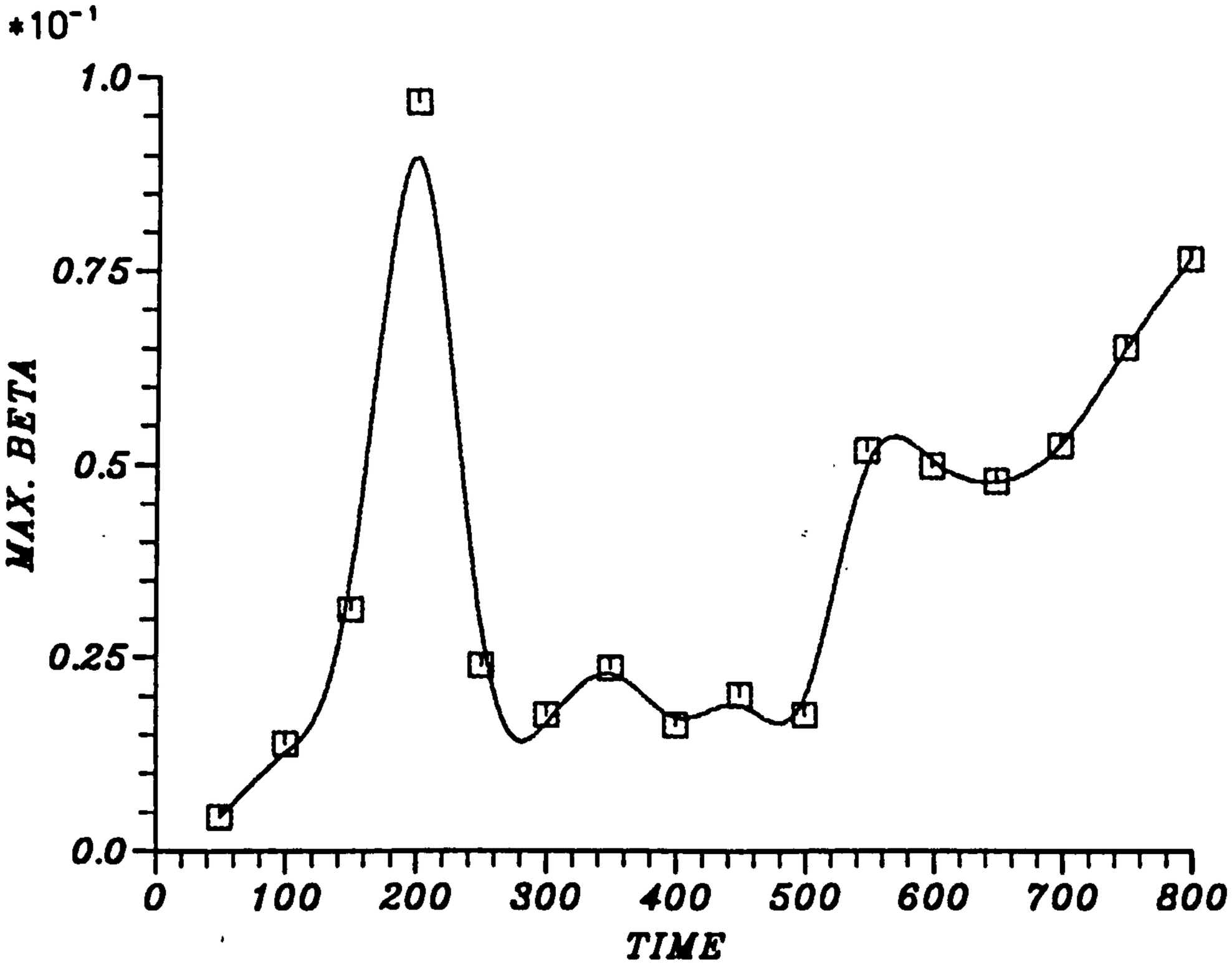

Figure 7.6: Maximum plasma beta vs time

7.5 COMPLETE SET OF TRANSPORT CO-EFFICIENTS

The aim of performing simulations including the full field terms was to find its effect on the growth of the Rayleigh-Taylor instability. The target selected for this particular problem is $5 \cdot 0 \mu m$ in both axial and radial directions. The parameters related to the laser and target are similar as used in section $5 \cdot 2$ but here both MAGN and BRAG switches are 'true'. We have performed simulations up to 500ps because the run was taking about 6 CPU hours to advance about 50ps from 450ps. We, therefore, stopped the calculations after this time

The density contour map is shown in figure $7 \cdot 7$ with an interval of 50ps. The pattern in both cases with and without the full set of coefficients is similar for both cases until 150ps but some extra high frequency modes have appeared in these complete simulations. Phase shifting has taken place because of the extra high frequency modes and the high density nodes have developed at different positions. Because of this phase shift the laser has started to penetrate through the target and then created a hole on the target axis after 300ps. At 500ps a phase shift

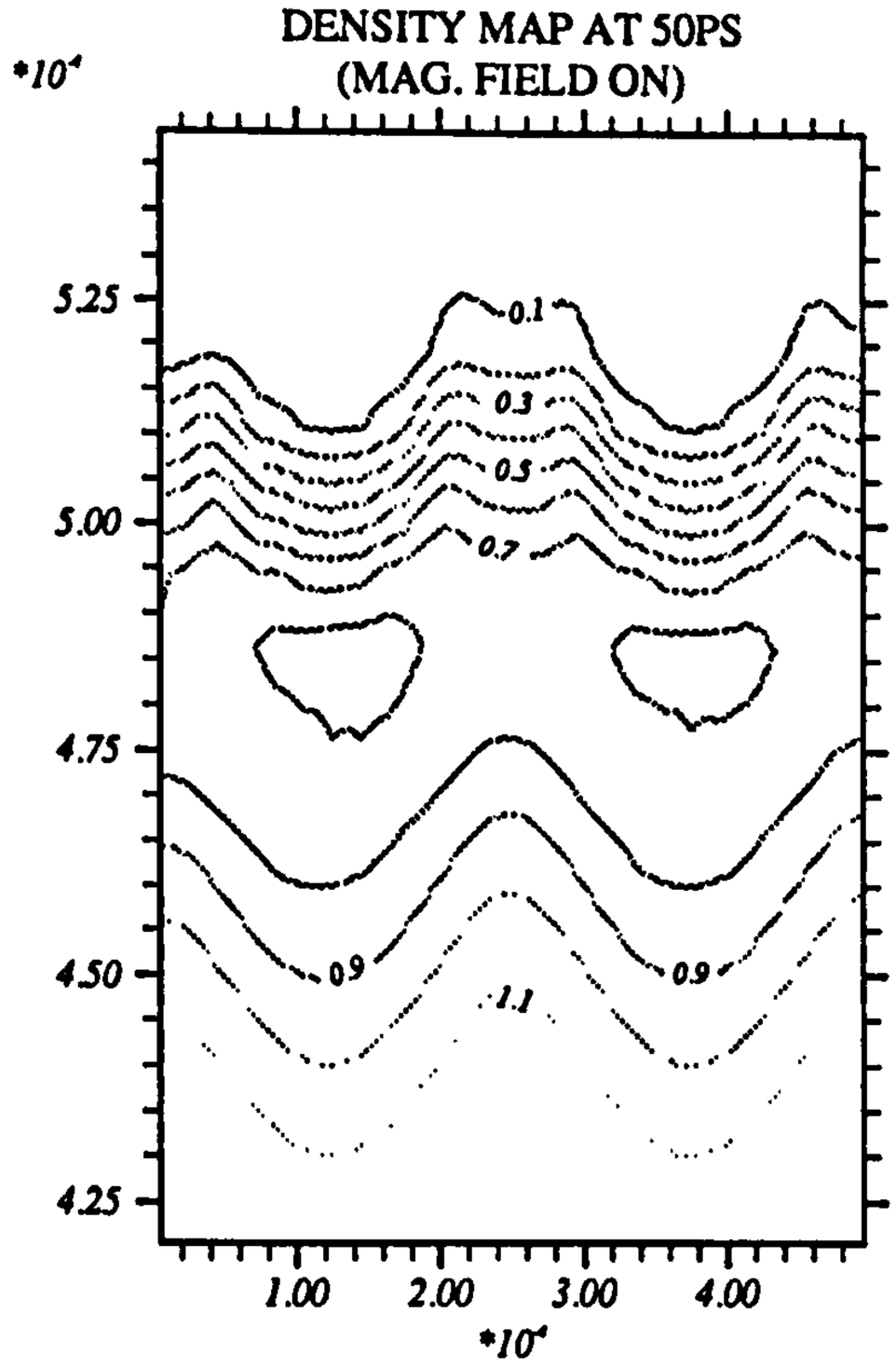

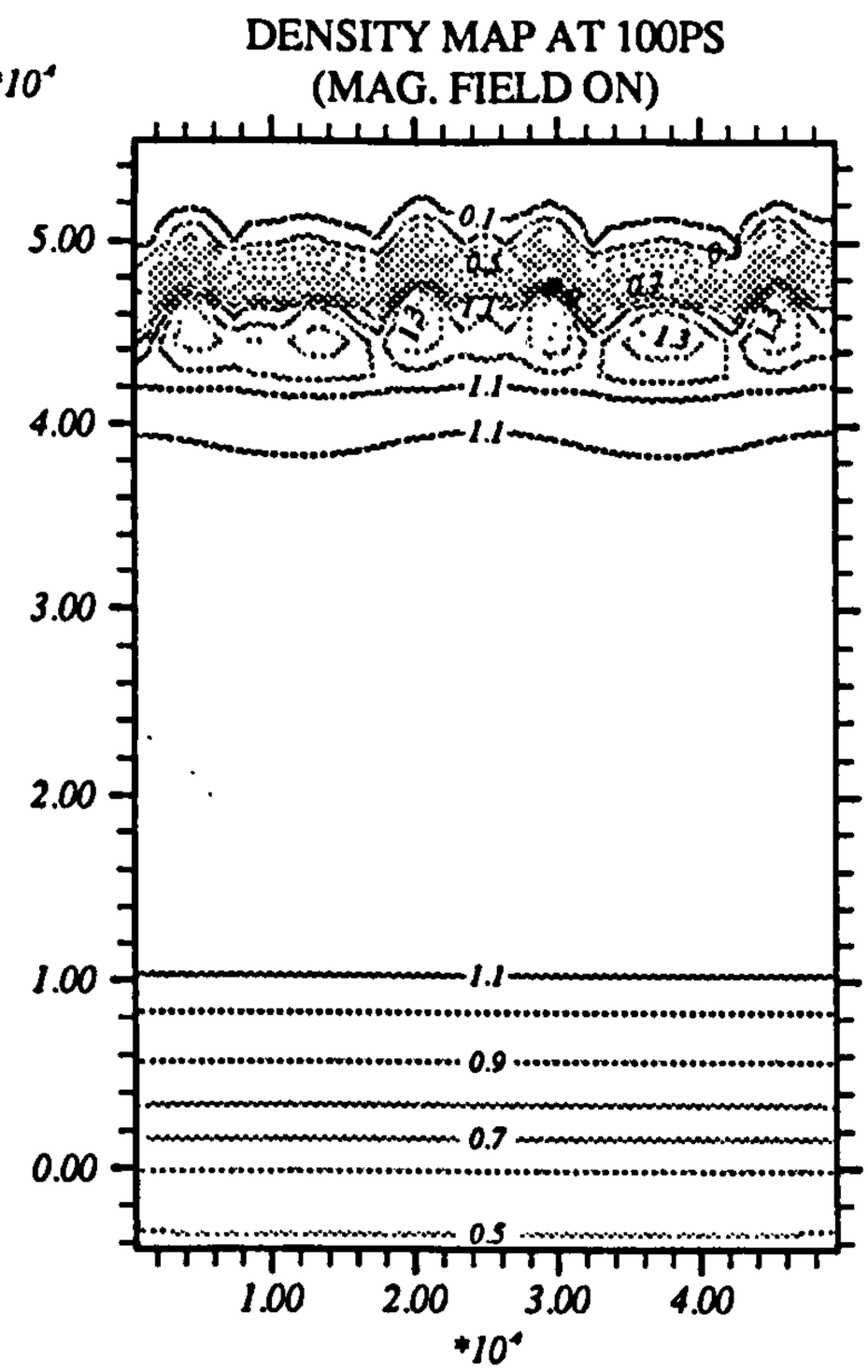

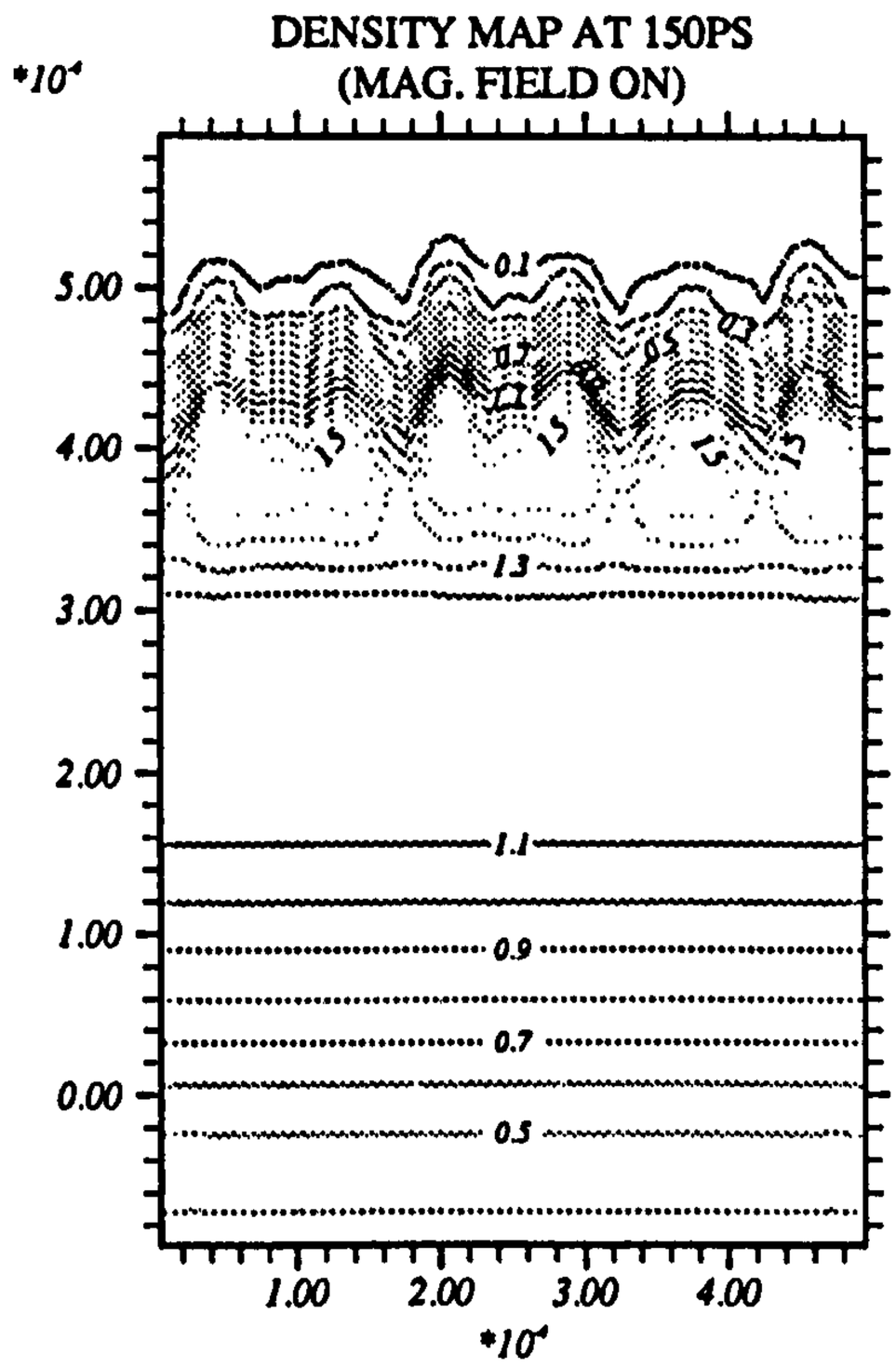

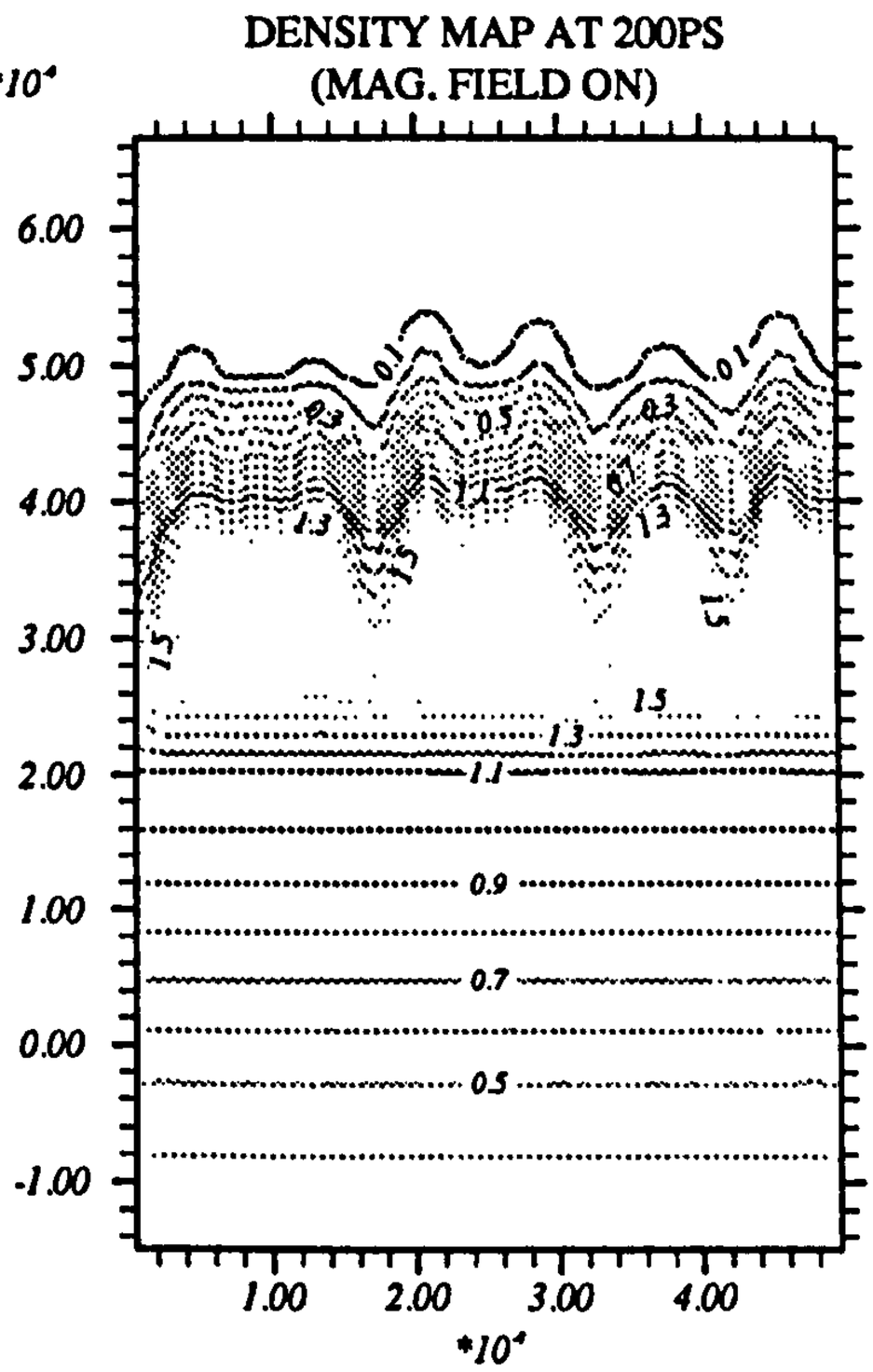

Figure 7.7: Density contour map for the target of $(5 \cdot 0\mu m \times 5 \cdot 0\mu m)$ including the full Braginskii coefficients.

DENSITY MAP AT 250PS
(MAG. FIELD ON)

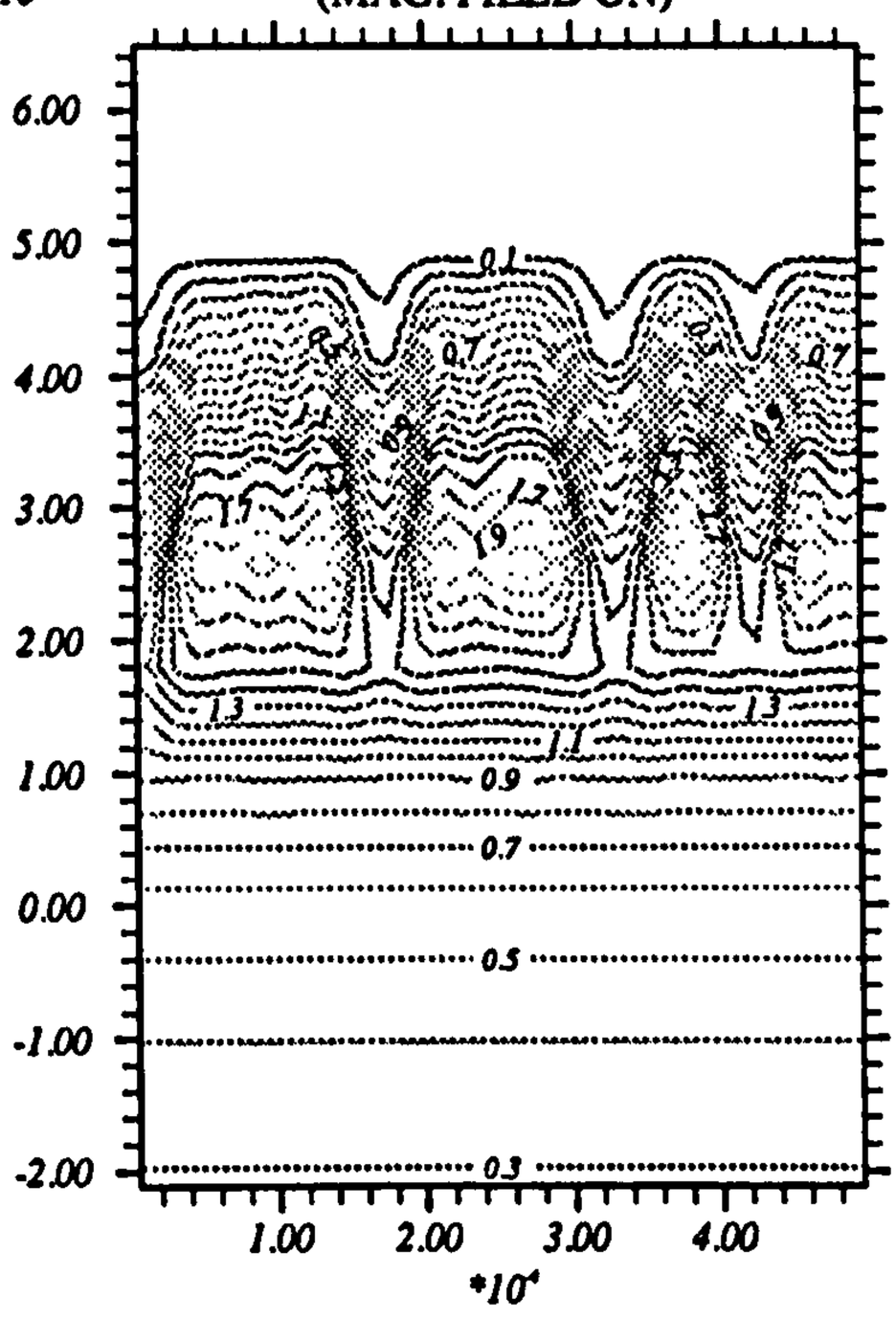

DENSITY MAP AT 300PS
(MAG. FIELD ON)

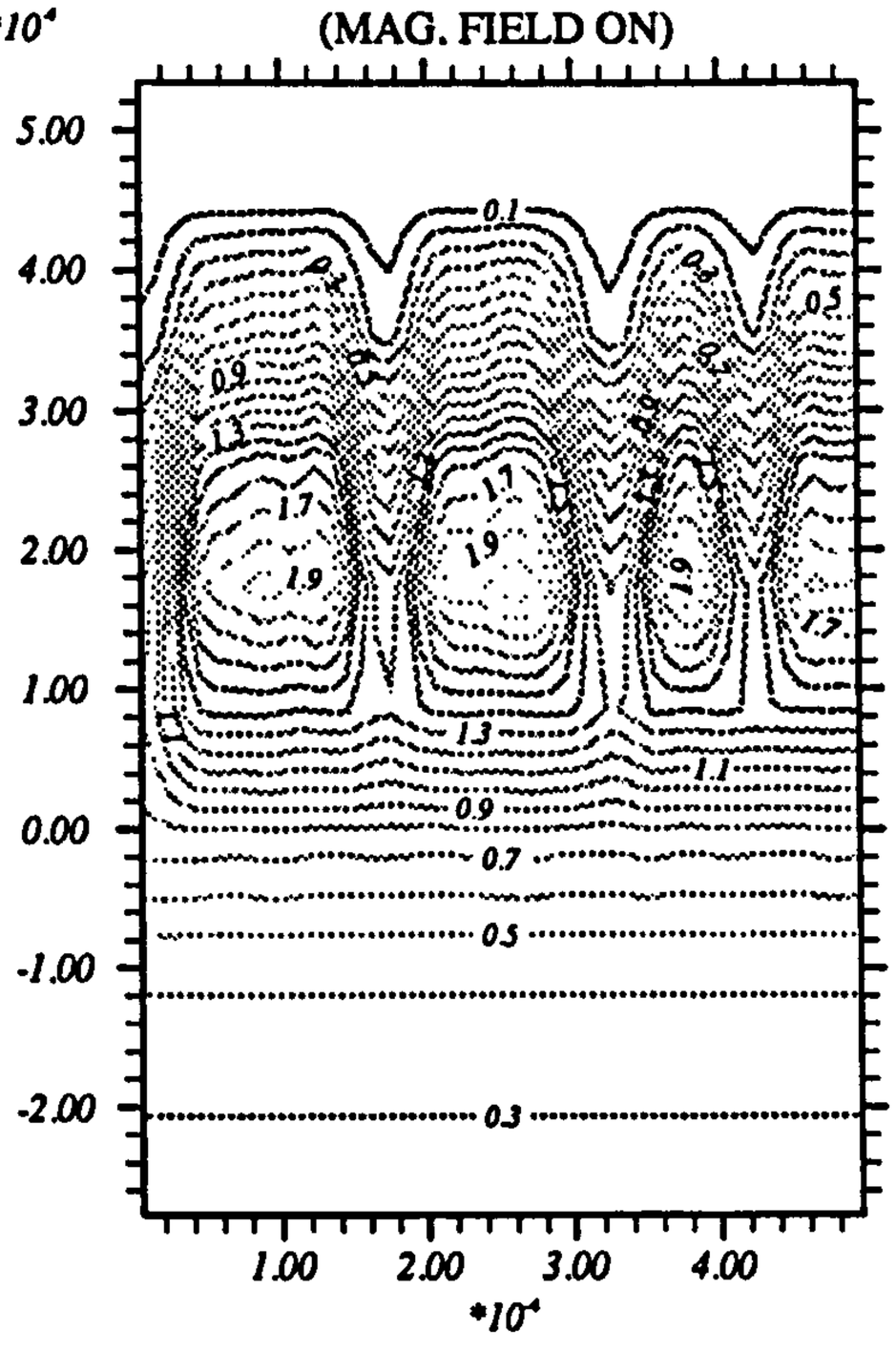

DENSITY MAP AT 350PS
(MAG. FIELD ON)

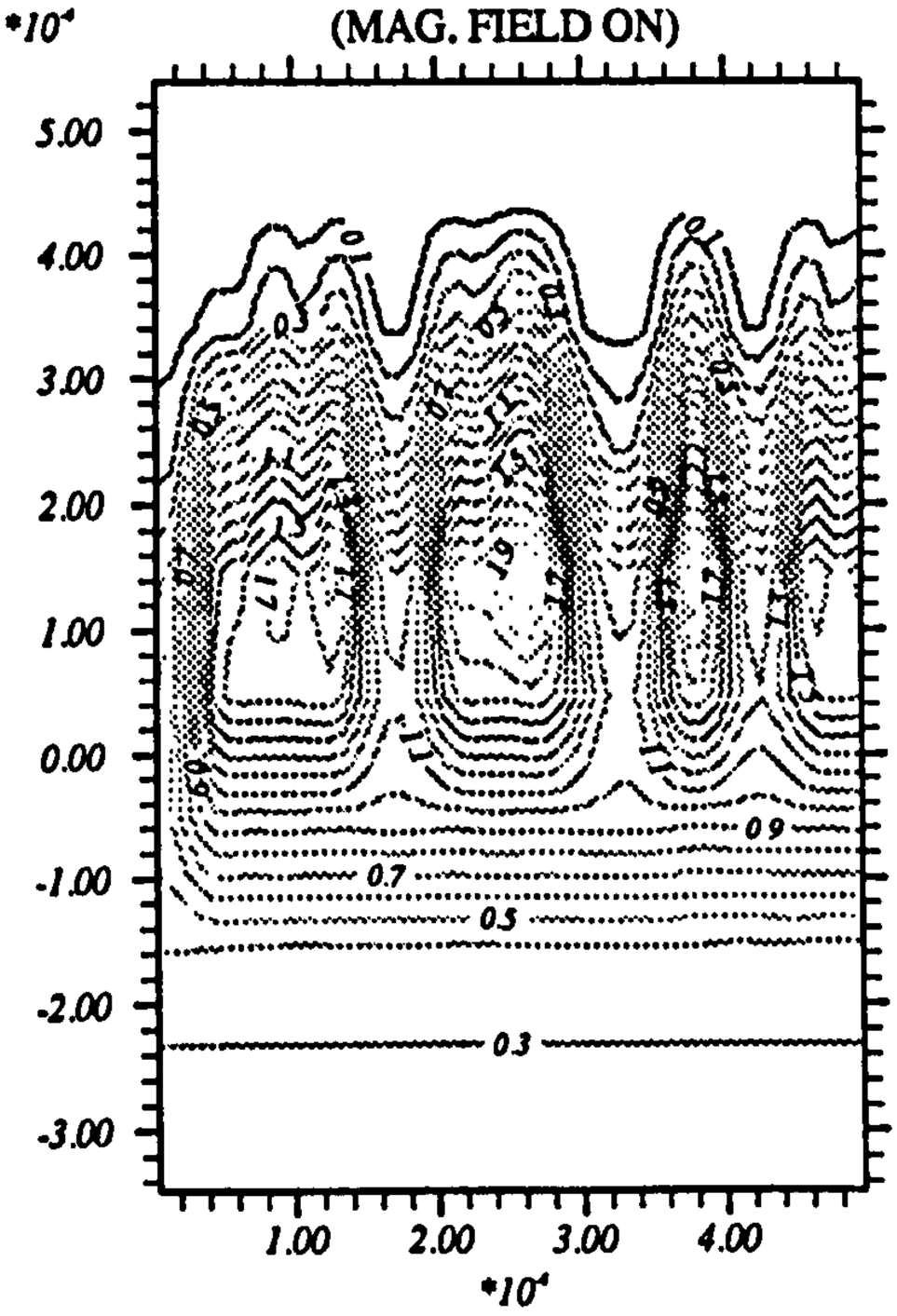

DENSITY MAP AT 400PS
(MAG. FIELD ON)

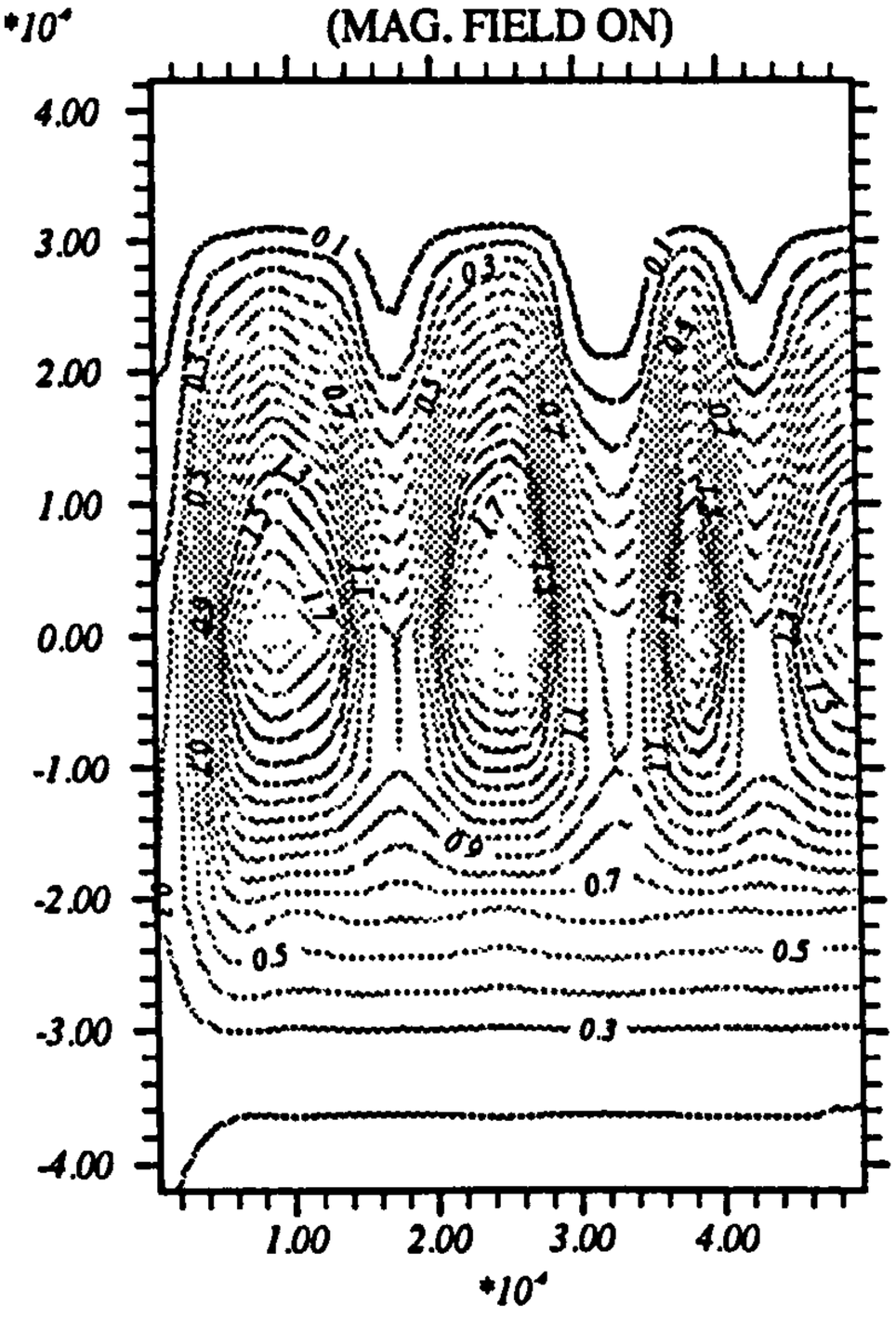

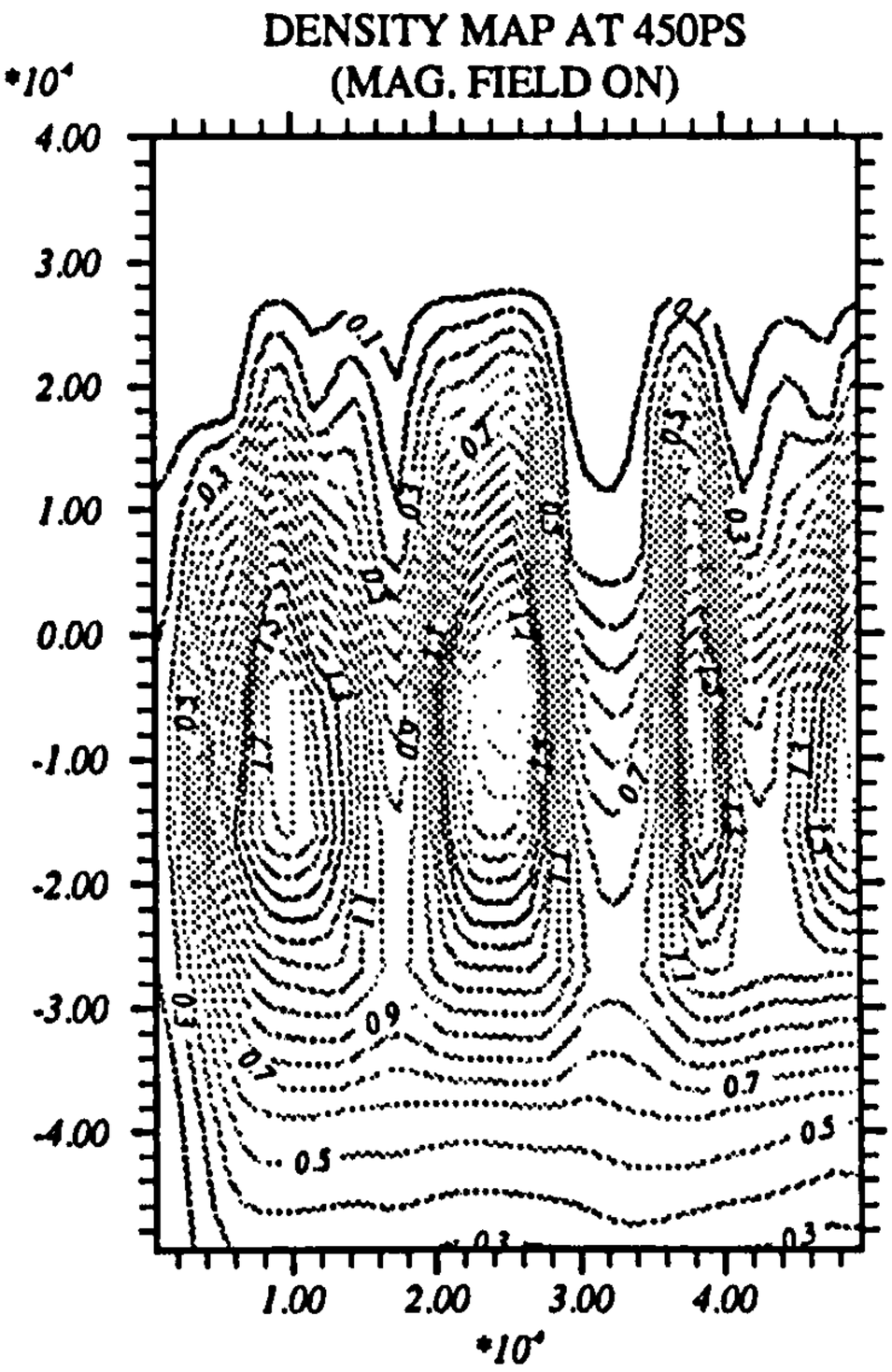
DENSITY MAP AT 450PS
(MAG. FIELD ON)
*10⁴
4.00
3.00
2.00
1.00
0.00
-1.00
-2.00
-3.00
-4.00
1.00
2.00
3.00
4.00
*10⁴

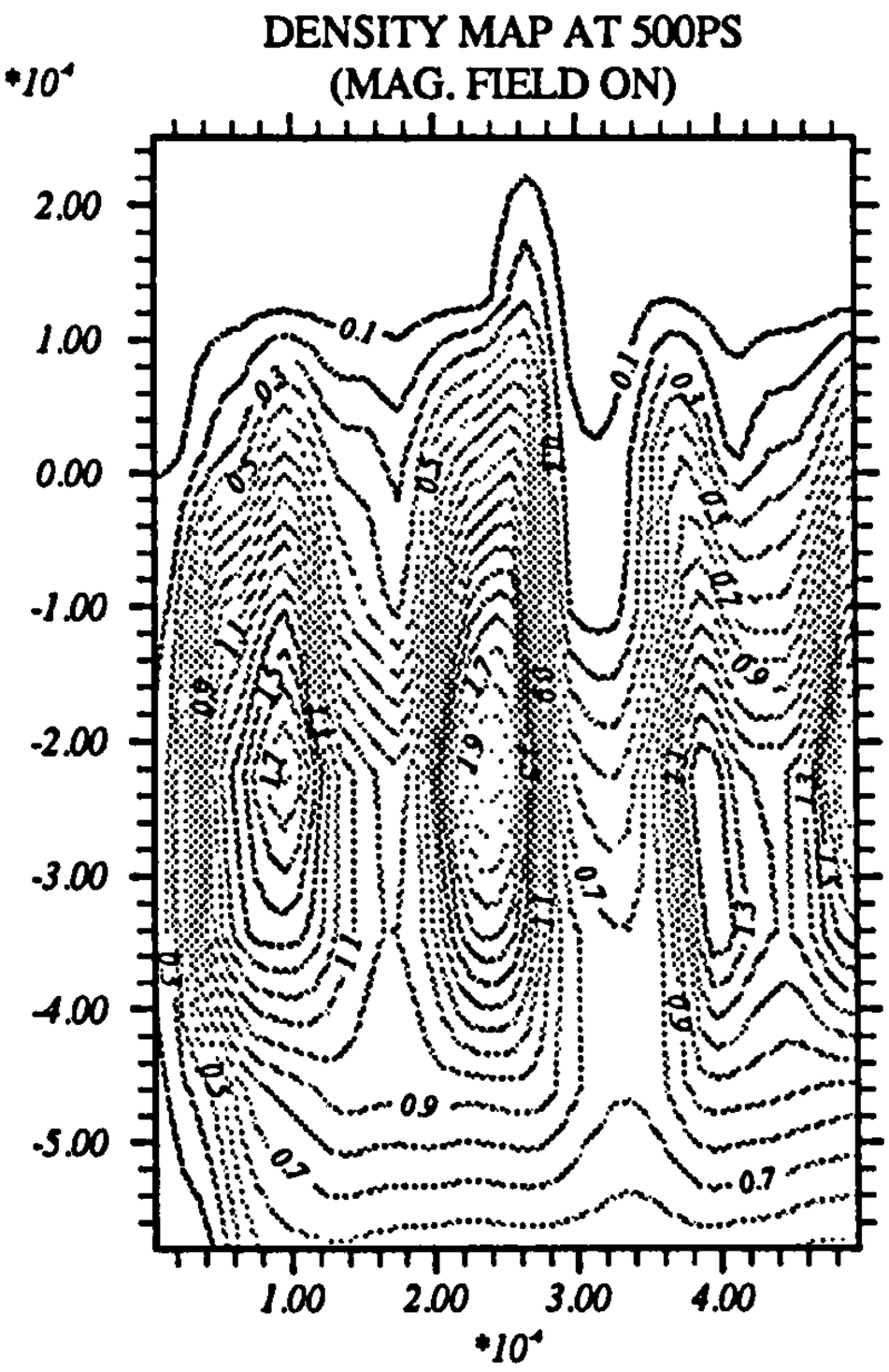
DENSITY MAP AT 500PS
(MAG. FIELD ON)
*10⁴
2.00
1.00
0.00
-1.00
-2.00
-3.00
-4.00
-5.00
1.00
2.00
3.00
4.00
*10⁴

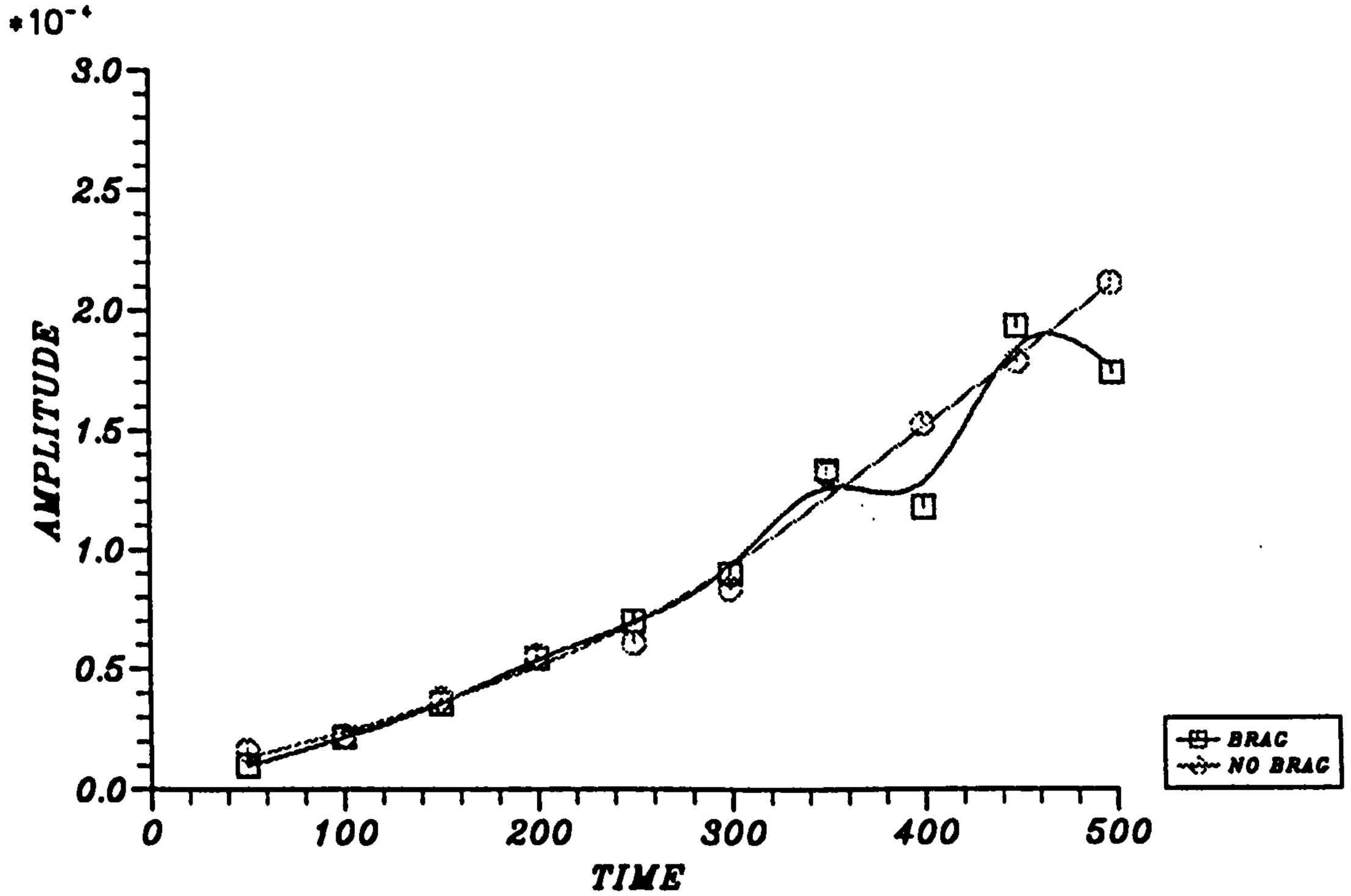

Figure 7.8: Amplitude-time graph for full

of about 90 is observed compared to section 5.2. Target acceleration is similar in both the case.

The amplitude as a function of time graph for both this and of section 5.2 is shown in figure 7 · 8. It is observed from this graph that the instability growth is very similar in both cases. We can, therefore, conclude from these simulations that the full field has not enhanced the growth of instability. It has only introduced some additional high frequency modes which have generated a shift in the density and have become a source which generates a hole on the target axis.

Chapter 8

CONCLUSIONS

The main objective of this research was to study the effect of self-generated magnetic fields on the growth of Rayleigh-Taylor instability in laser produced plasmas. The study of the instability is of crucial importance in Inertially Confined Fusion targets (whether imploded directly or indirectly) in the sense that the implosion must be symmetrical. The problem is tackled using computer simulations. The reason of using this approach is to observe the full range of physical processes during the time history of implosion which cannot be easily treated analytically.

In Chapter 2 we undertook a review of the Rayleigh-Taylor instability. The different growth phases were discussed in general terms and the factors which possibly affect the growth of instability were identified. In Inertially Confined Fusion targets Rayleigh-Taylor instability occurs twice: in the acceleration phase (where the low density abalator pushes the high density shell) and the deceleration phase (where the high density shell is stopped by lower density fuel). The main source of appearance of self-generated magnetic field was also discussed in the same Chapter.

In Chapter 3 an eigenvalue second order differential equation is derived from the standard fluid equations for incompressible fluid. This equation was applied to calculate the growth of Rayleigh-Taylor instability on linear and exponentially varying density profiles for different Atwood's numbers. For the linear density ramp it was observed that the instability growth is slower for small Atwood number ($a = 0 \cdot 1$) as compared to high Atwood numbers (e.g. $a = 0 \cdot 9$). The study of exponentially varying density profile was treated using both an approximate

analytical solution and direct numerical calculation. It was observed that for small kL values (~ 20) the approximate solution agreed with the computational results but for larger kL values the growth was slower for direct calculations compared to the approximate form. Problems arise in calculations due to the high frequency modes resulting from mode switching.

The main physical processes during the laser plasma interaction were reviewed in Chapter 4. It was also briefly discussed how these were used in the computer code MAGT2LD. The simulations were performed in Chapters 5-7 for different target sizes and varying certain parameters to investigate the growth of Rayleigh-Taylor instability with and without magnetic field. The simulations performed in this project required 4-40 CPU hours of computer on IBM-3070 at Rutherford Appleton Laboratory, depending on the size of the target and the field included/excluded options. It is observed that in most of the simulations the growth was nonlinear; or linear growth for a short time was followed by non-linear growth. The growth of the instability was observed by plotting the density contour maps; thereby measuring the width of the mix region, the amplitude-time graphs were drawn to find out the comparison of the instability growth for both magnetic field included and excluded. The magnetic field contour maps are also drawn to find its contribution towards the growth of Rayleigh-Taylor instability in our studies.

Very generally we observed the following important points;

- High frequency modes occur in the density contour maps in magnetic field included simulations in the early times. These high frequency modes are generated because of the non-linear terms in the self-generated field equations. The high frequency modes gradually disappeared.

- The high frequency modes then became the source to create a spatial phase shift of about 90° towards the axis in the density perturbation at late time intervals.

- In the most of the density contour maps with no field simulations, we observed a hole on the target axis. To clarify this effect we performed simulations by reversing the applied perturbations and this effect was thereby eliminated.

- Although our main aim was not to find the self-generated magnetic field strength, it was necessary to examine how the field affects the instability generation, thus we measured the field strength, which was observed to be of the order of $1 \cdot 8$ MG in most of the simulations.

- Plasma beta was found to reach a maximum value of around 10%.

- The instability growth is usually higher for the field on simulations compared to no field simulations. In the simulations where the perturbation was applied through density the instability growth is slightly faster for field on simulations in comparison to those with no field. However a significant difference was observed in the simulations when the perturbation was applied through the laser intensity.

- The instability growth is reduced by lowering the applied laser power.

- The phase shift towards the target axis is avoided if using the planar geometry rather than the cylindrical.

- The simulations performed in Chapter 7 using the thermoelectric coefficients of Braginskii as well as thermally generated magnetic fields do not generate any additional effect on the growth of the instability. In these simulations we have not observed any substantial difference in the magnetic field strength.

Clearly our computer simulations show that the self-generated magnetic fields significantly may enhance the instability growth. It would be advisible to extend this work to spherical geometry, which is used in Inertial Confinement Fusion experiments. However it is extremely difficult to model the magnetic field effects in this geometry and this will in consequence be an extremely expensive project in computer time. The research will become very interesting when the role of magnetic field in the instability growth can be measured experimentally and compared with experimental data. Another important parameter is the inclusion of better equation of state like Thomas-Fermi equation of state. It is finally necessary to give a cautionary remark that the reliability of the predictions made from computer simulations is dependant upon the quality of physical representations provided in the model.

Bibliography

[1] Chen F.F, *"Introduction to Plasma Physics and Controlled Fusion"*, Plenum Press, (1974).

[2] Nuckolls J., *Phys. Today*, **35**, 24 (1982).

[3] Rayleigh J.W., *"...Equilibrium of an Incompressible Heavy Fluid of Variable Density"*, *Proc. London Math. Soc.*, **XIV**, p. 170, (1883).

[4] Taylor G.I., *Proc. R.Soc.*, **A201**, 192 (1950).

[5] Smarr L., Wilson J.R., Barton R.T. and Bowers R.L., *Ap. J.* **246**, 515 (1981).

[6] Norman M.L., Smarr L., Wilson J.R. and Smith M.D., *Ap. J.*, **247**, 52 (1981).

[7] McCrory R.L., Montierth L., Murse R.L. and Verdon C.P., *Phys. Rev. Lett.*, **46**, 336 (1981).

[8] Evans R.J., Bennett A.J. and Pert G.J., *Phys. Rev. Lett.*, **49**, 1639 (1982).

[9] Emery M.H., Gardner J.H. and Boris J.P., *Phys. Rev. Lett.*, **48**, 667 (1982).

[10] Gerwin R.A. and Malone R.C., *Nucl. Fusion*, **19**, 155 (1979).

[11] Sharp D.H., *"An Overview of Rayleigh-Taylor Instability"*, Los Alamos National Laboratory Report, LA-UR-83-2130, (1983).

[12] Sharp D.H., *Physica*, **12D**, 1 (1984).

[13] Birkhoff G., *"Taylor Instability and Laminar Mixing"*, Los Alamos National Laboratory report LA-1862 (1955).

[14] Chandrasekhar S., *"Hydrodynamic and Hydromagnetic Stability"*, Oxford University Press, Oxford (1961).

[15] Lewis D.J., *Proc. Roy. Soc.*, **202A**, 81 (1950).

[16] Tritton D.J., *"Physical Fluid Dynamics"*, Van Nostrand (1977).

[17] Daly B.J., *Phys. Fluids*, **10(2)**, 297 (1967).

[18] Obenschain S.P., Grun J., Ripin B.H. and McLean E.A., *Phys. Rev. Letts.*, **46**, 1402 (1981).

[19] Whitlock R.R., Emery M.H., Stamper J.A., McLean E.A., Obenschain S.P. and Peckerar M.C., *Phys. Rev. Letts.*, **52** 819 (1984).

[20] Key M.H., *Phil. Trans. R. Soc. Lond.*, **A300**, 599 (1981).

[21] Key M.H., in '*"Laser-Plasma Interactions 3"*', ed. Hooper, SUSSP (1985).

[22] Kidder R.E., *Nucl. Fusion*, **16**, 3 (1976).

[23] Evans R.G., Bennett A.J. and Pert G.J., *J. Phys. D: Appl. Phys.* **15**, 1673 (1982).

[24] Bangerter R.O., *"Proc. IEEE Minicourse on ICF"*, Ch. 5, (1979).

[25] Nuckolls J., Wood L., Theissen A. and Zimmerman G., *Nature*, **239**, 139 (1972).

[26] Shiau J.N., Goldman E.B. and Weng C.I., *Phys. Rev. Letts.*, **32**, 352 (1974).

[27] Bodner S.E., *Phys. Rev. Letts.*, **33**, 761 (1974).

[28] Verdon C.P., McCrory R.L., Morse R.L., Baker D.I. and Orszag S.A., *Phys. Fluids*, **25**, 1653 (1982).

[29] Manheimer W.M. and Colombant D.G., *Phys. Fluids*, **27**, 983 (1984).

[30] Gamalii E.G., Rozanov V.B., Samarskii A.A., Tishkin V.F., Tyurina N.N and Favorskii A.P., *Sov. Phys. JETP*, **52**, 230 (1980).

[31] Duderstadt J.J. and Moses G.A., *"Inertial Confinement Fusion"*, Wiley (1982).

[32] Gardner J.H. and Bodner S.E., *Phys. Rev. Letts.*, **47**, 1137 (1981).

[33] Grun J., Emery M.H., Manka C.K., Lee T.N., McLean E.A., Mostovych A., Stamper J.A., Bodner S.E., Obenschain S.P. and Ripin B.H., *Phys. Rev. Letts.*, **58**, 2672 (1987).

[34] Obenschain S.P., Grun J., Herbst M.J., Kearny K.J., Manka E.J., McLean E.A., Mostovych A.N., Stamper J.A., Whitlock R.R., Bodner S.E., Gardner J.H. and Lehmberg R.H., *Phys. Rev. Letts.*, **56**, 2807 (1986).

[35] Johnson, T.H., *Proc. of IEEE*, **72**, 548 (1984).

[36] Kruer W.L. and Estabrook K., *Phys. Fluids*, **20**, 1688 (1977).

[37] Max C.E., Manheimer W.M. and Thomson J.J., *Phys. Fluids*, **21**, 128 (1978).

[38] Manheimer W.M., Max C.E. and Thomson J.J., *Lawrence Livermore Laboratory, Laser Program Annual Report*, UCRL-50021-77 4 (1977).

[39] Tidman D.A. and Stamper J.A., *Appl. Phys. Letts.* **22**, 498 (1973).

[40] Craxton R.S. and Haines M.G., *Phys. Rev. Letts.*, **35**, 1336 (1975).

[41] Pert G.J., *J. Plasma Phys.*, **18**, 227 (1977).

[42] Tidman D.A. and Shanny R.A., *Phys. Fluids*, **17**, 1207 (1974).

[43] Bol'shov L.A., Dreizin Yu.A. and Dyhkne A.M., *JETP Lett.*, **19**, 168 (1974).

[44] Al'terkop B.A., Mishin E.V. and Rukhadze A.A., *JETP Lett.*, **19**, 170 (1974).

[45] Colombant D.G., Tidman D.A. and Winsor N.K., *Appl. Phys. Letts.*, **29**, 401 (1976).

[46] Tidman D.A. and Burton L.L., *Phys. Rev. Letts.*, **37**, 1397 (1976).

[47] Tidman D.A., *Phys. Fluids*, **18**, 1454 (1975).

[48] Tidman D.A., *Phys. Rev. Letts.*, **32**, 1179 (1974).

[49] Max C.E. *"Theory of the Coronal Plasma in Laser Fusion Targets"*, **1**, LLNL Report, UCRL-53107 (1981).

[50] Potter D., *"Computational Physics"*, Wiley (1973).

[51] Schultz W.D., *"Methods in Computational Physics"*, **3**, (Academic Press, New York), 1964.

[52] Evans R.G., Bell A.R. and MacGowan B.J., *J. Phys. D: Appl. Phys.* **15** 711 (1982).

[53] Neumann J. Von and Richtmyer R.D., *J. Comp. Phys.*, **21**, 232 (1950).

[54] Boris J.P. and Book D.L., *J. Comp. Phys.*, **20**, 397 (1976).

[55] Pert G.J., *J. Comp. Phys.*, **49**, 1 (1983).

[56] Boris J.P. and Book D.L., in *"Methods in Computational Physics"*, Ed. Alder B., **16**, 85, (Academic Press New York), (1976).

[57] Anderson D.V., *J. Comp. Phys.*, **17**, 246 (1975).

[58] Craxton R.S. and McCrory R.L., *J. Comp. Phys.*, **33**, 432 (1979).

[59] Jacobs H., *"Influence of Gradual Density Transition and Non-Linear Saturation on Rayleigh-Taylor Instability Growth"*, Institut fur Neutronenphysik und Reaktortechnik, (1984).

[60] Kull H.J., *Phys Rev. Lett.*, **51**, 1434 (1983).

[61] Fermi E., Appendix F, Los Alamos Report LA-1927, (by Birkhoff G.) (1951).

[62] Emmons H.W., Chang C.T. and Watson B.C., *J. Fluid Mech.*, **7**, 177 (1960).

[63] Birkhoff G. and Carter D., *J. Math. Mech.*, **6**, 769 (1957).

[64] Garabedian P.R., *Proc. Roy. Soc.*, **A241**, 423 (1957).

[65] Baker G.R., Meiron D.I. and Orszag S.A., *Phys. Fluids*, **23**, 1485 (1980).

[66] Layzer D., *Astrophys J.*, **122**, 1 (1955).

[67] Henshaw M.J.De.C and Pert G.J., *Plasma Phys. Cont. Fus.*, **29**, 405 (1987).

[68] Youngs D.L., *Physica*, **12D**, 32 (1984).

[69] Read K.I., *Physica*, **12D**, 45 (1984).

[70] Pert G.J., *J. Comp. Phys.*, **43**, 111 (1981).

[71] Dawson J.M. and Oberman C.R., *Phys. Fluids*, **5**, 517 (1962).

[72] Pert G.J., in *"Laser-Plasm Interactions"*, ed. Cairns and Sanderson SUSSP (1979).

[73] Estabrook K.G., Valeo E.J. and Kruer W.L., *Phys. Fluids*, **18**, 1151 (1975).

[74] Manes K.R., Rupert V.C., Auerbach J.M., Lee P. and Swain J.E., *Phys. Rev. Letts.*, **39** 281 (1977).

[75] Spitzer L., *"Physics of Fully Ionised Gases"*, Interscience, NY, 2nd ed. (1962).

[76] Malone R.C., McCrory R.L. and Morse R.L., *Phys. Rev. Letts.*, **34**, 721 (1975).

[77] Bell A.R., Evans R.G. and Nicholas D.J., *Phys. Rev. Letts.*, **46**, 243, (1981).

[78] Evans R.G., *Laser and Particle Beams*, **3(3)**, 273, (1985).

[79] Nishiguchi A., Yabe T. and Haines M.G., *Phys. Fluids*, **28**, 3683 (1985).

[80] Colombant D.G. and Winsor N.K., *Phys. Rev. Letts.*, **38**, 697 (1977).

[81] Braginskii S.I., in *"Reviews of Plasma Physics"*, vol. 2, ed. Leontovich, M.A., Consultants Bureau, NY, (1965).

[82] Bennett A.J., PhD Thesis, University of Hull (1982).

[83] Kruer W.L., in *"Laser-Plasm Interactions"*, ed. Cairns and Sanderson SUSSP (1979).